

Investigation of blueschist and serpentized  
harzburgite from the Mariana forearc: Insights into the  
mechanisms of element mobilization in subduction  
zones and storage of fluid-mobile elements  
in the mantle wedge

**INAUGURAL – DISSERTATION**

zur Erlangung der Doktorwürde  
der Naturwissenschaftlich-Mathematischen Gesamtfakultät  
der Ruprecht-Karls-Universität  
Heidelberg

vorgelegt von  
Diplom-Geowissenschaftlerin  
**Sonja Pabst**  
aus Nordenham

Heidelberg, im Oktober 2009

Gutachter:  
PD Dr. Thomas Zack (Universität Mainz)  
Prof. Dr. Alan Woodland (Universität Frankfurt)

Tag der mündlichen Prüfung: 11.12.2009



# Contents

<b>Abstract</b>	<b>v</b>
<b>Zusammenfassung</b>	<b>vii</b>
<b>Chapter 1</b>	<b>1</b>
<b>Introduction</b>	
1.1 Aims and scope of the thesis	1
1.2 Thesis outline	2
1.3 Li, Be and B geochemistry	3
1.4 Boron isotope fractionation	4
1.5 Light elements in the Earth	6
1.5.1 Light elements in the subduction cycle	6
1.6 Geological setting	10
1.6.1 The geography of the Izu-Bonin-Mariana (IBM) subduction zone	10
1.6.2 History of the IBM arc system	12
1.6.3 Current subduction in the Mariana Arc	13
1.6.4 Serpentine mud volcanism and sample location	16
<b>Chapter 2</b>	<b>19</b>
<b>Analytical Techniques</b>	
2.1 Sample documentation	19
2.2 Electron probe micro analysis (EPMA)	21
2.3 Secondary ion mass spectrometry (SIMS)	22
2.4 Determination of boron isotope ratios by SIMS	23
2.5 Matrix correction for $\delta^{11}\text{B}$ analysis by SIMS	23
2.6 Time-of-flight Secondary Ion Mass Spectrometry (ToF-SIMS)	25
2.7 Micro-Raman spectroscopy	25
<b>Chapter 3</b>	<b>29</b>
<b>Evidence for boron incorporation into the serpentine crystal structure</b>	
3.1 Introduction	29
3.2 Analytical Techniques	29
3.3 Petrography and mineral compositions	30
3.4 Intragrain boron distribution in serpentine	32
3.5 Discussion and Conclusion	34
<b>Chapter 4</b>	<b>37</b>
<b>Serpentinization of the Mariana forearc mantle wedge: light elements as tracers for the hydration history</b>	
4.1 Introduction	37
4.2 Petrography of serpentinites and serpentine textures	37

4.2.1	Identification and discrimination of serpentine polymorphs and brucite	44
4.2.2	Serpentine polymorphs and brucite correlated with their textural position	45
4.3	Major element contents of serpentinite forming minerals	52
4.3.1	Olivine	52
4.3.2	Pyroxenes	53
4.3.3	Spinel	54
4.3.4	Brucite / Amakinite	55
4.3.5	Serpentine	56
4.3.6	Ca-(OH)-rich 'phase' in serpentinites	59
4.3.7	'Black serpentine'	60
4.4	Light element (Li, Be, B) contents of rock-forming minerals	61
4.4.1	Light element mappings by ToF-SIMS	61
4.4.2	Light element SIMS analyses	64
4.5	Boron isotope composition ( $\delta^{11}\text{B}$ ) of serpentine by in-situ SIMS	67
4.6	Interpretation of serpentine textures and mineral chemistry	68
4.6.1	Estimates of the degree of partial melting	69
4.6.2	Melt impregnation (refertilization / 'metasomatism')	70
4.6.3.1	Fe-distribution between serpentine-brucite-magnetite: evidence for serpentinization conditions	70
4.6.3.2	Serpentine polymorph distribution: evidence for variable fluid-rock ratios	73
4.6.4	Correlation between serpentine textures and their light element composition	74
4.6.5	Boron isotope evolution (serpentinizing fluid pulses)	76
<b>Chapter 5</b>		<b>79</b>
<b>Metamafic blueschist-facies rocks from the Mariana forearc: reactions at the slab-mantle interface</b>		
5.1	Introduction	79
5.2	Mineral Chemistry (major elements)	80
5.2.1	Amphibole	80
5.2.2	Phengite	81
5.2.3	Chlorite	82
5.2.4	Talc	83
5.2.5	Epidote and Allanite	83
5.2.6	Pyroxene	84
5.2.7	Garnet	85
5.2.8	Ti-phases (titanite, rutile, ilmenite, titano-magnetite)	86
5.2.9	Other phases (pumpellyite, apatite, quartz, plagioclase, zircon)	86
5.3	Petrography	86
5.3.1	Amphibole-Talc-Chlorite-Schists	88
5.3.1a)	metasomatic rind of ultra-mafite, i.e., serpentinized peridotite	89
5.3.1b)	metasomatic rind of mafic slab	92
5.3.2	Chlorite-Epidote-Rocks	95
5.3.2a)	blueschist-facies meta-basalt / endmember	95

5.3.3 Am-Chl-Phe-schists	99
5.3.3a) meta-sediment	99
5.3.3b) rind of meta-sediment	101
5.3.4 Rocks of magmatic origin	101
5.3.5 Andradite-bearing serpentinites (Grt + Srp) and Bt-Chl-rocks	103
5.4 Light element (Li,Be,B) contents and boron isotopic composition ( $\delta^{11}\text{B}$ ) of (rock forming) minerals	104
5.4.1 ToF-SIMS element maps	104
5.4.2 SIMS analyses: budgets of Li, Be and B	110
5.4.3 SIMS analyses: $\delta^{11}\text{B}$	111
5.5 Geothermobarometry	112
5.6 Calculated modal compositions: bulk rock and potential source material	115
5.7 Slab-mantle-interaction: evidence for an active subduction zone mélange formed by tectonic and metasomatic mixing	119
5.8 Light element behavior during dehydration and mélange metasomatism	124
5.9 Boron fractionation ( $\delta^{11}\text{B}$ ) during slab dehydration and slab-mantle-interaction (fractionation along the slab-mantle interface)	126
<b>Chapter 6</b>	<b>129</b>
<b>Synthesis: Fluid-rock interaction and light element recycling in the Mariana forearc</b>	
6.1 Subduction input - metamafic high-pressure rocks	130
6.2 Serpentinites of the forearc mantle wedge	132
6.3 Boron isotope evolution along the slab-mantle interface in the Mariana forearc	136
<b>References</b>	<b>139</b>
<b>Appendix A</b>	<b>159</b>
A1: Documentation of reference minerals for $\delta^{11}\text{B}$ SIMS analyses and matrix correction	160
A2: Composition of reference minerals	162
A3: List of mineral abbreviations	165
<b>Appendix B: Serpentinites</b>	<b>167</b>
B1: Sample BSE-images with EPMA, SIMS and Raman spots	168
B2: Electron probe micro analyses	169
B2.1: Serpentine and brucite minerals	169
B2.2: Spinel	170
B2.3: Olivine	170
B2.4: Clinopyroxene and orthopyroxene	171
B3: SIMS data	173
B4: Light element variation diagrams for different serpentinite samples	182
B5: Micro-Raman spectra of serpentine and brucite	185

<b>Appendix C: Metamafic rocks</b>	<b>195</b>
C1: Sample BSE-images with EPMA, SIMS and Raman spots	196
C2: Electron probe micro analyses	197
C2.1: Amphibole	197
C2.2: Chlorite	201
C2.3: Talc	202
C2.4: Pumpellyite, epidote and allanite	203
C2.5: Phengite and Biotite	205
C2.6: Garnet	206
C2.7: Pyroxene	207
C2.8: Spinel phases, titanite, rutile	208
C2.9: Apatite and zircon	209
C2.10: Serpentine (antigorite)	211
C3: SIMS data	212
C4: Micro-Raman spectra of andradite	218
<b>Appendix D: Supplementary Results</b>	<b>219</b>
D1: Sr - light element variation in blueschist minerals	220
D2: Sr - light element variation in serpentinites	220
D3: U concentration in rutile – a possibility for dating	221
D3.1 Analytic	222
<b>Danksagung</b>	
<b>Eidstattliche Erklärung</b>	
<b><i>Electronic Appendix (CD)</i></b>	

## Abstract

Numerous serpentinite seamounts on the forearc of the Izu-Bonin-Mariana (IBM) subduction zone present the only known locations worldwide where mantle wedge serpentinites and blueschist-facies metamafic fragments can be directly sampled. These fragments have been transported diapirically in a low temperature fluid-mud matrix from within this active subduction zone from a depth of >20 km below seafloor, i.e., directly from the slab-mantle-interface. At South Chamorro Seamount (ODP Leg 195), ~85 km distal from the trench axis, the slab surface is at ~27 km depth, where estimated temperatures are <350 °C, typical for blueschist-facies, sub-forearc subduction zone environments.

This is the first study which combines high-resolution results on light element (Li, Be, B) and  $\delta^{11}\text{B}$  distribution of both slab-derived metamafic rocks and serpentinitized mantle rocks from an active subduction zone. Mobile in aqueous fluids and sensitive as tracers of fluid source and mobilization, Li, Be and B in (Na-)amphibole, phengite, chlorite and serpentine provide (i) information to quantify devolatilization of the subducting mafic oceanic crust in shallow regions and (ii) information about fluid infiltration into the forearc mantle peridotite due to fluid transfer from the dehydrating slab into the overlying mantle wedge.

Analyses of Li, Be and B contents and B isotope ratios were performed using secondary ion mass spectrometry (SIMS). Light element distribution maps were made using Time-of-Flight SIMS. Micro-Raman was used to identify serpentine polymorphs and brucite in serpentinites.

The fine-grained metamafic fragments (<5 mm in diameter) comprise a large variety of mineral assemblages. These assemblages indicate a range of protoliths that have been subjected to mechanical mixing and metasomatism within a *mélange* zone at surprisingly shallow depths. Minerals such as chlorite, Na- and Ca-amphibole, phengite, epidote and Na-pyroxene in paragenesis with pumpellyite correlate with blueschist-facies conditions at ~27 km depth (at ~300 °C). The main Li, Be and B carriers are phengite > chlorite + amphibole. Estimated concentrations of light elements in bulk rocks are in the same range as in altered oceanic crust and subducting sediments, demonstrating that the major amount remains in the subducting slab and is not released with fluids. However, moderate B loss is suggested by the light  $\delta^{11}\text{B}$  values of phengite, chlorite and amphibole ( $-6 \pm 4 \text{‰}$ ). As B fractionation is most effective at low temperatures, this light B isotope signature can be explained by low fluid losses from the shallow slab, which originally had a slightly positive average  $\delta^{11}\text{B}$  value. Due to B isotope fractionation, the released (Li- and B-enriched) slab-fluids that correlate with a slab-residue with  $-6 \pm 4 \text{‰}$ , are positive reaching a  $\delta^{11}\text{B}$  value of up to  $\sim +20 \text{‰}$ .

In variably serpentinitized peridotites, the serpentine polymorphs lizardite, chrysotile and polygonal serpentine together with minor brucite are preferentially distributed between textures or serpentine generations. Li, Be and B abundances are variable and serpentine minerals show an enrichment for Li and B but also a depletion for Li compared to depleted mantle values. Be contents in serpentine are low and similar to primary minerals olivine, orthopyroxene and clinopyroxene. These results demonstrate that serpentinitization contributes to a general light element enrichment in the mantle wedge.

Early serpentine textures have high Li abundances (up to 30  $\mu\text{g/g}$ ) compared to the later serpentine, B abundances are variable. The dominant polymorph is lizardite, which indicates relatively low fluid-rock ratios. Late (youngest) serpentine generations are dominated by chrysotile, which indicates high fluid-rock ratios during serpentinization. This serpentine has lower Li abundances and is relatively enriched in B. The varying fluid-rock ratios between serpentine generations are suggested to be the key to explaining the large range in  $\delta^{11}\text{B}$  values of  $-14\text{‰}$  to  $+24\text{‰}$  found in serpentine. During early peridotite hydration, all fluid is completely consumed in small-scale serpentine areas and the averaging ( $\sim 25$  mm spot size) SIMS analyses reveal the positive B isotope signature of the slab-derived fluids. The negative  $\delta^{11}\text{B}$  values in serpentine can be well explained by strong B fractionation between fluid and serpentine at the low temperature and neutral to basic pH.



## Kurzfassung

Die zahlreichen Serpentin-Vulkane auf dem Forearc der Izu-Bonin-Mariana (IBM) Subduktionszone sind die weltweit einzigen bekannten Fundorte, wo Serpentine des Mantelkeils und Blauschiefer-fazielle metamafische Fragmente direkt beprobt werden können. Diese Fragmente wurden diapiirisch in einer Fluid-Schlamm-Matrix niedriger Temperatur innerhalb dieser aktiven Subduktionszone aus einer Tiefe von >20 km unter dem Meeresboden, also direkt von der Platten-Mantel-Grenze, befördert. Am South Chamorro Seamount (ODP Leg 195), ~85 km entfernt vom Graben, liegt die Oberfläche der subduzierenden Platte bei ~27 km Tiefe, wo Temperaturen <350 °C herrschen, typisch für eine Blauschiefer-fazielle Sub-Forearc-Subduktionszonen-Umgebung.

Dies ist die erste Studie, die hochauflösende Ergebnisse über die Verteilung leichter Elemente (Li, Be, B) und  $\delta^{11}\text{B}$  in Gesteinen der metamafischen Platte und des serpentinierten Mantels einer aktiven Subduktionszone vereint. Mobil in wässrigen Phasen und empfindlich als Tracer für Fluid-Quellen und –mobilisierung, liefern Li, Be und B in (Na-)Amphibol, Phengit, Chlorit und Serpentin a) Informationen, um die Entwässerung der subduzierenden mafischen ozeanischen Kruste in oberflächennahen Regionen zu quantifizieren und b) Informationen über Fluid Infiltration in den Forearc-Mantel-Peridotiten auf Grund von Fluid-Transfer von der entwässernden Platte in den darüber liegenden Mantelkeil.

Li-, Be- und B-Konzentrationen und B-Isotopenverhältnisse wurden mit dem Sekundär-Ionen-Massen-Spektrometer (SIMS) gemessen. Aufnahmen der Verteilung der leichten Elemente wurden mit dem Time-of-Flight SIMS (Flugzeitmassenspektrometer) erstellt. Mit dem Mikro-Raman wurden Serpentin Polymorphe und Brucit in den Serpentiniten bestimmt.

Die feinkörnigen metamafischen Fragmente (<5mm) bestehen aus einer Vielzahl von Mineralparagenesen. Diese Paragenesen deuten auf eine Reihe von Ausgangsgesteinen hin, die mechanischer Vermengung und Metasomatose innerhalb einer Mélange-Zone in erstaunlich niedriger Tiefe ausgesetzt waren. Minerale wie Chlorit, Na- und Ca-Amphibol, Phengit, Epidot und Na-Pyroxen in Paragenese mit Pumpellyit entsprechen Blauschiefer-faziellen Bedingungen in ~27 km Tiefe (bei ~300 °C). Die hauptsächlichen Li-, Be- und B-Träger sind Phengit > Chlorit + Amphibol. Abgeschätzte Gesamtgesteins-Konzentrationen leichter Elemente liegen im Bereich alterierter ozeanischer Kruste und subduzierender Sedimente; dies zeigt, dass der größte Teil der leichten Elemente in der subduzierenden Platte verbleibt und nicht mit Fluiden abgegeben wird. Jedoch deuten die leichten  $\delta^{11}\text{B}$  Werte von Phengit, Chlorite und Amphibol ( $-6 \pm 4 \text{‰}$ ) auf einen mäßigen B-Verlust hin. Da B-Isotopen-Fraktionierung bei niedrigen Temperaturen am stärksten ist, kann dieser negative  $\delta^{11}\text{B}$  Wert durch Fluid-Verlust von der Platte in niedriger Tiefe erklärt werden, welche einen im Mittel leicht positiven  $\delta^{11}\text{B}$  Ausgangswert hatte. Aufgrund von B-Isotopen-Fraktionierung haben die von der subduzierenden Platte freigesetzten (Li- und B-reichen) Fluide, die mit einem Residuum mit  $-6 \pm 4 \text{‰}$   $\delta^{11}\text{B}$  korrelieren, eine positive Isotopie von bis zu  $\sim +20 \text{‰}$ .

In den unterschiedlich stark serpentinierten Peridotiten sind die Serpentin Polymorphe Lizardit, Chrysotil und polygonaler Serpentin zusammen mit wenig Brucit unterschiedlich zwischen Texturen

und Serpentin-Generationen verteilt. Li-, Be- und B-Häufigkeiten sind variabel und Serpentin Minerale zeigen sowohl An- als auch Abreicherung an Li und Anreicherung in B im Vergleich zum verarmten Mantel. Be Konzentrationen sind niedrig und ähnlich wie in Primärmineralen Olivin, Orthopyroxen und Klinopyroxen. Diese Ergebnisse zeigen, dass Serpentinisierung zu einer allgemeinen Anreicherung leichter Elemente im Mantelkeil führt.

Frühe Serpentin Texturen haben hohe Li Konzentrationen (bis zu 30  $\mu\text{g/g}$ ) im Vergleich zu spät gebildetem Serpentin, die B Gehalte sind variabel. Das dominierende Polymorph ist Lizardit, was auf ein relativ niedriges Fluid-Gesteins-Verhältnis hinweist. Späte (also junge) Serpentin-Generationen sind von Chrysotil dominiert, was auf ein hohes Fluid-Gesteins-Verhältnis während der Serpentinisierung hinweist. Dieser Serpentin hat niedrige Li-Konzentrationen und ist relativ mit B angereichert. Die wechselnden Fluid-Gesteins-Verhältnisse zwischen Serpentin-Generationen sind die naheliegendste Erklärung für die große Spannweite der  $\delta^{11}\text{B}$  Werte von  $-14\text{‰}$  bis  $+24\text{‰}$  in Serpentin. Während früher Hydratisierung des Peridotits wird das Fluid komplett in kleinräumigen Serpentin-Bereichen aufgezehrt; somit weisen die SIMS Analysen, bei einer Messpunktgröße von  $\sim 25\text{ nm}$ , eine im Mittel positive B-Isotopie des von der subduzierenden Platte kommenden Fluids hin. Die negativen  $\delta^{11}\text{B}$  Werte im Serpentin können durch starke B-Isotopen-Fraktionierung zwischen Fluid und Serpentin bei niedriger Temperatur und neutralem bis basischem pH-Wert erklärt werden.

# Chapter 1

## Introduction

### 1.1 Aims and scope of the thesis

Subduction zones are the most dynamic and complex global structures in the Earth's interior. At these convergent plate margins, several input 'materials' (inputs) and output 'materials' (outputs) characterize geochemical cycling. Serpentinites of subducting variously altered oceanic crust and overlying sediments are important repositories of light elements. Recently, their inventory is more and more being constrained (Bonatti *et al.*, 1984; Ryan & Langmuir, 1987; Ishikawa & Nakamura, 1993; Decitre *et al.*, 2002; Vils *et al.*, 2008, 2009). Studies on arc-volcanoes revealed that light element concentrations and isotopic ratios change with increasing depth of the slab and/or distance from the subduction zone and that light element contents are enriched compared to unmetasomatized mantle (*e.g.*, Tatsumi, 1989; Ishikawa & Nakamura, 1994; Ryan *et al.*, 1995; Leeman, 1996; Rose *et al.*, 2001; Chan *et al.*, 1999, 2002b; Ryan, 2002; Tomascak *et al.*, 2002). Recent light element studies on enriched mantle wedge serpentinites, serpentinite muds, slab-derived pore waters, and metamafic rocks (Maekawa *et al.*, 1992, 1993; Maekawa, 1995; Fryer *et al.*, 1999; Benton *et al.*, 2001, 2004; Mottl *et al.*, 2003, 2004; Savov *et al.*, 2005b, 2007) stress the importance to understand the processes which control the light element mobilization, distribution and recycling within the 'Subduction Factory'.

To provide one of the first comprehensive working models for active subduction and backarc spreading, the NSF-MARGINS 'Subduction Factory Initiative' formed. The 'Subduction Factory' has received substantial attention from both the US and Japanese geoscience communities over the last decade. One focused investigation is the 'Ocean Drilling Program' research in the Izu-Bonin-Mariana (IBM) subduction system; large geophysical characterization (swath bathymetry, gravity and magnetics, deep magnetotellurics, computer modeling, and broadband and multichannel passive and active seismics) and geochemical studies (magmatic volatiles, volcanic gas sampling, cross-chain dredge sampling, forearc drilling) are integrated to model processes in active subduction zones.

To contribute to this initiative is the aim of the present PhD thesis. During this project, the abundance of light elements (Li, Be, B), their small-scale distribution and the B isotope systematics in rock-forming minerals of serpentinized mantle wedge peridotites and blueschist-facies metamafic slab rocks were studied. These samples are from the collection of I.P. Savov, who already studied serpentinites and metamafic bulk rocks for their light element inventory (Savov *et al.*, 2005a,b, 2007). To gain insight into the mobilization of fluids and associated light elements during prograde metamorphism with a related fluid transfer from the dehydrating slab into the overlying mantle wedge in the shallow region of subduction zones (~27 km), samples from Mariana serpentinite mud volcanoes have been studied: blueschist-facies mafic rock fragments and serpentinized harzburgites from South Chamorro Seamount (ODP Leg 195, Site 1200) and Conical Seamount (ODP Leg 125, Site 779).

This detailed study of various slab- and mantle-derived lithologies by petrologic, geochemical and B isotope geochemical means is the first systematic high quality dataset on the light element inventory of serpentized harzburgite and blueschist-facies mafic rocks from an active subduction zone. These data will influence the understanding of mass fluxes and geochemical interchanges at the slab-mantle-interface, *i.e.*, the décollement (*e.g.*, Kastner & Elderfield, 1993; Carson & Westbrook, 1995; Maltman *et al.*, 1997), as the non-accretionary Mariana margin is a unique locality, where the natural processes of serpentinite mud volcanism bring serpentized mantle wedge peridotites and blueschist-facies metamafics from great depths (~27 km) directly from the slab-mantle-interface to the surface (Fryer *et al.*, 2000; Mottl *et al.*, 2004). The results can be compared to ancient subduction zones in regions where erosion has exposed mélange zones, such as the Franciscan formation in California (*e.g.*, Essene & Fyfe, 1967; Coleman & Clark, 1968; Bebout, 1995). Furthermore, the detailed *in-situ* study on the serpentinite light element inventory in combination with serpentine textures, generations and serpentine polymorphs potentially contributes to the understanding of small- to large-scale Li and B redistribution during serpentization of the mantle wedge. The combination of the results obtained from H<sub>2</sub>O-rich slab- and mantle-rocks clearly influences existing models of the light element behavior and B isotope evolution in the ‘Subduction Factory’.

### 1.2 Thesis outline

This thesis is subdivided into six chapters, starting with this introduction including aims and scope of the thesis, a review on the geochemical behavior of the light elements Li, Be and B and of the B isotope systematics with the emphasis on processes related to the subduction cycle, and a geological overview of the IBM subduction zone. **Chapter 2** is a detailed description of all analytical methods applied for this study. **Chapter 3** presents a manuscript about the B incorporation into serpentine providing a basis for the light element analysis of serpentinites in Chapter 4. As the thesis is based on the investigation of serpentinites on one hand and high-pressure metamorphic rocks on the other hand, the results and discussions are separated into two chapters. **Chapter 4** provides a detailed petrological description of the mantle wedge serpentinites including textures, major element compositions and polymorphs identification. The main study concentrates on the light element inventory of serpentine and the discussion on the mobility of light elements during hydration. **Chapter 5** provides a detailed petrological description of the slab-derived high-pressure rocks including mineral paragenesis, major elements and estimated bulk rock composition. The main study concentrates on the light element and boron isotope signature of the mineral phases with the aim to give an overview of the light element behavior during progressive metamorphism and fluid release during subduction. **Chapter 6** is a synthesis of all results. A summary of the Li and B distribution and behavior in combination with B isotope signatures is given. The **Appendix** includes data tables, complementary images such as back-scattered electron images with spots of EPMA, micro-Raman and SIMS. Furthermore, the appendix provides results of the study which are not necessary for the previous discussion but yield important information and the basis for continuing research.

### 1.3 Li, Be and B geochemistry

In the last decade light elements, their behavior and cycle through the Earth have become an important topic for geochemists. Lithium (Li), beryllium (Be), and boron (B) are powerful tracers of the geochemical processes occurring at the interface between the different Earth's reservoirs. Li and B are highly fluid-mobile elements. Each has two isotopes with a large relative mass difference and with a large isotopic fractionation in nature. Be is rather fluid-immobile and mostly of low abundance. The incompatibility during magmatic processes and extreme mobility in hydrous fluids of the light elements under a wide range of temperatures give information on the transfer of chemical components during fluid or melt metasomatism and also during hydrothermal alteration. Light elements and their isotopes can hence be used to monitor many geological processes.

*Lithium* is a monovalent ( $\text{Li}^+$ ) alkali metal with the atomic number 3 and an atomic mass of 6.941 u. It has two stable isotopes,  $^6\text{Li}$  and  $^7\text{Li}$ , with a natural abundance of 7.59 % and 92.41 %, respectively. Due to the mass difference between the two isotopes, isotopic fractionation in nature is relatively large (up to 60 ‰). The atomic radius of  $\text{Li}^+$  in 6-fold coordination is 0.76 Å and thus can substitute for octahedrally coordinated  $\text{Mg}^{2+}$  (0.72 Å) and  $\text{Fe}^{2+}$  (0.76 Å) in silicates. In minerals like feldspar and amphibole,  $\text{Li}^+$  can substitute for  $\text{Na}^+$  and  $\text{K}^+$  on larger coordination sites (7, 8, 12). Major Li-bearing minerals are lipidolite (mica), spodumen (Li-pyroxene), and lithium carbonates. In hydrous fluids, lithium is tetrahedrally coordinated to four  $\text{H}_2\text{O}$  molecules (Olsher *et al.*, 1991).

*Beryllium* is a divalent ( $\text{Be}^{2+}$ ) alkaline metal with the atomic number 4 and an atomic mass of 9.012 u. The atomic radius of  $\text{Be}^{2+}$  is 0.26 Å, similar to that of  $\text{Si}^{4+}$  (0.27 Å). Due to the high charge difference, direct substitution of  $\text{Be}^{2+}$  and  $\text{Si}^{4+}$  is rare. In nature, Be is tetrahedrally coordinated to oxygen in minerals (Hawthorne & Huminicki, 2002) and generally substitutes for  $\text{Al}^{3+}$  (0.39 Å) or  $\text{B}^{3+}$  (0.11 Å) on the tetrahedral site. Be also can be incorporated into minerals in vacant tetrahedral sites (Hawthorne & Huminicki, 2002). Although twelve isotopes of beryllium exist, it has only one stable isotope  $^9\text{Be}$  and one cosmogenic isotope  $^{10}\text{Be}$ . Be (together with B) is relevant as an important tracer for subduction zones, as it partitions into slab-derived fluids that can be subsequently transported into the mantle wedge or the region of arc magma genesis (Tatsumi & Isoyama, 1988; Domanik *et al.*, 1993). The most abundant Be-containing mineral is beryl.

*Boron* is a trivalent ( $\text{B}^{3+}$ ) non-metallic element with the atomic number 5 and an atomic mass of 10.811 u. It has thirteen known isotopes of which the two stable ones  $^{10}\text{B}$  and  $^{11}\text{B}$  have natural abundances of 19.9 % and 80.1 %, respectively. The atomic radius of  $\text{B}^{3+}$  is 0.11 Å in tetrahedral coordination and 0.01 Å in trigonal coordination. In minerals, melts and fluids, B can be trigonally or tetrahedrally coordinated to oxygen (Hawthorne *et al.*, 1996). Substitution in silicates is limited to  $\text{Si}^{4+}$  and  $\text{Al}^{3+}$  on tetrahedral sites, which in case of  $\text{Si}^{4+}$  requires charge balancing and some distortion of the  $\text{TO}_4$  units due to the small ionic radius of  $\text{B}^{3+}$ . B is mostly bound to O, forming  $\text{B}(\text{OH})_3$  or  $\text{B}(\text{OH})_4$ . The coordination of B in fluids is highly pH-dependent; at low pH, B is trigonally (3-fold) coordinated to  $\text{H}_2\text{O}$ , while at high pH, B is tetrahedrally (4-fold) coordinated to  $\text{H}_2\text{O}$  (Schmidt *et al.*, 2005). After Palmer & Swihart (1996) significant concentrations of tetrahedrally coordinated boron complexes are present in fluids only at pH >8, at pH <6  $\text{B}(\text{OH})_4$  is absent in the fluid. Alteration

processes may enrich or deplete  $^{11}\text{B}$  in fluids compared to their residues. This geochemical behavior results in a wide range of natural fractionation ( $\sim 60\%$ ) of B isotopes. Boron-containing minerals are boron silicates (*e.g.*, tourmaline) and evaporite minerals (*e.g.*, probertite, rivadavite, borax).

## 1.4 Boron isotope fractionation

Isotopes of an element, which is characterized by the same number of electrons and protons, have different numbers of neutrons and thus different masses (*e.g.*,  $^{10}\text{B}$  and  $^{11}\text{B}$ ). Stable isotopes fractionate between different phases (minerals or fluids), *e.g.*, during incorporation of elements in minerals. Certain isotopes are preferred in different phases, which leads to fractionation in favor of one isotope. Equilibrium (not kinetic) stable isotope fractionation of an element is based on the different structural position in which it is incorporated in the various phases. If the coordination polyhedra of the element between the two phases is different, fractionation effects are notably large. In the case of B, coordination to oxygen is either trigonally or tetrahedrally in minerals, melts and fluids. Isotopic fractionation between different phases may therefore be large.  $^{11}\text{B}$  is preferentially incorporated into the trigonal sites compared to the tetrahedral site, due to the higher bond strength of the trigonal coordination (Chacko *et al.*, 2001), which leads to a relative enrichment of the light isotope  $^{10}\text{B}$  in the phase with tetrahedrally coordinated B (Palmer & Swihart, 1996). Therefore, equilibrium fractionation can be expressed by an exchange reaction of the isotopic composition of different phases (mineral-fluid or mineral-mineral in equilibrium). The fractionation factor between two isotopes is expressed as ‘alpha’ ( $\alpha$ ). For B isotopes the fractionation factor is

$$\alpha_{\text{A-B}} = \frac{\left(\frac{^{11}\text{B}}{^{10}\text{B}}\right)_{\text{A}}}{\left(\frac{^{11}\text{B}}{^{10}\text{B}}\right)_{\text{B}}} \quad (1.1)$$

The ratio of isotope abundance in a two-isotope system is commonly expressed in the delta notation (*e.g.*,  $\delta^{11}\text{B}$ ). It reflects the isotope ratio in a sample relative to the same ratio in a standard in permil ( $\%$ ) (equation 1.2).

$$\delta^{11}\text{B} = 1000 \left( \frac{\left(\frac{^{11}\text{B}}{^{10}\text{B}}\right)_{\text{sample}}}{\left(\frac{^{11}\text{B}}{^{10}\text{B}}\right)_{\text{standard}}} - 1 \right) \quad (1.2)$$

The formula is defined by the element of interest (here boron) and the mass numbers of the heavier and the lighter isotope ( $^{11}\text{B}/^{10}\text{B}$ ). For different isotope systems different standards are used. The common international isotope standard for B is boric acid NIST-SRM951 ( $\text{H}_3\text{BO}_3$ ) with an  $^{11}\text{B}/^{10}\text{B}$  isotope ratio of 4.043627 (Catanzaro *et al.*, 1970). The isotope fractionation between two phases A and B is expressed either by the fractionation factor  $\alpha_{\text{A-B}}$  or by the difference between  $\delta^{11}\text{B}$  values of the two phases (equation 1.3).

$$\Delta^{11}\text{B}_{\text{A-B}} = \delta^{11}\text{B}_{\text{A}} \pm \delta^{11}\text{B}_{\text{B}} \quad (1.3)$$

For natural samples and natural B isotope fractionation, the error introduced by the approximation

$$\Delta^{11}\text{B} \approx 1000 \ln \alpha \quad (1.4)$$

is negligible. Hence, both terms are often used equivalently.

Fractionation of isotopes is dependent on the water-rock interaction, but is also pH, temperature ( $T$ ) and pressure ( $P$ ) dependent. At low pH values, B is trigonally coordinated, at high pH the dominant B coordination is tetragonal (Spivack & Edmond, 1987; Boschi *et al.*, 2008). The possibility of B incorporation even changes with changes in polymorph coordination, *e.g.*, trigonally coordinated B is incorporated in calcite, tetrahedrally coordinated B in aragonite. In melts, B can be coordinated both trigonally and tetrahedrally.

The influence of  $T$  is much greater than that of  $P$  and the amount of fractionation decreases with increasing  $P$  and  $T$ . The temperature dependence of B isotopic fractionation between phases of different B coordination (*e.g.*, mica, amphibole, melt, fluid, tourmaline) has been experimentally studied in several studies (Fig. 1.1; *e.g.*, Peacock & Hervig, 1999; Williams *et al.*, 2001; Hervig *et al.*, 2002; Wunder *et al.*, 2005).

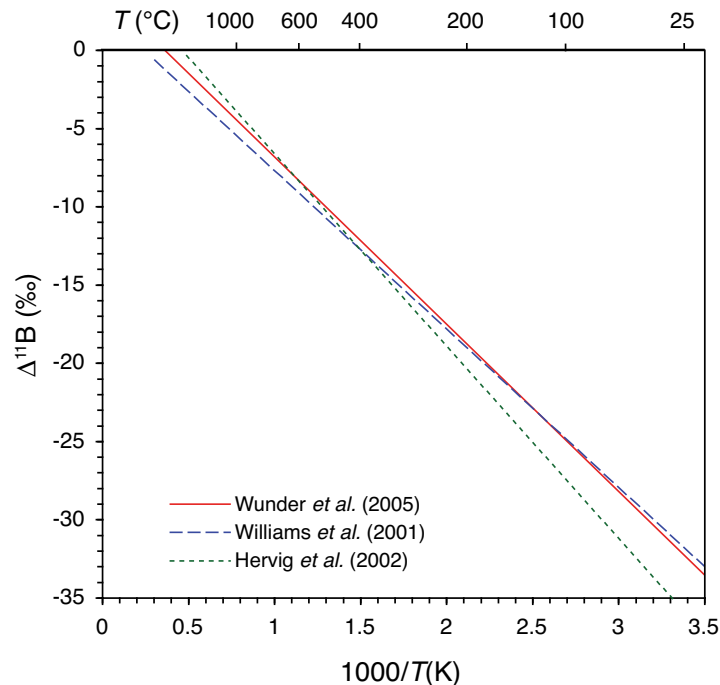


**Fig. 1.1:** Comparison of the temperature-dependence of the  $\Delta^{11}\text{B}_{\text{mineral}[4]-\text{fluid}[3]}$  equilibrium fractionation determined experimentally by Williams *et al.* (2001), Hervig *et al.* (2002) and Wunder *et al.* (2005).

The amount of fractionation decreases systematically between silicates and hydrous fluids with increasing temperature; calculated boron fractionation factors are:

$$\Delta^{11}\text{B} = -10.12 (1000/T[\text{K}]) + 2.44 \quad (\text{Williams } et al., 2001) \quad (1.5a)$$

$$\Delta^{11}\text{B} = -10.29 (1000/T[\text{K}]) + 5.68 \quad (\text{Hervig } et al., 2002) \quad (1.5b)$$

$$\Delta^{11}\text{B}_{(\text{solid}^{[4]} - \text{fluid}^{[3]})} = -10.69 (1000/T[\text{K}]) + 3.88 \quad (\text{Wunder } et al., 2005) \quad (1.5c)$$

In the most relevant temperature range in subduction zone metamorphic processes (300 to 700 °C), these models predict – within  $\pm 1\%$  – the same fractionation. Strongly basic conditions or the fluid-tourmaline system have a fractionation factor smaller by a factor of  $\sim 0.5\%$  (Palmer *et al.*, 1992; Wunder *et al.*, 2005).

## 1.5 Light elements in the Earth

### 1.5.1 Light elements in the subduction cycle

Subduction zones, also known as ‘Subduction Factory’, are undoubtedly the most dynamic and complex global structures in the Earth’s interior. Geologic processes at these convergent plate margins control geochemical cycling, seismicity, and deep biosphere activity within subduction zones. At a convergent plate boundary, variously altered oceanic crust, often together with overlaying sediments, is subducted into the Earth's mantle. As the slab descends, pressure and temperature increase continuously and H<sub>2</sub>O-rich fluids are released progressively from the slab; H<sub>2</sub>O-rich fluid is squeezed out of pores, removed from mineral surfaces and crystal-bound H<sub>2</sub>O is released by dehydration reactions. This dehydration of the subducting slab continues to depths of more than 100 km. The expelled fluids migrate upwards, hydrate and metasomatize (*i.e.*, serpentinize) the overlying mantle wedge, and escape in forms of hot springs and serpentine-mud volcanoes (seamounts) within the forearc system. Furthermore, subducted material is recycled and carried back to the surface by arc magmatism, which is the result of fluid-triggered melting of the hot section of the mantle wedge above the subducting plate and buoyant rise of magma. A fraction of elements and fluids is not released from the subducting slab and will be transported down to great depths. On a global scale, deeply recycled parts of ancient subducted plates form chemical heterogeneities within the Earth’s mantle, which are sampled by ocean island volcanoes.

The H<sub>2</sub>O-rich fluids are capable of transporting a wide range of elements, which causes large-scale redistribution of material between the different subduction zone entities. The chemical and isotopic signatures of subduction related island arc volcanics (*e.g.*, the enrichment of fluid-mobile elements Cs, Ba, K, Sr, U, Pb with respect to MORB) are interpreted as a result of metasomatism of the magma source by slab-derived fluids or melts underneath the volcanic front (*e.g.*, McCulloch & Gamble, 1991; Tatsumi & Eggins, 1995; Elliott *et al.*, 1997; Plank & Langmuir, 1998; Elliott, 2003). Geophysical observations provide evidence that the subduction related mantle wedge can be highly serpentinized (Bostock *et al.*, 2002; Kamimura *et al.*, 2002; Okino *et al.*, 2004). New subduction models incorporate a trace element laden serpentinized mantle dragged down by viscous coupling



(e.g., Hattori & Guillot, 2003) into the source region of island arc volcanics. This complexity increases the number of variables but can explain signatures of the subduction zone component such as non-mantle  $\delta^7\text{Li}$  and  $\delta^{11}\text{B}$  values of serpentinites (Benton *et al.*, 2001, 2004), high  $\delta^{18}\text{O}$  values in some island arc rocks (Dorendorf *et al.*, 2000) and the enrichment of fluid-mobile trace elements (B, Cs, Li, As and Sb) in forearc serpentinites thought to be lost during early dehydration (Hattori & Guillot, 2003; Savov *et al.*, 2007).

Experimentally determined mineral/fluid partition coefficients increase in the order  $D_{\text{B}} < D_{\text{Li}} \ll D_{\text{Be}}$  (clinopyroxene; Brenan *et al.*, 1998a), while mineral/melt partition coefficients increase in the order  $D_{\text{B}} \leq D_{\text{Be}} \ll D_{\text{Li}}$  (olivine, orthopyroxene, clinopyroxene; Ryan & Langmuir, 1988; Brenan *et al.*, 1998b; Blundy & Dalton, 2000). Abundances and isotopic systematics of light elements Li, Be, and B in subduction-related rocks can give important constraints on the mechanisms of slab-to-mantle transfer and slab-mantle-interaction.

Figure 1.2 shows a schematic cross-section through a Mariana-type subduction zone with indicated light element concentrations of the major subduction cycle compounds. Preferentially, data from the Mariana subduction zone are given.

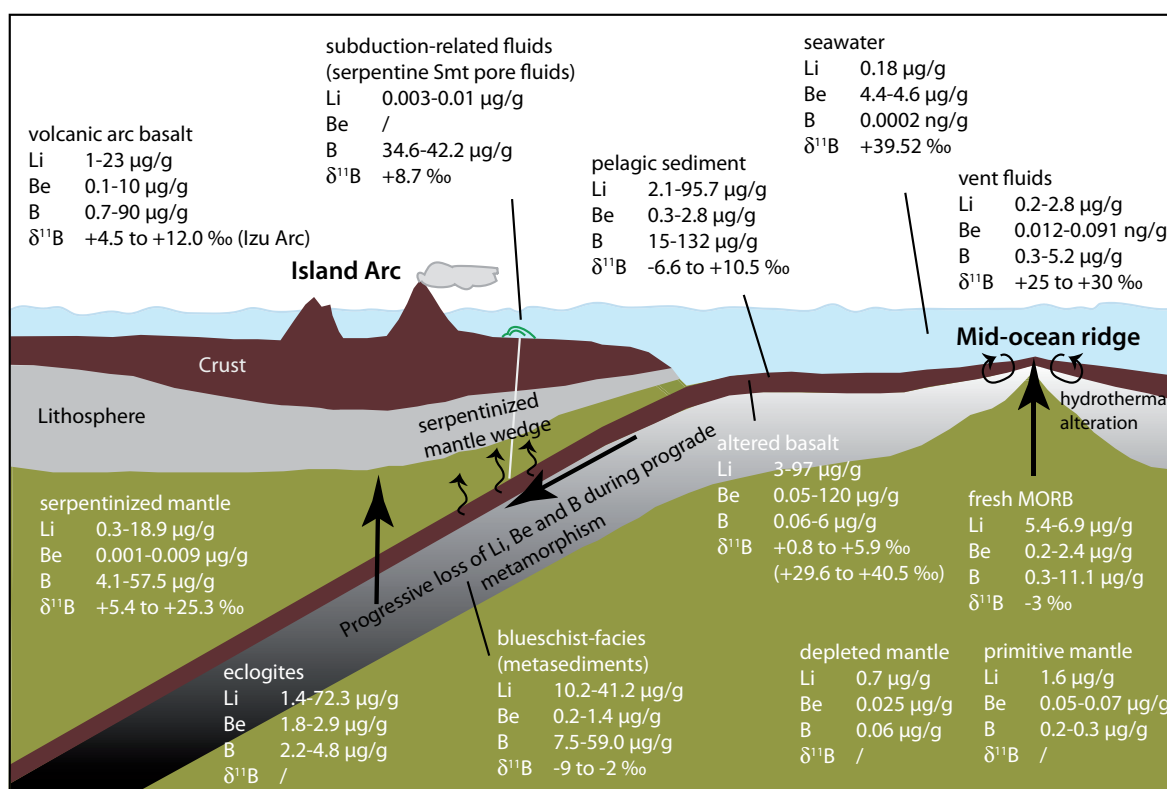


**Fig. 1.2:** Schematic vertical cross-section through a non-accretionary Mariana-type subduction zone, displaying the geochemical cycle of Li, Be and B on Earth. Modified after Vils (2009) and Pelletier (2008). See text for references.

The light element contents of the *primitive mantle* were estimated on the basis of element partition coefficients and are extremely low: 1.6  $\mu\text{g/g}$  Li, 0.05–0.07  $\mu\text{g/g}$  Be, and 0.2–0.3  $\mu\text{g/g}$  B (Ryan & Langmuir, 1993; McDonough & Sun, 1995; Ottolini *et al.*, 2004; Palme & O'Neill, 2004; Lyubetskaya & Korenaga, 2007a).

Salters & Stracke (2004) estimated a *depleted mantle* composition (as a residue after extraction of modern basalt) of 0.7  $\mu\text{g/g}$  Li, 0.025  $\mu\text{g/g}$  Be and 0.06  $\mu\text{g/g}$  B. Estimates for Li and B isotope ratios of primitive or depleted mantle do not exist. However, mid-ocean ridge basalt (MORB) values should be representative of the underlying mantle, as no fractionation between source material and magma occurs. Hart *et al.* (1999) give a  $\delta^{11}\text{B}$  value of  $-3\text{‰}$  for *N-MORB*, Spivack (1986) and Smith *et al.* (1995) also give a  $\delta^{11}\text{B}$  value of  $-3 \pm 1\text{‰}$  for *upper mantle*. *Fresh MORB* has light element concentrations of 5.4–6.9  $\mu\text{g/g}$  Li (Chan *et al.*, 1992), 0.2–2.4  $\mu\text{g/g}$  Be (Ryan & Langmuir, 1987) and 0.3–11.1  $\mu\text{g/g}$  B (Ryan & Langmuir, 1993 and references therein).

The subduction input comprises mainly *serpentinized oceanic crust* and the overlying, predominantly pelagic sediments. Altered, *i.e.*, serpentinized basaltic crust has variable light element composition. Serpentinized harzburgites from the Mid-Atlantic ridge ODP Leg 209 have 7–33  $\mu\text{g/g}$  Li, 2–120  $\mu\text{g/g}$  Be and 0.06–2.3  $\mu\text{g/g}$  B (*e.g.*, Vils *et al.*, 2008). Oceanic crust at IODP 1256D has B contents of 0.9–6  $\mu\text{g/g}$  (Sano *et al.*, 2001). Kelley *et al.* (2003) analyzed altered crust at ODP Site 801 in the Western Pacific by ICP-MS and give Li and Be concentrations of 3–97  $\mu\text{g/g}$  and 0.05–3.1  $\mu\text{g/g}$ , respectively. Ophiolitic altered oceanic crust studied by Smith *et al.* (1995) has B contents of 2.7–26  $\mu\text{g/g}$  and a boron isotope ratio between +0.8 and +5.9 ‰. Serpentinized oceanic crust from ODP 209 yields  $\delta^{11}\text{B}$  values from +29.6 to +40.5 ‰ (Vils *et al.*, 2009).

*Hydrothermal vent fluids* that are expelled from the oceanic crust after seawater percolating through the rock have light element concentrations of 0.2–2.8  $\mu\text{g/g}$  Li and 0.3–5.2  $\mu\text{g/g}$  B with  $\delta^{11}\text{B}$  values of +25 to +30 ‰ (Douville *et al.*, 2002; Foustoukos *et al.*, 2004, 2008; Boschi *et al.*, 2006; Schmidt *et al.*, 2007;). Beryllium concentrations are only available from hydrothermal fluids of the Guaymas Basin: 0.012–0.094  $\mu\text{g/g}$  (von Damm *et al.*, 1985).

Sediment input in the Mariana subduction zone is limited. The composition of *pelagic sediments* was given by Ishikawa & Nakamura (1993) with 2.1–95.7  $\mu\text{g/g}$  Li and 15–132  $\mu\text{g/g}$  B. Ryan & Langmuir (1987) summarized various Be literature data for *marine sediments* and give a range of 0.3–2.8  $\mu\text{g/g}$  Be. Boron isotope ratios of pelagic sediments range between  $-6.6$  and  $+10.5\text{‰}$  (Ishikawa & Nakamura, 1993). Spivack *et al.* (1987) report  $\delta^{11}\text{B}$  values between  $-4.3$  and  $+2.8\text{‰}$  in marine sediments (non-desorbable fraction).

Various studies on dredged abyssal peridotites have shown that reaction with seawater can enrich the lithospheric mantle in B (*e.g.*, Thompson & Melson, 1970; Bonatti *et al.*, 1984; Vils *et al.*, 2008), because B is abundant in *seawater* (4.4–4.6  $\mu\text{g/g}$ ; Quinby-Hunt & Turekian, 1983; Spivack & Edmond, 1987; Jean-Baptiste *et al.*, 1991; Mottl *et al.*, 2004) compared to depleted mantle. Li and Be concentrations of seawater are 25–26  $\mu\text{mol/kg}$ , *i.e.*, 0.18  $\mu\text{g/g}$  Li (Quinby-Hunt & Turekian, 1983;

Jean-Baptiste *et al.*, 1991; Douville *et al.*, 2002) and 0.2 ng/kg Be, *i.e.*, 0.0002 ng/g (Quinby-Hunt & Turekian, 1983). The boron isotope composition is +39.52 ‰ (Spivack & Edmond, 1987).

In subduction zones, there is a progressive release of Li and B from the subducted altered oceanic crust during dehydration reactions (Moran *et al.*, 1992; Bebout *et al.*, 1993, 1999; Domanik *et al.*, 1993; You *et al.*, 1995; Peacock & Hervig, 1999; Chan & Kastner, 2000; Benton *et al.*, 2001). Be can be released by melting (Johnson & Planck, 1999), but also by dehydration during high pressure and temperature metamorphism of the subducted altered oceanic crust (*e.g.*, Marschall *et al.*, 2007a).

Studies of *volcanic arc rocks* have shown that the magma source region was modified by slab-derived fluids or melts, indicated by an enrichment in Li, Be, and B compared to the unmetasomatized mantle (Tatsumi, 1989; Ishikawa & Nakamura, 1994; Leeman, 1996; Chan *et al.*, 1999, 2002a; Rose *et al.*, 2001; Ryan, 2002; Tomascak *et al.*, 2002). The light element compositions are variable with 1–23 µg/g Li, 0.1–2.6 µg/g Be (10 µg/g Be, Ryan, 2002) and 0.7–90 µg/g B (Ryan & Langmuir, 1988 and references therein; Ryan & Langmuir, 1993 and references therein; Leemann *et al.*, 1994; Ryan *et al.*, 1995; Smith *et al.*, 1997; Rose *et al.*, 2001; Ryan, 2002; Straub & Layne, 2002; Tomascak *et al.*, 2002). Boron isotope ratios range between –5.3 and +1.8 ‰ (Smith *et al.*, 1997) for the Lesser Antilles and between +4.5 and +12.0 ‰ for the Izu Arc (Ishikawa & Nakamura, 1994; Straub & Layne, 2002).

Slab-derived fluids are known to hydrate the overlying mantle wedge. *Partly serpentinized peridotites* from the Mariana subduction zone, recovered from serpentine seamounts, have 0.3–8.9 µg/g Li and 4.1–39.8 µg/g B at South Chamorro Seamount and 1.6–18.9 µg/g Li and 6.8–57.5 µg/g B at Conical Seamount (Benton *et al.*, 2001, 2004; Savov *et al.*, 2005b; Savov *et al.*, 2007). Be contents of South Chamorro serpentinites are very low (0.001–0.009 µg/g; Savov, personal communication). Boron isotope compositions vary between +5.4 and +25.3 ‰ at Conical Seamount (Benton *et al.*, 2001) and between +10.6 and +18.1 ‰ at South Chamorro Seamount (Savov *et al.*, 2004).

*Pore fluids*, upwelling at Conical (C. Smt.) and South Chamorro (S. Ch. Smt.) Seamount have enriched B but low Li concentrations: 34.6 µg/g B at C. Smt. and 42.2 µg/g B at S. Ch. Smt.; 0.003 µg/g Li at C. Smt. and 0.01 µg/g Li at S. Ch. Smt. (Mottl *et al.*, 2003, 2004 and references therein). The boron isotope signature of the upwelling fluids is positive with +8.7 ‰ (Savov *et al.*, 2004). Beryllium values for pore fluids are not reported.

During subduction, the slab reaches higher pressure and temperature regions and rocks in blueschist- and eclogite-facies are formed. *Blueschist-facies* metasedimentary rocks from onland studies (Catalina Schist) reveal a light element variation of 10.2–41.2 µg/g Li, 0.2–1.4 µg/g Be, and 7.5–59.0 µg/g B (Bebout *et al.*, 1993, 1999; King *et al.*, 2007). Boron isotope ratios range from –9 to –2 ‰ (King *et al.*, 2007). *Eclogite-facies* rocks have variable Li contents of 1.4–72.3 µg/g, Be and B contents are 1.8–2.9 µg/g and 2.2–4.8 µg/g, respectively (Zack *et al.*, 2003; Marschall, 2005; Marschall *et al.*, 2007a and references therein).

## 1.6 Geological setting

### 1.6.1 The geography of the Izu-Bonin-Mariana (IBM) subduction zone

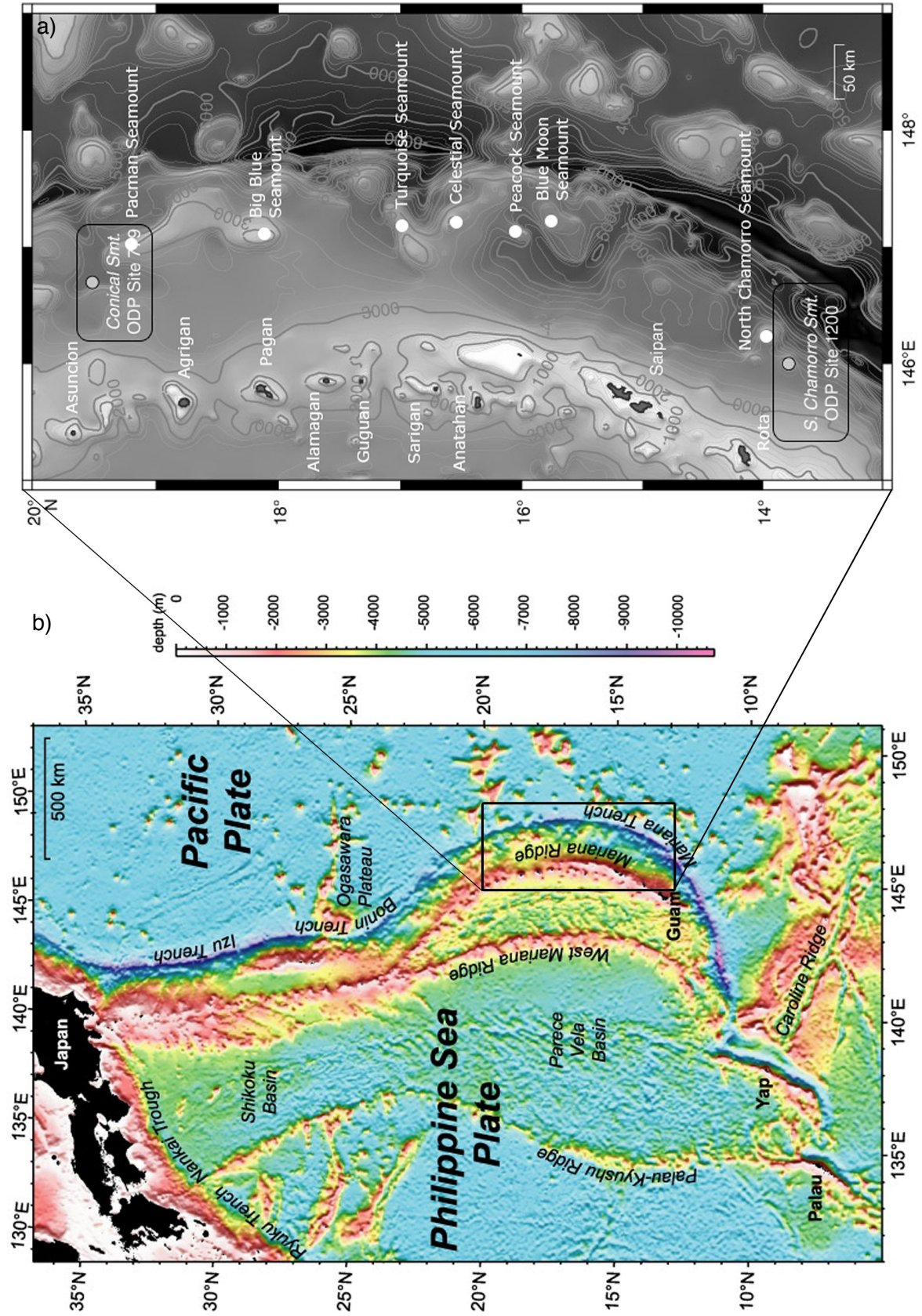
The Izu-Bonin-Mariana (IBM) subduction zone is a non-accretionary convergent plate margin, which ranges over ~2800 km from near Tokyo, Japan, to south of Guam, Mariana Islands (Fig. 1.3a). It lies along the eastern margin of the Philippine Sea Plate in the Western Pacific Ocean and formed as a result of subduction of the Western Pacific Plate. The southern boundary is located where the IBM trench meets the Palau-Kyushu Ridge at 11°N, the northern boundary is at 35°20'N close to southern Honshu (Stern *et al.*, 2003). The eastern boundary extends along a great trench (Fig. 1.3), which is almost 11 km deep in the Challenger Deep and less than 3 km, where the Ogasawara Plateau enters the trench (Fig. 1.3a; Stern *et al.*, 2003).

The IBM arc system can be morphologically divided into three segments, where forearc, active arc and back-arc are expressed differently; the Sofugan Tectonic Line (~29°30'N) separates the Izu and Bonin segments, and the northern end of the Mariana Trough back-arc basin (~23°N) marks the boundary between the Bonin and Mariana segments (Stern *et al.*, 2003).

The IBM forearc is very narrow in the south, but ~200 km wide between Guam and Honshu and differs from many other forearcs by not having an accretionary prism (Horine *et al.*, 1990). The Mariana magmatic arc is mostly defined by volcanic islands (*e.g.*, Asuncion, Anatahan, Rota; Fig. 1.3b) in the Central Island Province and is submarine to the north and south (Bloomer *et al.*, 1989a,b). Volcanoes erupting lavas of unusual composition – the shoshonitic province - are found in the transition between the Bonin and Mariana arc segments (Stern *et al.*, 2003).

The back-arc region of the three IBM segments varies markedly; (i) in the Izu segment several volcanic cross-chains extend SW away from the magmatic front (Ishizuka *et al.*, 1998), (ii) the Bonin arc has no back-arc basin, inter-arc rift or rear-arc cross chains, (iii) the Mariana segment comprises an active back arc basin (Fryer, 1995), the Mariana Trough, which shows seafloor spreading south of 19°15' and rifting farther north (Martinez *et al.*, 1995; Gribble *et al.*, 1998). South and west of Guam, the forearc region is very narrow and the intersection of the backarc basin spreading axis with the arc magmatic system is complex (Stern *et al.*, 2003).

**Fig. 1.3 (following page): a)** Bathymetry color map of the Izu-Bonin-Mariana arc-basin system (from and after Fryer & Salisbury, 2006), black rectangle indicates the area of figure b), **b)** Bathymetry map showing volcanic islands and serpentinite mud volcanoes, seamounts relevant for this study are Conical and South Chamorro Seamount (modified after Snyder *et al.*, 2005).



## 1.6.2 History of the IBM arc system

The IBM region developed since the Early-Middle Eocene (48 Ma ago) with the onset of westward subsidence of old, dense Jurassic-Cretaceous Pacific lithosphere beneath the Eocene Philippine Sea Plate (Fig. 1.4; Seno & Maruyama, 1984; Stern & Bloomer, 1992; Bloomer *et al.*, 1995; Cosca *et al.*, 1998). Igneous activity (depleted tholeiites, boninites and associated low-K

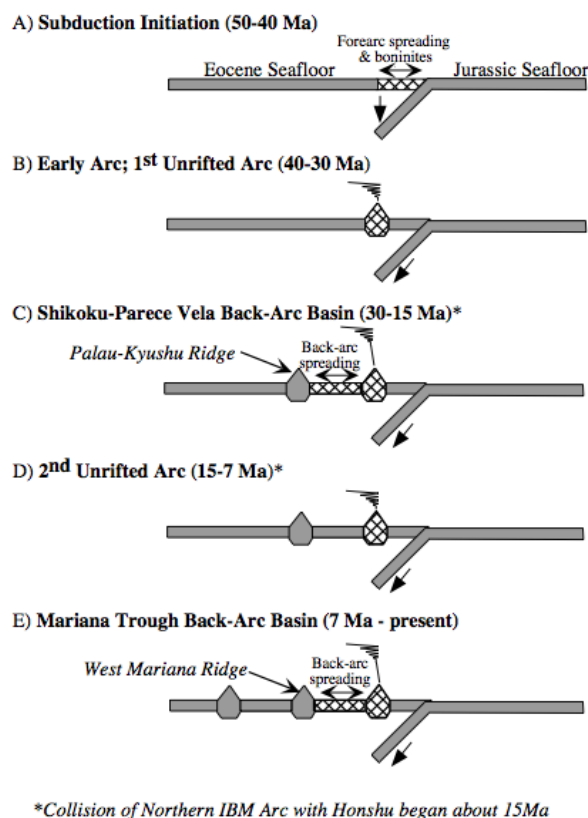


**Fig. 1.4:** Simplified history of the IBM arc system. Shaded areas are magmatically inactive, cross-hatched areas are magmatically active, from Stern *et al.* (2003).

The rifting split the arc and subsequent backarc spreading isolated the Kyushu-Palau Ridge remnant arc from the active Izu-Bonin-Mariana Arc. The systems, particularly the Parece Vela and Shikoku Basin spreading systems, rejoined 23 Ma ago and both basins shared a common spreading axis until 17–15 Ma ago (Stern *et al.*, 2003).

In the Late Miocene, the southern part of the arc was disrupted again and subsequent spreading occurred in the Mariana backarc basin. This led to isolation of the West Mariana Ridge remnant arc from the active Mariana Arc to form a separate magmatic system. Arc volcanism in the northern IBM is characterized by more depleted compositions compared to the relatively enriched compositions in the southern IBM (Bryant *et al.*, 1999). During subduction along the Nankai Trough in younger periods, at ~15 Ma, the northernmost IBM collided with Honshu (Stern *et al.*, 2003).

rhyodacites; Hickey & Frey, 1982; Stern *et al.*, 1991, 2004; Taylor *et al.*, 1994; Bloomer *et al.*, 1995; Macpherson & Hall, 2001) in the forearc allowed the sub-forearc mantle to stabilize and cool in the Late Eocene or Early Oligocene (Stern *et al.*, 2003).

True subduction with down-dip motion of the lithosphere began ~43 Ma ago, when the Pacific plate changed from a northerly to more westerly motion, indicated by the formation of the magmatic arc ~200 km away from the trench, close to its present position (Richards & Lithgow-Bertelloni, 1996). The arc stabilized until ~30 Ma ago, when the formation of an intra-oceanic volcanic arc rift induced the formation of the Parece Vela Basin in the south (Stern *et al.*, 2003). In the Early Oligocene, ~26 Ma ago, spreading in the northern part of the IBM arc began and propagated south to form the Shikoku Basin (Kobayashi *et al.*, 1995).

The Bonin Arc is in a still ongoing episode of rifting to form the Mariana Trough back-arc basin, which began sometime <10 Ma ago with seafloor spreading starting at ~3–4 Ma ago (Bibee *et al.*, 1980; Yamazaki & Stern, 1997). Then, ~2 Ma ago the Izu inter-arc rifts began to form (Taylor, 1992).

### 1.6.3 Current subduction in the Mariana Arc

Currently, mid-Jurassic to Early Cretaceous lithosphere, younger in the north and older in the south (including the oldest, ~170 Ma old oceanic crust) is being subducted and is a type example of an intra-ocean convergent margin. Converging rates of the Pacific plate were modeled by Seno *et al.* (1993) and reach ~20 mm/yr moving in NW direction at 12°N and ~60 mm/yr moving WNW at 34°N. In consequence, motions at the locations of Conical and South Chamorro Seamount should be 43 mm/yr and 23 mm/yr, respectively. The Mariana Trough is opening with a spreading rate of 30–50 mm/yr (Bibee *et al.*, 1980; Hussong & Uyeda, 1982; Yamazaki & Stern, 1997).

Engdahl *et al.* (1998) provided an earthquake catalogue of the IBM ‘Subduction Factory’. The results show that the dip of the Wadati-Benioff Zone steepens smoothly from ~40° to ~80° southwards and that seismicity diminishes between depths of ~150 and ~300 km. Deep earthquakes, seismic events  $\geq 300$  km, are common beneath parts of the IBM arc system, though less frequent than for most other subduction zones with deep seismicity (*e.g.*, Tonga/Fiji/Kermadec and South America; Stern *et al.*, 2003). Katsumata & Sykes (1969) outlined a lack of deep ( $\geq 300$  km) events beneath the Volcano Islands adjacent to the junction of the Izu-Bonin and Mariana trenches and a region of reduced shallow seismicity ( $\leq 70$  km).

Similarly, beneath the southern IBM, a double seismic zone was detected at 80 to 120 km depth (with the two zones separated by 30–35 km) generated either by unbending a plate which was originally deformed anelastically or by thermal stresses, where the curvature of the slab is greatest (Samowitz & Forsyth, 1981). Abers (1996) suggest that compositional variations in the subducting slab may also contribute to double seismic zones and Peacock (2001) proposes that double seismic zones represent the location of serpentine dehydration in the slab.

Currently, the Pacific plate in the Mariana segment descends at a ~20° dip angle to ~60 km depths, while at depths >100 km it sinks abruptly (almost vertically) beneath the Philippine Sea Plate (Engdahl *et al.*, 1998). Studies using several analysis techniques such as seismic anisotropy or travel-time tomography conclude that the cold, seismically fast slab beneath the northern IBM stagnates near the upper-lower mantle boundary (~660 km) leading to a depression of this discontinuity, whereas the slab beneath the southern and central IBM descends steeply through the upper mantle and appears to penetrate into the lower mantle to depths of 900–1000 km (Creager & Jordan, 1986; van der Hilst & Seno, 1993; Fukao *et al.*, 1992; Fouch & Fischer, 1996; Brudzinski *et al.*, 1997; Castle & Creager, 1998, 1999; Stern *et al.*, 2003).

Strong arc-parallel slip rates in the northern Mariana forearc of up to 30 mm/yr are fast enough to produce geologically significant effects such as unroofing of high-grade metamorphic rocks (McCaffrey, 1996). However, convergence in the Mariana Arc is nearly orthogonal, which could explain why the southern IBM forearc is tectonically more active. The IBM arc system south of the Ogasawara Plateau is bathymetrically 'rough' (Stern *et al.*, 2003), dominated by crude alignments of seamounts, atolls and islands defining three large, WNW-ESE trending chains, namely the Marcus-Wake-Ogasawara Plateau, the Magellan Chain and the Caroline Islands Ridge from N to S (Fig. 1.5; Winterer *et al.*, 1993). The first two chains formed by off-ridge volcanism during the Cretaceous and border the Pigafetta Basin, an abyssal plain. The Caroline Islands chain formed over the past 20 Ma during westward passage of the Pacific plate over a mantle hot-spot, marks the southern border of the East Mariana Basin, and comprises the only high volcanic islands on the NW Pacific plate (Stern *et al.*, 2003).

Seismic investigations of the southern Mariana subduction zone result in models that suggest a depth to the slab of roughly >20 km below sea level, *i.e.*, >17 km below seafloor (kmbsf) at ~85 km distance from the trench (below South Chamorro Smt; *e.g.*, Oakley *et al.*, 2008). Though the incoming Pacific plate includes numerous 2–3 km high seamounts inferring the Mariana subduction zone, there is a lack of a significant deformation of the Mariana forearc crust (Oakley *et al.*, 2008). Besides igneous intrusions, these seamounts may be responsible for the thickened oceanic crust in the Mariana region, which reaches ~7 km (Oakley *et al.*, 2008).

It is not possible to directly study the subducted materials that entered the trench 4–10 Ma ago and that are presently being processed by the IBM 'Subduction Factory' in 130 km depth, a possibility to fully understand the subduction processes beneath the IBM. Since the composition of the Western Pacific seafloor-oceanic crust (sediments, crust and mantle lithosphere) varies sufficiently systematically, it is possible to understand what is currently being processed by studying the material east of the IBM trench (Stern *et al.*, 2003). The Pacific plate is the oldest known crust on Earth, yielding MORB basement Ar-Ar ages of  $167 \pm 5$  Ma (Pringle, 1992) and a sediment age of Callovian or latest Bathonian (Jurassic, ~162 Ma, at Site 801C, Leg 129; Harland *et al.*, 1990). During subduction, seamount chains and aseismic ridges (see above) collided only with the Mariana and southern Izu-Bonin arcs. Yet, the IBM trench is devoid of a significant sediment cover (*e.g.*, Bellaiche, 1980); the ~500 m thick sediment cover observed at Site 801C is completely subducted with the downgoing plate (Shipboard Scientific Party, 1990c).

The MORB crust in the Pigafetta Basin (see above) is typically affected by low-temperature hydrothermal alteration and is overlain by a >3 m thick hydrothermal deposit (Alt *et al.*, 1992) and ~60 m alkali olivine basalt ( $157.4 \pm 0.5$  Ma; Pringle, 1992). The sediment sequence is dominated by chert, pelagic clay with little carbonate and volcanoclastic turbidites (Stern *et al.*, 2003). Investigation at Site 802 (Leg 129) in the East Mariana Basin provides (i) tuff in the first 238 m below seafloor interlayered by either pelagic clay or redeposited calcareous claystone and chalk and (ii) nanofossil chalk down to at least 310 m (Pratson *et al.*, 1992). Strong seafloor currents probably are responsible for the erosion or non-deposition of considerable sediment loads (Stern *et al.*, 2003).



The outer rise outboard of the trench elevates  $\sim 300$  m above the surrounding seafloor and is characterized by intensive trench parallel normal faults with step-like fault blocks promoting infiltrating fluids to be introduced deep into the soon-to-be-subducted plate (Bellaiche, 1980; Peacock, 2001; Stern *et al.*, 2003) allowing *e.g.* seawater to penetrate deeply into mantle lithosphere to generate serpentinites that carry substantial amounts of water into the ‘Subduction Factory’ (Peacock, 2001; Ranero *et al.*, 2003). This deep crustal hydration and the lack of significant sediment load suggests that during subduction, the amount of water released by pore space compaction of incoming sediments is insignificant compared to the amount of water contained in the subducting altered igneous oceanic crust (Oakley *et al.*, 2008).

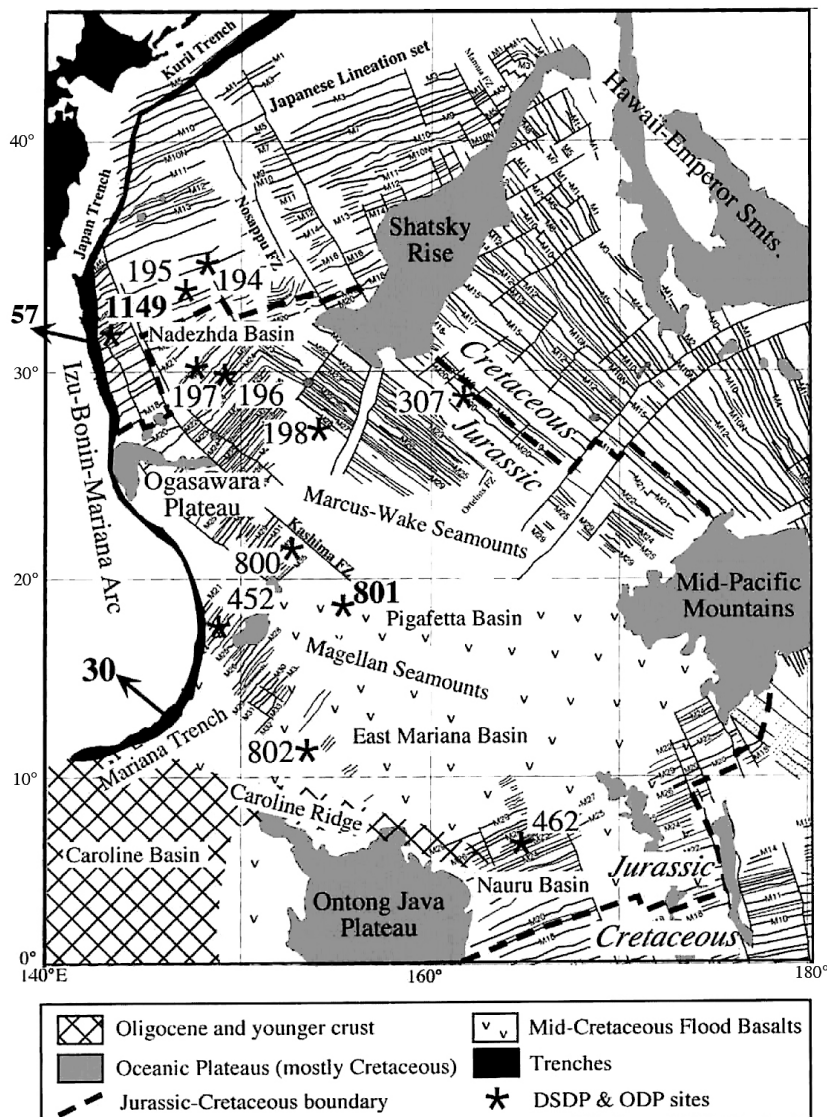


**Fig. 1.5:** Simplified geologic and magnetic map of the western Pacific from Stern *et al.* (2003): based on the work of Nakanishi *et al.* (1992). Relative motion of the Pacific plate with respect to the Philippine Sea Plate is shown with arrows, numbers correspond to velocities (mm/year), after Seno *et al.* (1993). Numbers with asterisks represent scientific drilling sites, especially Ocean Drilling Project and Deep Sea Drilling Program drillsites.

### 1.6.4 Serpentine mud volcanism and sample location

The Mariana forearc between the trench and the arc is pervasively faulted by tectonic activity and only minor sediment accretion occurred along the margin (Horine *et al.*, 1990; Salisbury *et al.*, 2002). As the Pacific plate descends, oceanic upper mantle, oceanic crust, overlying sediment, and water are transported into the deep mantle (Forsyth & Uyeda, 1975; Stern, 2002). Some material might be transferred from the subducting plate to the overlying plate, not being reincorporated into the Earth's interior. In the shallow to intermediate supra-subduction zone (SSZ) region, H<sub>2</sub>O-rich fluid is squeezed out of pores during porosity compaction, removed from mineral surfaces and dehydration reactions release pore fluids from bound volatiles in oceanic sediments and basalts of the downgoing plate as higher pressures and temperatures are encountered (*e.g.*, Fryer & Fryer, 1987; Peacock, 1987, 1990; Mottl, 1992; Liu *et al.*, 1996).

On the one hand, these released volatiles affect the physical properties in the contact region between the plates (the décollement) by the metamorphic formation of talc and serpentine (Peacock & Hyndman, 1999). Since acting directly and/or indirectly as lubricants, the presence or absence of fluids controls the occurrence of destructive earthquakes in shallow regions (up to 60 km depth) in subduction zones. The addition of fluids to these deeper regions (<60 km) lowers the melting temperature in the overlying mantle, generates arc and backarc magmas and affect the composition of these magmas that buoyantly rise from the deep and hot sections in the mantle wedge resulting subsequently in explosive (fluid-rich) volcanism at the Earth's surface.

On the other hand, large amounts of fluid rise along a steep pressure gradient through faults and fractures, carrying with it dissolved constituents from the subducting slab. In some cases fluids can vent as cold springs in the forearc (Mottl *et al.*, 2004). However, these slab-derived fluids hydrate and serpentinize the SSZ mantle peridotite. Recent geophysical investigations confirm that at least part of the Mariana forearc mantle wedge is indeed serpentinized (Bostock *et al.*, 2002; Kamimura *et al.*, 2002; Okino *et al.*, 2004). Within the deep reaching faults of the forearc, serpentinite fault gouges mix with the rising slab-derived fluids.

This mud-rock-mixture buoyantly rises in conduits along the fault planes until it ultimately protrudes on the seafloor to form numerous km-scale seamounts, *i.e.*, mud volcanoes, primarily composed of sedimentary serpentinite, situated on the outer forearc of the Mariana margin (*e.g.*, Hussong & Fryer, 1982; Fryer 1992). They are located in a trench-parallel zone ~30 to 100 km arcward of the trench axis (between trench and arc) and can reach up to 30–40 km in diameter and over 2 km in height (Fryer, 1992; Fryer *et al.*, 2000).

Unconsolidated flows of clay- to silt-sized serpentinite mud enclose up to boulder-sized clasts of variably serpentinized mantle peridotite and subordinately blueschist-facies clasts (Fryer & Hussong, 1982; Fryer *et al.*, 1990; Maekawa *et al.*, 1992; Maekawa, 1995; Fryer & Todd, 1999; Fryer *et al.*, 2000; Shipboard Scientific Party, 2002a). Hence, these compounds permit the direct sampling of slab-derived material (Fryer *et al.*, 1985; 1987; 1990; Mottl, 1992). The upwelling rates of such serpentinite muds are unknown. However, upwelling must be fast enough to maintain large boulder-

sized clasts of serpentinized peridotite suspended in its matrix, which is probably facilitated by the muds low density, apparently low yield strength, high ductility and overpressured and volatile-rich pore fluids at depth (*e.g.*, Phipps & Ballotti, 1992; Fryer *et al.*, 2006). Aragonite chimneys on the summit of the seamounts (*e.g.*, South Chamorro and Conical Seamount) have vent a fluid chemistry suggesting components derived by dehydration processes occurring in the subducting Pacific plate at the décollement zone (Mottl, 1992; Mottl *et al.*, 2003).

Since intra-ocean convergent margins hold not only thinner, denser and more refractory crust compared to Andean-type margins (*e.g.*, Japan or Andes), but also have a continuous thin sedimentary cover due to large distance or isolation from continents, the IBM subduction zone allows a confident assessment of mantle-to-crust fluxes and processes by studying *e.g.*, melts and fluids (Stern *et al.*, 2003). In this study samples from two serpentine mud volcanoes from the Mariana forearc region, South Chamorro and Conical Seamount, were investigated.

The South Chamorro Seamount is located at 13°47'N, 146°00'E, ~125 km east of Guam Island (Fig. 1.3b) and 85 km west of the trench and it was drilled by ODP during Leg 195 (Shipboard Scientific Party, 2002). It is a partly collapsed, roughly conical, structure ~2 km high and ~20 km wide with active serpentine/blueschist mud volcanism (*e.g.*, Maekawa 1995; Fryer *et al.*, 2000; Shipboard Scientific Party, 2002a,b). The subducting slab beneath this seamount is in ~26.5 km depth (Fryer *et al.*, 2000; Mottl *et al.*, 2004).

Conical Seamount (Fig. 1.3b) was drilled by ODP during Leg 125 (together with Torishima Seamount; Fryer, 1992). It is located at 19°35'N, 146°40'E, ~80 km west of the Mariana trench axis. It is situated ~30 km above the subducting Pacific plate and is a cone-shaped, 1500 m high structure with a diameter of 20 km (Fryer, 1992).



## Chapter 2

### Analytical Techniques

#### 2.1 Sample documentation

Samples investigated in this study are from the two serpentine mud volcanoes Conical Seamount (Smt.) and South Chamorro Seamount and were provided by I.P. Savov. They had been collected during two Ocean Drilling Program expeditions to the Mariana forearc basin: sampling of Conical Smt. (Site 779, Leg 125) took place during a cruise from 15-Feb to 17-Apr 1989 of the Drilling Vessel *JOIDES Resolution* (Fryer *et al.*, 1990) and South Chamorro Smt. (Site 1200, ODP Leg 195) was sampled from 2-Mar to 2-May 2001 during cruises of the Drilling Vessel *JOIDES Resolution* (Salisbury *et al.*, 2002). Figure 2.1 illustrates the different depths of the investigated samples from drill holes 1200D, 1200E, and 1200F.

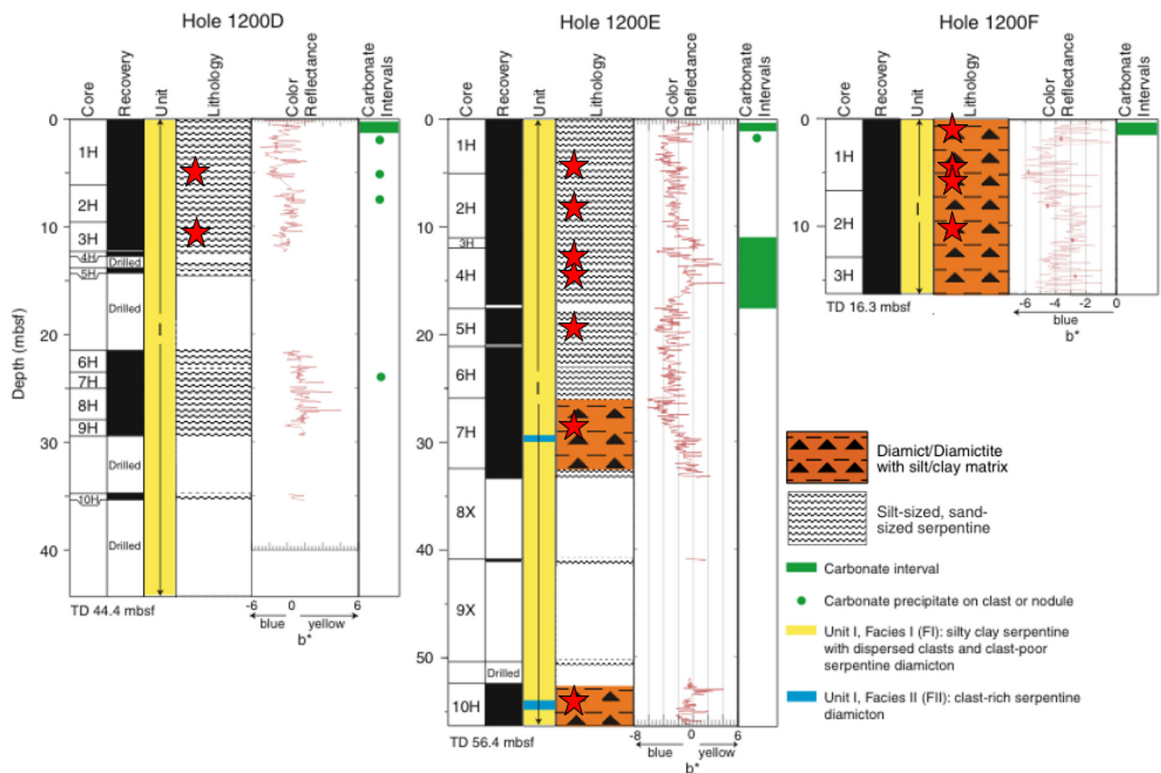


**Fig. 2.1:** Schematic depths profiles of drill sites 1200D, 1200E, and 1200F (from Shipboard Scientific Party, 2002b). The locations of investigated samples are marked by red stars. Similar detailed profiles for sites 1200A and 779A are not available.

Larger rock fragments, *i.e.*, of several cm in diameter, were already extracted from the recovered (drilled) serpentinite muds during the cruises. Clasts of serpentinitized peridotite as well as metamafic rocks (*e.g.*, chlorite-amphibole-schists) vary in size from <1 mm up to several cm. Serpentinite muds,

recovered as whole-round cores, were squeezed to mud-pellets and the pore waters were analyzed onboard (*e.g.*, Shipboard Scientific Party, 2002a). Selected mud-pellets, typically brownish or gray to blue-gray when less altered, were dissolved in distilled water and fragments of interest for this study (mainly only a few mm in diameter) were hand-picked and then sorted using a *Leica WILD M10* binocular microscope.

This time-consuming procedure was necessary due to the weak texture of most fragments. Approximately 500 serpentinite and metamafic clasts were chosen and prepared in 1-inch round polished microsections or slightly thickened ( $\sim 40\ \mu\text{m}$ ) 1-inch round thin sections (Fig. 2.2), to meet the technical requirements of the SIMS (see section 2.3).

Out of these, about 50 fragments with well-preserved mineral assemblages (Table 2.1) were chosen for electron probe micro analyses (EPMA) and secondary ion mass spectrometry (SIMS).



**Fig. 2.2:** Examples of 1-inch round samples: **a)** micro-section FIH4-2, **b)** thin-section A012R01W(3-5), partly serpentinitized areas appear green, entirely serpentinitized and brucite-bearing areas appear brownish to yellow.

Micro-analysis by electron probe and SIMS require detailed petrographic documentation of the samples (*e.g.*, serpentinite textures and mineral compounds) to choose appropriate analyzing areas; thin sections were pre-investigated by polarizing microscopy in combination with a digital camera and both thin sections and polished microsections were characterized by back-scattered electron (BSE) imaging using a *LEO 440* scanning electron microscope (SEM) at the Institut für Geowissenschaften, Universität Heidelberg, Germany. The applied accelerating voltage for BSE images was 15 kV and probe current was  $\sim 2\text{--}5\ \text{nA}$ .

**Table 2.1:** Summary of intervals investigated of holes 1200A, D, E, and F (South Chamorro Seamount) and hole 779A (Conical Seamount).

ODP Leg	Hole Core	Section	Interval	depth in mbsf*	label	sample type	serpentinite fragments	metamafic fragments
125	779A 10R	02	33-34	79.26	10R02	serpentinite-clast	x	
125	779A 26R	02	72-75	208.16	26R02	serpentinite-clast	x	
125	779A 34R	01	62-64	284.32	034-3	serpentinite-clast	x	
195	1200A 003R	01W	81-84	19.01	A003R01	serpentinite-clast	x	
195	1200A 007R	01W	38506	51.14	A007R01	serpentinite-clast	x	
195	1200A 007R	02W	38474	51.72	A007R02	serpentinite-clast	x	
195	1200A 007R	02W	40-43	52.09	7R-2-40	serpentinite-clast	x	
195	1200A 009R	01W	38569	70.46	A009R01	serpentinite-clast	x	
195	1200A 010R	01W	95-97	80.85	A010R01	serpentinite-clast	x	
195	1200A 011R	01W	40-42	89.8	A011R01-40	serpentinite-clast	x	
195	1200A 011R	01W	69-72	90.09	A011R01	serpentinite-clast	x	
195	1200A 012R	01W	38474	108.73	A012R01	serpentinite-clast	x	
195	1200A 013R	01W	25-27	108.95	A013R01-25	serpentinite-clast	x	
195	1200A 013R	01W	90-92	109.6	13R-1-90	serpentinite-clast	x	
195	1200A 013R	02W	40877	110.07	A013R01-12	serpentinite-clast	x	
195	1200A 015R	01W	40117	128.01	A015R01	serpentinite-clast	x	
195	1200A 017G	02W	26-28	> 147.20	17G-2-26	serpentinite-clast	x	
195	1200A 017G	02W	76-79	> 147.20	A017G02	serpentinite-clast	x	
195	1200D 001H	04WR	130-140	5.8	D1H4	mud-pellet	x	x
195	1200D 003H	01WR	130-140	11.2	D3H1	mud-pellet	x	x
195	1200E 001H	03WR	130-140	4.3	E1H3	mud-pellet	x	x
195	1200E 002H	02WR	130-140	8.9	E2H2	mud-pellet	x	x
195	1200E 004H	01WR	130-140	13.3	E4H1	mud-pellet	x	x
195	1200E 004H	02WR	130-140	14.8	E4H2	mud-pellet	x	x
195	1200E 005H	02W	81-83	19.86	E005H02	serpentinite-clast	x	
195	1200E 007H	02WR	130-140	28.7	MAK / E7H2	mud-pellet	x	x
195	1200E 010H	02W	63-65	54.53	E010H02	serpentinite-clast	x	
195	1200F 001H	01WR	90-105	0.9	F1H1	mud-pellet	x	x
195	1200F 001H	03WR	140-150	4.4	F1H3	mud-pellet	x	x
195	1200F 001H	04WR	140-150	5.9	F1H4	mud-pellet	x	x
195	1200F 002H	02WR	140-150	10.6	F2H2	mud-pellet	x	x

\* meters below seafloor, data from [http://iodp.tamu.edu/janusweb/coring\\_summaries/](http://iodp.tamu.edu/janusweb/coring_summaries/)

## 2.2 Electron probe micro analysis (EPMA)

Major element compositions of minerals in serpentinized peridotites and metamafic fragments were determined using a *Cameca SX 51* electron probe micro analyzer equipped with five wavelength-dispersive spectrometers at Institut für Geowissenschaften, Universität Heidelberg, Germany. Spot size was 1  $\mu\text{m}$  with an accelerating voltage of 15 kV, a probe current of 20 nA and counting times of generally 10 s for peak and 5 s for background for all elements using the setup label 'genani'. Synthetic and natural oxides and silicates were used as reference materials (Table 2.2). Matrix correction is based on the PAP-algorithm after Pouchou & Pichoir (1984).

**Table 2.2:** Analytical setup and parameters used for electron probe micro analyses.

Atomic number	Element	Spectrometer Crystal	Reference Material	Concentration (wt%) in reference material	Counting time (s)	Detection limit (wt%) at 15 kV and 20 nA
11	Na	TAP	Albite	8.71% Na	10	0.04% Na <sub>2</sub> O
12	Mg	TAP	MgO	60.31% Mg	20	0.05% MgO
13	Al	TAP	Al <sub>2</sub> O <sub>3</sub>	52.93% Al	30	0.03% Al <sub>2</sub> O <sub>3</sub>
14	Si	TAP	Wollastonite	24.08% Si	20	0.02% SiO <sub>2</sub>
19	K	PET	Orthoclase	12.18% K	10	0.03% K <sub>2</sub> O
20	Ca	PET	Wollastonite	34.12% Ca	30	0.02% CaO
22	Ti	PET	TiO <sub>2</sub>	59.95% Ti	20	0.05% TiO <sub>2</sub>
24	Cr	TAP	Cr <sub>2</sub> O <sub>3</sub>	68.42% Cr	20	0.05% Cr <sub>2</sub> O <sub>3</sub>
25	Mn	TAP	Rhodonite	33.68% Mn	10	0.08% MnO
26	Fe	TAP	hematite	100.00% Fe	10	0.11% Fe <sub>2</sub> O <sub>3</sub>
28	Ni	TAP	NiO	78.58% Ni	30	0.07% NiO

### 2.3 Secondary ion mass spectrometry (SIMS)

Concentrations of Li, Be and B of minerals, as well as Sr concentrations in some cases were analyzed by secondary ion mass spectrometry (SIMS) with a modified *Cameca ims 3f ion microprobe*, equipped with a primary beam mass filter (Institut für Geowissenschaften, Universität Heidelberg, Germany), following the procedure of Marschall & Ludwig (2004). In order to obtain B concentration data close to the detection limit of the SIMS (~1–5 ng/g) and to avoid surface contamination, the following procedure was implemented: (1) B-free glycol was used as a lubricant during thin section preparation, (2) sample surfaces were thoroughly wiped clean with acetone and then ultrasonic bathed in distilled water and finally in Milli-Q water (Millipore) for 2x15 min before gold coating, (3) every spot is pre-sputtered for six minutes by the primary ion beam, and (4) only the innermost 12 µm (later improvement of the machine by selecting a field aperture enabled analyses of smaller 6 µm) of secondary ions from an ~30 µm spot are allowed through the field aperture to minimize contamination from the rim of the crater produced during ion sputtering. This detection field enables the analyses of even very small sized minerals.

Analyses were performed using a 14.5 keV / 10–50 nA <sup>16</sup>O<sup>-</sup> primary ion beam. The energy window was set to 40 eV. Energy filtering with 75 eV offset to the nominal secondary accelerating voltage of 4.5 kV at a mass resolution (m/Δm) of about 1040 was applied to suppress interfering molecules and to minimize matrix effects (Ottolini *et al.*, 1993). Each analysis had 10 cycles and a total integration time of 220 s (for ‘LiBeBSi’; 247 s for ‘LiBeBSiSr’). For all silicates, secondary ion intensities of <sup>7</sup>Li, <sup>9</sup>Be, <sup>11</sup>B (and for some analyses <sup>86</sup>Sr and <sup>88</sup>Sr) were normalized to the count rate of <sup>30</sup>Si (SiO<sub>2</sub> concentration measured by EPMA) and calibrated against the NIST SRM 610 glass reference material using the concentrations (preferred averages) from Pearce *et al.*, 1997.

Accuracy for Li and B analyses is estimated to be better than 10% for concentrations in excess of 0.1 µg/g. Background near mass 11 was ≤10<sup>-2</sup> cps (≤1 ng/g). The setup used and the background of 0.02 ions/s lead to a detection limit (critical value) of 1.9 ng/g (Li), 1.8 ng/g (Be), 6.9 ng/g (B), and 20.2 ng/g (Sr) (Currie, 1968; Marschall & Ludwig, 2004). Results were not corrected for background.



Two strontium isotopes ( $^{86}\text{Sr}$  and  $^{88}\text{Sr}$ ) were detected to have the possibility to examine the reliability of the Sr concentration with respect to inferences.

## 2.4 Determination of boron isotope ratios by SIMS

Boron isotope ratios of serpentine, amphibole, chlorite and phengite were determined using the *Cameca ims 3f ion microprobe* at the Institut für Geowissenschaften, Universität Heidelberg, Germany. To avoid contamination, cleaning and analyses was done following the procedure of Marschall & Ludwig (2004). Primary ion beam was  $^{16}\text{O}^+$  accelerated to 10 keV with a beam current of 10–20 nA, resulting in count rates for  $^{11}\text{B}$  of  $\sim 40\text{--}60000$  cps and  $\sim 10\text{--}16000$  cps for  $^{10}\text{B}$  (in serpentine), collected by a single electron multiplier. The diameter of the 10 nA spot was  $<20\ \mu\text{m}$  and increased to  $\sim 40\ \mu\text{m}$  with 20 nA beam current. The energy window was set to 100 eV without offset to the secondary accelerating voltage. Mass resolution ( $m/\Delta m$ ) was 1175. On each analysis spot 400 cycles were measured (in some cases only 200) with counting times of  $2 \times 1.66$  s and 1.66 s on  $^{10}\text{B}$  and  $^{11}\text{B}$ , respectively. Presputtering time was 4 min resulting in a total analysis time for one spot of approximately 40 min (for 400 cycles). Reproducibility for standard analyses was  $\sim 0.5\ \text{‰}$  ( $1\ \sigma$ ). Internal precision of single analyses is always plotted as  $2\ \sigma$  in diagrams. The B6 Obsidian standard was used as reference material for the B isotope analyses with SIMS (Tonarini *et al.*, 2003).

## 2.5 Matrix correction for $\delta^{11}\text{B}$ analysis by SIMS

SIMS analyses of boron isotope ratios are very dependent on the matrix of the sample and values can differ from *e.g.*, TIMS values (Rosner *et al.*, 2008; Fig. 2.3). With the SIMS in Heidelberg, B isotopes have already been successfully analyzed for tourmaline and phengite. The results were cross-calibrated and thus matrix-matched with the same sample material analyzed by TIMS (Altherr *et al.*, 2004; Marschall *et al.*, 2006).

For this study, matrix corrections are particularly necessary for SIMS analyses of silicates such as serpentine, amphibole and phengite. In order to evaluate the  $\delta^{11}\text{B}$  matrix correction for serpentine, two pure serpentine crystal separates of known composition from two localities were chosen; ‘geiss’ from Geisspfad, Alps and ‘21826’ from Schweden. These samples each comprise numerous crystals with homogeneous (Li and B) compositions (Table 2.3; Fig. 2.3a). Using the B6 Obsidian as a standard, SIMS analyses give apparent compositions of  $-14.2\ \text{‰}$  and  $-18.1\ \text{‰}$  for ‘geiss’ and ‘21826’, respectively. The reference B isotope ratios of both samples analyzed at the TIMS laboratory in Pisa (by Sonia Tonarini) are  $-8.12\ \text{‰}$  and  $-12.05\ \text{‰}$  for ‘geiss’ and ‘21826’, respectively (Table 2.3; Fig. 2.3a). The offset between SIMS and TIMS analyses suggests a systematic shift of  $\sim 6\ \text{‰}$  for serpentine SIMS values against TIMS values towards lower values (Fig. 2.3a). To confirm this result, serpentine SIMS and bulk rock serpentinite TIMS data of two ODP 209 samples (studied by Flurin Vils; Vils *et al.*, 2009) are evaluated (Fig. 2.3a). Serpentes from the Mariana mantle wedge serpentinites have a very heterogeneous light element composition (see section 4.4). The bulk rock B isotope TIMS ratio of sample A013R01 (serpentine + Ol, Opx,

Cpx) is +19.4 ‰ (analyzed by Sonia Tonarini). B contents of serpentine in this sample is variable (~25–240  $\mu\text{g/g}$ ) and B isotope values analyzed by SIMS average at +12.7 ‰. This SIMS-TIMS difference further supports a required matrix correction of ~6 ‰ (Fig. 2.3a).

Matrix correction for phengite and amphibole analyses was applied after repeated analyses of several chemically homogeneous crystals of amphibole ‘21805’ and phengite ‘Phe-80-3’ (both samples provided by Thomas Zack, Mainz). As shown in table 2.3 and Fig. 2.3b, the discrepancy between SIMS and TIMS  $\delta^{11}\text{B}$  values suggests an offset of 2.8 ‰ for amphibole and 1.3 ‰ for phengite. As amphibole ‘21805’ is the more homogeneous sample, +3 ‰ matrix correction for both phengite and amphibole will be applied for SIMS data.

The  $\delta^{11}\text{B}$  values presented in the following chapters are matrix-corrected.

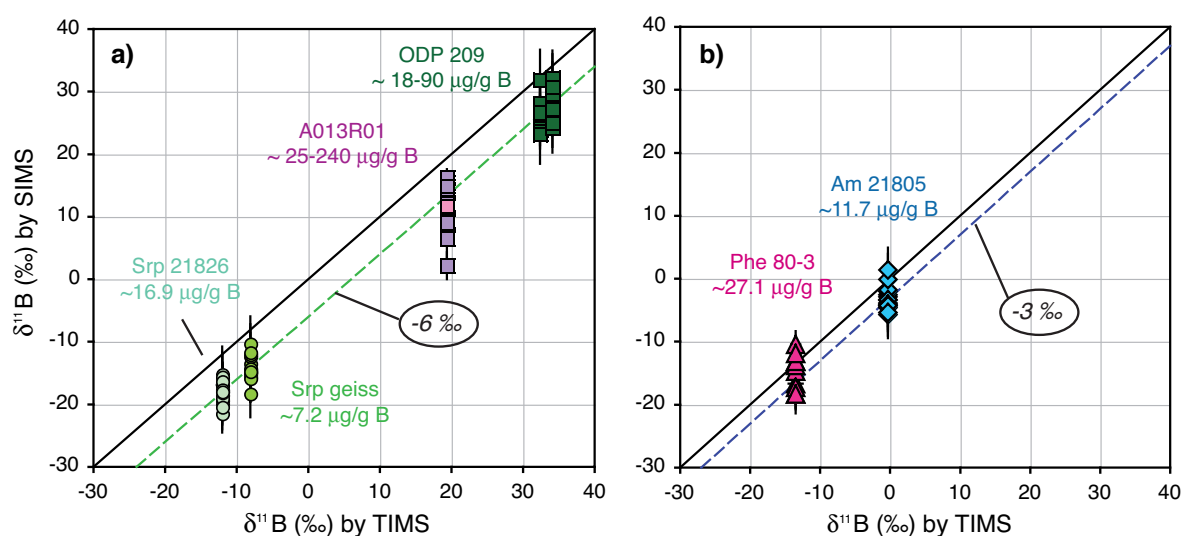


**Fig. 2.3:** Comparison of boron isotope ratios analyzed by TIMS versus SIMS for **a)** serpentine standards ‘geiss’ and ‘21826’ and various serpentine textures of two ODP Leg 209 serpentinites and A013R01 serpentinite (rose square is the mean), **b)** amphibole ‘21805’ and phengite ‘Phe-80-3’. Dashed lines indicate a matrix correction for SIMS analyses of +6 ‰ for serpentine and +3 ‰ for amphibole and phengite.

**Table 2.3:** Comparison of B isotope analyses by SIMS and TIMS.

	Srp ‘geiss’	Srp ‘21826’	Am ‘21805’	Phe ‘80-3’
<b>SIMS</b>				
mean Li content ( $\mu\text{g/g}$ )	5.7	7.8	0.09	32.1
1 $\sigma$	0.7	3.2	0.02	4.5
mean B content ( $\mu\text{g/g}$ )	7.2	16.9	11.7	27.1
1 $\sigma$	0.7	1.0	1.2	1.3
mean $\delta^{11}\text{B}$ (‰), $N = 36$	-14.1	-18.1	-3.1	-14.8
1 $\sigma$	2.0	1.4	1.9	2.8
$N =$	14	36	15	10
<b>TIMS</b>				
$\delta^{11}\text{B}$ (‰)	-8.1	-12.1	-0.3	-13.5
1 $\sigma$	0.3	0.4	0.4	0.3
deviation SIMS-TIMS	-6.0	-6.1	-2.8	-1.3

SIMS analyses were performed with 10–25 nA beam current and calibrated to B6 Obsidian.

## 2.6 Time-of-flight Secondary Ion Mass Spectrometry (ToF-SIMS)

Element distribution maps were obtained using the *ION-TOF TOF-SIMS IV* instrument at the Smithsonian Institution in Washington D.C., USA. ToF-SIMS is a surface-sensitive spectrometry that uses a pulsed low current primary ion beam (typically  $\text{Ga}^+$ ,  $\text{Cs}^+$  and  $\text{O}^+$ ) to remove molecules from the surface of the sample. Secondary ions or cluster ions are removed from atomic monolayers on the surface and then electrostatically accelerated into a ‘flight tube’ (field-free drift region), where a variety of mass ions are mass separated. Their mass is determined by measuring the exact time at which they reach the detector (*i.e.*, time-of-flight) to give a secondary ion mass spectrum. Data acquisition reveals modes such as depth profiles, and by rastering the finely focused beam across the sample surface, elemental maps are generated and presented as multi-color images.

For this study, a 25 kV  $^{69}\text{Ga}^+$  primary ion column was operated in ‘burst alignment’ single crossover mode with a cycle time of 50  $\mu\text{s}$ , allowing for optimum lateral resolution of  $\sim 300$  nm. To remove surface contamination, the mapping area was sputter-cleaned with a 3 keV  $\text{Ar}^+$  ion beam. For silicates, the sensitivity for the detection of  $\text{Li}^+$  is about 17 times higher than for  $\text{B}^+$  (Stephan, 2001).

## 2.7 Micro-Raman spectroscopy

Preliminary analyses were performed with a *DILOR LabRam 2* micro-Raman spectrometer at the ‘Universität Tübingen’. Finally, to identify particularly serpentine polymorphs, micro-Raman measurements were completed using a Horiba Jobin Yvon LabRam HR-UV 800 spectrometer with attached Olympus BX42 microscope at the ‘Institut für Geowissenschaften’, Universität Göttingen, Germany. Using the 488 nm excitation of an air cooled  $\text{Ar}^+$  laser (25 mW laser power at the laser exit), a holographic grating with 600 lines/mm and a Peltier-cooled CCD detector with 1024x256 pixels yielded a spectral dispersion of better than  $2\text{ cm}^{-1}$ . Using a 100x objective with a numerical aperture of 0.9 and closing the confocal hole to 100  $\mu\text{m}$  yielded a lateral resolution of about 1  $\mu\text{m}$  and a depth resolution of about 4  $\mu\text{m}$  (high confocality).

Correct calibration of the instruments was verified by checking the position of the Si band at  $\sim 520.4\text{ cm}^{-1}$ . To optimize the signal to noise ratio, spectra were acquired using 2 scans of 10 seconds for each spectral range. The characteristic spectral regions of serpentine minerals, 1200–100  $\text{cm}^{-1}$  and 4000–3000  $\text{cm}^{-1}$ , were considered. The similarity of serpentine polymorphs at lower wavenumbers requires the detection of the OH-vibrational bands at high wavenumbers (3000–4000  $\text{cm}^{-1}$ ), as they show the difference in asymmetry between chrysotile and lizardite peaks in this range (Auzende *et al.*, 2004). Spectra were processed by an automatic baseline subtraction using the Horiba Jobin Yvon LabRam software. The serpentine polymorphs were discriminated by comparison with published data (*e.g.*, Rinaudo *et al.*, 2003; Auzende *et al.*, 2004; Groppo *et al.*, 2006; Andreani *et al.* 2008).

Figure 2.5 shows the typical Raman spectra and Tables 2.4 and 2.5 summarize the bands for Mg-brucite, Fe-brucite, chrysotile, lizardite, antigorite, and polygonal serpentine. The variation of typical wavenumbers in this study can be  $\pm 2\text{ cm}^{-1}$ .

a) Chrysotile produces typical Raman bands at 232, 388, (525), 694, and 3699  $\text{cm}^{-1}$ . The low wavenumber bands can be related to O-H-O vibrations, to symmetric  $\text{SiO}_4$  and asymmetric Si-O<sub>b</sub>-Si stretching vibrations, respectively (Kloprogge *et al.*, 1999; Rinaudo *et al.*, 2003; Groppo *et al.*, 2006), and the high wavenumber bands to OH-vibrations (Kloprogge *et al.*, 1999; Auzende *et al.*, 2004). Many spectra show an additional peak of variable intensity at the left shoulder of the OH-vibrational band.

b) Typical Raman bands for lizardite at lower wavenumbers are 231, 385, (526), 690  $\text{cm}^{-1}$ , very similar to chrysotile. OH-vibrational bands are 3687 and 3705  $\text{cm}^{-1}$  and are easily discriminated from the chrysotile peak.

c) It has been discussed that polygonal serpentine is a complex assembly of lizardite layers arranged as an outer shell around chrysotile fibers (Cressey & Zussman, 1976; Middleton & Whittaker, 1976; Cressey, 1979). It can easily be determined by X-ray diffraction of serpentine powder (Whittaker & Zussman, 1956). Typical Raman bands for polygonal serpentine at lower wavenumbers are 230, 384, and 693  $\text{cm}^{-1}$ , very similar to chrysotile and lizardite. For the OH-vibrational bands at high wavenumbers, polygonal serpentine is characterized by a 'mixed' spectra between chrysotile and lizardite, as was already suggested by Auzende (personal communication, 2003). The strongest lizardite and chrysotile peaks at 3691  $\text{cm}^{-1}$  and 3702  $\text{cm}^{-1}$ , respectively, decrease in intensity and form an irregular broad band.

d) Similar to polygonal serpentine, antigorite shows a band shift of the symmetric  $\text{SiO}_4$  band to 380  $\text{cm}^{-1}$ . Other bands at lower wavenumbers are at 240, 530, and 690  $\text{cm}^{-1}$ . Furthermore, antigorite is characterized by an additional band at 1050  $\text{cm}^{-1}$ . Two typical distinct OH-vibrational bands are at  $\sim 3660$  and  $\sim 3700$   $\text{cm}^{-1}$ .

e) Micro-Raman spectroscopy of brucite is often hindered by strong fluorescence, which leads to relatively weak brucite spectra. Nevertheless, the analyses show that Fe- and Mg-rich brucite can be easily identified (Table 2.5). All brucite has a characteristic band at 444  $\text{cm}^{-1}$ . Fe-rich brucite has additional bands at about 531  $\text{cm}^{-1}$  and 705  $\text{cm}^{-1}$ . OH-vibrational bands are at lower wavenumbers compared to serpentine: at  $\sim 3638$   $\text{cm}^{-1}$  for Mg-rich brucite and  $\sim 3640$  and  $\sim 3649$   $\text{cm}^{-1}$  for Fe-rich brucite.

The similarities of the serpentine polymorphs in their lower wavenumbers obviously demonstrate the importance to detect the OH-vibrational bands at higher wavenumbers (3000–4000  $\text{cm}^{-1}$ ), as already discussed by Auzende *et al.* (2004). These bands are the major key for an easy characterization of any serpentine polymorph and even brucite, as is demonstrated with this study on natural samples.

**Table 2.4:** Raman band positions ( $\text{cm}^{-1}$ ) of serpentine polymorphs from Mariana mantle wedge serpentinites. Literature data with band assignments are reported for comparison.

Ctl	Liz	Pol	Atg	Ctl (3)	Atg (3)	Liz (3)	Ctl (2)	Ctl (1)	Band assignment for serpentine (1,3)
	<u>This study</u>			<u>Literature data</u>					
-	-	-	-	-	-	-	-	199	Al gmode of Mg(O,OH) <sub>6</sub>
232	231	230	240	231	230	233	-	231	Vibrations of O-H-O groups
-	-	-	-	-	-	-	-	304	Bending of SiO <sub>4</sub>
-	-	-	-	-	-	-	-	318	
-	-	-	-	345	-	350	-	345	
-	-	-	-	-	-	-	-	374	Symmetric Mg-OH vibrations
388	385	384	380	389	375	388	389	388	Symmetric v <sub>5(e)</sub> SiO <sub>4</sub>
-	-	-	-	-	-	-	432	432	Antisymmetric Mg-OH translation
-	-	-	-	-	-	-	-	458	v <sub>3(a1)</sub> SiO <sub>4</sub>
-	-	-	-	-	-	-	-	466	Mg-OH translation + v <sub>6(e)</sub> SiO <sub>2</sub>
(525)	(526)	-	530	-	520	510 (506,	-	-	SiO <sub>4</sub> - AlO <sub>4</sub> deformation modes
-	-	-	-	-	-	-	-	607	Vibration of inner Mg-OH
-	-	-	-	620	-	-	-	622	Antisymmetric OH-Mg-OH translation
-	-	-	-	-	-	-	-	629	
-	-	-	-	-	635	630	-	-	
694	690	693	690	692	683	690	-	692	vs Si-Ob-Si
-	-	-	-	-	-	-	-	705	Mg-OH outer symmetric translation
-	-	-	-	-	-	-	-	709	modes
-	-	-	1050	-	1044	-	-	-	v a Si-Ob-Si
-	-	-	-	1105	-	1096	-	1102	v as Si-Onb
-	-	-	3660	-	-	-	-	3643	Inner OH-stretch
-	-	-	-	-	-	-	-	3678	OH-stretch
-	3687	3691	-	-	-	-	-	3686	
3699	3705	3702	3700	-	-	-	-	3696	External OH-stretch

Liz: lizardite, Ctl: chrysotile, Pol: polygonal serpentine, Atg: antigorite  
(1) Klopogge et al. (1999), (2) Lewis et al. (1996), (3) Rinaudo et al. (2003)

**Table 2.5:** Raman band positions ( $\text{cm}^{-1}$ ) of Fe-rich and Mg-rich brucite from Mariana mantle wedge serpentinites in comparison to literature data.

Fe(OH) <sub>2</sub>	Mg(OH) <sub>2</sub>	Fe(OH) <sub>2</sub>	Mg(OH) <sub>2</sub>
	<u>This study</u>		<u>Literature data</u>
281	281	260 (1)	280 (4,5) 360 (5) 384 (5)
		407 (1)	408 (5)
444	444		443 (4) 445 (5)
531			
705			725 (4) 728 (5)
3640	3638	3573 (1) 3572 (2)	3655 (3) 3652 (5)
3649		3576 (1)	3661 (5)

(1) Lutz et al. (1994), (2) Speziale et al. (2005), (3) Kruger et al. (1989),  
(4) Dawson et al. (1973), (5) Duffy et al. (1995).

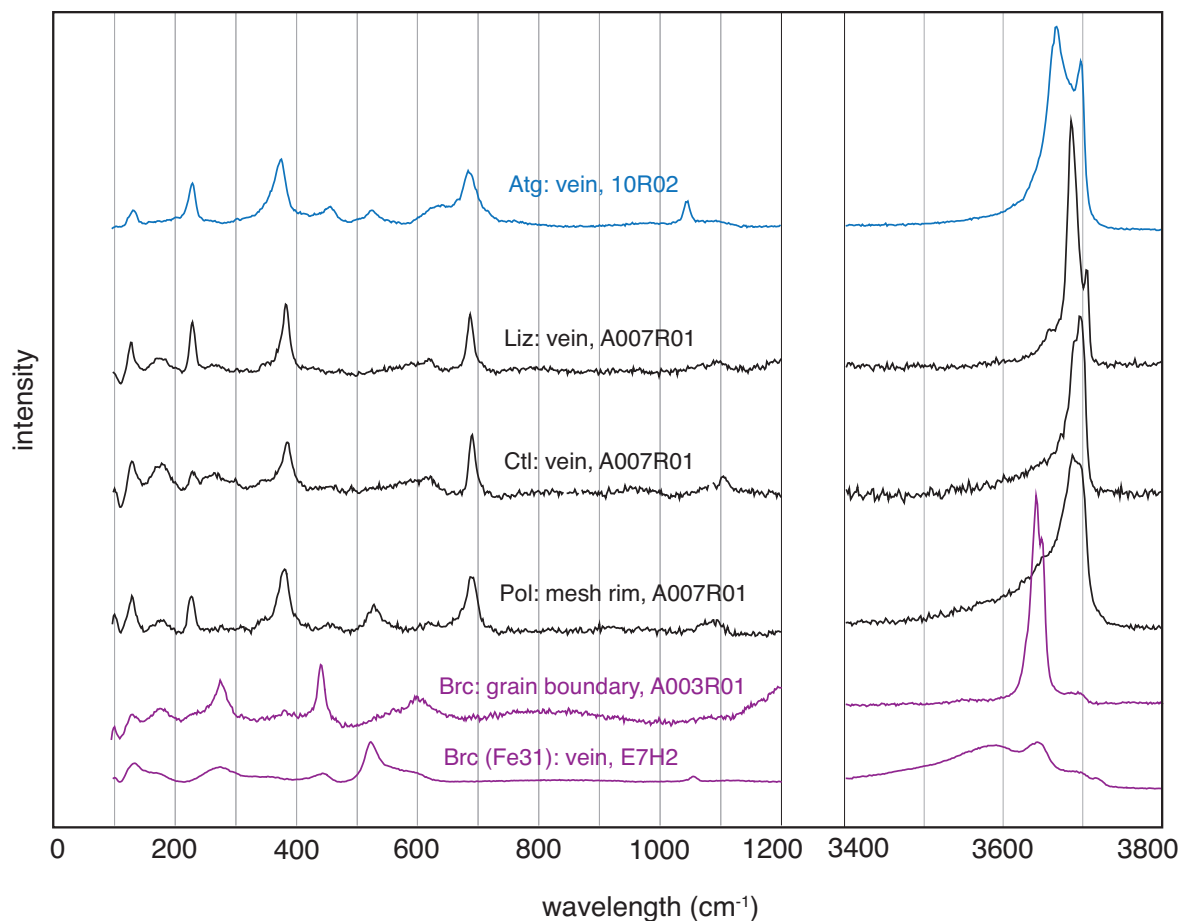


**Fig. 2.5:** Examples of micro-Raman spectra for the serpentine polymorphs antigorite (Atg), lizardite (Liz), chrysotile (Ctl), polygonal serpentine (Pol), and brucite (Brc). Most indicative for serpentine polymorphs are the OH-sensitive Raman bands between 3500 and 3800  $\text{cm}^{-1}$ . Brucite can be clearly distinguished from serpentine by a lower wavenumber OH-sensitive band ( $\sim 3649 \text{ cm}^{-1}$ ) and bands at 281 and 444  $\text{cm}^{-1}$ . If brucite is Fe-rich (amakinite endmember), additional strong bands at 531  $\text{cm}^{-1}$  and 3649  $\text{cm}^{-1}$  appear. Hence, brucite or amakinite admixtures to serpentine can be easily identified. Additional spectra can be found in Appendix B5.

## Chapter 3

### Evidence for boron incorporation into the serpentine crystal structure

#### 3.1 Introduction

Boron (B) is a highly fluid-mobile trace element incompatible during high temperature magmatic processes. Hence, B contents and B isotope composition of fluids and a wide variety of rocks (*e.g.*, high-pressure metamorphics, mantle wedge peridotites, trench sediments, arc and backarc volcanics) have been used as records for the elemental and isotope recycling processes and mass fluxes during subduction (*e.g.*, Smith *et al.*, 1995; Ryan *et al.*, 1996b; Palmer & Helvacı, 1997; Benton *et al.*, 2001; Tonarini *et al.*, 2001; Snyder *et al.*, 2005; Marschall *et al.*, 2006; Savov *et al.*, 2007;). Aqueous fluids released from the subducting slab can serpentinize the overlying depleted mantle; recent studies on variably serpentinized Mariana peridotites, exhumed at large serpentinite seamounts drilled during ODP Legs 125 and 195, give evidence that, within supra subduction zones, forearc serpentinites are a major sink for various trace elements such as B, Li, As, Sb, I and Cs (*e.g.*, Fryer *et al.*, 1990; Benton *et al.*, 2001; Mottl *et al.*, 2003; Savov *et al.*, 2007). Since primary minerals in serpentinized peridotites, such as olivine and pyroxene, are virtually devoid of B, minerals of the serpentine group (*e.g.*, chrysotile, lizardite and antigorite) have been presumed to be the main B sink in ultramafic rocks (*e.g.*, Bonatti *et al.*, 1984; Benton *et al.*, 2001; Ottolini *et al.*, 2004). Nonetheless, it remained still unclear, if and where B can be fixed in the serpentine crystal structure.

Serpentine [ $\text{Mg}_3\text{Si}_2\text{O}_5(\text{OH})_4$ ] is a tri-octahedral sheet silicate made up of stacked layers of a pseudo-hexagonal network of linked  $\text{SiO}_4$  tetrahedra with a joining brucite-like  $[\text{Mg}(\text{OH})_2]$  layer (Deer *et al.*, 1992). Boron hosted in-between the serpentine sheets, along grain boundaries or in microfractures would be leached out by infiltrating fluids at any temperature, while B incorporated in the serpentine crystal structure would only be released through serpentine recrystallization or breakdown reactions having major implications for B recycling and geodynamic models in subduction zones.

We have examined serpentine from Mariana mantle wedge serpentinites using micro-Raman spectroscopy, secondary ion mass spectrometry (SIMS) spot analysis traverses and time-of-flight (ToF)-SIMS elemental imaging. While it is impossible to examine single B atoms in a crystal structure, we combine these high spatial resolution methods and present, for the first time, evidence that B can indeed be sited in the serpentine crystal structure.

#### 3.2 Analytical Techniques

To study the B incorporation into serpentine minerals on a micron scale, thoroughly cleaned, coarse-grained and well-crystallized mineral grains are essential. Detailed optical and scanning electron microscopy, electron microprobe analyses and micro-Raman spectroscopy ensured later

analyses devoid of mineral inclusions (*e.g.*, magnetite), fractures and serpentine-brucite-intergrowths. We selected well-crystallized serpentine by large (>40  $\mu\text{m}$ ) serpentine areas showing optical continuity and sharp Raman spectral bands. For serpentine polymorph identification and crystallinity tests we applied the Horiba Jobin Yvon LabRam HR-UV 800 micro-Raman at the Universität Göttingen with a lateral resolution of <1  $\mu\text{m}$  using a 488 nm excitation source.

*In-situ* B and Li concentrations were determined with a modified Cameca ims 3f ion microprobe (magnetic sector SIMS) at the Universität Heidelberg, following procedures outlined in Marschall & Ludwig (2004). The lateral resolution of the SIMS analyses were  $\sim 5 \mu\text{m}$ . Accuracy for analyses is better than 10 % for B concentrations in excess of  $\sim 0.1 \mu\text{g/g}$ . Secondary ion images were performed with the ION-TOF TOF-SIMS IV instrument at the Smithsonian Institution in Washington D.C. with a lateral resolution of  $\sim 0.3 \mu\text{m}$ . The detection limits for B and Li are  $\sim 1 \mu\text{g/g}$ .

### 3.3 Petrography and mineral compositions

We selected two representative highly serpentinized (up to 80 %) harzburgite clasts ( $\sim 2 \text{ cm}$  in diameter) recovered from the South Chamorro Seamount during ODP Leg 195, Site 1200 (Salisbury *et al.*, 2002): 1200A-013R-01-25-27 (1-25 hereafter) drilled from depths of 108.95 mbsf (meters below sea floor) and 1200A-013R-02-12-15 (2-12 hereafter) from 110.07 mbsf. Olivine (avg Mg# 91.4) and enstatite are partly replaced by mesh textured serpentine and bastites (serpentine  $\pm$  brucite), respectively. Diopside and primary Cr-spinels (Cr#  $\sim 42\text{--}63$ ) are rare (<5 vol%) and much less affected by serpentinization. Both samples are crosscut by several generations of 1  $\mu\text{m}$  – 3 mm broad serpentine ( $\pm$  brucite) veins. Fine grained magnetite is enriched along former olivine grain boundaries and sporadically in serpentine mesh centers and veins. Serpentine major element compositions vary with textural type (Table 3.1); serpentine has Mg# of 81.8–95.3 in sample 1-25 and 84.6–94.9 in sample 2-12.

In this study we investigated i) a  $\sim 850 \mu\text{m}$  broad zoned serpentine vein (sample 1-25; Fig. 3.1a), intersected by ‘Frankenstein’-type veins (Fryer *et al.*, 1990), with a chrysotile marginal zone and a chrysotile and lizardite+spinel central zone (Table 3.1; Fig. 3.1 and 3.2), and ii) a serpentine area (sample 2-12; Fig. 3.1d) of homogeneous chrysotile mesh rims and lizardite mesh centers (Table 3.1; Fig. 3.1 and 3.2). All serpentine areas chosen for further detailed inspection are brucite-free.

The very sharp micro-Raman bands (Fig. 3.2) indicate a fully-crystalline serpentine structure (*e.g.*, Schenzel *et al.*, 2005; Strahm *et al.*, 2007). The optical continuity of the chrysotile vein and lizardite mesh center confirms the coarse-grained and well-crystallized character of the selected serpentines (Fig. 3.1b, c, e).



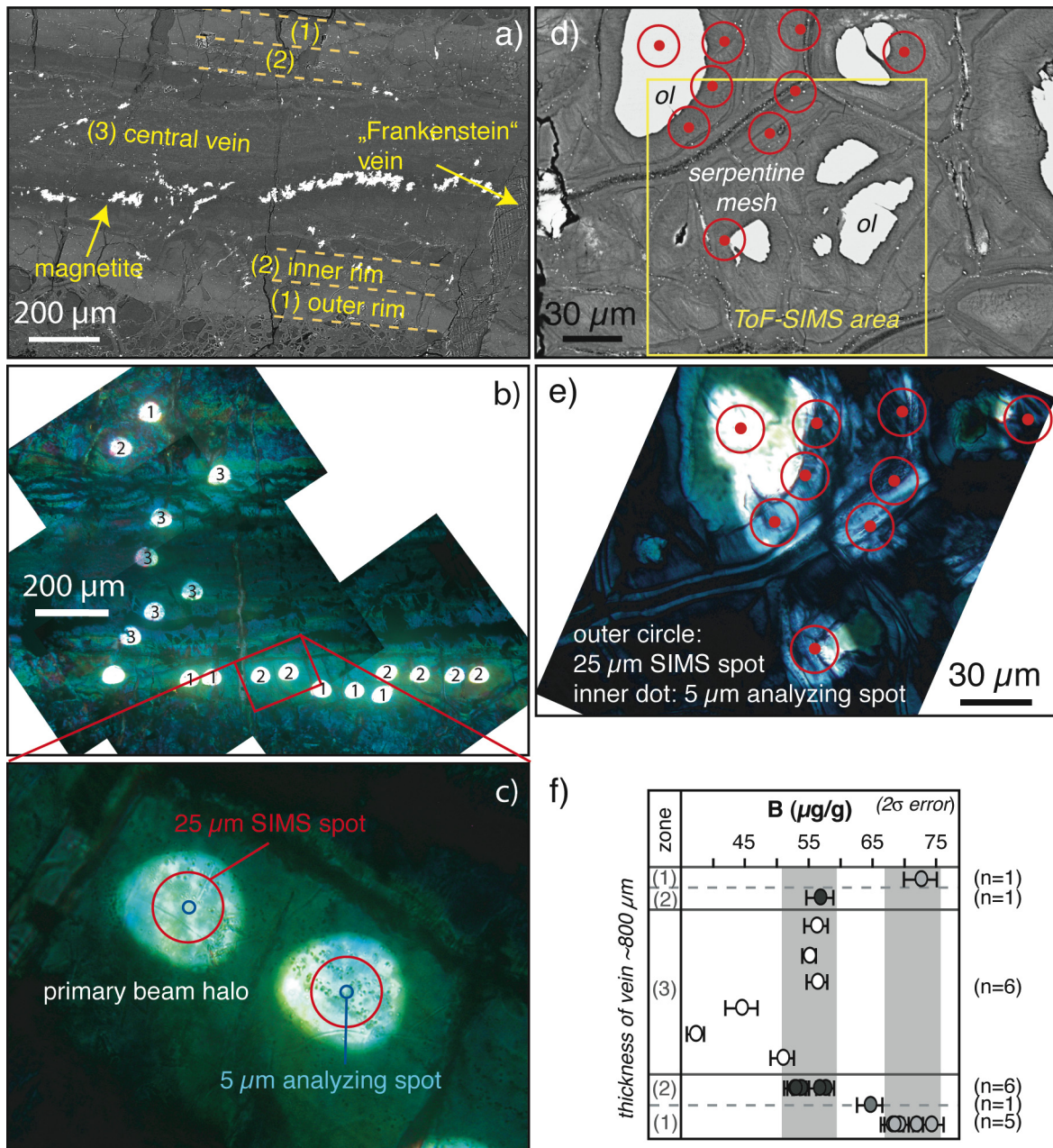


**Fig. 3.1:** **a)** Backscattered electron (BSE) image of a zoned serpentine vein ( $\sim 850 \mu\text{m}$  thick), intersected perpendicularly by 'Frankenstein'-type veins, sample 1-25. **b)** Optical microscope image (crossed polars) of a Au-coated thin-section with SIMS analyzing spots (bright). The two vein rim zones are optically continuous. Vein zones indicated by their respective numbers. **c)** Zoomed area of **b)** with SIMS analyzing spots within well-crystallized serpentine (optically continuous). Red circles:  $\sim 25 \mu\text{m}$  SIMS spots surrounded by a primary beam halo, blue circles:  $\sim 5 \mu\text{m}$  actual analyzing spots size. **d)** BSE image of serpentine mesh texture with relict olivine (white), sample 2-12. Yellow square: ToF-SIMS mapped area (cf. Fig. 3.3), red circles: SIMS spots. **e)** Optical microscope image (crossed polars) of a Au-coated thin-section with SIMS analyzing spots of optically continuous mesh centers. **f)** SIMS boron (B) concentrations. Compositions within the two chrysotile rim zones are homogenous along distance with (1) high B contents in the outer rim ( $\sim 76 \mu\text{g/g}$ ), (2) only  $\sim 60 \mu\text{g/g}$  B in the inner rim, and variable B-enrichment in the irregularly zoned vein centre with the lowest concentration in the lizardite + spinel zone.

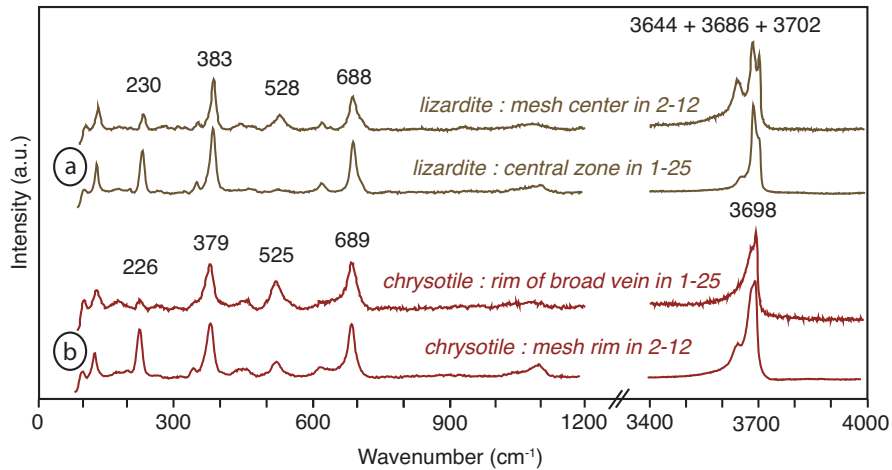


**Fig. 3.2:** Micro-Raman spectra of lizardite and chrysotile in different serpentine textures.

### 3.4 Intragrain boron distribution in serpentine

The serpentinite specimens in this study contain diverse serpentine textures with variable B concentrations ( $\sim 40\text{--}200\ \mu\text{g/g}$ ). The light element *in-situ* SIMS data (Table 3.1) reveal a homogeneous B distribution within large areas. The broad vein in sample 1-25 contains substantial amounts of B (Fig. 3.1f); the vein rim can be divided into a high-B ( $\sim 76\ \mu\text{g/g}$ ) and an intermediate-B ( $60\ \mu\text{g/g}$ ) zone (Fig. 3.1f). The vein centre is erratically zoned and has lower B concentrations ( $42\text{--}61\ \mu\text{g/g}$ ); here, the lowest B abundances appear to be associated with lizardite. SIMS traverses in the chrysotile vein rim zones show that along distances of up to  $\sim 1\ \text{mm}$  the B compositions are homogeneous (see discussion; Table 3.2). The lizardite mesh centers in sample 2-12 have constant high B concentrations of  $\sim 200\ \mu\text{g/g}$ . The thin mesh rims (and former grain boundaries) show intermediate B contents ( $\sim 85\ \mu\text{g/g}$ ). However, the B concentrations in relict olivine are very low ( $0.1\ \mu\text{g/g}$ ), consistent with the B-poor nature of mantle peridotites ( $0.07\text{--}0.1\ \mu\text{g/g}$ ; Ottolini *et al.*, 2004).

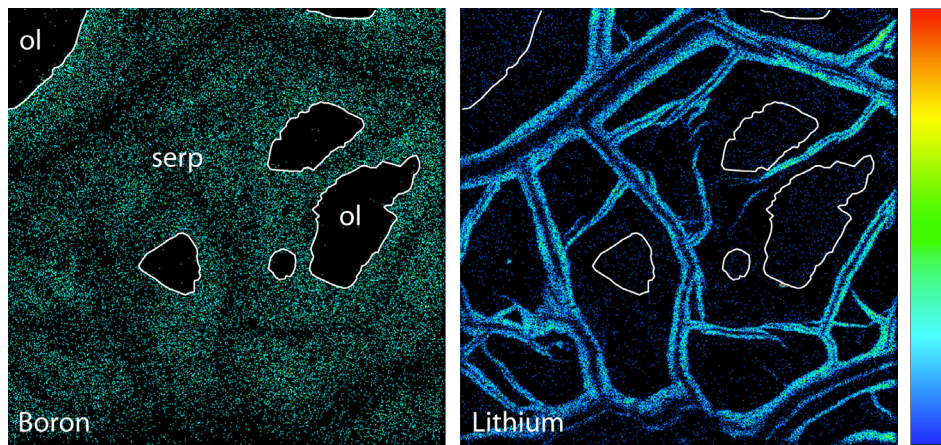


**Fig. 3.3:** ToF-SIMS false color elemental maps of a  $150\times 150\ \mu\text{m}$  mesh texture pseudomorphing olivine, sample 2-12. B is homogeneously distributed in the serpentine (mesh centers), while Li is only enriched in thin mesh rims along former olivine grain boundaries. Olivine (indicated by white contours) is extremely B-poor. The scale to the right represents the number of ions counted (increasing from bottom to top).

The light element ToF-SIMS images of the area containing lizardite replacing olivine in sample 2-12 (Fig. 3.1d and Fig. 3.3) is in agreement with the B (and Li) concentrations from SIMS spot analyses: B is homogeneously distributed within the serpentinized area at high concentrations (apart from former grain boundaries), whereas Li, shown for contrast, is enriched only in the thin mesh rims along former grain boundaries (Li  $\sim$ 6  $\mu$ g/g; Table 3.1, Fig. 3.3). A relatively heterogeneous Li distribution in serpentinites was already observed by Benton *et al.* (2004) and explained by a Li ‘concentration front’ with highest concentrations near serpentine veins. Relict olivine is extremely depleted in Li and B.

**Table 3.1:** Representative electron microprobe analyses and in-situ Li and B SIMS data of selected mineral phases of the serpentinized peridotites investigated from South Chamorro Seamount.

	hole-core-section-interval							
	A-013R-01-25-27 108.95 (mbsf)*				A-013R-02-12-15 110.07 (mbsf)*			
	vein - center	vein - rim	olivine	Cr-spinel	mesh center	mesh rim	olivine	Cr-spinel
(wt%)								
SiO <sub>2</sub>	41.40	41.04	41.21	0.00	39.66	40.79	41.18	0.01
TiO <sub>2</sub>	0.00	0.01	0.00	0.02	0.01	0.01	0.00	0.02
Al <sub>2</sub> O <sub>3</sub>	0.15	0.22	0.01	24.09	0.02	0.01	0.00	19.37
Cr <sub>2</sub> O <sub>3</sub>	0.00	0.01	0.00	43.14	0.00	0.00	0.00	47.65
FeO	3.65	7.14	8.15	20.53	4.98	4.79	8.34	24.12
MnO	0.05	0.14	0.08	0.06	0.02	0.06	0.07	0.21
MgO	39.03	36.33	50.67	11.12	39.81	38.44	50.33	8.95
CaO	0.18	0.21	0.02	0.00	0.15	0.22	0.00	0.01
Na <sub>2</sub> O	0.05	0.08	0.02	0.03	0.02	0.03	0.00	0.01
K <sub>2</sub> O	0.01	0.02	0.00	0.01	0.01	0.00	0.00	0.00
NiO	0.04	0.06	0.39	0.07	0.41	0.13	0.43	-
Total	84.56	85.25	100.53	99.07	85.07	84.47	100.35	100.34
oxygens	14	14	4	4	14	14	4	4
Si	4.01	4.01	1.00	0.00	3.86	3.98	1.00	0.00
Ti	0.00	0.00	0.00	0.00	0.00	0.00	0.00	0.00
Al	0.02	0.03	0.00	0.89	0.00	0.00	0.00	0.73
Cr	0.00	0.00	0.00	1.07	0.00	0.00	0.00	1.21
Fe <sup>2+</sup>	0.30	0.58	0.16	0.54	0.41	0.39	0.17	0.65
Mn	0.00	0.01	0.00	0.00	0.00	0.00	0.00	0.01
Mg	5.63	5.30	1.82	0.52	5.78	5.59	1.82	0.43
Ca	0.02	0.02	0.00	0.00	0.02	0.02	0.00	0.00
Na	0.01	0.01	0.00	0.00	0.00	0.01	0.00	0.00
K	0.00	0.00	0.00	0.00	0.00	0.00	0.00	0.00
Ni	0.01	0.02	0.03	0.01	0.14	0.04	0.04	0.00
sum	10.00	9.99	3.02	3.03	10.21	10.04	3.02	3.03
Mg#	94.95	89.88	91.66		93.42	93.39	91.44	
Cr#				54.58				62.27
Li ( $\mu$ g/g)	0.49	7.90	1.26	N.D. <sup>#</sup>	0.44	6.24	1.24	N.D. <sup>#</sup>
B ( $\mu$ g/g)	56.0	76.8	0.10	N.D. <sup>#</sup>	196.8	85.4	0.11	N.D. <sup>#</sup>

\*mbsf = meters below sea floor.  
<sup>#</sup> N.D. = not determined.

### 3.5 Discussion and Conclusion

The high spatial resolution ToF-SIMS boron distribution mapping reveals, within counting statistics, (i) absence of heterogeneities caused by B-rich inclusions, (ii) absence of B-enrichments in small voids, fractures or grain-boundaries on a submicrometer-scale, and (iii) a homogeneous B distribution within serpentine (Fig. 3.3).

A measure of homogeneity can be obtained by comparing the scatter in the SIMS dataset (lateral and depth) with the (statistical) variation that can be expected for a homogenous sample. (i) Depth or single spot variation. (Dynamic) SIMS is an in-depth analysis, where in the course of a single analysis with  $N$  cycles (here  $N = 10$ ) the sample is successively analyzed in deeper regions; typically 0.2–1  $\mu\text{m}$  deep. The relative standard error of the mean ( $RSEM$ ) of a single flawless  $N$ -cycle analysis on a perfectly homogeneous sample can be predicted by counting statistics:  $RSEM_{\text{count}} = 1/\sqrt{m}$ , where  $m$  is the total number of B ions that were counted. For multiple, flawless analyses on such a sample the average ratio  $r = RSEM/RSEM_{\text{count}}$  has to be  $r_{\text{mean}} = 1$ . For all B analyses of the zoned vein in sample 1-25, the average ratio is  $r = 0.92 \pm 0.21$  ( $1\sigma$ ). (ii) Lateral or spot-to-spot variation. For multiple flawless  $N$ -cycle analyses on a perfectly homogeneous sample, the standard deviation  $SD$  has to be equal to the average standard error of the mean ( $SEM$ ) of these analyses:  $SD = SEM_{\text{mean}}$ . The analyses of the outer vein rim ( $n=6$ ) yield an average B concentration of  $75.8 \pm 2.5 \mu\text{g/g}$  ( $SEM = 0.93 \mu\text{g/g}$ ) and of the inner vein rim ( $n=7$ )  $60.0 \pm 2.1 \mu\text{g/g}$  ( $SEM = 0.72 \mu\text{g/g}$ ). In both cases  $SD$  is only slightly higher than  $SEM_{\text{mean}}$ , indicating minor inhomogeneities ( $\leq 3\%$ ) within these regions (Table 3.2).

Both *in-situ* SIMS traverses and ToF-SIMS mapping display an even boron distribution in single serpentine crystals. Hypothetically, the serpentine structure itself could be B-free and such homogeneous B distribution could result from periodic B-rich interlayers between the  $\sim 7 \text{ \AA}$  thick serpentine sheets. While this is not resolvable by *in-situ* SIMS analyses, TEM (transmission electron microscopy) imaging is capable to show variations in the serpentine sheet spaces. Serpentine from B-rich serpentinites (10–50  $\mu\text{g/g}$ ; King *et al.*, 2004) from the Santa Ynez Fault in the Franciscan subduction mélangé (California) was examined by TEM and present regularly spaced serpentine layers without non-serpentine interlayers or inclusions (Andreani *et al.*, 2004).

By analogy, we can assume that B distribution in the form of B-rich interlayers is unlikely for the studied Mariana forearc serpentines. Furthermore, chrysotile nanotubes have been shown to accumulate Cl (Brearley *et al.*, 2007). Although B concentrations differ between serpentine textures and serpentine polymorphs in Mariana forearc serpentinites, particularly high and homogeneously distributed B contents were found in both chrysotile (nanotubes, cylindrical structure) and lizardite (planar structure). Hence, it is unlikely that chrysotile nanotubes are the dominant site for B, although small amounts of nanotube-bound B cannot be precluded.

Examination of a variety of serpentine textures by micro-Raman spectroscopy and high spatial resolution ToF-SIMS ion imaging and *in-situ* SIMS shows that B concentrations are not caused by (i) B hosted on mineral surfaces in cracks, (ii) interlayers or nanotubes, or (iii)  $\mu\text{m}$ -scale B-rich

“clusters”. Rather, our results consistently indicate that B resides in the serpentine crystal structure. Since brucite coexisting with serpentine in Mariana forearc serpentinites is B-poor ( $\sim 1.4 \mu\text{g/g}$  B; see 4.4.2), we reason that brucite-like layers cannot assign the highly enriched boron concentrations in serpentine.

Due to its small ionic size and high charge (+3), B should favor the crystallographic site of silica (Si) or aluminum (Al). In sheet silicates like borocookeite (a chlorite group mineral) and boromuscovite (mica), B partly replaces Al in tetrahedral coordination ( $^{41}\text{Al}$ ) (Foord *et al.*, 1991; Zagorsky *et al.*, 2003), in manandonite (another chlorite group mineral)  $\text{B}^{3+}$  predominantly enters the  $^{41}\text{Si}^{4+}$  site (Ranoroosa *et al.*, 1989). Compared to sheet silicates, nesosilicates like olivine have less stretched crystal structure and exotic trace elements cannot fit well. However, Kent & Rossman (2002) indicated a B-Si substitution in an unusual B-enriched ( $>10 \mu\text{g/g}$ ) olivine.

**Table 3.2:** SIMS B concentrations in the zoned vein in sample 2-12 with predicted error, standard deviation of the mean and their ratio.

zone	analysis	B concentration ( $\mu\text{g/g}$ )	std. dev. of the mean ( $N=10$ cycles) <i>RSEM</i>	predicted error <i>RSEM</i> <sub>count</sub>	$r =$ <i>RSEM</i> / <i>RSEM</i> <sub>count</sub>
outer rim	A013R01-54	77.67	1.67%	1.31%	1.27
inner rim	A013R01-53	61.87	1.71%	1.49%	1.14
zoned central vein	A013R01-52	61.29	1.49%	1.50%	0.99
zoned central vein	A013R01-51	60.19	0.86%	1.57%	0.55
zoned central vein	A013R01-50	61.41	1.31%	1.76%	0.74
zoned central vein	A013R01-49	49.56	2.55%	2.03%	1.25
zoned central vein	A013R01-48	42.34	1.60%	1.90%	0.84
zoned central vein	A013R01-47	56.00	1.64%	1.53%	1.07
inner rim	A013R01-45	61.76	1.32%	1.36%	0.97
inner rim	A013R01-44	57.98	1.49%	1.50%	0.99
inner rim	A013R01-43	62.71	1.13%	1.33%	0.85
inner rim	A013R01-42	57.80	0.89%	1.37%	0.65
inner rim	A013R01-38	58.88	1.12%	1.30%	0.86
inner rim	A013R01-37	58.72	0.77%	1.27%	0.60
mixed analysis	A013R01-46	69.70	1.42%	1.37%	1.04
outer rim	A013R01-36	73.51	1.03%	1.12%	0.92
outer rim	A013R01-35	73.18	1.18%	1.16%	1.02
outer rim	A013R01-41	79.32	1.25%	1.20%	1.04
outer rim	A013R01-40	74.27	1.51%	1.48%	1.02
outer rim	A013R01-39	76.92	0.72%	1.15%	0.63
<b>inner rim</b>					
	average	59.96	1.20%	1.37%	0.87
	<i>SD</i>	2.07	0.33%	0.09%	0.19
	<i>RSD</i>	3.45%			
	<i>SEM</i> <sub>count</sub>	0.72			
<b>outer rim</b>					
	average	75.81	1.23%	1.24%	0.98
	<i>SD</i>	2.51	0.34%	0.14%	0.21
	<i>RSD</i>	3.31%			
	<i>SEM</i> <sub>count</sub>	0.93			

Our results strongly indicate that B is directly incorporated into the serpentine crystal structure in tetrahedral coordination ( $^{14}\text{B}$ ) by the coupled substitution  $\text{B}(\text{OH})(\text{Si}^{4+}, \text{Al}^{3+})_{-1}\text{O}_{-1}$ . The mechanism of B incorporation into serpentine is independent of the degree of serpentinization, and also of serpentine polymorph or textural type. Being structurally bound into serpentine, B can only be extracted from serpentinized peridotites at high temperatures, which has major implications for B distributions, transfer mechanisms between deep source rocks (<60 km) within subduction zones and for modeling of the efficiency of cross arc fluid mobile element recycling in the Marianas and in other subduction zones with highly hydrated forearc mantle.

## Chapter 4

# Serpentinization of the Mariana forearc mantle wedge: light elements as tracers for the hydration history

### 4.1 Introduction

The serpentinite mud volcanoes situated on the extant oceanic forearc of the Izu-Bonin-Mariana (IBM) subduction zone are entities where serpentinitized peridotites can be studied. They represent supra subduction zone mantle wedge material serpentinitized by fluids derived from the dehydrating slab. The samples for this study are from suite of rocks recovered by drilling of South Chamorro and Conical Seamounts during Ocean Drilling Programs (ODP) Leg 195 and Leg 125. Most of the samples are rock fragments (clasts) and small in size, bedded in serpentine mud matrix. Therefore, interpretation of serpentinitization environments and emplacement in the mantle wedge are ambiguous.

This chapter begins with the petrology, mineralogy and major element composition of serpentinites by micro-Raman and electron microprobe analyses. The main focus of the study lies on the light element geochemistry (Li, Be, B) and boron isotope ( $\delta^{11}\text{B}$ ) composition of serpentine minerals. A great amount of these serpentinites were investigated for bulk geochemistry including light element and isotopic studies (Benton *et al.*, 2001; Savov *et al.*, 2004, 2007). These studies emphasize the importance of Li-B- $\delta^{11}\text{B}$  analyses to understand element transport in active subduction zones. Therefore, the high-resolution investigation of the light element distribution via ToF-SIMS and SIMS in various serpentines and textures will allow a better understanding of the complex nature of serpentinitization, the behavior of light elements and B isotope evolution during serpentinitization of the mantle wedge. Furthermore, correlations between serpentine polymorph – textural site – composition will be evaluated. These results will shed light on the nature and evolution of forearc mantle serpentinitization in the intra-oceanic supra subduction zone environment of the Marianas.

### 4.2 Petrography of serpentinites and serpentine textures

This section gives a description of serpentinitized peridotite fragments from different drill holes and sections (*i.e.*, different depths) within the serpentinite mud volcanoes South Chamorro Seamount (ODP Leg 195, Site 1200) and Conical Seamount (ODP Leg 125, Site 779) on the Mariana forearc. The majority of samples are derived from South Chamorro Sites 1200A and 1200E. The rocks exhibit various stages of serpentinitization. They are medium to heavily serpentinitized (~ 40–100 %) with generally lower degrees of serpentinitization in the larger clasts (several cm in diameter). Serpentinites are rocks composed of serpentine minerals, accessory magnetite, brucite and restitic primary Mg- and Ca-Al-silicates. In the samples studied these primary mantle minerals are preserved: orthopyroxene (Opx), clinopyroxene (Cpx), olivine (Ol) and spinel (Spl). Stronger serpentinitized clasts are weaker and broken into smaller pieces. In handspecimen and thinsections, the less serpentinitized peridotites have dark green color. Samples change to orange-brown color with increasing degree of

serpentinization and amount of brucite-rich veins. All larger harzburgite clasts have massive porphyroclastic fabrics. Foliation or deformation textures with some clastic disruptions can be observed only in some small completely serpentinized fragments (*e.g.*, E7H2).

The estimated original modal mineralogy of the rocks (for modal estimates only clasts >1 cm were used) is 75–99 % Ol, up to 20 % Opx, up to 5 % Cpx and up to 5 % Spl (Table 4.1). This mineralogy is typical for spinel harzburgite and dunite, visually presented in the ternary Ol-Opx-Cpx CIPW normative classification diagram for peridotites in Fig. 4.1 (orange field). Previous geochemical analyses of serpentinites from Site 1200 have shown that the serpentinite protoliths are dominantly harzburgites with minor dunites (and one lherzolite; Shipboard Scientific Party, 2002c; blue dots in Fig. 4.1).

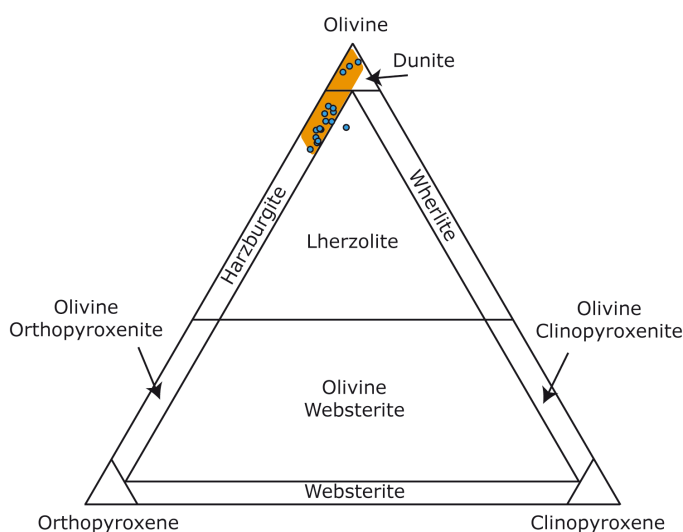
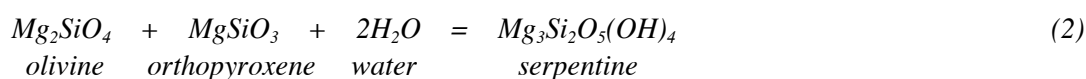
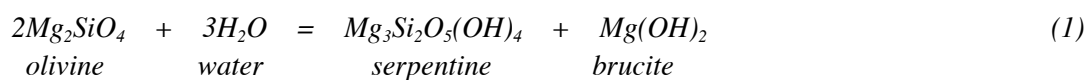


**Fig. 4.1:** CIPW normative compositions of serpentinites from Site 1200 plotted in the International Union of Geological Societies (IUGS) classification system for ultramafic rocks. Most of the Site 1200 clasts are harzburgites or dunites. Orange field: visually estimated composition of samples in this study, blue dots: results from Shipboard Scientific Party (2002c).

The formation of serpentine can be described by a number of general reactions including olivine and orthopyroxene (*e.g.*, Johannes, 1967, 1968; Allen & Seyfried, 2003; Evans, 2004). In a purely magnesian system, the reactions most commonly referred to are:



In an iron containing system, the serpentinization reaction leads to the formation of secondary spinel, *i.e.*, magnetite. It is present as small opaque grains. The serpentinization reaction including magnetite can be written as (*e.g.*, Mével, 2003):

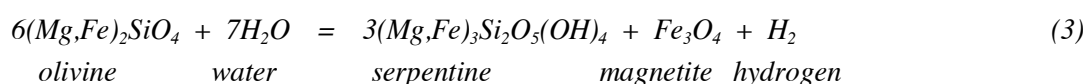




**Table 4.1:** List of studied serpentinite fragments with visually estimated mineral modes (vol%).

Site	Core and Section	Interval and piece number	Depth	Ø	Srp	Ol	Opx	Cpx	Cr-Al-Spl	Brc
<b>125-</b>										
779A	10R-02	33-34 #1	79.26	15	98	-	-	-	2	x
779A	26R-02	72-75 #1	208.16	17	99	-	-	-	1	x
779A	34R-01	62-64 #1	284.32	15	98	-	-	-	2	x
<b>195-</b>										
1200A	003R-01	81-84 #1	19.01	20	75	14	5	1	5	x
1200A	007R-01	4-6 #1	51.14	20	17	54	7	<1	2	x
1200A	007R-02	3-5 #1	51.72	18	71	25	2	<1	2	x
1200A	007R-02	40-42 #1	52.09	17	71	10	10	3	1	5
1200A	009R-01	6-8 #1	70.46	17	79	-	10	-	1	10
1200A	010R-01	95-97 #1	80.85	19	96	-	-	2	2	x
1200A	011R-01	40-42	89.80	17	80	-	-	-	<1	20
1200A	011R-01	69-72	90.09	16	73	20	5	<1	1	x
1200A	012R-01	3-5	108.73	16	52	32	12	4	<1	x
1200A	013R-01	25-27	108.95	17	79	12	6	<1	1	2
1200A	013R-01	90-92	109.60	16	70	26	-	2	2	x
1200A	013R-02	12-15	110.07	19	80	20	-	-	<1	x
1200A	015R-01	11-13	128.01	20	69	-	-	-	1	30
1200A	017G-02	76-79	> 147.20	17	51	40	3	1	5	x
1200E	005H-02	81-83	19.86	18	98	-	-	-	1	1
1200E	010H-02	63-65	54.53	14	80	-	-	-	<1	20
1200D	001H-04	130-140 #1c	5.80	6	88	-	-	-	2	10
1200D	001H-04	130-140 #3f	- "	7	93	-	-	-	2	5
1200D	001H-04	130-140 #4f	- "	4	97	-	-	-	3	-
1200D	001H-04	130-140 #4g	- "	3	100	-	-	-	-	x
1200D	001H-04	130-140 #6a	- "	13	100	-	-	-	-	x
1200D	003H-01	130-140 #6a	11.20	4	75	5	-	-	-	20
1200E	001H-03	130-140 #1C	4.30	6	95	-	-	-	5	x
1200E	001H-03	130-140 #2H	- "	5	95	-	-	-	-	5
1200E	001H-03	130-140 #3C	- "	3	95	-	-	-	-	5
1200E	004H-01	130-140 #1C	13.30	6	100	-	-	-	sulfide	x
1200E	004H-01	130-140 #1D	- "	6	99	-	-	-	1	x
1200E	004H-01	130-140 #4	- "	9	94	5	-	-	1	x
1200E	004H-02	130-140 #1	14.80	12	95	-	-	-	<1	5
1200E	004H-02	130-140 #2D	- "	4	100	-	-	-	<1	x
1200E	004H-02	130-140 #4	- "	12	80	-	-	-	<1	20
1200E	004H-02	130-140 #5D	- "	3	95	-	-	-	-	5
1200E	004H-02	130-140 #6	- "	15	56	15	15	2	2	10
1200E	007H-02	130-140 #1c	28.70	6	94	-	-	-	1	5
1200E	007H-02	130-140 #2b	- "	6	80	-	-	-	-	20 vein
1200E	007H-02	130-140 #2c	- "	8	80	-	-	-	-	10
1200E	007H-02	130-140 #2e	- "	5	100	-	-	-	<1	x
1200E	007H-02	130-140 #3b	- "	9	95	-	-	-	<1	5
1200E	007H-02	130-140 #3e	- "	8	80	-	-	-	-	20
1200E	007H-02	130-140 #4	- "	24	83	5	10	2	<1	x
1200E	007H-02	130-140 #5a	- "	5	99	-	-	-	-	1
1200E	007H-02	130-140 #5b	- "	6	95	-	-	-	-	5
1200E	007H-02	130-140 #7a	- "	5	100	-	-	-	-	x
1200E	007H-02	130-140 #8d	- "	2	95	-	-	-	-	5
1200E	007H-02	130-140 #8g	- "	2	94	-	-	-	1	5
1200E	007H-02	130-140 #8m	- "	2	100	-	-	-	-	x
1200E	007H-02	130-140 #8p	- "	2	85	-	-	-	10	5
1200E	007H-02	130-140 #8s	- "	2	100	-	-	-	-	x
1200F	002H-02	140-150 #2B	10.60	2.5	90	5	-	5	-	x

(x = only in traces)

The serpentine textures of the studied samples are described using the terminology of Wicks & Whittaker (1977). Serpentinization in the samples is pervasive (see Hébert *et al.*, 1990) and resulted in the formation of mesh texture after olivine (= **mesh rims** and **mesh centers**) and the formation of pseudomorphs after orthopyroxene (= **bastites**), both ‘replacing’ serpentinization (Fig. 4.2a–d). Furthermore, often due to stress in the mantle rock, in opening fissures serpentine crystallized in **veins**: in all serpentinite fragments several types and **generations of serpentine veins** cross the rock.

As the typical order of replacement is olivine - orthopyroxene - clinopyroxene - spinel, olivine appears to be the mineral most intensively serpentinized and, in some samples, is entirely altered into characteristic mesh textures with partly hourglass texture at the expense of olivine. Serpentinization starts along fractures (see veins) and **olivine** grain boundaries producing a mesh or web of serpentine veins separating (relict) olivine grains (*e.g.*, Shipboard Scientific Party, 1990d). Between such serpentine rims, *i.e.*, along the former olivine **grain boundaries**, thin serpentine veins or median lines are typically present, generally enriched in magnetite grains  $\pm$  brucite. These boundary veins outline crude polygons (Fig. 4.2a,b). In some samples, these polygons exhibit some distinct orientation (*e.g.*, E7H2-5B) and/or preferred orientation. Finally, areas of entirely serpentinized olivines exhibit tablets of mesh rim and mesh center serpentines. The pseudomorphing mesh rims can either be very thin and vein-like or quite broad around olivine. Fine-grained magnetite occasionally is concentrated in mesh centers, in rare cases, mesh centers are overgrown by brucite (Fig. 4.2c). Remnants of fresh olivine have irregularly rounded shape and the generally small crystals (‘neoblasts’) can exceed 200  $\mu\text{m}$  in diameter (with lobate grain boundaries).

Serpentinization of **orthopyroxene** begins along its exsolution lamellae (vein-like). Intensively serpentinized orthopyroxene is typically replaced by serpentine bastites  $\pm$  brucite with brucite-veins along the former cleavage planes. Relict orthopyroxene is irregularly shaped and often occurs as porphyroblasts (>1 mm; Fig. 4.2g,h). **Clinopyroxene** is less abundant (generally <5 vol%) and is hardly affected by the serpentinization. It has small grain size (<0.5 mm) with irregular shape and is often associated with orthopyroxene (Fig. 4.2d,g). Primary **spinel** is hardly serpentinized, but is irregularly rounded and the crystals have variable diameter of 0.1–2 mm (Fig. 4.2e,f). Only fragment D1H4-4F contains large spinel grains which reacted to surrounding serpentine coronas (Fig. 4.2s).

Some clinopyroxene occurs as interstitial discrete lobed to vermicular grains at triple junctions between (now serpentinized) olivine grains. These clinopyroxene grains may occur in symplectitic association with tiny grains of spinel (Fig. 4.2e,f,h) and sulfide (*e.g.*, Gréau *et al.*, 2007). Further observations are clinopyroxene-filled ‘en echelon’ microfractures that cross the serpentinized olivine matrix in discontinuous parallel veinlets extending over several millimeters, often linked by spinel veinlets (Fig. 4.2l). Sometimes, small clinopyroxene prisms or spindle-shaped grains grew on or replaced the thin and regular clinopyroxene exsolution lamellae within orthopyroxene (Fig. 4.2i,k). In some samples, serpentinization reached 100 % and even serpentinized the clinopyroxenes; these can be now identified by their former rounded and lobate shape (Fig. 4.2m,n).

Most orthopyroxene crystals have no exsolution lamellae and are partly serpentinized along their cleavage planes (Fig. 4.2d). Others have unserpentinized Cpx exsolution lamellae, even in the same

sample together with the Opx without exsolution lamellae (Fig. 4.2i,j). Kink-banding also can be observed in some orthopyroxenes (Fig. 4.2j).

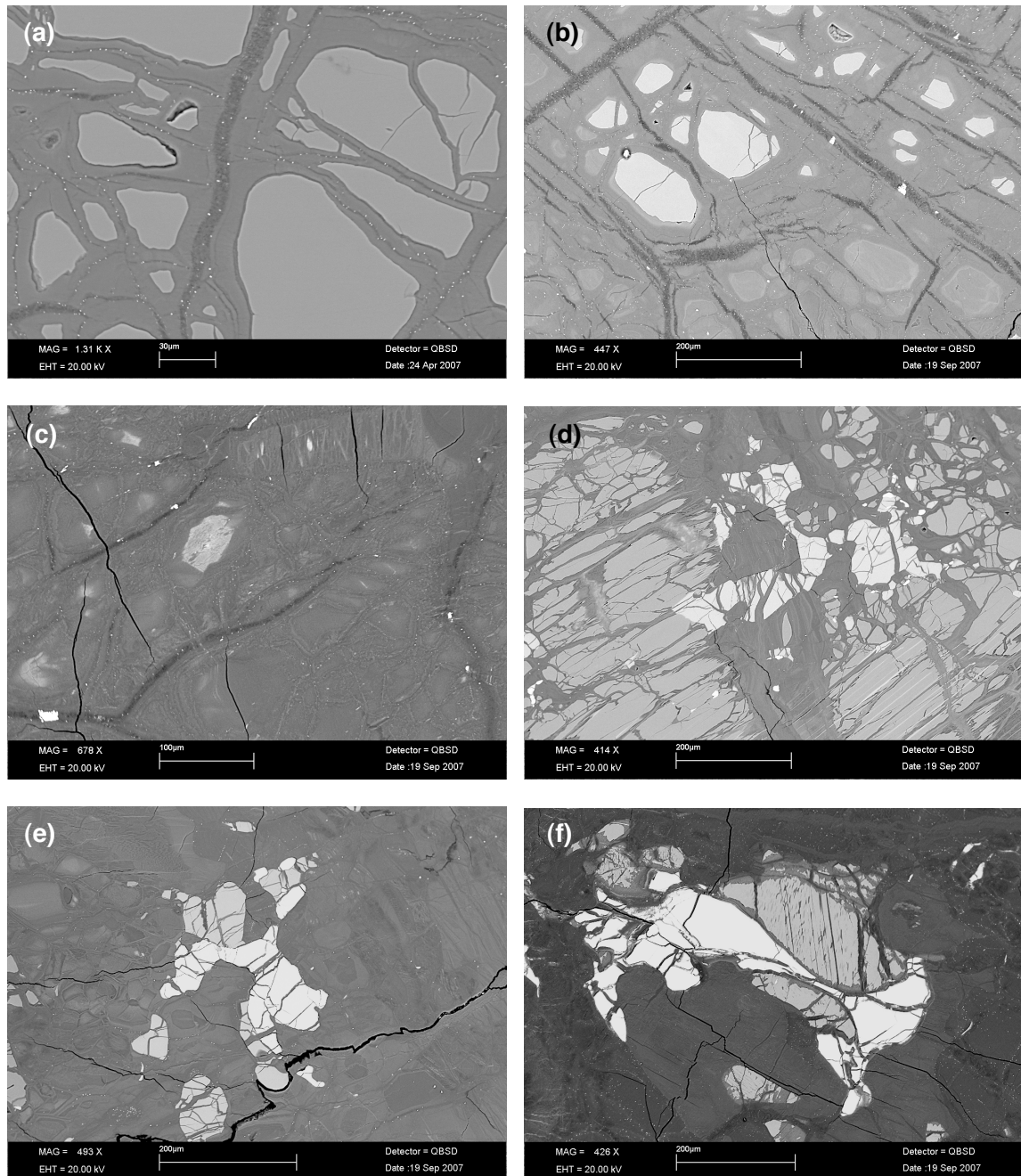


**Fig. 4.2:** Back-scattered electron (BSE) images of characteristic textures in serpentinites from the Mariana forearc mantle wedge.

- a)** Relict Ol cores (bright) surrounded by magnetite-free serpentine mesh rims and former grain boundaries with Mt (bright dots), sample A012R01(3-5),  
**b)** Transition between a partly serpentinized area with relict Ol (bright) and a completely serpentinized area (lower half), sample A003R01,  
**c)** Completely serpentinized brucite-rich area, the bright mesh center is amakinite, sample A011R01(40-42),  
**d)** Partly serpentinized Opx and Cpx (brighter phase in the centre), sample A007R01,  
**e)** Cpx with adjacent spinel (brighter phase in the centre) surrounded by mesh serpentine, sample A007R01,  
**f)** Cpx with adjacent spinel (brighter phase in the centre) surrounded by mesh serpentine, sample A010R01.

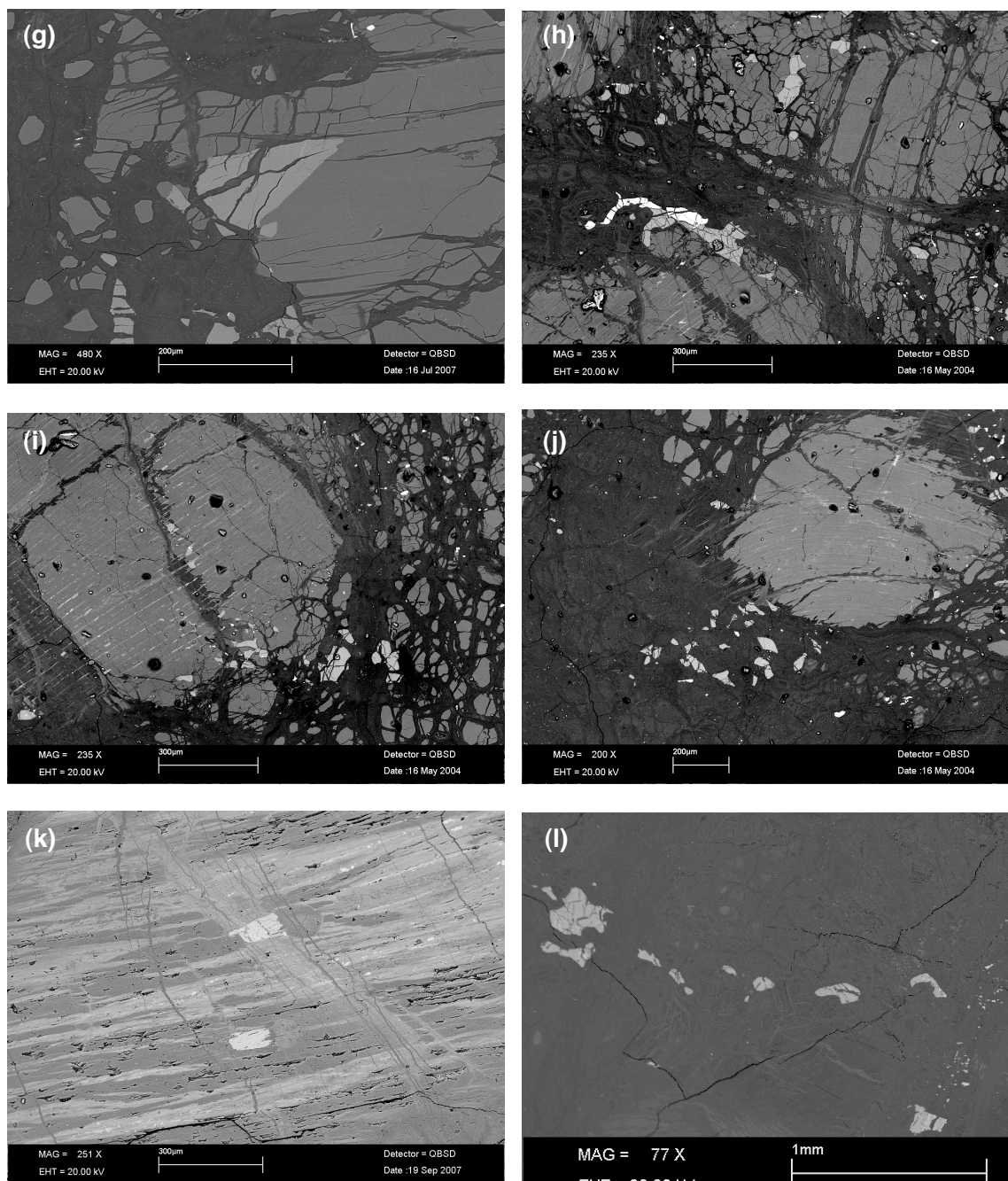


**Fig. 4.2 (continued):** BSE images of characteristic textures in serpentinites from the Mariana forearc mantle wedge.

- g)** Cpx in association with Opx, slightly serpentinized, sample A017G02,
- h)** Opx serpentinized along cleavage planes, Cpx exsolution lamellae in Opx (lower part), sample 7R01-4,
- i)** Cpx exsolution lamellae in Opx, sample 7R1-4,
- j)** Kink banding in Opx, sample 7R1-4,
- k)** Cpx crystals along serpentinized exsolution lamellae in Opx, sample A003R01,
- l)** Strings of spinel grains in mesh serpentine matrix, sample A012R01W.

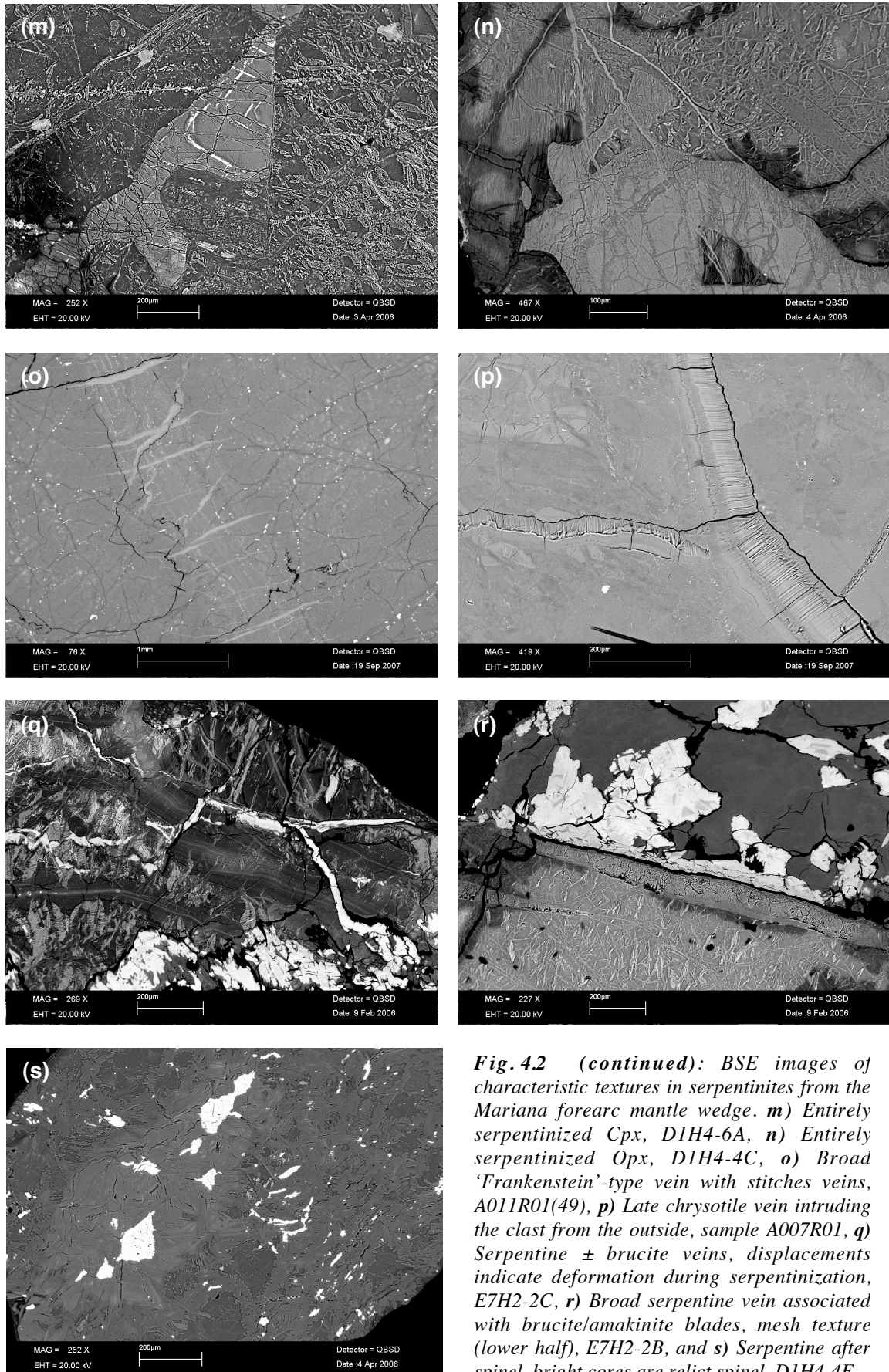


**Fig. 4.2 (continued):** BSE images of characteristic textures in serpentinites from the Mariana forearc mantle wedge. **m)** Entirely serpentinitized Cpx, DIH4-6A, **n)** Entirely serpentinitized Opx, DIH4-4C, **o)** Broad 'Frankenstein'-type vein with stitches veins, A011R01(49), **p)** Late chrysotile vein intruding the clast from the outside, sample A007R01, **q)** Serpentine ± brucite veins, displacements indicate deformation during serpentinitization, E7H2-2C, **r)** Broad serpentine vein associated with brucite/amakinite blades, mesh texture (lower half), E7H2-2B, and **s)** Serpentine after spinel, bright cores are relict spinel, DIH4-4F.

The most variable structural features in the serpentinized peridotites are veins. Several generations of veining can be recognized in all serpentinized clasts. The earliest serpentine veins formed during the first serpentinization steps when cracks in the mantle opened and aqueous fluids entered the peridotite. Some of these large veins are zoned; in the centre of the old vein serpentine crystallized out of later fluids (Fig. 4.2o). This kind of veining indicates further extension of the rock during ongoing serpentinization. Typically, these veins contain variable amounts of brucite and magnetite and are often zoned parallel to the vein boundaries.

Another consequence of such extension are so-called 'Frankenstein' textures; these large early veins have been intersected by a series of roughly perpendicular veins that extend across the serpentinization veins and a short distance into the surrounding rocks (Fig. 4.2o). This veining type, already described by Shipboard Scientific Party (1990c), was interpreted as indicating that the stress mechanism may be the expansion of the adjoining, less-serpentinized rock as it continues to serpentinize and expand. As the already existing serpentine vein cannot expand further, it experiences brittle failure in extension and the opening cracks fill with serpentine cross-fibers, resulting in 'Frankenstein' textures.

Later veins are generally thinner and with irregular orientation and paths within the rocks (Fig. 4.2p,q). They always cut through the textures already serpentinized. The latest veins, formed by fibrous serpentine, thin out from the outside to the inside of single clasts and are interpreted to have formed during ascent of the clasts within the serpentine mud (Fig. 4.2p). Some veins are even associated with brucite-veins (Fig. 4.2q,r) or comprise brucite-admixtures and/or magnetite. All the described veins crystallized as serpentine minerals out of an aqueous fluid, rather than having replaced former serpentine textures.

### 4.2.1 Identification and discrimination of serpentine polymorphs and brucite

Serpentine minerals in ultramafic rocks are characteristically abundant in a wide variety of microtextures, reflecting different P-T-fluid-strain conditions and fluid-rock ratios during formation (*e.g.*, Wicks & Whittaker, 1977; Moody, 1979; O'Hanley *et al.*, 1992, O'Hanley, 1996; O'Hanley & Wicks, 1995; Wunder *et al.*, 2001; Evans, 2004; Frost & Beard, 2007; Seyfried *et al.*, 2007). Factors like similar geochemistry, similar optical properties and fine-grained intergrowths of serpentine make it difficult to distinguish the various serpentine polymorph parageneses.

From crystallographic perspective, serpentine  $[\text{Mg}_3\text{Si}_2\text{O}_5(\text{OH})_4]$  is a tri-octahedral sheet/layer silicate consisting of alternating infinite sheets of 4-coordinated Si and 6-coordinated Mg. Serpentine can crystallize as four different polymorphs which are characterized by different wrapping modes of tetrahedral (T) and octahedral (O) sheets in response to their geometrical misfit, as the lateral dimension of O layers is 3 to 5 % greater than that of T layers (*e.g.*, Wicks & Whittaker, 1975; Deer *et al.*, 1992). The polymorphs are lizardite (planar structure), chrysotile (scrolled cylindrical structure), antigorite (modulated structure; the 1:1 layer periodically reverses, resulting in the loss of an octahedrally coordinated site) and polygonal serpentine (tubular with a polygonized section)

(Wicks & O'Hanley, 1988; Mével, 2003; Andreani *et al.*, 2007). After Whittaker & Zussman (1956), chrysotile can further be subdivided into the three structural varieties ortho-, clino- and parachrysotile. Polygonal serpentine is a complex assembly of lizardite and chrysotile, where layers of lizardite are arranged as an outer shell around chrysotile fibers (Cressey & Zussman, 1976; Middleton & Whittaker, 1976). Due to their different crystalline structures, serpentine polymorphs can be identified by their XRD patterns and TEM images. However, micro-Raman spectroscopy proved to be a quick, easy and reliable method and has been used as a technique complementary to optical microscopy and SEM-EDS for rapid determination of serpentine polymorphs (*e.g.*, Rinaudo *et al.*, 2003; Groppo *et al.*, 2006). This technique not only allows the discrimination of the four major serpentine polymorphs, but also the identification of associated phases like brucite (and excluding the existence of other secondary phases such as talc).

Optical examination and X-ray diffraction analyses of Mariana mantle wedge serpentinites reveal that chrysotile and lizardite are the most abundant serpentine polymorphs (Fryer *et al.*, 1990; Shipboard Scientific Party, 2002c). Preliminary bulk rock powder diffraction (XRD) analyses of South Chamorro serpentinites investigated in the present study, kindly performed by Ilse Glass ('Institut für Geowissenschaften', Universität Heidelberg) confirm this observation revealing the mineral assemblages clinochrysotile + lizardite + magnetite.

Micro-Raman spectra were obtained from selected areas of mineral grains that had previously been characterized by optical and electron (SEM-EDS) microscopy. Typical spectra for identified antigorite, lizardite, chrysotile, polygonal serpentine and brucite are summarized in Fig. 2.5, Chapter 2. Additional spectra are given in *Appendix B6*. Representative positions (*i.e.*, wavenumbers) of the micro-Raman bands related to the different polymorphs are presented in Table 2.4, Chapter 2.

The micro-Raman examination on Mariana serpentinites shows that serpentine polymorphs are lizardite > chrysotile > polygonal serpentine >> antigorite, in order of decreasing abundance. Antigorite was only identified in serpentinite from ODP Leg 125, Conical Seamount (10R02, 26R02), but not in serpentinites from ODP Leg 195, South Chamorro Seamount. The serpentine polymorphs occur in different microstructural positions and can be 'mixed' or intergrown with brucite.

#### 4.2.2 Serpentine polymorphs and brucite correlated with their textural position

The results of micro-Raman spectroscopy (*Appendix B6*) suggest that in the serpentinites recovered at South Chamorro Seamount the serpentine polymorphs chrysotile (Ctl), lizardite (Liz) and polygonal serpentine (Pol) can be assigned to different serpentine textures. However, the correlations are different between single clasts which may indicate different 'sample localities' within the serpentinized mantle wedge. The polymorph-texture correlation is an important observation that could indicate *PT*-conditions during formation and has rarely been described before. By contrast, Pelletier (2008) observed that in serpentinites from three different geological environments (oceanic, ophiolitic, alpine) texture and serpentine polymorph are not correlated.

A characteristic correlation valid for all studied Mariana mantle wedge serpentinites cannot be determined given the great variety of serpentinites. This variety can be explained by the broad range of serpentinization degree and, more significant, differences in the location in the mantle wedge and the moment (*i.e.*, the relative point in time) of serpentinization. Hence in the following representative examples will be described, whereas deviations in the polymorph-texture correlation are expected in the natural open system of the forearc mantle.

Sample A003R01 (Table 4.2) comprises (i) partly serpentinized regions with relict olivine grains (Fig. 4.3a) and (ii) regions that are completely serpentinized (Fig. 4.3b). Veins are relatively thin (<20  $\mu\text{m}$ ) and texturally late compared to mesh textures as they cross-cut mesh centres. These veins probably formed as a reaction to the volume expansion of the rock during serpentinization. One broad dominant vein through the studied fragment is slightly zoned by alternating lizardite/brucite abundances and zones of Cr-Spl enrichment (Fig. 4.3d). In areas with abundant relict olivine, former crystal boundaries (texturally early) are predominantly composed of brucite. Mesh rims around relict olivines are composed of chrysotile (+ bucite). Mesh centers are chrysotile (Fig. 4.3a,b). Bastites (here veins through relict Opx) are composed of lizardite (with tiny scattered Cr-Spl grains; Fig. 4.3c). Where the rock was serpentinized to a higher degree, former grain boundaries are composed of brucite with a lizardite component (Fig. 4.3b); a variable but Liz+Br composition of all crystal boundaries in the fragment is characteristic. Mesh rims around serpentine mesh centers are lizardite.

Sample A007R01 (Table 4.2) comprises (i) mainly areas with relict primary minerals (Ol, Opx, Cpx) and to a lesser extent (ii) entirely serpentinized parts (Fig. 4.4). The oldest textures are fibrous veins that must have crystallized out of the earliest fluids entering the rock; they are typically made up of chrysotile and cut irregularly into the fragment (Fig. 4.4c,d; from the outside to the inside). A broad zoned vein crosses the fragment and also crosses thinner lizardite + brucite veins which represent younger fluid generations (Fig. 4.4e). The zonation of the broad vein implies stepwise fluid pulses of changing composition leading to the assemblage polygonal serpentine + brucite of varying abundance ratios (Fig. 4.4e). Mesh rims around relict primary minerals (particularly Ol) are mixtures of lizardite and brucite (Fig. 4.4a). However, when serpentinization proceeds, mesh center olivine is replaced by lizardite and polygonal serpentine, mesh rims are mineral mixtures of lizardite and brucite (Fig. 4.4b). Magnetite grains exist along former grain boundaries which are composed of brucite with minor lizardite (Fig. 4.4a).

In sample A013R01(25-27) lizardite has a strong tendency to crystallize in mesh rims and of chrysotile to grow in veins. Polygonal serpentine can be identified in all textures. In sample A011R01(69-72), mesh rims are composed of lizardite and mesh centers are composed of pure chrysotile. Bastite serpentines and former grain boundaries (now thin serpentine veins) are composed of polygonal serpentine.



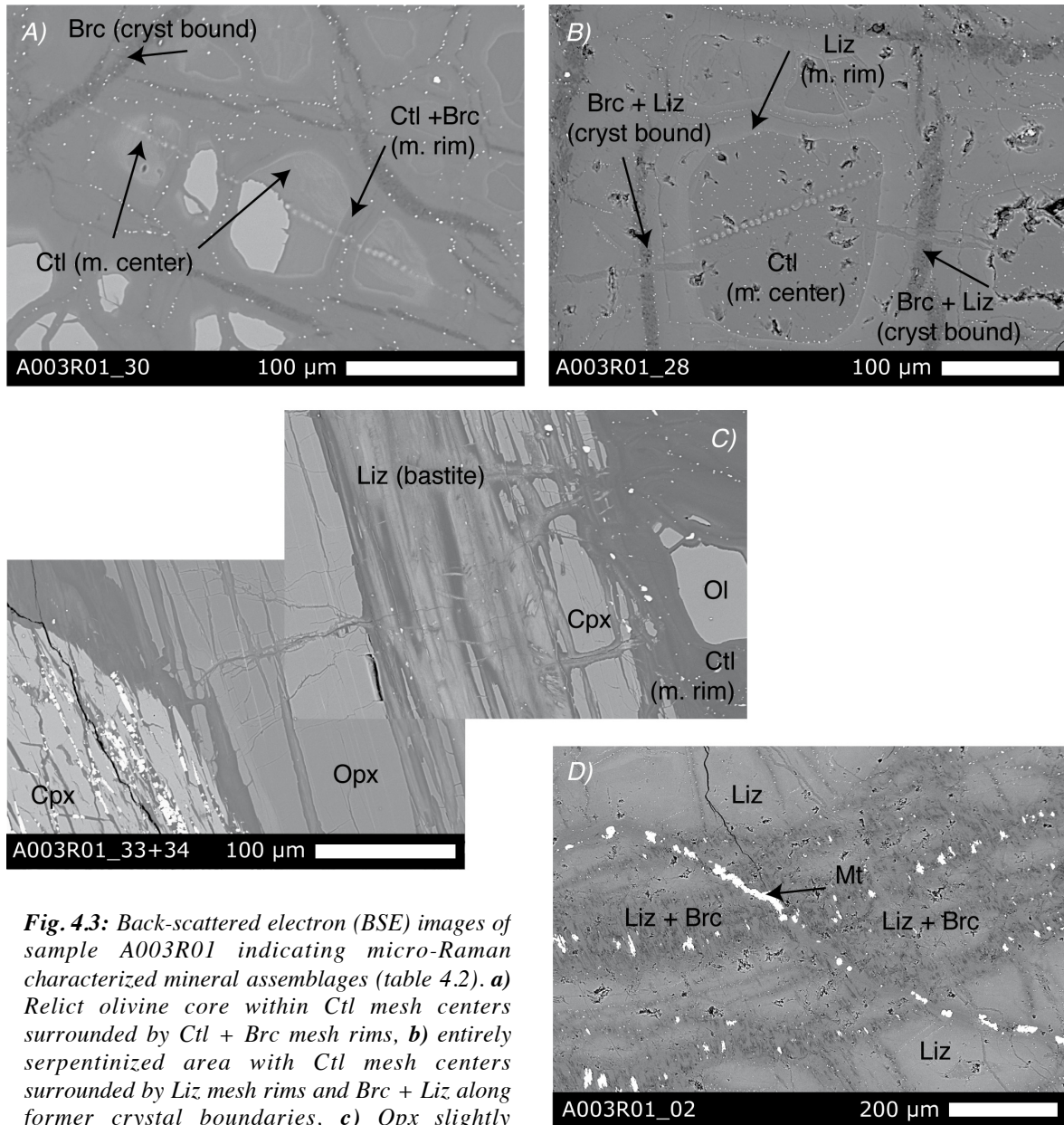


**Fig. 4.3:** Back-scattered electron (BSE) images of sample A003R01 indicating micro-Raman characterized mineral assemblages (table 4.2). **a)** Relict olivine core within Ctl mesh centers surrounded by Ctl + Brc mesh rims, **b)** entirely serpentinized area with Ctl mesh centers surrounded by Liz mesh rims and Brc + Liz along former crystal boundaries, **c)** Opx slightly serpentinized by Liz and Ctl mesh rim around olivine, and **d)** irregularly zone vein composed of Liz + Brc and Mt grains crossed by a thin Mt-rich vein.

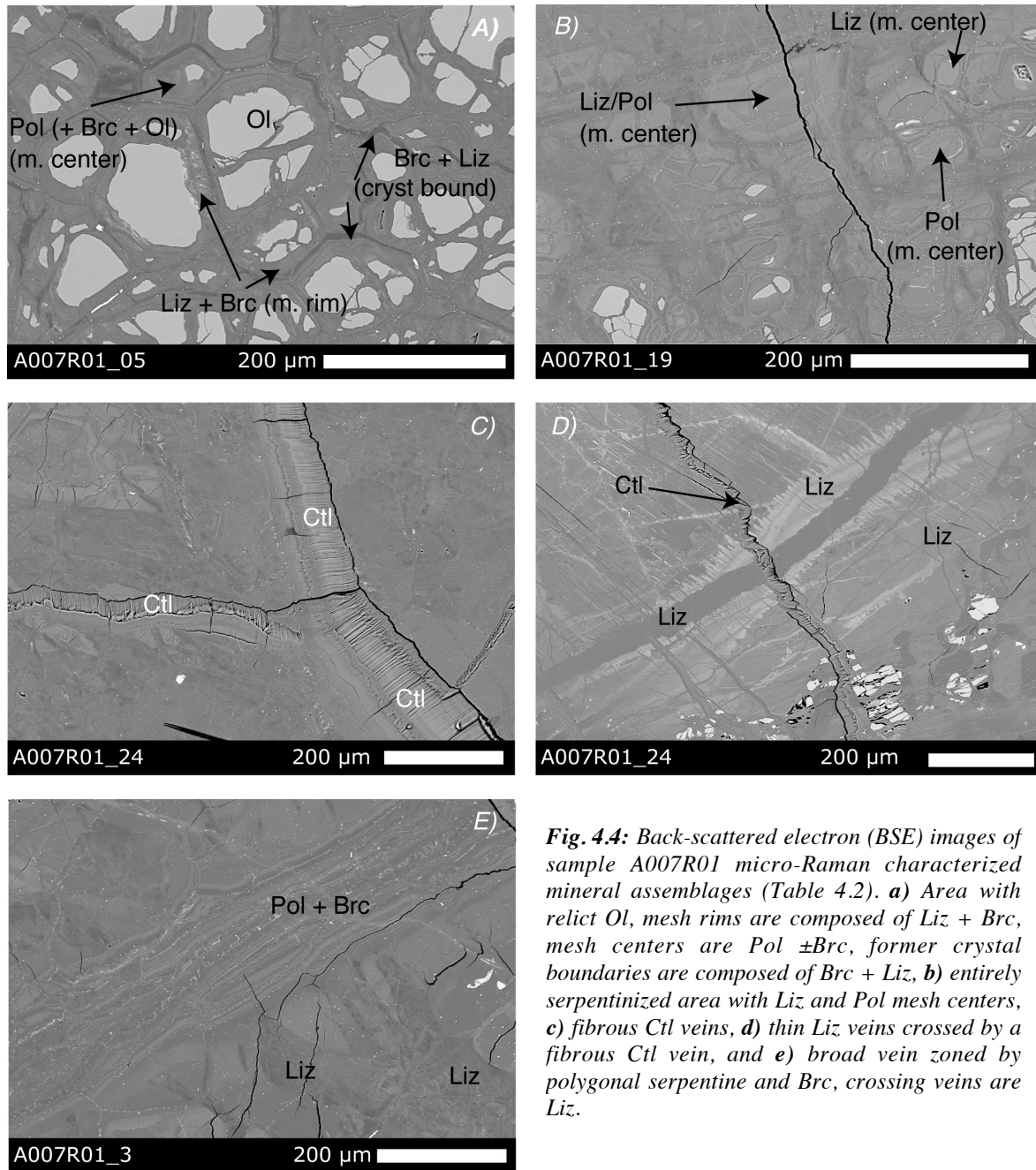


**Fig. 4.4:** Back-scattered electron (BSE) images of sample A007R01 micro-Raman characterized mineral assemblages (Table 4.2). **a)** Area with relict Ol, mesh rims are composed of Liz + Brc, mesh centers are Pol ± Brc, former crystal boundaries are composed of Brc + Liz, **b)** entirely serpentinized area with Liz and Pol mesh centers, **c)** fibrous Ctl veins, **d)** thin Liz veins crossed by a fibrous Ctl vein, and **e)** broad vein zoned by polygonal serpentine and Brc, crossing veins are Liz.

As described above, the serpentinized peridotites from South Chamorro Seamount comprise a great variety of textures that are representative for early to late serpentinization stages. The micro-Raman investigation (see also *Appendix B5*) suggests the following serpentine polymorph + brucite distribution between textures:

a) The serpentinite fragments are commonly crosscut by *early and late veins*. Early veins are broad and zoned, often known as ‘Frankenstein’-veins. In A013R01(25-27), chrysotile is the dominant serpentine in the broad vein, with lizardite in a thin central zone comprising also spinel. A zoned broad vein in A003R01 is brucite-rich and serpentine is lizardite. The same mineral polymorphs are observed in a zoned vein in A007R01 in alternation with polygonal + brucite vein

zones: perpendicularly crossing veins are lizardite + brucite. Another type of vein irregularly crosses most serpentinite fragments, entering from the outside: fibrous chrysotile veins. These veins can be interpreted as the latest, *i.e.*, youngest serpentine generation (*e.g.*, Viti & Mellini, 1998). Serpentine in veins with brucite or magnetite is predominantly lizardite.

b) *Former grain boundaries* are the first textural feature, when serpentinization of mainly olivine grains begins. As observed in sample A003R01, early thin grain boundaries are composed of brucite. As the degree of serpentinization increases, these veins are composed of brucite + lizardite. Similarly, lizardite with minor brucite but abundant magnetite is observed along former grain boundaries in sample A007R01. In entirely serpentinized areas like in samples A013R01(25-27) and A011R01(69-72), a transformation into polygonal serpentine can be observed. The mineralogy of these thin veins implies that early, Fe-rich (because of magnetite formation) fluids pass along grain boundaries and crystallize brucite + lizardite. Slow ongoing fluid percolation through the rock leads to pseudomorphosis of lizardite into polygonal serpentine.

c) Further serpentinization results in the formation of *mesh rim* textures around and replacing olivine grains. Changes from partly to entirely serpentinized zones in a clast indicate fluids that slowly percolate through the rock and use grain boundaries and cracks as pathways inducing serpentinization fronts. Early mesh rims around relict olivine are composed either of chrysotile ± brucite (A003R01), or lizardite ± brucite (A007R01). Mesh rims around serpentine mesh centers, *i.e.*, in entirely serpentinized areas, are composed of lizardite (± brucite). Also in other samples, lizardite ± brucite can be observed as the predominant assemblage in mesh rims.

d) *Mesh centers* form as pseudomorphs after relict olivine cores which are surrounded by already formed serpentine (± brucite) mesh rims. Early mesh centers are chrysotile or polygonal serpentine.

e) *Bastites* are pseudomorphs after orthopyroxene. Early serpentinization veins through Opx are composed of lizardite with tiny scarce Cr-spinel grains (A003R01, A007R01). In samples with advanced serpentinization, bastites are composed of polygonal serpentine (A011R01(69-72)).

In summary, the micro-Raman evaluation reveals that the investigated Mariana forearc serpentinites are characterized by a tendency of different serpentine polymorphs to crystallize in certain textures. As a simplified model, the following serpentinization steps are proposed:

- early 'Frankenstein'-veins: chrysotile, less lizardite (with spinel or brucite due to restitic fluids) or polygonal serpentine + brucite
- thin veins along former grain boundaries (early): brucite + lizardite
- mesh rims (early): predominantly lizardite ± brucite (rarely chrysotile ± brucite)
- bastites: polygonal serpentine with lizardite lamellae
- mesh centers (late): chrysotile ± magnetite (little polygonal serpentine)
- veins perpendicular to early veins ('Frankenstein' stitches): fibrous chrysotile (due to expansion, high water-rock-ratio)
- veins entering the clast from the outside, mostly late: fibrous chrysotile (due to high water-rock-ratios)

**Table 4.2:** Exemplary mineral phases identified by micro-Raman spectrometry with their textural site and related major element composition (wt%). Numbers of SIMS, Raman and EPMA are given for orientation.

Sample	area with relict minerals A003(81-84)										area entirely serpentinized A003(81-84)																				
	27	29	17	18	20	16	21	30	19		8	10	12	13	9	13	10	12	13	11	14	10	12	13	18-19	44-46	11				
SIMS No																															
Raman No																															
EPMA																															
texture	baustite		Cpx	mesh center	mesh center	mesh rim	mesh rim	mesh rim	mesh rim	Ol	cryst bound		mesh center	mesh center	mesh rim	mesh rim	mesh rim	mesh rim	mesh center	mesh center	mesh rim	mesh rim	mesh rim	mesh rim	mesh rim	mesh rim	mesh rim	mesh rim	mesh rim		
polymorph	Liz	Cpx	Cpx	Ctl	Ctl	Ctl+BrC	Ctl+BrC	Ctl+BrC	Ctl	Ol	BrC	Ctl	Ctl	Ctl	Ctl+BrC	Ctl+BrC	Ctl	Ctl	Ctl	Ctl	Ctl	Ctl	Ctl	Ctl	Ctl	Ctl	Ctl	Ctl	Liz		
SiO <sub>2</sub>	41.93	57.03	7.74	42.92	42.66	42.52	42.88	43.08	41.16		7.74	42.92	42.66	42.52	42.88	43.08	41.16	41.25	41.47	42.35	42.63	8.01	41.25	41.47	42.35	42.63	8.01	41.25	41.47	42.35	42.63
TiO <sub>2</sub>	0.00	0.00	0.01	0.01	0.00	0.00	0.00	0.00	0.00	0.00	0.01	0.01	0.00	0.00	0.00	0.00	0.00	0.00	0.01	0.01	0.00	0.00	0.00	0.00	0.00	0.00	0.00	0.00	0.00	0.00	
Al <sub>2</sub> O <sub>3</sub>	1.14	1.53	0.00	0.00	0.02	0.00	0.01	0.07	0.00	0.00	0.00	0.00	0.02	0.00	0.01	0.07	0.00	0.22	0.17	0.12	0.09	0.26	0.22	0.17	0.12	0.09	0.26	0.22	0.17	0.12	0.09
Cr <sub>2</sub> O <sub>3</sub>	0.38	0.68	0.03	0.04	0.00	0.02	0.01	0.05	0.00	0.00	0.03	0.04	0.00	0.02	0.01	0.05	0.00	0.00	0.00	0.03	0.00	0.01	0.00	0.03	0.00	0.00	0.01	0.00	0.03	0.00	
FeO	10.33	5.60	10.42	7.89	7.55	5.00	3.89	5.43	8.36	8.36	10.42	7.89	7.55	5.00	3.89	5.43	8.36	4.54	4.81	5.57	5.13	11.50	4.54	4.81	5.57	5.13	11.50	4.54	4.81	5.57	5.13
MnO	0.25	0.15	0.08	0.14	0.24	0.11	0.08	0.08	0.10	0.10	0.08	0.14	0.24	0.11	0.08	0.08	0.10	0.13	0.13	0.04	0.08	0.13	0.13	0.13	0.04	0.08	0.13	0.13	0.04	0.08	0.13
MgO	32.58	35.38	60.96	33.66	33.98	37.62	36.38	38.10	50.39	50.39	60.96	33.66	33.98	37.62	36.38	38.10	50.39	36.53	36.61	37.68	38.12	55.95	36.53	36.61	37.68	38.12	55.95	36.53	36.61	37.68	38.12
CaO	0.58	0.37	0.11	0.74	0.77	0.19	0.32	0.27	0.01	0.01	0.11	0.74	0.77	0.19	0.32	0.27	0.01	0.52	0.46	0.19	0.18	0.13	0.52	0.46	0.19	0.18	0.13	0.52	0.46	0.19	0.18
Na <sub>2</sub> O	0.09	0.00	0.02	0.06	0.06	0.09	0.07	0.06	0.04	0.04	0.02	0.06	0.06	0.09	0.07	0.06	0.04	0.06	0.04	0.04	0.07	0.36	0.06	0.04	0.04	0.07	0.36	0.06	0.04	0.07	0.36
K <sub>2</sub> O	0.04	0.00	0.00	0.12	0.12	0.02	0.05	0.07	0.01	0.01	0.00	0.12	0.12	0.02	0.05	0.07	0.01	0.05	0.03	0.04	0.05	0.04	0.05	0.03	0.04	0.05	0.04	0.05	0.03	0.04	0.05
NiO	0.04	0.08	0.04	0.25	0.27	0.04	0.18	0.09	0.38	0.38	0.04	0.25	0.27	0.04	0.18	0.09	0.38	0.07	0.08	0.04	0.00	0.05	0.07	0.08	0.04	0.00	0.05	0.07	0.08	0.04	0.00
Total	87.37	100.81	79.39	85.82	85.66	85.61	85.87	87.30	100.45	100.45	79.39	85.82	85.66	85.61	85.87	87.30	100.45	83.36	83.87	86.06	86.34	76.44	83.36	83.87	86.06	86.34	76.44	83.36	83.87	86.06	86.34
oxygens	14	6	14	14	14	14	14	14	4	4	14	14	14	14	14	14	4	14	14	14	14	14	14	14	14	14	14	14	14	14	14
Si	4.061	1.948	0.939	4.168	4.148	4.083	4.081	4.067	0.996	0.996	0.939	4.168	4.148	4.083	4.081	4.067	0.996	4.067	4.068	4.058	4.063	1.018	4.067	4.068	4.058	4.063	1.018	4.067	4.068	4.058	4.063
Ti	0.000	0.000	0.000	0.001	0.000	0.000	0.000	0.000	0.000	0.000	0.000	0.001	0.000	0.000	0.000	0.000	0.000	0.000	0.000	0.001	0.000	0.000	0.000	0.001	0.000	0.000	0.000	0.000	0.000	0.000	0.000
Al	0.130	0.062	0.000	0.000	0.003	0.000	0.001	0.008	0.000	0.000	0.000	0.000	0.003	0.000	0.001	0.008	0.000	0.025	0.020	0.014	0.010	0.038	0.025	0.020	0.014	0.010	0.038	0.025	0.020	0.014	0.010
Cr	0.029	0.018	0.002	0.003	0.000	0.001	0.001	0.004	0.000	0.000	0.002	0.003	0.000	0.001	0.001	0.004	0.000	0.000	0.000	0.002	0.000	0.001	0.000	0.002	0.000	0.000	0.001	0.000	0.000	0.000	0.000
Fe <sup>2+</sup>	0.837	0.160	1.058	0.640	0.614	0.402	0.310	0.429	0.169	0.169	1.058	0.640	0.614	0.402	0.310	0.429	0.169	0.374	0.394	0.446	0.409	1.222	0.374	0.394	0.446	0.409	1.222	0.374	0.394	0.446	0.409
Mn	0.020	0.004	0.008	0.011	0.020	0.009	0.006	0.006	0.002	0.002	0.008	0.011	0.020	0.009	0.006	0.006	0.002	0.011	0.011	0.003	0.007	0.014	0.011	0.011	0.003	0.007	0.014	0.011	0.003	0.007	0.014
Mg	4.704	1.802	11.027	4.873	4.926	5.385	5.445	5.361	1.818	1.818	11.027	4.873	4.926	5.385	5.445	5.361	1.818	5.368	5.354	5.382	5.416	10.593	5.368	5.354	5.382	5.416	10.593	5.368	5.354	5.382	5.416
Ca	0.060	0.014	0.014	0.077	0.080	0.020	0.033	0.027	0.000	0.000	0.014	0.077	0.080	0.020	0.033	0.027	0.000	0.054	0.049	0.019	0.018	0.18	0.054	0.049	0.019	0.018	0.18	0.054	0.049	0.019	0.018
Na	0.017	0.000	0.004	0.011	0.012	0.017	0.012	0.011	0.002	0.002	0.004	0.011	0.012	0.017	0.012	0.011	0.002	0.011	0.008	0.008	0.013	0.088	0.011	0.008	0.008	0.013	0.088	0.011	0.008	0.008	0.013
K	0.005	0.000	0.000	0.015	0.015	0.002	0.006	0.009	0.000	0.000	0.000	0.015	0.015	0.002	0.006	0.009	0.000	0.006	0.004	0.005	0.006	0.006	0.006	0.004	0.005	0.006	0.006	0.004	0.005	0.006	0.006
Ni	0.014	0.009	0.018	0.088	0.093	0.015	0.061	0.031	0.033	0.033	0.018	0.088	0.093	0.015	0.061	0.031	0.033	0.026	0.026	0.013	0.000	0.023	0.026	0.026	0.013	0.000	0.023	0.026	0.013	0.000	0.000
Total	9.878	4.017	13.070	9.887	9.910	9.933	9.957	9.953	3.021	3.021	13.070	9.887	9.910	9.933	9.957	9.953	3.021	9.943	9.940	9.948	9.941	13.021	9.943	9.940	9.948	9.941	13.021	9.943	9.940	9.948	9.941
Mg#	84.58	91.65	91.19	88.20	88.61	92.91	94.51	92.50	91.39	91.39	91.19	88.20	88.61	92.91	94.51	92.50	91.39	93.31	92.94	92.30	92.88	89.56	93.31	92.94	92.30	92.88	89.56	93.31	92.94	92.30	92.88

Ctl - chrysotile, Liz - lizardite, Pol - polygonal, BrC - brucite, Ol - olivine, Cpx - clinopyroxene / cryst bound - former crystal boundary.

**Table 4.2 (continued): Exemplary mineral phases identified by micro-Raman spectrometry with their textural site and related major element composition (wt%). Numbers of SIMS, Raman and EPMA are given for orientation.**

Sample	broad vein through the clast										area with relict minerals														
	A003(81-84)		vein		vein		vein		vein		in 20		in 5		2		3		7						
SIMS No	6	5	4	3	1	16	(9)	6	6	33	35	36	38	37	39	24	34	41	33	29	25	3	21	46	
Raman No	15	16	17	18	19	24	34	41	33	29	25	36	38	37	39	24	34	41	33	29	25	3	21	46	
EPMA	29	22	18	10	1	123	33	16	6	6	29	25	3	21	46	123	33	16	6	6	29	25	3	21	46
texture	vein	vein	vein	vein	vein	vein	cryst bound	mesh center	mesh rim	mesh rim	mesh rim	mesh rim	mesh rim	mesh rim	mesh rim	mesh rim	cryst bound	mesh center	mesh rim	mesh rim	mesh rim	mesh rim	olivine	mesh rim	
polymorph	Liz	Br+Liz	Liz+Br	Liz+Br	Liz	vein	Br+Liz	Pol(+Br+Ol)	Liz+Br	Liz+Br	Liz+Br	Liz+Br	Liz+Br	Liz+Br	Liz+Br	vein	Br+Liz	Pol(+Br+Ol)	Liz+Br	Liz+Br	Liz+Br	Liz+Br	Ol	Liz(+Br+Ol)	
SiO <sub>2</sub>	42.54	38.38	7.74	27.41	42.86	53.92	32.80	36.42	37.93	38.51	19.96	38.88	40.73	37.64	0.02	0.01	0.00	0.01	0.01	0.00	0.00	0.00	0.01	0.00	
TiO <sub>2</sub>	0.02	0.00	0.01	0.01	0.00	0.02	0.01	0.00	0.01	0.00	0.00	0.00	0.01	0.00	0.00	0.00	0.00	0.00	0.01	0.02	0.00	0.02	0.00	0.00	
Al <sub>2</sub> O <sub>3</sub>	0.09	0.05	0.01	0.03	0.07	1.33	0.00	0.01	0.01	0.02	0.00	0.02	0.00	0.00	0.00	0.00	0.00	0.01	0.01	0.02	0.00	0.02	0.00	0.00	
Cr <sub>2</sub> O <sub>3</sub>	0.00	0.00	0.02	0.00	0.00	0.35	0.02	0.00	0.00	0.00	0.00	0.03	0.01	0.00	0.00	0.00	0.00	0.00	0.00	0.00	0.03	0.01	0.00	0.00	
FeO	5.52	4.71	13.48	9.25	4.51	1.76	6.31	6.45	5.39	5.26	22.29	4.85	8.56	4.97	0.10	0.05	0.04	0.08	0.08	0.05	0.42	0.04	0.17	0.03	
MnO	0.11	0.11	0.23	0.11	0.08	0.10	0.05	0.04	0.08	0.05	0.42	0.04	0.17	0.03	0.11	0.08	0.04	0.08	0.05	0.42	0.04	0.17	0.03	0.03	
MgO	37.23	43.77	61.36	46.19	38.40	18.03	42.23	42.00	40.78	41.67	42.69	41.18	50.75	41.40	0.20	0.18	0.05	0.07	0.14	0.13	0.30	0.10	0.00	0.10	
CaO	0.20	0.18	0.05	0.09	0.17	24.60	0.09	0.07	0.14	0.13	0.30	0.10	0.00	0.00	0.10	0.13	0.09	0.07	0.14	0.13	0.30	0.10	0.00	0.10	
Na <sub>2</sub> O	0.10	0.13	0.05	0.07	0.07	0.08	0.02	0.00	0.04	0.00	0.01	0.03	0.00	0.00	0.00	0.02	0.00	0.00	0.04	0.00	0.01	0.03	0.00	0.00	
K <sub>2</sub> O	0.04	0.02	0.01	0.00	0.04	0.00	0.00	0.02	0.00	0.00	0.00	0.01	0.00	0.00	0.00	0.00	0.00	0.02	0.00	0.00	0.01	0.00	0.00	0.00	
NiO	0.02	0.06	0.00	0.17	0.05	0.03	0.31	0.39	0.34	0.40	0.32	0.32	0.39	0.32	0.02	0.03	0.31	0.39	0.34	0.40	0.32	0.32	0.39	0.32	
Total	85.87	87.40	82.93	83.31	86.25	100.23	81.84	85.40	84.71	86.04	86.00	85.45	100.62	84.46	14	14	14	14	14	14	14	14	4	14	
oxygens	14	14	14	14	14	6	14	14	14	14	14	14	4	14	14	14	14	14	14	14	14	14	4	14	
Si	4.083	3.666	0.914	2.906	4.074	1.954	3.412	3.599	3.738	3.732	2.263	3.780	0.986	3.715	0.001	0.000	0.001	0.000	0.001	0.000	0.000	0.000	0.000	0.000	
Ti	0.001	0.000	0.000	0.001	0.000	0.001	0.001	0.000	0.001	0.000	0.000	0.000	0.000	0.000	0.000	0.000	0.000	0.000	0.001	0.000	0.000	0.000	0.000	0.000	
Al	0.010	0.005	0.001	0.003	0.008	0.057	0.000	0.002	0.002	0.002	0.001	0.002	0.000	0.000	0.000	0.000	0.000	0.002	0.002	0.002	0.001	0.002	0.000	0.000	
Cr	0.000	0.000	0.001	0.000	0.000	0.010	0.001	0.000	0.000	0.000	0.000	0.000	0.000	0.000	0.000	0.000	0.000	0.000	0.000	0.000	0.000	0.000	0.000	0.000	
Fe <sup>2+</sup>	0.443	0.376	1.332	0.821	0.359	0.053	0.549	0.533	0.444	0.427	2.114	0.395	0.173	0.410	0.009	0.009	0.005	0.003	0.006	0.004	0.041	0.003	0.003	0.002	
Mn	0.009	0.009	0.023	0.010	0.006	0.003	0.005	0.003	0.006	0.004	0.004	0.003	0.003	0.002	0.000	0.000	0.000	0.000	0.006	0.002	0.002	0.003	0.003	0.002	
Mg	5.327	6.233	10.802	7.302	5.441	0.974	6.549	6.186	5.992	6.020	7.214	5.968	1.832	6.090	0.021	0.018	0.010	0.007	0.015	0.013	0.037	0.010	0.000	0.011	
Ca	0.021	0.018	0.006	0.010	0.017	0.955	0.010	0.007	0.015	0.013	0.007	0.002	0.000	0.000	0.000	0.019	0.004	0.000	0.007	0.001	0.002	0.005	0.000	0.000	
Na	0.019	0.024	0.011	0.013	0.013	0.006	0.004	0.000	0.007	0.001	0.000	0.005	0.000	0.000	0.005	0.005	0.004	0.000	0.007	0.001	0.002	0.005	0.000	0.000	
K	0.005	0.002	0.001	0.000	0.004	0.000	0.000	0.002	0.000	0.000	0.000	0.000	0.000	0.000	0.000	0.008	0.018	0.002	0.000	0.000	0.000	0.001	0.000	0.000	
Ni	0.008	0.019	0.000	0.064	0.015	0.004	0.118	0.138	0.121	0.138	0.131	0.138	0.034	0.115	0.008	0.008	0.004	0.138	0.121	0.138	0.131	0.138	0.034	0.115	
sum	9.926	10.353	13.091	11.130	9.939	4.017	10.648	10.471	10.324	10.337	11.803	10.278	3.030	10.343	9.926	9.926	9.926	9.926	9.926	9.926	9.926	9.926	9.926	9.926	
Mg#	92.18	94.18	88.85	89.79	93.72	94.53	92.21	92.02	93.01	93.32	77.00	93.76	91.20	93.66	92.18	92.18	92.18	92.18	92.18	92.18	92.18	92.18	91.20	93.66	

Cl - chrysotile, Liz - lizardite, Pol - polygonal, Br - brucite, Ol - olivine, Cpx - clinopyroxene / cryst bound - former crystal boundary.

### 4.3 Major element contents of serpentinite forming minerals

The studied samples contain some primary and secondary minerals. Relict primary minerals are olivine, orthopyroxene, clinopyroxene and spinel. Secondary minerals are pseudomorphing serpentine, brucite/amakinite and magnetite. Further products of serpentinization are Ca-(OH)-rich phases and ‘dark serpentine’. Major elements contents of minerals have been determined via electron probe micro analyses (EPMA). The results are listed in tables B2.1-B2.4 in *Appendix B*. Data were normalized assuming Fe as Fe<sup>2+</sup> in all minerals, except for spinel where Fe<sup>2+</sup> and Fe<sup>3+</sup> were calculated. Mg# was calculated as  $100 \times \text{Mg}/(\text{Mg} + \text{Fe}^{2+})$ , Cr# was calculated as  $100 \times \text{Cr}/(\text{Cr} + \text{Al})$ .

#### 4.3.1 Olivine

Olivine is the most abundant primary mineral in Mariana forearc peridotites and occurs as more or less rounded grains with a diameter of up to ~200  $\mu\text{m}$ . The forsterite (Fo) composition of olivine is very restricted in the range 90.3 to 92.8 (mean value of 91.4), typical for depleted upper mantle peridotites (Bonatti & Michael, 1989; Ishii *et al.*, 1992; Fig. 4.5). In particular, the mean Fo (= Mg#) of olivine is 91.4 in A003R01 and A007R01 and 91.3 in A011-69-72, A013-1-25 and A017G02. Values are the same as reported by *e.g.*, D’Antonio & Kristensen (2004; Mg# = 91.5-92.5). If comparing the Fo of olivine with the Cr# of chromian spinel (see later), the harzburgites plot in the olivine-spinel mantle array (Arai 1994; Fig. 4.5b). NiO contents are variable between 0.28 and 0.53 wt% (mean value of 0.41 wt%) which coincides well with the compositional range of mantle olivines (Takahashi *et al.*, 1987; Fig. 4.5a).

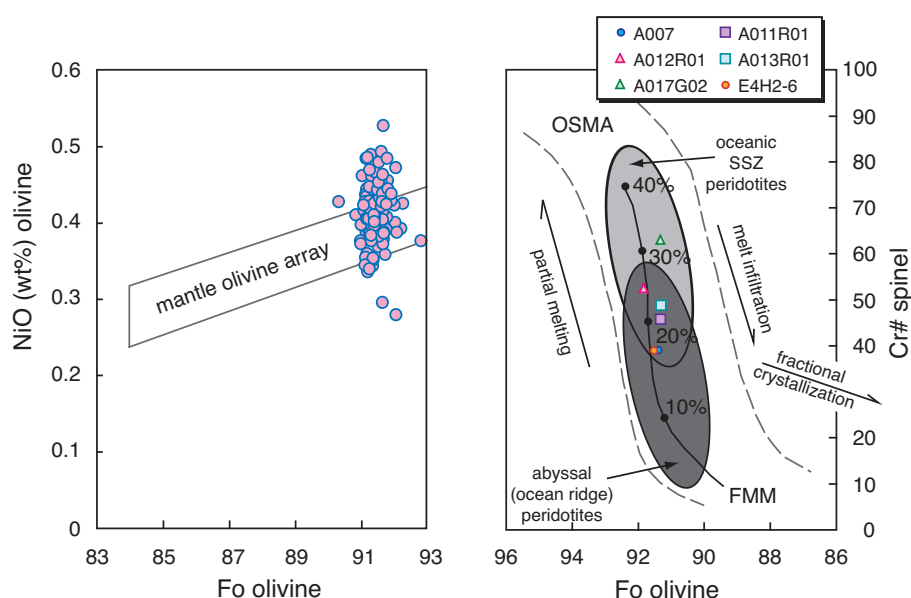
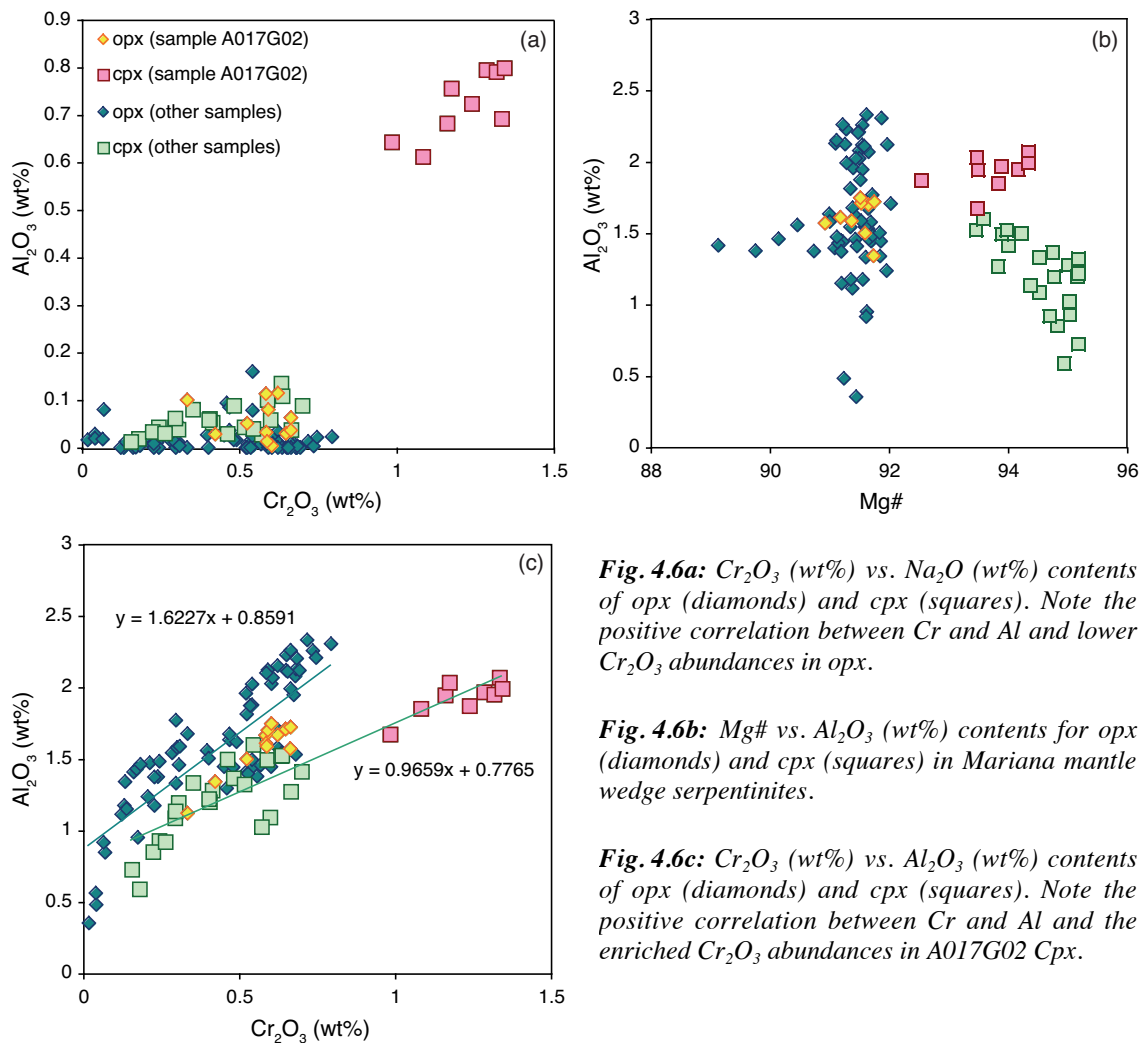


**Fig. 4.5:** **a)** Fo-content vs. NiO (wt%) in olivine from Mariana mantle wedge serpentinites. Solid lines show the compositional range of mantle olivines defined by those in mantle-derived xenoliths (Takahashi *et al.*, 1987). **b)** Cr-number in spinel vs. Fo-content in olivine from Mariana mantle wedge serpentinites. The light grey field represents values for oceanic SSZ peridotites and the dark grey field those for abyssal ocean ridge peridotites (from Pearce *et al.*, 2000 and references therein). OSMA, olivine-spinel mantle array after Arai (1994) and partial melting trend after Pearce *et al.* (2000 and references therein). FFM: fertile MORB mantle, SSZ: supra subduction zone. Modified after Pearce *et al.* (2000) and references therein.

## 4.3.2 Pyroxenes

Porphyroclasts of primary orthopyroxene (Opx) display a large compositional range within the field of enstatite and are variably affected by serpentinization. Mg# ranges from ~91 to ~92 (Fig. 4.6b). Some outlier at lower Mg#, can be interpreted as evidence for melt infiltration (Pelletier, 2008). Cr<sub>2</sub>O<sub>3</sub> contents are low but variable with up to 0.8 wt% and correlate with Al<sub>2</sub>O<sub>3</sub>. Al<sub>2</sub>O<sub>3</sub> contents range between 0.3 and 2.4 wt% (Fig. 4.6c). Al and Cr contents decrease with a drop in pressure and temperature. Na<sub>2</sub>O concentrations are well below 0.2 wt% (Fig. 4.6a). Cr<sub>2</sub>O<sub>3</sub> contents of Opx from sample A017G02 are higher at the same Al<sub>2</sub>O<sub>3</sub> content compared to other Opx (Fig. 4.6c). Some orthopyroxenes have clinopyroxene exsolution lamellae.



Clinopyroxenes (Cpx) are generally smaller than Opx crystals, are lobate and rounded and occur in much lower abundance (<5 vol%), mostly associated with Opx. Mg# of Cpx ranges from 92.4 to 95.5 (Fig. 4.6b). The composition varies in the field of Mg-rich diopside for the serpentinites with low Na<sub>2</sub>O and Cr<sub>2</sub>O<sub>3</sub> concentrations. Only Cpx in clast A017G02 is enriched in jadeite component, indicated by Na<sub>2</sub>O >0.6 wt%. It is also enriched in chromian compared to other Cpx (Cr<sub>2</sub>O<sub>3</sub> >1 wt%; Fig. 4.6a,c). Na increase in Cpx is usually assumed to indicate high-pressure melting; hence, sample

A017G02 may have originated from a deeper mantle portion or did not experience significant reequilibration (*e.g.*, Blundy *et al.*, 1995; Bazylev, 1996). The  $\text{Al}_2\text{O}_3$  content varies between 0.5 and 2.1 wt% which is in the same range as for orthopyroxene. The higher contents are represented by the A017G02 Cpx with  $\text{Al}_2\text{O}_3 > 1.7$  wt% and correlate positively with the  $\text{Cr}_2\text{O}_3$  content (Fig. 4.6c). The  $\text{TiO}_2$  contents are below 0.15 wt% and typical for a highly depleted peridotite.

Both orthopyroxene and clinopyroxene compositions are in good agreement with other subduction zone related peridotites and previously investigated South Chamorro harzburgites (*e.g.*,  $\text{Mg}\# = 90.1\text{--}92.4$  for Opx and  $92.2\text{--}95.6$  for Cpx; D'Antonio & Kristensen, 2004; Zanetti *et al.*, 2006).

### 4.3.3 Spinel

The majority of the peridotites contains unaltered Cr-Al-spinel which appears to be the most resistant mineral during serpentinization and alteration. It is commonly the only original phase remaining in the otherwise strongly serpentinized rocks. The Cr# of primary spinel in all serpentinite samples varies within the range of 28.0 and 70.2 (Fig. 4.7a), reflecting the refractory origin of these rocks (Ishii *et al.*, 1992). The Mg# ranges widely from 50.2 to 64.0. Similar Mg# and Cr# data for South Chamorro Seamount spinel are reported by Zanetti *et al.* (2006):  $\text{Mg}\# = 40.3\text{--}60.4$ ,  $\text{Cr}\# = 37\text{--}66$ .

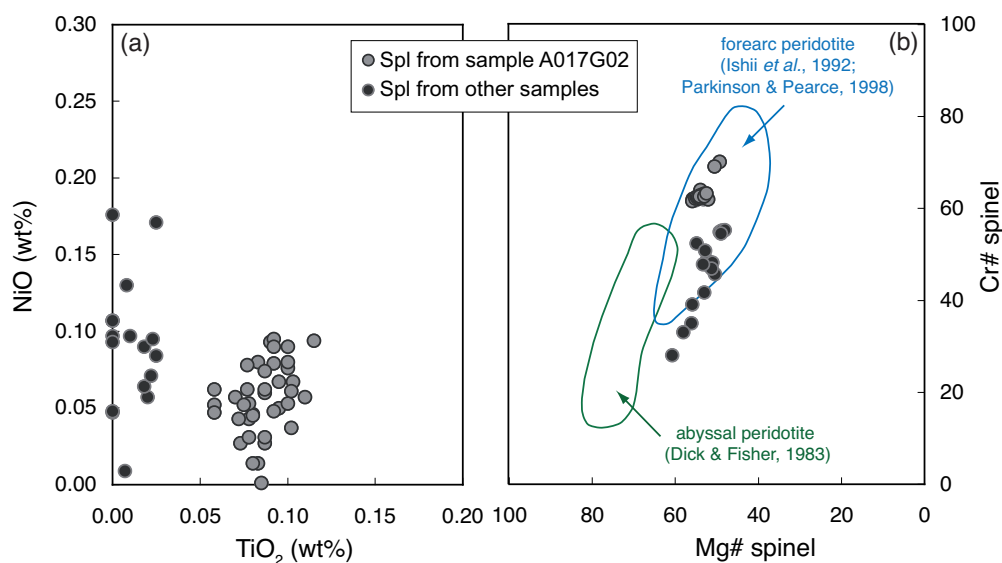


**Fig. 4.7:** **a)**  $\text{TiO}_2$  (wt%) and  $\text{NiO}$  (wt%) contents for Cr-Al-spinel in Mariana mantle wedge serpentinites. **b)** Mg# vs. Cr# for Cr-Al-spinel in Mariana mantle wedge serpentinites. Field for spinel from forearc peridotites: Ishii *et al.* (1992), Parkinson & Pearce (1998), field for spinel from abyssal spinel peridotite: Dick & Fisher (1984).  $\text{Cr}\# = \text{Cr}/(\text{Cr}+\text{Al})$ ,  $\text{Mg}\# = \text{Mg}/(\text{Mg}+\text{Fe}^{2+})$ .

As shown in Fig. 4.7a, the Mg# and Cr# of the Cr-Al-spinel in the Mariana mantle wedge serpentinites shows a linear relationship and plot in the compositional field defined by spinel from forearc peridotites (Ishii *et al.*, 1992; Parkinson & Pearce, 1998). Within the Cr-Al-range, Cr#



increases with increasing degrees of partial melting in the mantle (Dick & Bullen, 1984). For comparison, spinel from abyssal peridotites (Dick & Fisher, 1984; Dick & Bullen, 1984) has a composition at lower Cr# (well below 69) but higher Mg# (>60). TiO<sub>2</sub> contents of Cr-Al-spinel increase with increasing Cr#, while NiO contents decrease. The low TiO<sub>2</sub> concentrations are typical for spinel harzburgites. Cr-Al-spinel in sample A017G02 is enriched in TiO<sub>2</sub> and characterized by the Cr# >60 (Fig. 4.5b and Fig. 4.7a).

Due to the generally very small grain size of magnetite (<3 μm), EPM analyses are difficult, but the grains were identified as pure magnetite confirming observations of D'Antonio & Kristensen (2004).

#### 4.3.4 Brucite / Amakinite

During serpentinization, iron in olivine may redistribute, entering the structure of the serpentine minerals or brucite, or forming separate opaque phases: magnetite, awaruite, pentlandite, ferrit-chromite, etc. (Ashley, 1975). Brucite (Br) composition in the serpentinized peridotites rarely coincides with that of the pure endmember Mg(OH)<sub>2</sub>, but always contains a significant amount of amakinite (Am) – Fe(OH)<sub>2</sub> – and insignificant amounts of pyrochroite (Py) – Mn(OH)<sub>2</sub> –. In both veins and mesh textures these (Fe-Mg)-hydroxy-minerals occur as pure phases, *i.e.*, without serpentine admixtures. Pure brucite should contain ~30.9 wt% H<sub>2</sub>O, whereas lower water contents down to 21.6 wt% are expected in the Fe-Mn-rich varieties (D'Antonio & Kristensen, 2004). Thus, totals in the range 69–78 % are expected for natural brucite minerals, confirmed by EPM analyses in the present study.

Various early studies have already documented intensive substitution of iron for magnesium in brucite during serpentinization; 6 to 72 mole% with an average of about 15 mole% Fe(OH)<sub>2</sub> has been recorded (*e.g.*, Hostetler *et al.*, 1966; Mumpton & Thompson, 1966, 1975; Page, 1967a; Wicks & Plant, 1979). D'Antonio & Kristensen (2004) recently described Fe-bearing brucite in serpentinized peridotites from South Chamorro Seamount reporting compositions between Br<sub>89</sub>Am<sub>11</sub> and Br<sub>60</sub>Am<sub>40</sub> with most analyses between Br<sub>89</sub> and Br<sub>83</sub>. Compositions higher than Br<sub>76</sub> were all analyzed along a single vein. Compared to these data, this new study of South Chamorro Seamount serpentinites shows a much wider range in brucite-amakinite compositions between Br<sub>88</sub>Am<sub>12</sub> and very Fe-rich brucite, *i.e.*, amakinite with Br<sub>30</sub>Am<sub>70</sub> (Fig. 4.8). High iron abundances are mainly detected in veins.

The highest iron concentrations documented in literature was found in amakinite from the Daldyn-Alakit kimberlite field in Russia; 58.85 wt% FeO<sub>tot</sub> (30.4 wt% FeO + 31.58 wt% Fe<sub>2</sub>O<sub>3</sub>) with additional 3.63 wt% MnO and 10.10 wt% MgO (= Br<sub>14</sub>Am<sub>81</sub>Py<sub>5</sub>; Kozlov & Levshov, 1962). However, the amakinite analyzed in the presented Mariana forearc serpentinites has maximum MnO contents of 2.3 wt% (=Br<sub>60</sub>Am<sub>37</sub>Py<sub>3</sub>). Therefore, maximum total iron contents are higher compared to literature amakinite values in a Mn-poor system (Fig. 4.8).

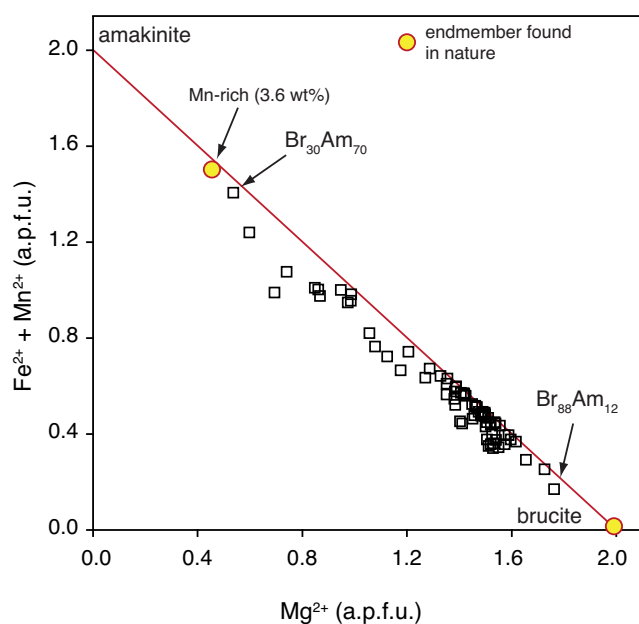


**Fig. 4.8:**  $Mg^{2+}$  vs  $Fe^{2+} + Mn^{2+}$  (a.p.f.u.) of brucite. Compositions vary between brucite and amakinite. Endmember compositions (yellow circles) from literature: brucite – Wood’s Chrome mine, Pennsylvania, USA ( $Mg_{0.99}Fe_{0.01}(OH)_2$ , (Anthony *et al.*, 1997; e.g., Bruce (1814), *American Min. Journal*: 1: 26 (as Native Magnesia), amakinite – Udachnaya-Vostochnaya pipe, Daldyn, Daldyn-Alakit kimberlite field, Saha Republic (Sakha Republic; Yakutia), Eastern-Siberian Region, Russia ( $Fe_{0.73}Mg_{0.22}Mn_{0.05}(OH)_2$ , Kozlov & Levshov, 1962; Shevschenko).

#### 4.3.5 Serpentine

The general formula of serpentines is  $Mg_5[Si_2O_5](OH)_4$ . Substitution of Al and  $Fe^{3+}$  for Si may occur in tetrahedral sites, and that of  $Fe^{2+}$ ,  $Fe^{3+}$ , Cr, Al, Ni and Mn for Mg in octahedral sites. It has been shown that lizardite tends to accept more substitution components than chrysotile and is typically more enriched in Al, although their compositions overlap (Wicks & Whittaker, 1975; Moody, 1976b; Wicks & O’Hanley, 1988; O’Hanley & Wicks, 1995). According to stoichiometry, pure serpentine minerals lizardite and chrysotile should contain ~13 wt%  $H_2O$ , whereas antigorite contains only ~12 wt% (e.g., D’Antonio & Kristensen, 2004). Deer *et al.* (1992) reported  $H_2O$  contents in the range 12.2–15.2 wt%, with lizardite and chrysotile showing the highest contents. Since water cannot be determined by electron microprobe, we take the difference from 100 wt% as a rough estimation for the amount of water present in the analyzed serpentine.

Serpentine minerals from the Mariana mantle wedge have variable chemical composition, especially concerning their  $MgO$ ,  $FeO_{tot}$ ,  $Al_2O_3$  and  $Cr_2O_3$  contents. The Mg# of all serpentines spans a total range of ~88 to ~97, although the majority of serpentine has a Mg# between 90 and 94. The Mg# is not consistent because it may be controlled by external factors such as the oxygen fugacity which influences magnetite formation and the  $Fe^{3+}/Fe^{2+}$  and Fe/Mg ratios in serpentine and associated phases (see 4.6.3.1).  $Cr_2O_3$  and  $Al_2O_3$  contents are primarily controlled by the composition of the minerals replaced; serpentine formed after olivine is low in both  $Al_2O_3$  and  $Cr_2O_3$  compared to bastites formed after orthopyroxene. Also serpentine after spinel can be highly enriched in  $Al_2O_3$  and  $Cr_2O_3$ .  $FeO_{tot}$  and  $MgO$  concentrations are similar in all serpentine textures. Serpentine mixed with

varying amounts of brucite and to a lower extent amakinite (Fe-brucite) shows mainly occurs in mesh rims, former grain boundaries and veins, as previously shown by micro-Raman analyses. These mineral mixtures are characterized by lower silica and higher magnesia and/or iron contents relative to pure serpentine minerals (with a chemical composition lying between the two minerals). They have already been described in other serpentinites and were attributed to brucite impurities in serpentine or to very fine-scale intergrowth of serpentine plus brucite (*e.g.*, Wicks & Plant, 1979; O'Hanley & Dyar, 1993; Dilek *et al.*, 1997).

Si-Mg-Fe mole fraction ternary diagrams represent well the variability and range of serpentine compositions (*e.g.*, Wicks & Plant, 1979; D'Antonio & Kristensen, 2004). Figure 4.9 presents a summary of >2400 electron microprobe analyses in the  $\text{Si}^{4+}$ - $\text{Mg}^{2+}$ - $\text{Fe}^{2+}$  system, showing variable serpentine compositions of Mariana mantle wedge serpentinites with intensive brucite and/or amakinite admixtures.

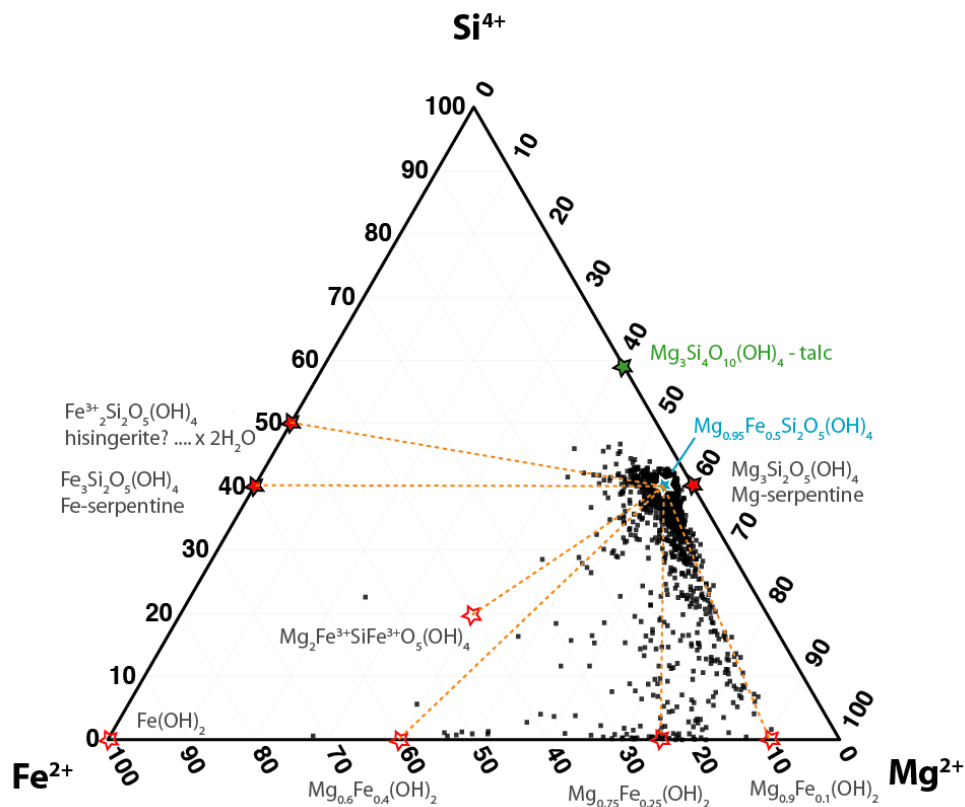


**Fig. 4.9:** Ternary diagram of molar %  $\text{Fe}^{2+}$ - $\text{Mg}^{2+}$ - $\text{Si}^{4+}$  (according to Wicks & Plant, 1979; Bach *et al.*, 2006) showing the chemical variability of serpentine minerals and serpentine + brucite mixtures from Site 1200 serpentinites. ( $n = 2450$ )

One of the first reactions during serpentinization is the formation of veins along mineral grain boundaries (*e.g.*, Fryer *et al.* 1990). As can be seen in Fig. 4.10a, such former grain boundaries have compositions lying between serpentine and brucite with Mg# 90. These thin grain boundary veins are Fe-rich in sample E4H2-6, with compositions between serpentine and Fe-rich brucite (Mg# 55).

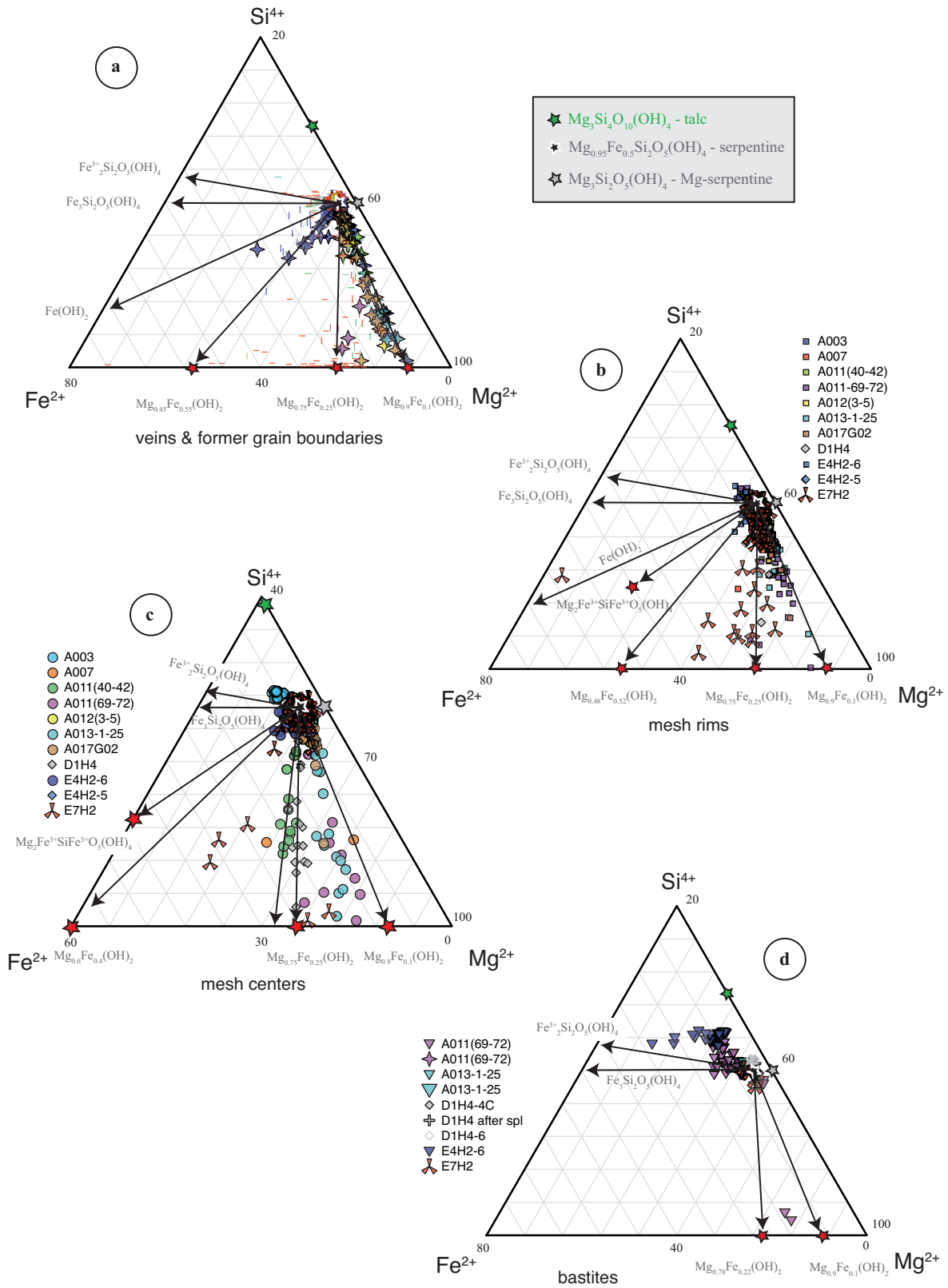


**Fig. 4.10:** Ternary diagram of mole%  $Fe^{2+}$ - $Mg^{2+}$ - $Si^{4+}$  showing the chemical variability of serpentine (+brucite) in **a**) veins (dashes) and crystal boundaries (stars). ( $n = 592$ ), **b**) mesh rims. ( $n = 962$ ), **c**) mesh centers. ( $n = 627$ ), and **d**) bastites. (bastites:  $n = 101$ ; serp after spl:  $n = 6$ ).

Also thin veins, crossing this sample, have Fe-rich composition. Veins in different E7H2 clasts are brucite-rich with a broad variety in Fe-Mg contents. Veins in E7H2-3B, a quite deformed clast, have Fe-rich serpentine composition (pink dashes in Fig. 4.10a). Veins and grain boundaries of sample A011R01(69-72) plot on a compositional line between brucite with Mg# 75 and the major trend of all grain boundaries towards brucite with Mg# 90 (Fig. 4.10a; rose). One vein in A013R01(25-27) has low MgO content with high FeO<sub>tot</sub> content (14.92 wt%) and is enriched in CaO and Al<sub>2</sub>O<sub>3</sub> (3.67 and 1.02 wt%, respectively), though the SiO<sub>2</sub> content is still high with 43.35 wt% (blue dash in Fig. 4.10a).

When serpentinization proceeds, static replacement of olivine forms mesh rims around relic olivine cores. Generally, the mesh rims of all studied serpentinites have quite similar composition of Mg-rich serpentine with a tendency to mix with a Mg-rich brucite component (Mg# 75–90; Fig. 4.10b). Only the mesh rims of sample E4H2-6 have a more Fe-rich brucite component, similar to veins and crystal boundaries in this sample.

Further hydration serpentinizes relic olivine cores and forms serpentine ± brucite or ± magnetite. Although the majority of mesh centers have a composition around Mg# ~92, in some samples mesh center serpentine tends to mix with a different brucite composition (Fig. 4.10c). Sample E4H2 contains some mesh centers with a mixing composition between serpentine and very Fe-rich brucite (Mg# 45). Furthermore, for samples A011R01(40-42) and D1H4 mixing trends between serpentine and brucite with Mg# 78 and Mg# 75, respectively can be observed. Serpentinities A011R01(69-72), A013R01(25-27), and A017G02 contain mesh centers with compositions between serpentine (Mg# ~92) and Mg-rich brucite (Mg# 88). Mesh centers of sample A003 cluster around a more Si-rich composition.

Generally, serpentine minerals in all textures are Al-poor. Though, serpentine in bastites, *i.e.*, after orthopyroxene, has elevated Al<sub>2</sub>O<sub>3</sub> and Cr<sub>2</sub>O<sub>3</sub> concentrations. In this case, Al and Cr substitute for Si. Since Al and Cr are not considered in the Si-Mg-Fe ternary diagram, Si concentrations consequently are shifted to overestimated values in Fig. 4.10d. Furthermore, bastite serpentine is characterized by lower Mg# in some samples compared to other serpentine textures.

As a rare finding, serpentinization after Cr-spinel can be observed in sample D1H4-4F. This serpentine is also enriched in both Al and Cr contents due to the primary spinel composition.

#### 4.3.6 Ca-(OH)-rich 'phase' in serpentinites

Some harzburgite samples contain irregular round blasts of 'Ca-(OH)-rich serpentine' (Fig. 4.11). This phase overgrows the existing serpentine mesh textures and partly contains small magnetite grains. Electron probe micro analyses have low totals (~74–79 %) indicating a hydrous mineral. The low sums similar to brucite minerals imply high amounts of water and/or CO<sub>2</sub> of up to ~26 %. However, SiO<sub>2</sub> concentrations are high and similar to serpentine minerals, MgO concentrations are <30 wt%, FeO contents vary in the range of ~3 to ~5 wt%. Hence, the Mg# are in the same range as

the other serpentinite minerals (*e.g.*, Srp, Ol, Opx): ~91 to ~95. CaO concentrations are high between ~10 and ~15 wt%. A possible composition, using 12 oxygens per formula, would be:  $\text{Ca}_{1.3}\text{Mg}_{4.3}\text{Fe}_{0.4}\text{Si}_3\text{O}_{10}(\text{OH})_2$ . Micro-Raman analyses were performed without success due to strong fluorescence.

O'Hanley (1996) described a similar 'phase' as carbonate overprinting lizardite in weathered serpentinite. It is not related to any serpentine textures, indicating that carbonate alteration must postdate serpentinization (O'Hanley, 1996). Furthermore, Mével (2003) summarized that carbonates (aragonite/calcite in veins and breccia matrix) in serpentinites correspond to very late stages and are not in equilibrium with the serpentine minerals. Thus, the formation of these Ca-rich phases in the serpentinized harzburgites could be interpreted as a late fluid related crystallization. This possibility is supported by the particular occurrence of this phase at the end of veins (Fig. 4.11). As fluids after serpentinization are known to be Ca-enriched (Palandri & Reed, 2004), they could explain an increased Ca concentration in the end of cracks. These 'restitic' fluids possibly 'overprint' the already formed serpentine.

Nevertheless, the final identification and explanation of this phase (or these phases) is beyond the scope of this thesis.

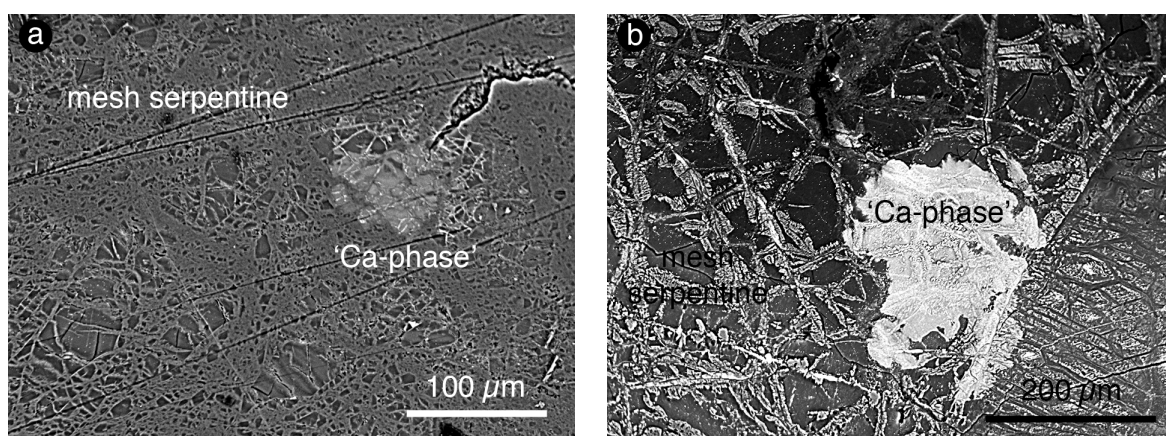


**Fig. 4.11:** Back-scattered electron (BSE) images of **a**) a mesh serpentine area with Ca-rich hydrous phase (bright) 'overprinting' serpentine at the end of a serpentine vein (E7H2-8S), and **b**) Ca-rich phase (bright) 'overprinting' the mesh serpentine, the former serpentine textures are still visible (D1H4-6A).

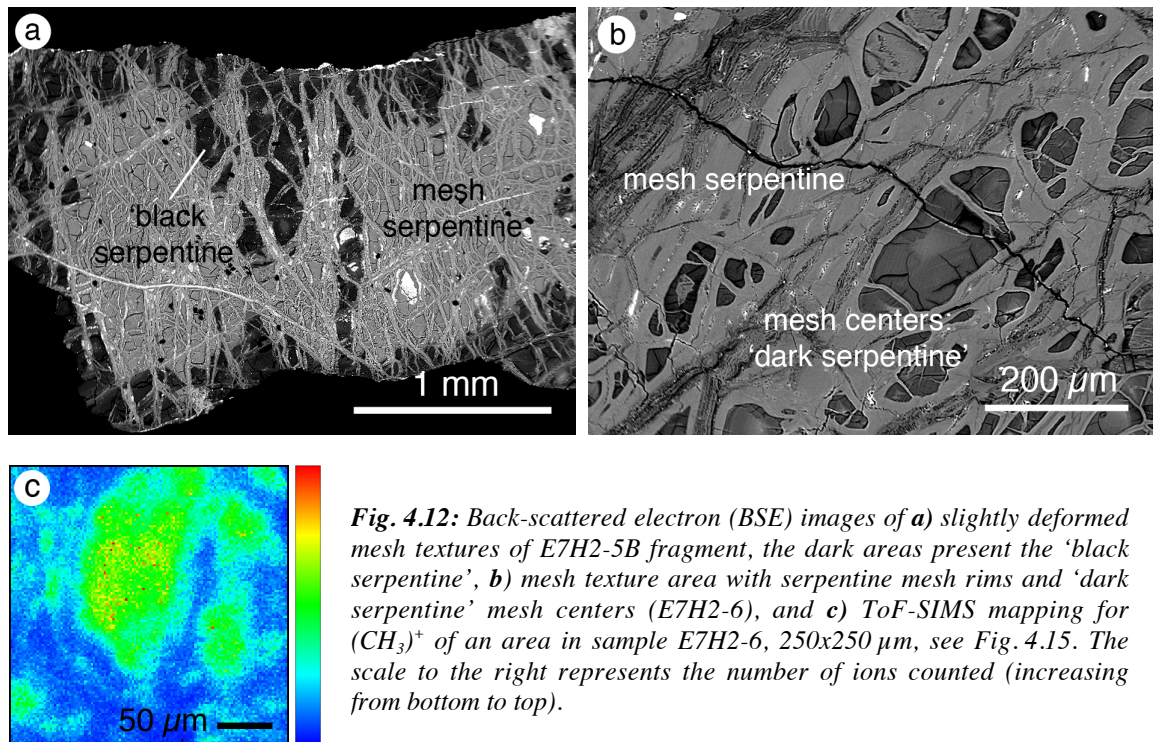
#### 4.3.7 'Black serpentine'

Strongly serpentinized harzburgites contain a finegrained and smooth mineral mixture with low EPMA sums of down to 60 wt%, but a Si/(Mg+Fe) ratio typical for serpentine. In back-scattered electron images, this phase is darker than serpentine (Fig. 4.12). In mesh centers, this phase contains also magnetite grains (like the mesh center serpentine), but has a deep topography with shrinking cracks (Fig. 4.12b). In some samples, this dark phase also occurs along the outer parts of broad veins; fine grained serpentine (even), 'black serpentine' and brucite also can be found in broad veins in alternation. Under the microscope, serpentine is colourless, the 'black serpentine', in mesh centers, is

dirty brown. Textural relationships suggest that the ‘black serpentine’ is the latest feature occurring in the samples (*e.g.*, 4.12a).

Micro-Raman analyses were not successful due to strong fluorescence, even with a laser of higher wavelength. Preliminary semi-quantitative analyses by SIMS on sample E7H2-5B (Fig. 4.12a) were made; calibration with dolomite at a given C/Mg ratio and the known MgO content of the ‘black serpentine’ resulted in CO<sub>2</sub> contents of up to 22 wt% which seems to be the missing portion for a sum of 100. Further work with a special SIMS setup and the selection of an appropriate and well characterized standard with either high MgO or SiO<sub>2</sub> content and high carbon concentration (*e.g.*, dolomite) are needed. A short-time ToF-SIMS element mapping of an area in sample E7H2-6 showed that carbon is enriched in these dark (in BSE images) areas (Fig. 4.12c).

However, these investigations are beyond the scope of this thesis, but a highly interesting point for future work. This phase will not be considered for the following discussions to avoid any secondary phase influences.



## 4.4 Light element (Li, Be, B) contents of rock-forming minerals

### 4.4.1 Light element mappings by ToF-SIMS

Light element ToF-SIMS images of serpentinites provide qualitative information about the distribution of elements in a mapped area (see chapter 3). Mapped samples include A013R-2-12, E4H2-6 and E7H2-2. Thin mesh rims and veins along former grain boundaries are strongly enriched in Li, whereas mesh centers after olivine have low Li content. B is generally homogeneously

distributed within the serpentinized area at high concentrations (apart from former grain boundaries) (see Fig. 3.3). The same Li and B distribution for serpentine after olivine is found in all mapped serpentinites (Fig. 4.13–4.16). Also serpentine veins through orthopyroxene, *i.e.*, along cleavage planes, are enriched in Li compared to bastite serpentine or Li-poor Opx (Fig. 4.14 and 4.15). All bastites, serpentinized cleavage planes and mesh serpentine are similarly enriched in B.

The mapped areas of most samples contain ‘black serpentine’ mesh centers (which should be excluded from further discussions, see 4.3.7); however, to demonstrate the Li enrichment in mesh rims and early veins, these examples are shown (*e.g.*, Fig. 4.13). Various veins in E4H2-6 have similar Li and B contents compared to mesh serpentine (Fig. 4.16). Relict olivine is extremely depleted in Li and B (Fig. 3.3 in chapter 3 and 4.15), orthopyroxene is B-poor (Fig. 4.15).

The results of the high resolution element mappings are in agreement with the B and Li concentrations detected by SIMS spot analyses (see chapter 3 and following pages).

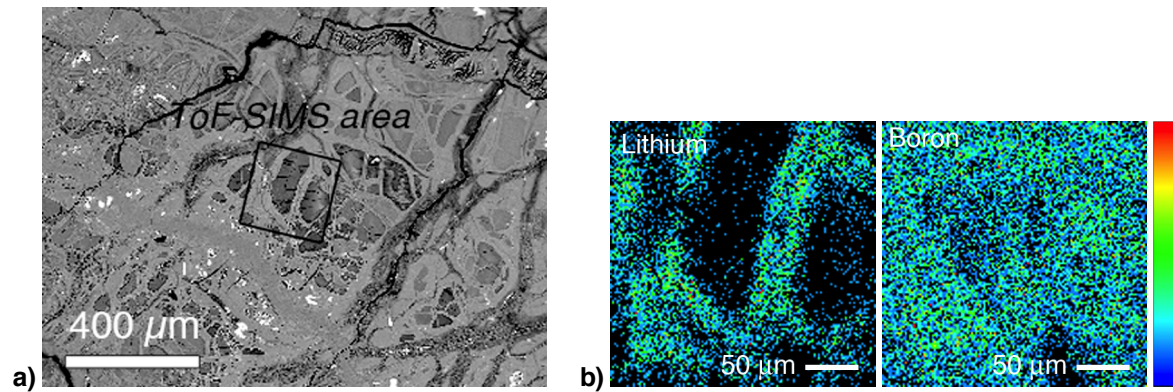


**Fig. 4.13:** a) Back-scattered electron image of partly serpentinized sample E4H2-6 with ‘black serpentine’ mesh centers, b) Li and B distribution, 250 x 250 μm (low counting time). The scale to the right represents the number of ions counted (increasing from bottom to top).

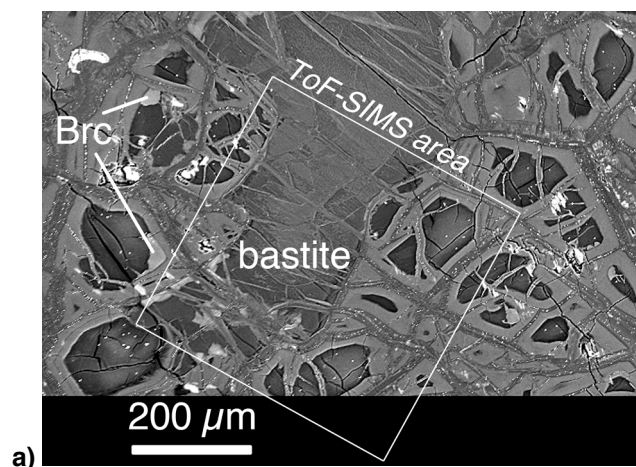


**Fig. 4.14:** a) Back-scattered electron image of entirely serpentinized sample E7H2-2E with bastite and ‘black serpentine’.



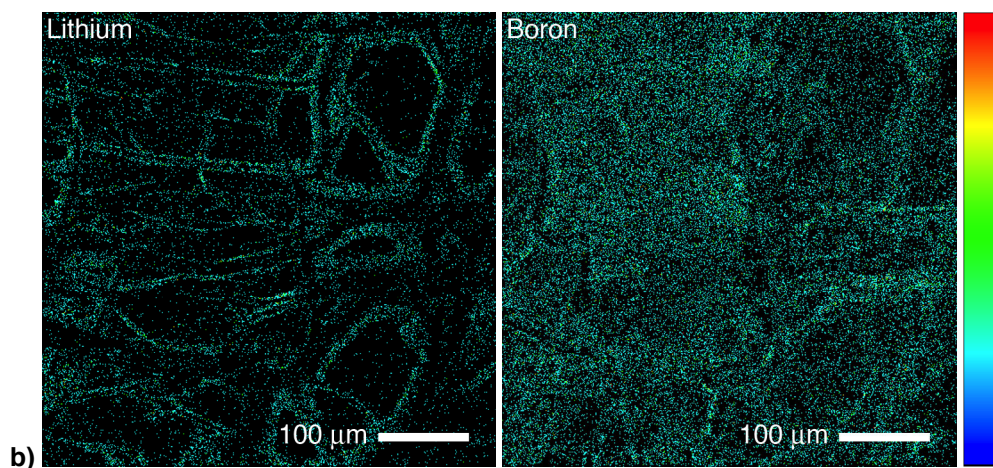


**Fig. 4.14 (continued): b)** ToF-SIMS images of sample E7H2-2E, Li and B distribution, 500 x 500  $\mu\text{m}$  (512x512 pixel, low acquisition time).

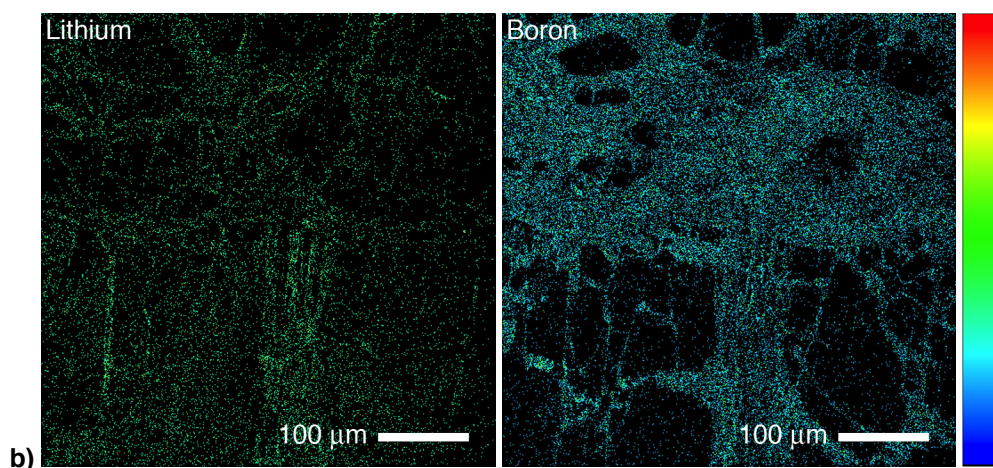
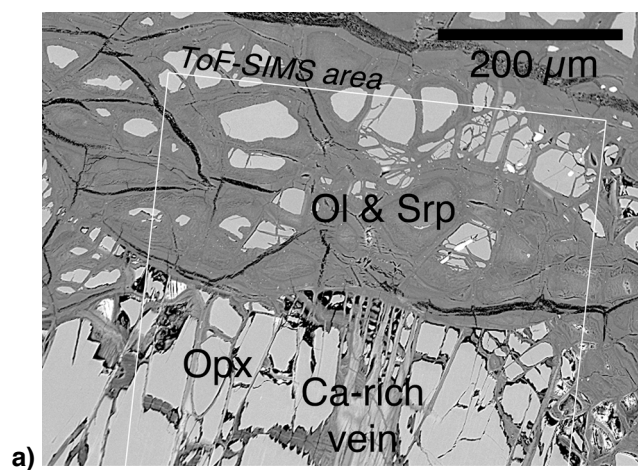


**Fig. 4.15: a)** Back-scattered electron image of partly serpentinized sample E4H2-6 with relict olivine and orthopyroxene. **b)** Li and B distribution, 500 x 500  $\mu\text{m}$  (512x512 pixel, low acquisition time).

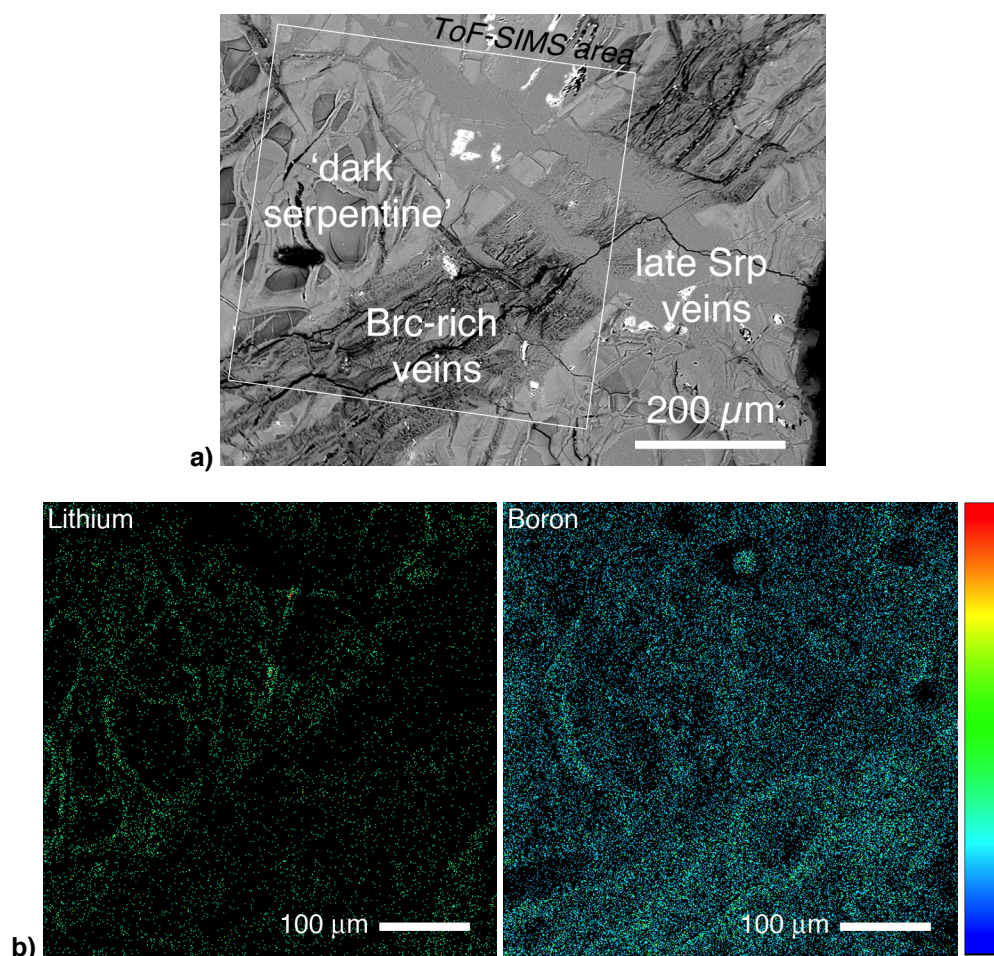


**Fig. 4.16:** **a)** Back-scattered electron image of partly serpentinized sample E4H2-6 with different vein generations and few 'black serpentine', **b)** Li and B distribution, 500 x 500 µm (512x512 pixel, low acquisition time).

#### 4.4.2 Light element SIMS analyses

Lithium (Li), beryllium (Be) and boron (B) concentrations of texturally well defined serpentine and primary minerals from South Chamorro and Conical Seamount (Smt.) mantle wedge harzburgites are given in *Appendix B3* and are graphically presented in Fig. 4.17. Rigorous analytical control avoided analyses of mineral mixtures (*e.g.*, Srp-Ol; see chapter 2).

Interstitial clinopyroxene has the highest Li contents of the primary minerals, ranging from 3.6 to 3.9 µg/g (Fig. 4.17a). Primary clinopyroxene (sample A017G02) has only 2.1 µg/g Li (Fig. 4.17b). Li concentrations in olivine and orthopyroxene overlap: 0.6–1.3 µg/g in olivine and 0.3–2.6 µg/g in orthopyroxene. B concentrations in olivine and pyroxenes are low and range from below the detection limit up to <4 µg/g in some minerals (Fig. 4.17a,b). Furthermore, these minerals have extremely low Be concentrations ranging from <0.1 µg/g down to <0.001 µg/g, reaching the Be detection limit (Fig. 4.17c). No correlation between Li, Be and B contents can be identified for olivine and pyroxene. The low light element abundances in primary minerals coincide well with primitive mantle rock values (Ryan & Langmuir, 1993; Ottolini *et al.*, 2004) or estimated depleted

mantle values ( $0.7 \mu\text{g/g}$  Li,  $0.06 \mu\text{g/g}$  B; Fig. 4.17a; Salters & Stracke, 2004). Hence, as stated before by other studies on serpentinites (Pelletier *et al.* 2008a, 2008b; Vils *et al.*, 2008) serpentinization has no influence on the composition of primary phases.

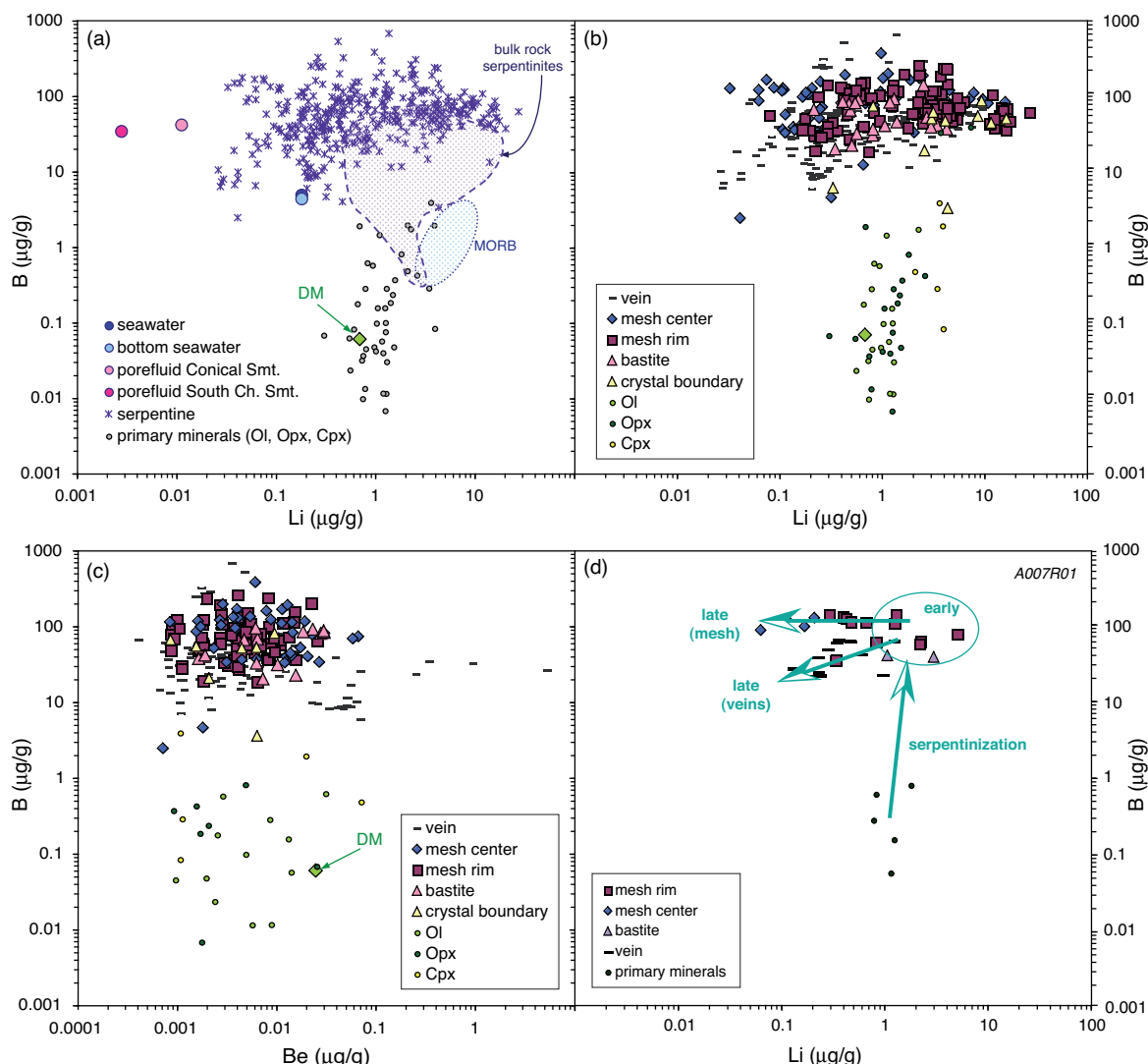


**Fig. 4.17:** **a)** Li vs. B concentration for Mariana serpentinite and primary minerals (Ol, Opx, Cpx) in comparison to fluids compositions (for references see text), depleted mantle (estimated by Salters & Stracke, 2004), MORB (Ryan & Langmuir, 1987; 1993) and bulk rock composition of serpentinites from South Chamorro Smt. (Savov *et al.*, 2005b, 2007), **b)** Li vs. B concentration of Mariana serpentinite and primary minerals, different symbols indicate different textural sites, **c)** Be vs. B concentration, for symbols see a) and b), and **d)** Li vs. B concentration of serpentinite and primary minerals in sample A007R01 to emphasize the different compositions between textures and serpentine generations.

The serpentines pseudomorphing olivine and pyroxene are characterized by generally high B, variable Li and low Be contents. A summary of all serpentine texture compositions (*e.g.*, vein, mesh center) shows a distinct ‘cloud’ of compositions at medium to high B content ( $\sim 2$  to  $\sim 400 \mu\text{g/g}$ ) and variable Li content ( $<0.001$  to  $<30 \mu\text{g/g}$ ; Fig. 4.17a). The majority of serpentine minerals shows B abundances between  $\sim 20$  and  $\sim 120 \mu\text{g/g}$  and an average Li abundances of  $\sim 2 \mu\text{g/g}$  (Fig. 4.17a,b). Be

concentrations of mesh serpentine are  $\leq 0.1 \mu\text{g/g}$  with an average of  $\sim 0.03 \mu\text{g/g}$ . As the Be content of serpentine is identical to primary minerals and similar to depleted mantle compositions (Fig. 4.17c), thus serpentinization has no influence on the beryllium composition of mantle peridotites and will therefore not be considered in the discussion. Brucite minerals are strongly depleted in both Li and B, Be abundances are below detection limit. Several veins of platy Fe-Mg-brucite in sample E7H2-2B are large enough for SIMS analyses; light element contents are low with  $1.19\text{--}1.63 \mu\text{g/g}$  B and  $0.6\text{--}1.6 \mu\text{g/g}$  Li.

B concentrations of serpentine minerals are much higher than those of primary minerals and relative to depleted mantle values (Fig. 4.17a). The average Li and B contents in primary minerals and serpentine agree with the B enrichment detected in bulk rock serpentinites from Conical Smt. ( $15.0 \mu\text{g/g}$  B) and South Chamorro Smt. ( $15.4 \mu\text{g/g}$  B) in greater depth below the seafloor (Benton *et al.*, 2001; Savov *et al.*, 2005b; Savov *et al.*, 2007; Fig. 4.17a). Down-hole B abundances in Conical Smt. serpentinites are generally highest near the seafloor (Benton *et al.*, 2001; Savov *et al.*, 2005b) due to the uptake of B from seawater ( $4.4\text{--}4.6 \mu\text{g/g}$ , Quinby-Hunt & Turekian, 1983; Spivack & Edmond, 1987; Jean-Baptiste *et al.*, 1991; Mottl *et al.*, 2004) by serpentine after emplacement. However, no simple positive correlation between the degree of serpentinization (= LOI) and B (and Li) whole rock contents was observed for South Chamorro peridotites (Savov *et al.*, 2005b).

The Li contents of serpentine minerals are both lower and higher than those of mantle minerals olivine, orthopyroxene and clinopyroxene (Fig. 4.17a,b). The Li contents in serpentine are within the whole rock Li range measured in serpentinites from Conical Smt. ( $\sim 4.6 \mu\text{g/g}$  Li; Benton *et al.*, 2004; Savov *et al.*, 2005b) and South Chamorro Smt. ( $\sim 2.5 \mu\text{g/g}$ ; Savov *et al.*, 2007), indicating a modest Li enrichment relative to depleted mantle values (Fig. 4.17a).

The serpentinites were carried in a water-mud-rock mixture to the surface. The corresponding pore fluids have B concentrations similar to serpentinites ( $34.6 \mu\text{g/g}$  B at Conical Smt. and  $42.2 \mu\text{g/g}$  B at South Chamorro Smt.). Compared to serpentine, primary minerals and seawater, these pore fluids have very low Li contents ( $0.003 \mu\text{g/g}$  Li at Conical Smt. and  $0.01 \mu\text{g/g}$  Li at South Chamorro Smt.; Mottl *et al.*, 2003, 2004 and references therein; Fig. 4.17a).

Similar to the major element compositions it is possible, though in a limited way, to distinguish light element contents for mesh textures, bastites and even veins (see section 4.3.5). Considering all serpentine minerals analyzed, the majority of serpentine mesh rims have a tendency to higher Li concentrations, whereas the majority of mesh centers tends to lower Li contents (Fig. 4.1b). Though highly variable, B abundances in mesh centers tend to higher B values. Bastite serpentines have a smaller compositional range around medium Li contents ( $\sim 0.2\text{--}4 \mu\text{g/g}$ ) and lower to medium B contents ( $\sim 20\text{--}150 \mu\text{g/g}$ ). Thin serpentine veins along former grain boundaries tend to high Li contents ( $\sim 0.3\text{--}17 \mu\text{g/g}$ ) at medium B contents ( $\sim 3\text{--}90 \mu\text{g/g}$ ) (Fig. 4.17b).

Serpentine veins have a quite variable light element concentration showing a broad trend from high B - high Li down to low B - low Li concentrations. Both mesh and bastite serpentines have low Be concentrations of  $< 0.001$  to  $\sim 0.09 \mu\text{g/g}$  (Fig. 4.17c) which is in the same range as the Be contents

of olivine and pyroxene. Generally, Be concentrations in veins and crystal boundaries are similar to mesh textures and bastites. However, some late veins reach high Be contents of up to  $>5 \mu\text{g/g}$ . These high Be contents were detected in (i) a serpentinite clast from Conical Seamount (10R02-3:  $2.01 \mu\text{g/g}$  Li,  $0.25 \mu\text{g/g}$  Be,  $23.55 \mu\text{g/g}$  B and 10R02-14:  $1.68 \mu\text{g/g}$  Li,  $5.28 \mu\text{g/g}$  Be,  $26.43 \mu\text{g/g}$  B), and (ii) in South Chamorro clast E7H2-2B (coarse-grained veins E7H2-2B-1:  $0.69 \mu\text{g/g}$  Li,  $0.34 \mu\text{g/g}$  Be,  $34.66 \mu\text{g/g}$  B and E7H2-2B-14:  $0.51 \mu\text{g/g}$  Li,  $0.96 \mu\text{g/g}$  Be,  $32.39 \mu\text{g/g}$  B). Currently there is no model to explain this observation.

#### 4.5 Boron isotope composition ( $\delta^{11}\text{B}$ ) of serpentine by SIMS

Boron isotope bulk rock data of Mariana serpentinites were already discussed by Benton *et al.* (2001). As bulk rock analyses cannot give information about the internal boron isotope variability of a sample, this study focusses on high lateral resolution SIMS analyses to evaluate the B isotope signature of single serpentine textures. The results demonstrate the compositional variability and textural complexity of serpentinized peridotites. Therefore, insights into the fluid-rock-interactions during serpentinization can be gained.

B isotope values ( $\delta^{11}\text{B}$ ) in serpentine minerals show considerable variation between very negative values of  $\sim -12\text{‰}$  and very positive values of  $\sim +24\text{‰}$  (Fig. 4.18). Though different serpentine textures tend to have different Li and B concentrations, this trend is hardly seen for  $\delta^{11}\text{B}$ . Nevertheless, most of the veins and former grain boundaries tend to have more negative  $\delta^{11}\text{B}$  values, whereas most mesh serpentines have more positive B isotope values (Fig. 4.18).

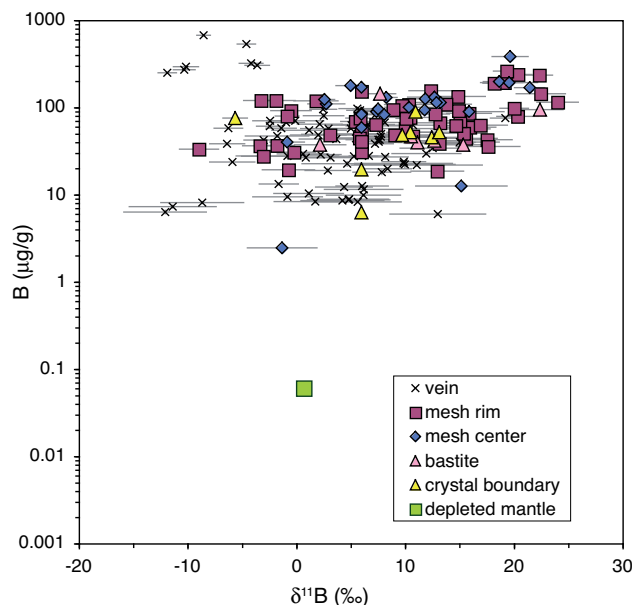


**Fig. 4.18:**  $\delta^{11}\text{B}$  vs. B of serpentine analyzed by SIMS. Errorbars indicate  $2\sigma$  values. Depleted mantle: Salters & Stracke (2004).

Serpentine after orthopyroxene has variable positive  $\delta^{11}\text{B}$  values between  $\sim +3$  and  $+22$  ‰. Some mesh centers have a very negative  $\delta^{11}\text{B}$  value of down to  $-14$  ‰ and most of these mesh centers are highly enriched in B. Also late veins show negative  $\delta^{11}\text{B}$  values (Fig. 4.18a). Strongly serpentinized samples show a tendency to have more negative  $\delta^{11}\text{B}$  values in serpentine. Although all samples include a broad range in  $\delta^{11}\text{B}$  values, the majority of serpentine textures has positive  $\delta^{11}\text{B}$  values. Within single clasts, *e.g.*, A007R01, high  $\delta^{11}\text{B}$  values correlate with high Li contents in early serpentine, such as mesh rims (Fig. 4.19). Late serpentine, however, has low Li contents at relatively negative B isotope ratios.

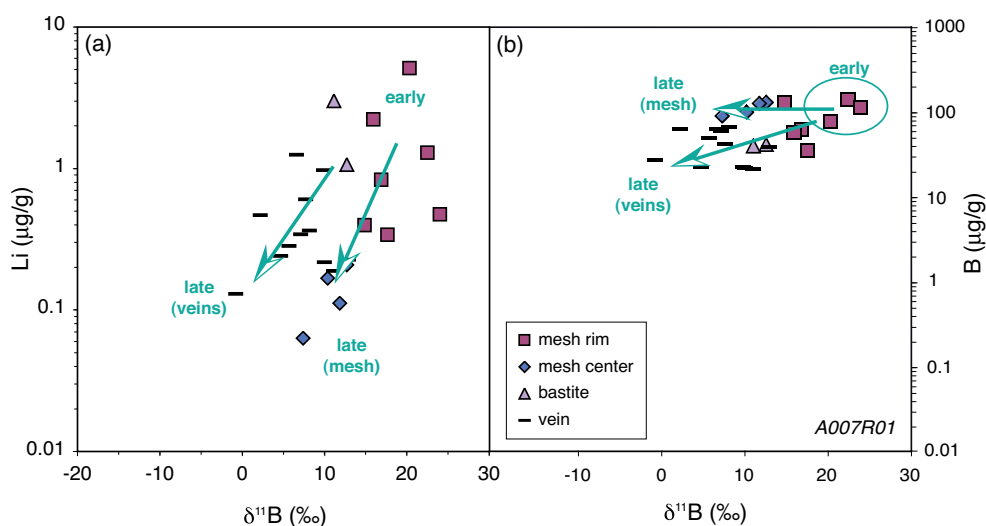


**Fig. 4.19:** a)  $\delta^{11}\text{B}$  vs. B and b)  $\delta^{11}\text{B}$  vs. Li of serpentine in sample A007R01. Arrows indicate the compositional change from early to late serpentine, *i.e.*, between serpentine generations.

Based on the abundance of single serpentine textures and their B concentrations, estimated average bulk rock  $\delta^{11}\text{B}$  values are positive with  $\sim +16$  ‰. This value is consistent with the positive signature between of  $+10$  to  $+20$  ‰ in bulk serpentinites and  $+8$  to  $+11$  ‰ in serpentinite muds from ODP 195 Site 1200 (Benton *et al.*, 2001; Savov *et al.*, 2004). The depleted mantle clearly has a lower B concentration and  $\delta^{11}\text{B}$  value of  $\sim 0$  (*e.g.*, Salters & Stracke, 2004). The results indicate that serpentinization of the Mariana mantle wedge peridotite leads to a strong increase in B concentration with, in average, positive  $\delta^{11}\text{B}$  values.

## 4.6 Interpretation of serpentine textures and mineral chemistry

The previous sections provided geochemical and textural evidence that the serpentinized spinel harzburgites from the Mariana mantle wedge experienced a complex history of deformation, melt infiltration, cooling and hydration. Finally, the forearc peridotite underwent serpentinization by slab-derived fluids, modifying the initial Li, Be and B content of the supra subduction zone mantle wedge. The distribution of light elements, B isotope signatures and serpentine polymorphs yields information about the hydration process and conditions within the mantle wedge.

#### 4.6.1 Estimates of the degree of partial melting

Primary mineral and bulk rock compositions of Mariana forearc serpentinites (South Chamorro and Conical Seamount) indicate a more depleted nature than those of abyssal peridotites (this study and *e.g.*, Ishii *et al.*, 1992; Shipboard Scientific Party, 2002a,c; Zanetti *et al.*, 2006). The serpentinites preserve a geochemical record of extensive partial melting of the upper mantle at spinel-facies conditions in the supra subduction zone mantle (*e.g.*, Jaques & Green, 1980; Pearce *et al.*, 2000; Hellebrand *et al.*, 2001, 2002). According to the Cr# of spinel (28.0 to 70.2) and the Mg# of olivine, the degree of partial melting was 18 and 31 % (see section 4.3) which implies a strong refractory nature of these mantle peridotites. The highest degree of melting is found for sample A017G02, a sample with extremely Cr-rich spinel and Na<sub>2</sub>O-rich Cpx. These results agree with the literature data; according to HREE and major element compositions, the Mariana ultramafic rocks experienced 15–30 % partial melting of depleted MORB mantle which has subsequently been modified by interaction with boninitic melt within the mantle wedge (Ishii *et al.*, 1992; Parkinson & Pearce, 1998; Shipboard Scientific Party, 2002a; Zanetti *et al.*, 2006). The initial partial melting event usually can be followed by metasomatizing by mafic alkaline to carbonatitic melts (*e.g.*, Grégoire *et al.*, 2000).

#### 4.6.2 Melt impregnation (refertilization / ‘metasomatism’)

The serpentinitized South Chamorro harzburgites show various textural and chemical evidence that the peridotite was infiltrated by melts prior to serpentinization (see Elthon, 1992; Niu, 1997; Niu & Hékinian, 1997). One textural indication for the presence of melt is interstitial clinopyroxene (+ Spl) that crystallized at triple junctions between olivine grains (Fig. 4.2d-e in section 4.2). These Cpx(-Spl) clusters are reminiscent of a quench texture and indicate that part of this melt has crystallized under lithospheric (cold) conditions. Small Cpx prisms or spindle-shaped grains in Opx exsolution lamellae (Fig. 4.2k in section 4.2) can be interpreted as having crystallized from incompletely extracted interstitial melts (Seyler *et al.*, 2001).

The light element contents of the interstitial clinopyroxene provides further evidence for a rock-interaction with interstitial melts. Li contents are higher compared to olivine and orthopyroxene and compared to normal mantle clinopyroxene. This Li enrichment in Cpx with a trend towards the MORB field (Fig. 4.17) can be related to metasomatism by mafic silicate melts or hydrous fluids (Seitz & Woodland, 2000). The preferential incorporation of Li in clinopyroxene during impregnation of peridotite by mafic melt was also reported by other studies (*e.g.*, McDade *et al.*, 2003; Ottolini *et al.*, 2004; Woodland *et al.*, 2004; Pelletier *et al.*, 2008b; Vils *et al.*, 2008). Li enrichment in clinopyroxene could alternatively be explained by fractionation upon cooling, leading to a Li depletion in olivine and orthopyroxene by inter-mineral diffusive re-equilibration (Coogan *et al.*, 2005; Jeffcoate *et al.*, 2007; Vils *et al.*, 2008).

However, olivine and orthopyroxene have Li concentrations similar to depleted mantle (Fig. 4.17 in section 4.4.2). Serpentinite A017G02 contains clinopyroxene grains with grain-to-grain borders to orthopyroxene. These clinopyroxenes have lower Li contents of ~2 µg/g, indicating a primary origin for Cpx which is an arguments against fractionation upon cooling. However, the Li enrichment in

interstitial clinopyroxene was principally controlled by impregnating melts except for clinopyroxene from sample A017G02 which does not show melt-related textures and composition.

### 4.6.3 Temperature conditions and fluid-rock ratios

B uptake during serpentinization and in analogy Li incorporation in serpentine is favored at temperatures below 350 °C (Seyfried & Dibble, 1980; Bonatti *et al.*, 1984; Seyfried *et al.*, 1998;). Furthermore, the potential role of pH on element enrichment/depletion during serpentinization was emphasized by several authors (*e.g.*, Palmer *et al.*, 1987). As especially B isotope compositions in serpentinites are highly pH dependent (see section 4.6.7; Boschi *et al.*, 2008; Vils *et al.*, 2009) the discussion of temperature, pH and fluid-rock ratios are important for the interpretation of element fluxes within the serpentinites.

#### 4.6.3.1 Fe-distribution between serpentine-brucite-magnetite: evidence for serpentinization conditions

Progressive serpentinization of peridotite produces mostly SiO<sub>2</sub>-undersaturated minerals (*e.g.*, Evans, 2008). The Mariana mantle wedge serpentinites comprise abundant magnetite grains in serpentine, intergrowth of serpentine with brucite/amakinite, and pure brucite/amakinite. Additionally, it is documented in natural serpentinite samples (*e.g.*, Hostetler *et al.*, 1966; Moody, 1976a,b, 1979; Wicks & Plant, 1979; Ishii *et al.*, 1992; Bach *et al.*, 2004, 2006; D'Antonio & Kristensen, 2004; Evans, 2004, 2008) and shown by experiments in ultramafic systems (*e.g.*, Allen & Seyfried, 2003 and references therein) that hydration of olivine can produce serpentine with brucite. Due to the stability of forsteritic olivine, this reaction does not occur at temperatures above 350 °C at 500 bars (Allen & Seyfried, 2003). Older studies have placed the temperature of the reaction of forsterite into Mg-rich brucite together with chrysotile and  $\pm$ magnetite at 350 to 450 °C and pressures below 2 GPa (*e.g.*, Moody, 1976b).

Compositions of serpentinites and serpentine minerals show that natural systems always involve an Fe-component. If the process of serpentinization is basically isochemical for Si, total Fe, and Mg (*e.g.*, O'Hanley, 1996; Shervais *et al.*, 2004), the growth of serpentine  $\pm$  brucite from olivine and orthopyroxene with high Mg# requires the precipitation of an additional Fe-rich mineral like magnetite (or nickel-iron) for mass balance (Evans, 2008). The serpentinization of the fayalitic component of olivine therefore results in the precipitation of magnetite with attendant production of dissolved H<sub>2</sub> and SiO<sub>2</sub> (Mével, 2003). It has been suggested that iron contents of serpentine and brucite minerals as well as the assemblage with magnetite may not only be an indication of the initial iron content of the replacing mineral (*e.g.*, olivine), but also can give further insight into the *PT*-conditions during serpentinization (*e.g.*, Hostetler *et al.*, 1966; Barnes *et al.*, 1972; Moody, 1976a,b; Foustoukos *et al.*, 2008 ).

The highest FeO content for pure serpentine in this study is 12.8 wt% (pure serpentine with Si/(Mg+Fe) = 0.67). Though, in Mariana mantle wedge serpentinites from South Chamorro



Seamount serpentine with even 14.5 wt% FeO were reported (D'Antonio & Kristensen, 2004) found. These high concentration exceed the general FeO range reported in the literature for most serpentines in metaperidotites (Wicks & Plant, 1979).

In the investigated Mariana samples, serpentine mesh rims have lower Fe/(Mg+Fe) ratios (Fe#) than the parent olivines, if magnetite occurs near the mesh rim along former grain boundaries (Fig. 4.20a; Fe# 0.07). Magnetite-free mesh centers have the same Fe# than the parent olivine (Fig. 4.20a; Fe# 0.09). If serpentine mesh centers are magnetite-bearing, the Fe# is lower than in the parent olivines (Fig. 4.20b; Fe# 0.07 vs Fe# 0.09 in Ol).

Bastite serpentine can have both higher and lower Fe contents than the parent orthopyroxene. In sample E7H2-2B, a vein of large blades of Fe-rich brucite (up to 33 wt% FeO), *i.e.*, amakinite coexists with a magnetite-free serpentine vein (Fig. 4.20c). The FeO content of this serpentine vein is lower (1.8–2.6 wt%) than the associated Mg-brucite- and magnetite-bearing mesh serpentine in this sample. Another vein in this sample, next and parallel to the low-Fe serpentine vein, is composed of coarse serpentine fibers and is free of brucite and magnetite (Fig. 4.20c). Serpentine FeO contents are between 4.1 and 5.2 wt%.

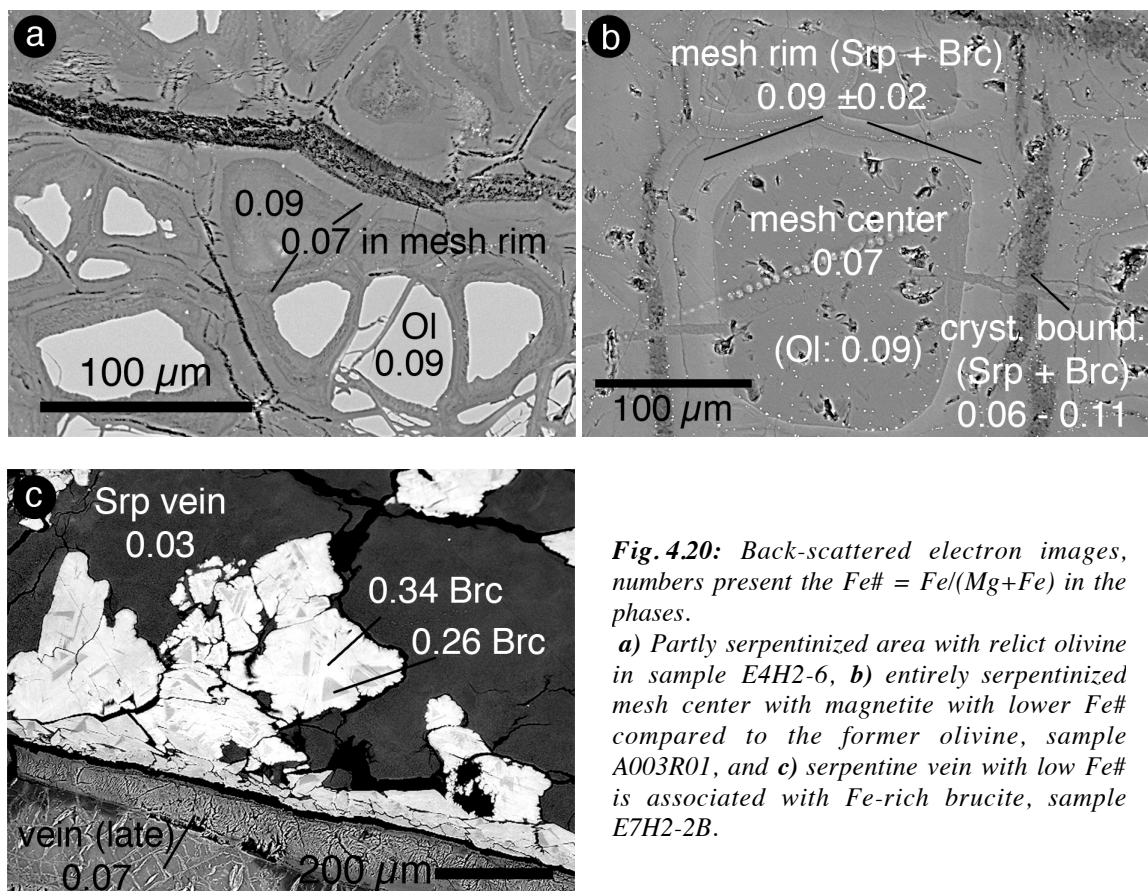


**Fig. 4.20:** Back-scattered electron images, numbers present the Fe# = Fe/(Mg+Fe) in the phases.

**a)** Partly serpentinized area with relict olivine in sample E4H2-6, **b)** entirely serpentinized mesh center with magnetite with lower Fe# compared to the former olivine, sample A003R01, and **c)** serpentine vein with low Fe# is associated with Fe-rich brucite, sample E7H2-2B.

These observations correlate with other studies on serpentine compositions (e.g., Hostetler *et al.*, 1966): serpentines possess lower Fe/(Mg+Fe) ratios than the parent olivines and pyroxenes, while coexisting brucite is richer in iron. Furthermore, high amounts of magnetite are associated with less iron in coexisting serpentine and olivine or, after Moody (1976a) even brucite minerals. In addition, in this study it was observed that available iron goes into magnetite or brucite minerals and serpentine rather is Fe-poor, when serpentine directly forms out of fluids (veins).

The observed Fe-allocation between serpentine, brucite and magnetite suggest the following serpentinization conditions.

(i) During magnetite precipitation accompanied by lower Fe# in serpentine, Si-activities were low, while magnetite-free serpentine (more Fe-rich) formed at higher Si-activity (Frost & Beard, 2007). The magnetite formation at low Si-activity further requires high  $f(\text{O}_2)$  or higher temperatures. Lower temperatures favor the iron substitution into brucite and lizardite rather than the formation of magnetite (Moody, 1976a). This explains the Fe-rich brucite in the vein coexisting with magnetite-free serpentine. Nevertheless, in an open system sufficient fluid flow will induce changes in rock composition by mass transfer of elements and a change in silica activity and  $f(\text{O}_2)$  (at constant  $P$  and  $T$ ) (Normand *et al.*, 2002; Frost & Beard, 2007; Evans, 2008).

(ii) Moreover, amakinite (Fe-rich brucite) forms at decreasing temperature, while the assemblage magnetite + Mg-rich brucite forms at the expense of amakinite at the high temperature end of the brucite stability field (for the same values  $f(\text{H}_2)$  and  $f(\text{H}_2\text{O})$ ; Moody, 1976a,b). Amakinite is most stable at temperatures well below 350 °C and at low  $f(\text{O}_2)$  (Moody, 1976a, b). Recently, Foustoukos *et al.* (2008) showed that Fe-rich brucite (25–30 %  $\text{Fe}(\text{OH})_2$ ) appears to be stable at temperatures lower than 250 °C which further limits the efficiency of magnetite formation and the extent of  $\text{H}_2(\text{aq})$  generation during serpentinization. It therefore can be concluded that the late amakinite veins in the serpentinites investigated formed at relatively low temperatures.

(iii) The high pH of the reacting fluid and the relatively low temperatures in 27 km depth (at the slab-mantle-interface) favors the uptake of B into serpentine during serpentinization (see next section). Foustoukos *et al.* (2008) suggest that Mg-bearing hydroxides might also be possible as mineral phases for in  $\text{BO}_3$  enriched sites and enhance fractionation with tetragonal B in solution. In addition, Pokrovsky *et al.* (2005) suggest a strong affinity of brucite to adsorb  $\text{B}(\text{OH})_3(\text{aq})$  at low temperatures (25 °C). However, brucite in the samples has very low B contents limiting the major B-containing phase to serpentine.

Mineral compounds, textures and the serpentine polymorphs lizardite and chrysotile indicate that serpentinization of the Mariana mantle wedge peridotite took place at relatively low temperatures of <350 °C. This low temperature during serpentinization first of all favors the precipitation of Fe into magnetite, causing serpentine to have a lower Fe# compared to the parent olivine. Nevertheless, brucite is a common secondary mineral in the samples which occurs as fine-grained and intimately intergrowth with e.g., lizardite in mesh textures and as monomineralic Fe-rich brucite veins. Brucite compositions of the samples show a very broad range of Fe-Mg composition from 12–70 %  $\text{Fe}(\text{OH})_2$ .

The variable assemblages of serpentine – brucite – magnetite with changing Fe-distribution indicate that serpentinization in the Mariana mantle wedge is characterized by an open system with sufficient fluid flow accompanied by changes in temperature, silica activity and  $f(\text{O}_2)$ .

#### 4.6.3.2 Serpentine polymorph distribution: evidence for variable fluid-rock ratios

Lizardite (Liz) and chrysotile (Ctl) were identified as the major serpentine polymorphs in Conical (C. Smt.) and South Chamorro Seamount (S. Ch. Smt.) serpentinites and occur together with variable amounts of magnetite and brucite (see previous section). Serpentinites from S. Ch. Smt. are antigorite-free, whereas in samples from C. Smt., antigorite (Atg) is present. During the last years it got commonly accepted that the direct transformation of olivine to serpentine and magnetite preferentially takes place below 250–300 °C (Wunder *et al.*, 2001; Allen & Seyfried, 2003; Mével, 2003; Bach *et al.*, 2004;). Particularly, Ctl formation takes place within temperature limits of 180 °C (Mével, 2003) or even lower (Barnes *et al.*, 1967) and 250 °C (stable reaction; 450 °C for metastable reactions; Mével, 2003). Within this temperature range, Evans (2004) argued that Ctl is a metastable phase whose occurrence is more determined by circumstances of growth rather than temperature and pressure. Liz appears to be the more stable phase over wide *PT*-ranges (Mével, 2003) and olivines in the rocks are directly pseudomorphed to Liz rather than to Ctl (O'Hanley, 1996), facilitated by its crystallographic texture (Evans, 2004).

The appearance of Fe-rich brucite limits the maximum temperature to 250°C (Foustoukos *et al.*, 2008) in some regions of the mantle wedge. Atg is known as a 'higher grade' serpentine polymorph (Berman, 1988; Ulmer & Trommsdorff, 1995; Wunder & Schreyer, 1997); it is stable under conditions up to 1.5 GPa and 650 °C (Evans *et al.*, 1976) or up to 7 GPa and 500 °C, respectively (*e.g.*, Ulmer & Trommsdorff, 1995; Peacock & Hervig 1999). Therefore, Atg is the most stable serpentine (with brucite or talc) above 310 °C (at 1 bar) (Evans, 2004). Its formation is shifted to lower temperatures for higher pressures during retrograde metamorphism (Evans *et al.*, 1976). So far, the *PT*-relations between serpentine polymorphs are still not sufficiently well known and their stability fields partially overlap. Thus, they give no precise indication of the serpentinization temperature (see discussion by Bach *et al.*, 2004), but at least a rough estimation.

However, the high abundance of lizardite and chrysotile with a lack of high-temperature minerals talc and antigorite clearly suggests a rather low temperature environment during serpentinization. A maximum temperature of 350 °C for the hydration of the Mariana mantle wedge can be estimated (within a transitional zone of coexisting Liz and Atg + Brc), as the serpentine polymorphs Ctl and Liz are not stable at higher temperatures (*e.g.*, Allen & Seyfried, 2003; Evans, 2004). The occurrence of Atg in C. Smt. serpentinites may suggest higher 'sampling depths' at higher temperatures; the slab is slightly deeper below C. Smt., situated at a greater distance from the trench compared to S. Ch. Smt. (*e.g.*, Mottl *et al.*, 2004).

The serpentine polymorphs identified in the Mariana mantle wedge serpentinites do not only provide information about the *PT*-conditions, but also can be indicative for the fluid-rock ratios

during their formation. The variability of serpentine polymorphs between different textures emphasizes the importance of fluid-rock ratios during serpentine growth. The preferred growth of lizardite and chrysotile requires different conditions (Evans, 2004). Firstly, the existence of space and enough fluids promotes crystallization of chrysotile, *i.e.*, oriented serpentine fibers (*e.g.*, Evans, 2004; Andreani *et al.*, 2005). This observation is comparable to field observations in low-temperature sheared serpentinites that indicate an increase of chrysotile abundance with increasing deformation degree (Coleman & Keith, 1971; Wicks, 1984). Low fluid-rock ratios should support slow lizardite growth (Evans, 2004). Furthermore, Evans (2004) interpreted the small grain size and poor crystallinity of rock-forming lizardite to be caused by low temperature crystallization at the site of serpentinization.

Since lizardite is the most abundant serpentine polymorph in the samples, serpentinization in the Mariana forearc must have occurred at generally low fluid-rock ratios. First intensive fluid pulses produced cracks in the fresh rock and triggered the formation of crack-filling chrysotile (with minor polygonal serpentine). These cracks eventually act as important fluid paths. However, serpentinites are dominated by early *in-situ* pseudomorphs such as mesh rims. The existence of lizardite in these textures suggests that the fluid-rock ratios were relatively low, *i.e.*, that the fluid was completely 'soaked' and consumed by the rock. Further fluid pulses increased the fluid-rock ratios and enabled chrysotile (with minor polygonal serpentine) pseudomorphs after relict minerals. Serpentinization weakened the rock and chrysotile vein formation indicates even late high fluid-rock ratios in the mantle wedge due to ongoing fluid pulses released from the subducting slab. The widespread occurrence of polygonal serpentine, due to its more evolved nature compared to chrysotile (Baronnet & Devouard, 1996), may reflect some 'recrystallization' or 'reorganization' of the serpentine polymorph structures (*e.g.*, Andreani *et al.*, 2005, 2007) more or less independent from fluid pulses or fluid-rock ratios.

Serpentinization in the Mariana mantle wedge is characterized by 1) complete fluid consumption associated with the formation of lizardite and 2) phases of high fluid-rock ratios leading to direct chrysotile and crack-filling chrysotile vein formation. These changing fluid-rock ratios at low serpentinization temperatures, reflected by different textural types, also have influence on the light element composition of the serpentines (see following sections).

#### 4.6.4 Correlation between serpentine textures and their light element composition

Though the major element composition of serpentine is primarily controlled by the composition of the mineral it replaces, the type of serpentine polymorph (*e.g.*, lizardite or chrysotile) and the Fe distribution between mineral phases (serpentine, brucite, magnetite) is controlled by pH, temperature and the fluid-rock ratio in combination with the textural site and by the serpentine generation (early or late). The variable light element (Li, Be, B) concentrations in serpentine minerals suggested that it is possible to distinguish between different serpentine textures (*e.g.*, mesh rims, bastites, veins), *i.e.*, that different textures may have characteristic light element signatures. Although compositions of single serpentinite clasts strongly overlap, the serpentinized peridotites are characterized by different

generations of serpentine that have typical Li and B contents for certain textures within single clasts (see section 4.4.2). B contents can be variable even within similar textures, whereas the Li abundance is more dependent on the textural position, *i.e.*, the serpentine generation.

Early fluid pulses, released from the subducting slab, migrate through cracks in the peridotite mantle wedge and along grain boundaries (*e.g.*, around olivine). Consequently, serpentinization begins with fracture-filling veins and the formation of mesh rims replacing olivine. These early serpentines are characterized by relatively high Li concentrations of generally  $>2 \mu\text{g/g}$  and high B concentrations ( $\sim 40\text{--}80 \mu\text{g/g}$ ) (Fig. 4.21). While concentrations vary between serpentinite fragments, they are consistent within a fragment. Nevertheless, brucite admixtures in mesh rims lead to a decrease in Li concentration (*e.g.*, A007).

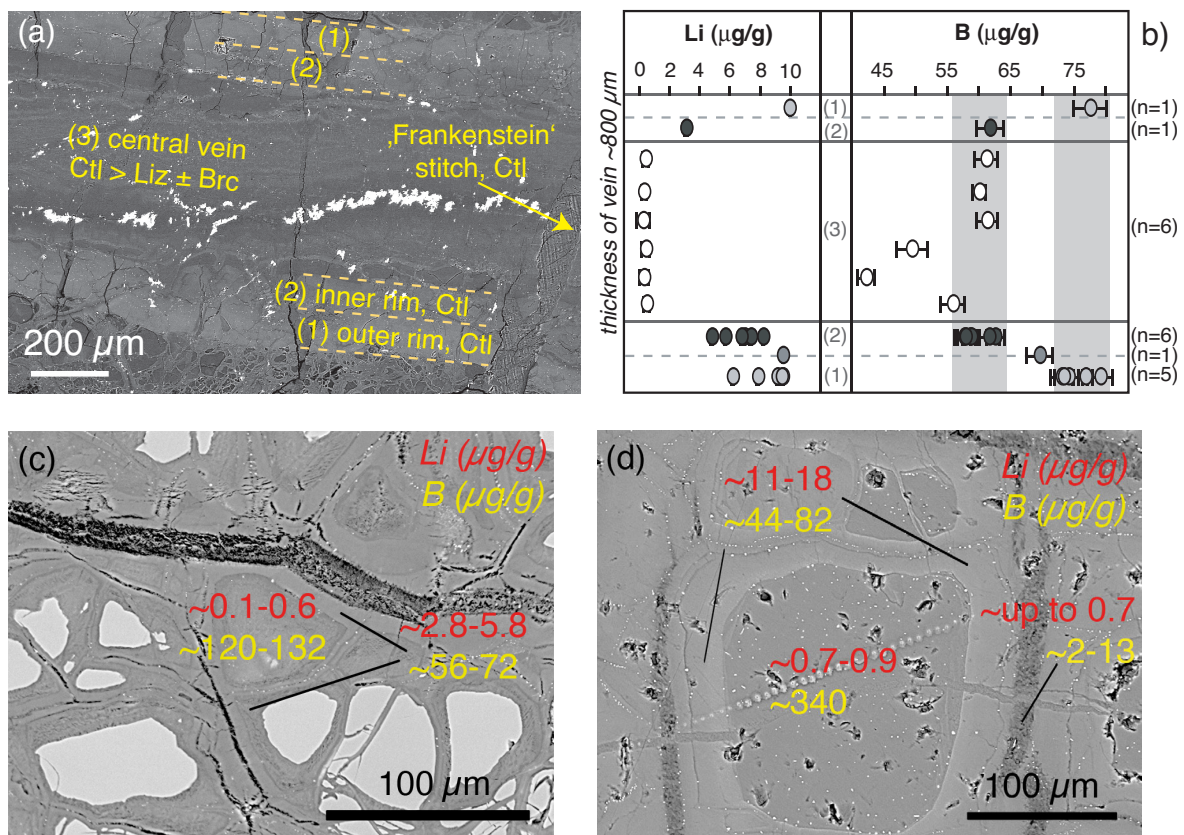


**Fig. 4.21:** **a)** Back-scattered electron (BSE) image of a zoned 'Frankenstein' vein (sample A013R01(25-27)), **b)** Li and B contents ( $\mu\text{g/g}$ ) in the zoned vein: the vein rim is enriched in Li and B, **c)** BSE image of partly serpentinized area with relict olivine cores (sample E4H2-6), and **d)** BSE image of a completely serpentinized area with serpentine mesh center (sample A003R01). Li and B contents are noted in **c)** and **d)**.

Textural relationships indicate that bastite formation after orthopyroxene already starts during early olivine serpentinization. Indeed, Li concentrations of thin early veins through bastites are high (similar to mesh rim compositions) and B concentrations are slightly lower compared to mesh rims (see above). Also early serpentine veins tend to have mesh texture compositions with high Li and high B concentrations (Fig. 4.21). The high Li contents in first generation serpentines suggest that Li

partitions immediately into the serpentine minerals. All these early textures, *i.e.*, the first generation serpentines, reflect the composition of the first fluids that entered the rock, as this fluid got completely ‘soaked’ by the serpentine formation. Thus, the initial slab-derived fluids were enriched in light elements.

Continuing serpentinization is typically characterized by high fluid-rock ratios and the formation of mesh centers replacing relict olivines. These mesh centers generally tend to lower Li concentrations (Fig. 4.21), but may also have compositions similar to the mesh rims and bastites formed earlier. However, the mesh rim composition is not changed by the continuing serpentinization; Li concentration remains high in mesh rims around entirely serpentinized mesh centers and indicates that light element compositions in already formed serpentine are not changed by ongoing serpentinization. The B content in mesh rims is often higher compared to early serpentine (Fig. 4.21). Texturally late veins, some of them brucite-bearing, tend to compositions more depleted in both B and Li. However, most veins and mesh centers are depleted in Li relative to primary minerals (depleted mantle composition) implying a depletion during late serpentinization in these cases.

Fluids released from the subducting slab have variable composition due to the mineralogical heterogeneity of the slab. The presented data reveal that these serpentinizing fluids can change their composition in the mantle wedge by element loss into serpentine and are modified by new fluid pulses coming from below. Serpentinization of the mantle wedge is very heterogeneous on all scales. Nevertheless, fluid pulses at relatively low fluid-rock ratios lead to Li-rich early serpentines, whereas late serpentine is characterized by serpentine polymorphs and light element compositions triggered by massive fluid supply. These differences should have influences not only on the light element concentrations, but also on the B isotope distribution in different serpentine generations.

### 4.6.5 Boron isotope evolution (serpentinizing fluid pulses)

The Pacific plate subducts beneath the Mariana forearc and dehydrates. The released water hydrates, *i.e.*, serpentinizes the overlying mantle wedge. This is not a sudden process but rather a series of stepwise reaction fronts fed by separate fluid pulses through the rock. The mud volcanoes are even formed by multiple episodes of mud depositions at the seafloor, an evidence for episodic discharge of serpentinite mud (Fryer *et al.*, 2006; Bickford *et al.*, 2008). These fluid pulses can have changing, constantly evolving composition.

Furthermore, as discussed above, the fluid-rock ratios during serpentinization can be highly variable which is the main reason for *e.g.*, the formation of lizardite and chrysotile in different textural sites (*e.g.*, mesh, vein). Also, serpentine textures or generations, respectively, can be correlated to distinct Li and B concentrations. Batches of fluid penetrate the mantle wedge and are either consumed or continuously evolve during interaction with the surrounding peridotite rock. This process is in line with the variation in light element contents and B isotope values of excess fluids that

ascend and are emitted through the Mariana forearc serpentinite mud volcanoes and exit as cold springs at their summits.

The distinctive composition of the interstitial water recovered from South Chamorro, Conical and Torishima Seamounts implies an origin by dehydration of the subducting Pacific Plate (Mottl *et al.*, 2003 and references therein). The temperature of the water emitted by springs on the seafloor is very low ( $\sim 2^\circ\text{C}$ ; Mottl *et al.*, 2003 and references therein), while the initial temperature of the slab originating fluids is  $\sim 150\text{--}250^\circ\text{C}$  at  $\sim 0.8$  GPa and  $\sim 27\text{--}29$  km depth at the top of the subducting Pacific Plate, estimated by steady state thermal models for the Mariana arc (Hussong & Fryer, 1982; Kincaid & Sacks, 1997; Peacock & Wang, 1999; Mottl *et al.*, 2003 and references therein; Peacock, 2003). These temperatures coincide with the temperature range not exceeding  $200\text{--}300^\circ\text{C}$  estimated based on the lizardite and chrysotile dominance in association with Fe-rich brucite assemblages in South Chamorro and Conical Seamount peridotites (this study; Fryer & Mottl, 1992; Heling & Schwarz, 1992; Shipboard Scientific Party, 2002a; D'Antonio & Kristensen, 2004).

Fluid directly released from the subducting slab has a neutral pH with the potential for large B isotope fractionation factors during serpentine formation. Pore fluids from Conical and South Chamorro Seamounts have high pH ( $\sim 12.5$ ), except near the seafloor, where the pH decreases to seawater values (Benton *et al.*, 2001; Mottl *et al.*, 2003). As serpentinization temperature in the Mariana forearc mantle wedge is very low and upwelling pore fluids have high pH, B can be assumed to be tetrahedrally coordinated  $[\text{B}(\text{OH})_4]$  in both serpentine and fluids (see chapter 1; Spivack & Edmond, 1987). Temperature ranges and pH favor the B uptake into serpentine at this supra subduction zone setting, leading to the observed elevated B contents in the serpentinized peridotites. According to Foustoukos *et al.* 2008; and references therein), fluids in equilibrium with peridotite have nearly basic pH at  $>250^\circ\text{C}$  and relatively low fluid-rock ratios and even acidic pH at high water-rock ratios (*e.g.*,  $w/r = 10$ ). Cooling of the fluid will increase the pH.

Hence, slab-derived fluids with neutral pH cool during ascend to the seafloor and the pH increases during this path. Although significant concentrations of  $\text{B}(\text{OH})_4$  complexes are present in fluids at  $\text{pH} > 8$  (Palmer & Swihart, 1996), a changing pH during serpentine formation could be responsible for the observed  $\delta^{11}\text{B}$  variation (Boschi *et al.*, 2008). The variation in Li and B contents as well as B isotope ratios in serpentine within and between samples cannot be satisfyingly explained by the pH and degree of serpentinization (*e.g.*, hydration = B enrichment). Rather, the light element budget and B isotope distribution should strongly depend on the water-rock ratios during serpentinization.

Early serpentine in the highly serpentinized Mariana peridotites is characterized by high Li contents and high  $\delta^{11}\text{B}$  values, whereas late serpentine has relatively low Li contents with low  $\delta^{11}\text{B}$  values of down to  $-14\text{‰}$  (Fig. 4.22). Compositions vary between clasts, but the highest  $\delta^{11}\text{B}$  values in early serpentine are  $\sim +15$  to  $+24\text{‰}$ . The broad range of serpentine  $\delta^{11}\text{B}$  values indicates variable fluid-rock ratios and varying fluid composition.

As described above, early serpentine formed during conditions with low fluid-rock ratios with the fluid getting completely consumed by serpentine. During olivine hydration the B fractionates and

forms serpentine of varying  $\delta^{11}\text{B}$  values. This early serpentines, however, are found along thin vein rims and small-scaled mesh rims around olivine cores ( $<30\ \mu\text{m}$ ). Therefore, SIMS spot analyses ( $\sim 25\ \mu\text{m}$ ) give an average composition which consequently reflects the average  $\delta^{11}\text{B}$  value from the serpentinizing fluid. As the early serpentine has high  $\delta^{11}\text{B}$  values, the slab-released fluid is expected to have variable but highly positive  $\delta^{11}\text{B}$  of up to  $\sim +20\text{‰}$ .

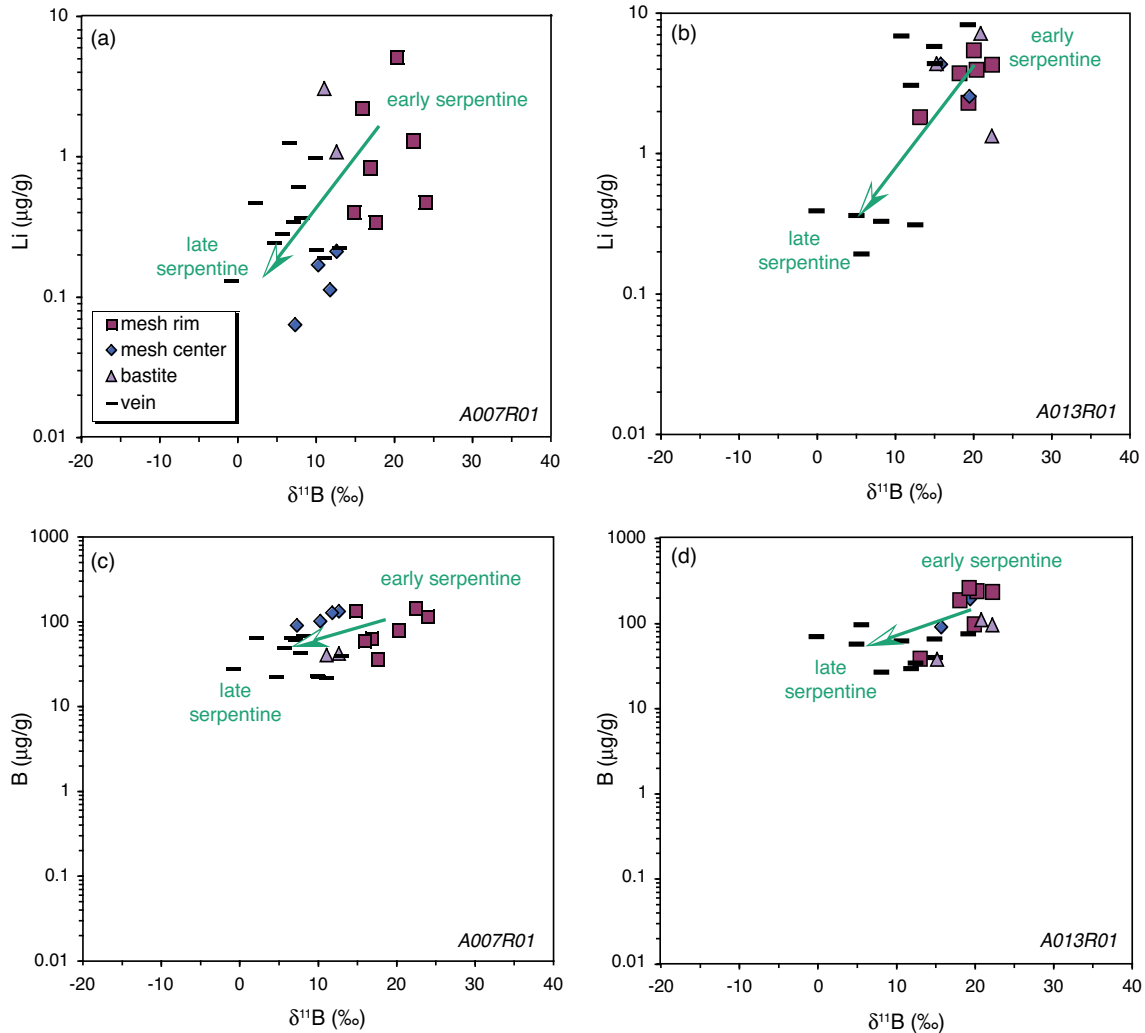


**Fig. 4.22:**  $\delta^{11}\text{B}$  vs  $\text{Li}$  and  $\delta^{11}\text{B}$  vs  $\text{B}$  for samples A007R01(a + c) and A013R01 (b + d). Vein serpentine tends to lower B isotope ratios compared to mesh serpentine. Further diagrams in Appendix B.

The high degrees of serpentinization and the high abundance of serpentine veins suggest a generally high fluid-rock ratio. During such periods of high fluid-rock ratios, texturally late serpentine formed (see above). These high amounts of fluid allow B fractionation during B incorporation into newly formed serpentine. In order to estimate  $\delta^{11}\text{B}$  compositions of coexisting fluids, fractionation factors between serpentine and fluid have to be considered in this case. The fractionation factor  $\Delta^{11}\text{B}$  (during fluid-from-slab release) is  $\sim -14\text{‰}$ , as pH is basic and temperatures are around  $300\text{ °C}$  (e.g., Wunder et al., 2001). In order to produce serpentine with the observed negative  $\delta^{11}\text{B}$  values, a fluid with neutral to positive  $\delta^{11}\text{B}$  values is required.



## Chapter 5

# Metamafic blueschist-facies rocks from the Mariana forearc: reactions at the slab-mantle interface

### 5.1 Introduction

Studies on metamafics from the Mariana subduction zone are rare (Maekawa, 1992, 1993, 1995; Fryer, 1999, 2000; Gharib, 2006) and focussed on petrologic descriptions and major element mineral compositions. For the first time, this study presents a detailed inventory of a large number of different metamafic clasts including petrology, *PT*-conditions of the metamorphic formation and the light element (Li, Be, B) contents and boron isotope composition of the rock-forming minerals. Major, trace and light element (Li, Be, B &  $\delta^{11}\text{B}$ ) compositions of minerals were analyzed to investigate the geochemical characteristics of slab metamorphism and mélangé formation along the active Mariana subduction zone slab–mantle interface.

To estimate the loss of fluid and fluid-mobile elements of the oceanic crust at a depth of >20 km, the trace element abundances of the blueschist-facies clasts can be compared to the compositions of basaltic oceanic crust, which is influenced by hydrothermal and ocean-floor alteration. The B isotope system is a widely applied and meaningful tracer of recycling processes occurring during subduction, primarily recording the thermal and fluid evolution of the subducting slab. During fluid loss the heavier B isotope is preferentially enriched in the fluid, leaving behind an isotopically lighter residual. As this process is most effective at low temperatures (Hervig *et al.*, 2002), large and measurable effects in the blueschist-facies mafic clasts are expected.

The only location where such slab-derived rocks are carried to the surface/ocean floor in an active subduction zone are the the Mariana forarc serpentinite seamounts (Maekawa *et al.*, 1992, 1993; Maekawa, 1995; Fryer *et al.*, 1999, 2000; Gharib, 2006). The compositional variations of seamount muds and slab-derived fluids (*e.g.*, Mottl *et al.*, 2004) suggest that the mafic material originates from the décollement region between the subducting Pacific Ocean lithosphere and the overlying forearc mantle wedge entrained into the rising serpentinite mud (*e.g.*, Fryer, 1992; Maekawa *et al.*, 1992; Mottl, 1992; Fryer *et al.* 1999). Therefore, these rocks offer a unique window into processes in the subducting slab.

Previous studies of metamorphosed mafic rocks recovered from a serpentinite forearc seamount in the Mariana region (*e.g.*, Maekawa *et al.*, 1993) recognized two types of metamorphism on the basis of mineral parageneses of the metamorphic rocks; one at low pressure and one at high pressure, the latter providing direct evidence of blueschist facies subduction zone metamorphism (Maekawa, 1995). The investigation of these incipient blueschist-facies rocks allowed the first empirical geochemical pressure and temperature estimates for sub-forearc subduction conditions from a modern subduction zone.

## 5.2 Mineral Chemistry (major elements)

Nearly 40 different types of metamafic rocks out of mud-pellets recovered from South Chamorro Seamount (ODP Leg 195, Site 1200) were studied. Most of the clasts are smaller than 0.5 mm in diameter and have a schistose foliation marked by oriented planar (Chl, Phe) and acicular (Am) minerals. Very fine-grained schists can be strongly folded. Other clasts have a patchy appearance of ‘intermingling’ mineral phases. The aligned metamorphic textures are a result of directed stress during metamorphism of the rock. The major mineral constituents of the studied rocks are amphibole, chlorite, phengite, epidote and titanite. Some samples contain low amounts of talc, others are nearly pure talc-aggregates. Minor minerals, present in some of the clasts, are ilmenite, magnetite, apatite, pyroxene, garnet, rutile, zircon and pumpellyite. Quartz and albite infrequently occur as inclusions in epidote.

Mineral compositions are specified in the following. Mineral nomenclature will be used according to Kretz (1983). Complementary back-scattered electron images with electron microprobe spots indicated are presented in *Appendix B*.

### 5.2.1 Amphibole

The amphiboles  $[(\text{Na},\text{K})_{0-1}(\text{Na},\text{Ca})_2(\text{Mg},\text{Fe}^{3+},\text{Fe}^{2+},\text{Al}^{\text{VI}})_5(\text{SiAl}^{\text{IV}})_8\text{O}_{22}(\text{OH},\text{Cl},\text{F})_2]$  often form acicular crystals in a chlorite matrix. According to the classification of Leake *et al.* (1997, 2004), they include calcic amphiboles (tremolite, actinolite, magnesio-hornblende, edenite, kaersutite), sodic-calcic amphiboles (richterite, barroisite), and sodic amphiboles (magnesio-riebeckite) (Fig. 5.1).

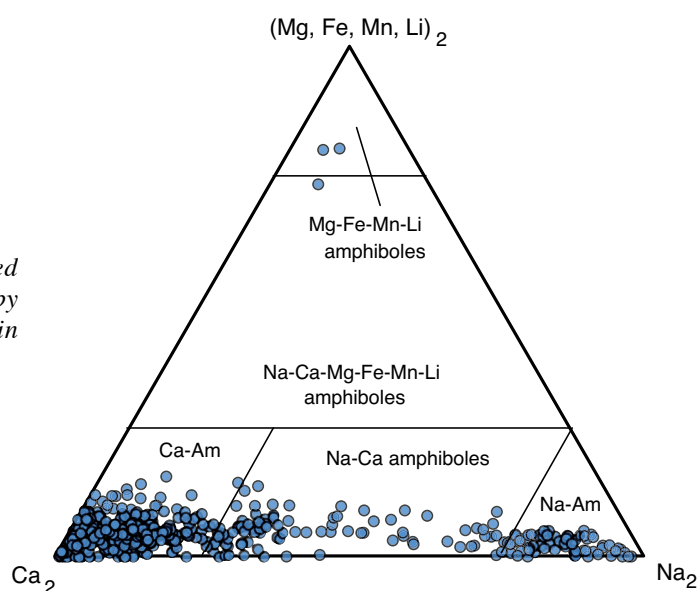


**Fig. 5.1:** Amphibole analyses plotted following the amphibole classification by Leake *et al.* (2004) for the five main groups of amphibole.

In sample D1H4-1A, few amphibole cores have a mangano-cummingtonite composition (Ca-Na-poor, ~9.9 wt% MnO). Typically, most of the metamafic clasts contain discontinuously zoned crystals with relatively calcic cores and more sodic rims. Some amphiboles show patchy zonation

with variable sodic-calcic composition. The Na content of the amphiboles in this study (up to 7.2 wt% Na<sub>2</sub>O) range as high as sodic amphiboles in the onland blueschist locality Syros (7.4 wt% Na<sub>2</sub>O; Marschall *et al.*, 2006).

Forneris & Holloway (2004) empirically demonstrated that relative abundances of Ca, Na, Al<sup>IV</sup>, and Al<sup>VI</sup> in amphiboles change approximately with pressure and temperature. A positive correlation between Al<sup>IV</sup> and Al<sup>VI</sup> in calcic amphiboles (Fig. 5.2a), which are assumed to be from earlier lower pressure metamorphic regimes, indicates increasing temperatures (Forneris & Holloway, 2004). Sodic amphiboles have a large range in Al<sup>VI</sup> and little Al<sup>IV</sup>. The calcic-sodic amphiboles have transitional composition and plot chemically between the calcic and sodic ones (Fig. 5.2a). In general, Na/Ca ratios in amphibole increase with pressure (Fig. 5.2b; Spear, 1993). Therefore, the Na-rich rims indicate crystallization with increasing *PT* and that the rise of the rocks to the seafloor was too rapid for significant retrograde metamorphism or metasomatism to more calcic rims.

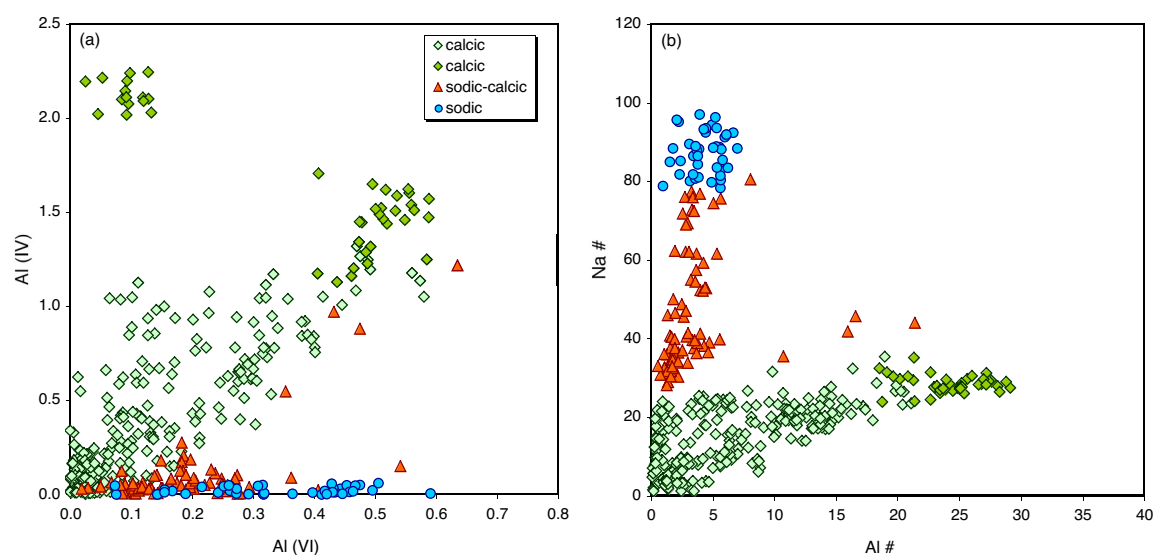
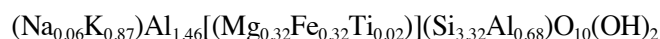


**Fig. 5.2:** **a)** Al<sup>VI</sup> vs Al<sup>IV</sup> in amphiboles. Calcic amphiboles show temperature-related trends, sodic amphiboles show pressure-related trends. **b)** Al# [100\*Al/(Al+Si)] vs Na# [100\*Na/(Na+Ca)] variation in amphiboles from Mariana metamafics.

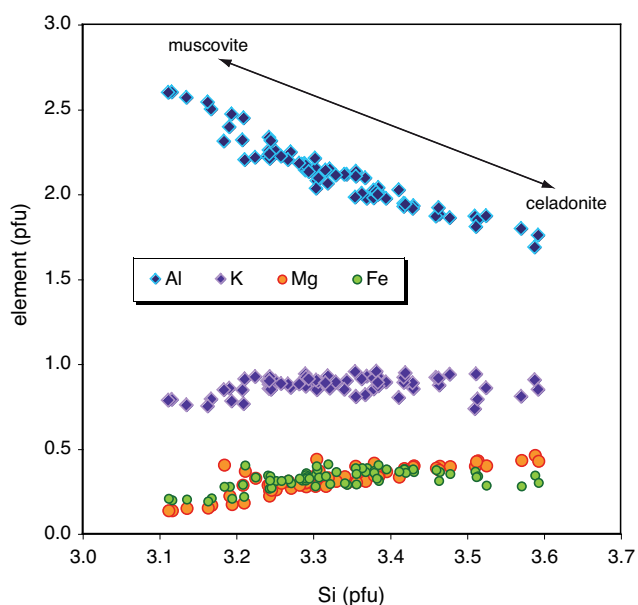
### 5.2.2 Phengite

Phengite in the Mariana metamafic rocks occurs as platy to very long sheaves together with chlorite and amphibole. Phengite is a high-Si, -Mg, and -Fe variety of muscovite that is stable at elevated pressures. It forms an incomplete solid solution between the muscovite and celadonite end-members (Fig. 5.3). This compositional range is defined by the reverse Tschermak substitution ( $\text{Fe}^{2+}\text{MgSi} \leftrightarrow \text{Al}^{\text{VI}}\text{Al}^{\text{IV}}$ ) with increasing Si, Mg and Fe as pressure increases (*e.g.*, Bucher & Frey, 2002; Fig. 5.3). One problem for formula calculation is the under-occupancy of the X-position (K+Na+Ca). The average composition for phengite in the metamafic rocks is:



Si occupies  $\sim 3.32$  pfu at an average celadonite composition of 0.32 in the muscovite-celadonite solid solution.

**Fig. 5.3:** Si (pfu) vs Al, K, Mg and Fe (pfu) for phengite minerals. Si, Mg and Fe increase with pressure.



### 5.2.3 Chlorite

In greenschist facies assemblages, chlorite is a common metamorphic mineral. It is one of the primary minerals and gives this facies its characteristic green color. The Mariana metamafic rocks contain platy chlorites with variable composition near to the Mg-rich clinochlore end-member on the clinochlore  $(\text{Mg}_5\text{Al})(\text{AlSi}_3)\text{O}_{10}(\text{OH})_8$  and chamosite  $(\text{Fe}_3\text{Al})(\text{AlSi}_3)\text{O}_{10}(\text{OH})_8$  solid solution (Tschermak substitution; Fig. 5.4a).

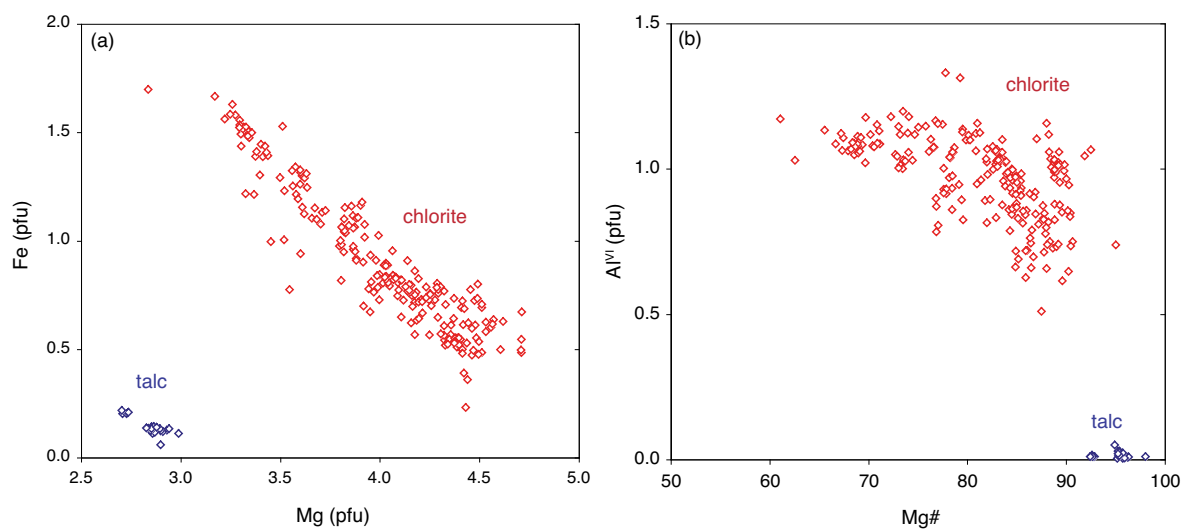


**Fig. 5.4:** **a)** Mg vs Fe (pfu) and **b)** Mg# (=  $\text{Mg}/(\text{Mg}+\text{Fe})$ ) vs  $\text{Al}^{\text{VI}}$  (pfu) for chlorite and talc in South Chamorro Seamount metamafic clasts. Calculation of formula units are based on 11 O for talc ( $\text{Fe}+\text{Mg}=3$ ) and 12 O for chlorite ( $\text{Fe}+\text{Mg}=5$ ).

Further substitution occurs between  $\text{Al}^{\text{IV}}\text{Al}^{\text{VI}}\text{-SiMg}$  (Fig. 5.4b). The ideal chlorite formula does not have significant octahedral vacancies, is not Si-rich and (Fe+Mg)-poor and has nearly equal amounts of tetrahedral and octahedral Al. However, quite common in the metamorphic chlorite minerals analyzed are measurable amounts of Ca, Na + K (up to: 1.0 wt% CaO, 0.7 wt%  $\text{Na}_2\text{O}$ , 0.6 wt%  $\text{K}_2\text{O}$ ), possibly due to smectite-layer ‘impurities’. Analyses with CaO >1 wt% are not considered as they might be analyses of chlorite mixed with other phases (*e.g.*, Amp).

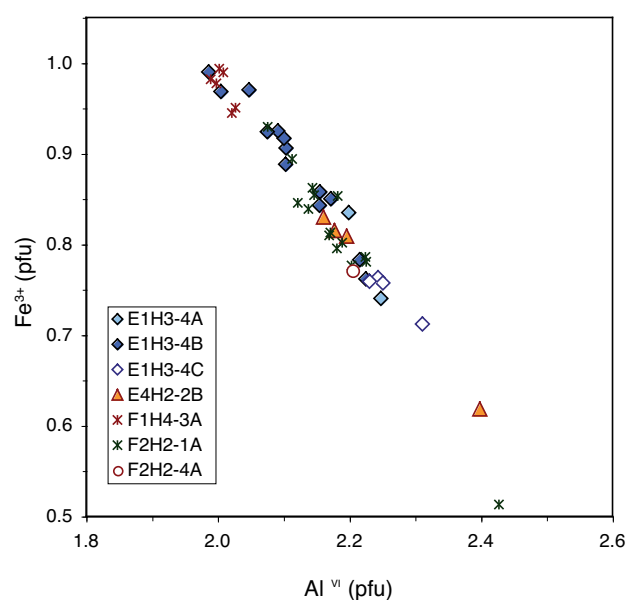
## 5.2.4 Talc

In some metamafic samples talc is associated with the matrix chlorite. Talc can be the dominant matrix forming mineral instead of chlorite implying metasomatic reactions. The composition averages around  $(\text{Mg}_{2.9}\text{Fe}_{0.1})\text{Si}_4\text{O}_{10}(\text{OH})$  with a minor Mg-Fe substitution (Fig. 5.4).

## 5.2.5 Epidote and Allanite

Epidote is found in eight metamafic samples. Its presence together with sodic amphibole is diagnostic of the epidote-blueschist facies (Evans, 1990). Even within a single clast, epidote shows different zonation patterns with a strong variation between the octahedral Al and Fe (Fig. 5.5). The solid solution between the clinozoisite ( $\text{Ca}_2\text{Al}_3\text{Si}_3\text{O}_{12}(\text{OH})$ ) and pistacite ( $\text{Ca}_2(\text{Al}_2\text{Fe}^{3+})\text{Si}_3\text{O}_{12}(\text{OH})$ ) end-members in the epidote group is defined by an  $\text{Al}^{\text{VI}}$  and  $\text{Fe}^{3+}$  substitution.

**Fig. 5.5:**  $\text{Al}^{\text{VI}}$  (pfu) vs  $\text{Fe}^{3+}$  (pfu) for epidote minerals. Increasing  $\text{Fe}^{3+}$  correlates with low temperatures or early crystallization.



Differences in composition are expressed by the pistacite end-member ( $X_{\text{ps}}$ ) calculated as  $\text{Fe}^{3+} / (\text{Al} + \text{Fe}^{3+})$ . Thereafter, epidote has a composition of  $X_{\text{ps}}$  from 0.17 to 0.33. Please note that  $X_{\text{ps}}$  is only reported for epidotes and not for the epidote group mineral allanite, which shows low EPMA totals and are bright in back-scattered images.

Furthermore, epidote has variable MnO contents in the range of 0.07–1.84 wt% and MgO content in the range of 0–0.37 wt%. Typical epidote cores and zonation are defined by allanite, with the general formula of  $\text{Ca}(\text{LREE})\text{Al}_2(\text{Fe}^{2+}, \text{Fe}^{3+})(\text{SiO}_4)(\text{Si}_2\text{O}_7)\text{O}(\text{OH})$ .

The epidotes can be assigned to the following groups defined by composition, zonation type and inclusions. Each epidote group includes epidote from several samples.

Epidote 1 ( $X_{\text{ps}} = 0.29$  in F2H2-1a): low-Fe epidote cores ( $X_{\text{ps}} = 0.17$ ) with quartz, epidote rim is irregular with some allanite zones.

Epidote 2 ( $X_{\text{ps}} = 0.25$  in E1H3 and 0.27 in F2H2-1a): epidote cores are compositionally homogeneous followed by an allanite-rich zone and an epidote outer rim.

Epidote 3 ( $X_{\text{ps}} = 0.26$ –0.33): epidote with titanite inclusions and allanite cores, strongly resorbed rims, often in contact with titanite.

Epidote 4 ( $X_{\text{ps}} = 0.33$ ): epidote of irregular habitus with allanite, albite and magnetite inclusions, partly reaction to or overgrowth by titanite (F1H4-3a).

Epidote 5 ( $X_{\text{ps}} = 0.27$ , E4H2-2b): single grains without zonation or inclusions, few core-like areas have lower iron but higher alumina contents ( $X_{\text{ps}} = 0.20$ ).

## 5.2.6 Pyroxene

Na-rich pyroxene in the metamafic samples has a narrow range in jadeite content (from ~7–26 mol%; see Fig. 5.6a) and is Fe<sup>3+</sup>-rich. These clinopyroxenes are aegirineaugite and aegirine with a broad spread along the path Q – ~Jd<sub>15</sub>Ac<sub>85</sub> (Fig. 5.6a).

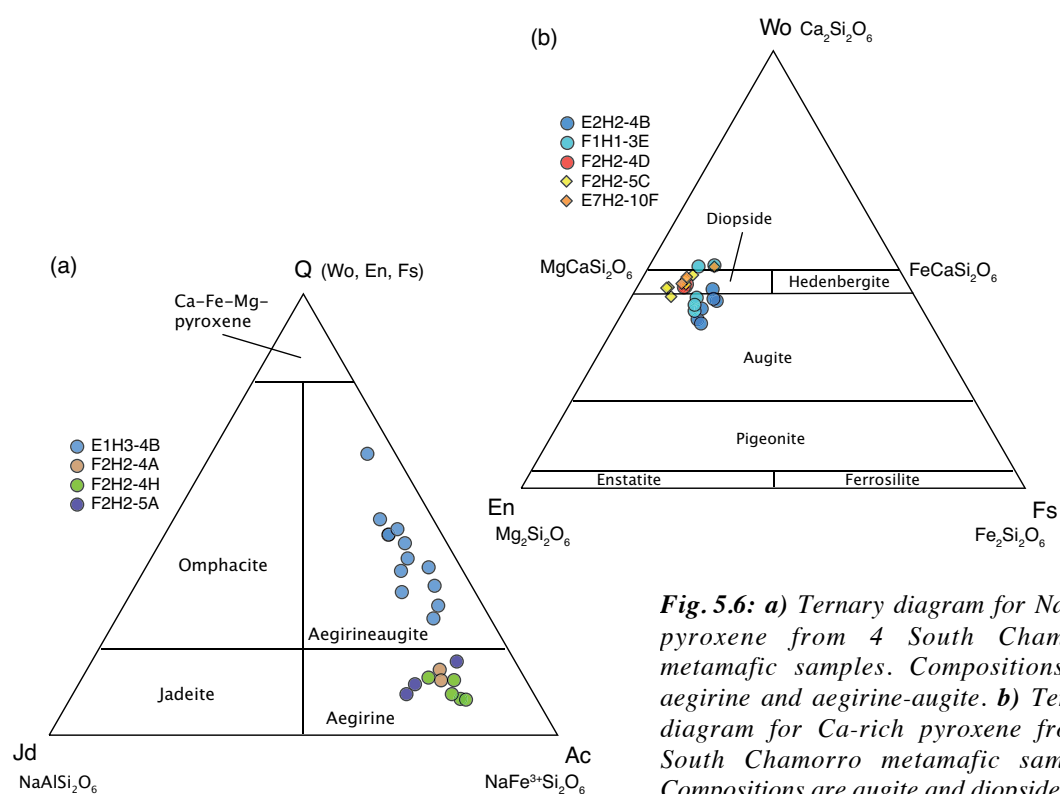


**Fig. 5.6:** **a)** Ternary diagram for Na-rich pyroxene from 4 South Chamorro metamafic samples. Compositions are aegirine and aegirine-augite. **b)** Ternary diagram for Ca-rich pyroxene from 5 South Chamorro metamafic samples. Compositions are augite and diopside.

Other samples also contain Ca-rich clinopyroxene of diopside and augite composition. Clinopyroxenes of individual samples form distinct compositional clusters (Fig. 5.6b). Magmatic clinopyroxene is regularly zoned (samples F2H2-5C and E7H2-10F) with Ti-rich cores.

### 5.2.7 Garnet

Garnet occurs with a chlorite-epidote rich mineral assemblage in one metamafic sample (E1H3-4C). The garnet shows zonation typical for growth under prograde conditions, characterized by increasing Mg# and MnO content and decreasing CaO content from core to rim (Fig. 5.8a). Central areas contain apatite inclusions. Nevertheless, the garnet compositions plots in a narrow field in the Ca-Fe-Mg triangle (Fig. 5.8b). Two other samples contain idiomorph andradite or Cr-rich ‘hydrous’ andradite with picotite (spinel) cores in a serpentine matrix (Fig. 5.8b).

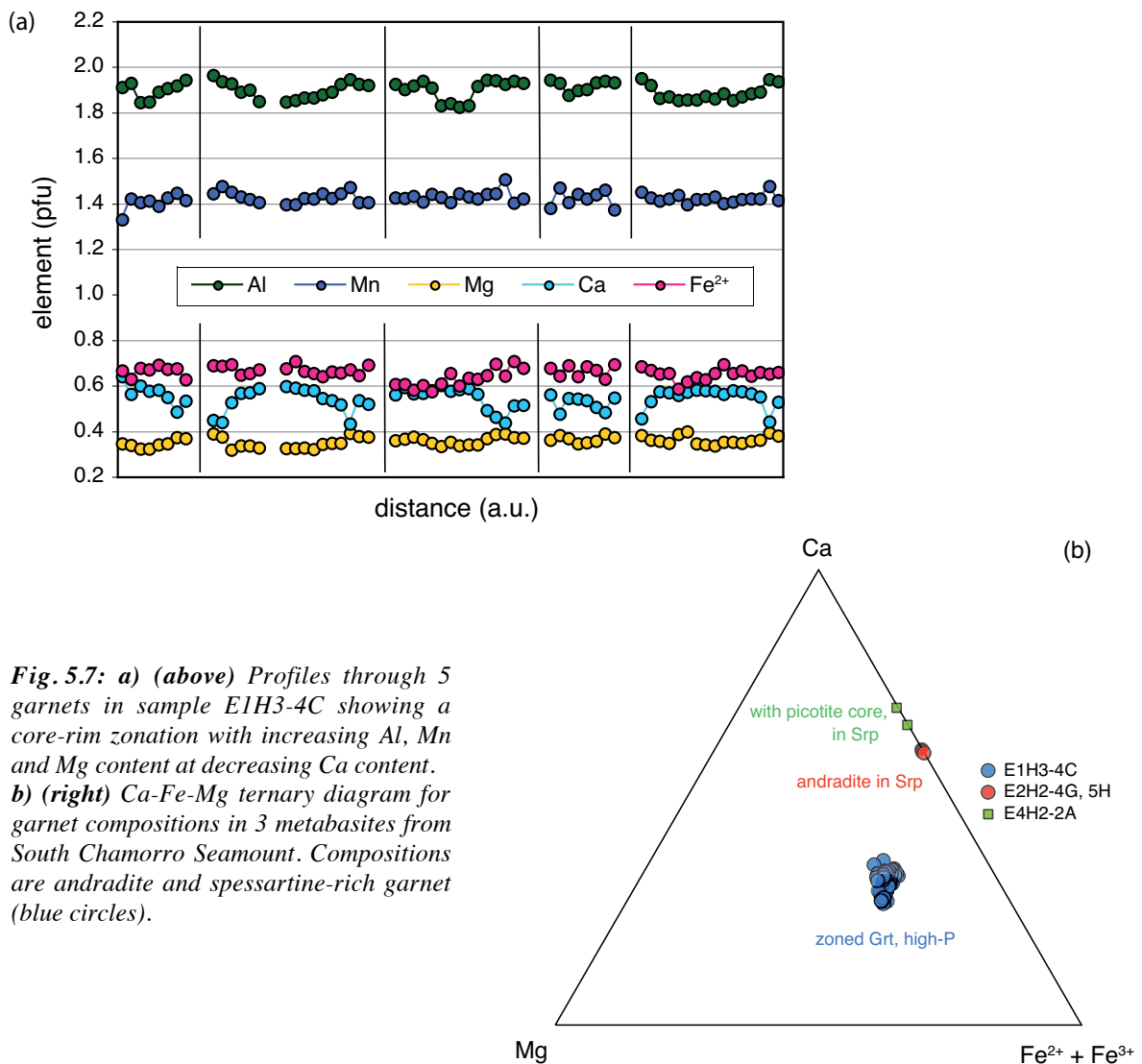


**Fig. 5.7:** *a) (above) Profiles through 5 garnets in sample E1H3-4C showing a core-rim zonation with increasing Al, Mn and Mg content at decreasing Ca content. b) (right) Ca-Fe-Mg ternary diagram for garnet compositions in 3 metabasites from South Chamorro Seamount. Compositions are andradite and spessartine-rich garnet (blue circles).*

Andradite in association with serpentine is known in metamorphosed oceanic mantle rocks in Idria, central California (reference) and in alpine-type serpentine schists (Tröger, 1959). Hydroandradite occurs in ophicalcites accompanying a partly serpentinized alpine-type peridotite from the Totalp serpentine complex, Davos, Switzerland (Peters, 1965).

### 5.2.8 Ti-phases (titanite, rutile, ilmenite, titanomagnetite)

Titanite is a calcium titanium silicate ( $\text{CaTiSiO}_5$ ) common in most of the metamafic samples investigated and has an  $\text{Al}_2\text{O}_3$  content of up to 5.2 wt%. In the amphibole dominated chlorite-schists of this study, titanite occurs as single grains, in epidote-bearing rocks in assemblage with rutile, pumpellyite and magnetite (e.g., E1H3-4B). Rutile (with up to 2.6 wt% FeO), ilmenite and titanomagnetite appear in most metamafic samples studied, often in assemblages of rutile + ilmenite + titanite + pumpellyite or epidote.

### 5.2.9 Other phases (pumpellyite, apatite, quartz, plagioclase, zircon)

In one metamafic sample (E1H3-4b), pumpellyite appears as single minerals and in assemblage with magnetite, titanite and rutile. The pumpellyite has Fe-rich composition between pumpellyite-(Mg) and pumpellyite-(Fe). However, it is less Fe-rich than common pumpellyite from zeolite and prehnite-pumpellyite facies. Apatite is a quite abundant mineral, which appears in various lithologies of the metamafic rocks. Quartz and the plagioclase albite have been identified (and verified by micro-Raman analyses); they occur only as inclusions in epidote.

## 5.3 Petrography

The metamafic rock fragments from South Chamorro Seamount comprise a great variety of mineral assemblages, i.e., various rock types. Clasts that show the same mineral content and textures and that were recovered from the same mud-pellet are summarized to one rock sample. Using these procedures, 50 fragments representing 38 different rock types were characterized. Petrographic comparison with lithologies described in literature suggests a rough classification of the Mariana metamafic fragments into amphibole-(talc)-chlorite-schists, epidote-schists and -rocks and phengite-schists.

To estimate the volume fraction of the minerals, gray-scale back-scattered images were evaluated using the visualizing software *ImageJ 1.39t* (National Institutes of Health, USA). Modal abundances of mineral assemblages in the recovered mafic clasts are reported in Table 5.1. Although the size of the rock fragments is very small, the volume% estimations are statistically representative due to the very small mineral grain size within the fragments. Figure 5.8 presents the volume% for each rock type as a color bar chart.



Table 5.1: Estimated modal composition (vol%) of blueschist-facies fragments from ODP Leg 195, Hole 1200, South Chamorro Seamount.

Sample/Label	depth (mbsf)	rock type	Srp	Tlc	Chl	Am	Phe	Ep	Aln	Ap	Ttn	Spl	Px	Pmp	Rt	Zrc	Grt	others
D3H1-8C	11.25	chl-phe-schist	-	-	55	-	42	3	-	-	-	<1	-	-	-	-	-	-
E2H2-4g,5h	8.95	serp-grt-zone	36	-	-	-	-	-	-	-	-	-	-	-	-	-	64	-
E4H1-1a	13.35	serpentinite	96	-	-	-	-	-	-	-	-	<1	-	-	-	-	-	4 Fe-sp
E4H2-2a	14.85	serpentinite	>50	-	-	-	-	-	-	-	-	-	-	-	-	-	-	Cc + picotite
E1H3-4b	4.35	chl-amph-epid-rock	-	-	27	62	<1	4	<1	-	2	<1	<1	<1	4	<1	-	-
E1H3-4c	4.35	chl-epid-grt-rock	-	-	50	4	-	25	<1	10	3	2	-	-	<1	<1	6	-
E4H2-2b	14.85	chl-epid-rock	-	-	38	-	-	58	-	2	2	-	-	-	-	-	-	-
F1H4-3a	5.95	chl-epid-rock	-	-	67	-	-	30	in Ep	-	3	<1	-	-	-	-	-	<1
F2H2-1A	10.65	amph-chl-epid-schist	-	-	26	30	-	22	1	20	1	-	-	-	-	<1	-	<1
E1H3-4a	4.35	phe-chl-amph-schist	-	-	38	16	37	<1	-	4	2	3	-	-	<1	<1	-	-
F2H2-4A,B,H	10.65	phe-amph-chl-schist	-	-	8	47	39	-	-	<1	3	-	3	-	-	<1	-	-
F2H2-5A	10.65	phe-amph-schist	-	-	13	59	23	-	-	<1	3	-	2	-	<1	<1	-	-
E1H3-3d	4.35	chl-amph-rock	-	-	90	8	-	-	-	2	-	-	-	-	-	-	-	-
E7H2-10F	28.75	px-chl-rock	-	-	43	-	-	-	-	-	-	4	53	-	-	-	-	-
F2H2-5C,D	10.65	px-chl-rock	-	-	65	-	-	-	-	-	-	1	34	-	-	-	-	-
F2H2-3F	10.65	amphibole-aggregate	-	-	-	100	-	-	-	-	-	-	-	-	-	-	-	-
F2H2-4D	10.65	chl-amph-schist	-	-	30	65	-	-	-	<1	<1	-	5	-	-	-	-	-
D1H4-2d	5.85	amph-chl-schist	-	-	59	33	-	-	-	2	6	-	-	-	-	<1	-	-
E1H3-5	4.35	amph-chl-schist (2x)	-	-	70	30	-	-	-	-	-	-	-	-	-	-	-	-
E2H2-4j	8.95	amphibole-aggregate	-	-	-	100	-	-	-	-	-	2	-	-	-	-	-	6
E2H2-5j	8.95	talc-aggregate	-	92	-	-	-	-	-	-	-	-	-	-	-	-	-	-
F1H1-3C	0.98	amph-chl-schist	-	-	50	50	-	-	-	-	-	-	-	-	-	-	-	-
F1H1-3F	0.98	amph-chl-schist	-	-	50	50	-	-	-	-	-	-	-	-	-	-	-	-
F1H3-2C	4.45	chl-tlc-amph-schist	-	76	8	16	-	-	-	-	-	<1	-	-	-	-	-	-
F1H3-2F	4.45	amph-(tlc)-rock	-	60	-	40	-	-	-	-	-	-	-	-	-	-	-	-
F1H4-5	5.95	amph-chl-schist	-	-	55	45	-	-	-	-	-	-	-	-	-	-	-	-
D1H4-1a	5.85	amph-chl-schist	-	5	32	63	-	-	-	-	-	-	-	-	-	-	-	-
D1H4	5.85	chlorite-aggregate	-	-	82	-	-	-	-	-	18	-	-	-	-	-	-	-
E2H2-4b	8.95	chl-amph-ap-rock	-	-	51(d) + 27(l)	10	-	-	-	1	1	-	10	-	-	-	-	-
E2H2-5d	8.95	amph-chl-tlc-rock	-	28	28	42	-	-	-	2	-	-	-	-	-	-	-	-
E4H1-2a	13.35	chlorite-amph	-	-	58	42	-	-	-	-	-	<1	-	-	-	-	-	-
E7H2-1a,b,2a,8a,b,10	28.75	amph-chl-schist	-	-	28	68	-	-	-	2	2	-	-	-	-	-	-	-
E7H2-6A	28.75	chlorite-aggregate	-	-	63(d) + 34(l)	-	-	-	-	2	3	-	-	-	-	-	-	-
F1H1-3E	0.98	amph-chl-rock	-	-	42	45	-	-	-	4	4	-	5	-	<1	-	-	-
F1H3-2D	4.45	chlorite-aggregate	-	-	91	-	-	-	-	-	9	-	-	-	-	-	-	-
F2H2-4E,G,5G	10.65	chl(-amph)-schist	-	7	69	22.5	-	-	-	<1	<1	1	-	-	-	<1	-	-
F2H2-4F,J	10.65	chl(-amph)-schist	-	5	85	10	-	-	-	-	-	-	-	-	-	-	-	-
E1H3-4d	4.35	phe-amph-chl-schist	-	-	25	42	30	-	-	-	3	-	-	-	-	-	-	-
F1H1-3D	0.98	chl(-phe)-schist	-	-	97	-	3	-	-	-	-	<1	-	-	-	-	-	-

Visual mineral volume% estimation. d = dark, l = light.

Mineral abbreviations - Srp: serpentinite, Tlc: talc, Chl: chlorite, Am: amphibole, Phe: phengite, Ep: epidote, Aln: allanite, Ap: apatite, Ttn: titanite, Spl: spinel, Px: (Na-)pyroxene, Pmp: pumpellyite, Rt: rutile, Zrc: zircon, Grt: garnet.

To date, a limited number of metamafic samples from Pacman, Big Blue, Conical and South Chamorro Seamounts were studied; the latter contains the significantly highest amount of metamafic clasts, the lowest amount is found in Big Blue seamount and no high pressure minerals were recovered from seamounts closer to the trench (<70 km; Maekawa *et al.*, 1992; Maekawa, 1995; Savov *et al.*, 2005a; Gharib, 2006). This suggests a potential depth-control on the advection of solid material that derives from the slab with a greater lithostatic load at greater depth combined with overpressured fluids controlling the eruptive frequency (Gharib, 2006). Mixing trends between serpentinite and metabasites compared to the serpentinite mud composition recovered at Conical and South Chamorro Seamounts reveals that the muds contain only up to 5% metabasites (Savov *et al.*, 2005a).

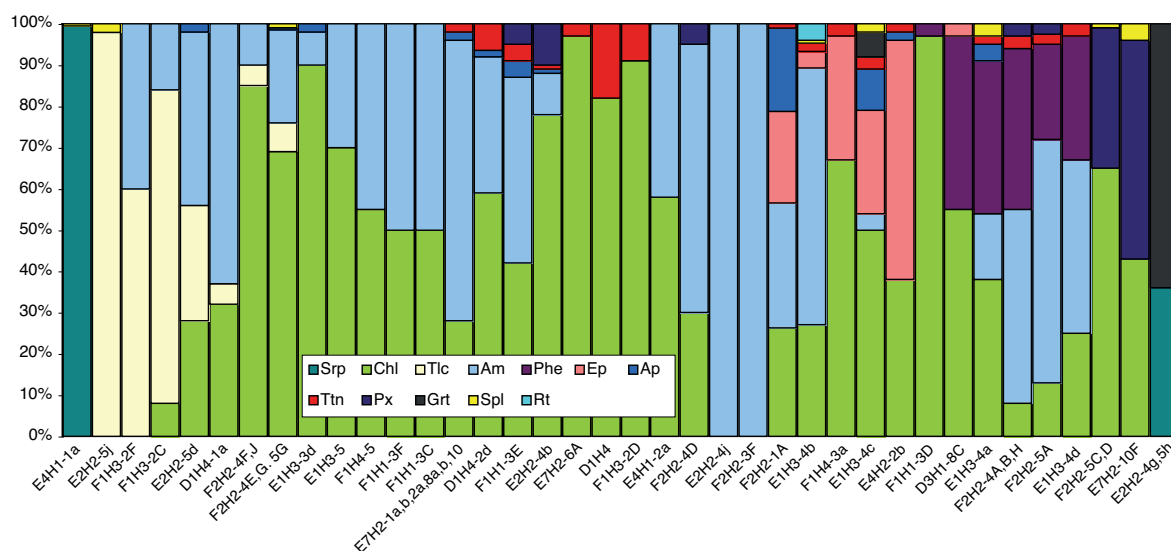


**Fig. 5.8:** Bar chart showing the modal composition (vol%) for metamafic rock types.

Mineralogical and texturally similar rocks are described from onland mélangé zones such as Catalina Schist (Sorensen, 1988; Bebout & Barton, 2002; King *et al.*, 2006) and Syros (Marschall *et al.*, 2006, 2007a,b; Miller *et al.*, 2009). These comprise ‘endmember’- and ‘rind’-rocks related to high-pressure metasomatic reactions and mechanical mixing between meta-basalts, meta-sediments and adjacent mantle peridotite. Hence, on the basis of the mineral abundance and assemblages in the Mariana metamafic samples, these fragments can be assigned to different entities within the subduction mélangé. However, in addition to these slab-derived metamafic rocks, some fraction may include mafic forearc crust (Johnson, 1992). This might be the case for fragments containing magmatic clinopyroxene in a chlorite matrix (*e.g.*, E7H2-10f), a fact that will be discussed later.

### 5.3.1 Amphibole-Talc-Chlorite-Schists

Most metamorphic schists are dominated by the paragenesis amphibole + chlorite (+ talc) of varying abundance. In addition, minerals as apatite, spinel, titanite, zircon, pyroxene, rutile and magnetite are present in some samples. Most rock fragments can be classified as metamorphic or

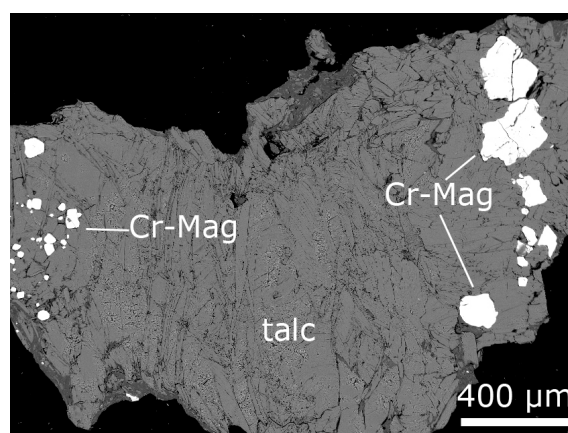
metasomatic rinds similar to rock types from the Catalina Schist and Syros mélangé zones (e.g., Sorensen, 1988; Bebout & Barton, 2002; King *et al.*, 2006; Miller *et al.*, 2009).

### 5.3.1a) metasomatic rind of ultra-mafite, i.e., serpentized peridotite

#### #1: Talc-zone (Talc-fels, blackwall)

**E2H2-5j** (Tlc >> Cr-Mag) is a talc aggregate composed of dominantly talc and minor chromian magnetite (3 wt% Cr<sub>2</sub>O<sub>3</sub>). Nearly monomineralic talc zones are typically found as blackwall zones due to SiO<sub>2</sub> transport around serpentinites (King *et al.*, 2003).

**Fig. 5.9:** Back-scattered electron (BSE) image of clast E2H2-5J: talc blades with large Cr-magnetite grains. >



#### #2: Tlc + tremolite, decreasing Tlc abundance (tremolite-dominated, blackwall)

**F1H3-2f** (Tlc > Am) consists of a talc matrix with fine-grained tremolite (Am) without any accessory minerals. The variably sized anhedral tremolite needles are embedded into this matrix with no preferred orientation (Fig. 5.10a).

**F1H3-2c** (Tlc >> Am > Chl + Mt) is a talc-amphibole-schist dominated by a fine-grained matrix that is composed of talc with few up to 80 µm large blades of chlorite and tiny amphibole grains. Up to 120 µm long subhedral unzoned calcic amphibole (tremolite) needles are embedded in this matrix with a slight orientation (Fig. 5.10b). The trace mineral is magnetite.

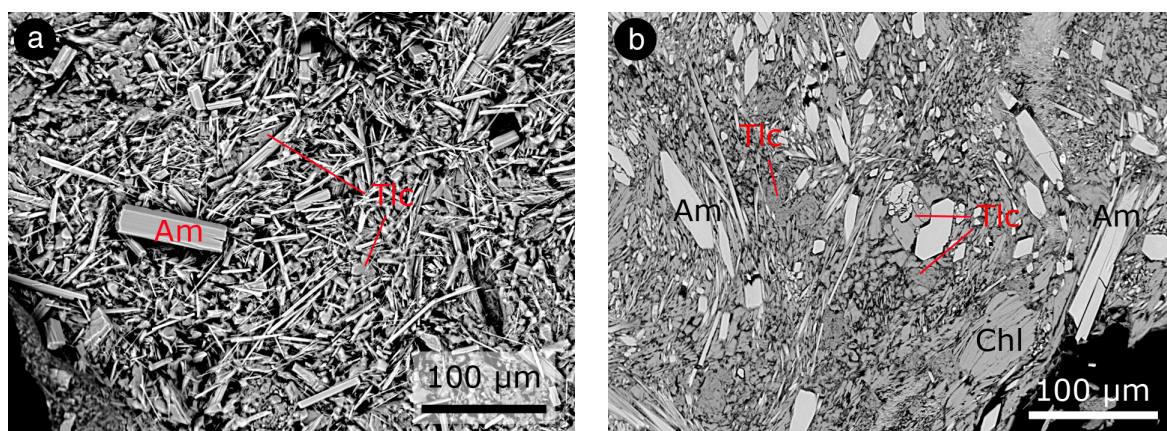


**Fig. 5.10:** BSE images of a) F1H3-2f, a talc-dominated amphibole schist and b) F1H3-2c, tremolite needles in a chlorite-talc-amphibole matrix.

**#3: Chl-Am-schist, foliated**

**E1H3-5-mud** (Chl > Am) is a small unconsolidated schist-fragment still embedded in serpentine mud and only consists of predominantly chlorite with amphibole (Fig. 5.11a). Amphibole is unzoned subhedral tremolite.

**F1H4-5** (Chl + Am) is a schist-fragment solitary composed of subhedral, up to 100  $\mu\text{m}$  sized amphibole, which is irregularly distributed in a chlorite matrix (Fig. 5.11b). The thin amphibole rims have actinolite composition, cores and smaller grains are tremolitic.

**F1H1-3f** (Chl + Am) is a schistous fragment with subhedral amphibole in a chlorite + fine-grained amphibole matrix without accessory mineral phases (Fig. 5.11c). Some larger amphiboles (~150  $\mu\text{m}$ ) have cores of edenite composition, the fibrous rims or single, tiny unzoned crystals are tremolite to actinolite (in one case).

**F1H1-3c** (Chl + Am) is a schist similar to F1H1-3f with subhedral amphibole needles in a chlorite (+ fine-grained amphibole) matrix without accessory mineral phases (Fig. 5.11d). Some amphiboles are zoned with an actinolite core and tremolite rim, other amphibole needles have either actinolite or tremolite composition. The two latter fragments indicate deformation by slight alignment of the amphibole needles.

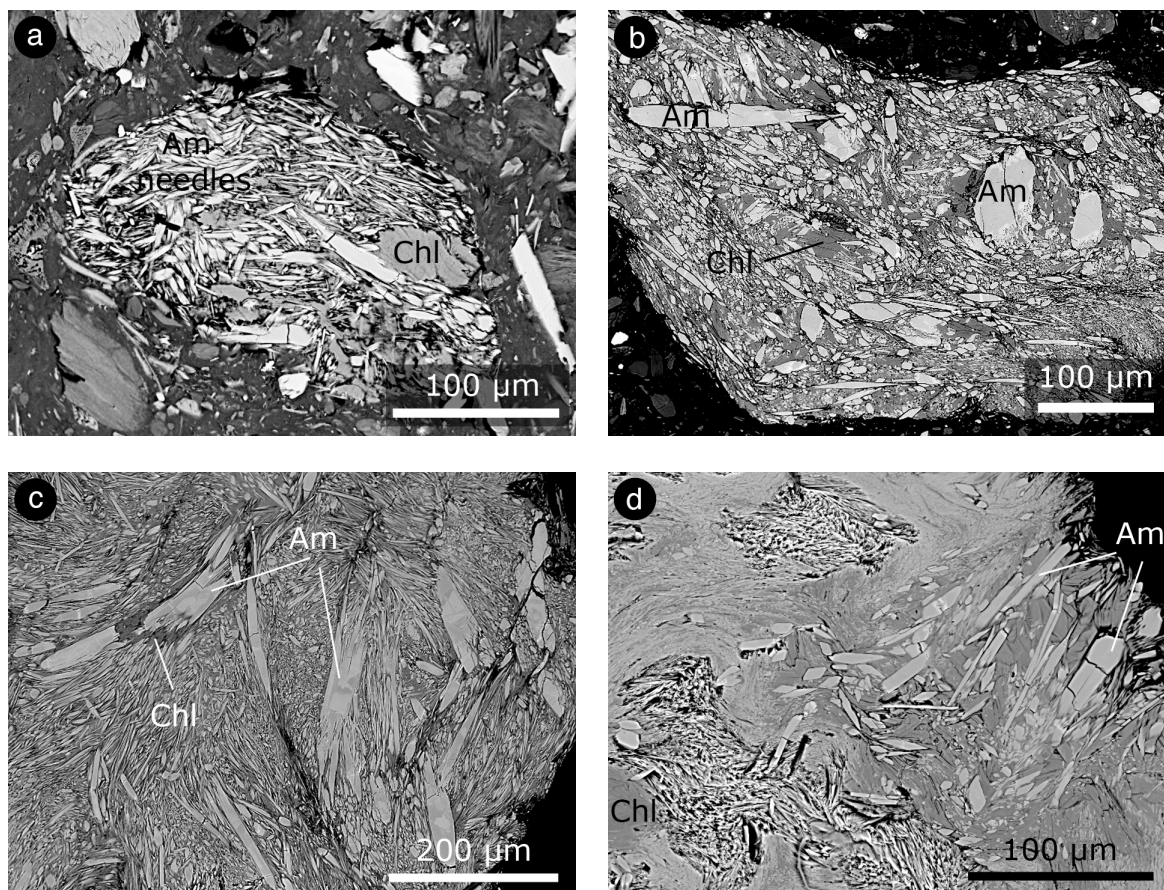


**Fig. 5.11:** BSE images of **a)** E1H3-5, Chl-Am-schist, **b)** F1H4-5, Chl-Am-schist, **c)** F1H1-3f, foliated Am-Chl-schist, **d)** F1H1-3c, foliated Am-Chl-schist.

**D1H4-2d** (Chl > Am > Ttn + Ap + Zrc) is a coarse-grained hardly foliated schist fragment. Matrix is made of platy chlorite. Amphibole occurs either as relative coarse subhedral unzoned grains (up to 200  $\mu\text{m}$ ) or as fine-grained crystal aggregates in the chlorite matrix, and has solely homogeneous actinolite composition. Titanite and apatite crystals are anhedral, whereas titanite also occurs as inclusions in amphibole. Of particular interest are tiny (size) zircon grains (Fig. 5.12).

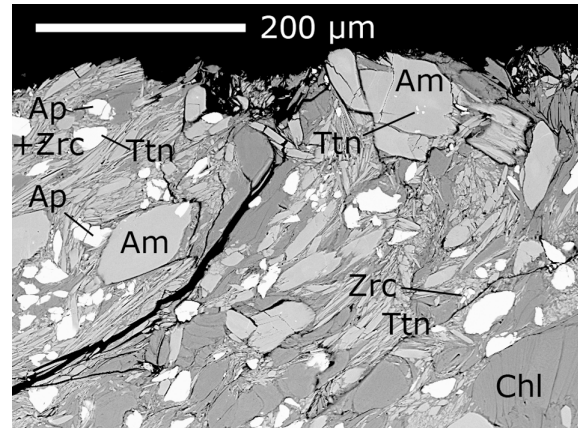


**Fig. 5.12:** BSE image of sample D1H4-2d, dominant phases are Am+Chl, minor minerals are Ttn+Ap.

#### **#4: amphibole aggregates**

**F2H2-4d** (Am > Chl > Px with inclusions of Ap + Tit) schist consists of euhedral unzoned amphibole crystals (actinolite) with two different types of chlorite occurring between amphibole. Chl 1 has a high Si/Al ratio and Chl 2 has lower Si/Al and a lower Mg# (see data in *Appendix*). At the border of the schist-fragment, a large diopside crystal with chlorite-filled cracks is embedded. Apatite and titanite are found as inclusions in this pyroxene (Fig. 5.13).

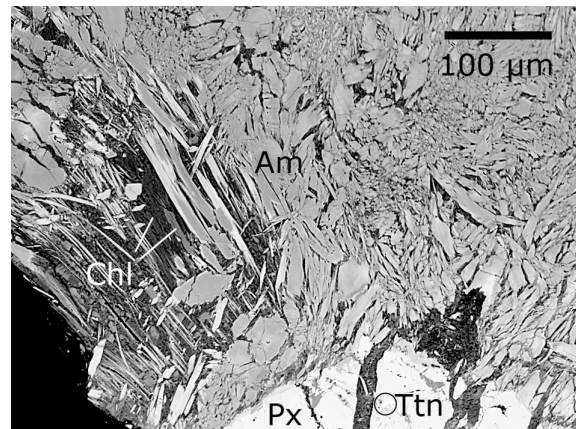


**Fig. 5.13:** BSE image of F2H2-4d, an Am-dominated fragment with a large diopside crystal (bottom).

Fragments **E2H2-4j** and **F2H2-3f** are pure amphibole-aggregates of tremolite and actinolite composition, respectively (Fig. 5.14). In the former, the crystals are quite large, in the latter they are fine-grained.

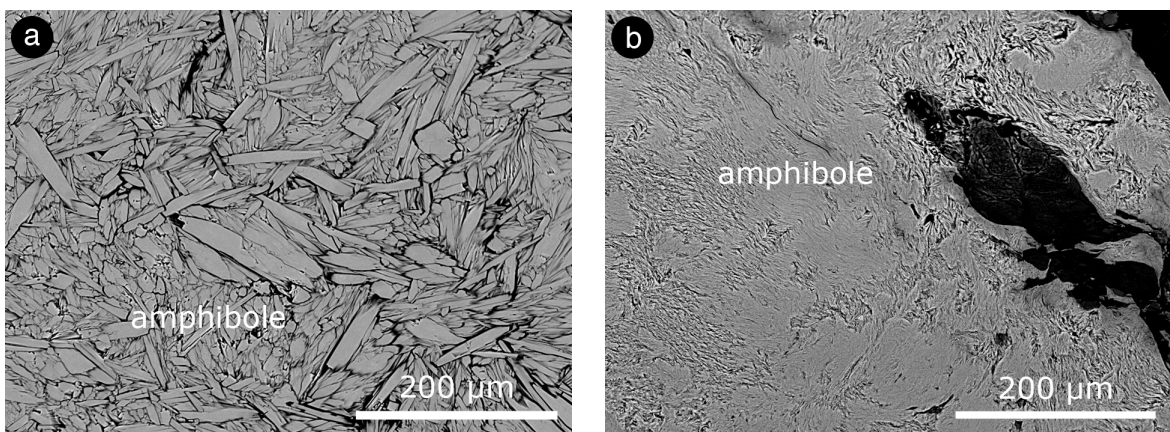


**Fig. 5.14:** Back-scattered electron (BSE) images of amphibole aggregates: **a)** E2H2-4j and **b)** F2H2-3f.

## 5.3.1b) metasomatic rind of mafic slab

**#1: Tlc + tremolite-actinolite, decreasing Tlc abundance**

**E2E2-5d** ( $Am > Chl + Tlc > Ap$ ) is a schist composed of predominantly amphibole needles and euhedral unzoned large Am-crystals of up to 180  $\mu m$  interfingering with a matrix composed of chlorite, talc, and small amphibole crystals (Fig. 5.15a). Apatite occurs as large euhedral crystals (up to 180  $\mu m$ ). Amphibole composition varies between actinolite, magnesio-hornblende and winchite (one small grain).

**D1H4-1A** ( $Am + Chl \gg Tlc$ ) is a small bluish schist fragment composed of variably sized (up to 100  $\mu m$  wide) mostly spiculeous amphibole with patchy zonation, embedded in a matrix of platy chlorite  $\pm$  talc (Fig. 5.15b). Amphibole compositions vary between actinolite/tremolite through magnesio-riebeckite to winchite ( $Na_2O$  up to 7 wt%). Bright (in BSE image) amphibole cores were identified as magnesio-cummingtonite ( $\sim 10$  wt% MnO). The schist is free of any accessory minerals.

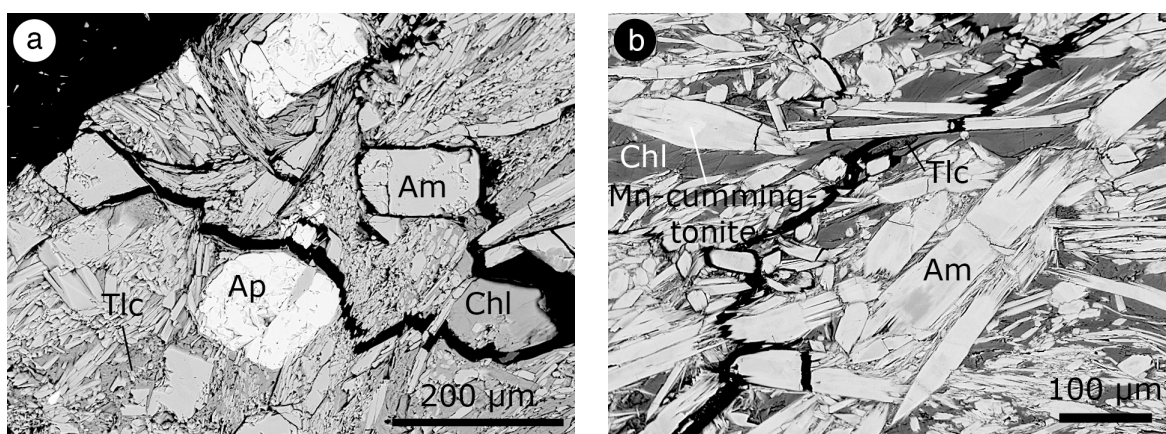


**Fig. 5.15:** BSE images of **a)** E2H2-5d, an Am-dominated schist with large apatite-grains, **b)** D1H4-1a, amphibole-chlorite(-talc)-schist with large Na-rich Am-needles.

**#2: Chl-Amph-schist, foliated**

**E7H2 (MAK-1A,B,2A,8A)** ( $Am > Chl \gg Ap + Ttn > Mag$  in Ap) greenish-bluish schist fragments, which comprise fine-grained anhedral amphibole and chlorite with minor anhedral titanite and euhedral apatite (Fig. 5.16). The texture is schistose with plication. Titanite and apatite are often concentrated in layers, magnetite may be found as inclusions in apatite. Single apatite grains can reach sizes of  $\sim 100 \mu m$ . Amphibole reaches  $>100 \mu m$  length; generally there are coarser grained areas within the fine grained fragments.

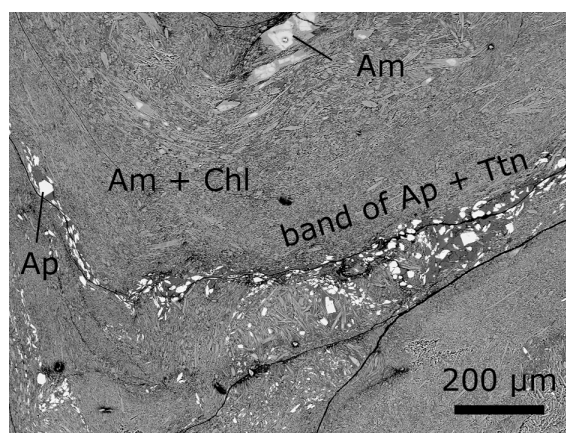


**Fig. 5.16:** BSE image of E7H2-1A, strongly foliated fine-grained Am-Chl-schist with Ap- and Ttn-rich bands.

The amphibole has a patchy zonation between actinolite and tremolite. Many amphiboles also have magnesio-hornblende or edenite composition. Amphibole cores are generally Fe-richer than the rims. However, there are also amphiboles with opposite composition of Fe-poorer cores and Fe-rich rims. Few amphibole has winchite composition. Chlorite composition shows strong Tschermak substitution.

### **#3: Chl-dominated**

**F2H2-4f,j** (Chl >> Am > Tlc) are chlorite-amphibole-schists dominated by platy well-crystallized and chemically homogeneous chlorite with minor, irregularly distributed amphibole needles and interstitial talc (Fig. 5.17a). Amphibole has tremolite composition, one analysis shows actinolite composition. Talc is coarse but poorly crystallized.

**F2H2-4e,g,5g** (Chl >> Am > Tlc + Ap + Ttn + Spl + Zrc) are chlorite-amphibole-schist with a matrix made up of platy well-crystallized chlorite with minor interstitial talc. Thin unzoned amphibole needles are irregularly distributed in this matrix (Fig. 5.17b) and have tremolite composition. Trace minerals are subhedral ilmenite, titanite, zircon, and apatite grains in the chlorite.

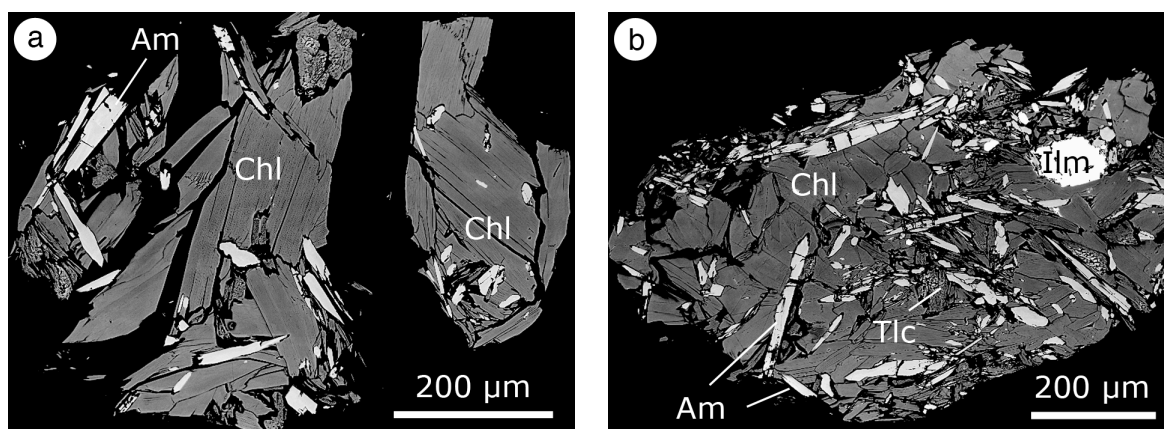


**Fig. 5.17:** BSE images of **a)** F2H2-4f, large Chl blades with Am needles, **b)** F2H2-4e, large Chl blades with minor Am needles and some ilmenite and talc.

### **#4: massive Chlorite-Titanite-rocks**

Chlorite-aggregate **E7H2-6a** (Chl 1 > Chl 2 >> Ttn) is composed of two different chlorite varieties that interfinger irregularly (Chl 2 seems to be later; Fig. 5.18a). Chlorite 1 is relatively fine-grained to massy with a Si-rich (Si/Al of 2.3) and Fe-poor (Fe/Mg of 0.3) composition (dark in BSE). Chlorite 2 is more platy and well-crystallized with a Si-poorer (Si/Al of 1.8) but Fe-richer (Fe/Mg of 0.9) composition (bright in BSE). Titanite (3 vol%) occurs as irregular grains in both chlorites.

Clast **D1H4** (Chl 1+2 >> Ttn) consists of titanite irregularly intergrown with fine-grained chlorite (Chl 1; Fig. 5.18b). This assemblage is intergrown with a more felty chlorite (Chl 2; darker in BSE image). Chl 1 (early) has a higher Si/Al compared to Chl 2 (later).

**F1H3-2d** (Chl >> Ttn) is dominated by massy to felty fine-grained Si-Mg-rich chlorite. Titanite occurs as irregular grains with reaction cores replacing chlorite (Fig. 5.18c).

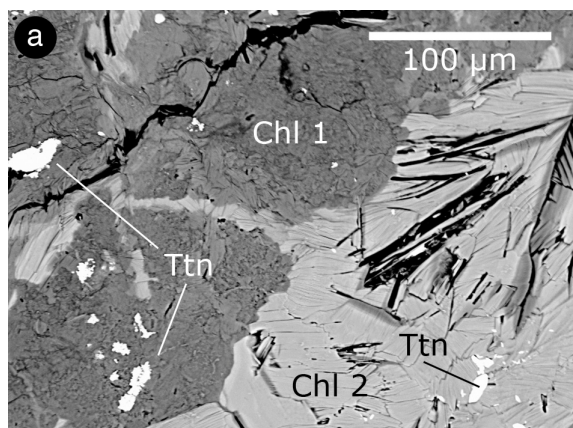
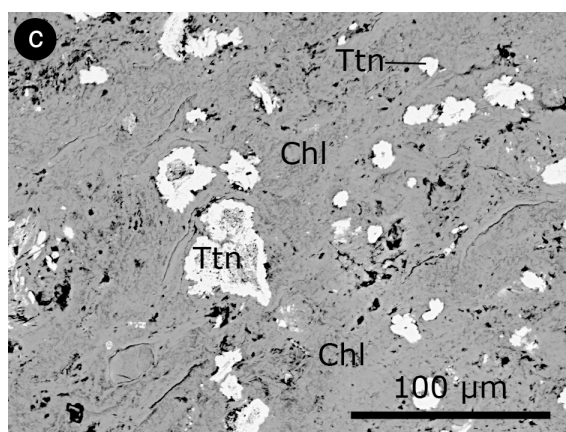
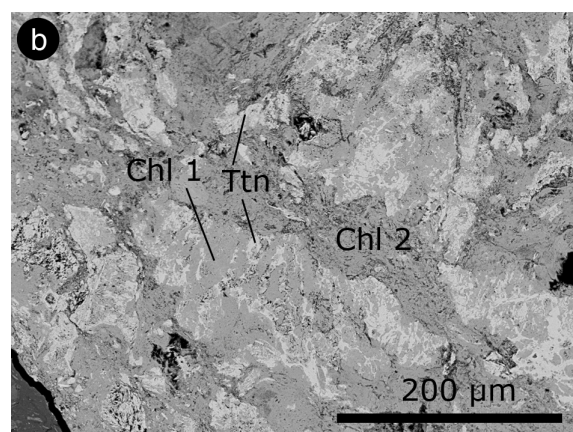


*Fig. 5.18 a): BSE images of E7H2-6a, Chl-aggregate with Ttn grains, of b) D1H4, Chl-Ttn-intergrowth and c) F1H3-2d, chlorite with irregular Ttn.*



### **#5: pyroxene-bearing schist**

**F1H1-3e** (Chl + Am >> Ap + Ttn + Px + Rt) has a chlorite matrix. Therein are predominantly unhehedral and unzoned amphiboles of magnesio-hornblendite to actinolite composition. Euhedral apatite (~4 vol%; up to 200 μm) and titanite (~4 vol%) grains are intensively intergrown with the amphibole. Pyroxene (5 vol%) occurs as tiny interstitial grains of  $En_{41}Fs_{13}Wo_{46}$  composition. Pyroxene can also be found as inclusions in amphibole. Accessory rutile is found as inclusions in titanite. Foliation is defined by amphibole and pyroxene (Fig. 5.19a), whereas amphibole seems to be the latest grown mineral phase.

**E2H2-4b** (Chl 1 > Chl 2 > Am + Px > Ap + Ttn) is a very fine-grained unfoliated schist that is dominated by two different types of chlorite; fine fibres of Chl 1 (high Si/Al with Fe/Mg of 0.2) and platy Chl 2 (low Si/Al with Fe/Mg 0.6). Embedded or intergrown with this matrix (Fig. 5.19b) are unzoned anhedral amphiboles of actinolite to magnesio-hornblende composition and pyroxene fibers of augite-diopside composition. Traces of euhedral apatite and titanite are found in the chlorite matrix.



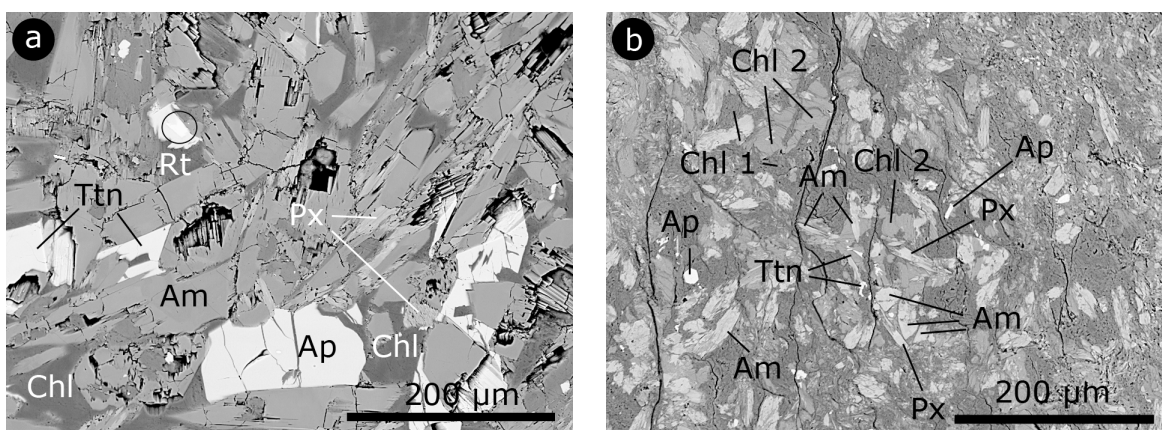
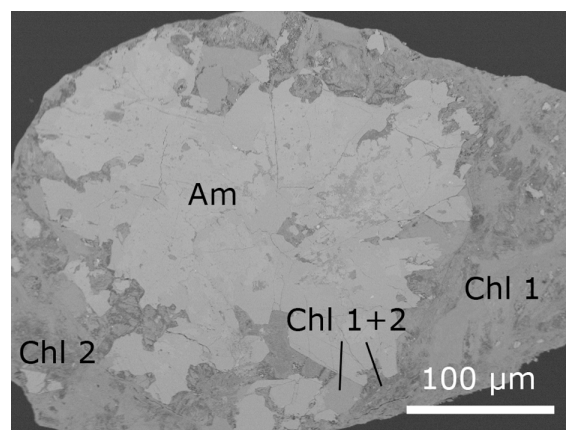


**Fig. 5.19:** BSE images of **a)** F1H1-3e, coarse-grained Am-Chl-schist with large Ap, **b)** E2H2-4b, intergrowth of Chl + Am + Px with Ttn and Ap grains.

### **#6: massive Chlorite-Amph-rocks**

In **E4H1-2a** (Chl + Am >> Mag) chlorite surrounds an amphibole aggregate (Fig. 5.20); again two different chlorite compositions can be identified with a Mg# between 69.7 and 87.4. Amphibole has a composition between Mg-hornblende, actinolite and edenite. Tiny trace magnetite grains occur along the amphibole rim.

**Fig. 5.20:** BSE image of a Chl-Am-aggregate, E4H1-2a. >



### 5.3.2 Chlorite-Epidote-Rocks

The chlorite-epidote rocks are characterized by epidote porphyroblasts in a chlorite matrix together with predominantly (Na-rich) amphibole and a great variety of further minerals such as ilmenite, titanite, apatite and garnet. Apatite, titanite, allanite, zircon and ilmenite are common trace minerals, whereas magnetite is relatively rare.

#### 5.3.2a) blueschist-facies meta-basalt / endmember

##### **#1: albite-bearing**

**F1H4-3a** (Chl + Ep + Ttn + Mag + Aln in Ep + Alb in Ep) is chlorite-epidote-schist, which is composed of fibrous chlorite with composition between 0.6 Fe/Mg and 0.2 Fe/Mg. Epidote occurs as up to 200 µm large hypidiomorph crystals (Fig. 5.21). Smaller grains form lineations with fine-grained titanite flakes (>3 vol%). Magnetite and albite occur as µm scale rounded inclusions in

epidote. Furthermore, patchy titanite forms inclusions in or overgrowths epidote and partly surrounds allanite. Epidote is characterized by a homogeneous pistacite composition ( $X_{ps} = 0.33$ ).

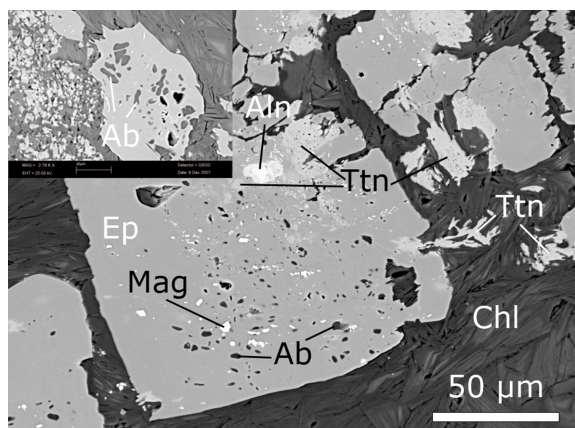


**Fig. 5.21:** Back-scattered electron (BSE) image of a large epidote grain with inclusions of magnetite, albite, allanite and titanite (FIH4-3a).

## #2: pumpellyite-bearing

The schist-fragment **E1H3-4b** (Am Chl Ep Phe Aln Ttn Ilm Px Pmp Rt Zrc Mag) offers a unique sample for studying complex metamorphic reactions (Fig. 5.22). The unfoliated clast is composed of dominantly amphibole with major chlorite, minor epidote (plus allanite), rutile, titanite, and traces of ilmenite, phengite, pyroxene, pumpellyite, zircon and magnetite. The matrix is made of chlorite with overgrown amphibole. Amphibole predominantly forms barely zoned, subhedral crystals of compositions varying between pargasite/Mg-hastingsite and more frequently edenite embedding large rutile-ilmenite and epidote crystals. Some μm sized parts within the edenite have actinolite composition. Patchy amphibole with Na-rich spots is Mg-hornblende. Rims of amphibole needles and some internal ‘stripes’ have Na-rich composition of winchite and richterite.

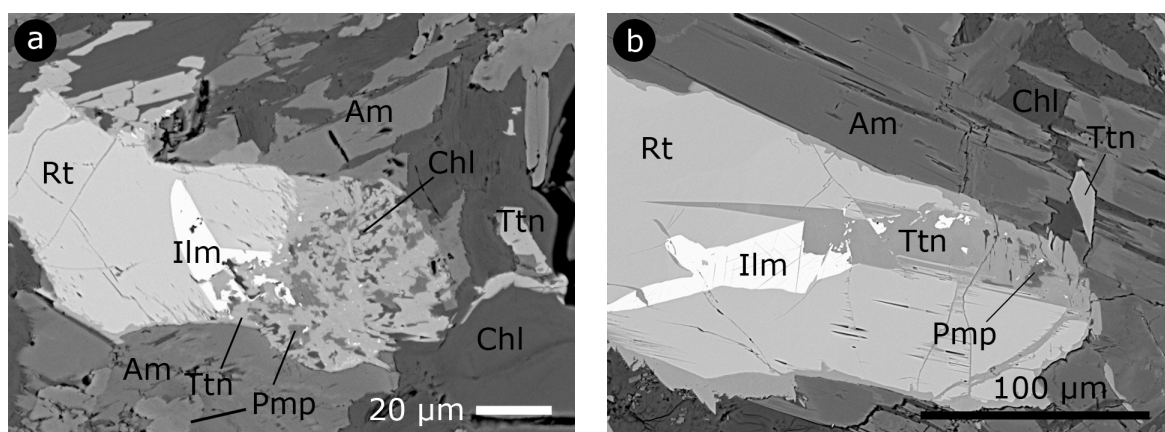


**Fig. 5.22:** Mineral parageneses showing various metamorphic stages and reactions in sample E1H3-4b. *a)* and *b)* show the reaction of  $Rt + Ilm \rightarrow Ttn + Pmp + Mag (+Chl)$ .

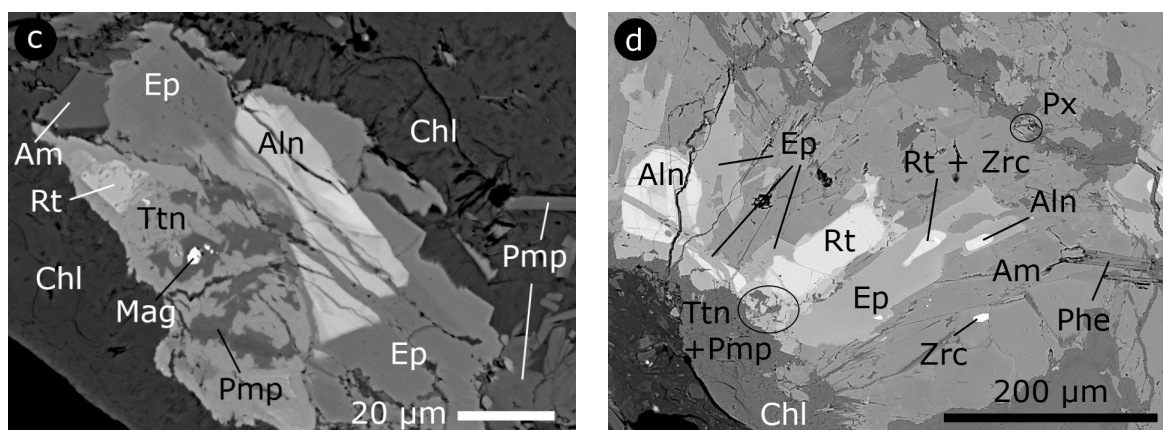


**Fig. 5.22 (continued):** Mineral parageneses showing various metamorphic stages and reactions in sample E1H3-4b. **c)** Rt, Pmp and Mag in Ttn with a resorption-like boundary to Ep+Aln, **d)** epidote with allanite and Rt+Zrc cores in assemblage with Rt, Ttn and Pmp.

Rutile and ilmenite always occur together, whereas ilmenite seems to be an exsolution from rutile (Fig. 5.22a,b,c). This assemblage partly reacted to (i) titanite, which surrounds the rutile, and (ii) larger titanite areas, which include patches of pumpellyite and minor chlorite. Pumpellyite can contain magnetite grains. The breakdown of  $Rt + Ilm$  to  $Ttn + Pmp + Mag$  requires Ca, which most likely comes from the consumption of the surrounding amphibole. Epidote has allanite cores and also has inclusions of rutile + zircon. Zircon also is found as single grains in the amphibole. Epidote is characterized by a heterogeneous  $Fe^{3+} / (Al + Fe^{3+})$  ratio of 0.30 (0.26–0.33), slightly lower compared to sample F1H4-3a. The assemblage epidote + allanite occurs with boundaries to the Rt-Ttn-Pmp-Mag assemblage. Pyroxene is in assemblage with amphibole and chlorite as euhedral crystals (Fig. 5.22d) and has variable aegirine-augite composition. Tiny phengite needles are aligned in amphibole near epidote assemblages (Fig. 5.22d).

### **#3: garnet-bearing**

Fragment **E1H3-4c** (Chl Ep Ap Grt Am Ttn Spl Aln Rt Zrc) is composed of a great variety of mineral assemblages. The dominant phase is platy matrix chlorite with irregularly distributed epidote, minor apatite, garnet, amphibole, titanite, spinel and trace amounts of rutile, zircon and allanite. Epidote grains are sub- to euhedral and sized up to 200  $\mu m$ . It is Al-rich with a homogeneous  $X_{ps}$  of 0.25. Some grains show a zonation of allanite-rich zones. Garnet occurs as single euhedral grains, often surrounded by epidote, titanite and chlorite, while it seems to replace epidote (Fig. 5.23a). Apatite occurs sub- to euhedral together with epidote, but is even found as inclusions in epidote and as tiny round inclusions in the garnet. The average garnet composition is  $Mn_{1.4}Ca_{0.6}Mg_{0.4}Fe_{0.6}Al_{1.9}Fe_{0.1}[SiO_4]_3$ . Garnet zonation profiles reveal (see section 5.2) that cores are enriched in FeO and CaO, but depleted in  $Al_2O_3$ , MgO and MnO.

Round apatite inclusions are found in the centre of the garnets. Cracks cut through the epidote and garnet grains are filled with chlorite. Zircon grains are found as inclusion in chlorite, apatite, and

epidote. Rutile and ilmenite inclusions are found in titanite, which on the other hand includes patches of epidote (Fig. 5.23b). Amphibole occurs as aggregates of small anhedral needles of winchite composition. Rutile and ilmenite had been described as relict inclusions in large titanite grains in blueschist-facies hybrid rocks from Syros (Greece) by Miller *et al.* (2009). This assemblage occurs in chlorite-rich rocks of a reaction zone between epidote-bearing rock and serpentinite; chlorite + titanite replace glaucophane and epidote as the dominant assemblage (Miller *et al.*, 2009).

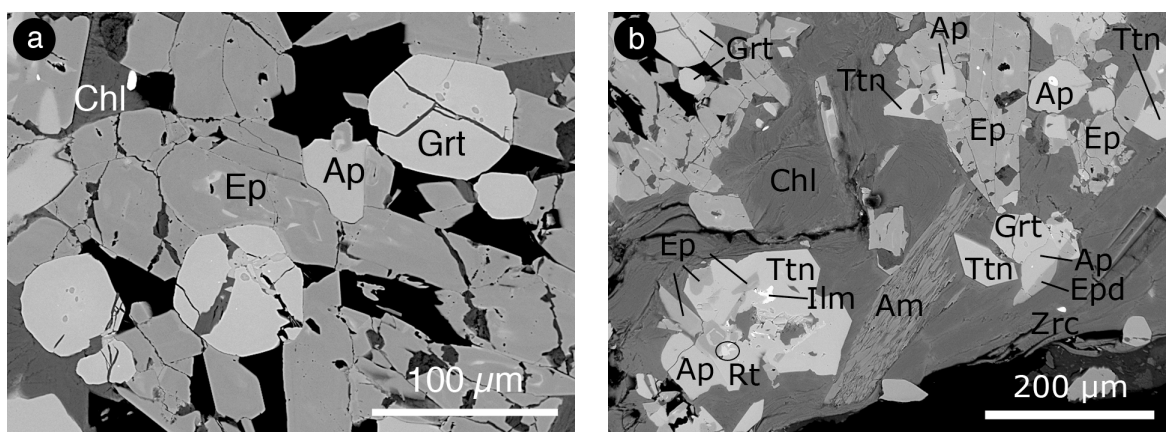


**Fig. 5.23:** BSE images of E1H3-4c with **a)** large Grt grains in assemblage with epidote and apatite, **b)** mineral paragenesis dominated by Chl, Ep, Ap, Ttn and Grt.

#### **#4: quartz-bearing**

Fragment **F2H2-1a** (Am Chl Ep+Aln Ap Ttn Zrc Qtz) is the only quartz-bearing one of all samples investigated. Coarse-grained major minerals are amphibole, epidote (plus trace amounts of allanite) and apatite embedded in a matrix of platy chlorite. Besides traces of titanite, further minerals are zircon and quartz (inclusions in epidote; Fig. 5.24a). Amphiboles are elongated and irregularly zoned crystals, some of them are a little bit patchy in the centre. Compositions vary from Mg-hornblende in the cores to glaucophane in the rim and a zonation between actinolite-winchite. Other Am-crystals have edenite cores surrounded by an actinolite-winchite zonation. Aside from amphibole-rich areas, there are epidote-apatite-rich areas in the sample.

Three different types of epidote can be identified (Fig. 5.24a-c; see section 5.2: epidote 1, 2 and 3). Epidote compositions range between 0.26 and 0.31  $X_{Ps}$  (avg 0.28), one dark (in BSE image) zone has an  $X_{Ps}$  of only 0.17. Round μm sized quartz-inclusions are found within the epidote cores. Allanite zonation in epidote is restricted to the outer zones of epidote 2. Epidote 3, with titanite inclusions, has irregular resorption boundaries and may border to titanite. In the Ep-Ap-rich area, epidote occurs with titanite and large (~100 μm) subhedral apatite crystals. Apatite and titanite also occur as single grain inclusions in amphibole.

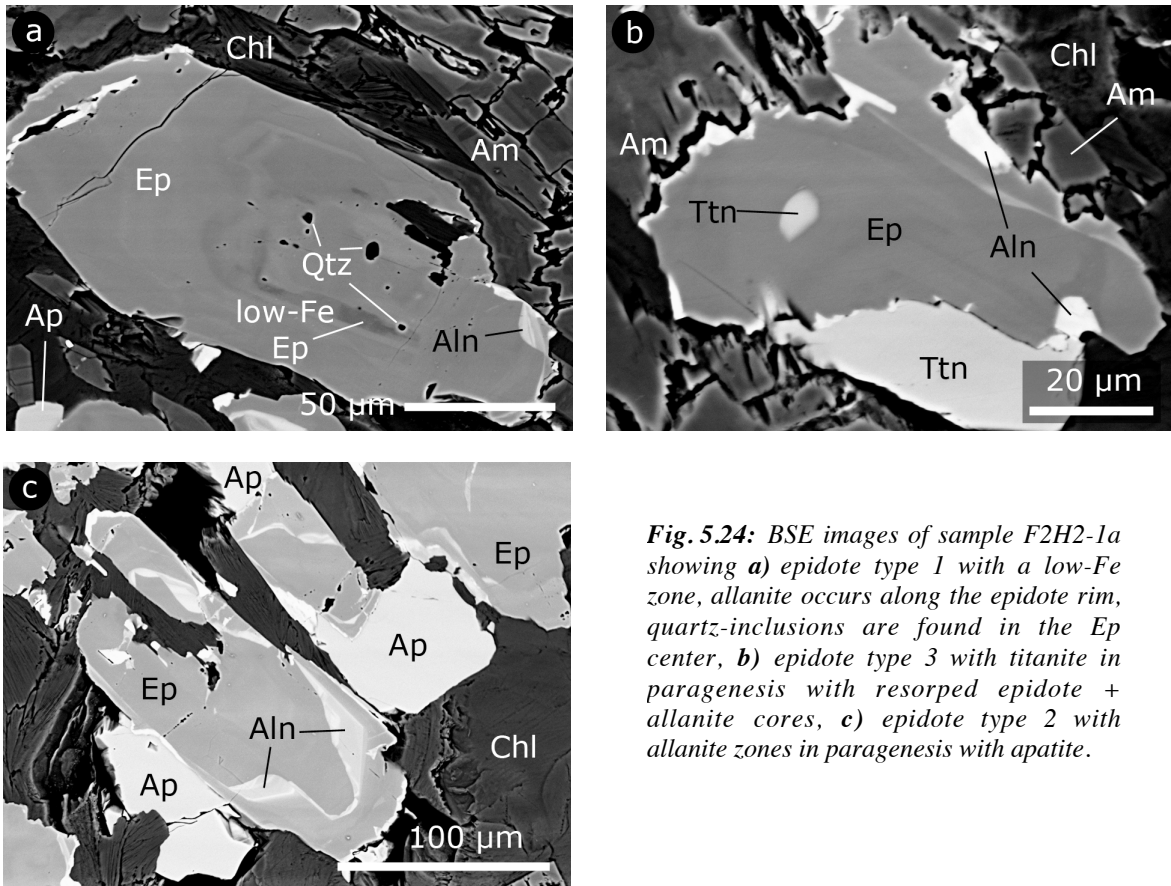
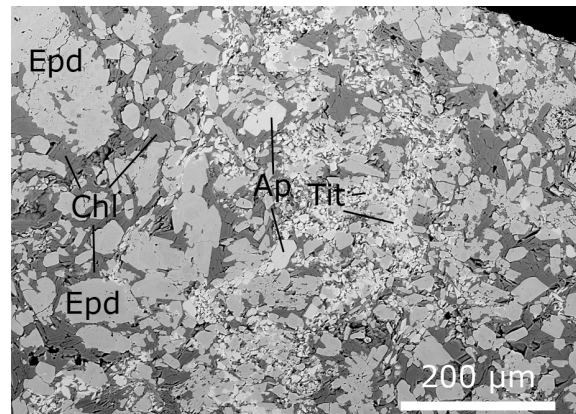


**Fig. 5.24:** BSE images of sample F2H2-1a showing **a)** epidote type 1 with a low-Fe zone, allanite occurs along the epidote rim, quartz-inclusions are found in the Ep center, **b)** epidote type 3 with titanite in paragenesis with resorped epidote + allanite cores, **c)** epidote type 2 with allanite zones in paragenesis with apatite.

#### **#5: epidote-apatite-titanite-aggregate**

**E4H2-2b** (Ep + Chl + Ap + Ttn) is a sample composed of variably sized epidote grains distributed in a chlorite matrix (Fig. 5.25). Up to 50 μm large apatite grains occur together with the epidote and titanite as accumulates in some areas of the sample. Epidote has a  $X_{\text{Ps}}$  of 0.27 (type 5) and 0.20 in some core areas.

**Fig. 5.25:** BSE image of epidote grains in a chlorite matrix with few apatite and accumulations of titanite, E4H2-2b. >



### 5.3.3 Am-Chl-Phe-schists

#### 5.3.3a) meta-sediment

Fragment **F2H2-5a** (Am > Phe > Chl > Ttn + Px + Zrc + Ap + Rt) is composed of elongated amphibole needles, phengite sheaves and minor pyroxene crystals with an interstitial chlorite matrix (Fig. 5.26a). Titanite occurs as interstitial irregular formed grains. Amphibole is very patchy with

compositions between actinolite, magnesio-hornblende and magnesio-riebeckite. Pyroxene has aegirine composition with up to 28% Jd component, the highest pyroxene Na<sub>2</sub>O content in all samples investigated. Trace minerals are rutile as inclusions in titanite and amphibole, apatite as inclusions in amphibole and tiny zircon grains. The fragment shows a foliation defined by oriented phengite and amphibole.

Fragments **F2H2-4a,b,h** ( $Am > Phe > Chl \gg Ttn + Px + Zrc + Ap$ ) are schists composed of patchy amphibole of up to >100  $\mu m$  size with interstitial phengite sheaves (Fig. 5.26b). Spaces are filled with chlorite. Titanite occurs as interstitial irregular formed grains. Na-rich pyroxene (aegirine with ~19% jadeite component) occurs as crystal aggregates. Amphibole is generally very Na-rich: core-like areas are actinolite with rare Mg-hornblende, rim-like areas are Mg-riebeckite, and thin fissure-like veins in amphibole are winchite. Trace minerals are zircon and apatite as inclusions in titanite. The fragment is foliated by oriented phengite and amphibole.

**E1H3-4a** ( $Chl + Phe > Am > Ap + Ttn + Ilm + Rt + Ep$ ) is a fine-grained fragment that consists of chlorite with interstitial phengite sheaves and amphibole crystals (Fig. 5.27). Large apatite grains occur in minor amounts, irregularly shaped ilmenite occurs in assemblages with titanite and epidote. Rutile, epidote and titanite occur as inclusions in ilmenite, epidote also in apatite. Amphibole is unzoned with winchite – Mg-riebeckite composition. Epidote inclusion in apatite has a  $X_{Ps}$  of 0.25, epidote in ilmenite 0.28. Phengite and amphibole form an oriented texture.

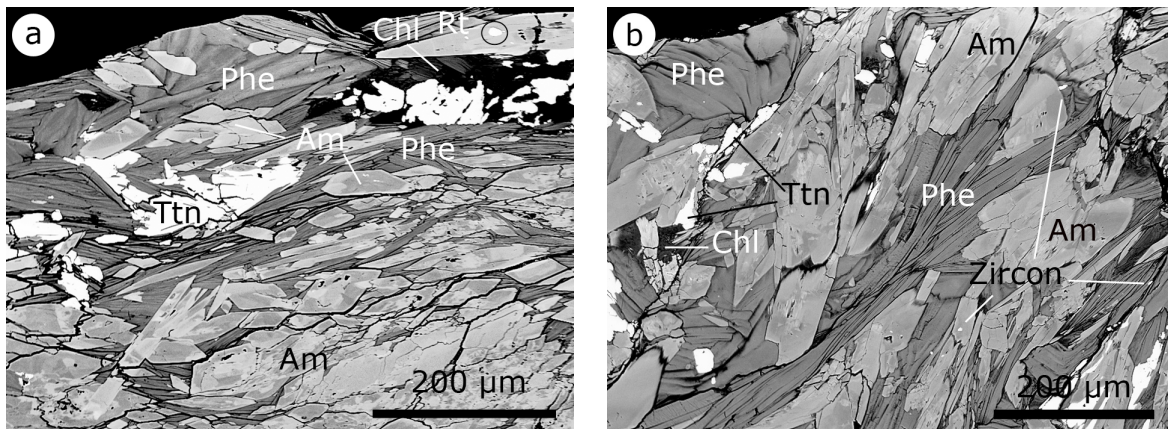


*Fig. 5.26: BSE images showing a) F2H2-5a, Am-Phe-Chl-schist, b) F2H2-4a, Phe-Am-schist with zircon.*

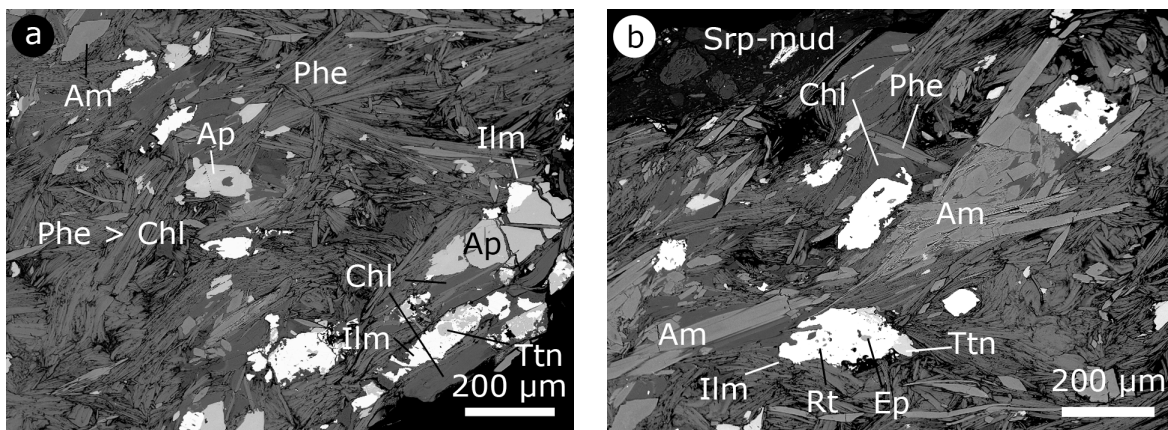


*Fig. 5.27: BSE images of E1H3-4a showing a) large apatite grains and b) Ilm-Ep-Ttn-assemblages.*

## 5.3.3b) rind of meta-sediment

**#1: large Phe sheaves (near rind)**

Fragment **E1H3-4d** ( $\text{Am} > \text{Phe} > \text{Chl} \gg \text{Ttn}$ ) is a phengite schist dominated by ~1 mm long, well-crystallized, large phengite sheaves with interstitial amphibole in a chlorite matrix. Large titanite grains are also intergrown with amphibole (Fig. 5.28a). The K concentration is slightly higher in the center of the phengite crystals. Mg-hornblende amphibole crystals are anhedral, unzoned and slightly oriented along and around the phengite.

**#2: Chl >> Phe (metasomatic rind)**

Chlorite-schist **F1H1-3d** ( $\text{Chl} + \text{Phe} + \text{Spl}$ ) is dominated by platy, well-crystallized chlorite (Fig. 5.28b). Phengite sheaves therein are irregularly distributed with little spinel.

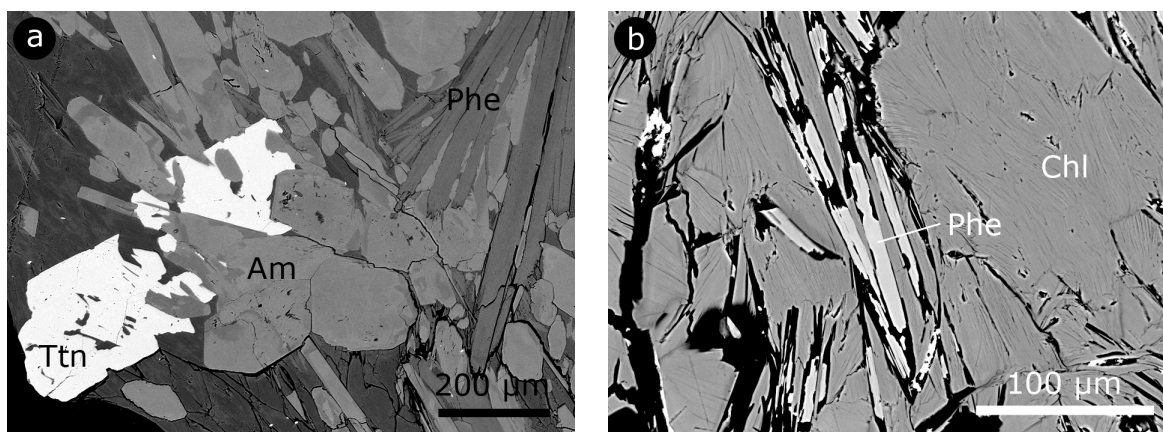


**Fig. 5.28:** BSE images showing **a)** E1H3-4d, large phengite sheaves with amphibole and titanite in a chlorite matrix, **b)** F1H1-3d, small Phe-sheaves in Chl.

## 5.3.4 Rocks of magmatic origin

**#1: Pyroxene-chlorite-rocks with magmatic relicts, Chl + Px**

Pyroxene-chlorite rocks are defined by three clasts, namely **F2H2-5c,d** and **E7H2-10f** (Fig. 5.29). Note, that the fragments representing the same rock, although they were sampled from different places within the serpentinite seamount. F2H2-5c and 5d are dominated by chlorite with pyroxene and few spinel. E7H2-10f is composed of pyroxene in chlorite and little spinel. The quite large sub-to euhedral and intensively zoned pyroxene minerals are irregularly distributed within the fine-grained chlorite matrix.

Such zoned clinopyroxenes in a fine-grained chlorite matrix are typical for volcanic rocks. The Px cores are Ti-rich diopside and the cpx rims are low-Ti diopside, which may imply magma mixing with a differentiated restitic melt of MORB.

One possible origin for such rock fragments is the Island Arc; erosion transports material from the arc into the trench. Another possible origin of these rocks are the volcanic seamounts situated on the subducting Pacific Plate. Nevertheless, the intensively zoned clinopyroxene with no evidence for higher-grade metamorphic overprint suggests that these samples did not experience subduction metamorphism at all, but rather originate from altered oceanic crust material. However, though representative, for further discussion these sample will not be considered as they don't seem to be slab-derived mafic material.

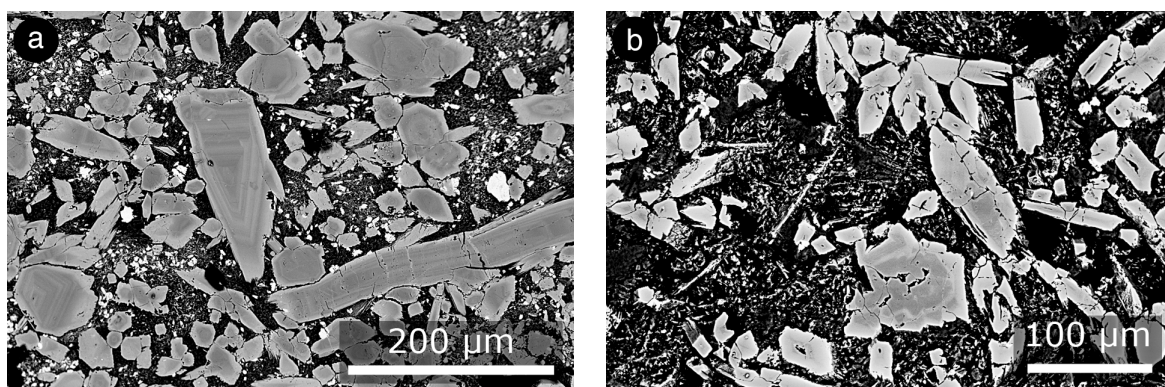


**Fig. 5.29:** BSE images showing oned magmatic clinopyroxene in fine-grained chlorite matrix, **a)** E7H2-10f and **b)** F2H2-5c.

## **#2: Chl > Am, magmatic amphibole**

Fragment **E1H3-3d** (Chl >> Am + Ap) is dominated by a fine-grained chlorite matrix with few subhedral amphibole grains and rare apatite (Fig. 5.30). Amphibole minerals have large cores, which had been identified as kaersutite. Apatite grains can be found as inclusions in these cores. The amphibole rims are feather-like with a composition changing from actinolite/tremolite to Mg-hornblende to winchite.

Kaersutite is an igneous amphibole found in upper mantle-derived peridotites and in alkalic rocks (Aoki, 1963; Pichler & Schmitt-Riegraf, 1997; Kesson & Price, 1972; McCubbin *et al.*, 2006), and even in alkaline plutonic complexes (Satoh *et al.*, 2004). As it is present mostly as phenocrysts but never occurs in the groundmass of these rocks, *P* and *T* were high when the kaersutite crystallized from the magma (Aoki, 1963). Furthermore, kaersutite represents an important phase in the fractionation of basic alkaline liquids over a wide range of pressures (Kesson & Price, 1972; Sr ranges from 532 to 1060 μg/g). Kaersutite often occurs in paragenesis with titan-augite, olivine, plagioclase, and apatite (Pichler & Schmitt-Riegraf, 1997).

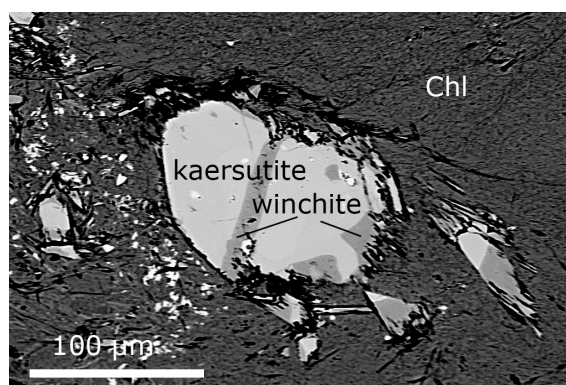


**Fig. 5.30:** Back-scattered electron (BSE) image of a large amphibole with kaersutite core and winchite rim, E1H3-3d.



Kaersutite and apatite in fragment E1H3-3d can be interpreted as the primary minerals in the rock before metamorphism. Metamorphism during subduction formed the chlorite matrix and the actinolite-winchite rims around irregular kaersutite cores.

### 5.3.5 Andradite-bearing serpentinites (Grt + Srp) and Bt-Chl-rocks

Fragments **E2H2-4g,5h** are characterized by idiomorph garnet minerals of andradite composition ( $\text{Ca}_3\text{Fe}_2\text{Si}_3\text{O}_{12}$ ) irregularly distributed in a fine-grained serpentine matrix (Fig. 5.31a). Micro-Raman analyses confirm andradite and show that the serpentine is antigorite, the high temperature polymorph.

Most garnets from ultramafic rocks have high pyrope and subordinate almandine contents (*e.g.*, Gustafson, 1974). However, idiomorph andradite crystals associated with serpentine have been found also in metamorphosed oceanic mantle rocks in Idria, central California (Fig. 5.31b) and in alpine-type serpentine schists (*e.g.*, Zermatt). Frost (1975) described various metaperidotite assemblages from the Paddy-Go-Easy Pass, Central Cascades; among these are serpentinites that contain relict chromite, chrome-magnetite and andradite or hydro-andradite. Further, hydroandradite occurs in opicalcites accompanying a partly serpentinitized alpine-type peridotite from the Totalp serpentine complex, Davos, Switzerland (Peters, 1965). The garnets occur with calcite, serpentine minerals (chrysotile and lizardite) and commonly with magnetite, which formed during serpentinization of peridotite, indicating the presence of considerable amounts of  $\text{H}_2\text{O}$ .

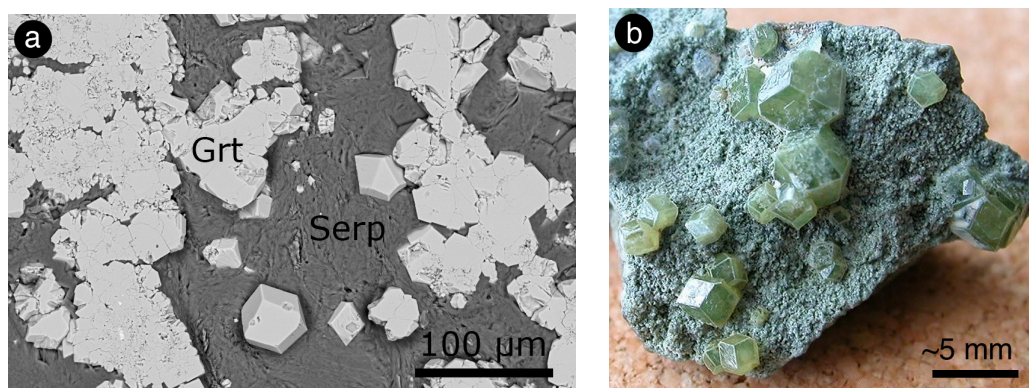


**Fig. 5.31:** **a)** Back-scattered electron image of sample E2H2-5H with andradite garnet crystals within an antigorite matrix, **b)** photograph of up to 5 mm large andradite crystals associated with serpentine, from metamorphosed oceanic mantle rocks, Idria, central California © 2004 Andrew Alden, licensed to About.com [<http://geology.about.com/od/minerals/ig/minpicgarnets/minpicandradite.htm>].

Fragment **E4H2-2a** is characterized by  $\pm$  idiomorph ‘hydrous Cr-garnet’ grains, which are distributed in the center of a serpentine matrix (Fig. 5.32). The garnet crystallized after spinel, as the cores of garnet are picotite. To the rim of the serpentine clast, calcite or aragonite ( $\text{CaCO}_3$ ) needles are radially embedded in the serpentine with increasing grain-size to the outside (up to  $50 \times 250 \mu\text{m}$ ). This sample might be similar to a finding within the Jijal Complex (northern Pakistan), where green

chromian andradite occurs associated with chrysotile in a chromitite layer. This garnet was formed during retrograde greenschist-facies metamorphism (Jan *et al.*, 1984).

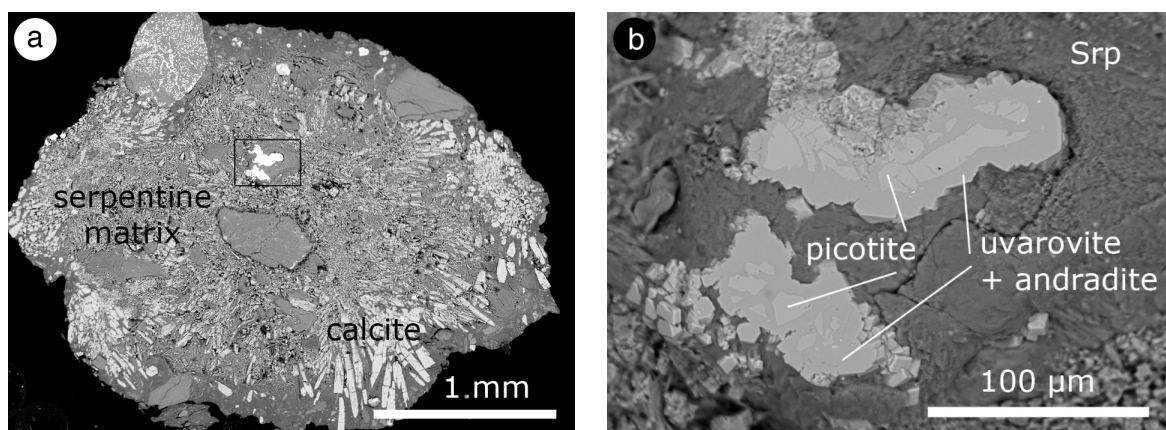


**Fig. 5.32:** BSE images of **a)** sample E4H2-2a serpentine matrix with calcite and **b)** andradite-uvarovite garnet with picotite cores embedded in this serpentine matrix.

Fragment **D3H1-8c** (Chl + Bt + Grt + Spl) is strongly foliated with an intergrowth of chlorite and biotite (Fig. 5.33). It also may be a replacement of biotite by chlorite. Tiny andradite grains are accumulated in some chlorite areas. Spinel occurs as accessory grains.

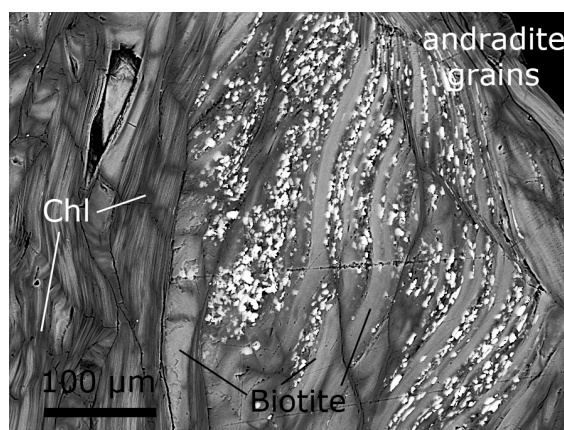


**Fig. 5.33:** BSE image of strongly foliated Chl-Bt with andradite grains (bright), D3H1-8c. >

## 5.4 Light element (Li, Be, B) contents and boron isotopic composition ( $\delta^{11}\text{B}$ ) of (rock forming) minerals

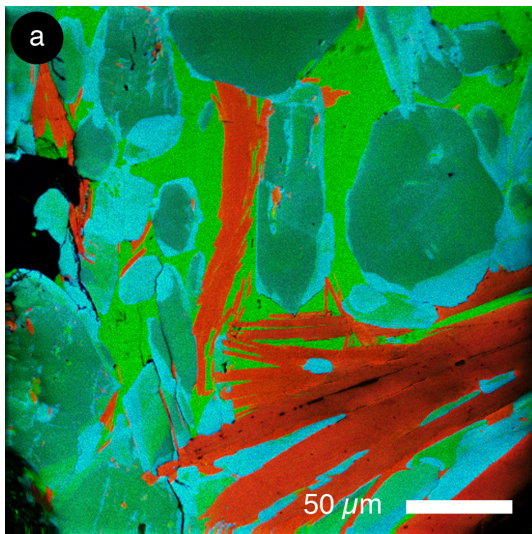
### 5.4.1 ToF-SIMS element maps

Distribution of Li and B of selected fragments was mapped in order to qualify their distribution between phases. As the ToF-SIMS is used in this study as a qualitative mapping technique with  $\mu\text{m}$ -scale resolution, the sensitivity of Li and B depends on the mineral, *e.g.*, identical Li contents produce higher count-rates in olivine than in serpentine (see chapter 3). In some cases, acquisition time was too short resulting in low total counts for some elements. Some images were processed into inverse color images with white background to visually intensify the element counts distribution. Chlorite and phengite were found to be the major Li- and B-carriers, whereas more variable and relatively lower Li and B count rates were found in amphibole. In the following, four sample metamafic rocks are shown.

**Example 1: E1H3-4d**

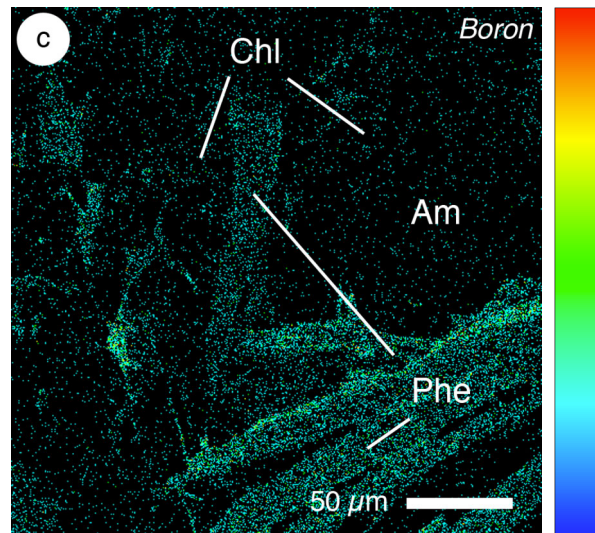
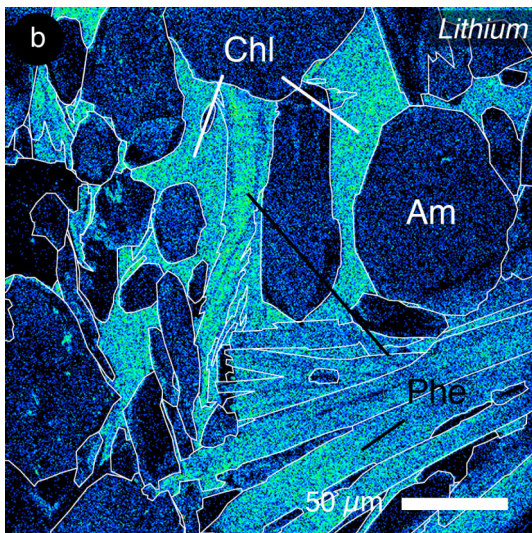
Figure 5.34a shows a ToF-SIMS multi-element map (500x500  $\mu\text{m}$ ) of sample E1H3-4d combining count rates for K (red color), Mg (green) and Na (blue). The bright green phase is chlorite, zoned amphibole is darker green to blue. The red sheaves are phengite. On the left is titanite (black). Figures 5.34b+c show Li and B distribution maps. The contours indicate boundaries of mineral phases. Chlorite and amphibole have low B contents, whereas phengite is strongly enriched in B. The highest Li concentration is found in chlorite and phengite, Li concentration in amphibole is lower.

A second area in the same rock (E1H3-4d) reveals the same results (Fig. 5.35, following page): Li and B are enriched in phengite and chlorite and less abundant in amphibole.



*Fig. 5.34 a) Multi-element map obtained by ToF-SIMS, K(red)Mg(green)Na(blue). Red needles are Phe, bright green is Chl and dark green to blue is Am. (500x500  $\mu\text{m}$ ).*

*(below) ToF-SIMS element distribution maps (500x500  $\mu\text{m}$ ) of b) lithium and c) boron. The scale to the right represents the number of ions counted (increasing from bottom to top).*



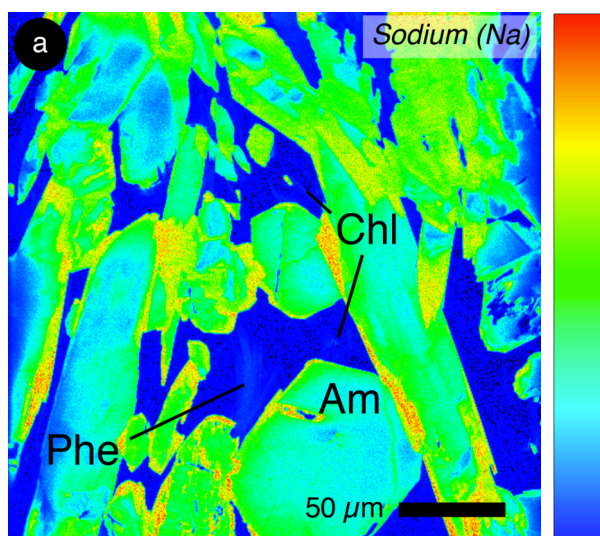
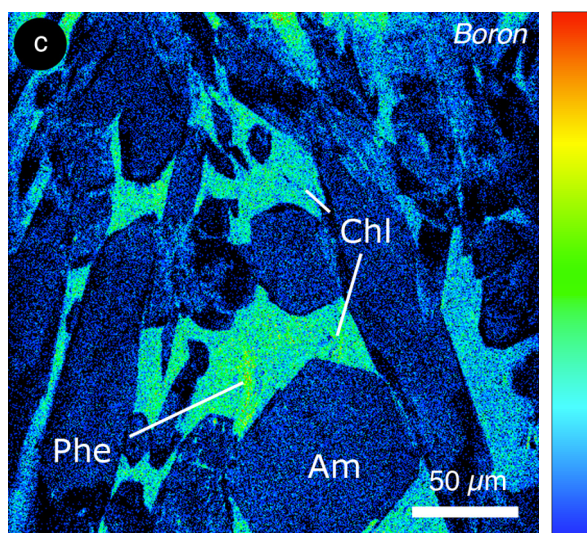
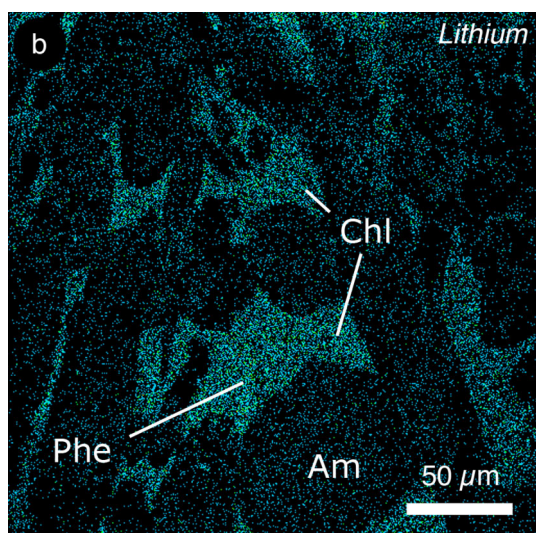


**Fig. 5.35 a):** ToF-SIMS mapping (500x500 μm) of E1H3-4d showing the Na distribution between phengite, chlorite and amphibole.

(below) ToF-SIMS element distribution maps (500x500 μm) of **b)** the lithium and **c)** boron distribution. Chl and Phe are enriched in both Li and B.

The scale to the right represents the number of ions counted (increasing from bottom to top).



### Example 2: E1H3-4b

Figure 5.36a shows a ToF-SIMS multi-element map (500x500 μm) of sample E1H3-4B combining count rates for K (red color), Mg (green) and Na (blue). The red sheaves in the upper left are phengite. Deep blue areas are Na-rich pyroxene (aegirin-augite:  $Jd_{19}Ac_{41}Q_{40}$ ), light blue areas of amphibole (dark green) have Na-rich composition (winchite-richterite). The light green phase is chlorite. Dark areas are Rt, Ttn, Ilm, Ep, Aln and Pmp (compare Fig. 5.22). Figures 5.36b+c show the B and Li distribution of the same area. The contours indicate boundaries of major minerals or mineral assemblages. Chlorite and phengite are generally enriched in B, whereas some chlorite areas have lower B contents (upper left in Fig. 5.36b). Li is highly enriched in chlorite and phengite, but less in amphibole.

Another mapped area of sample E1H3-4b is given in Fig. 5.37 (500x500 μm). To distinguish the phases Chl, Am, Phe, Ep+Aln and Rt a Mg-counts mapping is shown (Fig. 5.37a). Li concentrations are high in chlorite and phengite and lower in amphibole (Fig. 5.37b). Ep+Aln and Rt are virtually Li-free. Acquisition time in this case was too short to collect enough ions for a B distribution map.

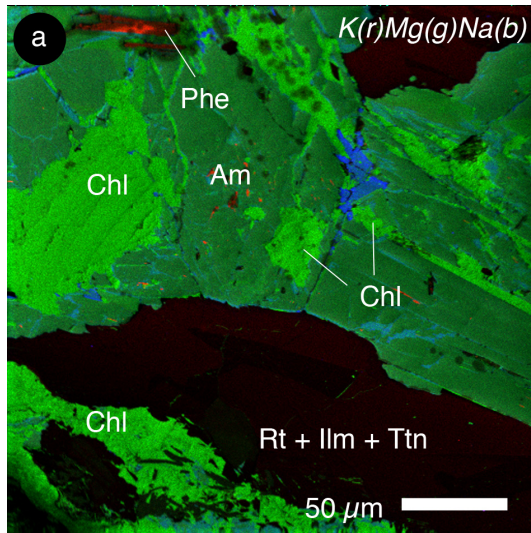


**Fig. 5.36 a):** ToF-SIMS mapping (500x500  $\mu\text{m}$ ) of EIH3-4b showing a multi-element distribution of K(red)Mg(green)Na(blue), the red phase is Phe, bright green is Chl, dark green is Am, blue is Na-Px.

(below): ToF-SIMS element distribution maps (500x500  $\mu\text{m}$ ) of **b)** the lithium and **c)** boron distribution. The scale to the right represents the number of ions counted (increasing from bottom to top).

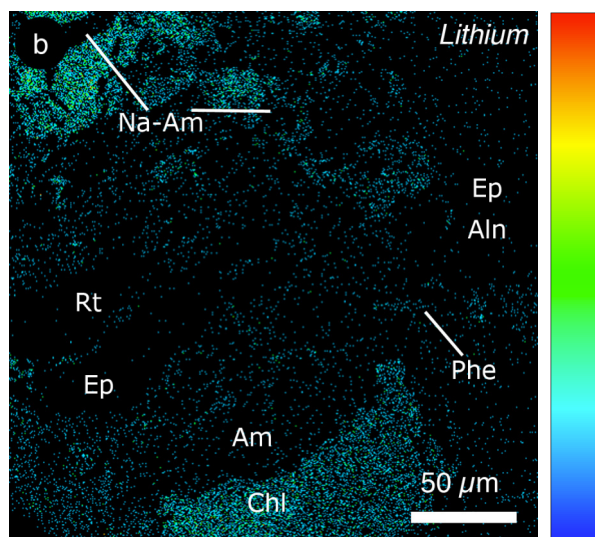
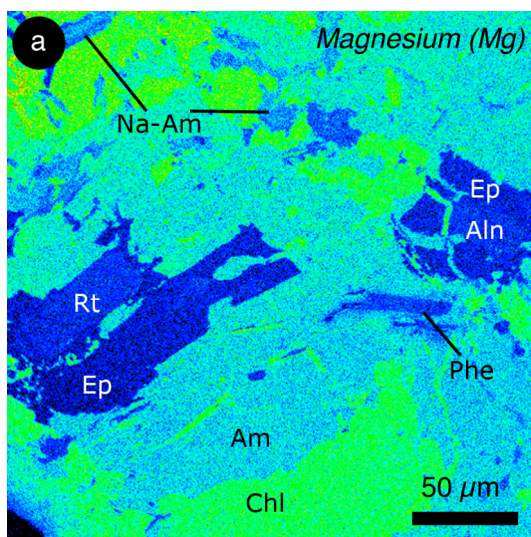
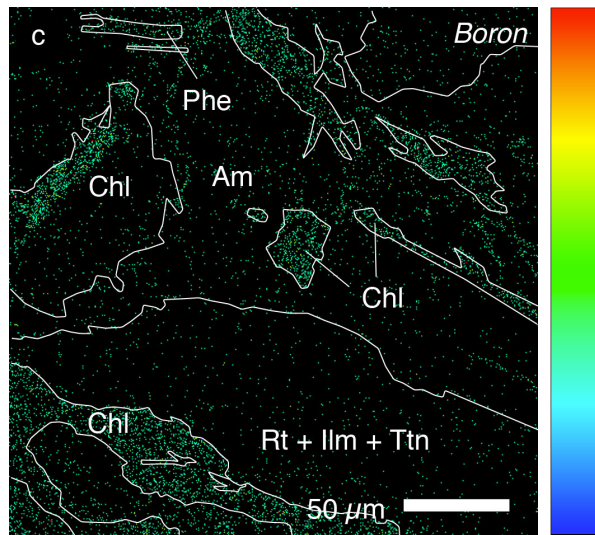
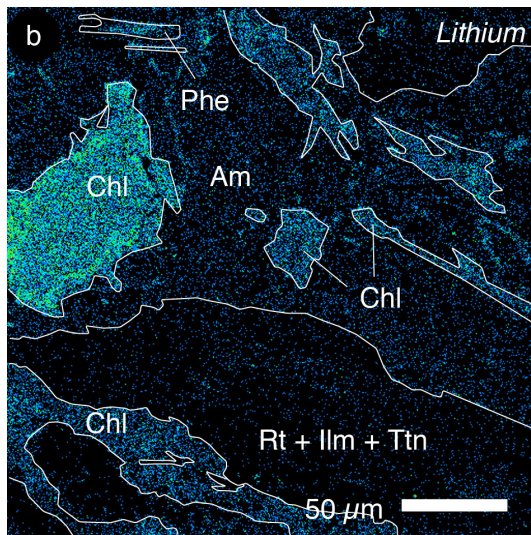
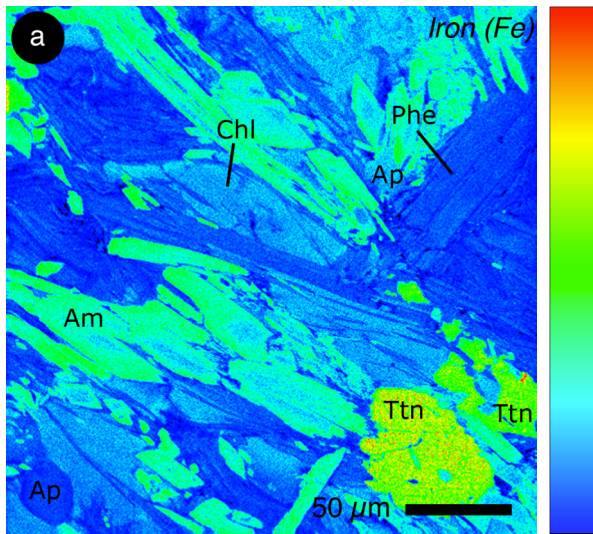


**Fig. 5.37:** ToF-SIMS mapping (500x500  $\mu\text{m}$ ) of sample EIH3-4b showing **a)** Mg count rates, major mineral phases can be easily distinguished, **b)** lithium count rates: Li is enriched predominantly in Chl.

**Example 3: E1H3-4a**

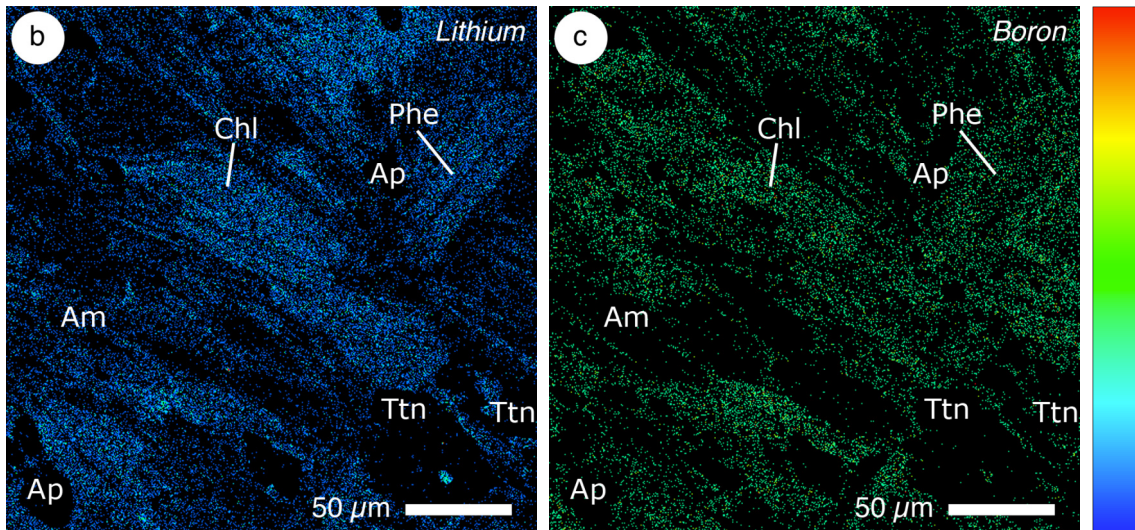
ToF-SIMS element mapping ( $500 \times 500 \mu\text{m}$ ) was performed for two areas in sample E1H3-4a (Fig. 5.38 and 5.39). Amphibole, chlorite and phengite phases can be well distinguished by Fe and Mg counts (Fig. 5.38a & 5.39a). A multi-element image combining Li and B counts in inverse color scale (Fig. 5.38b) shows that Chl and Phe are both enriched in Li and B, whereas Ap and Ttn are Li- and B-free.

Due to the very low acquisition time for the second mapped area in the sample (Fig. 5.39a), the count rate of B was too low to yield a map. As shown in Fig. 5.39b, Li is enriched in Chl and Phe relative to amphibole.



**Fig. 5.38 a):** ToF-SIMS mapping ( $500 \times 500 \mu\text{m}$ ) of E1H3-4a showing the Fe count rates, major mineral phases can be easily distinguished.

(below) ToF-SIMS element distribution maps ( $500 \times 500 \mu\text{m}$ ) of **b)** the lithium and **c)** boron distribution. The scale to the right represents the number of ions counted (increasing from bottom to top).



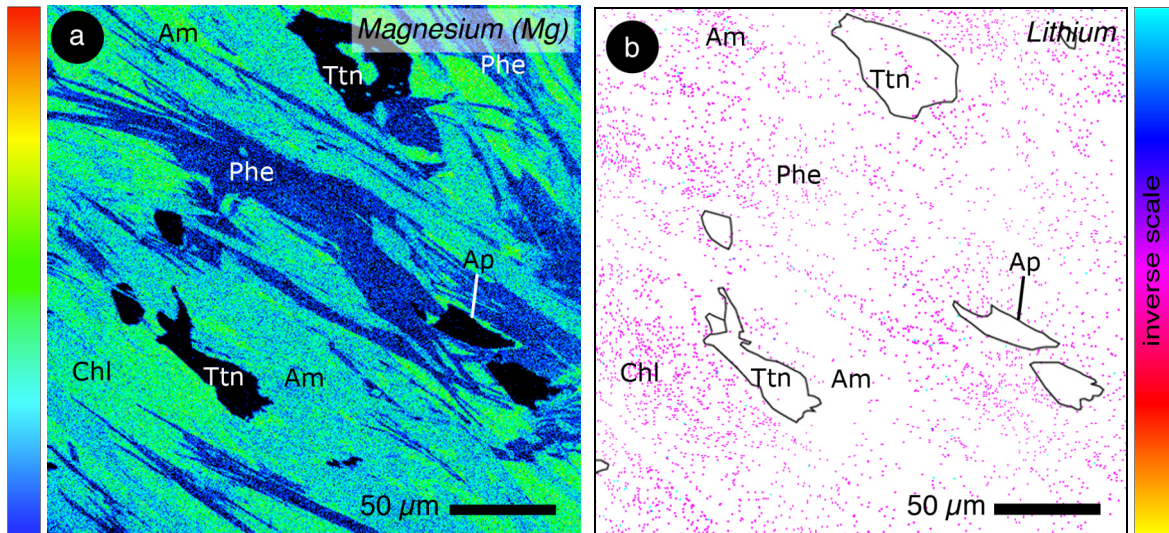


**Fig. 5.39:** ToF-SIMS maps (500x500 μm) showing **a)** Mg count intensities to distinguish between Chl, Am and Phe, **b)** Li counts distribution with inverse color scale).

#### Example 4: E1H3-4c

In sample E1H3-4C, a chlorite-rich epidote-bearing area was mapped (500x500 μm; Fig. 5.40a) Again, the acquisition time in this case was too short to collect enough ions for a B map. However, total Li counts were high (Fig. 5.40b) and the distribution map indicates a Li enrichment in chlorite. Garnet show few Li, while epidote, titanite and apatite are virtually Li-free.

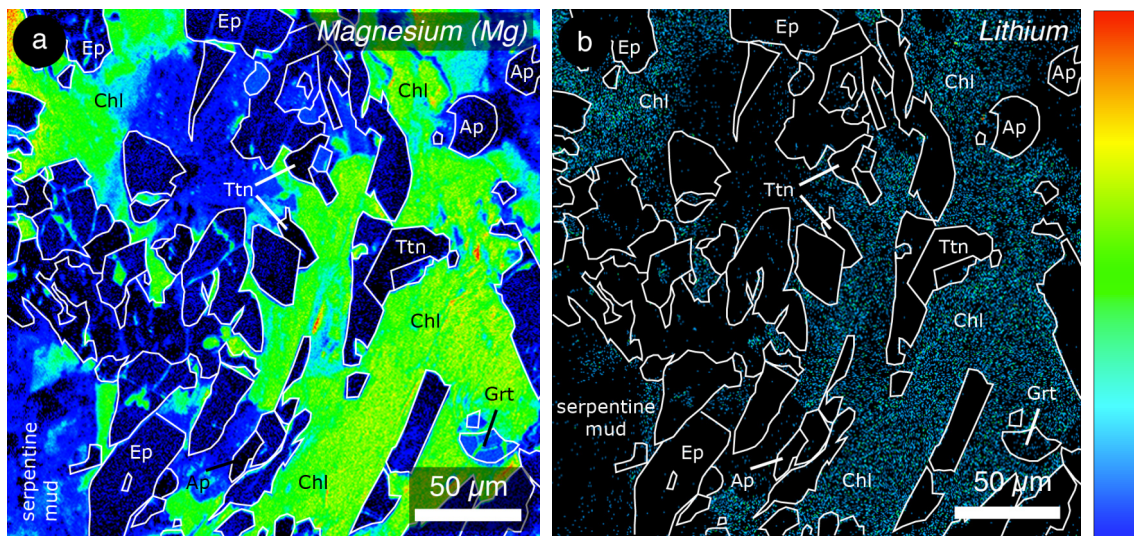


**Fig. 5.40:** ToF-SIMS maps (500x500 μm) showing **a)** the Mg counts distribution to distinguish the major phases and **b)** the lithium distribution. The scale to the right represents the number of ions counted (increasing from bottom to top).

### 5.4.2 SIMS analyses: budgets of Li, Be and B

SIMS analyses reveal that phengite and chlorite are the major Li- and B-bearing phases confirming the results of the qualitative ToF-SIMS mapping. Furthermore, amphibole and phengite are the major Be carrier in the metamafic rocks embedded in Mariana forearc serpentine mud of South Chamorro Seamount (Fig. 5.41). Analyses are given in *Appendix C3*.

*Amphibole* has variable Li and B concentrations with Li contents reaching  $\sim 40 \mu\text{g/g}$  and B reaching  $\sim 20 \mu\text{g/g}$ . Be contents vary between  $0.07\text{--}10 \mu\text{g/g}$ . Amphibole from the magmatic samples (kaersutite core composition) has distinct Li and Be ( $\sim 1 \mu\text{g/g}$ ; Fig. 5.41) and B contents ( $<0.5 \mu\text{g/g}$ ) lower to most other amphiboles.

*Chlorite* has similar B contents compared to amphibole ( $0.2\text{--}11 \mu\text{g/g}$ ), but higher Li contents up to  $105 \mu\text{g/g}$  (Fig. 5.41a). Be contents are below  $10 \mu\text{g/g}$ . The compositional field of chlorite partly overlaps with compositions of amphibole.

*Talc* is enriched in Li and B ( $\sim 10 \mu\text{g/g}$ ). Be contents are similar to the average Be content in chlorite ( $\sim 0.2 \mu\text{g/g}$ ).

*Phengite* composition plot in a relatively distinct field in the Li-B correlation diagram (Fig. 5.41); phengite has high Li ( $30\text{--}120 \mu\text{g/g}$ ) and B ( $20\text{--}70 \mu\text{g/g}$ ) contents. Be contents are similar to Be-rich chlorite and to the average amphibole Be contents ( $>1$  to  $2 \mu\text{g/g}$ ).

*Pyroxene* has a narrow range in Li contents ( $0.04\text{--}3 \mu\text{g/g}$ ), but has variable B contents between  $0.03\text{--}10 \mu\text{g/g}$ . Be compositions are in the range as for amphibole and chlorite. The very low Be and B contents are found in the calc-alkaline pyroxenes (volcanic sample). A linear positive correlation between Li-B, Be-B and Li-Be can be observed.

Some *epidote* (epidote in E4H2-2B) is similarly and even stronger enriched in B as phengite (Fig. 5.41). All other epidote has low B contents of  $<3 \mu\text{g/g}$  down to even  $0.05 \mu\text{g/g}$ . Li contents are usually low  $0.004\text{--}1 \mu\text{g/g}$  (one exception:  $7 \mu\text{g/g}$ ), with a tendency to higher contents with higher B. Also Be concentrations, ranging between  $0.01$  and  $1 \mu\text{g/g}$ , increase with increasing B concentrations.

*Pumpellyite* has a high B content in the range of the highest B contents in Chl and Am. The Li content is  $\sim 3 \mu\text{g/g}$ , Be content is high with  $8 \mu\text{g/g}$ .

*Garnet* within serpentine matrix (andradite) has B contents between  $1$  and  $3 \mu\text{g/g}$ , low Li contents, and is depleted in Be. Garnet in assemblage with Ep, Ttn, Ap and Chl (E1H3-4c) is Be- and B-depleted, but is Li-rich ( $4.4 \mu\text{g/g}$ ).



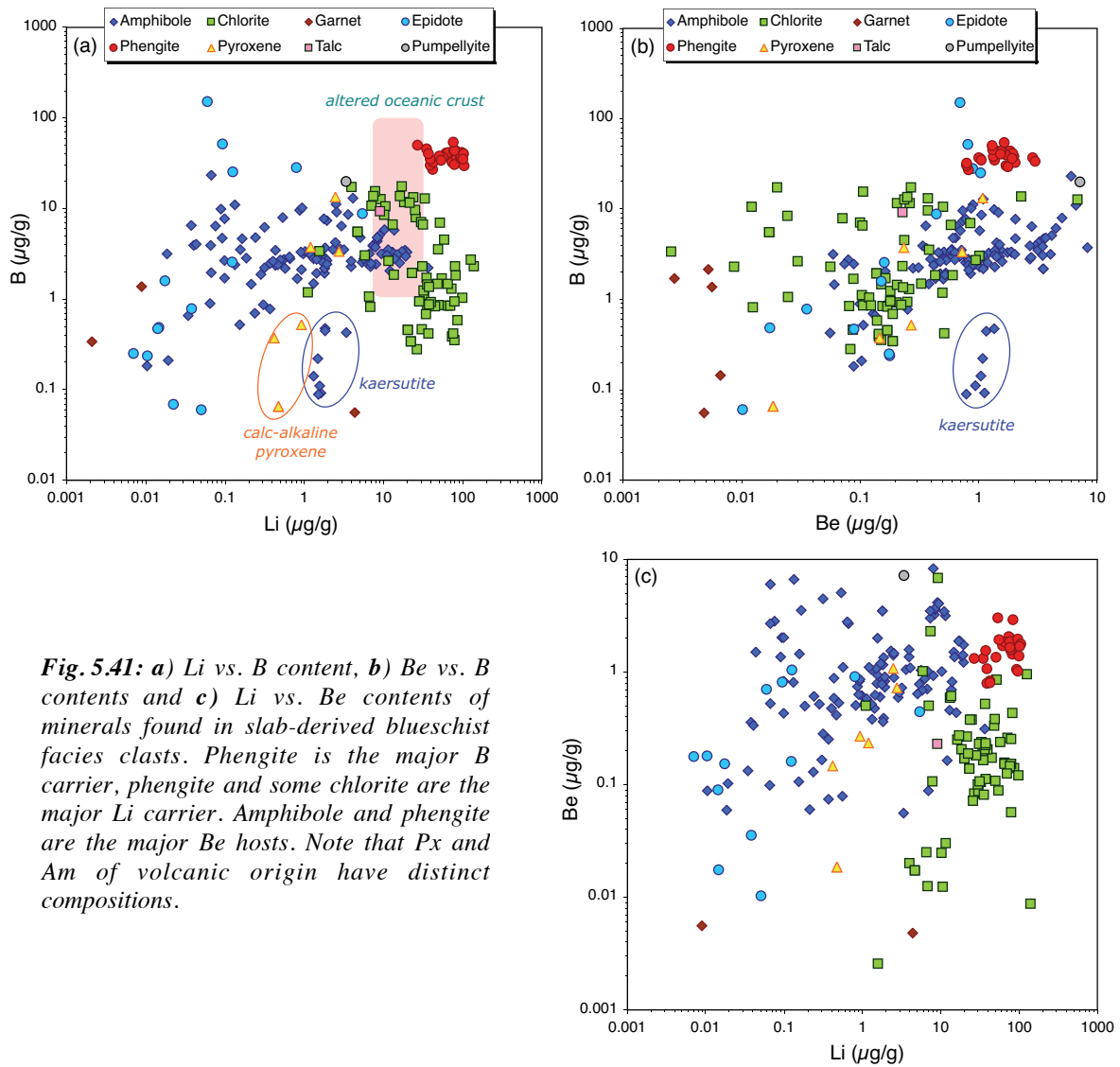


**Fig. 5.41:** a) Li vs. B content, b) Be vs. B contents and c) Li vs. Be contents of minerals found in slab-derived blueschist facies clasts. Phengite is the major B carrier, phengite and some chlorite are the major Li carrier. Amphibole and phengite are the major Be hosts. Note that Px and Am of volcanic origin have distinct compositions.

### 5.4.3 SIMS analyses: $\delta^{11}\text{B}$

In the blueschist-facies fragments recovered from South Chamorro Seamount, phengite, chlorite and amphibole are relatively B-rich (with decreasing B contents from Phe > Chl > Am). Also some epidotes and pyroxenes are B-rich. Due to the very small mineral grain size (generally <50  $\mu\text{m}$ ) a beam current of only 10 nA was chosen trading spot size for precision.

The B isotope analyses (Appendix C3) show that phengite of different samples define a narrow range between  $-2$  and  $-10$  ‰  $\delta^{11}\text{B}$  at high B concentrations. The majority of amphibole and chlorite confirms this negative B isotope signature which averages at  $-6 \pm 4$  ‰ (Fig. 5.42). However,  $\delta^{11}\text{B}$  values of amphibole, chlorite and epidote can be more negative or more positive relative to the range defined by phengite.

B isotope ratios vary significantly between minerals in a single fragment;  $\delta^{11}\text{B}$  may be higher in amphibole compared to chlorite, in other samples amphibole has similar or even lower  $\delta^{11}\text{B}$  relative

to chlorite (*Appendix C3*). However, this variation does not influence the average B isotope signature of  $-6\text{‰}$  defined by the B-rich minerals in the metamafic rocks.

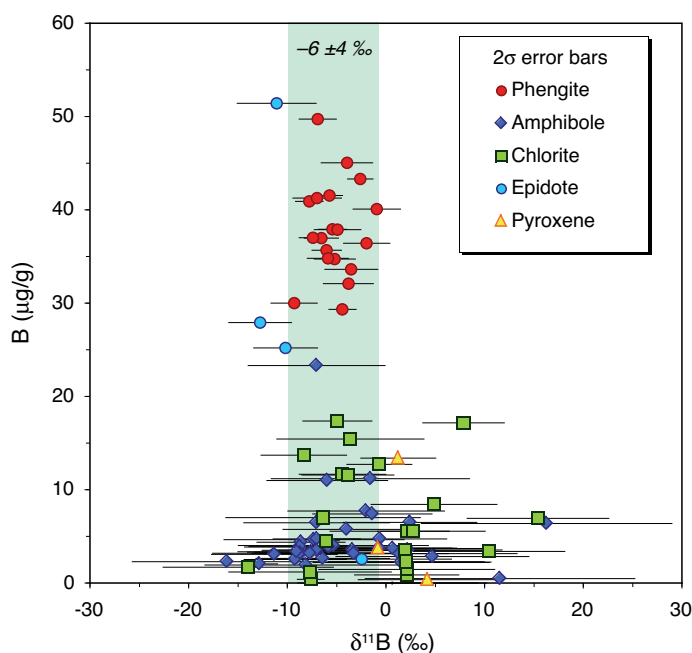


**Fig. 5.42:** B isotope ratios vs B concentrations for phengite, chlorite and amphibole in blueschist facies clasts by SIMS analyses. The correlation shows that bulk blueschists average at about  $-6\text{‰}$   $\delta^{11}\text{B}$ . Analyses of magmatic samples (e.g., some pyroxene and kaersutite amphibole) were excluded, as the samples relevant for later discussion and interpretation are restricted to slab-derived metamafic ones.

## 5.5 Geothermobarometry

In subduction-related complexes blueschist and greenschist facies rocks generally occur in intimate, even interlayered association (Bröcker, 1990). It has been established that during metamorphism, rocks and mineral compositions typically record ambient *PT*-conditions. Hence, mineral assemblages that are stable and in chemical equilibrium define metamorphic facies.

Subduction zones are characterized by greenschist- and blueschist-facies metamorphic rocks that formed under moderate-*P*/moderate-*T* or high-*P*/low-*T* conditions, respectively. Greenschist-facies minerals commonly include chlorite, actinolite, epidote, and albite in metamorphic rocks of basaltic primary rocks composition (Table 5.2; e.g., Evans, 1990). Temperatures range from  $\sim 350$  to  $500\text{ °C}$  at pressures between 0.2 and 1 GPa ( $\sim 5$ – $35$  km depth). The blueschist-facies can be considered to form under pressures equivalent to a depth of 15–18 km and a temperature range from 200 to  $500\text{ °C}$ . Common minerals associated with the blueschist-facies include sodic amphiboles (glaucophane), lawsonite or epidote, jadeite, albite or chlorite, garnet, aragonite and phengite (e.g., Ernst, 1973; Miyashiro, 1973; Evans, 1990). However, mineral formation is strongly influenced by factors such as water pressure,  $f(\text{O}_2)$  and bulk rock composition (e.g., Liou *et al.*, 1985; Maruyama *et al.*, 1986; Evans, 1990) which can lead to the intercalation of blue- and greenschist, depending e.g., on bulk compositions of the protoliths.

The metamafic rocks from South Chamorro Seamount comprise mainly (Na-)amphibole-schists and epidote-rocks and minor metasediments. To estimate the temperature and pressure conditions present during the formation of these metamafic rocks, sodic amphibole, chlorite, phengite, epidote,

pumpellyite, and rutile + ilmenite can be considered. First of all, there is no evidence for retrograde reactions such as replacement of blue amphibole by more calcic amphiboles (*e.g.*, Bröcker, 1990). Rather, amphibole rims are generally sodic-rich compared to the cores, indicating prograde metamorphism at blueschist-facies conditions. Chloritoid  $\pm$  glaucophane alter to paragonite + chlorite during retrograde paths (Bröcker, 1990); as phases such as paragonite were not observed in this study, retrograde reactions seem to be of minor importance.

**Table 5.2:** Metamorphic facies paragenesis in the system NCMASH after Evans (1990).

Facies	Stable paragenesis
Epidote Blueschist (EBS)	Na-amph + Epd + Qtz + H <sub>2</sub> O
Lawsonite Blueschist (LBS)	Na-amph + Laws
Pumpellyite-Actinolite (PA)	Pmp + Act + Chl + Ab + Qtz + H <sub>2</sub> O
Greenschist (GS)	Ab + Chl + Act + Ep + Qtz + H <sub>2</sub> O
Eclogite (E)	(Jd + Diop?) Omp + Grt + Qtz + H <sub>2</sub> O
Albite-Epidote-Amphibolite (AEA)	Jd $\pm$ Alb + Grt + Trem + Parag + Epd
Amphibolite (A)	Ab + Act/Hbl + Ep + absence of: Na-amph, Pl, Greenschist paragenesis (Ab + Chl + Ep + Act + Qtz)

Previous *PT* estimations for the metamafic fragments recovered at several seamounts in the Mariana forearc region are available in literature. Minerals in metamafic fragments from Conical Seamount include lawsonite, pumpellyite, calcic amphibole, incipient sodic pyroxene, phengite, chlorite and aragonite, some of them as secondary products (Maekawa *et al.*, 1992). Metamorphic conditions for these high-pressure minerals were estimated to be  $\sim 150\text{--}250$  °C (lawsonite+pumpellyite stability field) and 0.5–0.6 GPa (*e.g.*, aragonite-calcite phase transition) (Maekawa *et al.*, 1992). Maekawa *et al.* (1993) inferred that these metamorphic conditions are equivalent to depths of 16 to 21 km below seafloor. This is only slightly shallower than the slab depth of 29 km estimated for Conical Seamount, based on earthquake depths (Hussong & Fryer, 1982; Seno & Maruyama, 1984). Fryer *et al.* (2000) suggested similar conditions of  $\sim 350$  °C and  $\sim 0.8$  GPa, equivalent to a depth of  $\sim 26$  km for South Chamorro Seamount, close to the 27 km estimated by Mottl *et al.* (2004).

Mineral paragenesis generally used for *PT* estimations (at blueschist-facies conditions) include minerals such as prehnite, lawsonite, quartz and albite. However, the diagnostic mineral of this *PT* subduction zone metamorphism, *i.e.*, the blueschist-facies, is sodic amphibole. It can be observed that calcic amphibole undergoes systematic compositional changes becoming more sodic with increasing pressure (*e.g.*, Evans, 1990). Using the geobarometer from Maruyama *et al.* (1986) which is based on the influence of pressure on the Al<sub>2</sub>O<sub>3</sub> contents in sodic amphibole, Gharib (2006) estimated pressures of  $\sim 0.45$  to  $\sim 0.57$  GPa for the Mariana metamafic rocks. Na<sub>2</sub>O contents in these amphiboles are comparable to values measured in this study. However, as most rocks studied are free of albite and quartz, pressure estimations using the amphibole composition are just a rough approach. Furthermore,

jadeitic pyroxene of metamafic fragments in this study reach ~33% Jd. This value coincides with results from Maekawa *et al.* (1992) and confirms the *PT* estimations mentioned above.

Gharib (2006) evaluated several geothermometers for chlorite and concluded that for the Mariana metamafic clasts the temperatures after Cathelineau & Niveau (1985) and Xie *et al.* (1997) yield similar values; ~260 °C and ~280 °C, respectively. Chlorite from Conical Seamount samples (Maekawa *et al.*, 1992) yield a temperature of ~270 °C when applying the Cathelineau equation, (Gharib, 2006). However, geothermometers are calibrated for high temperatures which are well above the conditions expected at ~27 km depth. Therefore, *T* estimations on chlorite will not be considered in this study.

Epidote is typical for higher temperature blueschists, *i.e.*, the epidote-blueschist facies (*e.g.*, Taylor & Coleman, 1968; Murayama *et al.*, 1986; Evans, 1990). Because of their wide range of *PT* stability, epidote group minerals of variable composition may form in a single rock during several stages of metamorphic reequilibration. Especially at low temperatures, slow rates of intra-crystalline Al-Fe<sup>3+</sup> exchange preserve complex zonation patterns in individual grains, providing evidence for continuous or discontinuous prograde and retrograde reactions (Grapes & Hoskin, 2004). Hence, relic lower grade epidote is typically Fe-rich, whereas higher grade epidotes, often forming rims, are less Fe-rich (Grapes & Hoskin, 2004). Maruyama *et al.* (1986) calculated a series of equilibria for the ferric component of epidote along a continuous reaction between magnesio-riebeckite and glaucophane and found a positive *PT*-correlation with decreasing X<sub>ps</sub>. According to Maruyama *et al.* (1986 and Enami *et al.* (2004), Gharib (2006) applied isobars corresponding to glaucophane and pistacite X<sub>ps</sub> components (0.23–0.29 X<sub>ps</sub>) and suggested *PT* conditions of ~0.4 to ~0.5 GPa and ~240 to ~290 °C. However, compositional range is similar to the one observed in epidote from the present study (0.25 to 0.33 X<sub>ps</sub>, 0.17 in some epidote cores). However, these epidote compositions are comparable to blueschist-facies epidote from three Black Butte rocks (X<sub>ps</sub> = 0.28–0.33; Brown & Ghent, 1983) and hence confirm a blueschist-facies origin of the metamafic clasts studied.

Maekawa *et al.* (1992) and Maekawa (1995) described lawsonite in samples recovered from Conical Seamount. However, in the metamafic rocks Conical and South Chamorro Seamounts, lawsonite was not identified (this study; Gharib, 2006).

This study documents the existence of *pumpellyite* (sample E1H3-4b) in (i) association with titanite, magnetite, rutile, ilmenite and epidote surrounded by a chlorite + (Na)-amphibole (± Na-Px) matrix, as well as (ii) single pumpellyite crystals in amphibole. The comparative study of onland metamorphic terranes by Brown (1977) gives a petrogenetic grid for relative *PT*-range estimations (Fig. 5.43). Although the limiting phase relationships require quartz and albite, which do not occur in the Pmp-bearing sample, the Black Butte blueschist in the Franciscan includes the phase assemblage of Pmp + Ep + Na-Am (Fig. 5.43). Temperatures for these blueschists are 250–300 °C (Brown & Ghent, 1983) at about 0.7 GPa.

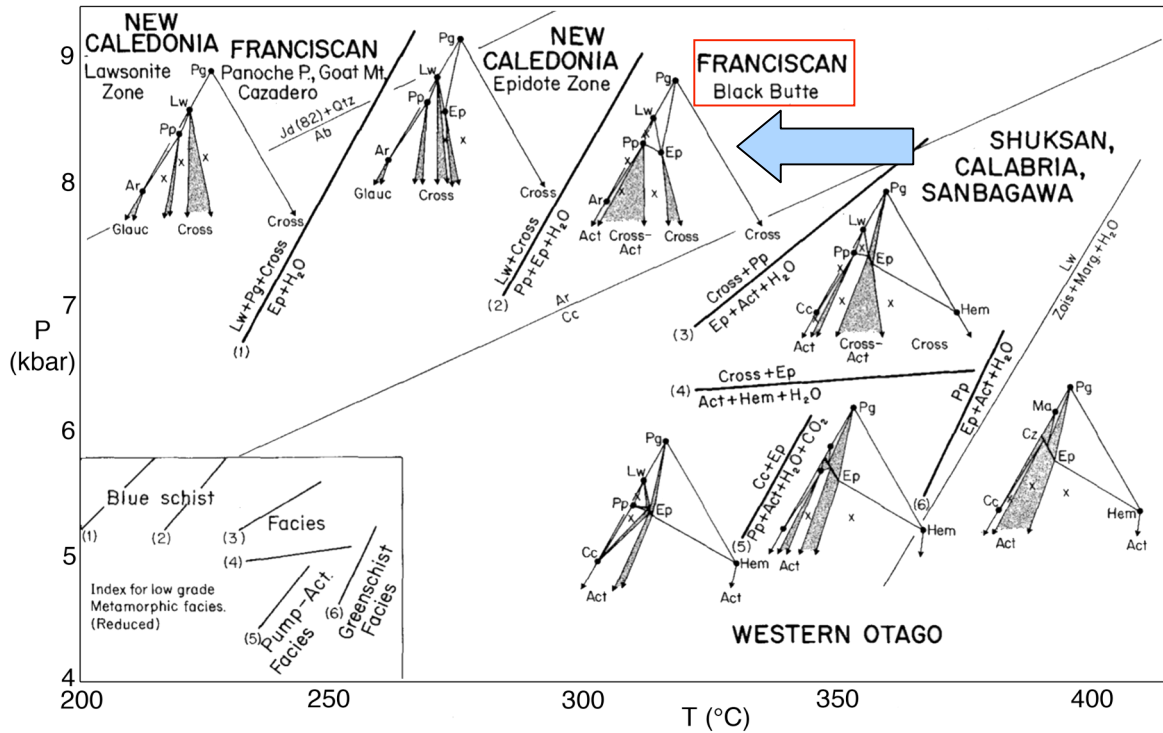


Fig. 5.43: Summary of PT-estimates and phase relations in the system Al-Ca-Fe<sup>3+</sup> (from Brown, 1977).

## 5.6 Calculated modal compositions: bulk rock and potential source material

To compare the metamafic rocks from the Mariana forearc region with literature data, the bulk rock composition of the mafic clasts was calculated and is reported in Table 5.3; combining the modal abundance and compositions of relevant mineral phases yields the bulk rock composition of each sample. The FeO content of minerals was recalculated to Fe<sub>2</sub>O<sub>3</sub> and rock compositions were calculated water-free to have consistency with literature data. It is important to note that calculated, *i.e.*, estimated bulk rock compositions are afflicted with a large error due to visual mineral vol% estimation and averaging of heterogeneous, *i.e.*, variable mineral compositions. The mineral assemblages and calculated bulk rock compositions are significantly more variable compared to samples investigated by Gharib (2006) indicating a large range of slab and slab-mantle-interface rocks sampled by South Chamorro Seamount.

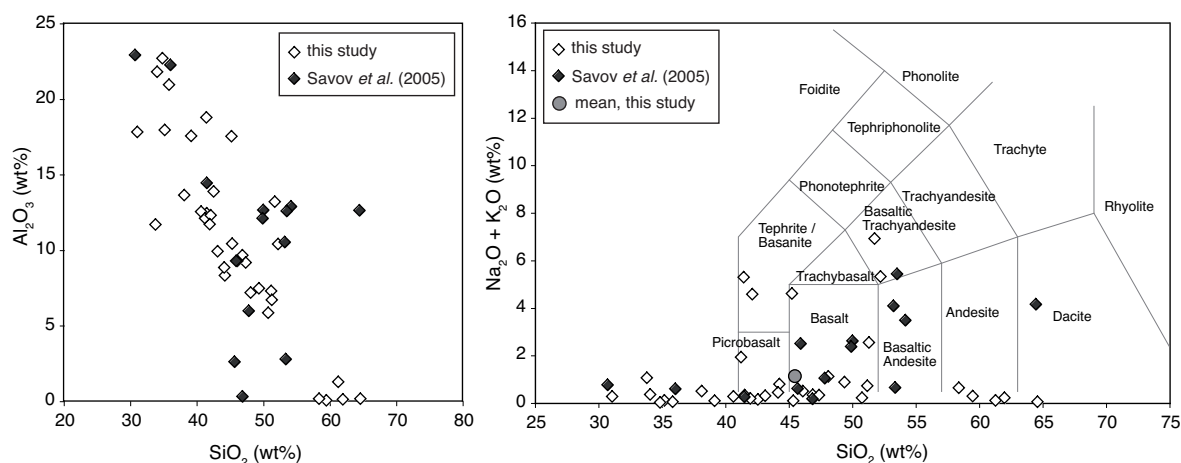
The metamafic rocks show a wide range from Si-depleted and Al-enriched to Si-enriched and Al-depleted compositions (Fig. 5.44a), equivalent to Si-undersaturated andesitic and trachybasaltic rocks in the TAS (total alkali vs silica) diagram (Fig. 5.44b). The large range in silica content (31–65 wt%) is caused by a large amount of nearly mono-mineralic fragments (*e.g.*, Chl, Am, Tlc). Talc- and/or amphibole-rich rocks have the highest SiO<sub>2</sub> contents, chlorite- and/or epidote-rich rocks are relatively silica-poor (Table 5.3). The estimated Mg# ranges from 39 to 92.

Table 5.3: Bulk rock composition (wt%) calculated after estimated mineral vol%.

Sample	SiO <sub>2</sub>	TiO <sub>2</sub>	Al <sub>2</sub> O <sub>3</sub>	Cr <sub>2</sub> O <sub>3</sub>	Fe <sub>2</sub> O <sub>3</sub>	MnO	MgO	CaO	Na <sub>2</sub> O	K <sub>2</sub> O	NiO	P <sub>2</sub> O <sub>5</sub>	LOI	Total (LOI-free)	Na <sub>2</sub> O + K <sub>2</sub> O	Mg#	Li (µg/g)	B (µg/g)
D1H4-1a	48.79	0.02	6.29	0.15	12.64	1.21	20.65	3.60	2.35	0.03	0.10	0.00	4.16	95.84	2.38	62.12	12.80	3.19
D1H4-2d	40.58	2.47	8.05	0.01	9.12	0.22	24.47	6.56	0.35	0.04	0.15	0.66	7.33	92.67	0.39	74.36	7.78	5.21
D3H1-8C	38.58	0.07	11.15	0.49	7.46	0.04	29.37	0.69	0.22	3.92	0.26	0.00	7.75	92.25	4.13	81.28		
E1H3-3d	33.31	0.36	11.77	0.01	11.28	0.24	28.29	2.26	0.34	0.09	0.08	0.82	11.14	88.86	0.43	73.10	20.60	10.64
E1H3-4a	38.87	1.10	17.35	0.05	14.38	0.28	13.03	3.24	1.08	3.80	0.03	1.64	5.15	94.85	4.88	49.61	51.92	18.23
E1H3-4b	39.12	5.01	11.30	0.14	13.88	0.32	15.94	8.16	1.64	0.16	0.04	0.00	4.30	95.70	1.80	55.40	22.70	4.84
E1H3-4c	28.84	1.89	16.28	0.10	14.92	1.91	12.62	13.06	0.23	0.01	0.10	4.10	5.93	94.07	0.24	45.11	22.91	0.88
E1H3-4d	42.85	1.46	16.40	0.14	11.31	0.41	13.50	4.98	1.31	2.99	0.05	0.00	4.60	95.40	4.30	56.02	48.90	13.77
E1H3-5	40.33	0.01	9.20	0.25	6.23	0.20	29.37	3.82	0.06	0.01	0.17	0.00	10.36	89.64	0.07	83.49		
E2H2-4b	37.67	0.41	11.12	0.03	12.45	0.17	25.25	4.13	0.21	0.07	0.08	0.41	8.00	92.00	0.28	68.91		
E2H2-4g,5h	36.76	0.01	0.18	0.01	23.79	0.04	13.55	21.37	0.03	0.01	0.02	0.00	4.24	95.76	0.04	38.69	0.61	53.58
E2H2-4j	58.69	0.00	0.04	0.03	3.72	0.10	22.52	13.29	0.23	0.05	0.04	0.00	1.29	98.71	0.28	86.72	0.26	2.46
E2H2-5d	48.41	0.05	6.82	0.23	8.39	0.51	23.40	5.62	0.64	0.03	0.18	0.82	4.90	95.10	0.67	74.36	13.61	4.40
E2H2-5j	60.45	0.02	0.13	0.10	3.41	0.01	29.30	0.00	0.03	0.00	0.34	0.00	6.20	93.80	0.04	90.49		
E4H1-2a	40.97	0.21	8.15	0.07	9.67	0.15	23.90	6.28	0.41	0.02	0.14	0.00	10.01	89.99	0.43	72.94	2.65	4.70
E4H2-2b	32.74	0.81	20.98	0.02	15.65	0.28	8.51	15.25	0.01	0.00	0.03	0.82	4.89	95.11	0.01	37.17	20.17	32.91
E7H2-10F	39.39	1.25	8.93	0.09	12.82	0.15	18.14	11.43	0.26	0.01	0.06	0.00	7.47	92.53	0.26	60.79		
E7H2-1a,b,2a,8a,b,10	45.88	0.93	6.76	0.03	11.23	0.41	19.66	9.12	0.99	0.05	0.09	0.82	4.01	95.99	1.04	65.11		
E7H2-6A	30.11	1.09	15.13	0.03	14.64	0.45	25.27	1.03	0.08	0.01	0.00	0.00	12.15	87.85	0.09	64.95		
F1H1-3C	44.18	0.02	8.47	0.50	8.72	0.38	24.83	6.21	0.28	0.02	0.24	0.00	6.13	93.87	0.30	75.08		
F1H1-3D	30.10	0.01	18.95	0.00	14.93	0.59	25.31	0.01	0.01	0.30	0.04	0.00	9.76	90.24	0.31	64.32		
F1H1-3E	41.71	1.63	7.75	0.13	7.23	0.45	20.35	10.26	0.70	0.03	0.14	1.64	7.99	92.01	0.74	74.52	70.85	2.46
F1H1-3F	45.07	0.03	6.75	0.12	10.10	0.20	24.98	6.57	0.76	0.03	0.19	0.00	5.20	94.80	0.79	72.87	8.20	9.11
F1H3-2C	57.84	0.01	1.18	0.03	3.55	0.14	29.20	2.08	0.08	0.01	0.43	0.00	5.45	94.55	0.09	89.75		
F1H3-2D	35.57	3.08	10.87	0.01	10.53	0.08	25.59	2.85	0.14	0.09	0.05	0.00	11.12	88.88	0.23	72.79	16.05	20.01
F1H3-2F	57.94	0.01	0.10	0.02	2.63	0.12	28.07	4.27	0.19	0.01	0.25	0.00	6.37	93.63	0.20	91.83		
F1H4-3a	32.66	1.02	18.82	0.01	12.75	0.56	18.80	7.68	0.02	0.01	0.03	0.00	7.64	92.36	0.03	60.96	66.59	1.32
F1H4-5	42.78	0.01	8.71	0.45	6.67	0.30	26.77	5.59	0.29	0.02	0.27	0.00	8.16	91.84	0.30	80.94		
F2H2-1A	31.89	0.42	10.89	0.02	12.68	0.77	10.33	18.90	0.92	0.06	0.06	8.20	4.85	95.15	0.99	45.86	0.57	1.34
F2H2-3F	57.12	0.01	0.15	0.06	7.14	0.14	20.47	12.02	0.54	0.07	0.29	0.00	1.99	98.01	0.61	75.68		
F2H2-4A,B,H	49.80	1.34	12.55	0.03	12.08	0.35	10.41	3.67	2.44	4.12	0.01	0.00	3.20	96.80	6.56	48.09	21.28	16.94
F2H2-4D	48.20	0.11	5.49	0.15	9.75	0.17	22.04	9.31	0.18	0.02	0.07	0.00	4.51	95.49	0.20	71.12	3.60	4.94
F2H2-4E,G,5G	37.83	0.10	12.22	0.26	8.04	0.49	27.34	2.98	0.12	0.01	0.19	0.21	10.23	89.77	0.13	77.94	27.59	1.45
F2H2-4F,J	34.46	0.03	15.31	0.22	7.60	0.43	29.37	1.19	0.07	0.01	0.22	0.00	11.09	88.91	0.07	80.14	21.96	1.23
F2H2-5A	50.52	1.12	9.93	0.04	12.09	0.48	13.45	4.50	2.72	2.35	0.02	0.00	2.77	97.23	5.07	54.19	22.50	14.97
F2H2-5C,D	38.40	0.58	10.58	0.19	13.21	0.18	21.98	7.38	0.16	0.01	0.11	0.00	7.23	92.77	0.16	64.54	14.71	6.93

Bulk rock compositions (wt%) calculated after estimated mineral vol%.  
Mg# = 100\*MgO/(MgO+MnO+FeO)

The average water-free composition (av LOI = 8.42 wt%) of all investigated metamafic clasts is basaltic. Mean weight percents are:  $\text{SiO}_2 = 45.57 \pm 8.4$ ,  $\text{TiO}_2 = 0.79$ ,  $\text{Al}_2\text{O}_3 = 10.3 \pm 6.5$ ,  $\text{Cr}_2\text{O}_3 = 0.13$ ,  $\text{Fe}_2\text{O}_3 = 10.35$ ,  $\text{MnO} = 0.39$ ,  $\text{MgO} = 24.21 \pm 7.8$ ,  $\text{CaO} = 7.00 \pm 5.5$ ,  $\text{Na}_2\text{O} = 0.58$ ,  $\text{K}_2\text{O} = 0.54$ ,  $\text{NiO} = 0.14$ ,  $\text{P}_2\text{O}_5 = 0.6$ . A similar average composition of Mariana metamafic rocks was already reported by Gharib (2006). However, the range in calculated bulk compositions of the metamafic rocks studied correlates well with previously analyzed metamafic fragments from Conical and South Chamorro Seamounts (Fig. 5.44) which have similar major and trace element composition to metabasalt and metadiabase (Johnson, 1992; Savov *et al.*, 2005a). Low Ni and Cr values, but high  $\text{TiO}_2$  abundances in most of the samples (not this study) suggest that they were derived from mid-ocean-ridge basalt (MORB-like) protoliths (Savov *et al.*, 2005a).



**Fig. 5.44:** Calculated bulk rock compositions of metamafic clasts from South Chamorro Seamount (open diamonds): **a)**  $\text{SiO}_2$  vs  $\text{Al}_2\text{O}_3$  contents and **b)** TAS diagram. Compositions of metabasites from Conical and South Chamorro Seamounts studied by Savov *et al.* (2005a; closed diamonds) are plotted for comparison. All values are based on LOI-free composition. The average composition of metabasites of this work is basaltic (large circle).

The composition of all studied metabasites is variable and similar to those of volcanic turbidites (Plank & Langmuir, 1998) in the sediment sequence being subducted at the Mariana convergent plate margin. Gharib (2006) illustrated that compositions are more similar to other subduction related rocks such as mid-ocean ridge basalt (MORB), basalts and associated phases from Sites 801 and 1149 outboard of the IBM margin (Kelley *et al.*, 2003), altered basalts from the Mid-Atlantic Ridge, a 1.8 km section of upper ocean crust drilled at ODP Hole 504B, seawater-altered basalt (Mottl, 1983; Alt *et al.*, 1986) and mean alkalic ocean island basalts (OIB) (Engel *et al.*, 1965).

The compositional range between samples suggests small scale heterogeneity of the sampled solid slab materials, *i.e.*, oceanic crust material which was subducted and then returned to the seafloor via serpentinite mud volcanoes.

Strong differences are found between phengite-rich rocks (high  $\text{K}_2\text{O}$  content) and epidote-rich rock (high  $\text{CaO}$ ). The high  $\text{MgO}$  content in talc- and amphibole-rich rocks, higher than in basalt, could be explained by Mg-metasomatism, during which Mg in solution is taken up by the rock,

typically into Mg-silicate clays. Such a Mg uptake during metasomatism is typical for high-temperature seawater-driven basalt alteration and is accompanied by leaching of major elements into the solution (*e.g.*, Mottl, 1983). The metamorphic rocks with typical volcanic clinopyroxene or amphibole suggest precursors such as hydrothermally altered OIBs from seamounts that were likely ripped off the subducting slab and incorporated into the fault gouge that erupted via the serpentinite mud volcano (*e.g.*, Sample & Karig, 1982; Yamazaki & Okamura, 1989; Shipley *et al.*, 1992; Cloos & Shreve, 1996; Scholz & Small, 1997; Mottl *et al.*, 1998).

Additionally to major elements compositions, Li and B concentrations of bulk rocks were estimated (Table 5.3). The Li and B contents are strongly controlled by their major carrier minerals phengite, chlorite and amphibole. Concentrations range from <1  $\mu\text{g/g}$  (Li and B) up to  $\sim 70 \mu\text{g/g}$  Li and up to  $\sim 33 \mu\text{g/g}$  B ( $\sim 44 \mu\text{g/g}$  B in the Srp+Grt-rock) (Fig. 5.45). Although the Li and B concentrations are rough approximations, the values coincide well with Mariana metamafic rocks analyzed for bulk rock compositions by Savov *et al.* (2005a; Fig. 5.45).

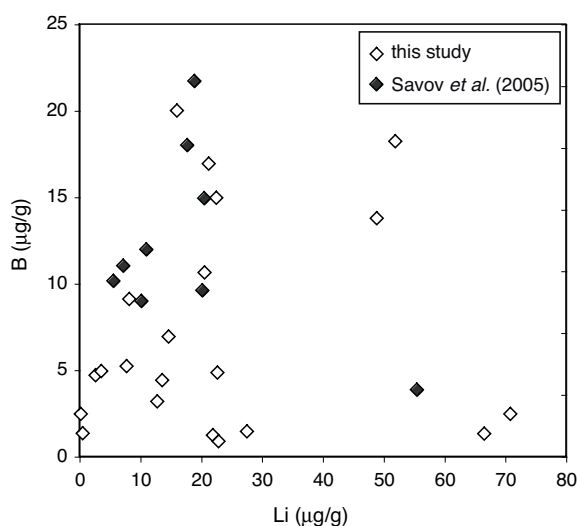


**Fig. 5.45:** Li vs. B of estimated bulk rock concentrations (open diamonds) compared to metamafic fragments from Conical and South Chamorro Seamounts studied by Savov *et al.* (2005a; closed diamonds).

Lithologies from onland blueschist occurrences that compose of various schist-assemblages (*e.g.*, Franciscan; Elekdag, Turkey; Syros) have bulk rock compositions varying between oceanic basalt and mantle wedge harzburgites (Altherr *et al.*, 2004; King *et al.*, 2007; Marschall *et al.*, 2007a). They originate from the interior of the slab or from a décollement region situated at the base of an accretionary wedge. These décollement regions, known as a mélange zones, are a serpentinite-rich and fluid-rich environment affected by strong mechanical mixing (*e.g.*, Bebout & Barton, 1989, 2002). The large amount of metamafic fragments which are composed of a variety of mineral assemblages, have an average composition suggesting that they originate from a broad region in the zone between the top of the subducting slab and the serpentinitized ultramafic material of the Mariana forearc mantle wedge.



So far, geochemical subduction zone models are based on onland blueschist deposits. Most of these onland blueschist-facies metabasites have not been transported through a supra-subduction mantle and due to tectonic uplift/exposure they experienced retrograde metasomatism. Therefore, they do not completely reflect actual top-of-slab conditions. A direct sampling of this slab-mantle interface is uniquely possible in the Mariana subduction zone.

### **5.7 Slab-mantle-interaction: evidence for an active subduction zone *mélange* formed by tectonic and metasomatic mixing**

One of the most characteristic features of subduction is the region known as a tectonic *mélange* which is found in most orogenic belts (*e.g.*, King *et al.*, 2006). Within accretionary prisms, this *mélange* forms highly deformed metasedimentary collages typical of incipient metamorphism (*e.g.*, Fisher, 1996). In forearc to sub-arc regions, the *mélange* is characterized by chaotic hybridized mixtures of peridotite, basalt and sediment produced at blueschist-, amphibolite-, or eclogite-facies conditions (*e.g.*, Bebout & Barton, 1989, 2002; Bebout *et al.*, 1993; Fisher, 1996; King *et al.*, 2003, 2006). The existence of *mélange* zones in active subduction settings is highly probable; Abers *et al.* (2006) reported seismic evidence for 1–7 km thick zones of anomalously slow material above subducting slabs which may represent hydrated *mélange* zones dominated by chlorite + talc (Bebout & Barton, 2002). The presence of such rheologically weak minerals formed during metamorphism (Reinen *et al.*, 1994; Peacock & Hyndman, 1999; Reinen, 2000) allows distributed deformation and the formation of *mélange* along the slab-mantle shear zone (Bebout & Barton, 1989, 2002; Bebout *et al.*, 1993) and affects the rheology and seismicity near the slab-mantle interface (Peacock & Hyndman, 1999).

*Mélange* formation appears intimately linked to reactive fluid flow leading to *metasomatic processes* accompanying *mechanical deformation/mixing* (*e.g.*, King *et al.*, 2006). Most observations so far were made on onland locations such as the Catalina Schist and Syros. Commonly, large blocks, sites of restricted or no fluid flow, are associated with areas that experienced strong metasomatism due to high fluid-flow and digestion of tectonic blocks (*e.g.*, Sorensen & Grossmann, 1989; Breeding *et al.*, 2004; King *et al.*, 2006).

Across the slab-mantle interface, *i.e.*, the *mélange* zone, there are severe contrasts in the chemical potentials, most notably for incompatible major and trace elements and their isotopic ratios, as well as volatile components. Thus, *mélange* zones act as a chemical bridge between the depleted peridotites of the mantle wedge and the evolved components of the subducting slab with fluids as agents of mass transfer to resolve the chemical gradient (King *et al.*, 2006). Metasomatic reactions observed in the onland Catalina *mélange* complex form metasomatic ‘rinds’ that are composed of minerals such as talc, chlorite and amphiboles replacing *e.g.*, olivine, pyroxenes and plagioclase of less ‘digested’ core material (Bebout & Barton, 1989, 2002; Sorensen & Grossmann, 1989; Breeding *et al.*, 2004; King *et al.*, 2006). Metasomatic rinds of SiO<sub>2</sub>-undersaturated serpentinized peridotite blocks are characterized by talc- and finally amphibole-rich assemblages (King *et al.*, 2003). The mineral assemblages suggest that metasomatism is characterized by the infiltration of Si-rich, slab-derived hydrous fluids during

subduction (Manning, 1997). This results in hybridized rock types or black-wall reaction zones that are not representative of any subduction input, *i.e.*, pre-subduction protolith (King *et al.*, 2003; Breeding *et al.*, 2004; Miller *et al.*, 2009). Mechanical mixing in the mélangé zones concentrates on the metasomatized rheological weaker minerals and is presented by deformation along these metasomatic reaction zones which enclose blocks of basalt, sediment, and peridotite.

Estimated major element compositions for the metamafic fragments show strong variations. Similar variations were observed for the Catalina Schist mélangé rocks (*e.g.*, Sorensen, 1988; Sorensen & Grossmann, 1989; Bebout & Barton, 2002; King *et al.*, 2006), without considering pegmatites and metasedimentary rocks from the Catalina Schist amphibolite unit (Sorensen & Grossman, 1989). Bebout & Barton (2002) defined two ‘endmembers’ for the mélangé interactions: a mafic endmember with a composition taken from the ‘non-migmatic blocks’ (Sorensen & Grossman, 1989) and an ultramafic endmember with the composition of serpentinite blocks. The strong mineralogical and textural similarities of the metamafic lithologies presented with metasomatic rocks from terrestrial subduction-related mélangé settings Catalina Schist and Syros (Bebout & Barton, 1989; Sorensen & Grossman, 1989; Bebout *et al.*, 1993; Manning, 1997; Breeding *et al.*, 2004; Marschall, 2005; Miller *et al.*, 2009) gives reason to classify the various metamafic fragments from South Chamorro Seamount into ‘endmember’- and ‘rind’-groups; Figure 5.46 shows a schematic assembly of the metamafic rock types with the three endmembers ‘serpentinite’, ‘epidote-rocks’ (~ subducted oceanic crust) and ‘meta-sediments’. This classification was already applied for the rock description in section 5.3. In detail, eclogite-rich metabasites are interpreted as the mafic endmember, though showing a broad compositional range. Schistose phengite-rich fragments are classified as meta-sediments and associated metasomatic rinds (Fig. 5.46).

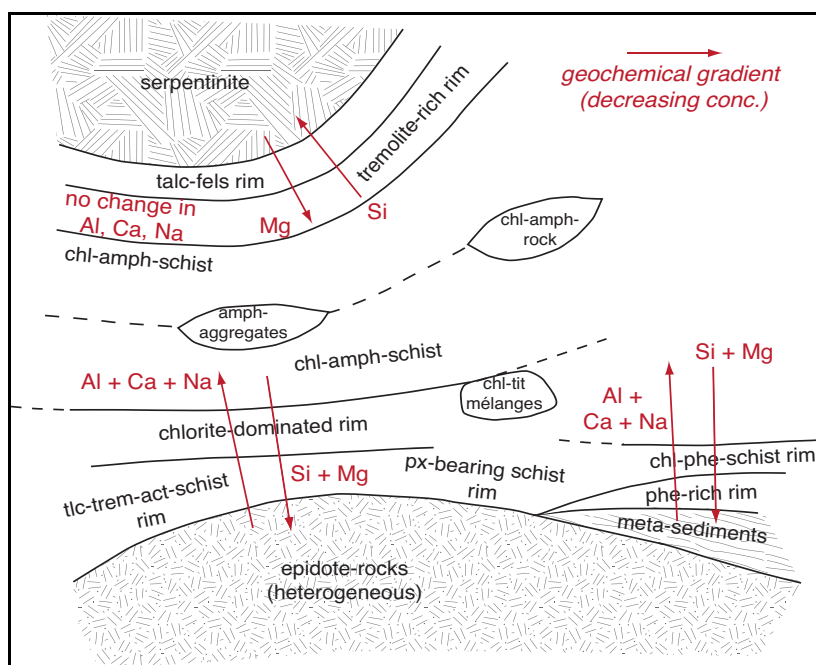


**Fig. 5.46:** Schematic assembly of observed metamafic rock types recovered from South Chamorro Seamount. Rocks can be allocated to endmembers (*e.g.*, meta-sediments) or schistose reaction rinds (*e.g.*, chl-amph-schists). Red arrows indicate decreasing geochemical gradients, *i.e.*, decreasing element concentrations during rind-formation.

The ultramafic endmember in the zone of slab-mantle-interaction is the mantle wedge serpentinite (Chapter 4). Serpentinites from Conical and South Chamorro Seamount (Savov *et al.*, 2005a,b, 2007) are used as endmember composition for the element variation diagrams (Fig. 5.47 and 5.48). Chlorite-amphibole-rich fragments are interpreted as metasomatic ‘rinds’ or *mélange* matrix, respectively. In the following, the compositional characteristics of the main lithologies are summarized:

1) The **ultramafic endmember** is the serpentinitized mantle peridotite (see chapter 4) with an average composition of 43 wt% SiO<sub>2</sub> and Mg# of 91–93 (Savov *et al.*, 2005a,b, 2007). The associated **metasomatic rinds** have a similar mineral inventory as described by authors like Sorensen & Grossmann (1989) and King *et al.* (2003). Representative samples of such rinds are the talc-‘fels’ and talc-dominated rocks with tremolitic to actinolitic amphibole (Fig. 5.46 and Fig. 5.47; see section 5.3.1). The petrological investigation of these metabasites suggests that the talc abundance decreases and chlorite becomes the major phase together with amphibole with distance to the serpentinite. Other rind parts are dominated by nearly monomineralic amphibole (see section 5.3.1).

2) The **mafic endmember**, *i.e.*, the metamorphosed oceanic crust, is represented by epidote-rich rocks which are enriched in Al<sub>2</sub>O<sub>3</sub> and CaO, but relatively depleted in SiO<sub>2</sub> (Fig. 5.48). Mineral paragenesis are dominated by chlorite, Na-amphibole, apatite, titanite and garnet. Some samples even contain rutile, pumpellyite, Na-pyroxene and garnet. All these phases do not necessarily occur together. Chlorite-rich Ca-Na-amphibole-schists with occasional talc and apatite ± titanite and chlorite-dominated schists with scarce tremolitic amphibole, talc and trace minerals (*e.g.*, apatite, titanite, zircon) are interpreted as **metasomatic rinds** that formed along the slab-mantle-interface, around epidote-rich mafic blocks (Fig. 5.46). Rocks with intergrown chlorite + titanite give evidence for tectonic mixing in the *mélange* matrix.

3) Phengite-rich amphibole-chlorite schists with pyroxene + titanite ± zircon ± apatite ± rutile ± epidote represent the **meta-sedimentary** rocks of the subducting slab. Similar mineral assemblages were described by Breeding *et al.* (2004) for meta-sedimentary rocks from Syros. These rocks are enriched in Al<sub>2</sub>O<sub>3</sub>, Na<sub>2</sub>O and K<sub>2</sub>O, but have low CaO (Fig. 5.47 and Fig. 5.48). Samples with predominantly chlorite and little phengite (F1H1-3d) are interpreted to be the related metasomatic rind zone (Fig. 5.46).

4) The Catalina Schist and Syros subduction complexes are characterized by a **mélange matrix**. Such a *mélange* matrix was formed by mechanical and geochemical mixing processes and consequently these zones are composed of weak material (see above). If such *mélange* material existed along the Mariana slab-mantle-interface, it probably was disaggregated in the uprising fluid-serpentine-mud mixture. However, evidence for strong tectonic mixing is given by the strongly foliated sample D3H1-8C; chlorite is intergrown with biotite, tiny andradite + spinel grains are concentrated in chlorite layers. The large amount of fine-grained amphibole-chlorite-schist fragments recovered at South Chamorro Seamount may represent the actual *mélange* matrix, although these samples are interpreted as metasomatic rinds in this study.

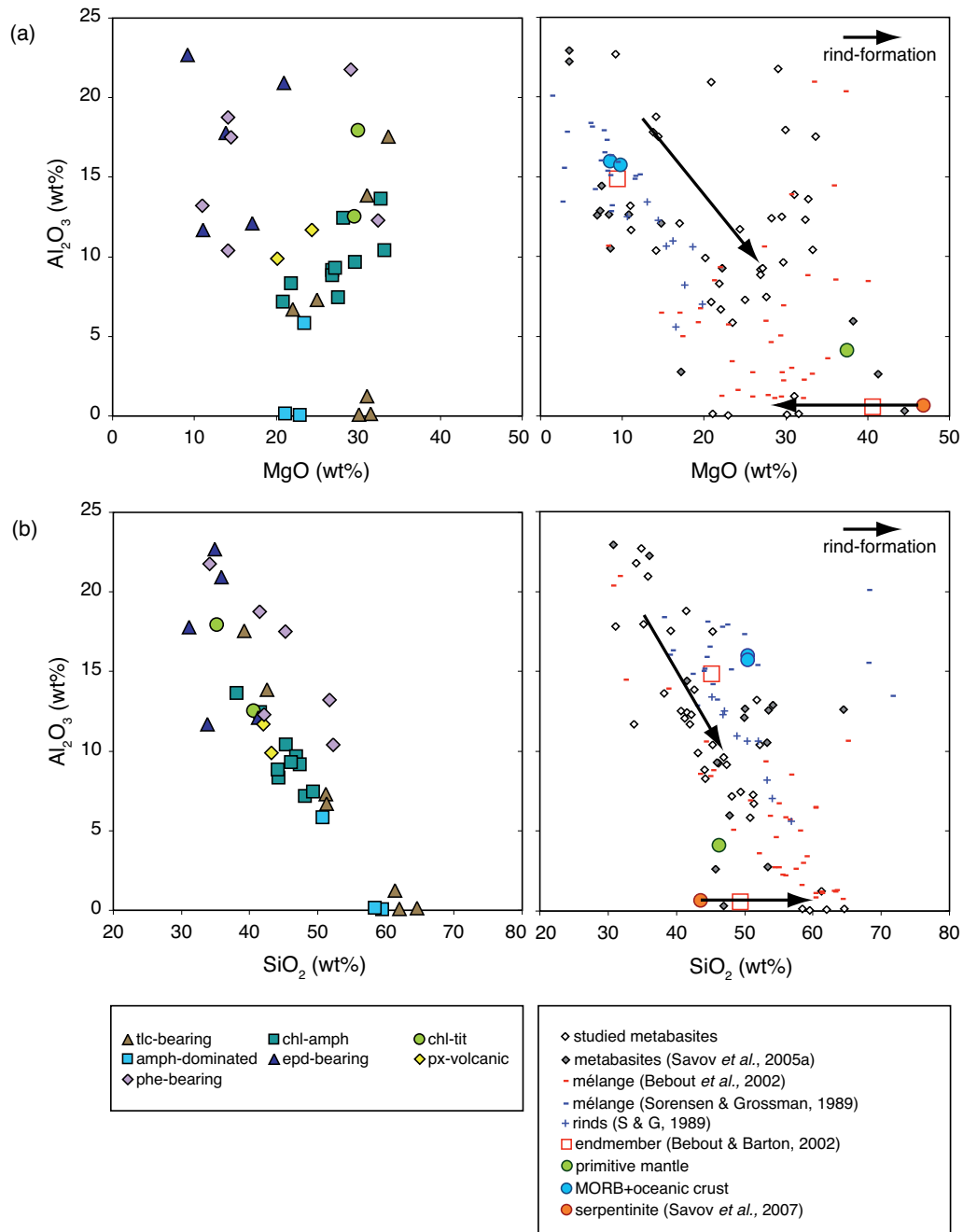


**Fig. 5.47:** Chemical discrimination diagrams, demonstrating the conceptual model for mixing in the *mélange* zone. **a)** MgO vs  $Al_2O_3$ , **b)**  $SiO_2$  vs  $Al_2O_3$ . Left diagrams: data of this study differentiated by lithology, right diagrams: comparison of the data from this study with literature data.

5) Some metamafic fragments give evidence for an OIB origin: zoned clinopyroxene crystals (augite-diopside) are embedded in a chlorite matrix. The Ti-rich core and Ti-poor rim composition of these clinopyroxenes suggests magma mixing during island arc formation. These samples likely are reworked clastic fragments from **island arc erosion** that were deposited in the trench region and then introduced into the subduction zone. Thick layers of turbidites of volcanic clasts are described for the sediment load of the Pacific plate (Stern *et al.*, 2003). Another sample gives evidence for an **upper mantle origin**; apatite and kaersutite amphibole of magmatic origin, the latter with Na-rich rims of

HP-metamorphic origin are embedded in a chlorite matrix. However, the high amount of chlorite in these samples is responsible for a major element composition similar to other chlorite-amphibole schists. Garnet-rich serpentinite samples will not be considered in the discussion, as their origin is not yet resolved.

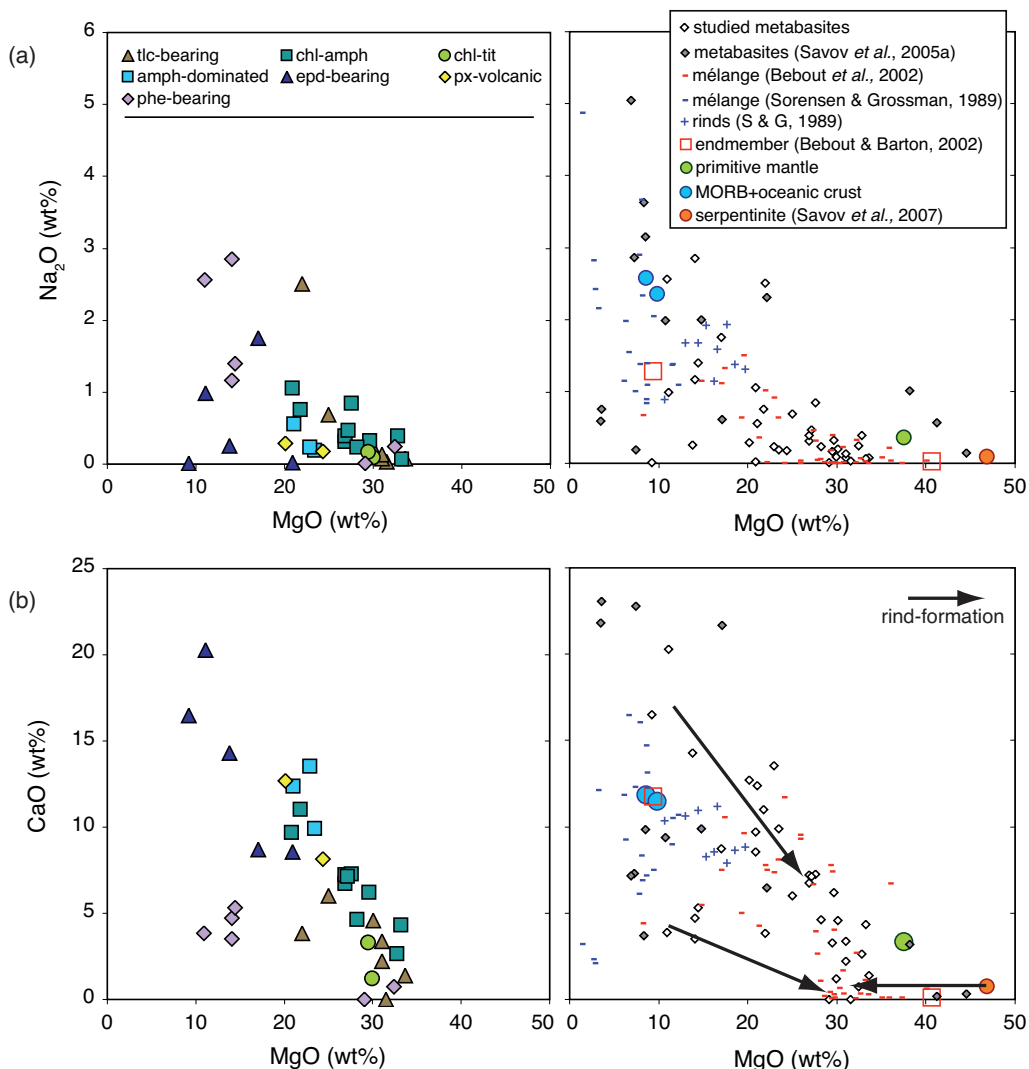


**Fig. 5.48:** Chemical discrimination diagrams, demonstrating the conceptual model for mixing in the *mélange* zone. **a)** MgO vs Na<sub>2</sub>O, **b)** MgO vs CaO. Left diagrams: data of this study differentiated by lithology, right diagrams: comparison of the data from this study with literature data.

To study the slab-mantle-interaction in the Mariana forearc region, the compositional variation between metabasites recovered from South Chamorro Seamount is compared to onland equivalents from the Catalina Schist. The variation diagrams (Fig. 5.47 and 5.48) are separated in plots showing (i) the data of metabasites of the present study with different symbols for each rock and (ii) the data of this study compared to literature metabasite data. South Chamorro Seamount metabasites correlate compositionally with the trend from high to low Al<sub>2</sub>O<sub>3</sub> contents at increasing MgO and SiO<sub>2</sub> contents of the *mélange* zone compositions reported from Catalina Schist samples (Fig. 5.47). The mafic slab rocks, including meta-sediments, have the highest Al<sub>2</sub>O<sub>3</sub> contents, while rind-related rocks decrease

in  $\text{Al}_2\text{O}_3$  contents (with distance to the slab endmember). Ultramafic rocks, *i.e.*, serpentinized peridotites, have the highest MgO contents. Rind formation (talc-rich rocks) is characterized by a decrease of MgO and increase of  $\text{SiO}_2$  contents at constant  $\text{Al}_2\text{O}_3$  content (Fig. 5.47).

$\text{Na}_2\text{O}$  contents of all metabasites are relatively low. Meta-sediments and eclogite-rich metabasites have the largest spread in  $\text{Na}_2\text{O}$  contents at low MgO (Fig. 5.48). Amphibole-chlorite-rich schists are characterized by low  $\text{Na}_2\text{O}$  contents below 1 wt%. These concentrations match matrix mélangé values of the Catalina Schist (Bebout & Barton, 2002). The CaO vs MgO distribution for the studied Mariana metabasites also matches the composition described for the Catalina Schist mélangé (Fig. 5.48). Metamafic slab samples and meta-sediments are characterized by parallel compositional trends for Ca-Mg during rind formation (Fig. 5.48). Talc-rich samples correlate geochemically with metasomatic rinds formed after ultramafic serpentinites, a compositional trend already suggested by Bebout & Barton (2002). Due to low  $\text{Na}_2\text{O}$ , MnO,  $\text{TiO}_2$ ,  $\text{Cr}_2\text{O}_3$  and  $\text{Fe}_2\text{O}_3$  bulk concentrations, endmembers and rinds are hardly identifiable on the basis of these elements.

Although the metamafic fragments do not give any information about their local relationship to each other, the mineralogy and calculated bulk rock composition yield the evidence that they derived from the slab-mantle interface. Major element correlations of the Mariana samples indicate chemical and mechanical mixing between crustal components and an ultramafic component (see also Bebout & Barton, 2002) by rind formation around metamafic and ultramafic rocks, comparable to the Catalina Schist mélangé rocks (*e.g.*, Sorensen & Grossman, 1989; Bebout *et al.*, 1993). King *et al.* (2006) interpreted those compositional trends as a direct result of metasomatic weakening of blocks through rind production (Sorensen & Grossman, 1989; Bebout *et al.*, 1993) and mechanical incorporation of these comparatively weak metasomatic minerals into the developing mélangé matrix (Bebout & Barton, 2002).

## 5.8 Light element behavior during dehydration and mélangé metasomatism

During progressive metamorphism in a subduction zone environment, the light elements Li, Be and B are important tracers of mass transfer. The bulk rock light element concentrations of the Mariana metabasites strongly vary from nearly zero to  $\sim 70 \mu\text{g/g}$  Li and  $\sim 35 \mu\text{g/g}$  B (Fig. 5.49). The average bulk composition is estimated to be  $\sim 23 \mu\text{g/g}$  Li and  $\sim 8 \mu\text{g/g}$  B. Mariana metabasites analyzed by Savov *et al.* (2005a) have higher bulk rock B contents (Fig. 5.49b). This discrepancy suggests that calculated light element abundances of the metamafic rocks investigated in this work have to be used carefully. Due to the very small size (<2 mm) of the fragments and the visual approximation of mineral abundances, calculated bulk element concentrations may not be sufficiently representative for light elements, but rather may be over- or under-estimated. Additionally, bulk rock analyses (Savov *et al.*, 2005a) include Li and B bound in cracks and along grain boundaries. Note that bulk light element calculations are not available for all samples.

The  $\text{Al}_2\text{O}_3$  abundance of the metamafic fragments turned out to be most indicative to discriminate between 'endmember' slab-derived metabasites and metasomatic rinds within the slab-mantle-

interface mélangé (see previous section). As phengite > chlorite + amphibole are the major hosts of B, metabasites rich in these phases have the highest B concentration (Fig. 5.49). Rind formation is characterized by decreasing Li and B abundance from epidote- and phe-rich rocks to rind-related amphibole-chlorite-schists ( $\pm$  phe  $\pm$  tlc) (Fig. 5.49a,b). The metasomatic rinds have Li and B abundances of <10  $\mu\text{g/g}$ . Highest calculated Li whole-rock abundances are found in few phengite-rich and amph-chl-schist samples: >48  $\mu\text{g/g}$  (Fig. 5.49a). The average Be concentrations of the metamafic rocks is considerably <1  $\mu\text{g/g}$ .

The Li, Be and B abundances in bulk metamafic rocks are variable, though in the same range as for altered oceanic crust (AOC) and sediments being subducted (Fig. 5.49). The average composition of the subducting slab can hardly be estimated due to the fact that it is not possible to determine the volume% of AOC and sediments ‘sampled’ by the metamafic fragments in this study. The smallest variation is given for AOC directly east of the Mariana trench with 0.05–3.1  $\mu\text{g/g}$  B (Kelley *et al.*, 2003; Fig. 5.49b). Variable amounts of sediments are expected to be added to the subducting load, which would increase the average B contents of the slab, *i.e.*, of the precursor of the metabasites studied. Nevertheless, as average B contents of metamafics are also low, a strong B-loss by dehydration during subduction until 27 km depth below South Chamorro Seamount can be excluded. Li concentrations in AOC and sediments strongly vary. Therefore, an estimation about Li-loss hardly is possible.

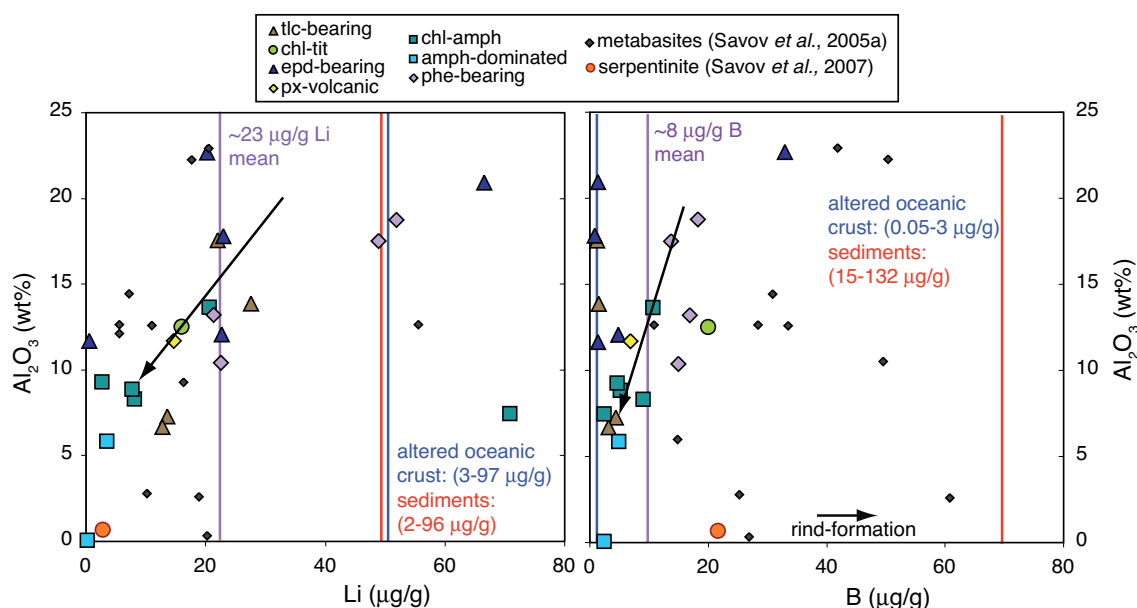


**Fig. 5.49:** Variation diagrams for South Chamorro metabasites in comparison with literature data of metabasites from South Chamorro and Conical Seamounts (Savov *et al.*, 2005a). **a)** Li vs  $\text{Al}_2\text{O}_3$ , **b)** B vs  $\text{Al}_2\text{O}_3$ . Average concentrations for altered oceanic crust from Kelley *et al.* (2003) and for sediments from Ishikawa & Nakamura (1993).

This very low light element loss, nevertheless, is understandable, as the metamorphic grade is relatively low compared to metamorphic conditions suggested for most onland mélangé zones. The results of the Li and B bulk inventory in Mariana metabasics can be compared to literature; Bebout *et*

*al.* (1993, 1999) examined Li, Be and B whole rock abundances of metasediments and metamafic rocks from the Catalina Schist which demonstrate a range in metamorphic grade from lawsonite-albite via greenschist and epidote-amphibolite facies. With increasing metamorphic grade, mean B abundances in metasediments decrease from 92  $\mu\text{g/g}$  to 15  $\mu\text{g/g}$  implying a possible B loss of ~85 % during prograde metamorphism. Large amounts of B along with other highly fluid-mobile elements are lost from subducting sediments already at shallow depths. Li and Be bulk rock abundances (0.1 to ~5  $\mu\text{g/g}$  Be and ~6 to ~45  $\mu\text{g/g}$  Li) and B/Be ratios (<30) in these metamafic rocks do not change significantly with metamorphic grade. This implies that B is preferentially removed from the subducting slab relative to Be and Li and the high B/Be ratios typically found in oceanic sediments and altered oceanic crust are not retained to subarc depths (Moran *et al.* 1992; Bebout *et al.*, 1999).

The Li, Be and B abundances of the Mariana metabasites are in the same range as in altered oceanic crust and sediments. Nevertheless, their average abundances imply that most of the Li and Be remained in the subducting Pacific slab and was not released with hydrous fluids, while B contents slightly decreased during progressive subduction until the 'sampled' depth of ~27 km below the South Chamorro Seamount.

### **5.9 Boron fractionation ( $\delta^{11}\text{B}$ ) during slab dehydration and slab-mantle-interaction (fractionation along the slab-mantle interface)**

Boron isotope systematics have proven to be important tracers in studies about material recycling in subduction zones, *i.e.*, in the 'Subduction Factory'. In hydrous fluids and in silicate melts Li and B are relatively mobile and element concentrations in the slab are decreasing with increasing depth of subduction, due to dehydration and fluid release. Be is relatively immobile in hydrous fluids but mobile in silicate melts. B redistribution and the fractionation of its isotopic species strongly depends on the thermal evolution and resulting devolatilization history of subducted materials (*e.g.*, Moran *et al.*, 1992; Bebout *et al.*, 1993, 1999; Peacock & Hervig, 1999; Nakano & Nakamura, 2001; Bebout & Nakamura, 2003; Marschall *et al.*, 2007a; King *et al.*, 2007). The preferential loss of the heavier isotope  $^{11}\text{B}$  (Leeman & Sisson, 2002; Ryan, 2002; Palmer & Swihart, 1996) results in decreasing  $\delta^7\text{Li}$  and  $\delta^{11}\text{B}$  values in the subducting material. B concentrations and  $\delta^{11}\text{B}$  values in subduction-related volcanic rocks decrease across-arc, from trench to back-arc (*e.g.*, Ryan & Langmuir, 1987, 1988, 1993).

Fresh mantle and magmatic rocks show very low Li, Be and B concentrations and no isotopic anomalies. Subducting sediments (enriched in Be), altered (serpentinized) oceanic crust and serpentinized ultramafic rocks (mantle wedge) are important reservoirs for the light elements and show  $\delta^{11}\text{B}$  values higher than MORB (or mantle), due to a preferential enrichment of the heavy isotopes during the interaction with seawater or slab-derived fluids. Therefore, the hydrous portion of the subducting slab introduces large amounts of Li and B into the subduction zone (Zack *et al.*, 2003; Marschall *et al.*, 2006).



The mineral assemblages of the studied blueschist-facies clasts are diverse; major components are Na-amphibole, chlorite, phengite and also epidote and rutile. Some rare findings are pumpellyite and Na-rich pyroxene (Acm-Di-Jd). SIMS and ToF-SIMS analyses show that in the shallow subducted slab Li resides in phengite  $\geq$  chlorite  $>$  amphibole and that B preferentially resides in both phengite and chlorite. B isotope ratios of the dominant minerals Na-amphibole, phengite and chlorite are negative: mean  $\delta^{11}\text{B}$  values are  $-6\text{‰}$  with a variation from  $-10$  to  $-2\text{‰}$  for most analyses (Fig. 5.42).

The B isotopic composition of oceanic crust may vary between  $-4.3\text{‰}$  to  $+24.9\text{‰}$  depending on fluid-rock ratios, temperature, the extent of alteration and other parameters during seafloor metamorphism (Oman and Cyprus ophiolites; Smith *et al.*, 1995). The average B content of altered oceanic crust is assumed to be  $5.2 \pm 1.7\ \mu\text{g/g}$  with an average  $\delta^{11}\text{B}$  of  $+3.4 \pm 1.1\text{‰}$  (Smith *et al.*, 1995). The B isotope signature of seafloor pelagic sediments range from  $-6.6$  to  $+11\text{‰}$  with B concentrations of  $80\text{--}160\ \mu\text{g/g}$  (Ishikawa & Nakamura, 1993),  $\delta^{11}\text{B}$  values for trench turbidites range from  $-6$  to  $-1\text{‰}$  (You *et al.*, 1995). Marschall *et al.* (2007a) presented a model for the quantification of trace element release during dehydration of progressively subducting oceanic crust and used altered oceanic crust as a starting material with a B isotope ratio of  $+0.8\text{‰}$  and a B concentration of  $26\ \mu\text{g/g}$ . Also King *et al.* (2007) modelled the B isotope fractionation during progressive fluid loss during subduction. Thereafter, to summarize a model for the subducted Mariana slab, we assume an altered oceanic subducting crust, *i.e.*, the slab, with a  $\delta^{11}\text{B}$  of  $\sim +4.3\text{‰}$  (Smith *et al.*, 1995). During progressive metamorphism, in the metamafic epidote-rich rocks from South Chamorro Seamount, *i.e.*, the metamafic slab endmember in the mélangé zone, and in the phengite-bearing metasediment B isotope composition is lowered to a value of  $\sim -6\text{‰}$  with mean B concentrations of  $\sim 8\ \mu\text{g/g}$  as it reaches blueschist facies conditions at  $\sim 27$  km depth.

This B isotope value is considerably lower than compositional ranges of mantle and MORB. Consequently, during subduction-related dehydration reactions the heavy B ( $^{11}\text{B}$ ) must have been preferentially and progressively removed from the slab minerals by released B-rich aqueous fluids. The B isotopes fractionate by Rayleigh fractionation (Peacock & Hervig, 1999), thereby increasing the  $\delta^{11}\text{B}$  in the fluid fraction and lowering  $\delta^{11}\text{B}$  in the subducting slab. To discuss the B fractionation for the Mariana subduction, a temperature of  $300\text{--}350\text{ °C}$  at  $\sim 27$  km depth at the slab-mantle-interface is applied, as has been estimated above. At such temperatures, a B isotope fractionation value ( $\Delta^{11}\text{B}$ ) between boromuscovite and fluid of  $-14.8$  and  $-13.3\text{‰}$  (stronger fractionation at lower temperature) has been experimentally determined by Wunder *et al.* (2005). This is in agreement with experimentally derived isotope fractionation factor of B between silicates ( $\text{B}^{[4]}$ ) and water ( $\text{B}^{[3]}$ ) between  $-15.2$  and  $-13.8\text{‰}$  at  $300$  and  $350\text{ °C}$ , respectively (Williams *et al.*, 2001).

The progressive removal of B from the rock during subduction decreased the  $\delta^{11}\text{B}$  values of the rock and the released fluid. Peacock & Hervig (1999) calculated that the removal of 50% of the B decreases the  $\delta^{11}\text{B}$  value of the rock from 0 to  $-8\text{‰}$  for the case where the evolved fluid is enriched in  $^{11}\text{B}$  by a constant  $10\text{‰}$  relative to the rock. This B isotope fractionation model implies a general B-loss in order to explain the low observed  $\delta^{11}\text{B}$  values of the metamafic blueschists from the Mariana forearc. Applying a  $\Delta^{11}\text{B}$  of  $-14\text{‰}$ , the fluids released from the blueschist-facies slab with a negative

$\delta^{11}\text{B}$  ( $-6\text{‰}$ ) carry a positive  $\delta^{11}\text{B}$  of  $+8\text{‰}$ , with a variation of  $\pm 4\text{‰}$  due to slab composition variability. However, it has to be considered that the altered oceanic slab, *i.e.*, the blueschist-facies fragments have a variable B and B isotope composition. Furthermore, slab dehydration begins already in lower depths at moderate *PT* conditions. At temperatures of  $200\text{ °C}$ ,  $\Delta^{11}\text{B}$  is  $\sim -21\text{‰}$  (Williams *et al.*, 2001; Wunder *et al.*, 2005) producing fluids with an even stronger positive  $\delta^{11}\text{B}$  signature.

This study presents for the first time B isotope data of high-pressure metamorphic rocks of a currently subducting slab. Previous studies were only based on onland exposed metamorphic complexes and experiments (Bebout *et al.*, 1999; Peacock & Hervig, 1999; Marschall *et al.*, 2006; King *et al.*, 2007). Previous studies have estimated the  $\delta^{11}\text{B}$  value of subducted sediments to be  $-8$  or  $-10\text{‰}$  (Ishikawa & Tera, 1997; Smith *et al.*, 1997). Metabasalt samples studied by Peacock & Hervig (1999) have undergone subduction zone metamorphism and show  $\delta^{11}\text{B}$  values of  $-3$  to  $-7\text{‰}$ . Blueschist-facies rocks from the Catalina Schist have B concentrations of  $7.5\text{--}9\text{ }\mu\text{g/g}$  and  $\delta^{11}\text{B}$  values of  $-2$  to  $-9\text{‰}$  (Bebout *et al.*, 1992, 1999; King *et al.*, 2007). These isotope values are substantially lower than those for altered oceanic crust.

Combined with data from this study, a consistent pattern emerges where the release of aqueous fluids from subducted sediments and subducted basaltic oceanic crust will decrease the  $\delta^{11}\text{B}$  value of the rocks during slab metamorphism, *i.e.*, metamorphic dehydration reactions. The moderately negative  $\delta^{11}\text{B}$  composition of the metamafic slab-derived rocks ( $-6\text{‰}$ ) implies that slab-released fluids are B-rich with a positive  $\delta^{11}\text{B}$  signature due to a large fractionation at  $\sim 27\text{ km}$  depth and the given temperatures. These fluids infiltrate and serpentinize the overlying mantle wedge peridotite, where B further fractionates between fluid and serpentine.

## Chapter 6

### Synthesis

#### Fluid-rock interaction and light element recycling in the Mariana forearc

This chapter presents a synthesis of the studies on 1) variably serpentinized Mariana forearc mantle wedge peridotites and 2) blueschist-facies metamafic samples directly from the active subducting Pacific slab.

Light element concentrations and  $\delta^{11}\text{B}$  values of bulk rocks already provided information that helps to understand the rock and fluid chemical evolution within the Mariana ‘Subduction Factory’. To date, no (published) micro-analytical light element data exist on serpentinites and metamafic fragments from any serpentinite mud volcano; this study fills the gap. The results of this study make it possible to create a model of the light element distribution and behavior in an active subduction zone, in particular between the subducting slab and the overlying mantle wedge (Fig. 6.1).

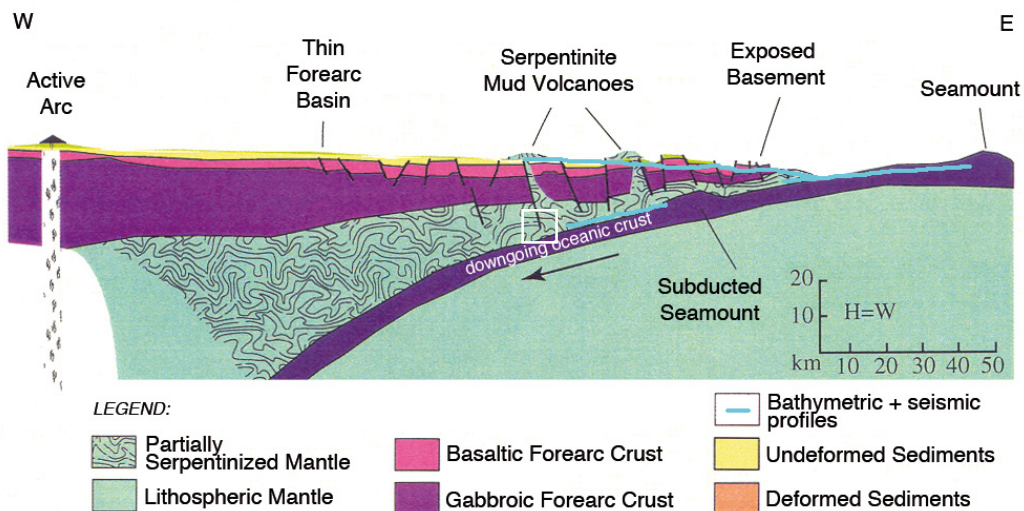


**Fig. 6.1:** Cross-section of the non-accretionary Mariana subduction zone in the area of the South Chamorro Seamount, modified after Stern et al. (2002) and Mottl et al. (2007). The top of the downgoing Pacific Plate and the top of the Philippine Sea Plate were located bathymetrically and seismically by Oakley et al. (2008). The dipping angle of the subducting slab is about  $12^\circ$  and  $4^\circ$  E' of the trench. The location of the South Chamorro Seamount is equivalent with the westernmost serpentinite mud volcano in the sketch,  $\sim 85$  km W' of the trench and above the slab in  $\sim 27$  km. The white box indicates the likely origin of the metamafic rocks and serpentinites studied in this work.

## 6.1 Subduction input - metamafic high-pressure rocks

Several geochemical studies on high-pressure metamorphic rocks and adjacent serpentinites exist (*e.g.*, Sorensen & Grossmann, 1989; Bebout, 1995; King *et al.*, 2006; Marschall *et al.*, 2006; Pelletier *et al.*, 2008b). Such rock suites are only outcropping in regions where erosion has exposed an ancient subduction zone, accompanied by retrograde metasomatism, such as the Franciscan formation (California), Syros (Greece), and Elekdag (Turkey) (*e.g.*, Essene & Fyfe, 1967; Coleman & Clark, 1968; Bebout, 1995; Altherr *et al.*, 2004; Breeding *et al.*, 2004; Marschall *et al.*, 2007; Miller *et al.*, 2009). Therefore, the Mariana forearc serpentinite seamounts offer a unique opportunity for detailed petrological investigation of a great variety of slab-derived metamafic rocks with the focus on light element and B isotope micro-analyses of blueschist-facies minerals such as amphibole, chlorite, phengite and epidote. The results can be summarized in the following main facts.

- 1) The metamafic rock types from South Chamorro Seamount are often composed of similar single clasts from different locations in the serpentinite volcano. Hence, the suite of rock types can be assumed to be representative for the lithology of the subducting Pacific slab or the slab-mantle-interface. The amphibole-chlorite-schists and phengite- to epidote-dominated rocks comprise a great variety of lithologies with minerals including phengite, chlorite, talc, jadeitic pyroxene, Ca- and Na-amphiboles, epidote, garnet, pumpellyite, ilmenite, rutile, zircon, sphene, apatite and even albite and quartz (the latter two as inclusions in epidote). Similar lithologies and mineral parageneses are found in exhumed old subduction zones; *e.g.*, typical occurrences in the Franciscan formation are talc- and tremolite-dominated blackwall-rocks as well as Na-Am-Chl-Lws-dominated blueschist-facies metamafic rocks (*e.g.*, King *et al.*, 2006). Na-rich amphibole together with jadeitic pyroxene and the mineral assemblage Pmp-Ttn-Rt-Ilm-Ep in the Mariana metamafic rocks indicate blueschist-facies conditions at a temperature of ~150–350 °C and a pressure of ~0.4–0.6 GPa (Maekawa *et al.*, 1992; Gharib, 2006), equivalent to minimum depths of 12 to 18 km below seafloor. Fryer *et al.* (2000) estimated that the metamafic fragments from South Chamorro Seamount derived from a region of ~350 °C at ~0.8 GPa. The latter conditions are equivalent to depths of <26 to ~27 km depth of the subducting slab surface (Fryer *et al.*, 2002; Mottl *et al.*, 2004). These *PT* estimates closely match lithologically similar blueschist-facies rocks from Black Butte, California (Brown & Ghent, 1983).
- 2) On the one hand, the geochemistry of the metamafic rocks, though highly variable, indicates that the average protoliths of these rocks were oceanic basalts with minor sediments (see section 5.5). On the other hand, the major element variation in estimated bulk rock compositions tells us that the metabasites present rocks and schists of a mélangé zone, where mechanical mixing and metasomatism along the slab-mantle-boundary change the mineral assemblages and rock compositions (see section 5.6; Bebout & Barton, 2002; Breeding *et al.*, 2004; Bebout *et al.*, 2007). The latter interpretation is based on comparison with onland ‘subduction zone’ sections from the Catalina Schist sequence (California) and Syros (Greece). The mélangé metasomatism influences the major element concentrations; rind formation due to the slab-mantle-interaction produced a chemical gradient with increasing

Mg and decreasing Si contents from the ‘endmembers’ mafic slab and meta-sediments to their rinds. Decreasing Mg with increasing Si and constant Al contents are observed during (talch-, chl-, tremolite-) rind formation around serpentinite. The observations indicate that mélange formation is already significant at relatively low depth (only ~27 km in the Mariana forearc region).

- 3) The study presented provides further significant information about the Li and B distribution between minerals. Li and B are variably but strongly enriched in the metamafic minerals. The main Li carriers are chlorite (up to 105 µg/g) and phengite (30–120 µg/g). B is variably enriched in chlorite (0.2–11 µg/g) and amphibole (up to 40 µg/g), the highest B values are found in phengite (20–70 µg/g). Some epidotes and pyroxenes are enriched in B, but less in Li (see section 5.3.2). Estimated bulk rock concentrations are variable between ~0 and ~70 µg/g for both Li and B (chapter 5.5). The protolith of the metamafic rocks is the subducting Pacific plate which experienced low temperature reactions of seawater alteration and hence is enriched in Li and B compared to depleted mantle (Thompson & Melson, 1970; Bonatti *et al.*, 1984; Spivack & Edmond, 1987; Kelley *et al.*, 2003; Salters & Stracke, 2004; Sano *et al.*, 2004; Vils *et al.*, 2008). Additionally, the subducting sediments are also enriched in Li, but less in B (Ishikawa & Nakamura, 1993). The average composition of this subducting load is variable. As the light element concentrations in the metamafic rocks are still high and as B is the more fluid-mobile element, the prograde metamorphism and slab dehydration on the way down to ~27 km depth is characterized by low B-loss and very limited Li-loss (see 5.7) and most Li and B is yet to be released with the fluids during further subduction.
- 4) Furthermore, this study presents  $\delta^{11}\text{B}$  values of micro-analyses in the B-rich phases. These B isotope results are the first documented in metamafic rocks from the Mariana forearc, *i.e.*, from an active subducting slab. The SIMS data were matrix corrected (chapter 2.5), thus providing reliable information about the  $\delta^{11}\text{B}$  inventory of the subducting slab at blueschist-facies conditions. Phengite minerals are the B-richest phase in the metamafics studied; their  $\delta^{11}\text{B}$  values give a limited range of  $-6 \pm 4 \text{‰}$  (Fig. 6.2). Although B contents of most amphiboles and chlorites are much lower, their  $\delta^{11}\text{B}$  values correlate well with this phengite-defined range (chapter 5.3). However, some minerals have lower or higher  $\delta^{11}\text{B}$  values suggesting earlier or later dehydration (and B fractionation) of these single minerals.
- 5) During subduction and progressive fluid loss, the average positive slab  $\delta^{11}\text{B}$  signature for the slightly altered oceanic crust ( $\sim +3.4 \text{‰}$ ; Smith *et al.*, 1995) with minor volcanoclastic and pelagic sediments ( $\sim -7$  to  $+11 \text{‰}$ ) will evolve by Rayleigh fractionation: the released fluids extract B from the dehydrating slab and carry a more positive  $\delta^{11}\text{B}$  value, while the residual rock retains a more negative  $\delta^{11}\text{B}$  value (Fig. 6.2; Peacock & Hervig, 1999; Benton *et al.*, 2001; Williams *et al.*, 2001; Rosner *et al.*, 2003). The degree of B fractionation decreases with increasing temperature and depth; at ~27 km depth and low temperatures (~200 °C) a fractionation ( $\Delta^{11}\text{B}$ ) of  $-21 \text{‰}$  is expected between sheet silicates and fluids of neutral to basic pH (*e.g.*, Wunder *et al.*, 2005a). The  $\delta^{11}\text{B}$  values of phengite, amphibole and chlorite

can therefore be explained by temperature-dependant B isotope fractionation models between slab-fluid and slab-restite (Fig. 6.2): taking the altered oceanic crust (AOC) as the starting material with a  $\delta^{11}\text{B}$  value of  $+3.4\text{‰}$ , progressive dehydration of the subducting slab with increasing metamorphic grade (increasing  $PT$ ) more and more lowers the  $\delta^{11}\text{B}$  value of both the released fluids and the slab. Thereafter, the fluid released from the slab minerals (at  $\sim 27$  km depth), *i.e.*, predominantly phengite, chlorite and amphibole ( $-6 \pm 4\text{‰}$ ), will have a positive average B isotope value of  $+14 \pm 4\text{‰}$ . As the mineral compositions are variable and fluid release is heterogeneous (rather than constant and homogeneous), the fluid composition is variable and might reach even values of  $>20\text{‰}$ , if chlorite and amphibole with a positive B isotope signature dehydrates (chapter 5.3).

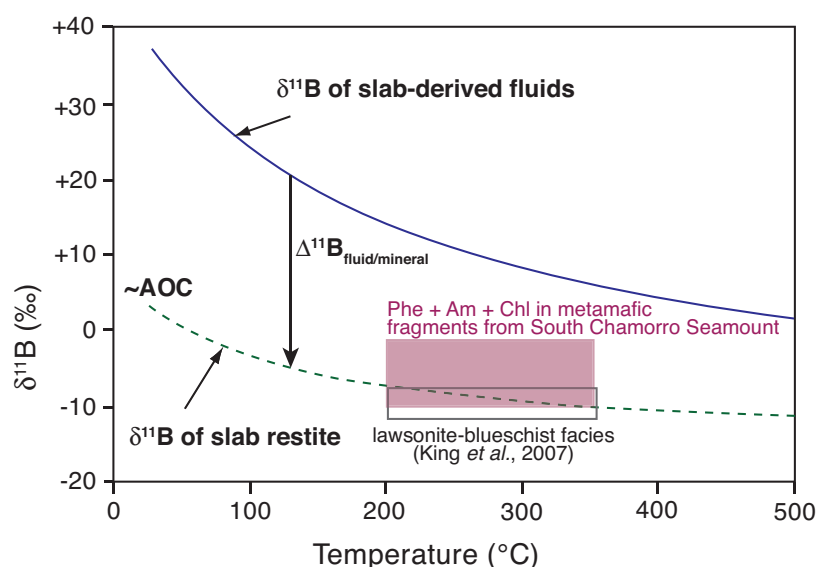


**Fig. 6.2:** The evolution of  $\delta^{11}\text{B}$  as a function of metamorphic temperature (=increase of fluid loss) for the metamafic minerals Phe, Am and Chl from South Chamorro Seamount, Mariana forearc (pink box) and comparison to the field of lawsonite-blueschist facies rocks from of the Catalina Schist (King *et al.*, 2007). The temperature dependence of fractionation lines of the residual slab and slab-derived fluids were modeled by Peacock & Hervig (1999), Benton *et al.* (2001), Bebout & Nakamura (2003) and Rosner *et al.* (2003). AOC marks the approximate  $\delta^{11}\text{B}$  of altered oceanic crust ( $+3.4 \pm 1\text{‰}$ ; Smith *et al.*, 1995).

## 6.2 Serpentinites of the forearc mantle wedge

Serpentinites from the Mariana forearc region in the southern part of the Izu-Bonin-Mariana ‘Subduction Factory’ have long been of interest in various petrological studies (*e.g.*, Fryer *et al.*, 1990, 1992, 2006; Mottl *et al.*, 2003, 2004; D’Antonio *et al.*, 2004; Savov *et al.*, 2007; Benton *et al.*, 2001, 2004). The two serpentinite mud volcanoes Conical Seamount and South Chamorro Seamount provide variably serpentinitized spinel-harzburgites comprising a variety of textures and different serpentine  $[\text{Mg}_3\text{Si}_2\text{O}_5(\text{OH})_4]$  polymorphs (lizardite > chrysotile > polygonal serpentine >> antigorite). Relict primary minerals are olivine, orthopyroxene, clinopyroxene and Cr-spinel, with decreasing grade of serpentinitization. The detailed petrologic serpentinite investigation leads to the following main results which are summarized in Table 6.1 and schematically pictured in Fig. 6.3.

**Table 6.1:** Schematic summary of the relationship between polymorphs, textural location, brucite composition, Li and B contents and  $\delta^{11}\text{B}$  values.

	fluid/rock	after olivine	veins	brucite	Li conc.	B conc.	$\delta^{11}\text{B}$
<b>early:</b>	low, complete consumption	Liz $\pm$ Brc (mesh rim)	Liz	Mg-rich	high	medium to high	up to +24 ‰
<b>late:</b>	high	Ctl $\gg$ Liz (mesh center)	Ctl	Fe-rich	low	variable	down to -14 ‰

1. The serpentine major element composition of the various textures (*e.g.*, mesh rims, veins) is predominantly dependent on the mineral which is replaced (Ol, Opx) as well as dependent on possible brucite admixtures and magnetite abundance in the serpentine. For instance, serpentine after orthopyroxene has higher Al and Cr contents compared to other serpentine. The variable degrees of serpentinization, the variety of textures and the different degrees of mantle melting suggest that the peridotitic mantle was sampled at different locations (*i.e.*, depths). The predominance of lizardite and chrysotile together with Fe-rich brucite and the absence of antigorite (aside from Conical Seamount serpentinites) limits the temperature range of extensive hydration to well below 350 °C down to <250 °C.
2. Previous studies (*e.g.*, Allen & Seyfried, 2003; Evans, 2008; Foustoukos *et al.*, 2008; Frost & Beard, 2007; Moody, 1976a, 1976b, 1979) have shown that pH, *T*, Si-activity and oxygen-fugacity have a strong influence on the Fe/Mg ratio, *i.e.* the Fe distribution between serpentinization-related mineral phases. The samples reveal that mesh rim serpentine after olivine has Fe/Mg ratios of the former olivine (*e.g.*, 0.09) and that mesh rims have enriched Fe/Mg ratios due to brucite-admixtures. Mesh center serpentine is dominated by lower Fe/Mg ratios than the former olivine, if magnetite is abundant. Magnetite-free mesh centers can also contain brucite of different Fe-concentration which varies between samples. However, low-Fe serpentine, also in veins, is associated with Fe-precipitation into magnetite and/or brucite. The variable assemblages of serpentine – brucite – magnetite with changing Fe-distribution indicate that serpentinization in the Mariana mantle wedge is characterized by an open system with sufficient fluid flow accompanied by changes in temperature, silica activity and  $f(\text{O}_2)$ .
3. Further, serpentine polymorphs chrysotile (Ctl), lizardite (Liz) and polygonal serpentine (Pol) correlate with certain serpentine textures (microstructural positions) and serpentine generations. This serpentine polymorph distribution in the samples reveals crucial information about the fluid-rock ratios apparent during serpentinization of the forarc mantle wedge. Liz predominantly occurs in early serpentine textures such as former crystal boundaries, veins and mesh rims. This polymorph forms at relatively low fluid-rock ratios and complete fluid consumption. Later serpentinization, characterized by the formation of mesh center and late veins, crystallized Ctl which predominantly occurs at high fluid-rock ratios. Pol, *e.g.*, in serpentine after orthopyroxene, suggests ‘medium’ conditions or

polymorph transformation due to further fluid supply. These results show that serpentinization in the Mariana forearc mantle wedge is characterized by changing fluid-rock ratios fed by recurring (fresh) fluid pulses (released from the subducting Pacific plate). This range in fluid-rock ratios likely has an influence on the chemistry of serpentine.

4. The examination of a variety of serpentine textures by micro-Raman spectroscopy and high spatial resolution ToF-SIMS ion imaging and SIMS shows that B concentrations are not caused by (i) B hosted on mineral surfaces in cracks, (ii) interlayers or nanotubes, or (iii)  $\mu\text{m}$ -scale B-rich 'clusters'. Therefore it can be concluded that B measurements in serpentine of this work are a reliable indicator of B in the crystal structure.
5. The Li and B contents of serpentine minerals result from the low temperature interaction of the depleted forearc mantle wedge peridotite with slab fluids derived from early dehydration of the subducting slab (Hattori & Guillot, 2003). Previous studies on bulk rock serpentinites already demonstrated large but selective fluid-mobile element enrichment patterns (*e.g.*, Li, B, As, Cs, Sb) in serpentinites and serpentinized muds (*e.g.*, Benton *et al.*, 2001, 2004; Savov *et al.*, 2005a, 2007). However, those averaging bulk rock element concentrations cannot give sufficient information for understanding the course of serpentinization and the element distribution between different serpentine types or generations. The present study shows that especially Li and B are variably enriched in serpentine relative to depleted mantle (minerals). Compositions of different serpentine textures overlap in the range of  $\sim 0\text{--}20 \mu\text{g/g}$  Li and  $\sim 2\text{--}200 \mu\text{g/g}$  B. Nevertheless, within single serpentinite clasts, a systematic texture-related variation of Li and B concentrations is observed, predominantly between early and late serpentine. Early thin veins along former grain boundaries, mesh rims around relict olivine and thin veins through orthopyroxene have variable B, but enriched Li contents. Late mesh centers and late veins can have higher B contents, but are significantly depleted in Li relative to mesh rims (see model summary). The early mesh serpentines, and also texturally early veins, are the first serpentinization products; serpentinization during this period of complete fluid consumption (see above) seems to favor the uptake of Li into the serpentine minerals. Continuing serpentinization does not change the (light element) content of the once formed serpentine (*e.g.*, mesh center serpentinization via mesh rims); Li concentrations remain unchanged in mesh rims and along former crystal boundaries during ongoing serpentinization. This clearly shows that (Li) compositions of serpentine once formed (early generation) do not change.

A relatively heterogeneous Li distribution in serpentinite bulk rocks was already observed by Benton *et al.* (2004) and explained by a Li 'concentration front' with highest concentrations near serpentine veins. Nevertheless, the results presented show that the Li distribution within serpentinites is predominantly controlled by the fluid-rock ratios, *i.e.*, early or late serpentinization events which also might be true for the B and  $\delta^{11}\text{B}$  distribution.

6. SIMS analyses of serpentine from the mantle wedge serpentinites reveal that B isotope fractionation is not only controlled by pH and temperature, but also by water-rock ratios.  $\delta^{11}\text{B}$  ranges from very negative to very positive values considering all serpentinites: from



–14 ‰ to +24 ‰. Though ranges are different between serpentinite clasts,  $\delta^{11}\text{B}$  tends to high values in association with high Li contents in early serpentine textures, whereas the lowest, most negative  $\delta^{11}\text{B}$  values are found in late serpentine textures, *e.g.*, late veins (Table 6.1; see Fig. 4.19 in chapter 4). Bulk rock compositions reveal positive  $\delta^{11}\text{B}$  values ( $\sim +15$  ‰; Benton *et al.*, 2001; Savov *et al.*, 2004) which correlate with the weighted mean of single serpentine  $\delta^{11}\text{B}$ . The variability in  $\delta^{11}\text{B}$  values suggests changing fluid composition during serpentinization as well as fresh fluid supply from depth, rather than a differentiation path or constant fluid evolution. The ‘Subduction Factory’ is an open and variable system; therefore, the serpentinizing fluids released from the slab must have a well defined but still variable (light element) composition and B isotope signature (see chapter 5).

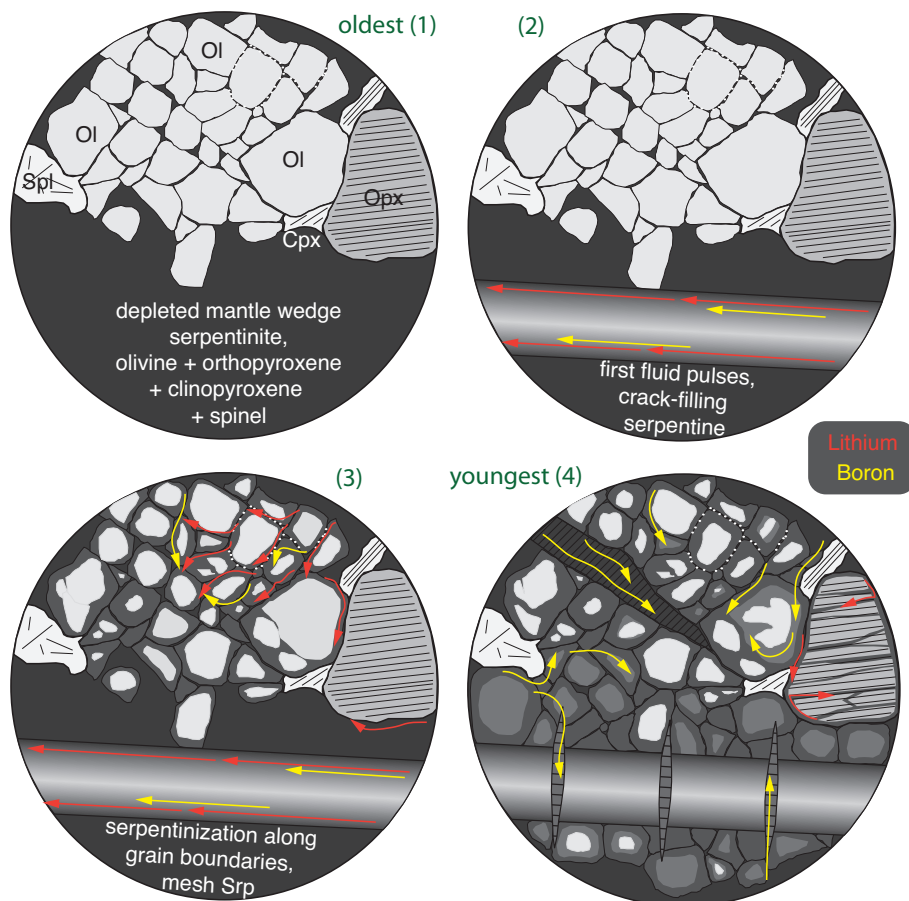


**Fig. 6.3:** Schematic model of peridotite serpentinization steps with color indicated Li and B infiltration: **1)** juvenile mantle peridotite, only primary minerals Ol, Opx, Cpx and Spl, **2)** first veins with high Li and B contents in the rims, **3)** continuing serpentinization affects rims of olivine grain producing Li-rich serpentine with variable B content associated with complete fluid consumption, and **4)** late serpentine veins and mesh centers form and have typically enriched B contents and relatively low Li contents.

### 6.3 Boron isotope evolution along the slab-mantle interface in the Mariana forearc

The results of the light element study on blueschist-facies slab-derived metamafic rocks and variably serpentinized mantle wedge peridotites from the Mariana forearc region (Fig. 6.4) allows to explain the Li and B distribution in serpentinite textures and the B isotope evolution in rocks and fluids during subduction, slab-dehydration and mantle hydration.

As demonstrated above, the metamafic slab-derived rocks have a  $\delta^{11}\text{B}$  spread from  $-10\text{‰}$  to  $-2\text{‰}$  ( $-6 \pm 4\text{‰}$ ) and are enriched in Li and B. This B isotope signature can be explained by progressive fluid loss during subduction. The sediments and hydrated oceanic crust carry large quantities of  $\text{H}_2\text{O}$ . The major fraction of  $\text{H}_2\text{O}$  is bound in hydrous minerals, such as chlorite, amphibole and phengite. As the subducting altered oceanic crust has a positive  $\delta^{11}\text{B}$  value ( $\sim +3\text{‰}$ ), fluids released at the onset of dehydration, where temperatures are very low and B fractionation is large, have positive  $\delta^{11}\text{B}$  values, significantly above the ranges of mantle and MORB (Marschall *et al.*, 2007). When subduction proceeds, the  $\delta^{11}\text{B}$  values of the released fluids decrease and reach negative  $\delta^{11}\text{B}$  values, even lower than those of the mantle, while the  $\delta^{11}\text{B}$  value of the slab also decreases. As temperatures increase with depths, the B fractionation factor will decrease (Peacock & Hervig, 1999; Wunder *et al.*, 2005). Consequently, at the temperature of  $200\text{--}350\text{ °C}$  in  $\sim 27\text{ km}$  depth, a slab-released fluid with positive  $\delta^{11}\text{B}$  ( $+14\text{‰}$ ) can be expected, leaving behind the slab with a  $\delta^{11}\text{B}$  of  $-6\text{‰}$ . The metamafic rocks from the slab-mantle-interface in the Mariana forearc are characterized by a lithology typical for a *mélange* zone. Therefore, a compositional heterogeneity of the fluids can be expected. These fluids are available for the hydration of the overlying mantle wedge and their positive B isotopic signature explains the  $\delta^{11}\text{B}$  value of upwelling fluids ( $\sim +9$  to  $+13\text{‰}$ ; Benton *et al.*, 2001; Savov *et al.*, 2004). Consistently, Mottl *et al.* (2003, 2004) already suggested a single deep fluid source for these fresh upwelling fluids such as dehydration of sediment and altered basalt at the top of the subducting Pacific Plate.

However, these relatively low-temperature slab-derived fluids are likely to be B- and Li-rich and hydrate the depleted mantle. The Mariana serpentinites record a variable Li and B enrichment and a large range of  $\delta^{11}\text{B}$  values ( $-14$  to  $+24\text{‰}$ ) in serpentine minerals. This weighted mean of this well represents the average bulk serpentinite rock compositions of  $\sim +15\text{‰}$  (Benton *et al.*, 2001; Savov *et al.*, 2004). In order to explain this range, the question whether the mafic rocks subducted are the direct source for the serpentinizing fluids can be raised.

The variability of  $\delta^{11}\text{B}$  values and their correlation with different serpentine generations strongly implies that the fluid-rock ratio is the major key to explain the light element distribution in serpentinites. One can envision that during earliest serpentinization (*e.g.*, mesh rims) and complete consumption of fluid by olivine to serpentine transformation, B as well is fully consumed and the fluid composition is virtually 'taken' up by the serpentine structure. As a matter of course, the B fractionates during olivine hydration and forms serpentine of varying  $\delta^{11}\text{B}$  values. This early serpentines, however, are found along thin vein rims and small-scaled mesh rims around olivine cores ( $<30\text{ }\mu\text{m}$ ); SIMS spot analyses ( $\sim 25\text{ }\mu\text{m}$ ) consequently give an average composition which therefore

reflects the average  $\delta^{11}\text{B}$  value from the serpentinizing fluid. Such a model can explain the formation of early serpentine with the very positive  $\delta^{11}\text{B}$  values of up to +24 ‰.

Texturally late serpentine that forms at high fluid-rock ratios, predominantly triggered by recurring fluid pulses, incorporates B via strong Rayleigh fractionation. At the low temperatures and neutral to basic pH in the deep mantle wedge near the subducting slab, the fractionation factor  $\Delta^{11}\text{B}$  varies between  $\sim -14$  ‰ (at 350°C) and  $\sim -21$  ‰ (at 200 °C; *e.g.*, Hervig & Peacock, 1999; Winter *et al.*, 2001; Wunder *et al.*, 2005) and therefore enable to produce serpentine with very negative  $\delta^{11}\text{B}$  values, when starting with a positive  $\delta^{11}\text{B}$  in the hydrating slab-derived fluids.

The results of this thesis are an important contribution to the investigation of ‘Subduction Factories’, as the Mariana forearc mafic and ultramafic rocks are a link between input materials (*e.g.*, altered oceanic crust), deep subduction related lithologies such as eclogites and output materials such as arc magmas.

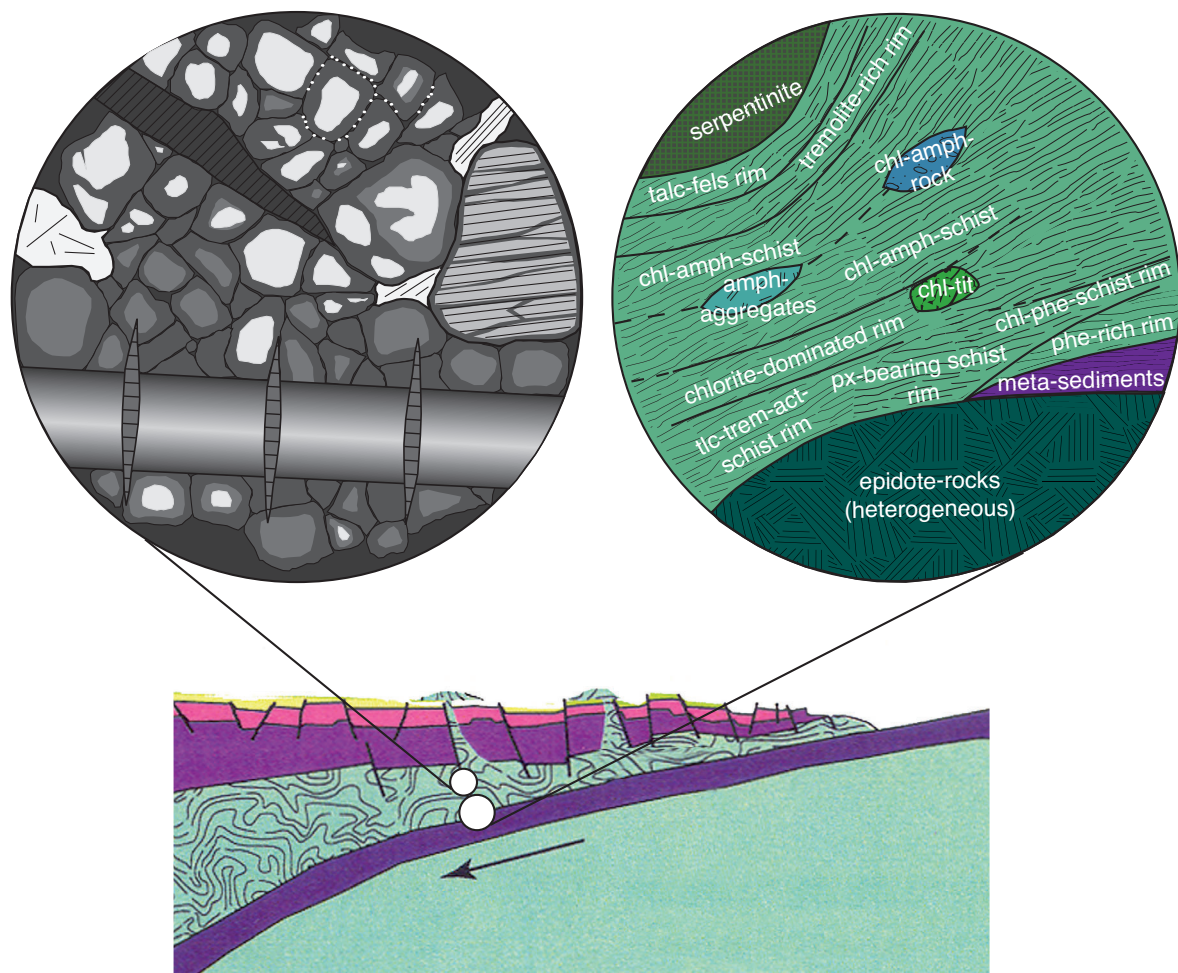


**Fig. 6.4:** Schematic presentation of the Mariana forearc. White circles indicate sampling locations, zoomed images present the characteristic serpentinite textures (left) and the metamafic lithologies of the slab or slab-mantle-mélange (right).



## References

- Abers GA (1996) Plate structure and the origin of double seismic zones. In: Bebout GE, et al. (ed) *Subduction: Top to Bottom*, AGU Geophysical Monograph 96, Washington, D.C.
- Abers GA, van Keken PE, Kneller EA, Ferris A and Stachnik JC (2006) The thermal structure of subduction zones constrained by seismic imaging: Implications for slab dehydration and wedge flow. *Earth and Planetary Science Letters* 241(3-4):387-397
- Allen DE and Seyfried WE (2003) Compositional controls on vent fluids from ultramafic-hosted hydrothermal systems at mid-ocean ridges: An experimental study at 400°C, 500 bars. *Geochimica Et Cosmochimica Acta* 67(8):1531-1542
- Alt J, Honnorez J, Laverne C and Emmermann R (1986) Hydrothermal Alteration of A 1 km Section Through the Upper Oceanic Crust, Deep Sea Drilling Project Hole 504B: Mineralogy, Chemistry and Evolution of Seawater-Basalt Interactions *Geophysical Research* 91
- Altherr R, Topuz G, Marschall H, Zack T and Ludwig T (2004) Evolution of a tourmaline-bearing lawsonite eclogite from the Elekdag area (Central Pontides, N Turkey): evidence for infiltration of slab-derived B-rich fluids during exhumation. *Contributions to Mineralogy and Petrology* 148(4):409-425
- Andreani M, Baronnet A, Boullier AM and Gratier JP (2004) A microstructural study of a "crack-seal" type serpentine vein using SEM and TEM techniques. *European Journal of Mineralogy* 16(4):585-595
- Andreani M, Boullier AM and Gratier JP (2005) Development of schistosity by dissolution-crystallization in a Californian serpentinite gouge. *Journal of Structural Geology* 27(12):2256-2267
- Andreani M, Grauby O, Baronnet A and Munoz M (2008) Occurrence, composition and growth of polyhedral serpentine. *European Journal of Mineralogy* 20(2):159-171
- Andreani M, Mevel C, Boullier AM and Escartin J (2007) Dynamic control on serpentine crystallization in veins: Constraints on hydration processes in oceanic peridotites. *Geochemistry Geophysics Geosystems* 8
- Anthony JW, Bideaux RA, Bladh KW and Nichols MC (1997) Handbook of Mineralogy. *Mineralogical Magazine* 3(67):406-408
- Aoki K (1963) The Kaersutites and Oxykaersutites from alkalic rocks of Japan and surrounding areas. *Journal of Petrology* 4(2):198-210
- Arai S (1994) Characterization of spinel peridotites by olivine-spinel compositional relationships: Review and interpretation. *Chemical Geology* 113(3-4):191-204
- Arai S, Takada S, Michibayashi K and Kida M (2004) Petrology of peridotite xenoliths from Iraya volcano, Philippines, and its implication for dynamic mantle-wedge processes. *Journal of Petrology* 45(2):369-389
- Ashley PM (1974) Opaque mineral assemblage formed during serpentinization in the Coolac ultramafic belt, New South Wales. *Australian Journal of Earth Sciences: An International Geoscience Journal of the Geological Society of Australia* 22(1):91 - 102
- Auzende AL, Daniel I, Reynard B, Lemaire C and Guyot F (2004) High-pressure behaviour of serpentine minerals: a Raman spectroscopic study. *Physics and Chemistry of Minerals* 31(5):269-277
- Bach W, Garrido CJ, Paulick H, Harvey J and Rosner M (2004) Seawater-peridotite interactions: First insights from ODP Leg 209, MAR 15 degrees N. *Geochemistry Geophysics Geosystems* 5
- Bach W, Paulick H, Garrido CJ, Ildefonse B, Meurer WP and Humphris SE (2006) Unraveling the sequence of serpentinization reactions: petrography, mineral chemistry, and petrophysics of serpentinites from MAR 15 degrees N (ODP Leg 209, Site 1274). *Geophysical Research Letters* 33(13)
- Bach W, Peucker-Ehrenbrink B, Hart SR and Blusztajn JS (2003) Geochemistry of hydrothermally altered oceanic crust: DSDP/ODP Hole 504B - Implications for seawater-crust exchange budgets and Sr- and Pb-isotopic evolution of the mantle. *Geochemistry Geophysics Geosystems* 4

## References

---

- Barnes I, LaMarche VC, Jr. and Himmelberg G (1967) Geochemical Evidence of Present-Day Serpentinization. *Science* 156(3776):830-832
- Barnes I, Sheppard RA, Gude AJ, Rapp JB and Oneil JR (1972) Metamorphic Assemblages and Direction of Flow of Metamorphic Fluids in 4 Instances of Serpentinization. *Contributions to Mineralogy and Petrology* 35(3):263
- Baronnet A and Devouard B (1996) Topology and crystal growth of natural chrysotile and polygonal serpentine. *Journal of Crystal Growth* 166(1-4):952-960
- Bayliss P (1975) Nomenclature of the trioctahedral chlorites. *The Canadian Mineralogist* 13(2):178-180
- Bazylev BA (1996) Compositions of clinopyroxene and spinel in restite hyperbasites as indicators of the generation conditions and compositions of coupled primary mantle magmas. *Geochemistry International* 33(3):115-124
- Bebout GE (1995) The impact of subduction-zone metamorphism on mantle-ocean chemical cycling. *Chemical Geology* 126(2):191-218
- Bebout GE and Barton MD (1989) Fluid-flow and metasomatism in a subduction zone hydrothermal system: Catalina Schist terrane, California. *Geology* 17(11):976-980
- Bebout GE and Barton MD (2002) Tectonic and metasomatic mixing in a high-T, subduction-zone mélange--insights into the geochemical evolution of the slab-mantle interface. *Chemical Geology* 187(1-2):79-106
- Bebout GE and Nakamura E (2003) Record in metamorphic tourmalines of subduction-zone devolatilization and boron cycling. *Geology* 31(5):407-410
- Bebout GE, Ryan JG and Leeman WP (1993) B-Be systematics in subduction-related metamorphic rocks: Characterization of the subducted component. *Geochimica Et Cosmochimica Acta* 57(10):2227-2237
- Bebout GE, Ryan JG, Leeman WP and Bebout AE (1999) Fractionation of trace elements by subduction-zone metamorphism -effect of convergent-margin thermal evolution. *Earth and Planetary Science Letters* 171(1):63-81
- Bellaiche G (1980) Sedimentation and structure of the Izu-Ogasawara (Bonin) trench off Tokyo - new lights on the results of a diving campaign with the bathyscape "archimede". *Earth and Planetary Science Letters* 47(1):124-130
- Benton LD, Ryan JG and Savov IP (2004) Lithium abundance and isotope systematics of forearc serpentinites, Conical Seamount, Mariana forearc: Insights into the mechanics of slab-mantle exchange during subduction. *Geochemistry Geophysics Geosystems* 5
- Benton LD, Ryan JG and Tera F (2001) Boron isotope systematics of slab fluids as inferred from a serpentine seamount, Mariana forearc. *Earth and Planetary Science Letters* 187(3-4):273-282
- Berman RG (1988) Internally-Consistent Thermodynamic Data for Minerals in the System Na<sub>2</sub>O-K<sub>2</sub>O-CaO-MgO-FeO-Fe<sub>2</sub>O<sub>3</sub>-Al<sub>2</sub>O<sub>3</sub>-SiO<sub>2</sub>-TiO<sub>2</sub>-H<sub>2</sub>O-CO<sub>2</sub>. *Petrology* 29(2):445-522
- Bibee LD, Shor GG and Lu RS (1980) Inter-arc spreading in the Mariana trough. *Marine Geology* 35(1-3):183-197
- Bickford ME, Siegel DI, Mottl MJ, Hill BM and Shosa J (2008) Strontium isotopic relations among pore fluids, serpentine matrix, and harzburgite clasts, South Chamorro Seamount, Mariana forearc. *Chemical Geology* 256(1-2):24-32
- Bloomer SH and Fisher RL (1987) Petrology and Geochemistry of Igneous Rocks from the Tonga Trench: Implications for its Structure. *Geology* 95:469-495
- Bloomer SH and Hawkins JW (1987) Petrology and geochemistry of boninite series volcanic rocks from the Mariana trench. *Contributions to Mineralogy and Petrology* 97:361-377
- Bloomer SH, Stern RJ, Fisk E and Geschwind CH (1989a) Shoshonitic volcanism in the northern Mariana arc. 1. mineralogic and major and trace element characteristics. *Journal of Geophysical Research-Solid Earth and Planets* 94(B4):4469-4496
- Bloomer SH, Stern RJ and Smoot NC (1989b) Physical volcanology of the submarine Mariana and Volcano Arcs. *Bulletin of Volcanology* 51(3):210-224
- Bloomer SH, Taylor B, MacLeod CJ, Stern RJ, Fryer P, Hawkins JW and Johnson L (1995) Early Arc

- volcanism and the Ophiolite problem: A perspective from drilling in the Western Pacific. In: Taylor B and Natland J (ed) *Active Margins and Marginal Basins of the Western Pacific*, American Geophysical Union, Washington D.C., pp 67-96
- Blundy J and Dalton J (2000) Experimental comparison of trace element partitioning between clinopyroxene and melt in carbonate and silicate systems, and implications for mantle metasomatism. *Contributions to Mineralogy and Petrology* 139(3):356-371
- Blundy JD, Falloon TJ, Wood BJ and Dalton JA (1995) Sodium partitioning between clinopyroxene and silicate melts. *Journal of Geophysical Research* 100:15,501-515,515
- Bonatti E, Lawrence JR and Morandi N (1984) Serpentinization of oceanic peridotites: temperature dependence of mineralogy and boron content. *Earth and Planetary Science Letters* 70(1):88-94
- Bonatti E and Michael PJ (1989) Mantle peridotites from continental rifts to ocean basins to subduction zones. *Earth and Planetary Science Letters* 91(3-4):297-311
- Boschi C, Dini A, Früh-Green GL and Kelley DS (2008) Isotopic and element exchange during serpentinization and metasomatism at the Atlantis Massif (MAR 30°N): Insights from B and Sr isotope data. *Geochimica Et Cosmochimica Acta* 72(7):1801-1823
- Boschi C, Früh-Green G, Delacour A, Karson JA and Kelley DS (2006) Mass transfer and fluid flow during detachment faulting and development of an oceanic core complex, Atlantis Massif (MAR 30°N). *Geochemistry Geophysics Geosystems* 7:1-39
- Bostock MG, Hyndman RD, Rondenay S and Peacock SM (2002) An inverted continental Moho and serpentinization of the forearc mantle. *Nature* 417(6888):536-538
- Brearley AJ, Barnes JD and Sharp ZD (2007) Chrysotile Nanotubes: Potential Host of Insoluble Chlorine in Serpentinized Oceanic Crust. *AGU Fall Meeting Abstracts, #V11E-04*
- Breeding CM, Ague JJ and Brocker M (2004) Fluid-metasedimentary rock interactions in subduction-zone melange: Implications for the chemical composition of arc magmas. *Geology* 32(12):1041-1044
- Brenan JM, Neroda E, Lundstrom CC, Shaw HF, Ryerson FJ and Phinney DL (1998a) Behaviour of boron, beryllium, and lithium during melting and crystallization: constraints from mineral-melt partitioning experiments. *Geochimica Et Cosmochimica Acta* 62(12):2129-2141
- Brenan JM, Ryerson FJ and Shaw HF (1998b) The role of aqueous fluids in the slab-to-mantle transfer of boron, beryllium, and lithium during subduction: Experiments and models. *Geochimica Et Cosmochimica Acta* 62(19-20):3337-3347
- Bröcker M (1990) Blueschist-to-greenschist transition in metabasites from Tinos Island, Cyclades, Greece: Compositional control or fluid infiltration? *Lithos* 25(1-3):25-39
- Brown EH and Ghent ED Mineralogy and phase relations in the blueschist facies of the Black Butte and Ball Rock areas, northern California Coast Ranges.
- Brown EH and Ghent ED (1983) Mineralogy and phase relations in the blueschist facies of the Black Butte and Ball Rock areas, northern California Coast Ranges. *American Mineralogist* 68(3-4):365-372
- Brown EHT (1977) The crossite content of Ca-amphibole as a guide to pressure of metamorphism. *Journal of Petrology* 18:53-72
- Brudzinski MR, Chen W-P, Nowack RL and Huang B-S (1997) Variations of P wave speeds in the mantle transition zone beneath the northern Philippine Sea. *Journal of Geophysical Research* 102
- Bryant CJ, Arculus RJ and Eggins SM (1999) Laser ablation-inductively coupled plasma-mass spectrometry and tephros: A new approach to understanding arc-magma genesis. *Geology* 27(12):1119-1122
- Bucher K and Frey M (2002) *Petrogenesis of Metamorphic Rocks*, vol. Springer, Heidelberg
- Carson B and Westbrook GK (1995) Modern fluid flow in the Cascadia accretionary wedge; a synthesis. In: Carson B, Westbrook, Graham K., Musgrave, Robert J. et al. (ed) *Proceedings of the Ocean Drilling Program, Scientific Results, Part I, 146*, College Station, TX (Ocean Drilling Program), pp 413-421
- Castle JC and Creager KC (1998) Topography of the 660-km seismic discontinuity beneath Izu-Bonin: Implications for tectonic history and slab deformation. *Journal of Geophysical Research* 103
- Castle JC and Creager KC (1999) A steeply dipping discontinuity in the lower mantle beneath Izu-Bonin.

## References

---

- Journal of Geophysical Research* 104
- Catanzaro F, Champion CE, Garner EL, Marinenko G, Sappenfield KM, Shields WR (1970) Boric acid: isotopic and assay standard reference materials. *National Bureau of Standards (US) Special Publications* 260:1-70
- Cathelineau M (1988) Cation site occupancy in chlorites and illites as a function of temperature. *Clay Minerals* 23(4):471-485
- Cathelineau M and Niveau D (1985) A chlorite solid-solution geothermometer. The Los-Azufres (Mexico) geothermal system. *Contributions to Mineralogy and Petrology* 91(3):235-244
- Chacko T, Cole DR and Horita J (2001) Equilibrium Oxygen, Hydrogen and Carbon Isotope Fractionation Factors Applicable to Geologic Systems. *Reviews in Mineralogy and Geochemistry* 43(1):1-81
- Chan LH, Alt JC and Teagle DAH (2002b) Lithium and lithium isotope profiles through the upper oceanic crust: a study of seawater-basalt exchange at ODP Sites 504B and 896A. *Earth and Planetary Science Letters* 201(1):187-201
- Chan LH, Edmond JM, Thompson G and Gillis K (1992) Lithium isotopic composition of submarine basalts: implications for the lithium cycle in the oceans. *Earth and Planetary Science Letters* 108(1-3):151-160
- Chan LH and Kastner M (2000) Lithium isotopic compositions of pore fluids and sediments in the Costa Rica subduction zone: implications for fluid processes and sediment contribution to the arc volcanoes. *Earth and Planetary Science Letters* 183(1-2):275-290
- Chan LH, Leeman WP and You CF (1999) Lithium isotopic composition of Central American Volcanic Arc lavas: implications for modification of subarc mantle by slab-derived fluids. *Chemical Geology* 160(4):255-280
- Chan LH, Leeman WP and You CF (2002a) Lithium isotopic composition of Central American volcanic arc lavas: implications for modification of subarc mantle by slab-derived fluids: correction. *Chemical Geology* 182(2-4):293-300
- Chauvel C, Goldstein SL and Hofmann AW (1995) Hydration and dehydration of oceanic crust controls Pb evolution in the mantle. *Chemical Geology* 126(1):65-75
- Cloos M and Shreve RL (1996) Shear zone thickness and the seismicity of Chilean- and Mariana-type subduction zones. *Geology* 24(2):107-110
- Coleman RG and Clark JR (1968) Pyroxenes in the blueschist facies of California. *American Journal of Science* 266(1):43-59
- Coleman RG and Keith TE (1971) A Chemical Study of Serpentinization-Burro Mountain, California. *Petrology* 12(2):311-328
- Coogan LA, Kasemann SA and Chakraborty S (2005) Rates of hydrothermal cooling of new oceanic upper crust derived from lithium-geospeedometry. *Earth and Planetary Science Letters* 240(2):415-424
- Coombs DS, Nakamura Y and Vuagnat M (1976) Pumpellyite-actinolite facies schists of Taveyanne formation near Loeche, Valais, Switzerland. *Journal of Petrology* 17(4):440-471
- Cosca MA, Arculus RJ, Pearce JA and Mitchell JG (1998) Ar-40/Ar-39 and K-Ar geochronological age constraints for the inception and early evolution of the Izu-Bonin-Mariana arc system. *The Island Arc* 7(3):579-595
- Creager KC and Jordan TH (1986) Slab Penetration Into the Lower Mantle Beneath the Mariana and Other Island Arcs of the Northwest Pacific. *Journal of Geophysical Research* 91
- Cressey BA and Zussman J (1976) Electron microscope studies of serpentinites. *The Canadian Mineralogist* 14:307-313
- Curie LA (1968) Limits for Qualitative Detection and Quantitative Determination. *Analytical Chemistry* 40:586-593
- D'Antonio M and Kristensen MB (2004) Serpentine and brucite of ultramafic clasts from the South Chamorro Seamount (Ocean Drilling Program Leg 195, Site 1200): inferences for the serpentinization of the Mariana forearc mantle. *Mineralogical Magazine* 68(6):887-904
- Dawson P, Hadfield CD and Wilkinson GR (1973) The polarized infra-red and Raman spectra of Mg(OH)<sub>2</sub> and



- Ca(OH)<sub>2</sub>. *Journal of Physics and Chemistry of Solids* 34(7):1217-1225
- Decitre S, Deloule E, Reisberg L, James R, Agrinier P and Mevel C (2002) Behavior of Li and its isotopes during serpentinization of oceanic peridotites. *Geochemistry Geophysics Geosystems* 3
- Deer WA, Howie RA and Zussman J (1992) *An Introduction to the Rock-Forming Minerals*. 2nd ed., Longman Scientific and Technical, New York
- Dick HJB and Bullen T (1984) Chromian spinel as a petrogenetic indicator in abyssal and alpine-type peridotites and spatially associated lavas. *Contributions to Mineralogy and Petrology* 86(1):54-76
- Dick HJB and Fisher RL (1984) Mineralogic studies of the residues of mantle melting: abyssal and alpine-type peridotites. In: Kornprobst J (ed) *Proc. the 3rd Int. Kimberlite Conference*, Elsevier, Amsterdam, pp 295-308
- Dick HJB, Fisher RL and Bryan WB (1984) Mineralogic variability of the uppermost mantle along mid-ocean ridges. *Earth and Planetary Science Letters* 69(1):88-106
- Dilek Y, Coulton A and Hurst SD (1997) Serpentinization and hydrothermal veining in peridotites at Site 920 in the MARK area. In: Karson JA, Cannat, Mathilde, Miller, D. Jay et al. (ed) *Proceedings of the Ocean Drilling Program, Scientific Results, 153*. College Station, TX (Ocean Drilling Program), pp 35-59
- Domanik KJ, Hervig RL and Peacock SM (1993) Beryllium and boron in subduction zone minerals: An ion microprobe study. *Geochimica Et Cosmochimica Acta* 57(21-22):4997-5010
- Dorendorf F, Wiechert U and Wörner G (2000) Hydrated sub-arc mantle: a source for the Kluchevskoy volcano, Kamchatka/Russia. *Earth and Planetary Science Letters* 175(1-2):69-86
- Douville E, Charlou JL, Oelkers EH, Biennu P, Jove Colon CF, Donval JP, Fouquet Y, Prieur D and Appriou P (2002) The rainbow vent fluids (36°14'N, MAR): the influence of ultramafic rocks and phase separation on trace metal content in Mid-Atlantic Ridge hydrothermal fluids. *Chemical Geology* 184(1-2):37-48
- Duffy TS, Meade C, Fei YW, Mao HK and Hemley RJ (1995) High-pressure phase transition in brucite, Mg(OH)<sub>2</sub>. *American Mineralogist* 80(3-4):222-230
- Elliott T (2003) Tracers of the Slab. In: Eiler JM (ed) *Inside the Subduction Factory*, American Geophysical Union, Washington, DC, pp 23-45
- Elliott T, Plank T, Zindler A, White W and Bourdon B (1997) Element transport from slab to volcanic front at the Mariana arc. *Geophysical Research* 102
- Elthon D (1992) Chemical trends in abyssal peridotites: Refertilization of depleted subocean mantle. *Geophysical Research* 97
- Enami M, Liou JG and Mattinson CG (2004) Epidote minerals in high P/T metamorphic terranes: subduction zone and high- to ultrahigh-pressure metamorphism. In: Liebscher A, Franz, G. (ed) *Epidotes*, Reviews in Mineralogy and Geochemistry 56, Mineralogical Society of America and Geochemical Society, pp 347-398
- Engdahl ER, van der Hilst R and Buland R (1998) Global teleseismic earthquake relocation with improved travel times and procedures for depth determination. *Bulletin of the Seismological Society of America* 88(3):722-743
- Engel AEJ, Engel CG and Havens RG (1965) Chemical Characteristics of Oceanic Basalts and the Upper Mantle. *Geological Society of America Bulletin* 76
- Ernst WG (1973) Interpretative synthesis of the metamorphism in the Alps. *Bull. Geol. Soc. Amer.* 84:2053-2078
- Evans BW (1977) Metamorphism of Alpine Peridotite and Serpentinite. *Annual Review of Earth and Planetary Sciences* 5(1):397-447
- Evans BW (1990) Phase relations of epidote-blueschists. *Lithos* 25(1-3):3-23
- Evans BW (2004) The serpentinite multisystem revisited: Chrysotile is metastable. *International Geology Review* 46(6):479-506
- Evans BW (2008) Control of the Products of Serpentinization by the (FeMg<sub>1</sub>)-Mg<sub>2</sub> Exchange Potential of Olivine and Orthopyroxene. *Journal of Petrology* 49(10):1873-1887

## References

---

- Evans BW, Johannes W, Oterdoom H and Tommsdorff V (1976) Stability of crysotile and antigorite in the serpentinite multisystem. *Schweizerische Mineralogische und Petrographische Mitteilungen* 56:79–93
- Fisher DM (1996) Fabrics and veins in the forearc: A record of cyclic fluid flow at depths of <15 km (Overview). In: Bebout GE, Scholl, D.W., Kirby, S.H., Platt, J. (ed) *Subduction Top to Bottom*, Geophysical Monograph 96, pp 75-89
- Foord EE, Martin RF, Fitzpatrick JJ, Taggart JE and Crock Jr. JG (1991) Boromuscovite, a new member of the mica group, from the Little Three mine pegmatite, Ramona district, San Diego County, California. *American Mineralogist* 76:1998-2002
- Fornieris JF and Holloway JR (2004) Evolution of mineral compositions during eclogitization of subducting basaltic crust. *American Mineralogist* 89(10):1516-1524
- Forsyth D and Uyedaf S (1975) On the Relative Importance of the Driving Forces of Plate Motion. *Geophysical Journal of the Royal Astronomical Society* 43(1):163-200
- Fouch MJ and Fischer KM (1996) Mantle anisotropy beneath northwest Pacific subduction zones. *Journal of Geophysical Research* 101
- Foustoukos DI, James RH, Berndt ME and Seyfried WE (2004) Lithium isotopic systematics of hydrothermal vent fluids at the Main Endeavour Field, Northern Juan de Fuca Ridge. *Chemical Geology* 212(1-2):17-26
- Foustoukos DI, Savov IP and Janecky DR (2008) Chemical and isotopic constraints on water/rock interactions at the Lost City hydrothermal field, 30 degrees N Mid-Atlantic Ridge. *Geochimica Et Cosmochimica Acta* 72(22):5457-5474
- Frost BR (1975) Contact metamorphism of serpentinite, chlorite blackwall and rodingite at Paddy-Go-Easy Pass, Central Cascades, Washington. *Journal of Petrology* 16(2):272-313
- Frost BR and Beard JS (2007) On silica activity and serpentinization. *Journal of Petrology* 48(7):1351-1368
- Fryer P (1987) Results of Alvin studies of Mariana forearc serpentinite diapirism *EOS, Trans AGU* 68(44):1534
- Fryer P, Pearce, Julian A., Stokking, Laura B. et al. (1990) Bonin/Mariana region, covering Leg 125 of the cruises of the drilling vessel JOIDES Resolution, Apra Harbor, Guam, to Tokyo, Japan, sites 778-786. In: Fryer P, Pearce, JA, Stokking, LB et al. (ed) *Proceedings of the Ocean Drilling Program, Initial Reports, 125*. College Station, TX (Ocean Drilling Program), pp 367-380
- Fryer P (1992 ) A synthesis of LEG 125 Drilling of serpentine seamounts on the Mariana and Izu-Bonin Forearcs. In: Fryer P, Pearce, J A, Stokking, L B et al. (ed) *Proceedings of the Ocean Drilling Program, Scientific Results, 125*. College Station, TX (Ocean Drilling Program)
- Fryer P (1995) Geology of the Mariana Trough In: Taylor B (ed) *Backarc Basins: Tectonics and Magmatism*, vol. Plenum Press, New York, pp 237-279
- Fryer P, Ambros EL and Hussong DM (1985) Origin and emplacement of Mariana Forearc seamounts. *Geology* 13:774-777
- Fryer P and Fryer GJ (1987) Origins of nonvolcanic seamounts in a forearc environment. In: Keating BH, Fryer P, Batiza, R, Boehlert, GW (ed) *Seamounts, Islands, and Atolls*, Geophysical Monograph 43, pp 61-69
- Fryer P, Gharib J, Ross K, Savov I and Mottl MJ (2006) Variability in serpentinite mudflow mechanisms and sources: ODP drilling results on Mariana forearc seamounts. *Geochemistry, Geophysics, Geosystems* 7
- Fryer P, Lockwood JP, Becker N, Phipps S and Todd CS (2000) Significance of serpentine mud volcanism in convergent margins. *Geological Society of America Special Papers* 349:35-51
- Fryer P and Mottl MJ (1992) Lithology, mineralogy, and origin of serpentine muds recovered from Conical and Torishima forearc seamounts: results of Leg 125 drilling. In: Fryer P, Pearce, J.A., Stokking, L.B., et al. (ed) *Proceedings Ocean Drilling Program, Science Results, 125*. College Station, TX (Ocean Drilling Program), pp 343–362
- Fryer P, Wheat CG and Mottl MJ (1999) Mariana blueschist mud volcanism: Implications for conditions within the subduction zone. *Geology* 27(2):103-106
- Fryer PB and Salisbury MH (2006) 1. Leg 195 Synthesis: Site 1200—Serpentinite Seamounts of the Izu-Bonin/Mariana Convergent Plate Margin (ODP Leg 125 and 195 Drilling Results). In: Shinohara M, Salisbury, M.H., and Richter, C. (ed) *Proceedings of the Ocean Drilling Program, 195*. College Station,

- TX (Ocean Drilling Program), pp 1-30
- Fukao Y, Obayashi M, Inoue H and Nenbai M (1992) Subducting Slabs Stagnant in the Mantle Transition Zone. *Journal of Geophysical Research* 97
- Gharib J (2006) *Clastic metabasites and authigenic minerals within serpentinite protrusions from the Mariana forearc: implications for sub-forearc subduction processes*. University of Hawaii, USA. PhD thesis
- Gill JB, Hiscott RN and Vidal P (1994) Turbidite geochemistry and evolution of the Izu-Bonin arc and continents. *Lithos* 33(1-3):135-168
- Gill JB, Morris JD and Johnson RW (1993) Timescale for producing the geochemical signature of island arc magmas: U-Th-Po and Be-B systematics in recent Papua New Guinea lavas. *Geochimica Et Cosmochimica Acta* 57(17):4269-4283
- Grapes RH and Hoskin PWO (2004) Epidote Group Minerals in Low-Medium Pressure Metamorphic Terranes *Reviews in Mineralogy and Geochemistry* 56(1):301-345
- Gréau Y, Godard M and Alard O (2007) Evidence of melt stage refertilization and metasomatism in abyssal peridotites from Hess Deep (ODP LEG 147). *European Mantle Workshop (EMAW 2007)*
- Gregoire M, Moine BN, O'Reilly SY, Cottin JY and Giret A (2000) Trace element residence and partitioning in mantle xenoliths metasomatized by highly alkaline, silicate- and carbonate-rich melts (Kerguelen Islands, Indian Ocean). *Journal of Petrology* 41(4):477-509
- Gribble RF, Stern RJ, Newman S, Bloomer SH and O'Hearn T (1998) Chemical and isotopic composition of lavas from the Northern Mariana Trough: Implications for magmagenesis in back-arc basins. *Journal of Petrology* 39(1):125-154
- Groppo C, Rinaudo C, Cairo S and Gastaldi D (2006) Micro-Raman spectroscopy for a quick and reliable identification of serpentine minerals from ultramarines. *European Journal of Mineralogy* 18(3):319-329
- Gustafson W (1974) Stability andradite, hedenbergite, and related minerals in system Ca-Fe-Si-O-H. *Journal of Petrology* 15(3):456-496
- Harland WB, Armstrong R, Cox AV, Craig L, Smith A and Smith D (1990) *A Geologic Time Scale 1989*, Cambridge Univ. Press, Cambridge
- Hart SR, Blusztajn J, Dick HJB, Meyer PS and Muehlenbachs K (1999) The fingerprint of seawater circulation in a 500-meter section of ocean crust gabbros. *Geochimica Et Cosmochimica Acta* 63(23-24):4059-4080
- Hattori KH and Guillot S (2003) Volcanic fronts form as a consequence of serpentinite dehydration in the forearc mantle wedge. *Geology* 31(6):525-528
- Hawthorne FC and Huminicki DMC (2002) The Crystal Chemistry of Beryllium. In: Grew E (ed) *Beryllium: mineralogy, petrology and geochemistry*. Reviews in Mineralogy 50, Mineralogical Society of America, Washington, DC, pp 333-403
- Hawthorne Y, Burns P and Grice J (1996) The crystal chemistry of boron In: Grew ES (ed) *Boron: Mineralogy, Petrology and Geochemistry*, Reviews in Mineralogy 33, Mineralogical Society of America, Washington, DC, pp 41-116
- Hébert R, Adamson AC and Komor SC (1990) Metamorphic petrology of ODP Leg 109, Hole 670A serpentinitized peridotites: serpentinitization processes at a slow spreading ridge environment. In: Detrick R, Honnorez, J., Bryan, W.B., Juteau, T., et al. (ed) *Proceedings of the Ocean Drilling Program, Scientific Results, 106/109*. College Station, TX (Ocean Drilling Program), pp 103-115
- Heling D and Schwarz A (1992) Iowaitite in serpentinite muds at Sites 778, 779, 780, and 784: a possible cause for the low chlorinity of pore waters. In: Fryer P, Pearce, J.A., Stokking, L.B., et al. (ed) *Proceedings of the Ocean Drilling Program, Scientific Results, 125*. College Station, TX (Ocean Drilling Program), pp 313-323
- Hellebrand E, Snow JE, Dick HJB and Hofmann AW (2001) Coupled major and trace elements as indicators of the extent of melting in mid-ocean-ridge peridotites. *Nature* 410(6829):677-681
- Hellebrand E, Snow JE and Muhe R (2002) Mantle melting beneath Gakkel Ridge (Arctic Ocean): abyssal peridotite spinel compositions. *Chemical Geology* 182(2-4):227-235
- Hervig RL, Moore GM, Williams LB, Peacock SM, Holloway JR and Roggensack K (2002) Isotopic and elemental partitioning of boron between hydrous fluid and silicate melt. *American Mineralogist* 87(5-

- 6):769-774
- Hickey RL and Frey FA (1982) Rare-earth element geochemistry of Mariana fore-arc volcanics; Deep Sea Drilling Project Site 458 and Hole 459B. *Leg 60 of the cruises of the drilling vessel Glomar Challenger; Apra, Guam to Apra, Guam; March-May 1978* 60:735-742
- Horine RL, Moore GF and Taylor B (1990) Structure of the outer Izu-Bonin Forearc from seismic-reflection profiling and gravity modeling. In: Fryer P, JA, Stokking, LB et al. (ed) *Proceedings of the Ocean Drilling Program, Initial Reports, 125*. College Station, TX (Ocean Drilling Program), pp 81-94
- Hostetler PB, Coleman RG, Mumpton FA and Evans BW (1966) Brucite in alpine serpentinites. *American Mineralogist* 51:75-98
- Hussong DM and Fryer P (1982) Structure and tectonics of the Mariana arc and forearc: drillsite section surveys. *Initial Reports of the Deep Sea Drilling Project, 60*
- Hussong DM and Uyeda S Mariana arc and fore-arc background and objectives. *Initial Reports of the Deep Sea Drilling Project, 60*
- Hussong DM, Uyeda S, Knapp R, Ellis H, Kling S and Natland J (1982) Deep sea Drilling project LEG 60: Cruise objectives, principal results, and explanatory notes. *Initial Reports of the Deep Sea Drilling Project, 60*
- Ishii T, Robinson PT, Maekawa H and Fiske R (1992) Petrological studies of peridotites from diapiric serpentinite seamounts in the Izu-Ogasawara-Mariana forearc, LEG 1251. In: Fryer P, Pearce, J A, Stokking, L B et al. (ed) *Proceedings of the Ocean Drilling Program, Scientific Results, 125*. College Station, TX (Ocean Drilling Program)
- Ishii T, Sato H, Haraguchi S, Fryer P, Fujioka K, Bloomer S and Yokose H (2000) Petrological characteristics of peridotites from serpentinite seamounts in the Izu-Ogasawara-Mariana forearc. *The water in the slab and the material circulation in the mantle* 109(4):517-530
- Ishikawa T and Nakamura E (1993) Boron isotope systematics of marine sediments. *Earth and Planetary Science Letters* 117(3-4):567-580
- Ishikawa T and Nakamura E (1994) Origin of the slab component in arc lavas from across-arc variation of B and Pb isotopes. *Nature* 370(6486):205-208
- Ishikawa T and Tera F (1997) Source, composition and distribution of the fluid in the Kurile mantle wedge: Constraints from across-arc variations of B/Nb and B isotopes *Earth and Planetary Science Letters* 152(1):123-138
- Ishiwatari A and Tsujimori T (2003) Paleozoic ophiolites and blueschists in Japan and Russian Primorye in the tectonic framework of East Asia: A synthesis. *The Island Arc* 12:190-206
- Ishizuka O, Uto K, Yuasa M and Hochstaedter A (1998) K-Ar ages from seamount chains in the back-arc region of the Izu-Ogasawara arc. *The Island Arc* 7:408-421
- Jacobson CE (1995) Qualitative thermobarometry of inverted metamorphism in the Pelona and Rand Schists, southern California, using calciferous amphibole in mafic schist. *Journal of Metamorphic Geology* 13(1):79-92
- Jan MQ, Windley BF and Wilson RN (1984) Chromian andradite and olivine-chromite relations in a chromitite layer from the Jijal Complex, northwestern Pakistan. *The Canadian Mineralogist* 22(2):341-345
- Jaques AL and Green DH (1980) Anhydrous melting of peridotite at 0–15 Kb pressure and the genesis of tholeiitic basalts. *Contributions to Mineralogy and Petrology* 73(3):287-310
- Jean-Baptiste P, Charlou JL, Stievenard M, Donval JP, Bougault H and Mevel C (1991) Helium and methane measurements in hydrothermal fluids from the mid-Atlantic ridge: The Snake Pit site at 23°N. *Earth and Planetary Science Letters* 106(1-4):17-28
- Jeffcoate AB, Elliott T, Kasemann SA, Ionov D, Cooper K and Brooker R (2007) Li isotope fractionation in peridotites and mafic melts. *Geochimica Et Cosmochimica Acta* 71(1):202-218
- Johannes W (1967) Zur Bildung und Stabilität von Forsterit, Talk, Serpentin, Quarz und Magnesit im System MgO-SiO<sub>2</sub>-H<sub>2</sub>O-CO<sub>2</sub>. *Contributions to Mineralogy and Petrology* 15(3):233-250
- Johannes W (1968) Experimental investigation of the reaction forsterite + H<sub>2</sub>O serpentine + brucite. *Contributions to Mineralogy and Petrology* 19(4):309-315

- Johnson LE (1992) Mafic clasts in serpentine seamounts: petrology and geochemistry of a diverse crustal suite from the outer Mariana forearc. In: Fryer P, Pearce, J A, Stokking, L B et al. (ed) *Proceedings of the Ocean Drilling Program, Scientific Results*, College Station, TX (Ocean Drilling Program)
- Johnson M and Plank T (1999) Dehydration and melting experiments constrain the fate of subducted sediments. *Geochemistry, Geophysics, Geosystems* 1
- Kamimura A, Kasahara J, Shinohara M, Hino R, Shiobara H, Fujie G and Kanazawa T (2002) Crustal structure study at the Izu-Bonin subduction zone around 31°N: implications of serpentized materials along the subduction plate boundary. *Physics of The Earth and Planetary Interiors* 132(1-3):105-129
- Kapp P, Yin A, Manning CE, Murphy M, Harrison TM, Spurlin M, Lin D, Deng XG and Wu CM (2000) Blueschist-bearing metamorphic core complexes in the Qiangtang block reveal deep crustal structure of northern Tibet. *Geology* 28(1):19-22
- Kastner M and Elderfield H (1993) Data report: compositions of fluids and authigenic phases in sediments of the Nankai Trough accretionary complex. In: Hill IA, Taira, A., Firth, J.V., et al., (ed) *Proceedings of the Ocean Drilling Program, Scientific Results, 131 / 34*. College Station, TX (Ocean Drilling Program)
- Katsumata M and Sykes LR (1969) Seismicity and Tectonics of the Western Pacific: Izu-Mariana-Caroline and Ryukyu-Taiwan Regions. *Journal of Geophysical Research* 74
- Kelley KA, Plank T, Ludden J and Staudigel H (2003) Composition of altered oceanic crust at ODP Sites 801 and 1149. *Geochemistry Geophysics Geosystems* 4
- Kent AJR and Rossman GR (2002) Hydrogen, lithium, and boron in mantle-derived olivine: The role of coupled substitutions. *American Mineralogist* 87(10):1432-1436
- Kesson S and Price RC (1972) The major and trace element chemistry of kaersutite and its bearing on the petrogenesis of alkaline rocks. *Contributions to Mineralogy and Petrology* 35(2):119-124
- Kincaid C and Sacks IS (1997) Thermal and dynamical evolution of the upper mantle in subduction zones. *Journal of Geophysical Research-Solid Earth* 102(B6):12295-12315
- King RL, Bebout GE, Grove M, Moriguti T and Nakamura E (2007) Boron and lead isotope signatures of subduction-zone mélangé formation: Hybridization and fractionation along the slab-mantle interface beneath volcanic arcs. *Chemical Geology* 239(3-4):305-322
- King RL, Bebout GE, Kobayashi K, Nakamura E and van der Klauw S (2004) Ultrahigh-pressure metabasaltic garnets as probes into deep subduction zone chemical cycling. *Geochemistry Geophysics Geosystems* 5
- King RL, Bebout GE, Moriguti T and Nakamura E (2006) Elemental mixing systematics and Sr-Nd isotope geochemistry of mélangé formation: Obstacles to identification of fluid sources to arc volcanics. *Earth and Planetary Science Letters* 246(3-4):288-304
- King RL, Kohn MJ and Eiler JM (2003) Constraints on the petrologic structure of the subduction zone slab-mantle interface from Franciscan Complex exotic ultramafic blocks. *Geological Society of America Bulletin* 115(9):1097-1109
- Klopprogge JT, Frost RL and Rintoul L (1999) Single crystal Raman microscopic study of the asbestos mineral chrysotile. *Physical Chemistry Chemical Physics* 1(10):2559-2564
- Kobayashi K, Kasuga S, Okino K and (1995) Basin and its margins. In: Taylor B (ed) *Backarc Basins; Tectonics and Magmatism*, Plenum Press, New York, pp 381-405
- Kozlov IT and Levshov PP (1962) Amakinite, a new mineral of the brucite-pyrochroite group (original russian text). *Zap. Vses. Mineral. Obshch.* 91:72-77
- Kretz R (1983) Symbols for rock-forming minerals. *American Mineralogist* 68(1-2):277-279
- Kruger MB, Williams Q and Jeanloz R (1989) Vibrational spectra of Mg(OH)<sub>2</sub> and Ca(OH)<sub>2</sub> under pressure. *Journal of Chemical Physics* 91(10):5910-5915
- Laird J and Albee AL (1981) Pressure, temperature, and the indicators in mafic schist: their application to reconstructing the polymetamorphic history of Vermont. *American Journal of Science* 281(2):127-175
- Laure P (2008) *The oceanic mantle as an important repository for the light elements Li, Be and B*. University of Neuchatel, Swiss. Phd thesis
- Leake BE, Woolley AR, Arps CES, Birch WD, Gilbert MC, Grice JD, Hawthorne FC, Kato A, Kisch HJ,

## References

---

- Krivovichev VG, Linthout K, Laird J, Mandarino JA, Maresch WV, Nickel EH, Rock NMS, Schumacher JC, Smith DC, Stephenson NCN, Ungaretti L, Whittaker EJW and Guo Youzhi (1997) Nomenclature of amphiboles; Report of the Subcommittee on Amphiboles of the International Mineralogical Association, Commission on New Minerals and Mineral Names. *American Mineralogist* 82(9-10):1019-1037
- Leake BE, Woolley AR, Birch WD, Burke EAJ, Ferraris G, Grice JD, Hawthorne FC, Kisch HJ, Krivovichev VG, Schumacher JC, Stephenson NCN and Whittaker EJW (2004) Nomenclature of amphiboles: Additions and revisions to the International Mineralogical Association's amphibole nomenclature. *American Mineralogist* 89(5-6):883-887
- Leeman W (1996) Boron and other fluid-mobile elements in volcanic arc lavas: implications for subduction processes. *Geophysical Monograph Series* 96:269-276
- Leeman WP, Carr MJ and Morris JD (1994) Boron geochemistry of the Central American Volcanic Arc: Constraints on the genesis of subduction-related magmas. *Geochimica Et Cosmochimica Acta* 58(1):149-168
- Leeman WP and Sisson VB (2002) Geochemistry of boron and its implications for crustal and mantle processes. In: Grew ES, Anovitz, L.M. Editors (2nd edn.) (ed) *Boron: Mineralogy, Petrology and Geochemistry*, Reviews in Mineralogy 33. Mineralogical Society of America, Washington, DC pp 645-708
- Lewis IR, Chaffin NC, Gunter ME and Griffiths PR (1996) Vibrational spectroscopic studies of asbestos and comparison of suitability for remote analysis. *Spectrochimica Acta Part A: Molecular and Biomolecular Spectroscopy* 52(3):315-328
- Liou JG, Maruyama S and Cho M (1985) Phase equilibria and mineral parageneses of metabasites in low-grade metamorphism. *Mineralogical Magazine* 49:321-333
- Liu J, Bohlen SR and Ernst WG (1996) Stability of hydrous phases in subducting oceanic crust. *Earth and Planetary Science Letters* 143(1-4):161-171
- Locock AJ (2008) An Excel spreadsheet to recast analyses of garnet into end-member components, and a synopsis of the crystal chemistry of natural silicate garnets. *Computers & Geosciences* 34(12):1769-1780
- Lutz HD, Möller H and Schmidt M (1994) Lattice vibration spectra. Part LXXXII. Brucite-type hydroxides  $M(OH)_2$  ( $M = Ca, Mn, Co, Fe, Cd$ ) -- IR and Raman spectra, neutron diffraction of  $Fe(OH)_2$ . *Journal of Molecular Structure* 328:121-132
- Lykins RW and Jenkins DM (1992) Experimental determination of pargasite stability relations in the presence of orthopyroxene. *Contributions to Mineralogy and Petrology* 112(2-3):405-413
- Lyubetskaya T and Korenaga J (2007a) Chemical composition of Earth's primitive mantle and its variance: 1. Method and results. *Journal of Geophysical Research-Solid Earth* 112(B3)
- Lyubetskaya T and Korenaga J (2007b) Chemical composition of Earth's primitive mantle and its variance: 2. Implications for global geodynamics. *Journal of Geophysical Research-Solid Earth* 112(B3)
- Macpherson CG and Hall R (2001) Tectonic setting of Eocene boninite magmatism in the Izu-Bonin-Mariana forearc. *Earth and Planetary Science Letters* 186(2):215-230
- Maekawa H (1995) Metamorphic rocks from serpentinite seamounts in the Mariana and Izu-Bonin forearcs In: Tokuyama Hea (ed) *Geology and Geophysics of the Philippine Sea*, Terra Scientific Publishing Company, Tokyo, pp 357-369
- Maekawa H (2001) A Speculation on Stress Regime of the High-Pressure Metamorphic Belts in the Circum-Pacific Regions. *Gondwana Research* 4(4):695-695
- Maekawa H, Shozui M, Ishii T, Saboda KL and Ogawa Y (1992) Metamorphic rocks from the serpentinite seamounts in the Mariana and Izu-Ogasawara forearcs. In: Fryer P, Pearce, JA, Stokking, LB et al. (ed) *Proceedings of the Ocean Drilling Program, Scientific Results, 125*. College Station, TX (Ocean Drilling Program)
- Maekawa H, Shozul M, Ishii T, Fryer P and Pearce JA (1993) Blueschist metamorphism in an active subduction zone. *Nature* 364(6437):520-523
- Maltman AJ, Labaume P and Housen BA (1997) Structural geology of the decollement at the toe of the

- Barbados accretionary prism. In: Shipley TH, Ogawa, Yujiro, Blum, Peter et al. (ed) *Proceedings of the Ocean Drilling Program, Scientific Results, 156*. College Station, TX (Ocean Drilling Program), pp 279-292
- Manning CE (1997) Coupled reaction and flow in subduction zones: silica metasomatism in the mantle wedge. In: Jamtveit B and Yardley BWD (eds) *Fluid flow and transport in rocks: mechanisms and effects*, Chapman & Hall, London, pp 139-148
- Marschall HR (2005) *Lithium, beryllium and boron in high-pressure metamorphic rocks from Syros (Greece)*. Mathematisch-Naturwissenschaftlichen Gesamtfakultät, Ruprecht-Karls-Universität, Heidelberg, Germany. Phd thesis
- Marschall HR, Altherr R and Rupke L (2007a) Squeezing out the slab - modelling the release of Li, Be and B during progressive high-pressure metamorphism. *Chemical Geology* 239(3-4):323-335
- Marschall HR and Ludwig T (2004) The low-boron contest: minimising surface contamination and analysing boron concentrations at the ng/g-level by secondary ion mass spectrometry. *Mineralogy and Petrology* 81(3):265-278
- Marschall HR, Ludwig T, Altherr R, Kalt A and Tonarini S (2006) Syros metasomatic tourmaline: Evidence for very high-delta B-11 fluids in subduction zones. *Journal of Petrology* 47(10):1915-1942
- Marschall HR, Pogge von Strandmann PAE, Seitz H-M, Elliott T and Niu Y (2007b) The lithium isotopic composition of orogenic eclogites and deep subducted slabs. *Earth and Planetary Science Letters* 262(3-4):563-580
- Martinez F, Fryer P, Baker NA and Yamazaki T (1995) Evolution of backarc rifting: Mariana Trough, 20°-24°N. *Journal of Geophysical Research-Solid Earth* 100(B3):3807-3827
- Maruyama S, Cho M and Liou JG (1986) Experimental investigations of blueschist-greenschist transition equilibrium: pressure dependence of Al<sub>2</sub>O<sub>3</sub> contents in sodic amphiboles: a new geobarometer. In: Evans BW and Brown EH (eds) *Blueschists and Eclogites*, Geological Society of America Memoir 164, pp 1-16
- McCaffrey R (1996) Estimates of modern arc-parallel strain rates in fore arcs. *Geology* 24(1):27-30
- McCubbin FM, Nekvasil H and Lindsley DH (2006) Oxy-component in kaersutite: How much can be a primary magmatic feature? *EOS, Trans AGU* 87(36)
- McCulloch MT and Gamble JA (1991) Geochemical and geodynamical constraints on subduction zone magmatism. *Earth and Planetary Science Letters* 102(3-4):358-374
- McDade P, Blundy JD and Wood BJ (2003) Trace element partitioning between mantle wedge peridotite and hydrous MgO-rich melt. *American Mineralogist* 88(11-12):1825-1831
- McDonough WF and Sun SS (1995) The composition of the earth. *Chemical Geology* 120(3-4):223-253
- Mével C (2003) Serpentinization of abyssal peridotites at mid-ocean ridges. *Comptes Rendus Geosciences* 335(10-11):825-852
- Middleton AP and Whittaker EJW (1976) Structure of povlentype chrysotile. *The Canadian Mineralogist* 14:301-306
- Miller DP, Marschall HR and Schumacher JC (2009) Metasomatic formation and petrology of blueschist-facies hybrid rocks from Syros (Greece): Implications for reactions at the slab-mantle interface. *Lithos* 107(1-2):53-67
- Miyashiro A (1973) *Metamorphism and metamorphic belts*, Allen & Unwin, London
- Moody JB (1976a) An experimental study on the serpentinization of iron-bearing olivines. *The Canadian Mineralogist* 14(4):462-478
- Moody JB (1976b) Serpentinization: a review. *Lithos* 9(2):125-138
- Moody JB (1979) Serpentinites, spilites and ophiolite metamorphism. *The Canadian Mineralogist* 17(4):871-887
- Moran AE, Sisson VB and Leeman WP (1992) Boron depletion during progressive metamorphism: Implications for subduction processes. *Earth and Planetary Science Letters* 111(2-4):331-349
- Moriguti T, Shibata T and Nakamura E (2004) Lithium, boron and lead isotope and trace element systematics of

## References

---

- Quaternary basaltic volcanic rocks in northeastern Japan: mineralogical controls on slab-derived fluid composition. *Chemical Geology* 212(1-2):81-100
- Mottl MJ (1983) Metabasalts, axial hot springs, and the structure of hydrothermal systems at mid-ocean ridges. *Geological Society of America Bulletin* 94(2):161-180
- Mottl MJ (1992) Pore waters from seamounts in Mariana and Izu-Bonin forearcs, Leg 125: evidence for volatiles from the subduction slab. In: Fryer P, Pearce, J.A., Stokking, L.B., et al. (ed) *Proceeding Ocean Drilling Program, Scientific Results, 125*. College Station, TX (Ocean Drilling Program), pp 373-385
- Mottl MJ, Fryer P and Wheat CG (2007) Decarbonation, Serpentinization, Abiogenic Methane, and Extreme pH beneath the Mariana Forearc. In: *Subduction Factory Studies in the Izu-Bonin-Mariana Arc System: Results and Future Plans, Joint NSF-MARGINS and IFREE Workshop*
- Mottl MJ, Komor SC, Fryer P and Moyer CL (2003) Deep-slab fuel extremophilic Archaea on a Mariana forearc serpentinite mud volcano: Ocean Drilling Program Leg 195. *Geochemistry Geophysics Geosystems* 4
- Mottl MJ, Wheat CG, Fryer P, Gharib J and Martin JB (2004) Chemistry of springs across the Mariana forearc shows progressive devolatilization of the subducting plate. *Geochimica Et Cosmochimica Acta* 68(23):4915-4933
- Mottl MJ, Wheat G, Baker E, Becker N, Davis E, Feely R, Grehan A, Kadko D, Lilley M, Massoth G, Moyer C and Sansone FT (1998) Warm springs discovered on 3.5 Ma oceanic crust, eastern flank of the Juan de Fuca Ridge. *Geology* 26(1)
- Mumpton FA and Thompson CS (1966) The stability of brucite in the weathering zone of the New Idria serpentinite. *Clays Clay Minerals* 14:249-257
- Mumpton FA and Thompson CS (1975) Mineralogy and origin of the Coalinga asbestos deposit. *Clays and Clay Minerals* 23(2):131-143
- Nakanishi M, Tamaki K and Kobayashi K (1992) Magnetic anomaly lineations from Late Jurassic to Early Cretaceous in the west-central Pacific Ocean. *Geophysical Journal International* 109(3):701-719
- Nakano T and Nakamura E (2001) Boron isotope geochemistry of metasedimentary rocks and tourmalines in a subduction zone metamorphic suite. *Phys. Earth Planet. Inter.* 127:233-252
- Niu Y (1997) Mantle Melting and Melt Extraction Processes beneath Ocean Ridges: Evidence from Abyssal Peridotites. *Journal of Petrology* 38(8):1047-1074
- Niu Y and Hékinian R (1997) Basaltic liquids and harzburgitic residues in the Garrett Transform: a case study at fast-spreading ridges. *Earth and Planetary Science Letters* 146(1-2):243-258
- Normand C, Williams-Jones AE, Martin RF and Vali H (2002) Hydrothermal alteration of olivine in a flow-through autoclave: Nucleation and growth of serpentine phases. *American Mineralogist* 87(11-12):1699-1709
- Oakley AJ, Taylor B and Moore GF (2008) Pacific Plate subduction beneath the central Mariana and Izu-Bonin fore arcs: New insights from an old margin. *Geochemistry Geophysics Geosystems* 9
- O'Hanley DS (1996) *Serpentinites, records of tectonic and petrological history*, Oxford Monographs on Geology and Geophysics 34, Oxford University Press, New York, Oxford
- O'Hanley DS and Dyar MD (1993) The composition of lizardite 1T and, the formation of magnetite in serpentinites. *American Mineralogist* 78(3-4):391-404
- O'Hanley DS, Schandl ES and Wicks FJ (1992) The origin of rodingites from Cassiar, British-Columbia, and their use to estimate T and P(H<sub>2</sub>O) during serpentinization. *Geochimica et Cosmochimica Acta* 56: pp 97-108
- O'Hanley DS and Wicks FJ (1995) Conditions of formation of lizardite, chrysotile and antigorite, Cassiar, British-Columbia. *The Canadian Mineralogist* 33:753-773
- Okino K, Matsuda K, Christie DM, Nogi Y and Koizumi K (2004) Development of oceanic detachment and asymmetric spreading at the Australian-Antarctic Discordance. *Geochemistry Geophysics Geosystems* 5
- Olsher U, Izatt RM, Bradshaw JS and Dalley NK (1991) Coordination chemistry of lithium ion. A crystal and molecular-structure review. *Chemical Reviews* 91(2):137-164



- Ottolini L, Bottazzi P and Vannucci R (1993) Quantification of lithium, beryllium, and boron in silicates by secondary-ion mass-spectrometry using conventional energy-filtering *Analytical Chemistry* 65(15):1960-1968
- Ottolini L, Le Fevre B and Vannucci R (2004) Direct assessment of mantle boron and lithium contents and distribution by SIMS analyses of peridotite minerals. *Earth and Planetary Science Letters* 228(1-2):19-36
- Page NJ (1967a) Serpentinization at Burro Mountain, California. *Contributions to Mineralogy and Petrology* 14(4):321-342
- Page NJ (1967b) Serpentinization considered as a constant volume metasomatic process: a discussion. *American Mineralogist* 52:545-549
- Palandri JL and Reed MH (2004) Geochemical models of metasomatism in ultramafic systems: serpentinization, rodingitization, and sea floor carbonate chimney precipitation. *Geochimica Et Cosmochimica Acta* 68(5):1115-1133
- Palmer MR and Helvacı C (1997) The boron isotope geochemistry of the neogene borate deposits of western Turkey. *Geochimica Et Cosmochimica Acta* 61(15):3161-3169
- Palmer MR, London D, Morgan Vi GB and Babb HA (1992) Experimental determination of fractionation of  $^{11}\text{B}/^{10}\text{B}$  between tourmaline and aqueous vapor: A temperature- and pressure-dependent isotopic system. *Chemical Geology: Isotope Geoscience section* 101(1-2):123-129
- Palmer MR, Spivack AJ and Edmond JM (1987) Temperature and pH controls over isotopic fractionation during adsorption of boron on marine clay. *Geochimica Et Cosmochimica Acta* 51(9):2319-2323
- Palmer MR and Swihart GH (1996) Boron isotope geochemistry: an overview. In: Grew ES and Anovitz IM (eds) *Boron: Mineralogy, Petrology and Geochemistry*, Reviews in Mineralogy 33, pp 709-744
- Parkinson IJ and Pearce JA (1998) Peridotites from the Izu-Bonin-Mariana Forearc (ODP Leg 125): Evidence for Mantle Melting and Melt-Mantle Interaction in a Supra-Subduction Zone Setting. *Petrology* 39(9):1577-1618
- Peacock SA (1990) Fluid Processes in Subduction Zones. *Science* 248(4953):329-337
- Peacock SM (1987) Creation and Preservation of Subduction-Related Inverted Metamorphic Gradients. *Journal of Geophysical Research* 92
- Peacock SM (1996) Thermal and petrologic structure of subduction zones In: Bebout GE, et al. (ed) *Subduction: Top to Bottom*, AGU Geophysical Monograph 96, Washington, D.C., pp 119-133
- Peacock SM (2001) Are the lower planes of double seismic zones caused by serpentine dehydration in subducting oceanic mantle? *Geology* 29(4):299-302
- Peacock SM (2003) Thermal structure and metamorphic evolution of subducting slabs. In: Eiler JM (ed) *Inside the Subduction Factory*, Geophysical Monograph Series, American Geophysical Union, Washington, DC, pp 7-22
- Peacock SM and Hervig RL (1999) Boron isotopic composition of subduction-zone metamorphic rocks. *Chemical Geology* 160(4):281-290
- Peacock SM and Hyndman RD (1999) Hydrous minerals in the mantle wedge and the maximum depth of subduction thrust earthquakes. *Geophysical Research Letters* 26(16):2517-2520
- Peacock SM and Wang K (1999) Seismic consequences of warm versus cool subduction metamorphism: Examples from southwest and northeast Japan. *Science* 286(5441):937-939
- Pearce JA, Barker PF, Edwards SJ, Parkinson IJ and Leat PT (2000) Geochemistry and tectonic significance of peridotites from the South Sandwich arc-basin system, South Atlantic. *Contributions to Mineralogy and Petrology* 139(1):36-53
- Pearce NJG, Perkins WT, Westgate JA, Gorton MP, Jackson SE, Neal CR and Chenery SP (1997) A compilation of new and published major and trace element data for NIST SRM 610 and NIST SRM 612 glass reference materials. *Geostandards Newsletter-the Journal of Geostandards and Geoanalysis* 21(1):115-144
- Pelletier L (2008) *The oceanic mantle as an important repository for the light elements Li, Be and B*. University of Neuchâtel, Swiss. Phd thesis

## References

---

- Pelletier L, Müntener O, Kalt A, Vennemann TW and Belgya T (2008a) Emplacement of ultramafic rocks into the continental crust monitored by light and other trace elements: An example from the Geisspfad body (Swiss-Italian Alps). *Chemical Geology* 255(1-2):143-159
- Pelletier L, Vils F and Kalt A (2006) Li, Be and B in Pindos and Vourinos mantle rocks (Greece): Evidence against a supra-subduction origin. *Geochimica Et Cosmochimica Acta* 70(18, Supplement 1):A481-A481
- Pelletier L, Vils F, Kalt A and Gmeling K (2008b) Li, B and Be Contents of Harzburgites from the Dramala Complex (Pindos Ophiolite, Greece): Evidence for a MOR-type Mantle in a Supra-subduction Zone Environment. *Petrology*:57
- Peters T (1965) A water-bearing andradite from total serpentine (Davos Switzerland). *American Mineralogist* 50(9):1482-1486
- Phipps SP and Ballotti DL (1992) Rheology of serpentinite muds in the Mariana-Izu-Bonin forearc. In: Fryer P, Pearce, JA, Stokking, LB et al. (ed) *Proceedings of the Ocean Drilling Program, Bonin/Mariana region, 125*. College Station, TX (Ocean Drilling Program), pp 363-372
- Pichler H and Schmitt-Riegraf C (1997) *Rock-forming Minerals in Thin Section*, Springer, Netherland
- Plank T and Langmuir CH (1998) The chemical composition of subducting sediment and its consequences for the crust and mantle. *Chemical Geology* 145(3-4):325-394
- Pokrovsky OS, Schott J and Castillo A (2005) Kinetics of brucite dissolution at 25°C in the presence of organic and inorganic ligands and divalent metals. *Geochimica Et Cosmochimica Acta* 69(4):905-918
- Pouchou JL and Pichoir F (1984) A new model for quantitative analyses. I. Application to the analysis of homogeneous samples. *La Recherche Aérospatiale* 3:13-38
- Quinby-Hunt MS and Turekian KK (1983) Distribution of elements in sea water. *EOS* 64:130-132
- Ranero CR, Morgan PJ, McIntosh K and Reichert C (2003) Bending-related faulting and mantle serpentinization at the Middle America trench. *Nature* 45:367-373
- Ranoroosa N, Fontan F and Fransolet AM (1989) Rediscovery of manandonite in the Sahatany Valley, Madagascar. *European Journal of Mineralogy* 1(5):633-638
- Rea DK and Ruff LJ (1996) Composition and mass flux of sediment entering the world's subduction zones: Implications for global sediment budgets, great earthquakes, and volcanism. *Earth and Planetary Science Letters* 140(1-4):1-12
- Reinen LA (2000) Seismic and aseismic slip indicators in serpentinite gouge. *Geology* 28(2):135-138
- Reinen LA, Weeks JD and Tullis TE (1994) The frictional behavior of lizardite and antigorite serpentinites: Experiments, constitutive models, and implications for natural faults. *Pure and Applied Geophysics* 143(1):317-358
- Richards MA and Lithgow-Bertelloni C (1996) Plate motion changes, the Hawaiian-Emperor bend, and the apparent success and failure of geodynamic models. *Earth and Planetary Science Letters* 137(1-4):19-27
- Rinaudo C, Gastaldi D and Belluso E (2003) Characterization of chrysotile, antigorite and lizardite by FT-Raman spectroscopy. *The Canadian Mineralogist* 41:883-890
- Rose EF, Shimizu N, Layne GD and Grove TL (2001) Melt production beneath Mt. Shasta from boron data in primitive melt inclusions. *Science* 293(5528):281-283
- Rosner M, Erzinger J, Franz G and Trumbull RB (2003) Slab-derived boron isotope signatures in arc volcanic rocks from the Central Andes and evidence for boron isotope fractionation during progressive slab dehydration. *Geochemistry, Geophysics, Geosystems* 4
- Rosner M, Wiedenbeck M and Ludwig T (2008) Composition-Induced Variations in SIMS Instrumental Mass Fractionation during Boron Isotope Ratio Measurements of Silicate Glasses. *Geostandards and Geoanalytical Research* 32(1):27-38
- Ryan JG (2002) Trace-elements systematics of beryllium in terrestrial materials. In: ES G (ed) *Beryllium: mineralogy, petrology and geochemistry*, Reviews in Mineralogy and Geochemistry 50, Mineralogical Society of America, Washington, DC, pp 121-145

- Ryan JG and Langmuir CH (1987) The systematics of lithium abundances in young volcanic rocks. *Geochimica Et Cosmochimica Acta* 51(6):1727-1741
- Ryan JG and Langmuir CH (1988) Beryllium systematics in young volcanic-rocks - implications for Be-10. *Geochimica Et Cosmochimica Acta* 52(1):237-244
- Ryan JG and Langmuir CH (1993) The systematic of boron abundances in young volcanic-rocks. *Geochimica Et Cosmochimica Acta* 57(7):1489-1498
- Ryan JG, Leeman WP, Morris JD and Langmuir CH (1996a) The boron systematics of intraplate lavas: implications for crustal and mantle evolution. *Geochimica et Cosmochimica Acta* 60:415-422
- Ryan JG, Morris J, Bebout G and Leeman WP (1996b) Describing chemical fluxes in subduction zones: insights from "depth profiling" studies of arc and forearc rocks. In: Bebout GE SD, Kirby SH, Platt JP (ed) *Geophysical Monograph Series* 96. pp 263-268
- Ryan JG, Morris J, Tera F, Leeman WP and Tsvetkov A (1995) Cross-arc geochemical variations in the Kurile-arc as a function of slab depth. *Science* 270(5236):625-627
- Salisbury M, Shinohara, M, Richter, C, et al., (2002) Initial Reports 195. In: *Proceeding of the Ocean Drilling Program, 195*, College Station, TX (Ocean Drilling Program)
- Salisbury MH, Shinohara, Masanao, Richter, Carl, et al. (2002) Leg 195 summary. In: Salisbury MH, Shinohara, Masanao, Richter, Carl, et al. (ed) *Proceedings of the Ocean Drilling Program, Initial Reports, 195*. College Station, TX (Ocean Drilling Program), p 63
- Salters VJM and Stracke A (2004) Composition of the depleted mantle. *Geochemistry Geophysics Geosystems* 5(5)
- Samowitz IR and Forsyth DW (1981) Double Seismic Zone Beneath the Mariana Island Arc. *Journal of Geophysical Research* 86
- Sample JC and Karig DE (1982) A volcanic production rate for the Mariana island arc. *Journal of Volcanology and Geothermal Research* 13 73-82
- Sano T, Hasenka T, Shimaoka A, Yonezawa C and Fukuoka T (2001) Boron contents of Japan Trench sediments and Iwate basaltic lavas, Northeastern Japan: estimation of sediment-derived fluid contribution in mantle wedge. *Earth and Planetary Science Letters* 186:187-198
- Satoh H, Yamaguchi Y and Makino K (2004) Ti-substitution mechanism in plutonic oxy-kaersutite from the Larvik alkaline complex, Oslo rift, Norway. *Mineralogical Magazine* 68(4):687-697
- Savov IP, Guggino S, Ryan JG, Fryer P and Mottl MJ (2005a) Geochemistry of serpentinite muds and metamorphic rocks from the Mariana forearc, ODP Sites 1200 and 778-779, South Chamorro and Conical Seamounts. In: Shinohara M, Salisbury, M.H. and Richter, C. (ed) *Proceedings of the Ocean Drilling Program, Scientific Results*. College Station, TX (Ocean Drilling Program)
- Savov IP, Ryan JG, D'Antonio M and Fryer P (2007) Shallow slab fluid release across and along the Mariana arc-basin system: Insights from geochemistry of serpentinitized peridotites from the Mariana fore arc. *Journal of Geophysical Research-Solid Earth* 112
- Savov IP, Ryan JG, D'Antonio M, Kelley K and Mattie P (2005b) Geochemistry of serpentinitized peridotites from the Mariana Forearc Conical Seamount, ODP Leg 125: Implications for the elemental recycling at subduction zones. *Geochemistry Geophysics Geosystems* 6
- Savov IP, Tonarini S, Ryan J and Mottl M (2004) Boron isotope geochemistry of serpentinites and porefluids from Leg 195, Site 1200, S.Chamorro Seamount, Mariana forearc region. *International Geological Congress (IGC), Florence, Italy*
- Schenzel K, Fischer S and Brendler E (2005) New Method for Determining the Degree of Cellulose I Crystallinity by Means of FT Raman Spectroscopy. *Cellulose* 12(3):223-231
- Shipboard Scientific Party, 2002a. Leg 195 summary. In: Salisbury, M.H., Shinohara, M., Richter, C., et al., *Proc. ODP, Init. Repts., 195*. College Station, TX (Ocean Drilling Program), 1-63
- Shipboard Scientific Party, 2002b. Explanatory notes. In: Salisbury, M.H., Shinohara, M., Richter, C., et al., *Proceedings of the Ocean Drilling Program, Initial Reports, 195*. College Station, TX (Ocean Drilling Program), 1-56
- Shipboard Scientific Party, 2002c. Site 1200. In: Salisbury, M.H., Shinohara, M., Richter, C., et al.,

## References

---

- Proceedings of the Ocean Drilling Program, Initial Reports, 195*. College Station, TX (Ocean Drilling Program), 1–173
- Shipboard Scientific Party, 1990a. Site 779. In: Fryer, P., Pearce, J.A., Stokking, L.B., et al., *Proceedings of the Ocean Drilling Program, Initial Reports, 125*. College Station, TX (Ocean Drilling Program), 115–145
- Shipboard Scientific Party, 1990b. Site 780. In: Fryer, P., Pearce, J.A., Stokking, L.B., et al., *Proceedings of the Ocean Drilling Program, Initial Reports, 125*. College Station, TX (Ocean Drilling Program), 147–178
- Shipboard Scientific Party, 1990c. 7. Site 779. In: Fryer, P., Pearce, J. A., Stokking, L. B., et al., *Proceedings of the Ocean Drilling Program, Initial Reports, 125*. College Station, TX (Ocean Drilling Program)
- Shipboard Scientific Party, 1990d. 8. Site 801. In: Lancelot, Y., Larson, R. L., et al., *Proceedings of the Ocean Drilling Program, Initial Reports, 129*. College Station, TX (Ocean Drilling Program)
- Schmidt C, Thomas R and Heinrich W (2005) Boron speciation in aqueous fluids at 22 to 600 degrees C and 0.1 MPa to 2 GPa. *Geochimica Et Cosmochimica Acta* 69:275-281
- Schmidt K, Koschinsky A, Garbe-Schönberg D, de Carvalho LM and Seifert R (2007) Geochemistry of hydrothermal fluids from the ultramafic-hosted Logatchev hydrothermal field, 15°N on the Mid-Atlantic Ridge: Temporal and spatial investigation. *Chemical Geology* 242(1-2):1-21
- Scholz CH and Small C (1997) The effect of seamount subduction on seismic coupling. *Geology* 25:487-490
- Seitz HM and Woodland AB (2000) The distribution of lithium in peridotitic and pyroxenitic mantle lithologies - an indicator of magmatic and metasomatic processes. *Chemical Geology* 166(1-2):47-64
- Seno T and Maruyama S (1984) Paleogeographic reconstruction and origin of the Philippine Sea. *Tectonophysics* 102(1-4):53-84
- Seno T, Stein S and Gripp AE (1993) A Model for the Motion of the Philippine Sea Plate Consistent With NUVEL-1 and Geological Data. *Geophysical Research* 98
- Seyfried Jr WE and Dibble Jr WE (1980) Seawater-peridotite interaction at 300°C and 500 bars: implications for the origin of oceanic serpentinites. *Geochimica Et Cosmochimica Acta* 44(2):309-321
- Seyfried WE, Chen X and Chan LH (1998) Trace Element Mobility and Lithium Isotope Exchange During Hydrothermal Alteration of Seafloor Weathered Basalt: An Experimental Study at 350°C, 500 Bars - Implications for fluid processes at shallow depths in subduction zones. *Geochimica Et Cosmochimica Acta* 62:949-960
- Seyfried WE, Foustoukos DI and Fu Q (2007) Redox evolution and mass transfer during serpentinization: An experimental and theoretical study at 200 degrees C, 500 bar with implications for ultramafic-hosted hydrothermal systems at Mid-Ocean Ridges. *Geochimica Et Cosmochimica Acta* 71(15):3872-3886
- Seyler M, Toplis MJ, Lorand JP, Luguët A and Cannat M (2001) Clinopyroxene microtextures reveal incompletely extracted melts in abyssal peridotites. *Geology* 29(2):155-158
- Sharma A and Jenkins DM (1999) Hydrothermal synthesis of amphiboles along the tremolite-pargasite join and in the ternary system tremolite-pargasite-cummingtonite. *American Mineralogist* 84(9):1304-1318
- Shervais J, Kimbrough D, Renne P, Hanan B, Murchey B, Snow C, Schuman MZ and Beaman J (2004) Multi-Stage Origin of the Coast Range Ophiolite, California: Implications for the Life Cycle of Supra-Subduction Zone Ophiolites. *International Geology Review* 46(4):289 - 315
- Shibley TH, McIntosh KD, Silver EA and Stoffa PL (1992) Three-Dimensional Seismic Imaging of the Costa Rica Accretionary Prism: Structural Diversity in a Small Volume of the Lower Slope. *Journal of Geophysical Research* 97
- Smith HJ, Leeman WP, Davidson J and Spivack AJ (1997) The B isotopic composition of arc lavas from Martinique, Lesser Antilles. *Earth and Planetary Science Letters* 146(1-2):303-314
- Smith HJ, Spivack AJ, Staudigel H and Hart SR (1995) The boron isotopic composition of altered oceanic crust. *Chemical Geology* 126(2):119-135
- Snyder GT, Savov IP and Muramatsu Y (2005) Iodine and boron in Mariana serpentinite mud volcanoes (ODP Legs 125 and 195): implications for forearc processes and subduction recycling. In: Shinohara M, Salisbury, M.H., and Richter, C. (ed) *Proceedings of the Ocean Drilling Program, Scientific Results, 195*. College Station, TX (Ocean Drilling Program), pp 1-18

- Sorensen SS (1988) Petrology of amphibolite-facies mafic and ultramafic rocks from the Catalina schist, Southern-California - metasomatism and migmatization in a subduction zone metamorphic setting. *Journal of Metamorphic Geology* 6(4):405-435
- Sorensen SS and Grossman JN (1989) Enrichment of trace-elements in garnet amphibolites from a Paleosubduction zone-Catalina schist, Southern California. *Geochimica Et Cosmochimica Acta* 53(12):3155-3177
- Spear FS (1993) Metamorphic phase equilibria and pressure-temperature-time path. *Mineralogical Society of America Monograph*:482-483
- Speziale S, Jeanloz R, Milner A, Pasternak MP and Zaug JM (2005) Vibrational spectroscopy of Fe(OH)<sub>2</sub> at high pressure: Behavior of the O-H bond. *Physical Review B* 71(18)
- Spivack AJ and Edmond JM (1987) Boron isotope exchange between seawater and the oceanic crust. *Geochimica Et Cosmochimica Acta* 51(5):1033-1043
- Spivack AJ, Palmer MR and Edmond JM (1987) The sedimentary cycle of the boron isotopes. *Geochimica Et Cosmochimica Acta* 51(7):1939-1949
- Stephan T (2001) TOF-SIMS in cosmochemistry. *Planetary and Space Science* 49(9):859-906
- Stern RJ (2002) Subduction zones. *Reviews of Geophysics* 40(4)
- Stern RJ and Bloomer SH (1992) Subductions zone infancy- examples from the Eocene Izu-Bonin- Mariana and Jurassic California arcs *Geological Society of America Bulletin* 104(12):1621-1636
- Stern RJ, Fouch MJ and Klemperer S (2003) An overview of the Izu-Bonon-Mariana subduction factory. *Geophysical Monograph Series* 138:175-223
- Stern RJ, Morris J, Bloomer SH and Hawkins JW (1991) The source of the subduction component in convergent margin magmas: Trace-element and radiogenic isotope evidence from Eocene boninites, Mariana forearc. *Geochimica Et Cosmochimica Acta* 55(5):1467-1481
- Strahm B, Howling AA, Sansonnens L and Hollenstein C (2007) Plasma silane concentration as a determining factor for the transition from amorphous to microcrystalline silicon in SiH<sub>4</sub>/H<sub>2</sub> discharges. *Plasma Sources Science & Technology* 16(1):80-89
- Straub SM and Layne GD (2002) The systematics of boron isotopes in Izu arc front volcanic rocks. *Earth and Planetary Science Letters* 198(1-2):25-39
- Straub SM and Layne GD (2003) The serpentinization of subduction zones - evidence from the Izu arc volcanic front. *State-of-the-arc (SOTA) meeting*, Timberline Lodge, Mt. Hood, Oregon, USA.
- Takahashi E, Uto K and Schilling JG (1987) Primary magma compositions and Mg / Fe ratios of their mantle residues along Mid Atlantic Ridges 29°N to 73°N. *Technical Report ISEI, Okayama University A-9:1-12*
- Tatsumi Y (1989) Migration of fluid phases and genesis of basalt magma at subduction zones. *Journal of Geophysical Research* 94:4697-4707
- Tatsumi Y and Eggins SM (1995) *Subduction Zone Magmatism*, Blackwell, Oxford
- Tatsumi Y and Isoyama H (1988) Transportation of beryllium with H<sub>2</sub>O at high pressure implication for magma genesis in subduction zones. *Geophysical Research Letters* 15(2):180-183
- Taylor B (1992) Rifting and the volcanic-tectonic evolution of the Izu-Bonin-Mariana Arc. In: Taylor B. FK (ed) *Proceedings of the Ocean Drilling Program, Scientific Results, 126*. College Station, TX (Ocean Drilling Program), pp 627-651
- Taylor HPJ and Coleman RG (1968) <sup>18</sup>O/<sup>16</sup>O ratios of coexisting minerals in glaucophane-bearing metamorphic rocks. *Bull. Geol. Soc. Am.* 79:1727-1756
- Taylor RN, Nesbitt RW, Vidal P, Harmon RS, Auvray B and Croudace IW (1994) Mineralogy, chemistry, and genesis of the boninite series of volcanics, Chichijima, Bonon-Islands, Japan. *Journal of Petrology* 35(3):577-617
- Thompson G and Melson WG (1970) Boron contents of serpentinites and metabasalts in the oceanic crust: Implications for the boron cycle in the oceans. *Earth and Planetary Science Letters* 8(1):61-65
- Tomascak PB, Widom E, Benton LD, Goldstein SL and Ryan JG (2002) The control of lithium budgets in

## References

---

- island arcs. *Earth and Planetary Science Letters* 196(3-4):227-238
- Tomkins HS, Powell R and Ellis DJ (2007) The pressure dependence of the zirconium-in-rutile thermometer. *Journal of Metamorphic Geology* 25(6):703-713
- Tonarini S, Armienti P, D'Orazio M and Innocenti F (2001) Subduction-like fluids in the genesis of Mt. Etna magmas: evidence from boron isotopes and fluid mobile elements. *Earth and Planetary Science Letters* 192(4):471-483
- Tonarini S, Forte C, Petrini R and Ferrara GB (2003) Melt/biotite B-11/B-10 isotopic fractionation and the boron local environment in the structure of volcanic glasses. *Geochimica Et Cosmochimica Acta* 67(10):1863-1873
- Tröger E (1959) The garnet group relation between mineral chemistry and rock type. *Neues Jahrbuch der Mineralogie* 93:1-44
- Ulmer P and Trommsdorff V (1995) Serpentinite stability to mantle depths and subduction-related magmatism. *Science* 268(5212):858-861
- Uyeda S (1982) Subduction zones: An introduction to comparative subductology. *Tectonophysics* 81(3-4):133-159
- van der Hilst R and Seno T (1993) Effects of relative plate motion on the deep structure and penetration depth of slabs below the Izu-Bonin and Mariana island arcs. *Earth and Planetary Science Letters* 120(3-4):395-407
- Vils F (2009) *Light elements in oceanic and ophiolitic serpentinites*. University of Neuchâtel, Swiss. Phd thesis
- Vils F, Pelletier L, Kalt A and Müntener O (2006) Potential input of light elements into subduction zones- Insights from ODP leg 209. *Geochimica Et Cosmochimica Acta* 70(18, Supplement 1):A674-A674
- Vils F, Pelletier L, Kalt A, Müntener O and Ludwig T (2008) The Lithium, Boron and Beryllium content of serpentinized peridotites from ODP Leg 209 (Sites 1272A and 1274A): Implications for lithium and boron budgets of oceanic lithosphere. *Geochimica Et Cosmochimica Acta* 72(22):5475-5504
- Vils F, Tonarini S, Kalt A and Seitz H-M (2009) Boron, lithium and strontium isotopes as tracers of seawater-serpentinite interaction at Mid-Atlantic ridge, ODP Leg 209. *Earth and Planetary Science Letters* 286(3-4):414-425
- Viti C and Mellini M (1998) Mesh textures and bastites in the Elba retrograde serpentinites *European Journal of Mineralogy* 10(6):1341-1359
- Von Damm KL, Edmond JM, Measures CI and Grant B (1985) Chemistry of submarine hydrothermal solutions at Guaymas Basin, Gulf of California. *Geochimica Et Cosmochimica Acta* 49(11):2221-2237
- Whittaker EJW and Zussman J (1956) The characterization of serpentine minerals by X-ray diffraction. *Mineralogical Magazine* 233:107-126
- Wicks FJ (1984) Deformation histories as recorded by serpentinites; II, Deformation during and after serpentinization. *The Canadian Mineralogist* 22(1):197-203
- Wicks FJ and O'Hanley FC (1988) Serpentine minerals: Structures and petrology. In: Bailey SWE (ed) *Hydrous Phyllosilicates (exclusive of micas)*, vol 19. Reviews in Mineralogy, Mineralogical Society of America, Chantilly, Virginia, pp 91-159
- Wicks FJ and Plant AG (1979) Electron-microprobe and X-ray microbeam studies of serpentine textures. *The Canadian Mineralogist* 17(4):785-830
- Wicks FJ and Whittaker EJW (1975) A reappraisal of the structures of the serpentine minerals *The Canadian Mineralogist* 13(3):227-243
- Wicks FJ and Whittaker EJW (1977) Serpentine textures and serpentinization. *The Canadian Mineralogist* 15:459-488
- Williams IB (2002) Application of boron isotopes to the understanding of fluid-rock interactions in a hydrothermally stimulated oil reservoir in the Alberta Basin, Canada. *Fuel and Energy Abstracts* 43(4):240-241
- Williams LB, Wieser ME, Fennell J, Hutcheon I and Hervig RL (2001) Application of boron isotopes to the understanding of fluidrock interactions in a hydrothermally stimulated oil reservoir in the Alberta Basin,

- Canada. *Geofluids* 1:229-240
- Winterer EL, Natland JH, Van Waagsbergen RJ, Duncan RA, McNutt MK, Wolfe CJ, Silva IP, Sager WW and Sliter WV (1993) Cretaceous Guyots in the Northwest Pacific: An overview of their Geology and Geophysics. In: Prigle MSS, W.W. Sliter, W.V. Stein, S. (ed) *The Mesozoic Pacific: Geology, Tectonics, and Volcanism*, Geophysical Monograph 97, American Geophysical Union, pp 307-334
- Woodland AB, Seitz HM and Yaxley GM (2004) Varying behaviour of Li in metasomatised spinel peridotite xenoliths from western Victoria, Australia. *Lithos* 75(1-2):55-66
- Wunder B, Meixner A, Romer RL, Wirth R and Heinrich W (2005) The geochemical cycle of boron: Constraints from boron isotope partitioning experiments between mica and fluid. *Lithos* 84(3-4):206-216
- Wunder B and Schreyer W (1997) Antigorite: High pressure stability in the system MgO-SiO<sub>2</sub>-H<sub>2</sub>O (MSH). *Lithos* 41(1-3):213-227
- Wunder B, Wirth R and Gottschalk M (2001) Antigorite: Pressure and temperature dependence of polysomatism and water content. *European Journal of Mineralogy* 13(3):485-495
- Xie XG, Byerly GR and Ferrell RE (1997) IIb trioctahedral chlorite from the Barberton greenstone belt: Crystal structure and rock composition constraints with implications to geothermometry. *Contributions to Mineralogy and Petrology* 126(3):275-291
- Yamazaki T and Okamura Y (1989) Subducting seamounts and deformation of overriding forearc wedges around Japan. *Tectonophysics* 160(1-4)
- Yamazaki T and Stern RJ (1997) Topography and magnetic vector anomalies in the Mariana Trough. *JAMSTEC Deep Sea Resolution*, 13:31-45
- You CF, Spivack AJ, Gieskes JM, Rosenbauer R and Bischoff JL (1995) Experimental study of boron geochemistry: Implications for fluid processes in subduction zones. *Geochimica Et Cosmochimica Acta* 59(12):2435-2442
- Zack T, Tomascak PB, Rudnick RL, Dalpé C and McDonough WF (2003) Extremely light Li in orogenic eclogites: The role of isotope fractionation during dehydration in subducted oceanic crust. *Earth and Planetary Science Letters* 208(3-4):279-290
- Zagorsky VY, Peretyazhko, IS, Sapozhnikov, AN, Zhukhlistov, AP, and Zvyagin, BB (2003) Borocookeite, a new member of the chlorite group from the Malkhan gem tourmaline deposit, Central Transbaikalia, Russia. *American Mineralogist* 88, p. 830-836
- Zanetti A, D'Antonio M, Spadea P, Raffone N, Vannucci R and Brugeir O (2006) Petrogenesis of mantle peridotites from the Izu-Bonin-Mariana (IBM) forearc. *Ophioliti* 31(2):189-206





## Appendix A

A1: Documentation of reference minerals for $\delta^{11}\text{B}$ SIMS analyses and matrix correction	160
A2: Composition of reference minerals	162
A3: List of mineral abbreviations	165

**A1: Documentation of reference minerals for  $\delta^{11}\text{B}$  SIMS analyses and matrix correction**

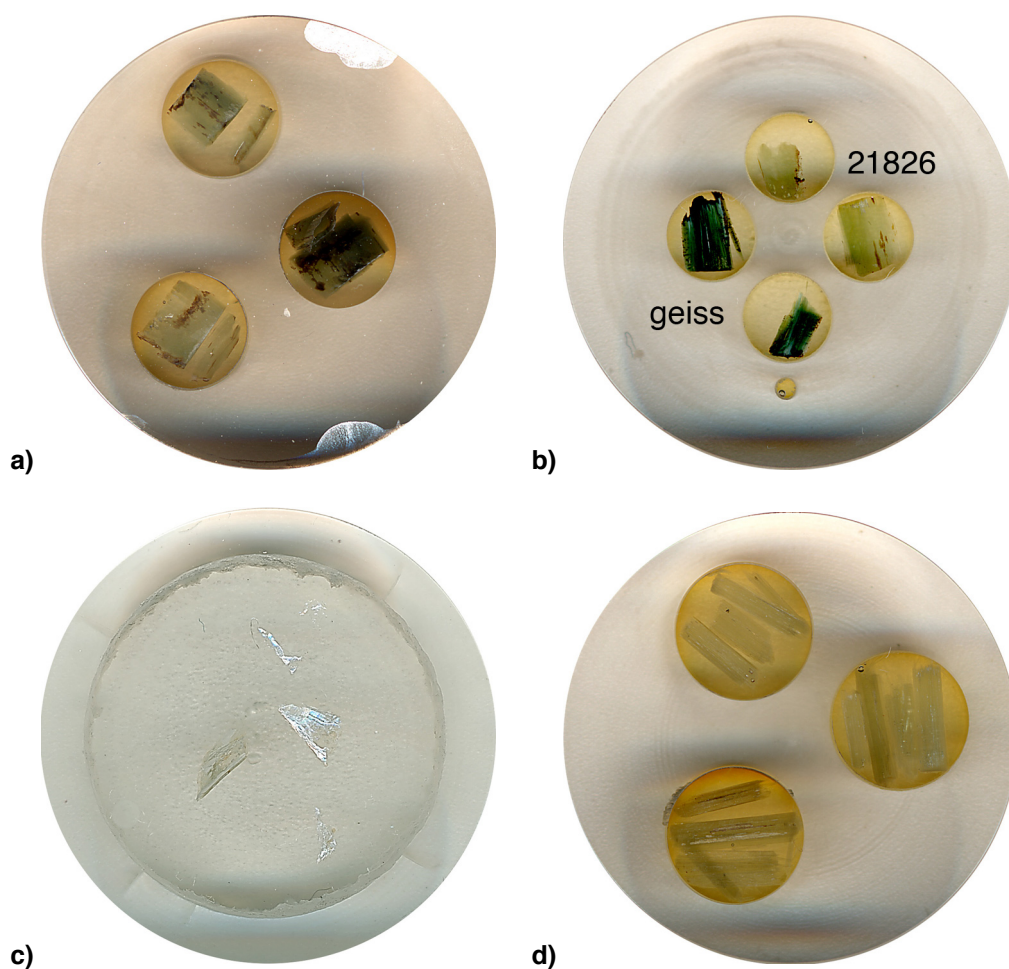


**Fig. A1:** Scans of 1-inch round samples with embedded crystals, **a)** serpentine 21826, **b)** serpentine '21826' and 'geiss', **c)** phengite 80-3, and **d)** amphibole '21805'.

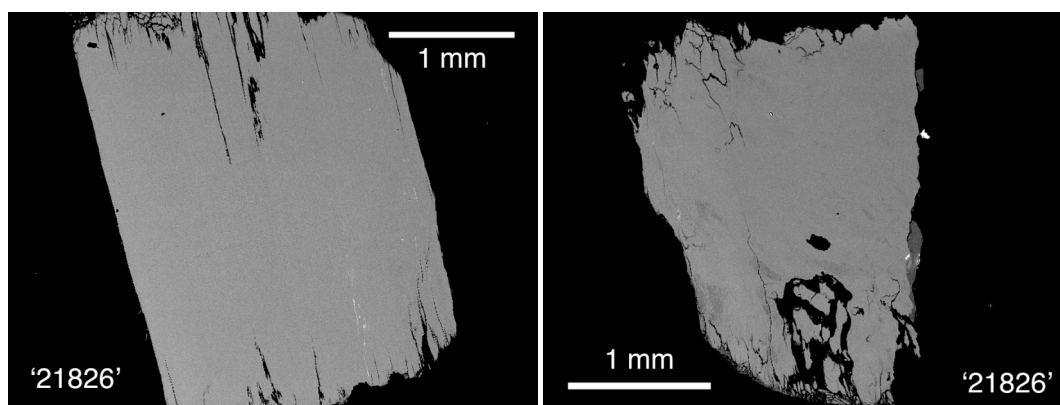


**Fig. A2:** Back-scattered electron (BSE) images of serpentine '21826'.

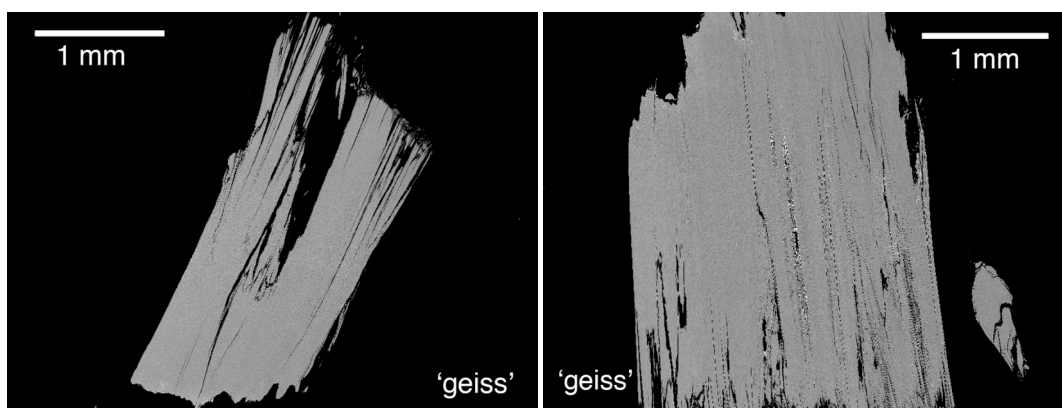


**Fig. A3:** Back-scattered electron (BSE) images of serpentine 'geiss'.

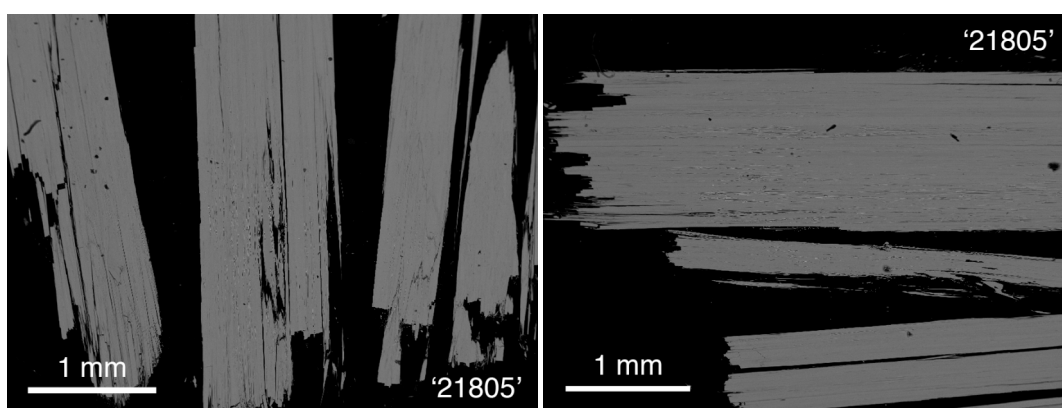


**Fig. A4:** Back-scattered electron (BSE) images of amphibole '21805'.

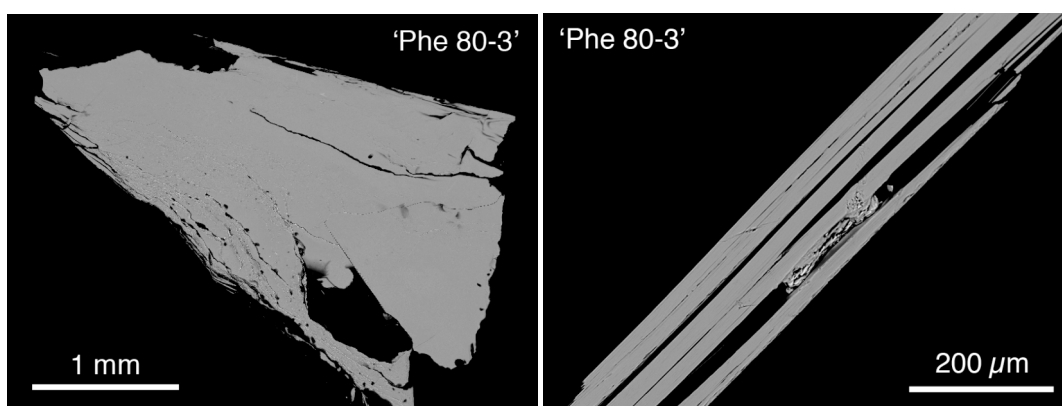


**Fig. A5:** Back-scattered electron (BSE) images of phengite 'Phe 80-3'.

## A2: Composition of reference minerals

*Table A1: Representative composition of serpentine minerals 'geiss'.*

Analysis	geiss	geiss	geiss	geiss	geiss	geiss	geiss	geiss	geiss	geiss	geiss	geiss	geiss
<b>SiO<sub>2</sub></b>	43.34	43.12	42.87	42.85	43.03	42.88	42.46	42.48	42.29	42.75	43.11	42.68	45.81
<b>TiO<sub>2</sub></b>	0.02	0.02	0.02	0.03	0.04	0.06	0.03	0.03	0.05	0.01	0.02	0.02	0.02
<b>Al<sub>2</sub>O<sub>3</sub></b>	2.10	2.32	2.22	2.22	2.22	2.21	2.49	2.45	2.56	2.35	2.38	2.16	2.07
<b>Cr<sub>2</sub>O<sub>3</sub></b>	0.14	0.12	0.15	0.13	0.11	0.14	0.11	0.12	0.14	0.11	0.09	0.11	0.11
<b>FeO</b>	4.90	4.89	4.88	5.11	4.94	4.93	5.30	5.20	5.21	5.07	4.80	4.87	4.76
<b>MnO</b>	0.12	0.07	0.19	0.09	0.09	0.05	0.11	0.13	0.12	0.20	0.04	0.08	0.10
<b>NiO</b>	36.21	36.46	36.30	36.81	36.46	36.60	36.60	36.74	36.68	36.68	36.33	36.25	35.82
<b>MgO</b>	0.05	0.07	0.05	0.06	0.07	0.07	0.06	0.04	0.02	0.05	0.10	0.05	0.05
<b>CaO</b>	0.01	0.00	0.00	0.02	0.02	0.00	0.00	0.02	0.01	0.01	0.01	0.01	0.02
<b>Na<sub>2</sub>O</b>	0.02	0.00	0.01	0.00	0.01	0.00	0.00	0.01	0.01	0.01	0.01	0.03	0.00
<b>K<sub>2</sub>O</b>	0.22	0.21	0.24	0.19	0.18	0.14	0.16	0.16	0.11	0.19	0.17	0.19	0.20
<b>Total</b>	87.12	87.27	86.92	87.51	87.16	87.06	87.32	87.37	87.17	87.42	87.06	86.46	88.96
<b>Si</b>	4.066	4.039	4.036	4.013	4.039	4.031	3.991	3.990	3.982	4.009	4.045	4.039	4.182
<b>Ti</b>	0.002	0.001	0.001	0.002	0.003	0.004	0.002	0.002	0.003	0.001	0.001	0.002	0.002
<b>Al</b>	0.232	0.256	0.246	0.245	0.246	0.244	0.275	0.271	0.284	0.260	0.264	0.241	0.223
<b>Cr</b>	0.010	0.009	0.011	0.010	0.008	0.010	0.008	0.009	0.010	0.008	0.007	0.008	0.008
<b>Fe</b>	0.385	0.383	0.384	0.400	0.387	0.388	0.417	0.408	0.410	0.398	0.377	0.386	0.363
<b>Mn</b>	0.009	0.005	0.015	0.007	0.007	0.004	0.009	0.010	0.009	0.015	0.003	0.007	0.008
<b>Mg</b>	5.064	5.091	5.095	5.139	5.101	5.128	5.129	5.145	5.148	5.128	5.082	5.113	4.875
<b>Ca</b>	0.005	0.007	0.005	0.006	0.007	0.007	0.006	0.004	0.002	0.005	0.010	0.005	0.005
<b>Na</b>	0.001	0.000	0.000	0.003	0.003	0.000	0.000	0.004	0.001	0.001	0.001	0.002	0.004
<b>K</b>	0.002	0.000	0.001	0.000	0.001	0.000	0.000	0.001	0.001	0.001	0.002	0.004	0.000
<b>Ni</b>	0.074	0.069	0.083	0.065	0.062	0.046	0.054	0.055	0.037	0.065	0.058	0.065	0.064
<b>Total</b>	9.850	9.862	9.876	9.891	9.864	9.861	9.891	9.898	9.887	9.890	9.849	9.870	9.735
<b>Mg#</b>	92.78	92.91	92.73	92.65	92.82	92.91	92.35	92.49	92.47	92.54	93.04	92.87	92.93

Cation calculation is based on 14 oxygen.

*Table A2: Representative composition of serpentine minerals '21826'.*

Analysis	21826	21826	21826	21826	21826	21826	21826	21826	21826	21826	21826	21826	21826
<b>SiO<sub>2</sub></b>	43.05	42.76	43.32	43.40	43.66	43.42	42.99	43.20	43.13	42.80	43.13	43.00	43.17
<b>TiO<sub>2</sub></b>	0.04	0.01	0.03	0.05	0.03	0.04	0.03	0.03	0.06	0.05	0.01	0.03	0.03
<b>Al<sub>2</sub>O<sub>3</sub></b>	2.69	2.40	2.26	2.40	2.15	2.27	2.39	2.65	2.85	2.73	2.42	2.76	2.74
<b>Cr<sub>2</sub>O<sub>3</sub></b>	0.12	0.12	0.16	0.13	0.14	0.15	0.13	0.11	0.12	0.12	0.12	0.11	0.12
<b>FeO</b>	3.53	3.46	3.46	3.29	3.60	3.46	3.64	3.44	3.36	3.51	3.52	3.54	3.37
<b>MnO</b>	0.08	0.07	0.09	0.05	0.04	0.01	0.06	0.04	0.10	0.09	0.00	0.07	0.06
<b>NiO</b>	37.57	37.53	37.70	37.63	37.81	37.73	37.71	37.45	37.44	37.52	37.68	37.41	37.47
<b>MgO</b>	0.02	0.02	0.00	0.00	0.01	0.01	0.02	0.02	0.03	0.02	0.01	0.02	0.02
<b>CaO</b>	0.11	0.12	0.14	0.07	0.04	0.10	0.02	0.11	0.12	0.08	0.14	0.11	0.14
<b>Na<sub>2</sub>O</b>	0.15	0.21	0.44	0.09	0.10	0.12	0.10	0.16	0.16	0.17	0.28	0.27	0.25
<b>K<sub>2</sub>O</b>	0.14	0.18	0.15	0.17	0.13	0.12	0.18	0.08	0.17	0.12	0.13	0.15	0.15
<b>Total</b>	87.49	86.88	87.75	87.29	87.70	87.44	87.26	87.28	87.53	87.20	87.44	87.45	87.52
<b>Si</b>	4.004	4.007	4.024	4.035	4.045	4.035	4.009	4.022	4.004	3.995	4.015	4.002	4.011
<b>Ti</b>	0.003	0.001	0.002	0.003	0.002	0.003	0.002	0.002	0.004	0.003	0.001	0.002	0.002
<b>Al</b>	0.295	0.265	0.247	0.263	0.235	0.249	0.263	0.290	0.311	0.300	0.266	0.303	0.300
<b>Cr</b>	0.008	0.009	0.012	0.010	0.010	0.011	0.010	0.008	0.009	0.009	0.009	0.008	0.008
<b>Fe</b>	0.275	0.271	0.269	0.256	0.279	0.269	0.284	0.268	0.261	0.274	0.274	0.276	0.262
<b>Mn</b>	0.007	0.005	0.007	0.004	0.003	0.001	0.005	0.003	0.008	0.007	0.000	0.005	0.005
<b>Mg</b>	5.209	5.242	5.220	5.214	5.224	5.227	5.241	5.198	5.182	5.221	5.229	5.191	5.190
<b>Ca</b>	0.001	0.002	0.000	0.000	0.001	0.001	0.002	0.001	0.003	0.002	0.001	0.002	0.002
<b>Na</b>	0.020	0.022	0.026	0.013	0.007	0.018	0.004	0.019	0.022	0.015	0.025	0.019	0.026
<b>K</b>	0.017	0.025	0.052	0.011	0.012	0.014	0.011	0.019	0.019	0.020	0.033	0.031	0.030
<b>Ni</b>	0.045	0.060	0.050	0.058	0.044	0.039	0.061	0.028	0.058	0.039	0.045	0.051	0.050
<b>Total</b>	9.883	9.909	9.909	9.867	9.861	9.867	9.891	9.860	9.881	9.885	9.898	9.891	9.885
<b>Mg#</b>	94.88	94.99	94.98	95.25	94.88	95.09	94.79	95.04	95.07	94.90	95.01	94.86	95.11

Cation calculation is based on 14 oxygen.

Table A3: Representative composition of amphibole minerals '21805'.

Analysis	mg-kato	mg-kato	barroisite	mg-kato	mg-kato	barroisite	mg-kato	mg-kato	barroisite	mg-kato	mg-kato	barroisite	mg-kato
	21805	21805	21805	21805	21805	21805	21805	21805	21805	21805	21805	21805	21805
<b>SiO<sub>2</sub></b>	58.26	58.32	58.23	58.96	58.22	57.90	57.90	58.14	57.82	58.58	58.62	57.03	58.62
<b>TiO<sub>2</sub></b>	0.00	0.02	0.00	0.00	0.01	0.00	0.01	0.05	0.00	0.01	0.02	0.00	0.02
<b>Al<sub>2</sub>O<sub>3</sub></b>	0.11	0.14	0.17	0.12	0.12	0.12	0.15	0.12	0.11	0.05	0.03	0.93	0.12
<b>Cr<sub>2</sub>O<sub>3</sub></b>	0.01	0.01	0.01	0.00	0.03	0.01	0.00	0.00	0.02	0.01	0.00	0.03	0.01
<b>Fe<sub>2</sub>O<sub>3</sub></b>	3.03	2.79	3.54	3.03	2.79	3.54	3.03	2.79	3.54	3.03	2.79	3.54	3.03
<b>FeO</b>	11.03	10.61	6.46	11.03	10.61	6.46	11.03	10.61	6.46	11.03	10.61	6.46	11.03
<b>MnO</b>	0.20	0.19	0.18	0.15	0.23	0.18	0.16	0.19	0.20	0.19	0.08	0.19	0.19
<b>MgO</b>	21.52	21.74	21.70	21.78	21.07	21.03	21.73	21.02	21.02	22.21	22.61	22.66	21.81
<b>CaO</b>	12.68	12.56	12.51	12.62	12.61	12.55	12.69	12.65	12.66	13.15	13.17	12.09	12.84
<b>Na<sub>2</sub>O</b>	0.02	0.06	0.08	0.06	0.04	0.07	0.05	0.06	0.03	0.05	0.05	0.07	0.08
<b>K<sub>2</sub>O</b>	0.04	0.04	0.03	0.01	0.05	0.05	0.04	0.06	0.02	0.02	0.02	0.05	0.06
<b>H<sub>2</sub>O</b>	2.05	2.03	2.06	2.05	2.03	2.06	2.05	2.03	2.06	2.05	2.03	2.06	2.05
<b>Total</b>	99.16	98.02	97.28	99.16	98.02	97.28	99.16	98.02	97.28	99.16	98.02	97.28	99.16
<b>T-site</b>													
<b>Si</b>	7.031	7.121	7.454	7.031	7.121	7.454	7.031	7.121	7.454	7.031	7.121	7.454	7.031
<b>Al<sup>(iv)</sup></b>	0.969	0.879	0.546	0.969	0.879	0.546	0.969	0.879	0.546	0.969	0.879	0.546	0.969
<b>C-site</b>													
<b>Al<sup>(vi)</sup></b>	0.433	0.475	0.354	0.433	0.475	0.354	0.433	0.475	0.354	0.433	0.475	0.354	0.433
<b>Ti</b>	0.057	0.047	0.011	0.057	0.047	0.011	0.057	0.047	0.011	0.057	0.047	0.011	0.057
<b>Fe<sup>3+</sup></b>	0.334	0.310	0.387	0.334	0.310	0.387	0.334	0.310	0.387	0.334	0.310	0.387	0.334
<b>Cr</b>	0.026	0.004	0.016	0.026	0.004	0.016	0.026	0.004	0.016	0.026	0.004	0.016	0.026
<b>Mg</b>	2.844	2.900	3.467	2.844	2.900	3.467	2.844	2.900	3.467	2.844	2.900	3.467	2.844
<b>Mn</b>	0.050	0.043	0.089	0.050	0.043	0.089	0.050	0.043	0.089	0.050	0.043	0.089	0.050
<b>Fe<sup>2+</sup></b>	1.257	1.220	0.675	1.257	1.220	0.675	1.257	1.220	0.675	1.257	1.220	0.675	1.257
<b>B-site</b>													
<b>Mg</b>	0.000	0.000	0.000	0.000	0.000	0.000	0.000	0.000	0.000	0.000	0.000	0.000	0.000
<b>Mn</b>	0.000	0.000	0.000	0.000	0.000	0.000	0.000	0.000	0.000	0.000	0.000	0.000	0.000
<b>Fe<sup>2+</sup></b>	0.095	0.088	0.111	0.095	0.088	0.111	0.095	0.088	0.111	0.095	0.088	0.111	0.095
<b>Ca</b>	1.352	1.389	1.388	1.352	1.389	1.388	1.352	1.389	1.388	1.352	1.389	1.388	1.352
<b>Na</b>	0.552	0.523	0.501	0.552	0.523	0.501	0.552	0.523	0.501	0.552	0.523	0.501	0.552
<b>A-site</b>													
<b>Na</b>	0.582	0.470	0.258	0.582	0.470	0.258	0.582	0.470	0.258	0.582	0.470	0.258	0.582
<b>K</b>	0.032	0.048	0.008	0.032	0.048	0.008	0.032	0.048	0.008	0.032	0.048	0.008	0.032
<b>Total</b>	15.615	15.518	15.266	15.615	15.518	15.266	15.615	15.518	15.266	15.615	15.518	15.266	15.615

FeO, Fe<sub>2</sub>O<sub>3</sub>, and H<sub>2</sub>O were calculated stoichiometrically. Cation calculation is based on 22 oxygen and 2 OH.  
mg-kato = magnesio-katophorite

Table A4: Composition of phengite minerals '80-3'.

Analysis	Phe-80-3	Phe-80-3	Phe-80-3	Phe-80-3	Phe-80-3	Phe-80-3	Phe-80-3	Phe-80-3	Phe-80-3	Phe-80-3
	<b>SiO<sub>2</sub></b>	52.88	50.79	50.95	49.93	30.65	51.48	51.46	51.33	51.72
<b>TiO<sub>2</sub></b>	0.39	0.35	0.38	0.38	0.23	0.42	0.42	0.41	0.39	0.38
<b>Al<sub>2</sub>O<sub>3</sub></b>	25.60	25.74	25.13	26.32	15.33	24.81	25.49	24.84	25.49	25.04
<b>Cr<sub>2</sub>O<sub>3</sub></b>	0.04	0.05	0.03	0.04	0.04	0.03	0.03	0.04	0.05	0.02
<b>FeO</b>	1.35	1.31	1.23	1.11	0.80	1.20	1.32	1.24	1.05	1.39
<b>MnO</b>	0.00	0.00	0.00	0.00	0.02	0.02	0.00	0.00	0.00	0.00
<b>NiO</b>	0.05	0.05	0.06	0.04	0.03	0.07	0.00	0.06	0.05	0.03
<b>MgO</b>	4.79	4.02	4.01	3.69	2.35	4.12	3.97	3.92	4.07	4.20
<b>CaO</b>	0.00	0.00	0.00	0.00	0.00	0.00	0.00	0.00	0.00	0.02
<b>Na<sub>2</sub>O</b>	0.50	0.57	0.48	0.61	0.26	0.50	0.47	0.48	0.45	0.39
<b>K<sub>2</sub>O</b>	9.13	9.63	9.89	9.58	4.62	9.72	9.75	9.74	9.65	9.34
<b>H<sub>2</sub>O</b>	4.53	4.40	4.38	4.37	2.62	4.40	4.42	4.39	4.44	4.37
<b>Total</b>	99.26	96.91	96.55	96.06	56.94	96.77	97.32	96.43	97.36	96.01
<b>Si</b>	3.497	3.458	3.484	3.428	3.504	3.507	3.487	3.510	3.495	3.487
<b>Al<sup>(iv)</sup></b>	0.503	0.542	0.516	0.572	0.496	0.493	0.513	0.490	0.505	0.513
<b>Al<sup>(vi)</sup></b>	1.493	1.524	1.510	1.558	1.570	1.499	1.523	1.511	1.525	1.511
<b>Ti</b>	0.020	0.018	0.020	0.019	0.019	0.022	0.021	0.021	0.020	0.020
<b>Cr</b>	0.002	0.002	0.002	0.002	0.004	0.002	0.001	0.002	0.002	0.001
<b>Fe<sup>2+</sup></b>	0.075	0.075	0.070	0.064	0.076	0.068	0.075	0.071	0.059	0.080
<b>Mn</b>	0.000	0.000	0.000	0.000	0.002	0.001	0.000	0.000	0.000	0.000
<b>Mg</b>	0.472	0.408	0.409	0.378	0.400	0.418	0.401	0.400	0.410	0.430
<b>Ca</b>	0.000	0.000	0.000	0.000	0.000	0.000	0.000	0.000	0.000	0.001
<b>Na</b>	0.064	0.076	0.064	0.081	0.058	0.065	0.061	0.063	0.059	0.051
<b>K</b>	0.770	0.837	0.863	0.840	0.673	0.844	0.842	0.850	0.832	0.817
<b>Total</b>	6.896	6.940	6.938	6.942	6.802	6.920	6.925	6.917	6.908	6.911

FeO, Fe<sub>2</sub>O<sub>3</sub>, and H<sub>2</sub>O were calculated stoichiometrically. Cation calculation is based on 11 oxygen and 2 OH.

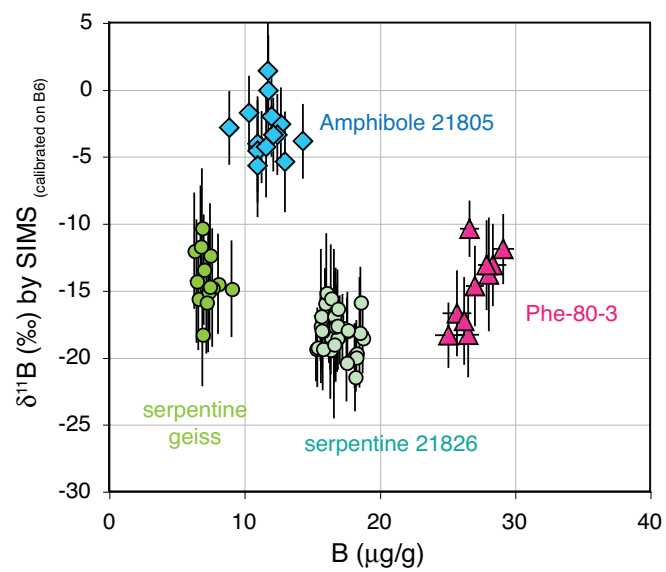


**Fig. A6:**  $B$  vs  $\delta^{11}B$  of reference minerals '21826', 'geiss', '21805', and 'Phe 80-3'. The  $\delta^{11}B$  analyses calibrated to B6 Obsidian.

**A3: List of mineral abbreviations**

Ab	Albite
Act	Actinolite
Alm	Almandine
Aln	Allanite
Am	Amphibole
Andr	Andradite
Ap	Apatite
Atg	Antigorite
Brc	Brucite
Bt	Biotite
Cc	Calcite
Chl	Chlorite
Cpx	Clinopyroxene
Ctl	Chrysotile
Di	Diopside
Enst	Enstatite
Ep	Epidote
Fa	Fayalite
Fs	Ferrosilite
Gln	Glaucophane
Grs	Grossular
Grt	Garnet
Ilm	Ilmenite
Jd	Jadeite
Laws	Lawsonite
Liz	Lizardite
Mag	Magnetite
Ol	Olivine
Opx	Orthopyroxene
Phe	Phengite
Plg	Plagioclase
Pmp	Pumpellyite
Pol	Polygonal serpentine
Px	Pyroxene
Qtz	Quartz
Rt	Rutile
Spl	Spinel
Sps	Spessartine
Srp	Serpentine
Ttn	Titanite
Tlc	Talc
Zrc	Zircon





## Appendix B: Serpentinites

B1: Sample BSE images with EPMA, SIMS and Raman spots	168
B2: Electron probe micro analyses	169
B2.1: Serpentine and brucite minerals	169
B2.2: Spinel	170
B2.3: Olivine	170
B2.4: Clinopyroxene and Orthopyroxene	171
B3: SIMS data	173
B4: Light element variation diagrams for different serpentinite samples	182
B5: Micro-Raman spectra of serpentine and brucite	185

**B1: Sample BSE images with EPMA, SIMS and Raman spots**

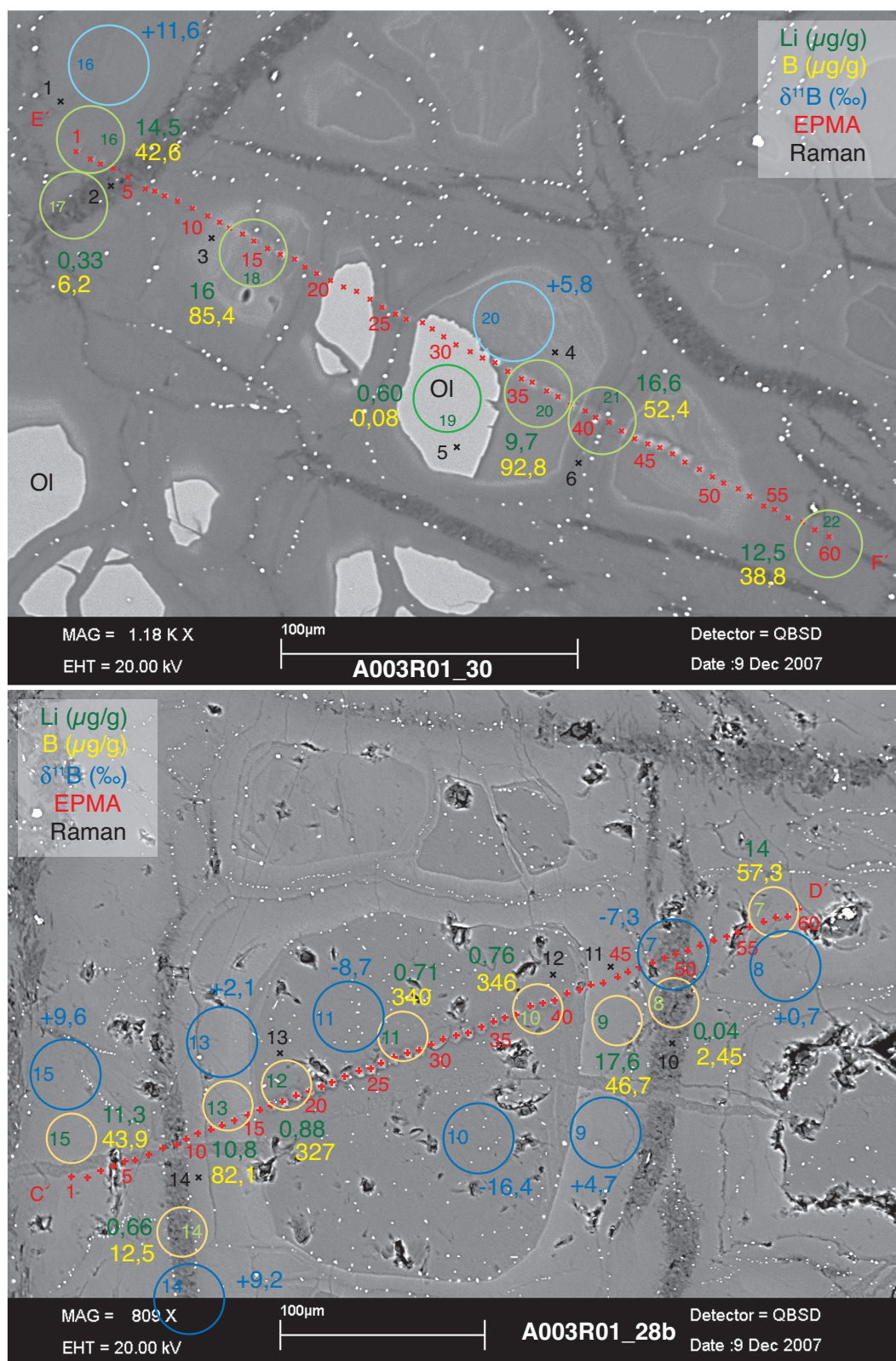


**Fig. B2:** Back-scattered electron (BSE) images of sample A003R01 with indicated spots of electron probe micro analyses, secondary ion electron spectrometry and micro-Raman analyses. Further images in electronic appendix.

## B2: Electron probe micro analyses

## B2.1: Serpentine and brucite minerals

Table B2.1: Representative composition of brucite and serpentine (in wt%), further analyses in electronic appendix.

Analysis	brucite										serpentine									
	E4H2- 6_145	E4H2- 6_18	E4H2- 6_78	A013_10	A013_10	A007R01	A007R01	A007R01	A007R01	A007R01	A13R01_52	E4H2- 6_117	E4H2- 6_118	E4H2- 6_125	MAK8P- 01	MAK8P- 12				
SiO <sub>2</sub>	0.77	0.36	0.46	0.38	0.26	33.15	38.09	38.36	40.25	40.80	40.97	39.44	41.20	42.35	42.12					
TiO <sub>2</sub>	0.01	0.04	0.00	0.00	0.00	0.02	0.01	0.00	0.01	0.00	0.01	0.03	0.00	0.00	0.01					
Al <sub>2</sub> O <sub>3</sub>	0.67	0.67	0.87	0.11	0.09	0.00	0.00	0.00	0.03	0.00	0.06	0.07	0.00	0.11	0.29					
Cr <sub>2</sub> O <sub>3</sub>	0.01	0.03	0.03	0.00	0.02	0.02	0.00	0.00	0.00	0.00	0.00	0.07	0.02	0.04	0.33					
FeO	44.38	40.06	37.53	27.40	25.60	11.30	5.48	6.01	4.46	5.06	4.38	4.16	5.11	4.89	3.94					
MnO	0.42	0.21	0.80	0.64	0.60	0.10	0.05	0.09	0.12	0.08	0.09	0.03	0.03	0.07	0.05					
MgO	21.16	19.42	19.13	49.74	47.58	42.18	41.73	38.99	39.62	39.70	38.85	39.93	39.17	40.92	36.99					
CaO	0.08	0.07	0.08	0.07	0.05	0.15	0.07	0.21	0.13	0.15	0.10	0.11	0.07	0.06	2.47					
Na <sub>2</sub> O	0.16	0.05	0.07	0.01	0.00	0.02	0.02	0.04	0.09	0.03	0.02	0.01	0.03	0.05	0.04					
K <sub>2</sub> O	0.01	0.01	0.02	0.00	0.02	0.00	0.00	0.01	0.02	0.01	0.01	0.04	0.01	0.03	0.01					
NiO	1.28	1.37	1.39	0.15	0.14	0.33	0.34	0.25	0.32	0.41	0.16	0.04	0.58	0.00	0.00					
Total	68.95	62.29	60.37	78.50	74.34	87.26	85.77	83.95	85.05	86.25	84.64	83.91	86.20	88.52	86.24					
Si	0.021	0.011	0.014	0.008	0.005	3.326	3.710	3.818	3.905	3.911	3.980	3.878	3.944	3.947	4.030					
Ti	0.000	0.001	0.000	0.000	0.000	0.001	0.001	0.000	0.001	0.000	0.001	0.002	0.000	0.000	0.001					
Al	0.021	0.023	0.031	0.003	0.002	0.000	0.000	0.000	0.003	0.000	0.007	0.008	0.000	0.012	0.033					
Cr	0.000	0.001	0.001	0.000	0.000	0.001	0.000	0.000	0.000	0.000	0.000	0.005	0.001	0.003	0.025					
Fe	0.999	0.997	0.955	0.463	0.456	0.948	0.446	0.500	0.362	0.406	0.356	0.342	0.409	0.381	0.315					
Mn	0.010	0.005	0.021	0.011	0.011	0.009	0.004	0.008	0.009	0.006	0.007	0.002	0.003	0.006	0.004					
Mg	0.849	0.862	0.868	1.499	1.512	6.309	6.060	5.785	5.731	5.674	5.626	5.853	5.589	5.685	5.276					
Ca	0.002	0.002	0.003	0.002	0.001	0.016	0.008	0.022	0.014	0.016	0.010	0.011	0.007	0.006	0.253					
Na	0.008	0.003	0.004	0.000	0.000	0.004	0.003	0.007	0.017	0.006	0.004	0.002	0.005	0.009	0.006					
K	0.000	0.000	0.001	0.000	0.000	0.000	0.000	0.001	0.003	0.001	0.002	0.005	0.001	0.004	0.001					
Ni	0.124	0.147	0.152	0.011	0.011	0.119	0.118	0.089	0.111	0.142	0.055	0.013	0.199	0.000	0.000					
Total	2.034	2.051	2.048	1.997	1.999	10.733	10.349	10.230	10.158	10.162	10.046	10.123	10.158	10.052	9.944					
Mg#	45.70	46.23	47.08	75.97	76.39	91.83	94.35	93.46	93.91	93.23	93.94	94.45	93.14	93.62	94.30					

Cation calculation based on 12 oxygens for serpentine and 4 for brucite.

## B2.2: Spinel

*Table B2.2: Representative composition of spinel (in wt%), further analyses in electronic appendix.*

Analysis	A3R1W- 11	A12R1-I1	A13R01- 73	A12R1-I1	A12R1-I1	A13R01- 03	A13R01- 09	A017G0 2-line	A017G0 2-line	A017G0 2-line	A017G0 2-line	A017G0 2-line	A017G0 2-line
TiO <sub>2</sub>	0.00	0.02	0.00	0.02	0.00	0.01	0.03	0.07	0.10	0.08	0.10	0.08	0.08
Al <sub>2</sub> O <sub>3</sub>	0.00	0.35	0.00	23.51	23.57	26.09	32.38	20.36	20.30	20.54	20.67	19.97	19.67
Cr <sub>2</sub> O <sub>3</sub>	0.04	3.35	0.01	43.14	43.40	42.83	34.56	50.01	49.73	49.59	49.72	50.00	50.58
Fe <sub>2</sub> O <sub>3</sub>	67.60	66.02	68.67	0.00	0.00	0.00	0.00	0.00	0.00	0.00	0.00	0.00	0.00
FeO	29.84	30.73	30.70	20.88	20.19	18.13	19.30	17.46	17.14	17.01	17.50	18.60	18.30
MnO	0.09	0.01	0.06	0.19	0.17	0.15	0.17	0.10	0.16	0.16	0.07	0.10	0.17
MgO	0.29	0.45	0.07	11.28	10.59	12.50	12.36	12.20	12.18	12.18	12.37	11.83	11.45
CaO	0.00	0.02	0.02	0.00	0.00	0.02	0.00	0.00	0.01	0.00	0.00	0.00	0.00
<b>Total</b>	<b>97.85</b>	<b>100.95</b>	<b>99.53</b>	<b>99.02</b>	<b>97.91</b>	<b>99.72</b>	<b>98.80</b>	<b>100.19</b>	<b>99.61</b>	<b>99.57</b>	<b>100.42</b>	<b>100.58</b>	<b>100.25</b>
Ti	0.000	0.001	0.000	0.000	0.000	0.000	0.001	0.002	0.002	0.002	0.002	0.002	0.002
Al	0.000	0.016	0.000	0.871	0.882	0.940	1.148	0.748	0.750	0.758	0.757	0.735	0.728
Cr	0.001	0.100	0.000	1.073	1.090	1.035	0.822	1.233	1.232	1.227	1.221	1.235	1.256
Fe <sup>3+</sup>	1.999	1.883	2.000	0.000	0.000	0.000	0.000	0.000	0.000	0.000	0.000	0.000	0.000
Fe <sup>2+</sup>	0.980	0.974	0.993	0.549	0.536	0.464	0.486	0.455	0.449	0.445	0.455	0.486	0.480
Mn	0.003	0.000	0.002	0.005	0.005	0.004	0.004	0.003	0.004	0.004	0.002	0.003	0.005
Mg	0.017	0.025	0.004	0.529	0.502	0.570	0.554	0.567	0.569	0.569	0.573	0.551	0.536
Ca	0.000	0.001	0.001	0.000	0.000	0.001	0.000	0.000	0.000	0.000	0.000	0.000	0.000
<b>Total</b>	<b>3.000</b>	<b>3.000</b>	<b>3.000</b>	<b>3.028</b>	<b>3.014</b>	<b>3.012</b>	<b>3.015</b>	<b>3.008</b>	<b>3.007</b>	<b>3.005</b>	<b>3.009</b>	<b>3.013</b>	<b>3.006</b>

FeO, Fe<sub>2</sub>O<sub>3</sub> were calculated stoichiometrically. Cation calculation based on 4 oxygens.

## B2.3: Olivine

*Table B2.3: Representative composition of olivine (in wt%), further analyses in electronic appendix.*

Analysis	A3R1-I3	A3R1-I3	A007R01- 21	A007R01- 26	A011R01 W-line	A011R01 W-line	A011R01 W-line	A017G0 2-line	A017G0 2-line	E4H2- 6_53	E4H2- 6_49	A12R1-I2	A12R1-I2
SiO <sub>2</sub>	41.16	41.67	40.73	40.21	41.08	41.23	40.97	41.37	41.57	40.50	40.63	40.72	40.54
TiO <sub>2</sub>	0.00	0.00	0.01	0.00	0.00	0.00	0.00	0.01	0.00	0.00	0.00	0.00	0.00
Al <sub>2</sub> O <sub>3</sub>	0.00	0.00	0.00	0.01	0.00	0.00	0.00	0.03	0.03	0.02	0.00	0.01	0.00
Cr <sub>2</sub> O <sub>3</sub>	0.00	0.00	0.01	0.00	0.03	0.03	0.00	0.03	0.03	0.02	0.01	0.00	0.01
FeO	8.36	8.07	8.56	8.50	8.42	8.49	8.66	8.17	8.78	8.31	8.41	7.91	7.58
MnO	0.10	0.19	0.17	0.18	0.04	0.10	0.12	0.13	0.07	0.10	0.08	0.14	0.11
MgO	50.39	50.88	50.75	50.81	50.78	50.90	50.75	50.92	51.11	50.93	50.67	51.17	50.95
CaO	0.01	0.00	0.00	0.01	0.01	0.00	0.02	0.06	0.00	0.00	0.00	0.01	0.01
Na <sub>2</sub> O	0.04	0.00	0.00	0.02	0.00	0.00	0.01	0.02	0.00	0.00	0.00	0.00	0.04
K <sub>2</sub> O	0.01	0.00	0.00	0.01	0.00	0.00	0.00	0.02	0.00	0.00	0.01	0.00	0.01
NiO	0.38	0.38	0.39	0.42	0.45	0.47	0.36	0.30	0.41	0.38	0.41	0.43	0.39
<b>Total</b>	<b>100.45</b>	<b>101.18</b>	<b>100.62</b>	<b>100.15</b>	<b>100.81</b>	<b>101.21</b>	<b>100.88</b>	<b>101.04</b>	<b>102.01</b>	<b>100.26</b>	<b>100.21</b>	<b>100.39</b>	<b>99.63</b>
Si	0.996	0.999	0.986	0.979	0.991	0.991	0.990	0.995	0.992	0.984	0.987	0.986	0.987
Ti	0.000	0.000	0.000	0.000	0.000	0.000	0.000	0.000	0.000	0.000	0.000	0.000	0.000
Al	0.000	0.000	0.000	0.000	0.000	0.000	0.000	0.001	0.001	0.000	0.000	0.000	0.000
Cr	0.000	0.000	0.000	0.000	0.000	0.000	0.000	0.000	0.000	0.000	0.000	0.000	0.000
Fe	0.169	0.162	0.173	0.173	0.170	0.171	0.175	0.164	0.175	0.169	0.171	0.160	0.154
Mn	0.002	0.004	0.003	0.004	0.001	0.002	0.002	0.003	0.001	0.002	0.002	0.003	0.002
Mg	1.818	1.819	1.832	1.845	1.826	1.824	1.827	1.826	1.819	1.844	1.835	1.846	1.850
Ca	0.000	0.000	0.000	0.000	0.000	0.000	0.001	0.001	0.000	0.000	0.000	0.000	0.000
Na	0.002	0.000	0.000	0.001	0.000	0.000	0.000	0.001	0.000	0.000	0.000	0.000	0.002
K	0.000	0.000	0.000	0.000	0.000	0.000	0.000	0.001	0.000	0.000	0.000	0.000	0.000
Ni	0.033	0.033	0.034	0.036	0.039	0.041	0.031	0.026	0.035	0.033	0.036	0.037	0.034
<b>Total</b>	<b>3.021</b>	<b>3.017</b>	<b>3.030</b>	<b>3.039</b>	<b>3.028</b>	<b>3.029</b>	<b>3.026</b>	<b>3.018</b>	<b>3.025</b>	<b>3.033</b>	<b>3.031</b>	<b>3.033</b>	<b>3.031</b>
<b>Mg#</b>	<b>91.39</b>	<b>91.66</b>	<b>91.20</b>	<b>91.26</b>	<b>91.46</b>	<b>91.36</b>	<b>91.16</b>	<b>91.62</b>	<b>91.14</b>	<b>91.52</b>	<b>91.41</b>	<b>91.89</b>	<b>92.19</b>

Cation calculation based on 4 oxygens.

## B2.4: Clinopyroxene and Orthopyroxene

*Table B2.4: Representative composition of clinopyroxene (in wt%), further analyses in electronic appendix.*

Analysis	A3R1-14	A3R1-14	A3R1-14	A3R1-14	A007R01 _121	A007R01 _123	A13R01_ 13	A13R01_ 14	A13R01_ 16	A017G0 2-line	A017G0 2-line	A017G0 2-line	A017G0 2-line
<b>SiO<sub>2</sub></b>	50.45	53.63	54.41	54.28	54.06	53.92	54.14	54.34	54.13	53.42	54.27	53.51	53.62
<b>TiO<sub>2</sub></b>	0.02	0.01	0.01	0.01	0.02	0.02	0.01	0.01	0.03	0.06	0.06	0.05	0.07
<b>Al<sub>2</sub>O<sub>3</sub></b>	1.09	1.41	1.03	1.27	1.37	1.33	1.50	1.52	1.53	1.67	1.95	1.87	2.04
<b>Cr<sub>2</sub>O<sub>3</sub></b>	0.60	0.70	0.57	0.67	0.48	0.35	0.59	0.63	0.64	0.98	1.16	1.24	1.17
<b>FeO</b>	4.32	2.09	1.67	2.04	1.74	1.76	1.96	2.15	1.96	2.20	2.10	2.49	2.17
<b>MnO</b>	0.11	0.07	0.00	0.05	0.02	0.10	0.09	0.05	0.06	0.04	0.05	0.10	0.03
<b>MgO</b>	19.36	18.93	17.90	17.86	17.80	18.03	17.64	17.59	17.70	17.99	17.27	18.00	17.60
<b>CaO</b>	21.95	23.52	25.19	24.70	24.86	24.60	24.12	24.31	24.33	21.84	22.54	21.87	21.68
<b>Na<sub>2</sub>O</b>	0.06	0.09	0.03	0.04	0.09	0.08	0.10	0.14	0.11	0.64	0.68	0.72	0.76
<b>K<sub>2</sub>O</b>	0.00	0.02	0.00	0.00	0.00	0.00	0.00	0.00	0.01	0.01	0.01	0.00	0.00
<b>NiO</b>	0.05	0.06	0.03	0.04	0.01	0.03	0.08	0.07	0.03	0.10	0.06	0.00	0.08
<b>Total</b>	98.01	100.52	100.83	100.96	100.46	100.22	100.22	100.81	100.51	98.96	100.14	99.84	99.20
<b>Si</b>	1.861	1.928	1.957	1.952	1.950	1.948	1.961	1.958	1.954	1.950	1.964	1.936	1.954
<b>Ti</b>	0.001	0.000	0.000	0.000	0.001	0.001	0.000	0.000	0.001	0.002	0.001	0.001	0.002
<b>Al</b>	0.048	0.060	0.043	0.054	0.058	0.057	0.064	0.065	0.065	0.072	0.083	0.080	0.087
<b>Fe<sup>3+</sup></b>	0.133	0.063	0.027	0.025	0.034	0.042	0.003	0.010	0.016	0.041	0.002	0.061	0.020
<b>Cr</b>	0.017	0.020	0.016	0.019	0.014	0.010	0.017	0.018	0.018	0.028	0.033	0.035	0.034
<b>Fe<sup>2+</sup></b>	0.000	0.000	0.023	0.036	0.019	0.011	0.056	0.054	0.043	0.026	0.062	0.014	0.046
<b>Mn</b>	0.003	0.002	0.000	0.002	0.001	0.003	0.003	0.001	0.002	0.001	0.001	0.003	0.001
<b>Mg</b>	1.064	1.015	0.960	0.957	0.957	0.971	0.952	0.945	0.952	0.979	0.932	0.971	0.956
<b>Ca</b>	0.868	0.906	0.971	0.952	0.961	0.952	0.936	0.939	0.941	0.854	0.874	0.848	0.847
<b>Na</b>	0.004	0.006	0.002	0.003	0.006	0.006	0.007	0.010	0.008	0.046	0.048	0.051	0.053
<b>K</b>	0.000	0.001	0.000	0.000	0.000	0.000	0.000	0.000	0.001	0.000	0.000	0.000	0.000
<b>Total</b>	4.000	4.000	4.000	4.000	4.000	4.000	4.000	4.000	4.000	4.000	4.000	4.000	4.000
<b>Mg#</b>	100.00	100.00	97.68	96.35	98.06	98.92	94.41	94.56	95.68	97.44	93.78	98.54	95.44
<b>Wo</b>	44.9	47.2	49.7	48.9	49.6	49.2	48.1	48.4	48.6	45.9	46.8	46.2	45.8
<b>En</b>	55.1	52.8	49.1	49.2	49.4	50.2	49.0	48.8	49.2	52.7	49.9	53.0	51.7
<b>Fs</b>	0.0	0.0	1.2	1.9	1.0	0.5	2.9	2.8	2.2	1.4	3.3	0.8	2.5

Cation calculation based on 6 oxygens.

**Table B2.4:** Representative composition of orthopyroxene (in wt%), further analyses in electronic appendix.

Analysis	A3R1-14	A3R1-14	A11R01- line	A11R01- line	A13R01_ 11	A13R01_ 10	A13R01- line	A13R01_ 08	A017G0 2-line	A017G0 2-line	E4H2- 6_25	E4H2- 6_99	E4H2- 6_61
<b>SiO<sub>2</sub></b>	55.34	57.03	56.35	56.73	55.22	56.38	53.05	53.27	53.16	54.02	56.92	57.71	56.69
<b>TiO<sub>2</sub></b>	0.00	0.00	0.01	0.02	0.02	0.02	0.01	0.02	0.02	0.03	0.00	0.01	0.01
<b>Al<sub>2</sub>O<sub>3</sub></b>	1.45	1.53	1.95	1.99	1.56	1.37	0.85	0.56	1.12	1.67	2.21	1.68	2.07
<b>Cr<sub>2</sub>O<sub>3</sub></b>	0.45	0.68	0.68	0.67	0.40	0.24	0.07	0.04	0.34	0.62	0.75	0.34	0.61
<b>FeO</b>	5.82	5.60	5.52	5.75	6.35	6.24	5.91	7.43	5.22	7.09	5.64	5.83	5.46
<b>MnO</b>	0.14	0.15	0.19	0.18	0.14	0.16	0.05	0.19	0.20	0.17	0.17	0.15	0.18
<b>MgO</b>	34.66	35.38	34.70	34.90	34.58	35.20	35.80	34.54	36.19	33.02	35.05	35.64	34.80
<b>CaO</b>	1.18	0.37	1.11	0.70	0.64	0.50	0.28	0.41	0.98	0.55	0.54	0.22	0.55
<b>Na<sub>2</sub>O</b>	0.03	0.00	0.01	0.01	0.03	0.01	0.08	0.02	0.10	0.12	0.02	0.00	0.01
<b>K<sub>2</sub>O</b>	0.02	0.00	0.01	0.01	0.01	0.02	0.02	0.06	0.02	0.04	0.00	0.01	0.00
<b>NiO</b>	0.05	0.08	0.10	0.10	0.06	0.08	0.07	0.06	0.06	0.03	0.13	0.06	0.16
<b>Total</b>	99.13	100.81	100.60	101.05	99.01	100.21	96.20	96.61	97.39	97.35	101.43	101.63	100.53
<b>Si</b>	1.932	1.948	1.934	1.937	1.932	1.944	1.911	1.924	1.893	1.931	1.934	1.953	1.941
<b>Ti</b>	0.000	0.000	0.000	0.000	0.001	0.000	0.000	0.001	0.000	0.001	0.000	0.000	0.000
<b>Al</b>	0.059	0.062	0.079	0.080	0.064	0.056	0.036	0.024	0.047	0.070	0.088	0.067	0.083
<b>Cr</b>	0.012	0.018	0.018	0.018	0.011	0.007	0.002	0.001	0.009	0.018	0.020	0.009	0.016
<b>Fe</b>	0.170	0.160	0.158	0.164	0.186	0.180	0.178	0.225	0.156	0.212	0.160	0.165	0.156
<b>Mn</b>	0.004	0.004	0.005	0.005	0.004	0.005	0.002	0.006	0.006	0.005	0.005	0.004	0.005
<b>Mg</b>	1.804	1.802	1.775	1.776	1.803	1.809	1.922	1.860	1.921	1.760	1.775	1.798	1.776
<b>Ca</b>	0.044	0.014	0.041	0.026	0.024	0.018	0.011	0.016	0.037	0.021	0.020	0.008	0.020
<b>Na</b>	0.002	0.000	0.001	0.001	0.002	0.001	0.006	0.001	0.007	0.008	0.001	0.000	0.001
<b>K</b>	0.001	0.000	0.000	0.001	0.001	0.001	0.001	0.003	0.001	0.002	0.000	0.000	0.000
<b>Ni</b>	0.007	0.009	0.012	0.012	0.007	0.010	0.010	0.008	0.008	0.004	0.016	0.007	0.019
<b>Total</b>	4.036	4.017	4.024	4.020	4.035	4.030	4.078	4.069	4.086	4.031	4.021	4.012	4.019
<b>Mg#</b>	91.40	91.85	91.81	91.54	90.66	90.96	91.52	89.23	92.51	89.24	91.73	91.59	91.91

Cation calculation based on 6 oxygens.

## B3: SIMS data

Table B3: Li, Be, B, Sr contents and  $\delta^{11}\text{B}$  values of serpentinites, analyzed by SIMS, analyses also in electronic appendix.

Texture	Analysis	Li ( $\mu\text{g/g}$ )	$2\sigma_{\text{mean}}$	Be ( $\mu\text{g/g}$ )	$2\sigma_{\text{mean}}$	B ( $\mu\text{g/g}$ )	$2\sigma_{\text{mean}}$	Sr ( $\mu\text{g/g}$ )	$2\sigma_{\text{mean}}$	Analysis	$I_p$ (nA)	n	$^{11}\text{B}/^{10}\text{B}$ measured	$\alpha_{\text{inst}}$	$^{11}\text{B}/^{10}\text{B}$ corrected	$\delta^{11}\text{B}$ (‰) <sup>#</sup>	$2\sigma_{\text{mean}}$
basite	D1H4-4C_10	0.51	6.2%	0.016	0.016	22.61	33.5%	2.03	5.7%	-	-	400	3.811	1.054	4.016	-0.80	0.32%
basite	D1H4-4C_11	0.35	6.8%	0.007	0.007	20.20	69.7%	2.04	0.7%	-	-	400	3.818	1.054	4.024	1.16	0.32%
basite	D1H4-4C_13	0.82	6.9%	0.010	0.010	30.97	65.0%	1.22	4.1%	-	-	400	3.821	1.054	4.027	1.77	0.38%
serp 1	D1H4-4F-6	0.17	16.8%	0.009	0.009	51.87	57.2%	1.47	3.9%	-	-	400	3.833	1.054	4.039	4.89	0.36%
serp 2	D1H4-4F-2	1.00	4.2%	0.008	0.008	65.29	63.2%	0.48	1.7%	-	-	400	3.830	1.054	4.037	4.26	0.38%
serp 2	D1H4-4F-4	0.05	18.2%	0.002	0.002	29.39	96.6%	0.32	3.5%	-	-	400	3.832	1.054	4.039	4.82	0.38%
serp 2	D1H4-4F-5	0.26	10.5%	0.004	0.004	47.50	116.4%	0.59	1.3%	-	-	400	3.836	1.054	4.042	5.65	0.40%
mesh	D1H4-4C_3	0.23	8.5%	0.026	0.026	70.09	32.6%	1.71	2.2%	-	-	400	3.823	1.054	4.029	2.49	0.22%
mesh	D1H4-4C_4	0.24	8.6%	0.030	0.030	81.28	28.4%	1.60	1.6%	-	-	400	3.836	1.054	4.043	5.87	0.12%
mesh	D1H4-4C_12	0.28	11.5%	0.027	0.027	67.55	34.9%	1.88	2.4%	-	-	400	3.829	1.054	4.035	3.92	0.18%
mesh	D1H4-4G-5	0.13	15.4%	0.006	0.006	20.78	49.3%	1.67	1.7%	-	-	400	3.836	1.054	4.042	5.67	0.10%
mesh	D1H4-4G-7	0.47	7.0%	0.010	0.010	41.86	38.2%	1.02	2.4%	-	-	400	3.834	1.054	4.041	5.30	0.22%
basite	D1H4-4C_2	0.59	4.2%	0.023	0.023	91.43	35.8%	2.35	3.0%	-	-	400	3.842	1.054	4.049	7.35	0.12%
basite	D1H4-4C_5	0.48	5.8%	0.028	0.028	80.94	25.6%	2.50	2.6%	-	-	400	3.852	1.054	4.059	9.89	0.20%
basite	D1H4-4C_6	0.55	8.4%	0.030	0.030	83.15	4.2%	1.78	4.2%	-	-	400	3.832	1.054	4.039	4.82	0.38%
vein 1	D1H4-4G-2	0.16	12.8%	0.004	0.004	31.31	84.7%	0.66	1.9%	-	-	400	3.836	1.054	4.042	5.65	0.40%
vein 1	D1H4-4G-4	0.19	15.9%	0.015	0.015	55.14	62.0%	1.30	2.2%	-	-	400	3.823	1.054	4.029	2.49	0.22%
vein 1	D1H4-4G-6	0.19	9.8%	0.010	0.010	64.76	36.3%	2.36	2.8%	-	-	400	3.836	1.054	4.043	5.87	0.12%
vein 3	D1H4-4G-9	0.19	9.5%	0.004	0.004	14.82	84.5%	0.38	2.2%	-	-	400	3.811	1.054	4.016	-0.80	0.32%
vein	26R02-1	0.24	11.0%	0.026	0.026	9.41	37.5%	0.58	3.9%	26R02-1	30	400	3.811	1.054	4.016	-0.80	0.32%
vein	26R02-2	0.29	11.1%	0.064	0.064	10.26	20.8%	0.45	3.5%	26R02-2	30	400	3.818	1.054	4.024	1.16	0.32%
vein	26R02-3	0.31	13.7%	0.051	0.051	11.34	35.6%	0.31	2.7%	-	-	400	3.821	1.054	4.027	1.77	0.38%
vein	26R02-4	0.23	16.3%	0.047	0.047	8.26	24.8%	0.56	3.1%	26R02-3	30	400	3.821	1.054	4.027	1.77	0.38%
vein	26R02-5	0.26	10.7%	0.057	0.057	8.83	21.1%	0.53	2.4%	26R02-4	30	400	3.833	1.054	4.039	4.89	0.36%
vein	26R02-6	0.21	11.5%	0.042	0.042	8.52	25.7%	0.38	1.7%	26R02-5	30	400	3.830	1.054	4.037	4.26	0.38%
vein	26R02-7	0.21	13.4%	0.051	0.051	9.12	28.1%	0.80	2.7%	-	-	400	3.832	1.054	4.039	4.82	0.38%
vein	26R02-8	0.25	14.4%	0.044	0.044	8.66	19.8%	1.38	3.2%	26R02-6	30	400	3.832	1.054	4.039	4.82	0.38%
vein	26R02-9	0.21	7.6%	0.034	0.034	8.24	42.3%	1.25	2.5%	26R02-7	30	400	3.836	1.054	4.042	5.65	0.40%
vein	26R02-10	1.01	6.7%	0.006	0.006	32.02	84.9%	0.99	2.1%	-	-	400	3.823	1.054	4.029	2.49	0.22%
vein	26R02-11	0.72	5.3%	0.040	0.040	34.16	35.1%	1.62	1.4%	26R02-8	30	400	3.823	1.054	4.029	2.49	0.22%
vein	26R02-13	0.05	21.7%	b.d.l.	b.d.l.	92.38	0.6%	1.32	2.1%	26R02-11	30	400	3.836	1.054	4.043	5.87	0.12%
vein	26R02-14	0.29	13.4%	0.079	0.079	48.30	28.4%	3.20	1.2%	-	-	400	3.836	1.054	4.043	5.87	0.12%
vein	26R02-15	0.31	13.0%	0.056	0.056	16.86	24.7%	0.91	2.0%	-	-	400	3.829	1.054	4.035	3.92	0.18%
mesh texture	26R02-16	0.42	8.9%	b.d.l.	b.d.l.	38.85	39.3%	2.83	1.3%	26R02-12	30	400	3.829	1.054	4.035	3.92	0.18%
vein	26R02-17	0.10	17.4%	b.d.l.	b.d.l.	91.38	0.9%	2.83	1.3%	26R02-13	30	400	3.836	1.054	4.042	5.67	0.10%
vein	26R02-18	1.01	3.6%	0.039	0.039	38.43	33.5%	1.14	2.7%	-	-	400	3.834	1.054	4.041	5.30	0.22%
vein	26R02-19	0.81	4.8%	0.003	0.003	27.34	96.6%	0.67	1.4%	26R02-14	30	400	3.834	1.054	4.041	5.30	0.22%
vein	26R02-20	0.05	33.9%	b.d.l.	b.d.l.	83.48	0.7%	4.79	12.3%	26R02-10	30	400	3.842	1.054	4.049	7.35	0.12%
vein	26R02-22	0.66	6.3%	0.002	0.002	28.72	126.5%	0.51	46.0%	-	-	400	3.852	1.054	4.059	9.89	0.20%
vein	26R02-23	0.63	6.3%	0.002	0.002	23.68	126.5%	0.32	46.0%	26R02-20	30	400	3.852	1.054	4.059	9.89	0.20%
vein	26R02-24	0.87	4.6%	0.001	0.001	28.55	189.7%	0.84	32.8%	-	-	400	3.852	1.054	4.059	9.89	0.20%
vein	26R02-25	0.72	5.7%	0.070	0.070	25.52	25.9%	0.87	2.0%	-	-	400	3.852	1.054	4.059	9.89	0.20%

# = matrix corrected

Table B3 (continued): Li, Be, B, Sr contents and  $\delta^{11}\text{B}$  values of serpentinites, analyzed by SIMS, analyses also in electronic appendix.

Texture	Analysis	Li ( $\mu\text{g/g}$ )	$2\sigma_{\text{mean}}$	Be ( $\mu\text{g/g}$ )	$2\sigma_{\text{mean}}$	B ( $\mu\text{g/g}$ )	$2\sigma_{\text{mean}}$	Sr ( $\mu\text{g/g}$ )	$2\sigma_{\text{mean}}$	Analysis	$I_p$ (nA)	n	$^{11}\text{B}/^{10}\text{B}$ measured	$\alpha_{\text{inst}}$	$^{11}\text{B}/^{10}\text{B}$ corrected	$\delta^{11}\text{B}$ (‰) <sup>#</sup>	$2\sigma_{\text{mean}}$
vein	26R02-26	0.85	7.4%	0.001	189.7%	27.61	3.7%	0.87	22.2%	26R02-19	30	400	3.839	1.054	4.046	6.69	0.18%
vein	26R02-27	0.23	20.0%	0.052	30.9%	11.40	3.1%	0.73	27.5%	26R02-17	30	400	3.838	1.054	4.044	6.21	0.36%
vein	26R02-28	0.85	5.4%	0.001	189.7%	19.70	1.6%	0.89	35.8%	26R02-18	30	400	3.846	1.054	4.053	8.39	0.22%
vein	26R02-29	0.20	13.2%	0.023	34.9%	9.86	2.6%	0.79	32.3%	26R02-16	30	400	3.838	1.054	4.044	6.17	0.34%
vein	26R02-31	0.21	15.8%	0.070	31.1%	5.95	3.2%	0.53	32.2%	26R02-15	30	400	3.864	1.054	4.072	13.01	0.44%
vein	10R02-1	3.77	2.4%	0.001	189.7%	46.07	0.7%	2.89	15.3%	10R02-1	30	200	3.873	1.046	4.051	7.77	0.17%
vein	10R02-2	3.83	1.9%	0.002	96.6%	49.26	0.4%	2.21	6.0%	10R02-2	30	200	3.874	1.046	4.051	7.82	0.15%
vein	10R02-3	2.01	3.9%	0.254	19.9%	23.55	1.1%	1.00	19.2%	10R02-3	30	200	3.821	1.046	3.996	-5.87	0.21%
vein	10R02-4	4.58	2.5%	0.003	77.5%	42.47	1.2%	3.91	13.0%	10R02-4	30	200	3.872	1.046	4.050	7.55	0.16%
vein	10R02-5	2.35	4.5%	0.001	126.5%	44.16	1.1%	2.29	9.5%	10R02-5	30	200	3.865	1.046	4.042	5.49	0.16%
vein	10R02-6	20.47	1.7%	0.004	84.6%	36.80	1.7%	3.43	12.3%	10R02-6	30	200	3.880	1.046	4.058	9.45	0.17%
mesh texture	10R02-7	4.91	1.3%	0.004	96.7%	76.27	0.7%	8.41	1.9%	10R02-7	30	200	3.852	1.046	4.028	2.14	0.11%
vein	10R02-8	5.54	1.7%	0.003	77.5%	38.21	1.0%	3.82	8.1%	10R02-8	30	200	3.871	1.046	4.049	7.24	0.17%
vein	10R02-9	3.37	2.7%	0.001	189.7%	14.58	2.6%	2.64	10.6%	-	-	-	-	-	-	-	-
mesh texture	10R02-10	1.78	3.7%	0.003	77.5%	70.75	1.1%	0.70	16.6%	10R02-9	30	200	3.869	1.046	4.046	6.60	0.13%
vein	10R02-11	1.45	3.1%	0.062	39.4%	11.42	1.7%	0.71	24.3%	10R02-10	30	200	3.860	1.046	4.037	4.43	0.34%
vein	10R02-12	5.36	1.7%	0.003	145.2%	39.11	2.1%	3.42	7.9%	-	-	-	-	-	-	-	-
vein	10R02-13	4.70	2.3%	b.d.l.	-	40.24	1.0%	4.20	7.0%	10R02-11	30	200	3.873	1.046	4.050	7.58	0.15%
vein	10R02-14	1.68	3.3%	5.282	10.1%	26.43	5.3%	6.22	11.9%	10R02-12	30	200	3.855	1.046	4.032	3.14	0.23%
vein	10R02-15	3.26	2.0%	0.002	135.1%	61.73	0.9%	1.38	17.6%	10R02-13*	30	200	3.877	1.046	4.055	8.76	0.15%
mesh texture	10R02-16	0.48	4.6%	0.025	44.5%	38.76	1.6%	8.47	5.4%	-	-	-	-	-	-	-	-
vein	10R02-17	0.82	6.1%	0.006	101.2%	18.51	1.6%	147.05	5.0%	-	-	-	-	-	-	-	-
basalt	E4H2-59	1.19	5.8%	0.019	47.7%	84.63	5.1%	4.46	8.0%	-	-	-	-	-	-	-	-
basalt	E4H2-16	2.75	2.8%	b.d.l.	-	53.53	1.1%	31.17	4.5%	-	-	-	-	-	-	-	-
crystal boundary	E4H2-20	3.17	2.5%	0.001	189.7%	62.64	1.6%	38.12	5.3%	-	-	-	-	-	-	-	-
vein	E4H2-60	3.19	3.1%	b.d.l.	-	22.09	1.7%	26.34	4.1%	E4H2-21	30	200	3.890	1.046	4.069	12.20	0.18%
Cpx	E4H2-1	3.45	3.2%	0.001	189.7%	0.29	23.2%	0.95	42.1%	E4H2-20*	30	400	3.794	1.046	3.967	-12.87	1.00%
Cpx	E4H2-62	3.94	2.2%	0.001	189.7%	0.08	28.2%	0.43	24.6%	-	-	-	-	-	-	-	-
Ol	E4H2-24	0.97	3.5%	0.002	126.5%	0.05	44.0%	0.35	30.5%	-	-	-	-	-	-	-	-
Ol	E4H2-25	0.80	5.0%	0.001	189.7%	0.05	50.3%	0.40	40.8%	E4H2-9*	30	400	3.762	1.046	3.934	-21.06	2.32%
Ol	E4H2-46	0.73	4.7%	b.d.l.	-	0.03	43.7%	0.39	46.5%	-	-	-	-	-	-	-	-
opx relict	E4H2-3	1.26	5.0%	b.d.l.	-	0.08	24.6%	0.23	37.8%	E4H2-19*	30	400	3.920	1.046	4.099	19.81	0.71%
opx relict	E4H2-45	0.75	4.9%	b.d.l.	-	0.04	52.5%	0.04	96.6%	E4H2-25*	30	400	3.800	1.046	3.974	-11.16	1.68%
opx relict	E4H2-48	0.54	11.3%	b.d.l.	-	0.06	34.8%	0.08	70.5%	-	-	-	-	-	-	-	-
opx relict	E4H2-57	1.56	5.9%	0.001	189.7%	0.37	15.2%	0.57	32.8%	-	-	-	-	-	-	-	-
opx relict	E4H2-58	1.41	4.5%	0.002	126.5%	0.18	13.6%	0.24	44.6%	E4H2-22*	30	400	3.811	1.046	3.986	-8.28	1.27%
opx relict	E4H2-61	1.52	3.0%	b.d.l.	-	0.05	29.4%	0.13	59.8%	-	-	-	-	-	-	-	-
reddish vein	E4H2-50	0.08	13.2%	0.001	189.7%	22.04	7.6%	3.73	16.5%	-	-	-	-	-	-	-	-
reddish vein	E4H2-31	0.13	16.0%	0.002	126.5%	69.93	3.0%	39.38	3.3%	E4H2-7	30	200	3.834	1.046	4.010	-2.40	0.16%
reddish vein	E4H2-39	0.14	10.4%	0.002	96.6%	28.68	3.4%	38.66	4.9%	E4H2-2	30	200	3.852	1.046	4.028	2.24	0.19%
reddish vein	E4H2-51	0.15	16.6%	0.004	85.1%	37.68	4.0%	15.41	10.7%	-	-	-	-	-	-	-	-

# = matrix corrected



Table B3 (continued): Li, Be, B, Sr contents and  $\delta^{11}\text{B}$  values of serpentinites, analyzed by SIMS, analyses also in electronic appendix.

Texture	Analysis	Li ( $\mu\text{g/g}$ )	$2\sigma_{\text{mean}}$	Be ( $\mu\text{g/g}$ )	$2\sigma_{\text{mean}}$	B ( $\mu\text{g/g}$ )	$2\sigma_{\text{mean}}$	Sr ( $\mu\text{g/g}$ )	$2\sigma_{\text{mean}}$	Analysis	$I_p$ (nA)	n	$^{11}\text{B}/^{10}\text{B}$ measured	$\alpha_{\text{inst}}$	$^{11}\text{B}/^{10}\text{B}$ corrected	$\delta^{11}\text{B}$ (‰) <sup>#</sup>	$2\sigma_{\text{mean}}$
reddish vein	E4H2-12	0.18	8.0%	0.001	189.7%	60.79	0.8%	12.46	5.4%	E4H2-14	30	200	3.834	1.046	4.010	-2.44	0.12%
reddish vein	E4H2-38	0.20	12.3%	0.004	77.5%	66.69	1.1%	23.81	7.2%	E4H2-3	30	200	3.840	1.046	4.016	-0.93	0.17%
reddish vein	E4H2-41	0.32	7.7%	0.002	126.7%	57.63	2.0%	152.10	2.5%	E4H2-1	30	200	3.838	1.046	4.014	-1.38	0.14%
reddish vein	E4H2-7	0.72	5.9%	0.001	189.7%	57.33	0.9%	97.76	6.8%	E4H2-17	30	200	3.819	1.046	3.994	-6.23	0.13%
reddish vein	E4H2-11	1.91	5.6%	0.003	96.6%	94.38	1.0%	55.99	2.6%	E4H2-15	30	200	3.853	1.046	4.029	2.48	0.12%
mesh center	E4H2-54	0.06	10.9%	0.009	65.3%	123.22	1.2%	4.61	9.3%	E4H2-23	30	200	3.853	1.046	4.030	2.59	0.09%
mesh center	E4H2-10	0.18	16.3%	0.001	189.7%	113.53	0.6%	4.84	9.5%	-	-	-	-	-	-	-	-
mesh center	E4H2-30	0.97	5.8%	0.002	126.5%	117.16	0.9%	6.17	8.9%	-	-	-	-	-	-	-	-
mesh center	E4H2-55	0.25	9.4%	0.008	73.5%	160.13	0.9%	5.45	10.3%	-	-	-	-	-	-	-	-
mesh center	E4H2-35	1.25	5.3%	0.003	96.6%	103.41	1.3%	4.63	8.6%	-	-	-	-	-	-	-	-
mesh center	E4H2-23	0.11	14.5%	b.d.l.	b.d.l.	119.76	0.8%	23.79	4.4%	-	-	-	-	-	-	-	-
mesh center	E4H2-36	0.60	9.2%	0.005	70.0%	134.37	0.9%	3.73	16.0%	-	-	-	-	-	-	-	-
mesh center	E4H2-32	0.03	36.3%	b.d.l.	b.d.l.	130.09	0.8%	4.87	8.9%	E4H2-6	30	200	3.875	1.046	4.053	8.29	0.10%
mesh center	E4H2-6	1.40	5.9%	0.002	126.5%	98.76	2.1%	21.47	5.7%	-	-	-	-	-	-	-	-
mesh rim	E4H2-47	0.79	6.2%	b.d.l.	b.d.l.	96.34	0.9%	8.60	9.1%	-	-	-	-	-	-	-	-
mesh rim	E4H2-63	1.98	4.8%	0.002	126.5%	60.60	1.3%	51.65	3.5%	-	-	-	-	-	-	-	-
mesh rim	E4H2-18	2.36	2.7%	b.d.l.	b.d.l.	83.45	1.1%	27.97	7.8%	E4H2-11	30	200	3.893	1.046	4.071	12.76	0.13%
mesh rim	E4H2-19	2.99	1.5%	b.d.l.	b.d.l.	63.45	1.1%	25.04	4.7%	E4H2-10	30	200	3.871	1.046	4.049	7.30	0.11%
mesh rim	E4H2-22	3.65	2.6%	b.d.l.	b.d.l.	49.87	0.7%	38.97	3.5%	-	-	-	-	-	-	-	-
mesh rim	E4H2-53	4.34	2.7%	0.011	55.8%	65.95	2.8%	4.54	9.3%	-	-	-	-	-	-	-	-
mesh rim	E4H2-4	0.62	8.6%	0.003	96.6%	105.56	1.1%	22.35	5.3%	-	-	-	-	-	-	-	-
mesh rim	E4H2-26	3.11	4.7%	b.d.l.	b.d.l.	118.79	1.4%	5.52	19.4%	-	-	-	-	-	-	-	-
mesh rim	E4H2-40	2.26	3.8%	0.005	96.1%	84.76	0.7%	2.56	12.8%	-	-	-	-	-	-	-	-
mesh rim	E4H2-17	0.95	6.3%	0.002	126.5%	104.60	0.5%	38.84	3.4%	E4H2-12	30	200	3.881	1.046	4.059	9.71	0.10%
mesh rim	E4H2-13	0.42	8.2%	0.001	189.7%	91.10	1.2%	75.47	2.7%	E4H2-13	30	200	3.901	1.046	4.080	14.92	0.10%
mesh rim	E4H2-2	1.28	12.8%	0.001	189.7%	120.79	2.9%	16.37	7.8%	-	-	-	-	-	-	-	-
mesh rim	E4H2-33	2.64	3.3%	0.001	189.7%	68.75	1.1%	4.47	16.1%	E4H2-5	30	200	3.864	1.046	4.041	5.44	0.13%
mesh rim	E4H2-28	3.11	4.4%	0.001	189.7%	78.83	1.1%	5.79	6.7%	-	-	-	-	-	-	-	-
mesh rim	E4H2-37	3.91	2.9%	0.006	70.8%	74.63	1.0%	4.31	17.7%	E4H2-4	30	200	3.882	1.046	4.060	10.09	0.09%
mesh rim	E4H2-27	4.81	3.3%	0.001	189.7%	48.31	1.5%	27.52	6.0%	E4H2-8	30	200	3.878	1.046	4.056	9.06	0.12%
mesh rim	E4H2-5	0.53	4.6%	0.001	189.7%	93.80	2.0%	17.59	4.5%	E4H2-18	30	200	3.878	1.046	4.055	8.90	0.10%
vein	E4H2-9	0.08	15.2%	0.001	189.7%	29.13	1.3%	1.07	18.9%	E4H2-16	30	200	3.846	1.046	4.022	0.62	0.24%
vein	E4H2-8	0.11	15.3%	0.001	189.7%	36.25	1.9%	1.02	16.0%	-	-	-	-	-	-	-	-
vein	E4H2-56	0.13	19.4%	0.006	57.8%	64.35	2.9%	1.43	16.4%	-	-	-	-	-	-	-	-
vein	E4H2-52	0.04	25.5%	0.002	135.2%	18.93	5.0%	0.66	27.8%	E4H2-24	30	200	3.855	1.046	4.031	2.92	0.21%
vein	E4H2-49	0.07	15.2%	0.002	126.5%	20.22	3.0%	1.50	22.2%	-	-	-	-	-	-	-	-
basaltic crystal boundary	E4H2-6-66	3.47	3.8%	b.d.l.	b.d.l.	42.04	2.5%	39.46	6.4%	E4H2-6-88	20	400	3.813	1.048	3.997	-5.61	0.11%
OI	E4H2-6-68	0.82	8.3%	0.010	102.0%	75.42	2.2%	14.67	14.3%	-	-	-	-	-	-	-	-
Opx	E4H2-6-68	0.66	11.6%	0.003	189.7%	0.18	37.6%	0.29	67.2%	-	-	-	-	-	-	-	-
Opx	E4H2-6-72	0.78	9.4%	b.d.l.	b.d.l.	0.01	105.1%	0.09	104.9%	-	-	-	-	-	-	-	-
Opx	E4H2-6-64	1.01	4.5%	b.d.l.	b.d.l.	0.04	65.9%	0.18	69.0%	-	-	-	-	-	-	-	-
Opx	E4H2-6-73	1.05	7.2%	b.d.l.	b.d.l.	0.16	37.6%	0.55	50.5%	-	-	-	-	-	-	-	-
Opx	E4H2-6-65	1.26	7.4%	0.002	189.7%	0.01	189.7%	0.16	90.9%	-	-	-	-	-	-	-	-

# = matrix corrected

Table B3 (continued): Li, Be, B, Sr contents and  $\delta^{11}\text{B}$  values of serpentinites, analyzed by SIMS, analyses also in electronic appendix.

Texture	Analysis	Li ( $\mu\text{g/g}$ )	$2\sigma_{\text{mean}}$	Be ( $\mu\text{g/g}$ )	$2\sigma_{\text{mean}}$	B ( $\mu\text{g/g}$ )	$2\sigma_{\text{mean}}$	Sr ( $\mu\text{g/g}$ )	$2\sigma_{\text{mean}}$	Analysis	$I_p$ (nA)	n	$^{11}\text{B}/^{10}\text{B}$ measured	$\alpha_{\text{inst}}$	$^{11}\text{B}/^{10}\text{B}$ corrected	$\delta^{11}\text{B}$ (‰) <sup>#</sup>	$2\sigma_{\text{mean}}$
mesh rim	E4H2-6-71	0.56	8.1%	0.002	189.7%	121.27	1.0%	12.57	8.0%	-	-	400	3.831	1.048	4.016	-0.83	0.11%
mesh rim	E4H2-6-69	2.77	3.3%	b.d.l.	85.3%	61.68	1.4%	32.16	5.7%	-	-	400	3.857	1.048	4.043	5.88	0.13%
mesh rim	E4H2-6-84	3.41	5.2%	0.009	189.7%	69.66	2.8%	9.22	14.7%	-	-	400	3.831	1.048	4.016	-0.83	0.11%
mesh rim	E4H2-6-67	3.59	4.2%	0.002	189.7%	56.02	1.4%	19.91	9.5%	-	-	400	3.857	1.048	4.043	5.88	0.13%
mesh rim	E4H2-6-83	3.89	4.0%	0.009	63.2%	60.18	1.7%	5.90	14.4%	-	-	400	3.831	1.048	4.016	-0.83	0.11%
mesh rim	E4H2-6-91	3.99	2.7%	0.007	77.5%	79.61	1.3%	7.24	13.6%	E4H2-6-90	20	400	3.831	1.048	4.016	-0.83	0.11%
mesh rim	E4H2-6-79	4.17	1.5%	0.004	126.5%	75.49	2.3%	2.75	8.5%	E4H2-6-79	20	400	3.857	1.048	4.043	5.88	0.13%
mesh rim	E4H2-6-89	4.28	4.4%	0.007	77.5%	54.19	2.0%	11.12	14.3%	-	-	400	3.831	1.048	4.016	-0.83	0.11%
mesh rim	E4H2-6-78	4.68	2.2%	0.005	96.6%	57.54	1.3%	3.98	12.6%	-	-	400	3.831	1.048	4.016	-0.83	0.11%
mesh rim	E4H2-6-90	5.75	4.2%	0.013	70.7%	71.76	2.5%	3.65	16.7%	-	-	400	3.831	1.048	4.016	-0.83	0.11%
mesh rim	E4H2-6-75	4.30	5.3%	0.002	189.7%	71.50	1.7%	32.49	5.2%	-	-	400	3.831	1.048	4.016	-0.83	0.11%
vein	E4H2-6-86	0.06	24.8%	0.002	189.7%	16.76	4.4%	0.98	28.5%	-	-	400	3.831	1.048	4.016	-0.83	0.11%
vein dense	MAK2B-15	0.03	36.6%	0.001	189.7%	7.23	3.5%	0.06	105.0%	MAK2B-1	10	400	3.770	1.054	3.973	-11.35	0.40%
vein dense	MAK2B-16	0.04	31.0%	0.002	126.5%	8.07	2.5%	0.05	96.6%	MAK2B-2	10	400	3.781	1.054	3.984	-8.64	0.38%
vein dense	MAK2B-17	0.03	39.3%	b.d.l.	189.7%	6.30	4.6%	0.16	48.8%	MAK2B-3	10	400	3.768	1.054	3.971	-12.05	0.38%
vein dense	MAK2B-3	0.04	26.2%	0.001	189.7%	9.82	2.7%	0.16	65.4%	-	-	400	3.811	1.054	4.016	-0.83	0.16%
vein dense	MAK2B-4	0.03	17.9%	b.d.l.	104.9%	10.50	3.0%	0.13	49.2%	-	-	400	3.807	1.054	4.012	-1.76	0.16%
vein dense	MAK2B-5	0.10	17.2%	b.d.l.	42.2%	39.91	4.8%	0.40	45.7%	-	-	400	3.801	1.054	4.006	-3.33	0.16%
vein dense	MAK2B-6	0.08	21.2%	b.d.l.	84.7%	24.05	2.4%	0.16	70.1%	MAK2B-6	10	400	3.829	1.054	4.035	3.96	0.16%
mesh center	MAK2B-7	0.28	9.2%	0.021	42.2%	39.87	1.8%	2.85	13.2%	-	-	400	3.829	1.054	4.035	3.96	0.16%
mesh rim	MAK2E-8	4.32	2.4%	0.006	84.7%	70.71	1.5%	3.63	12.2%	-	-	400	3.829	1.054	4.035	3.96	0.16%
mesh rim + center	MAK2B-12	0.17	12.3%	0.008	77.6%	36.51	1.3%	1.30	19.8%	MAK2B-5	10	400	3.807	1.054	4.012	-1.76	0.16%
mesh rim + center	MAK2B-13	0.36	9.0%	0.016	50.7%	36.26	1.6%	1.42	25.8%	MAK2B-4	10	400	3.801	1.054	4.006	-3.33	0.16%
m. rim + cr. bound.	MAK2E-1	0.46	13.8%	0.003	126.5%	59.32	1.1%	5.14	10.2%	-	-	400	3.829	1.054	4.035	3.96	0.16%
m. rim + cr. bound.	MAK2E-6	0.66	9.0%	0.004	126.6%	40.35	1.5%	14.08	21.9%	-	-	400	3.829	1.054	4.035	3.96	0.16%
m. rim + cr. bound.	MAK2E-7	0.33	11.2%	0.010	81.4%	45.87	2.7%	4.38	19.3%	-	-	400	3.829	1.054	4.035	3.96	0.16%
coarse fibers	MAK2B-9	0.44	13.8%	0.002	126.5%	48.29	3.4%	1.76	15.8%	MAK2B-8	10	400	3.829	1.054	4.035	3.96	0.16%
vein coarse	MAK2B-1	0.69	6.0%	0.344	9.5%	34.66	2.1%	2.10	13.8%	-	-	400	3.829	1.054	4.035	3.96	0.16%
vein coarse	MAK2B-11	0.50	6.3%	0.012	46.0%	25.33	1.5%	1.22	17.7%	-	-	400	3.829	1.054	4.035	3.96	0.16%
vein coarse	MAK2B-14	0.51	5.4%	0.958	10.2%	32.39	1.5%	1.58	27.3%	-	-	400	3.829	1.054	4.035	3.96	0.16%
basaltic	A003R01-27	13.71	1.7%	b.d.l.	40.91	40.91	1.6%	27.58	6.9%	A003R01-27	10	400	3.899	1.045	4.073	13.26	0.28%
basaltic	A003R01-28	4.50	3.2%	b.d.l.	26.06	26.06	2.2%	17.76	7.2%	-	-	400	3.899	1.045	4.073	13.26	0.28%
crystal boundary	A003R01-17	0.33	6.6%	b.d.l.	6.21	6.21	3.4%	2.70	5.7%	-	-	400	3.842	1.045	4.014	-1.30	0.32%
crystal boundary	A003R01-8	0.04	21.9%	0.001	189.7%	2.45	7.4%	1.46	12.6%	A003R01-7	10	400	3.842	1.045	4.014	-1.30	0.32%
crystal boundary	A003R01-14	0.66	13.8%	b.d.l.	85.41	85.41	4.8%	4.31	20.0%	A003R01-14	10	400	3.906	1.045	4.081	15.18	0.42%
mesh center	A003R01-18	15.97	1.2%	0.002	189.7%	85.41	0.9%	41.56	6.2%	-	-	400	3.893	1.045	4.067	11.81	0.19%
mesh center	A003R01-20	9.67	1.8%	b.d.l.	92.75	92.75	3.3%	43.88	1.1%	A003R01-20	10	400	3.879	1.045	4.052	8.08	0.23%
mesh rim	A003R01-13	10.84	1.9%	b.d.l.	82.13	82.13	1.8%	9.78	8.1%	A003R01-13	10	400	3.908	1.045	4.082	15.59	0.29%
mesh rim	A003R01-15	11.31	1.9%	b.d.l.	43.93	43.93	2.1%	8.38	11.1%	A003R01-15	10	400	3.915	1.045	4.090	17.55	0.23%
mesh rim	A003R01-16	14.47	3.0%	b.d.l.	42.55	42.55	1.7%	11.49	6.9%	A003R01-16	10	400	3.915	1.045	4.090	17.55	0.23%
mesh rim	A003R01-21	16.63	1.2%	0.002	189.7%	52.38	1.8%	14.60	6.6%	-	-	400	3.915	1.045	4.090	17.55	0.23%

# = matrix corrected

Table B3 (continued): Li, Be, B, Sr contents and  $\delta^{11}\text{B}$  values of serpentinites, analyzed by SIMS, analyses also in electronic appendix.

Texture	Analysis	Li ( $\mu\text{g/g}$ )	$2\sigma_{\text{mean}}$	Be ( $\mu\text{g/g}$ )	$2\sigma_{\text{mean}}$	B ( $\mu\text{g/g}$ )	$2\sigma_{\text{mean}}$	Sr ( $\mu\text{g/g}$ )	$2\sigma_{\text{mean}}$	Analysis	$I_p$ (nA)	n	$^{11}\text{B}/^{10}\text{B}$ measured	$\alpha_{\text{first}}$	$^{11}\text{B}/^{10}\text{B}$ corrected	$\delta^{11}\text{B}$ (‰) <sup>#</sup>	$2\sigma_{\text{mean}}$
mesh rim	A003R01-22	12.47	2.3%	b.d.l.	b.d.l.	38.82	1.8%	11.04	9.9%	-	10	400	3.924	1.045	4.100	19.84	0.31%
mesh rim	A003R01-30	16.15	4.2%	b.d.l.	b.d.l.	36.33	3.7%	17.11	4.1%	A003R01-30	10	400	3.924	1.045	4.100	19.84	0.31%
mesh rim	A003R01-7	13.96	1.9%	0.002	189.7%	57.27	1.6%	10.11	11.1%	A003R01-8	10	400	3.873	1.045	4.046	6.66	0.21%
mesh rim	A003R01-9	17.64	1.8%	0.002	189.7%	46.72	1.6%	8.09	9.6%	A003R01-9	10	400	3.889	1.045	4.063	10.70	0.25%
Ol	A003R01-19	0.60	10.2%	b.d.l.	b.d.l.	0.08	34.6%	0.40	47.1%	-	-	-	-	-	-	-	-
Opx	A003R01-25	2.10	5.8%	b.d.l.	b.d.l.	1.97	6.7%	0.37	37.8%	-	-	-	-	-	-	-	-
Opx	A003R01-26	2.26	5.2%	b.d.l.	b.d.l.	1.75	12.0%	0.53	39.6%	A003R01-26	10	400	3.900	1.045	4.075	13.74	1.54%
Opx	A003R01-29	2.61	3.9%	0.002	189.7%	0.43	14.9%	0.18	58.2%	A003R01-29	10	400	3.891	1.045	4.065	11.21	1.31%
vein	A003R01-1	7.30	2.2%	0.002	189.7%	40.06	1.7%	9.22	12.7%	A003R01-1	10	400	3.900	1.045	4.074	13.52	0.28%
vein	A003R01-3	3.72	4.1%	b.d.l.	b.d.l.	33.76	2.0%	7.48	6.8%	A003R01-3	10	400	3.883	1.045	4.056	9.17	0.33%
vein	A003R01-4	0.20	14.5%	b.d.l.	b.d.l.	12.63	4.5%	4.00	18.6%	A003R01-4	10	400	3.854	1.045	4.027	1.85	0.38%
vein	A003R01-5	1.10	5.3%	0.002	189.7%	43.39	4.8%	12.07	7.2%	A003R01-5	10	400	3.861	1.045	4.034	3.68	0.34%
vein	A003R01-6	7.10	1.9%	b.d.l.	b.d.l.	45.55	1.2%	10.16	9.0%	A003R01-6	10	400	3.887	1.045	4.061	10.29	0.27%
vein	A003R01-2	0.46	8.0%	b.d.l.	b.d.l.	35.43	4.9%	8.63	7.6%	-	-	-	-	-	-	-	-
mesh center	A007R01-6	0.21	36.9%	b.d.l.	b.d.l.	130.40	2.9%	-	-	A007R01-6	10	400	3.895	1.045	4.071	12.71	0.25%
mesh rim	A007R01-14	0.68	20.4%	0.015	96.6%	154.74	2.8%	-	-	A007R01-14	10	400	3.893	1.045	4.069	12.37	0.20%
mesh rim	A007R01-2	0.40	19.9%	0.004	189.7%	132.70	2.2%	-	-	A007R01-2	10	400	3.903	1.045	4.080	14.88	0.25%
mesh rim	A007R01-10	0.43	30.1%	0.005	189.7%	127.45	2.3%	-	-	-	-	-	-	-	-	-	-
mesh rim	A007R01-11	0.30	26.8%	b.d.l.	b.d.l.	142.34	3.3%	-	-	-	-	-	-	-	-	-	-
mesh rim	A007R01-5	0.34	19.8%	0.004	189.7%	35.58	2.3%	-	-	A007R01-5	10	400	3.914	1.045	4.091	17.64	0.29%
mesh rim	A007R01-12	1.27	16.5%	b.d.l.	b.d.l.	108.45	3.3%	-	-	-	-	-	-	-	-	-	-
mesh rim	A007R01-4	1.29	19.5%	b.d.l.	b.d.l.	143.34	2.8%	-	-	A007R01-4	10	400	3.932	1.045	4.110	22.49	0.23%
mesh rim	A007R01-8	2.25	11.0%	0.026	84.6%	63.36	3.0%	-	-	-	-	-	-	-	-	-	-
mesh rim	A007R01-9	0.67	16.5%	b.d.l.	b.d.l.	113.34	2.8%	-	-	-	-	-	-	-	-	-	-
mesh rim	A007R01-7	0.83	17.1%	0.011	126.5%	62.34	4.6%	-	-	A007R01-7	10	400	3.911	1.045	4.088	16.91	0.25%
mesh rim	A007R01-1	1.16	15.2%	0.014	96.6%	0.06	96.6%	-	-	-	-	-	-	-	-	-	-
Ol	A007R01-13	0.83	19.1%	0.031	126.5%	0.62	63.3%	-	-	-	-	-	-	-	-	-	-
Ol	A007R01-3	0.79	24.2%	0.009	189.7%	0.28	78.3%	-	-	-	-	-	-	-	-	-	-
Opx	A007R01-15	1.81	8.3%	0.005	189.7%	0.81	27.9%	-	-	-	-	-	-	-	-	-	-
vein	A007R01-17	0.22	46.7%	0.011	126.5%	22.17	8.0%	-	-	A007R01-17	10	400	3.884	1.045	4.060	9.99	0.46%
vein	A007R01-18	0.14	50.8%	0.005	189.7%	20.62	5.0%	-	-	-	-	-	-	-	-	-	-
vein	A007R01-19	0.23	36.6%	b.d.l.	b.d.l.	24.67	6.3%	-	-	-	-	-	-	-	-	-	-
mesh rim	A007R01-20	5.13	5.7%	0.005	189.7%	78.61	3.3%	-	-	A007R01-20	10	400	3.924	1.045	4.102	20.36	0.19%
mesh rim	A007R01-21	0.47	34.2%	0.015	96.6%	113.94	3.5%	-	-	A007R01-21	10	400	3.938	1.045	4.117	24.04	0.19%
Ol	A007R01-22	1.24	16.2%	0.013	126.5%	0.16	96.6%	-	-	-	-	-	-	-	-	-	-
mesh rim	A007R01-23	2.22	5.6%	b.d.l.	b.d.l.	58.81	2.3%	-	-	A007R01-23	10	400	3.907	1.045	4.084	15.96	0.24%
vein	A007R01-24	0.13	47.7%	b.d.l.	b.d.l.	27.77	6.4%	-	-	A007R01-24	10	400	3.842	1.045	4.016	-0.81	0.47%
vein	A007R01-25	0.24	26.5%	0.005	189.7%	22.54	5.7%	-	-	A007R01-25	10	400	3.864	1.045	4.038	4.69	0.41%
mesh center	A007R01-26	0.17	26.4%	b.d.l.	b.d.l.	99.74	0.7%	30.88	5.4%	A007R01-26	10	400	3.885	1.045	4.061	10.36	0.22%
mesh center	A007R01-27	0.06	28.4%	b.d.l.	b.d.l.	89.21	1.3%	25.68	5.4%	A007R01-27	10	400	3.874	1.045	4.049	7.38	0.16%
basaltic	A007R01-28	1.07	9.3%	0.002	189.7%	41.49	2.2%	16.91	8.7%	A007R01-28	10	400	3.895	1.045	4.071	12.72	0.28%
basaltic	A007R01-29	3.02	3.4%	b.d.l.	b.d.l.	39.55	3.6%	21.62	9.5%	A007R01-29	10	400	3.888	1.045	4.064	11.14	0.31%

# = matrix corrected

**Table B3 (continued): Li, Be, B, Sr contents and  $\delta^{11}\text{B}$  values of serpentinites, analyzed by SIMS, analyses also in electronic appendix.**

Texture	Analysis	Li ( $\mu\text{g/g}$ )	$2\sigma_{\text{mean}}$	Be ( $\mu\text{g/g}$ )	$2\sigma_{\text{mean}}$	B ( $\mu\text{g/g}$ )	$2\sigma_{\text{mean}}$	Sr ( $\mu\text{g/g}$ )	$2\sigma_{\text{mean}}$	Analysis	$I_p$ (nA)	n	$^{11}\text{B}/^{10}\text{B}$ measured	$\alpha_{\text{inst}}$	$^{11}\text{B}/^{10}\text{B}$ corrected	$\delta^{11}\text{B}$ (‰) <sup>#</sup>	$2\sigma_{\text{mean}}$
vein	A007R01-30	0.36	5.7%	0.000	189.7%	67.03	1.0%	7.55	4.0%	A007R01-30	10	400	3.877	1.045	4.052	8.17	0.27%
vein	A007R01-30b	0.36	8.6%	0.002	189.7%	65.46	1.6%	24.33	25.0%	-	-	-	-	-	-	-	-
vein	A007R01-31	1.25	6.1%	b.d.l.	b.d.l.	63.64	2.1%	34.65	2.6%	A007R01-31	10	400	3.871	1.045	4.046	6.61	0.24%
vein	A007R01-32	0.60	18.9%	b.d.l.	b.d.l.	42.55	2.7%	24.29	9.2%	A007R01-32	10	400	3.875	1.045	4.050	7.69	0.31%
vein	A007R01-33	0.34	12.0%	b.d.l.	b.d.l.	61.12	2.0%	36.98	5.4%	A007R01-33	10	400	3.873	1.045	4.048	7.10	0.25%
vein	A007R01-34	0.97	11.7%	b.d.l.	b.d.l.	22.81	2.4%	13.11	7.5%	A007R01-34	10	400	3.884	1.045	4.059	9.86	0.45%
vein	A007R01-35	0.19	19.8%	b.d.l.	b.d.l.	21.68	2.7%	10.00	10.0%	A007R01-35	10	400	3.888	1.045	4.064	11.08	0.60%
vein	A007R01-36	0.23	17.5%	b.d.l.	b.d.l.	39.39	9.7%	9.78	12.3%	A007R01-36	10	400	3.895	1.045	4.072	12.93	0.35%
vein	A007R01-37	0.28	11.6%	0.001	189.7%	49.41	1.4%	0.88	22.6%	A007R01-37	10	400	3.867	1.045	4.042	5.69	0.23%
vein	A007R01-38	0.47	10.9%	0.004	126.5%	64.02	2.0%	1.93	24.9%	A007R01-38	10	400	3.854	1.045	4.028	2.17	0.21%
mesh center	A007R01-39	0.11	17.5%	b.d.l.	b.d.l.	125.21	1.4%	13.13	16.7%	A007R01-39	10	400	3.891	1.045	4.067	11.87	0.17%
mesh center	A011(40-42)																
mesh center	A011R01-14	2.31	14.5%	b.d.l.	b.d.l.	177.25	12.9%	10.73	9.4%	-	-	-	-	-	-	-	-
vein major	A011R01-7	2.55	5.8%	b.d.l.	b.d.l.	303.57	2.5%	6.06	12.4%	A011R01-7	10	400	3.833	1.045	4.005	-3.58	0.11%
vein major	A011R01-9	0.48	9.5%	0.002	189.7%	319.48	3.1%	1.37	26.4%	A011R01-9	10	400	3.831	1.045	4.003	-4.14	0.11%
mesh rim	A011R01-13	3.29	5.8%	b.d.l.	b.d.l.	119.35	11.0%	14.22	15.6%	A011R01-13	10	400	3.840	1.045	4.012	-1.87	0.18%
mesh rim	A011R01-15	1.44	10.6%	b.d.l.	b.d.l.	118.39	9.1%	11.64	10.7%	A011R01-15	10	400	3.854	1.045	4.027	1.81	0.20%
mesh rim	A011R01-3	0.23	20.5%	0.002	189.7%	248.47	0.8%	1.80	29.1%	A011R01-17	10	400	3.805	1.045	4.006	-3.23	0.16%
vein stiches	A011R01-4	0.26	12.9%	b.d.l.	b.d.l.	268.52	1.6%	26.58	5.7%	A011R01-3	10	400	3.971	1.045	3.971	-11.86	0.08%
vein stiches	A011R01-5	0.30	9.5%	0.002	189.7%	247.48	1.3%	344.40	2.5%	A011R01-4	10	400	3.807	1.045	3.978	-10.31	0.10%
vein stiches	A011R01-6	0.27	15.5%	b.d.l.	b.d.l.	240.26	0.9%	47.50	11.5%	-	-	-	-	-	-	-	-
vein stiches	A011R01-1	0.27	21.8%	b.d.l.	b.d.l.	323.71	1.2%	119.08	4.6%	-	-	-	-	-	-	-	-
basalte	A011R01-12	0.82	17.7%	b.d.l.	b.d.l.	37.09	6.8%			*A011R01-12	10	400	3.854	1.045	4.028	2.21	0.24%
basalte	A011R01-13	2.55	14.8%	b.d.l.	b.d.l.	143.20	2.7%			A011R01-13	10	400	3.877	1.045	4.051	7.71	0.15%
basalte	A011R01-9	0.57	19.8%	0.006	126.6%	32.57	3.5%			-	-	-	-	-	-	-	-
crystal boundary	A011R01-6	11.65	4.2%	b.d.l.	b.d.l.	45.04	3.6%			A011R01-6	10	400	3.895	1.045	4.070	12.46	0.29%
crystal boundary	A011R01-5	9.36	5.0%	b.d.l.	b.d.l.	88.93	2.6%			*A011R01-5	10	400	3.888	1.045	4.064	10.96	0.24%
crystal boundary	A011R01-4	16.30	4.0%	0.006	189.7%	51.47	5.5%			*A011R01-4	10	400	3.896	1.045	4.073	13.15	0.26%
mesh center	A011R01-30									*A011R01-30	10	400	3.880	1.045	4.055	8.82	0.20%
mesh center	A011R01-10	1.00	14.7%	0.014	77.5%	113.08	3.0%			A011R01-10	10	400	3.899	1.045	4.073	13.28	0.21%
mesh center	A011R01-11	2.80	7.5%	0.019	96.0%	116.40	2.3%			A011R01-11	10	400	3.880	1.045	4.054	8.53	0.17%
mesh center	A011R01-26	0.84	14.7%	0.023	84.5%	77.88	2.4%			*A011R01-11	10	400	0.000	1.045	4.054	7.49	0.00%
mesh center	A011R01-27	0.32	11.7%	0.002	96.6%	4.61	3.3%			-	-	-	-	-	-	-	-
mesh center	A011R01-28	0.69	12.6%	0.030	54.0%	81.64	1.4%			-	-	-	-	-	-	-	-
mesh center	A011R01-29	0.40	16.1%	0.015	84.9%	83.05	2.8%			-	-	-	-	-	-	-	-
mesh center	A011R01-7	5.37	4.0%	0.005	126.5%	50.28	2.6%			-	-	-	-	-	-	-	-
mesh rim	A011R01-3	2.93	7.3%	0.005	126.5%	108.59	1.8%			A011R01-7	10	400	3.907	1.045	4.082	15.40	0.21%
mesh rim	A011R01-8	1.25	13.7%	0.005	189.7%	76.24	2.5%			A011R01-3	10	400	3.900	1.045	4.075	13.76	0.24%
mesh rim	A011R01-25	2.49	13.9%	0.006	189.7%	44.25	6.2%			*A011R01-8	10	400	3.886	1.045	4.062	10.46	0.19%
mesh rim	A011R01-23	0.69	18.0%	0.004	189.7%	91.28	3.4%			*A011R01-25	10	400	3.868	1.045	4.043	5.82	0.26%
OI	A011R01-1	1.28	10.2%	0.006	189.7%	0.01	189.7%			*A011R01-23	10	400	3.844	1.045	4.017	-0.48	0.19%

<sup>#</sup> = matrix corrected

Table B3 (continued): Li, Be, B, Sr contents and  $\delta^{11}\text{B}$  values of serpentinites, analyzed by SIMS, analyses also in electronic appendix.

Texture	Analysis	Li ( $\mu\text{g/g}$ )	$2\sigma_{\text{mean}}$	Be ( $\mu\text{g/g}$ )	$2\sigma_{\text{mean}}$	B ( $\mu\text{g/g}$ )	$2\sigma_{\text{mean}}$	Sr ( $\mu\text{g/g}$ )	$2\sigma_{\text{mean}}$	Analysis	$I_p$ (nA)	n	$^{11}\text{B}/^{10}\text{B}$ measured	$\alpha_{\text{first}}$	$^{11}\text{B}/^{10}\text{B}$ corrected	$\delta^{11}\text{B}$ (‰) <sup>#</sup>	$2\sigma_{\text{mean}}$
Ol	A011R01-2	1.19	14.9%	0.009	0.009	0.01	189.7%			-							
Opx	A011R01-24	2.15	12.1%	b.d.l.	b.d.l.		0.0%			-							
vein	A011R01-15	1.61	17.6%	0.005	0.005	45.05	5.3%			-							
vein	A011R01-16	1.70	9.2%	0.007	0.007	48.51	2.8%			-							
vein	A011R01-18	1.55	15.5%	b.d.l.	b.d.l.	48.07	2.4%			-							
vein	A011R01-19	1.25	14.2%	0.005	0.005	49.02	4.4%			*A011R01-18	10	400	3.855	1.045	4.028	2.03	0.26%
vein	A011R01-14	1.71	15.4%	0.003	0.003	44.97	2.1%			*A011R01-19	10	400	3.857	1.045	4.032	3.05	0.26%
vein	A011R01-17	1.62	16.2%	0.017	0.017	54.65	2.9%			-							
vein	A011R01-21	1.24	9.8%	0.008	0.008	53.63	3.9%			-							
vein	A011R01-20	1.64	12.8%	0.009	0.009	52.40	2.8%			-							
vein	A011R01-22	1.70	14.2%	0.015	0.015	46.88	3.3%			-							
crystal boundary	A012R01-8	3.05	4.4%	0.002	0.002	51.64	2.2%	14.69	6.9%	*A011R01-22	10	400	3.839	1.045	4.012	-1.75	0.29%
mesh center	A012R01-4	7.19	3.3%	0.004	0.004	95.34	6.2%	14.03	8.1%	A012R01-8	10	400	3.888	1.045	4.062	10.49	0.22%
mesh center	A012R01-7	7.91	4.5%	b.d.l.	b.d.l.	113.46	17.2%	16.01	6.9%	A012R01-4	10	400	3.876	1.045	4.050	7.53	0.23%
mesh rim	A012R01-1	14.65	3.5%	0.003	0.003	70.78	5.9%	15.91	7.5%	A012R01-7	10	400	3.897	1.045	4.072	12.91	0.20%
mesh rim	A012R01-2	12.34	3.1%	0.002	0.002	51.20	2.5%	11.63	8.5%	-							
mesh rim	A012R01-3	0.95	7.7%	b.d.l.	b.d.l.	48.24	4.5%	6.91	7.6%	A012R01-3	10	400	3.859	1.045	4.032	3.10	0.23%
mesh rim	A012R01-6	27.72	1.5%	b.d.l.	b.d.l.	61.72	2.4%	7.93	13.5%	A012R01-6	10	400	3.904	1.045	4.079	14.69	0.21%
Ol	A012R01-5	1.10	10.2%	b.d.l.	b.d.l.	1.46	9.8%	0.47	37.9%	A012R01-5	10	400	3.841	1.045	4.012	-1.74	2.00%
basaltic	A012R01-9	1.40	10.0%	b.d.l.	b.d.l.	46.35	4.3%	14.18	8.1%	A012R01-9	10	400	3.886	1.045	4.062	10.57	0.29%
mesh rim	A012R01-12	16.59	2.1%	0.004	0.004	69.98	1.2%	2.14	26.8%	A012R01-12	10	400	3.904	1.045	4.080	15.06	0.23%
mesh rim	A012R01-13	15.33	2.9%	0.004	0.004	66.10	1.7%	2.41	19.3%	A012R01-13	10	400	3.896	1.045	4.073	13.21	0.24%
Ol	A012R01-15	0.74	10.1%	b.d.l.	b.d.l.	0.01	126.5%	0.25	58.8%	A012R01-15	10	400	3.859	1.045	4.034	3.62	1.01%
Ol	A012R01-19	0.56		0.002	0.002	0.02	0.36	0.36		-							
Opx	A012R01-14	1.19	4.7%	b.d.l.	b.d.l.	0.04	48.9%	0.03	189.7%	A012R01-14	10	400	3.897	1.045	4.074	13.46	1.71%
Opx	A012R01-20	1.48		0.002	0.002	0.24		0.10		-							
vein	A012R01-10	1.17	5.3%	b.d.l.	b.d.l.	79.77	6.1%	14.37	9.8%	A012R01-10	10	400	3.855	1.045	4.030	2.53	0.19%
vein	A012R01-16	1.42	6.2%	b.d.l.	b.d.l.	56.49	2.8%	3.44	30.2%	A012R01-16	10	400	3.904	1.045	4.080	15.10	0.27%
vein	A012R01-17	1.16	8.5%	0.002	0.002	291.98	0.8%	2.88	11.1%	A012R01-17	10	400	3.806	1.045	3.978	-10.15	0.12%
mesh center	A013R01-12	1.90	10.3%	0.012	0.012	167.37	2.0%	16.54	12.4%	A013R01-12	10	400	3.926	1.046	4.106	21.47	0.14%
basaltic	A013R01-17	1.32	7.5%	0.006	0.006	94.17	2.1%	6.43	10.5%	A013R01-17	10	400	3.929	1.046	4.110	22.41	0.21%
vein	A013R01-30	0.19	16.2%	b.d.l.	b.d.l.	96.23	1.5%	2.60	6.9%	A013R01-30	10	400	3.865	1.046	4.042	5.64	0.17%
vein	A013R01-8	0.39	11.4%	0.003	0.003	69.73	2.1%	12.47	5.7%	A013R01-8	10	400	3.844	1.045	4.019	-0.08	0.26%
vein	A013R01-31	0.31	15.1%	0.002	0.002	34.04	3.8%	8.04	13.8%	A013R01-31	10	400	3.891	1.046	4.070	12.54	0.30%
vein	A013R01-32	0.33	16.8%	b.d.l.	b.d.l.	26.89	4.7%	8.24	12.6%	A013R01-32	10	400	3.874	1.046	4.052	8.18	0.21%
vein	A013R01-28	0.36	14.9%	0.002	0.002	57.05	1.7%	10.23	8.9%	A013R01-28	10	400	3.862	1.046	4.040	5.02	0.26%
vein	A013R01-27	6.87	3.4%	0.007	0.007	62.31	1.3%	11.09	11.4%	A013R01-27	10	400	3.884	1.046	4.063	10.73	0.21%
vein	A013R01-29	5.80	2.8%	0.002	0.002	65.52	0.9%	10.83	8.9%	A013R01-29	10	400	3.900	1.046	4.080	14.93	0.22%
mesh center	A013R01-15	2.52	6.9%	0.013	0.013	191.65	1.5%	11.59	16.3%	A013R01-15	10	400	3.918	1.046	4.099	19.57	0.26%
mesh center	A013R01-18	0.98	12.1%	0.006	0.006	380.13	1.0%	15.85	9.6%	A013R01-18	10	400	3.919	1.046	4.099	19.67	0.17%
mesh center	A013R01-3	4.29	10.2%	b.d.l.	b.d.l.	89.03	2.8%	29.09	19.3%	A013R01-3	10	400	3.906	1.045	4.084	15.90	0.32%

\* = matrix corrected

**Table B3 (continued): Li, Be, B, Sr contents and  $\delta^{11}\text{B}$  values of serpentinites, analyzed by SIMS, analyses also in electronic appendix.**

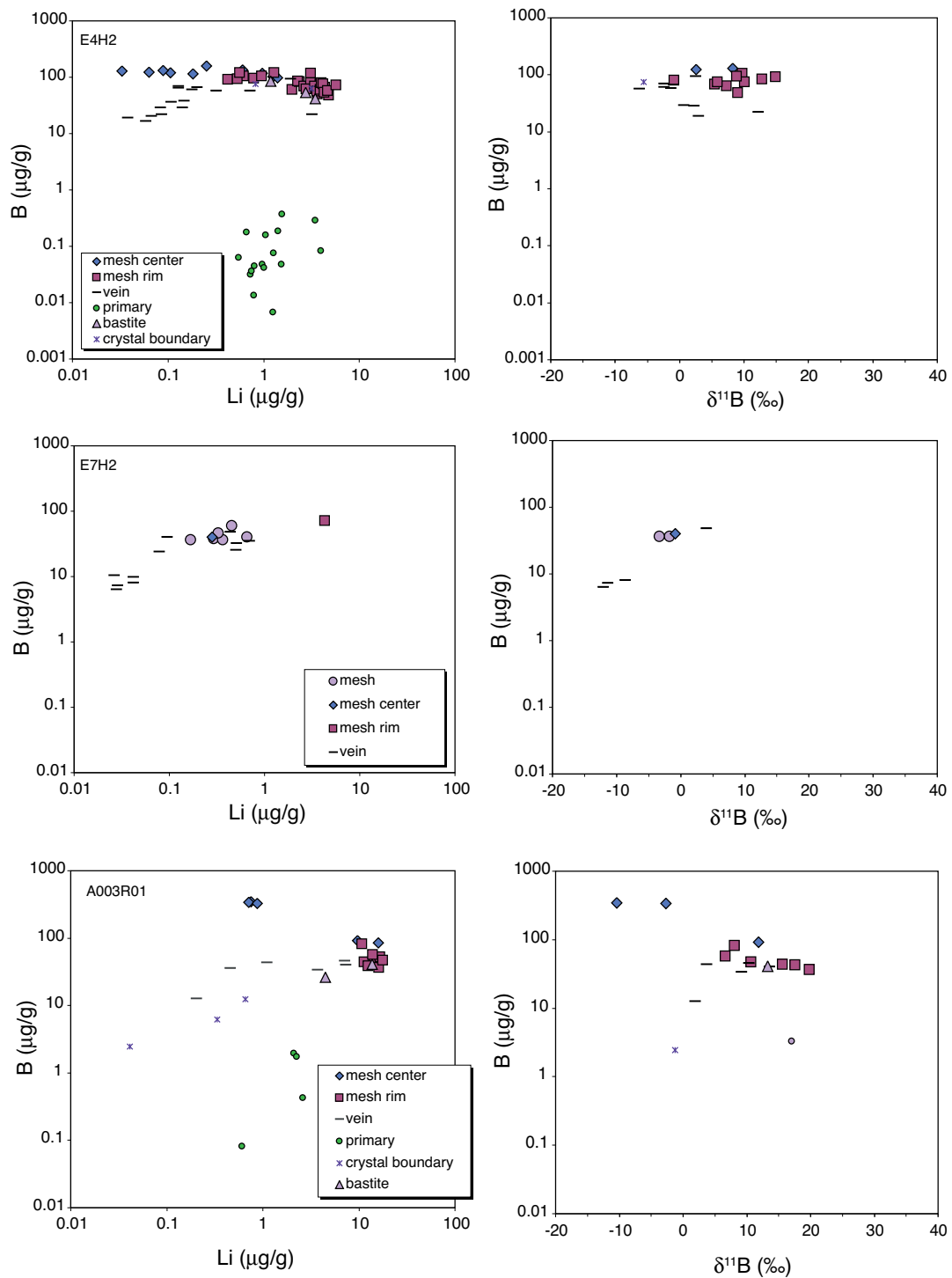
Texture	Analysis	Li ( $\mu\text{g/g}$ )	$2\sigma_{\text{mean}}$	Be ( $\mu\text{g/g}$ )	$2\sigma_{\text{mean}}$	B ( $\mu\text{g/g}$ )	$2\sigma_{\text{mean}}$	Sr ( $\mu\text{g/g}$ )	$2\sigma_{\text{mean}}$	Analysis	$I_p$ (nA)	n	$^{11}\text{B}/^{10}\text{B}$ measured	$\alpha_{\text{inst}}$	$^{11}\text{B}/^{10}\text{B}$ corrected	$\delta^{11}\text{B}$ (‰) <sup>#</sup>	$2\sigma_{\text{mean}}$
mesh rim	A013R01-9	5.41	2.1%	0.004	0.004	97.29	1.5%	13.71	7.3%	A013R01-9	10	400	3.920	1.046	4.100	20.04	0.13%
mesh rim	A013R01-10	3.73	5.9%	b.d.l.	b.d.l.	187.61	1.4%	8.49	7.9%	A013R01-10	10	400	3.913	1.046	4.093	18.20	0.10%
mesh rim	A013R01-13	3.95	6.1%	0.008	77.5%	237.86	1.3%	8.66	12.4%	A013R01-13	10	400	3.922	1.046	4.102	20.40	0.13%
mesh rim	A013R01-14	4.28	5.0%	0.002	189.7%	233.57	1.3%	11.12	10.4%	A013R01-14	10	400	3.929	1.046	4.110	22.36	0.12%
mesh rim	A013R01-19	2.30	4.1%	0.004	189.7%	260.25	1.1%	6.83	10.0%	A013R01-19	10	400	3.918	1.046	4.098	19.37	0.12%
mesh rim	A013R01-4	1.81	7.7%	0.008	96.7%	38.64	2.9%	10.71	11.5%	A013R01-4	10	400	3.896	1.045	4.073	13.16	0.31%
Ol	A013R01-33	1.26	9.5%	b.d.l.	b.d.l.	0.10	26.9%	0.25	37.7%	-	-	-	-	-	-	-	-
Opx	A013R01-34	1.29	5.5%	b.d.l.	b.d.l.	0.29	24.1%	0.12	84.7%	-	-	-	-	-	-	-	-
mesh	A013R01-2	7.08	3.7%	0.002	189.7%	108.79	2.1%	13.42	10.0%	A013R01-2	10	400	3.926	1.045	4.104	20.97	0.15%
basaltic	A013R01-1	4.30	2.2%	0.002	189.7%	37.29	2.4%	17.88	4.5%	A013R01-1	10	400	3.904	1.045	4.081	15.35	0.25%
vein	A013R01-11	4.36	4.9%	0.002	189.7%	39.75	1.6%	8.49	9.2%	A013R01-11	10	400	3.901	1.046	4.080	15.04	0.36%
vein	A013R01-16	8.26	3.4%	0.007	105.3%	75.09	1.1%	4.11	21.5%	A013R01-16	10	400	3.917	1.046	4.097	19.23	0.14%
vein	A013R01-20	3.06	3.6%	0.005	126.5%	29.54	3.7%	10.84	13.1%	A013R01-20	10	400	3.889	1.046	4.068	11.97	0.32%
vein	A013R01-39	7.90	6.0%	b.d.l.	b.d.l.	76.92	1.4%	-	-	-	-	-	-	-	-	-	-
vein	A013R01-40	9.55	5.4%	0.004	189.7%	74.27	3.0%	-	-	-	-	-	-	-	-	-	-
vein	A013R01-41	9.19	4.0%	0.011	77.5%	79.32	2.5%	-	-	-	-	-	-	-	-	-	-
vein	A013R01-35	9.47	6.2%	0.014	84.3%	73.18	2.4%	-	-	-	-	-	-	-	-	-	-
vein	A013R01-36	6.22	6.1%	b.d.l.	b.d.l.	73.51	2.1%	-	-	-	-	-	-	-	-	-	-
vein	A013R01-37	8.25	2.9%	0.007	135.0%	58.72	1.5%	-	-	-	-	-	-	-	-	-	-
vein	A013R01-38	7.00	4.1%	b.d.l.	b.d.l.	58.88	2.2%	-	-	-	-	-	-	-	-	-	-
vein	A013R01-42	7.43	4.9%	0.005	126.5%	57.80	1.8%	-	-	-	-	-	-	-	-	-	-
vein	A013R01-43	4.82	8.1%	0.011	77.5%	62.71	2.3%	-	-	-	-	-	-	-	-	-	-
vein	A013R01-44	5.72	4.0%	0.003	189.7%	57.98	3.0%	-	-	-	-	-	-	-	-	-	-
vein	A013R01-45	6.81	6.5%	0.003	189.7%	61.76	2.6%	-	-	-	-	-	-	-	-	-	-
vein	A013R01-46	9.56	1.9%	0.009	96.6%	69.70	2.8%	-	-	-	-	-	-	-	-	-	-
vein	A013R01-47	0.49	19.9%	b.d.l.	b.d.l.	56.00	3.3%	-	-	-	-	-	-	-	-	-	-
vein	A013R01-48	0.31	28.1%	0.011	96.6%	42.34	3.2%	-	-	-	-	-	-	-	-	-	-
vein	A013R01-49	0.43	26.4%	0.010	126.5%	49.56	5.1%	-	-	-	-	-	-	-	-	-	-
vein	A013R01-50	0.27	41.7%	b.d.l.	b.d.l.	61.41	2.6%	-	-	-	-	-	-	-	-	-	-
vein	A013R01-51	0.32	17.5%	0.007	126.5%	60.19	1.7%	-	-	-	-	-	-	-	-	-	-
vein	A013R01-52	0.41	20.1%	0.006	126.5%	61.29	3.0%	-	-	-	-	-	-	-	-	-	-
vein	A013R01-53	3.12	8.8%	0.007	126.5%	61.87	3.4%	-	-	-	-	-	-	-	-	-	-
vein	A013R01-54	10.01	4.0%	0.010	96.6%	77.67	3.3%	-	-	-	-	-	-	-	-	-	-
mesh rim	A013R01-55	1.64	14.1%	0.023	77.5%	200.92	1.9%	-	-	-	-	-	-	-	-	-	-
mesh center	A013R01-56	2.40	18.3%	b.d.l.	b.d.l.	225.18	1.5%	-	-	-	-	-	-	-	-	-	-
Cpx	A017G02-15	2.09	13.5%	0.071	43.9%	0.48	25.1%	-	-	-	-	-	-	-	-	-	-
crystal boundary	A017G02-10	4.15	11.0%	0.005	189.7%	48.29	4.2%	-	-	A017G02-10	10	400	3.885	1.045	4.059	9.76	0.37%
crystal boundary	A017G02-7	8.63	9.3%	b.d.l.	b.d.l.	55.33	4.8%	-	-	A017G02-7	10	400	3.879	1.045	4.053	8.29	0.28%
mesh center	A017G02-11	0.08	65.6%	0.004	189.7%	168.90	1.3%	-	-	-	-	-	-	-	-	-	-
mesh center	A017G02-8	0.11	43.9%	0.004	189.7%	130.34	3.1%	-	-	-	-	-	-	-	-	-	-
mesh center	A017G02-2	2.06	9.5%	0.003	189.7%	33.71	4.8%	-	-	A017G02-2	10	400	3.859	1.045	4.031	2.91	0.17%
mesh center	A017G02-3	0.11	34.8%	b.d.l.	b.d.l.	58.40	3.8%	-	-	-	-	-	-	-	-	-	-

# = matrix corrected

Table B3 (continued): Li, Be, B, Sr contents and  $\delta^{11}\text{B}$  values of serpentinites, analyzed by SIMS, analyses also in electronic appendix.

Texture	Analysis	Li ( $\mu\text{g/g}$ )	$2\sigma_{\text{mean}}$	Be ( $\mu\text{g/g}$ )	$2\sigma_{\text{mean}}$	B ( $\mu\text{g/g}$ )	$2\sigma_{\text{mean}}$	Sr ( $\mu\text{g/g}$ )	$2\sigma_{\text{mean}}$	Analysis	$I_p$ (nA)	n	$^{11}\text{B}/^{10}\text{B}$ measured	$\alpha_{\text{first}}$	$^{11}\text{B}/^{10}\text{B}$ corrected	$\delta^{11}\text{B}$ (‰) <sup>#</sup>	$2\sigma_{\text{mean}}$
mesh center	A017G02-4	0.62	26.8%	0.005	189.7%	151.47	3.3%			-		400	3.858	1.045	4.031	2.76	0.17%
mesh center	A017G02-6	0.19	30.6%	0.011	134.4%	109.81	2.5%			-		400	3.879	1.045	4.052	8.13	0.28%
mesh rim	A017G02-9	0.49	12.4%	0.004	189.7%	26.94	3.3%			A017G02-12	10	400	3.886	1.045	4.060	10.02	0.25%
mesh rim	A017G02-12	0.08	79.9%	0.011	126.6%	57.20	3.8%			-		400					
mesh rim	A017G02-14	0.24	25.8%	0.008	126.5%	100.18	1.9%			-		400					
mesh rim	A017G02-17	0.74	24.1%	0.006	189.7%	18.56	6.5%			A017G02-17	10	400	3.897	1.045	4.072	12.97	0.24%
mesh rim	A017G02-5	0.22	32.0%	0.003	189.7%	30.71	4.1%			-							
Ol	A017G02-13	1.02	16.9%	0.005	189.7%	0.10	84.8%			-							
Ol	A017G02-1	1.30	17.5%	b.d.l.		0.03	126.5%			-							
Opx	A017G02-16	0.30	30.5%	0.026	126.3%	0.07	77.5%			-							
Ol	2-12-01	0.94	10.4%	0.003	189.7%	0.58	13.8%	0.38	69.1%	-							
mesh center	2-12-02	4.58	4.4%	0.003	189.7%	122.25	2.2%	12.40	11.2%	-		400	3.903	1.046	4.084	15.91	0.21%
mesh rim + crystal	2-12-03	6.24	3.9%	b.d.l.		85.42	1.9%	11.77	9.0%	2-12-03	10	400					
mesh center	2-12-04	1.15	9.8%	b.d.l.		203.81	1.6%	22.21	11.3%	-							
mesh rim + crystal	2-12-05	3.80	6.5%	0.012	77.5%	110.46	2.0%	15.30	11.6%	-							
mesh center	2-12-06	0.44	10.1%	0.003	189.7%	196.82	1.3%	2.39	31.7%	2-12-06	10	400	3.914	1.046	4.095	18.67	0.15%
mesh rim (+ center)	2-12-07	4.32	7.2%	0.003	189.7%	147.34	2.3%	8.82	9.8%	-							
mesh rim + crystal	2-12-08	2.39	10.1%	b.d.l.		102.67	1.6%	9.76	11.0%	-							
mesh rim + crystal	2-12-09	2.32	5.3%	0.003	189.7%	191.89	1.6%	11.28	12.2%	2-12-09	10	400	3.916	1.046	4.097	19.15	0.17%
brucite vein	E7H2-2C-1	1.99	4.0%	b.d.l.		2.17	8.8%	10.67	13.1%	-							
brucite vein	E7H2-2C-2	1.56	7.3%	0.002	189.7%	2.30	7.6%	6.91	9.9%	-							
brucite, bright	E7H2-2B-2	0.88	12.3%	0.004	126.5%	1.43	12.8%	3.04	10.9%	-							
brucite, bright	E7H2-2B-5	1.40	5.6%	b.d.l.		1.56	8.2%	9.66	7.0%	-							
brucite, bright	E7H2-2B-7	1.19	6.1%	b.d.l.		1.19	13.4%	5.48	13.2%	-							
brucite, bright	E7H2-2B-9	1.30	11.4%	b.d.l.		1.38	9.0%	4.12	17.7%	-							
brucite, bright	E7H2-2B-12	0.93	13.5%	b.d.l.		1.83	7.9%	3.02	18.9%	-							
brucite, bright	E7H2-2B-13	1.60	5.2%	0.002	189.7%	1.34	12.6%	8.83	9.3%	-							
brucite, bright	E7H2-2B-15	2.08	4.1%	b.d.l.		1.77	9.1%	1.62	26.3%	-							
brucite, bright	E7H2-2B-3	0.78	6.2%	0.002	189.7%	1.90	6.3%	1.81	21.3%	-							
brucite, dark	E7H2-2B-6	1.15	7.8%	0.002	189.7%	1.40	9.5%	3.33	19.2%	-							
brucite, dark	E7H2-2B-10	0.59	12.4%	0.002	189.7%	1.33	10.3%	0.65	24.4%	-							
brucite, dark	E7H2-2B-14	1.07	10.3%	b.d.l.		1.63	12.4%	0.94	37.8%	-							
mesh center	E7H2-2D-1	0.19	12.3%	0.011	71.8%	46.06	2.0%	12.21	10.2%	-							
mesh center	E7H2-2D-2	0.21	15.6%	0.003	126.5%	40.18	3.7%	8.33	16.1%	-							
vein	E7H2-2B-4	0.06	27.0%	0.001	189.7%	6.47	3.7%	0.12	77.4%	-							
vein	E7H2-2B-8	0.03	49.1%	0.001	189.7%	7.89	4.2%	0.13	66.7%	-							
vein	E7H2-2B-11	0.04	22.0%	0.001	189.7%	6.67	3.5%	0.10	57.5%	-							
vein	E7H2-2D-3	0.27	9.0%	0.006	85.9%	19.69	1.7%	2.21	17.5%	-							

# = matrix corrected

**B4: Light element variation diagrams for different serpentinite samples**

**Fig. B4:** Li vs B and  $\delta^{11}\text{B}$  vs B of different serpentinite samples.



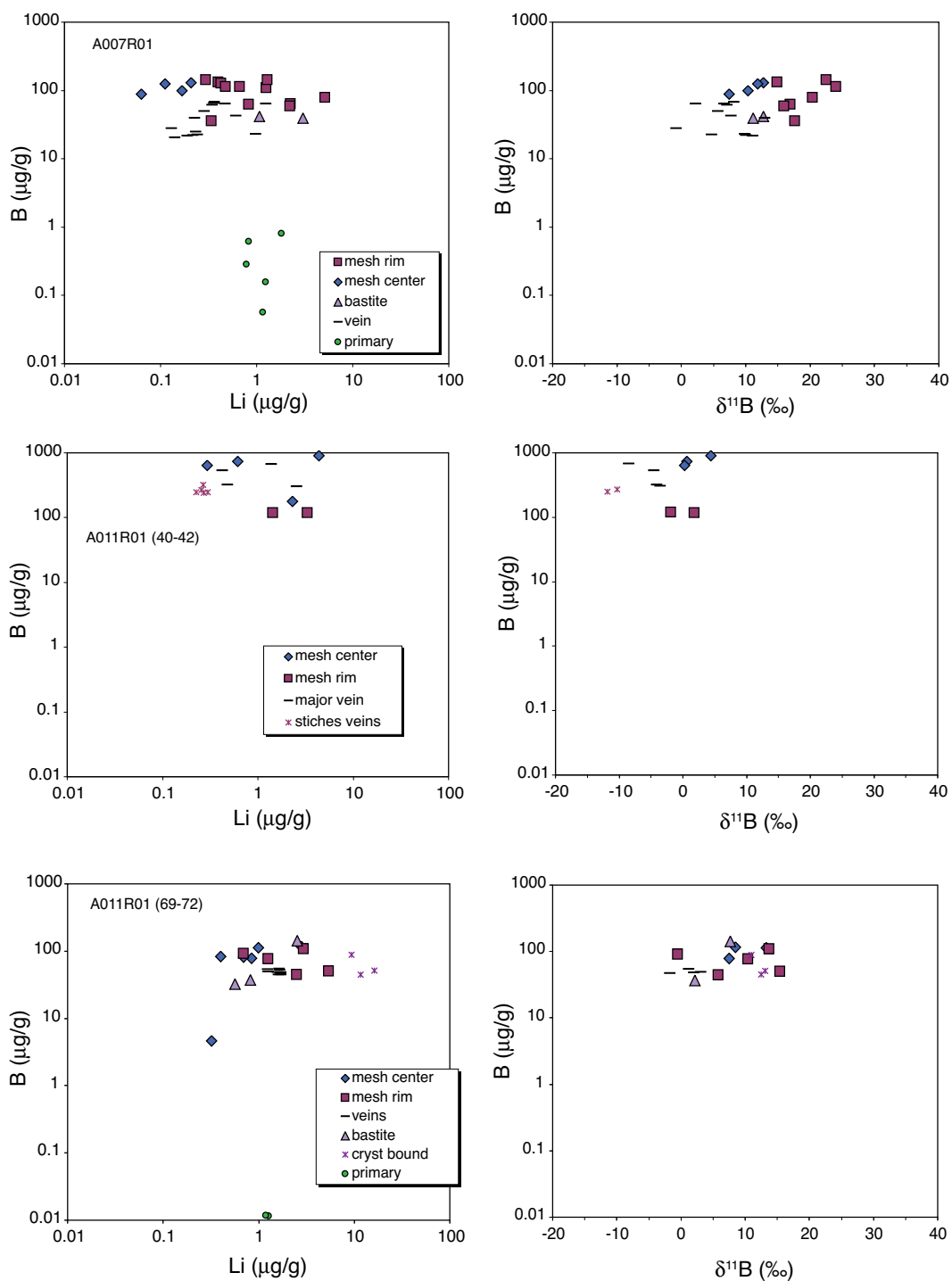


**Fig. B4 (continued):** *Li vs B and  $\delta^{11}B$  vs B of different serpentinite samples.*

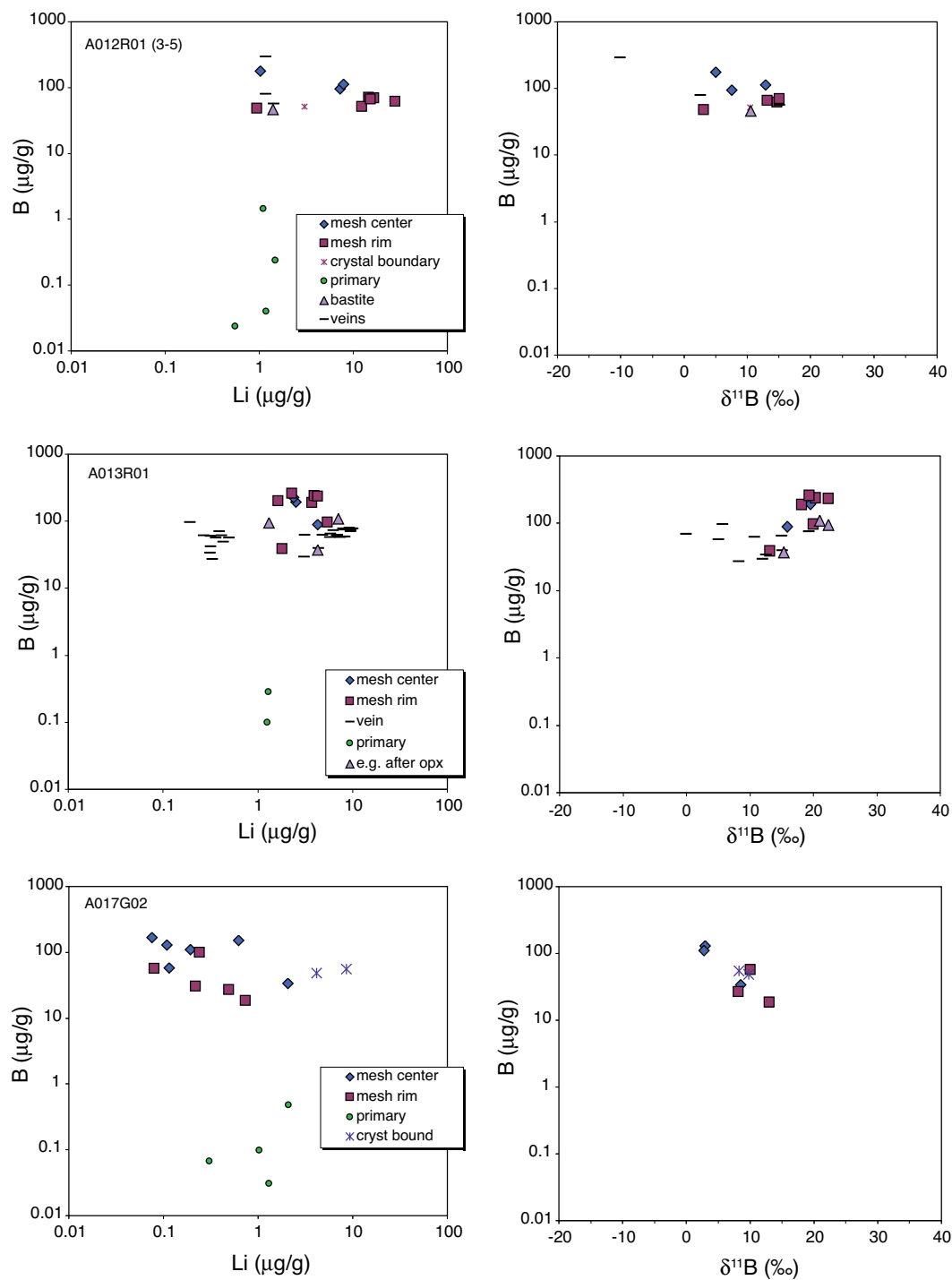


**Fig. B4 (continued):** Li vs B and  $\delta^{11}\text{B}$  vs B of different serpentinite samples.

### B5: Micro-Raman spectra of serpentine and brucite

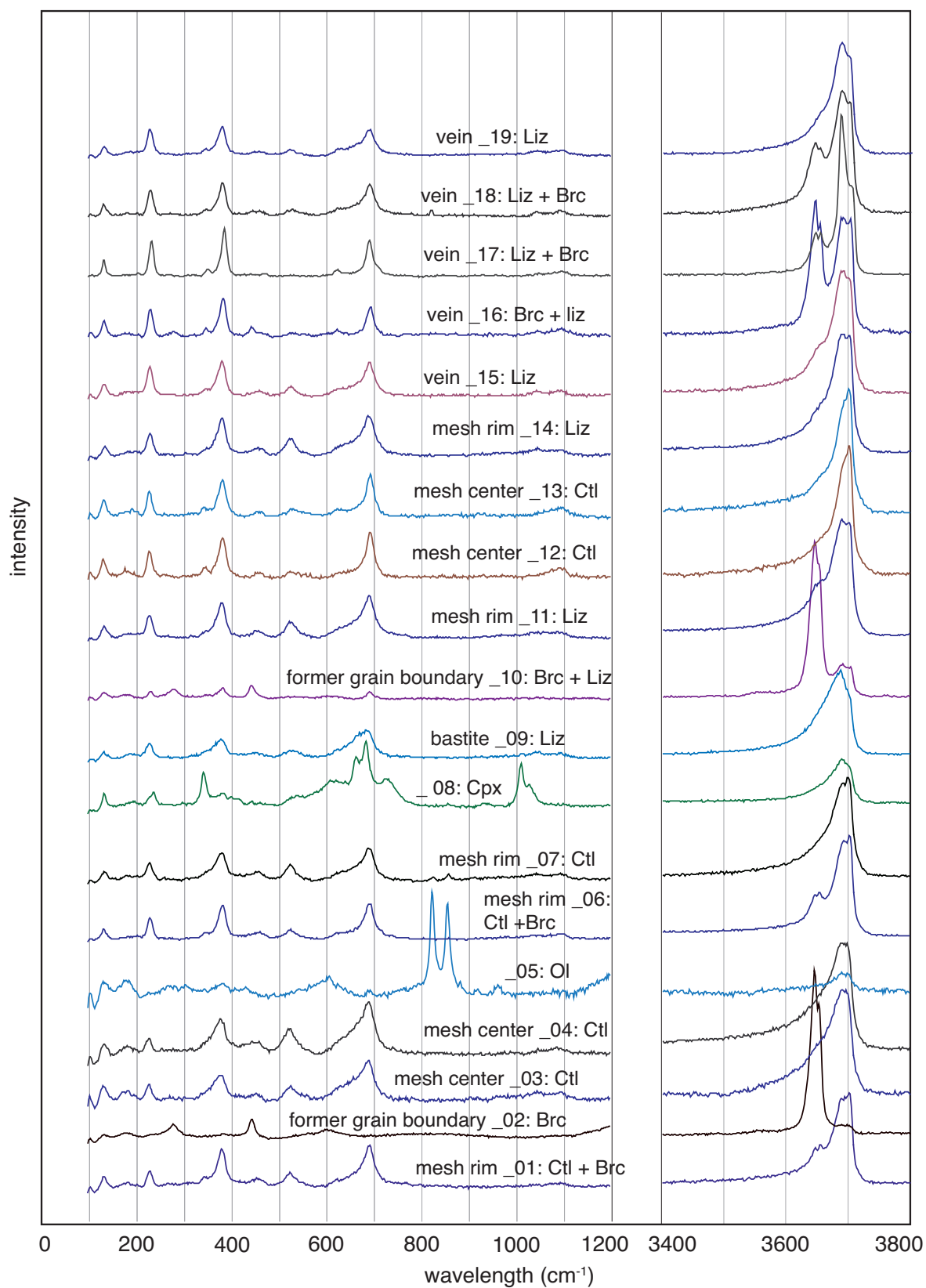


*Fig. B5: Micro-Raman spectra of textures in sample A003R01.*

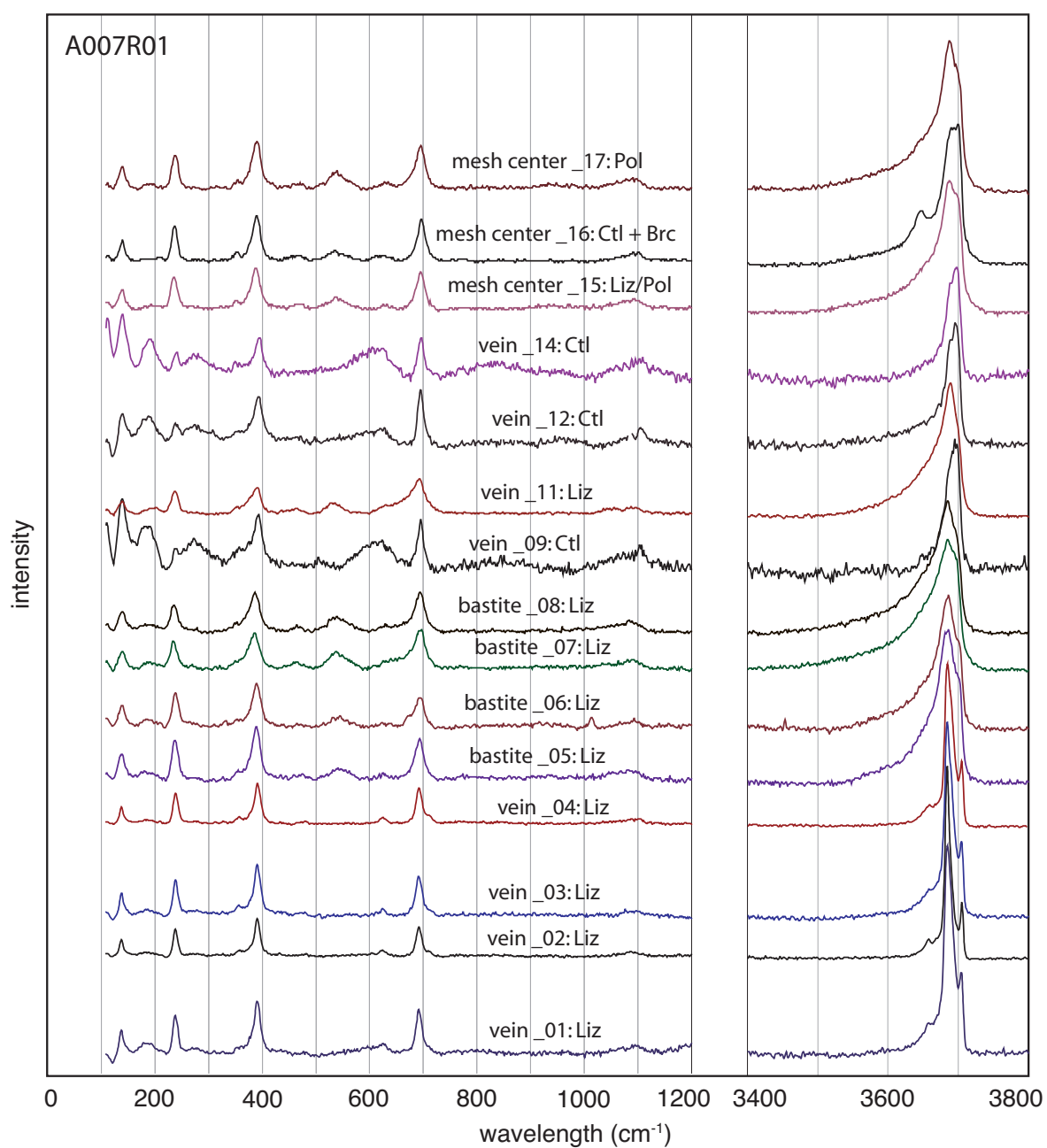


**Fig. B5 (continued):** Micro-Raman spectra of textures in sample A007R01.

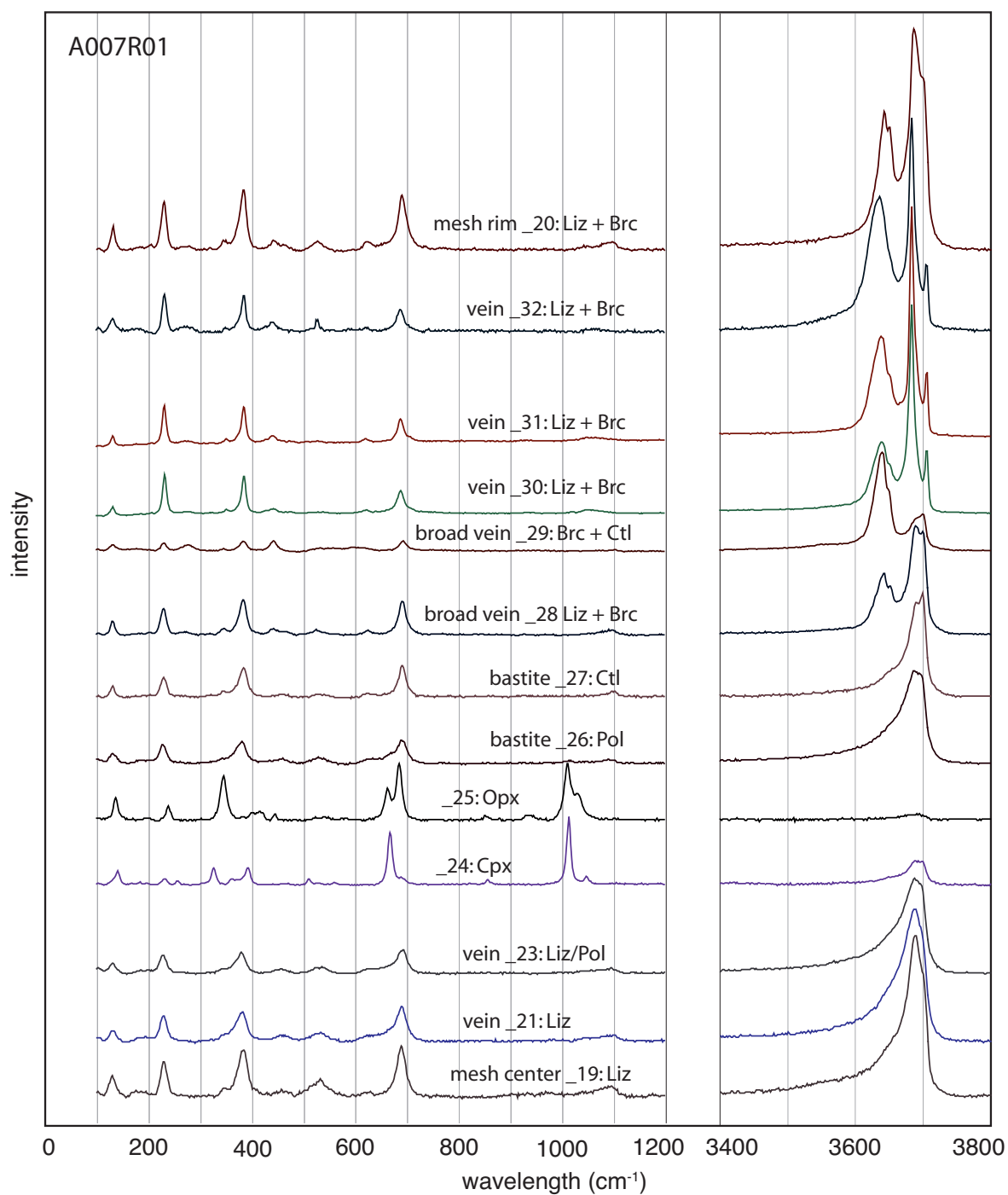


*Fig. B5 (continued): Micro-Raman spectra of textures in sample A007R01.*

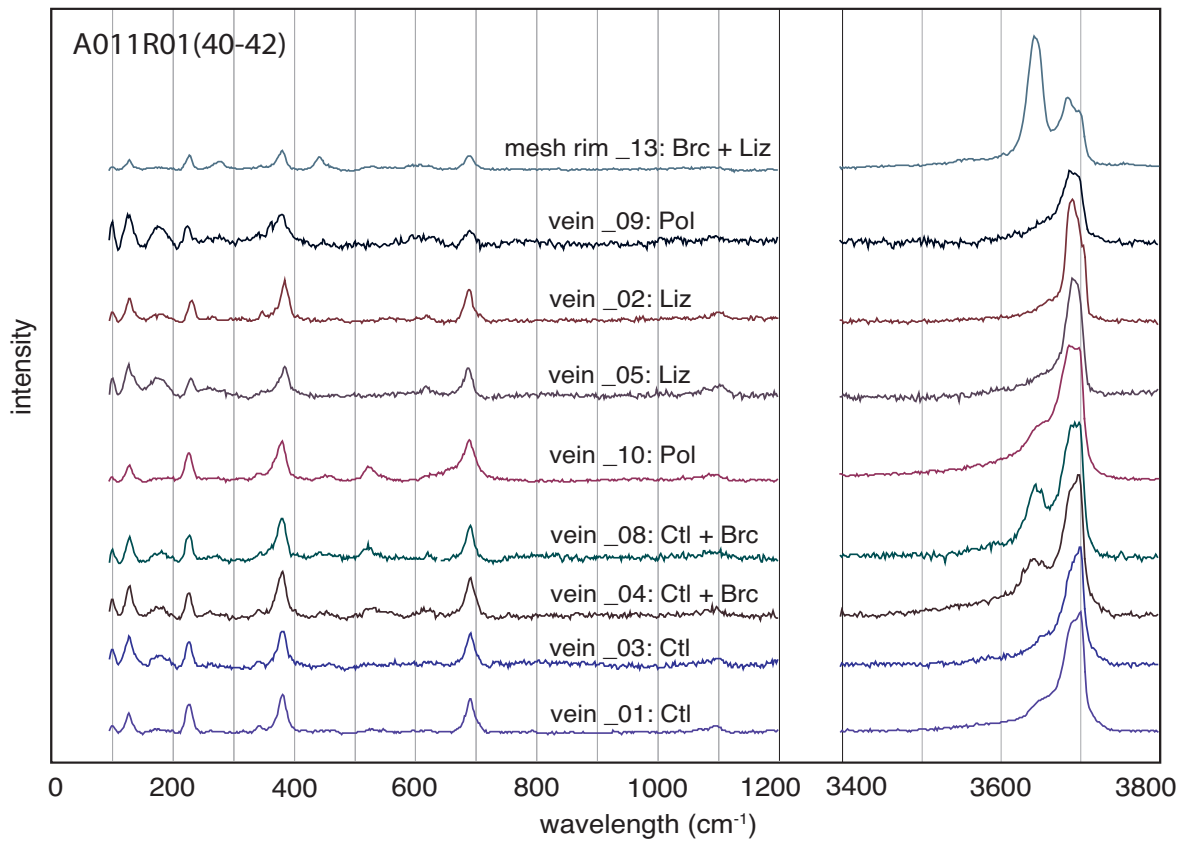
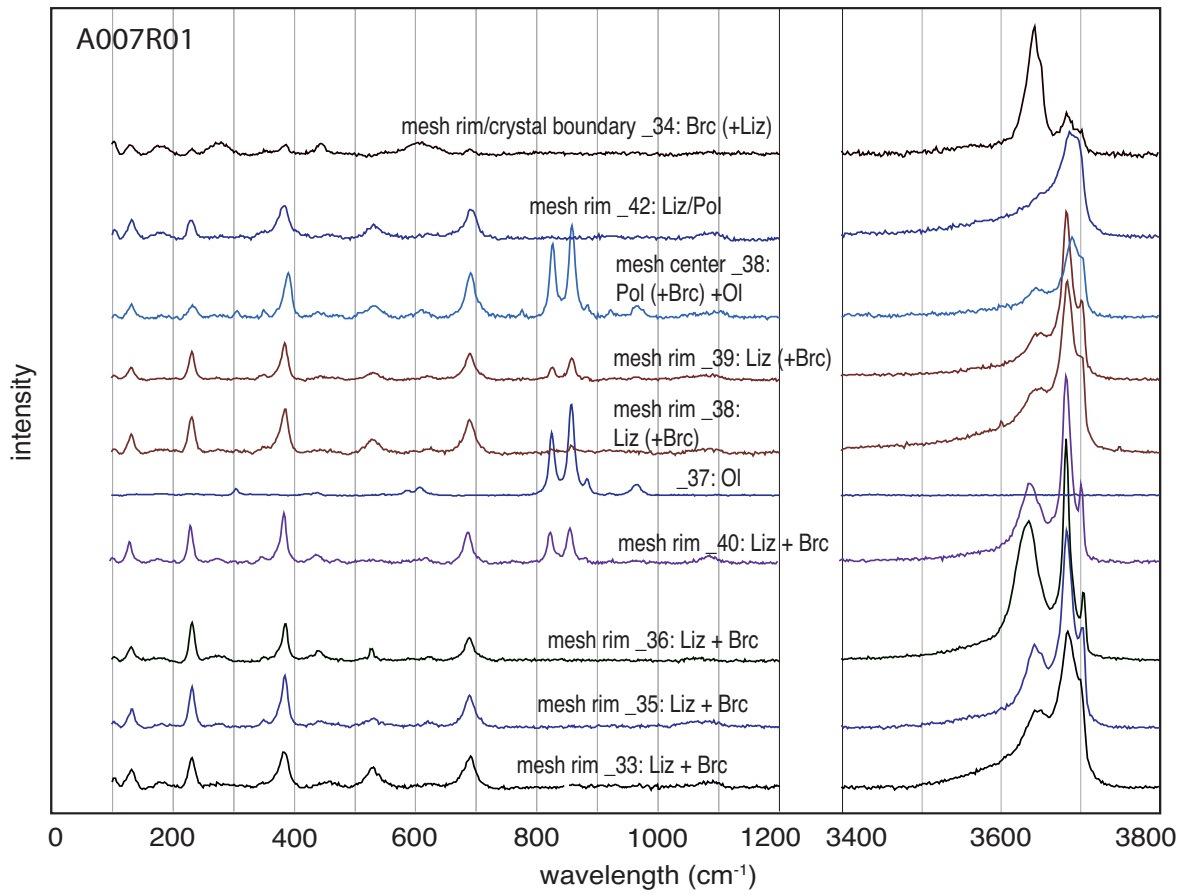


**Fig. B5 (continued):** Micro-Raman spectra of textures in samples A007R01 and A011R01(40-42).

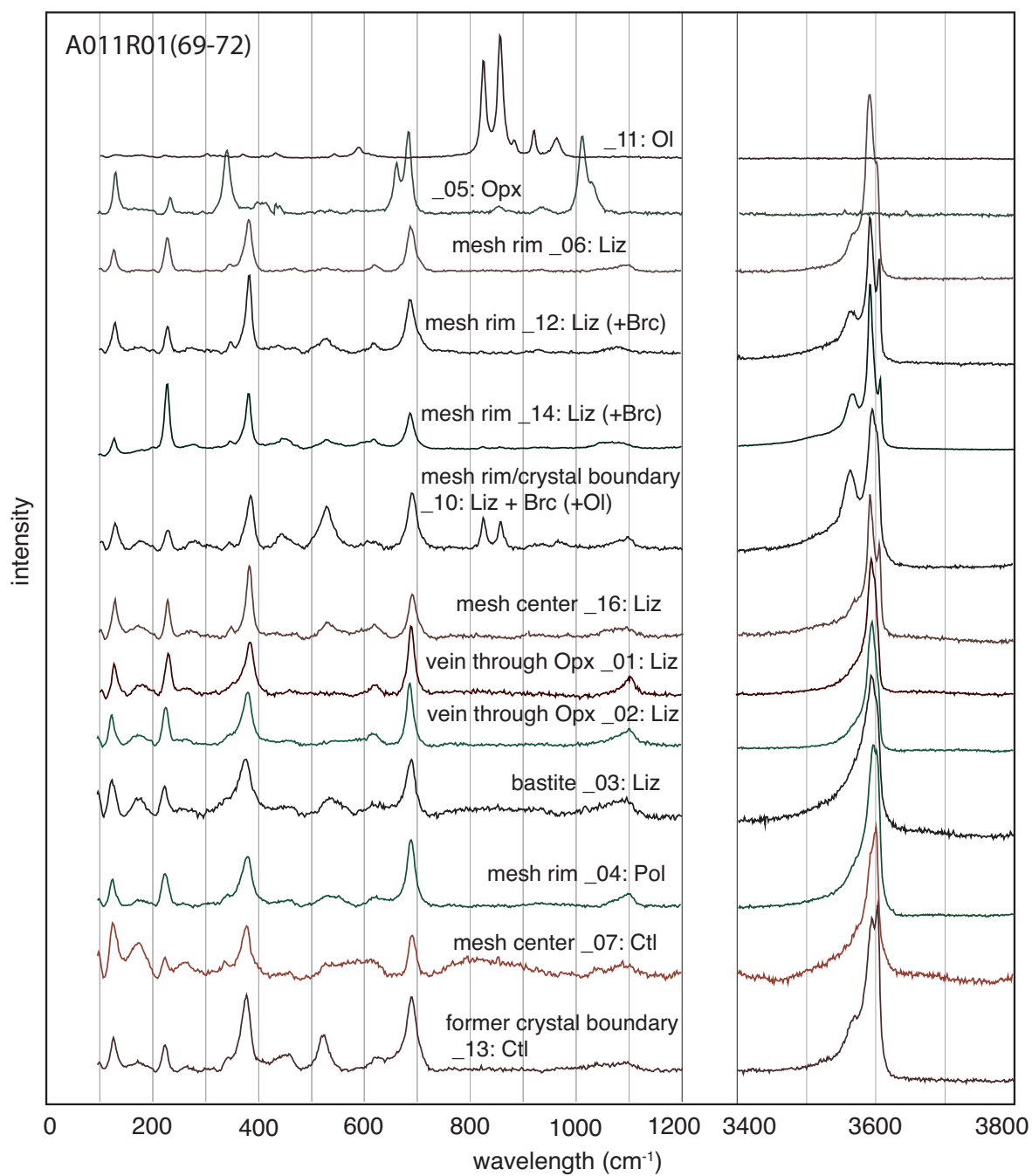


**Fig. B5 (continued):** Micro-Raman spectra of textures in sample A011R01(69-72).

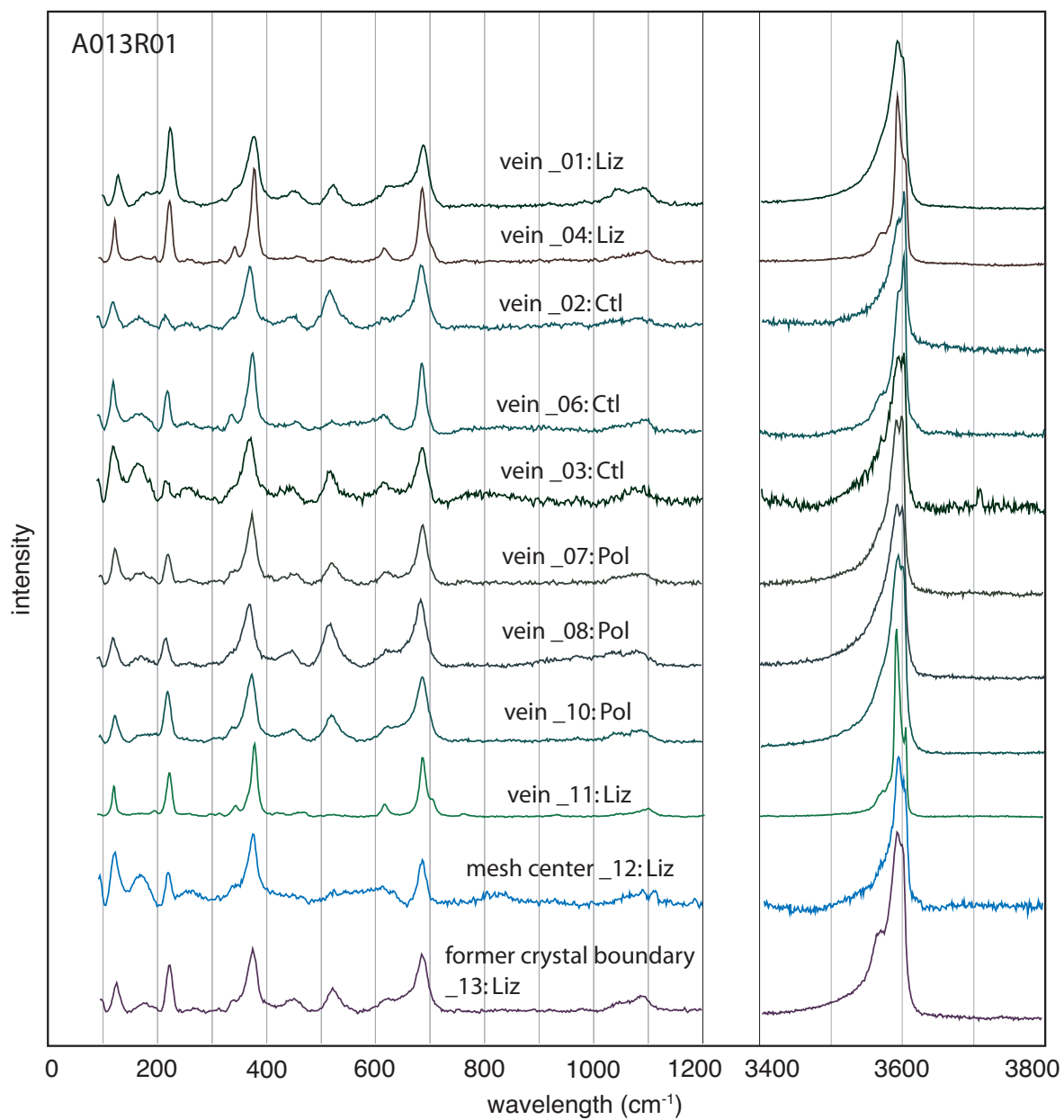


**Fig. B5 (continued):** Micro-Raman spectra of textures in sample A013R01(25-27).



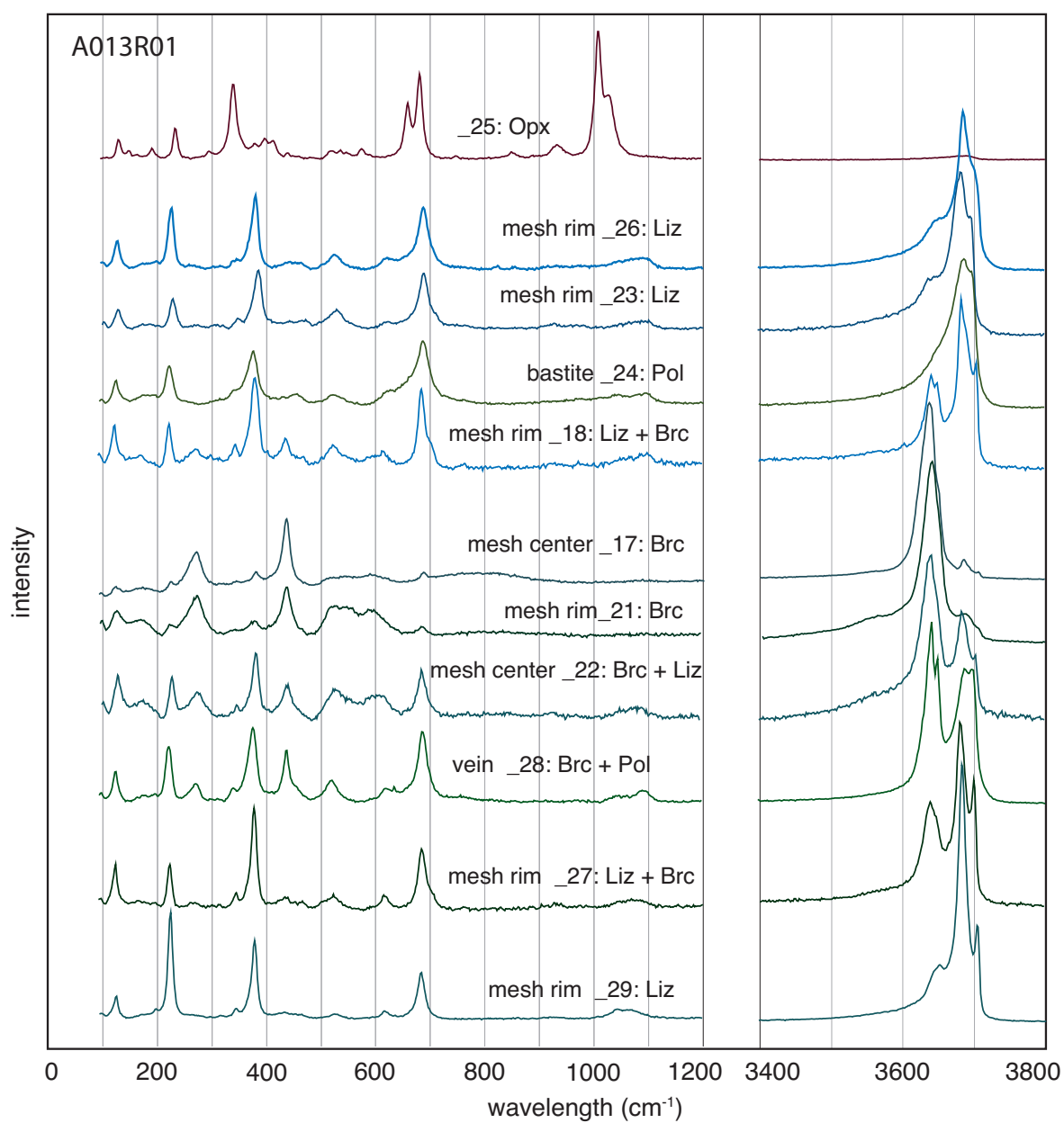


*Fig. B5 (continued): Micro-Raman spectra of textures in sample A013R01(25-27).*

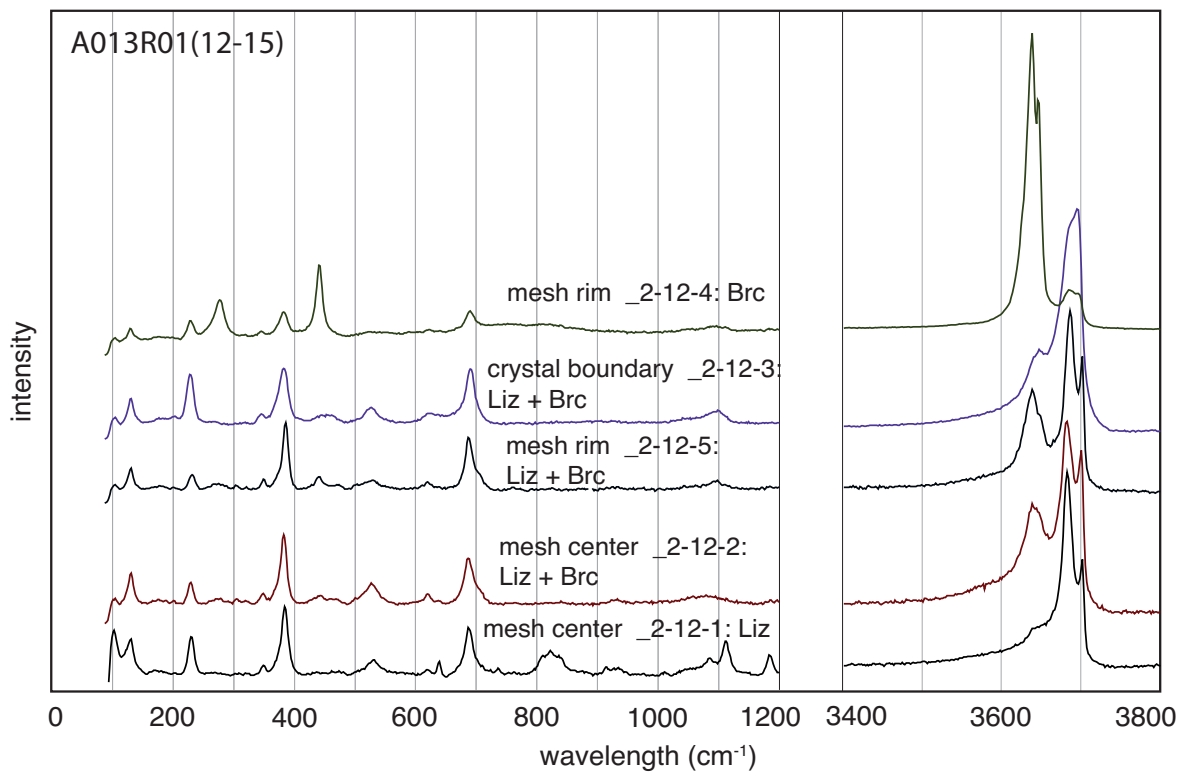


**Fig. B5 (continued):** Micro-Raman spectra of textures in sample A013R01(12-15).

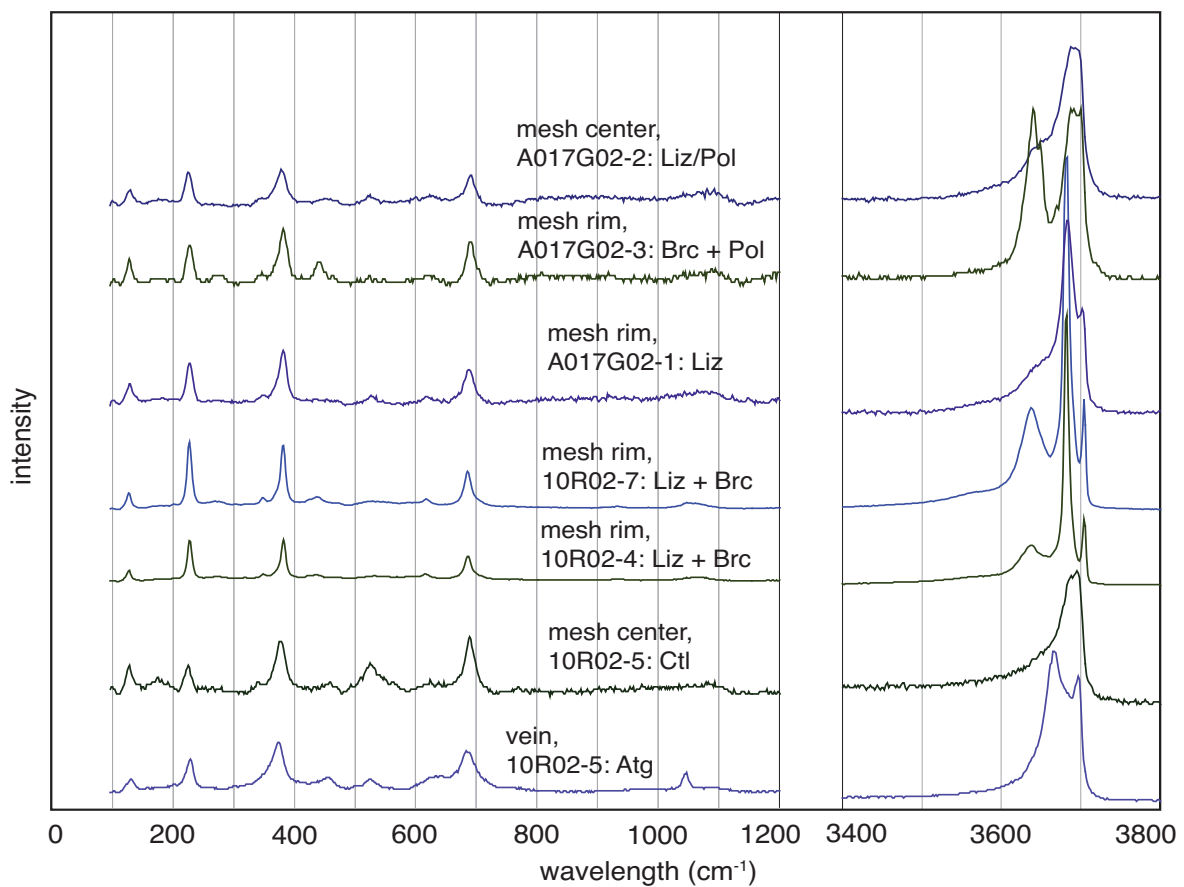


**Fig. B5 (continued):** Micro-Raman spectra of textures in samples A017G02 and 10R02.

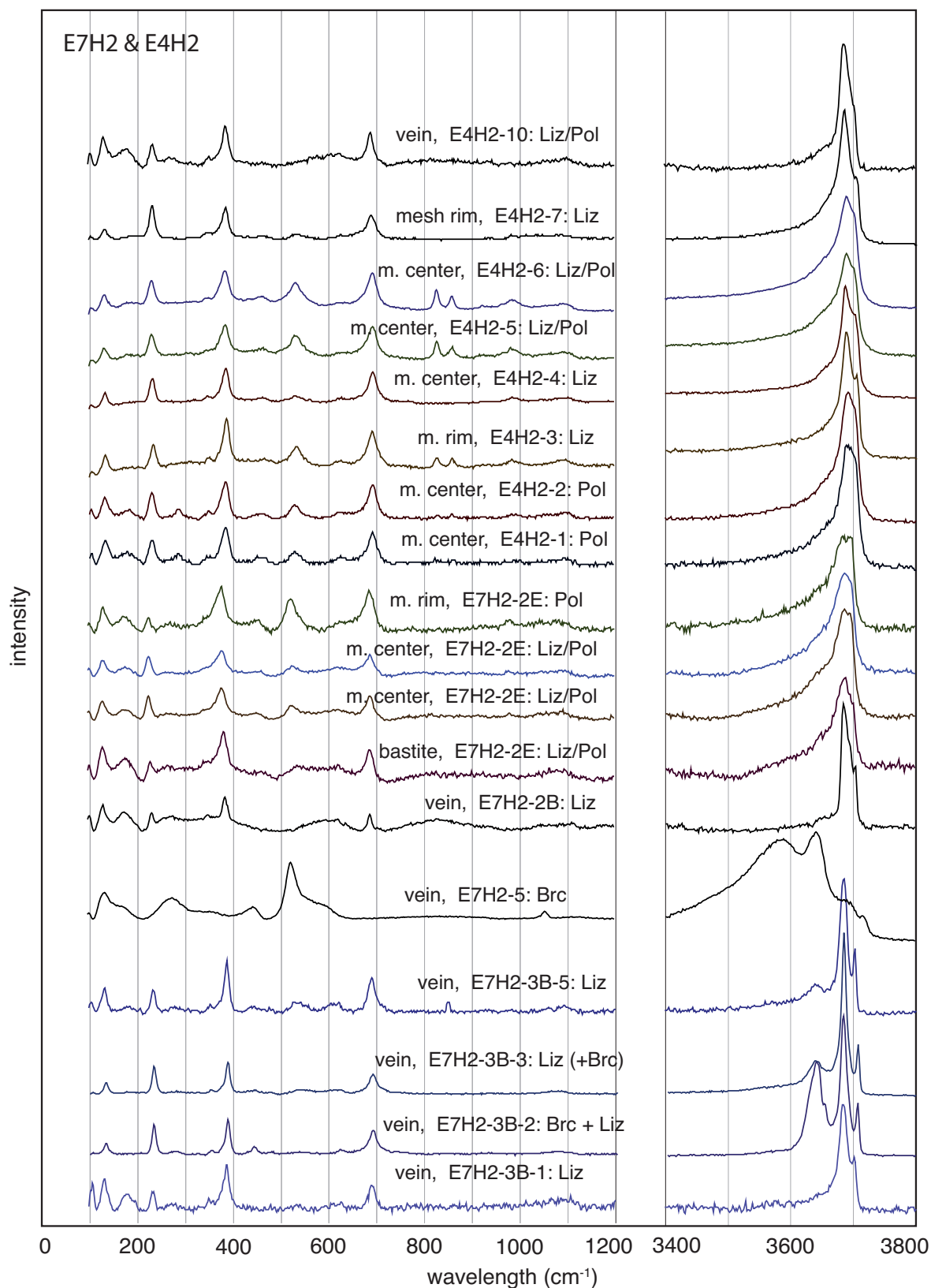


**Fig. B5 (continued):** Micro-Raman spectra of textures in samples E7H2 and E4H2.



## Appendix C: Metamafic rocks

C1: Sample BSE-images with EPMA, SIMS and Raman spots	196
C2: Electron probe micro analyses	197
C2.1: Amphibole	197
C2.2: Chlorite	201
C2.3: Talc	202
C2.4: Pumpellyite, epidote and allanite	203
C2.5: Phengite and Biotite	205
C2.6: Garnet	206
C2.7: Pyroxene	207
C2.8: Rutile, titanite, ilmenite, picotite and magnetite	208
C2.9: Apatite and zircon	209
C2.10: Serpentine (antigorite)	211
C3: SIMS data	212
C4: Micro-Raman spectra of andradite	218

**C1: Sample BSE-images with EPMA, SIMS and Raman spots**

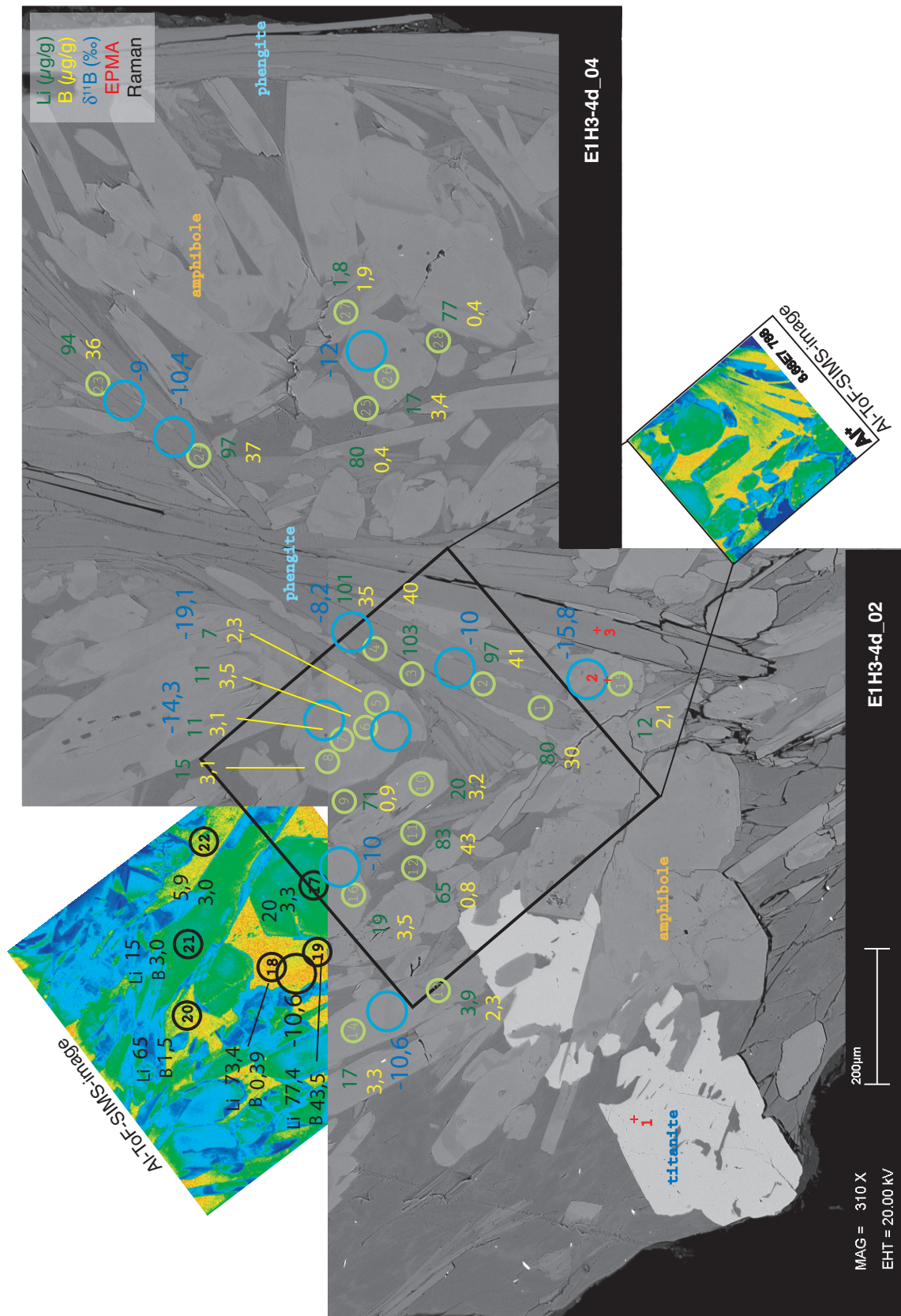


**Fig. C1:** Back-scattered electron (BSE) images of sample A003R01 with indicated spots of electron probe micro analyses, secondary ion electron spectrometry and micro-Raman analyses. Further images in electronic appendix.

## C2: Electron probe micro analyses

## C2.1: Amphibole

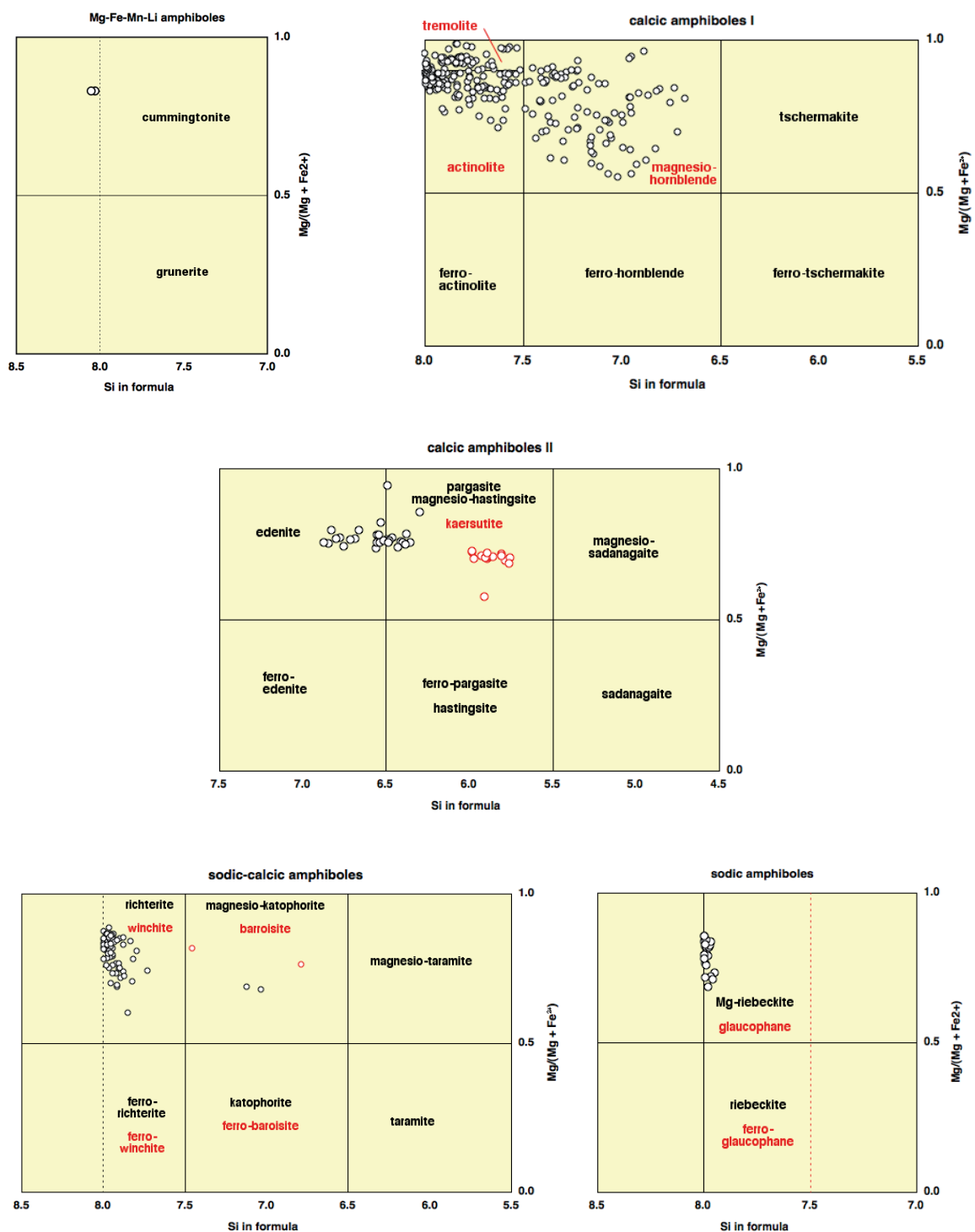


Fig. C2: Amphibole classification (after Leake et al., 1997, 2004).

**Table C2.1:** Representative composition of calcic amphiboles (in wt%), further analyses in electronic appendix.

Analysis	mg-hbl	mg-hbl	mg-hbl	act	act	act	trem	trem	mg-hast	kaers	kaers	prg	prg	edenite
	E1H3- 5_61	E2H2-4B 04	E1H3- 4B_100	D1H4- 2D_09	E1H3- 3D_23	E1H3- 5_50	E1H3- 5_59	F1H1-3C 06	E1H3- 4B_93	E1H3- 3D_34	E1H3- 3D_35	E1H3- 4B_01	E1H3- 4B_02	E1H3- 4B_104
<b>SiO<sub>2</sub></b>	51.38	51.96	48.03	57.58	56.66	52.62	57.10	57.46	43.32	39.28	38.74	43.51	43.37	45.83
<b>TiO<sub>2</sub></b>	0.20	0.36	0.48	0.07	0.09	0.08	0.00	0.04	0.50	5.26	6.02	0.67	0.47	0.53
<b>Al<sub>2</sub>O<sub>3</sub></b>	6.01	3.38	7.99	0.28	0.18	4.13	0.49	0.44	12.33	12.46	13.54	12.22	12.40	10.59
<b>Cr<sub>2</sub>O<sub>3</sub></b>	0.33	0.31	0.14	0.02	0.00	0.26	0.04	0.14	0.14	0.02	0.03	0.09	0.08	0.10
<b>Fe<sub>2</sub>O<sub>3</sub></b>	4.09	1.36	4.84	1.77	2.43	3.27	0.38	2.80	7.74	2.37	1.96	3.01	2.91	2.91
<b>FeO</b>	3.85	8.89	7.61	4.62	5.83	3.75	4.28	3.82	4.48	9.12	9.59	8.08	8.19	7.07
<b>MnO</b>	0.96	0.24	0.28	0.26	0.20	0.73	0.61	0.35	0.32	0.14	0.15	0.25	0.33	0.39
<b>MgO</b>	18.04	17.03	15.19	20.33	19.53	18.78	21.65	20.24	15.02	13.24	12.76	14.10	14.04	15.32
<b>CaO</b>	10.47	12.37	9.72	11.33	10.50	10.54	11.83	10.56	10.69	10.91	11.11	11.59	11.57	11.67
<b>Na<sub>2</sub>O</b>	1.42	0.92	2.55	1.28	1.41	1.32	0.30	1.59	2.21	2.37	2.32	2.41	2.56	2.03
<b>K<sub>2</sub>O</b>	0.08	0.17	0.21	0.18	0.01	0.05	0.02	0.03	0.28	1.12	1.14	0.27	0.31	0.23
<b>H<sub>2</sub>O</b>	2.11	2.08	2.07	2.16	2.13	2.10	2.15	2.16	2.06	2.00	2.02	2.03	2.03	2.06
<b>Total</b>	98.94	99.06	99.10	99.87	98.96	97.62	98.84	99.61	99.09	98.28	99.37	98.22	98.26	98.74
<b>T-site</b>														
<b>Si</b>	7.283	7.488	6.957	7.994	7.981	7.516	7.965	7.980	6.295	5.890	5.757	6.413	6.399	6.660
<b>Al<sup>(IV)</sup></b>	0.717	0.512	1.043	0.006	0.019	0.484	0.035	0.020	1.705	2.110	2.243	1.587	1.601	1.340
<b>C-site</b>														
<b>Al<sup>(VI)</sup></b>	0.287	0.061	0.321	0.040	0.010	0.212	0.045	0.052	0.408	0.092	0.128	0.536	0.556	0.474
<b>Ti</b>	0.022	0.039	0.052	0.008	0.009	0.009	0.000	0.004	0.054	0.593	0.673	0.074	0.052	0.058
<b>Fe<sup>3+</sup></b>	0.436	0.147	0.527	0.185	0.258	0.351	0.040	0.292	0.846	0.268	0.219	0.334	0.323	0.318
<b>Cr</b>	0.037	0.035	0.016	0.002	0.000	0.029	0.004	0.015	0.016	0.003	0.003	0.010	0.009	0.011
<b>Mg</b>	3.812	3.658	3.278	4.208	4.101	3.999	4.501	4.190	3.254	2.959	2.827	3.098	3.087	3.318
<b>Mn</b>	0.115	0.029	0.035	0.031	0.023	0.088	0.072	0.041	0.039	0.018	0.019	0.031	0.042	0.047
<b>Fe<sup>2+</sup></b>	0.292	1.031	0.770	0.526	0.598	0.312	0.337	0.406	0.382	1.067	1.130	0.917	0.931	0.773
<b>B-site</b>														
<b>Mg</b>	0.000	0.000	0.000	0.000	0.000	0.000	0.000	0.000	0.000	0.000	0.000	0.000	0.000	0.000
<b>Mn</b>	0.000	0.000	0.000	0.000	0.000	0.000	0.000	0.000	0.000	0.000	0.000	0.000	0.000	0.000
<b>Fe<sup>2+</sup></b>	0.165	0.041	0.152	0.010	0.089	0.136	0.162	0.038	0.162	0.076	0.062	0.079	0.080	0.086
<b>Ca</b>	1.590	1.910	1.508	1.685	1.584	1.613	1.769	1.572	1.664	1.753	1.770	1.831	1.829	1.817
<b>Na</b>	0.245	0.049	0.340	0.306	0.327	0.251	0.070	0.390	0.174	0.171	0.168	0.090	0.091	0.098
<b>A-site</b>														
<b>Na</b>	0.144	0.209	0.377	0.038	0.059	0.116	0.012	0.037	0.448	0.517	0.499	0.598	0.642	0.475
<b>K</b>	0.015	0.032	0.038	0.031	0.001	0.009	0.004	0.005	0.052	0.215	0.216	0.050	0.058	0.043
<b>Total</b>	15.159	15.240	15.414	15.069	15.060	15.124	15.016	15.042	15.500	15.732	15.715	15.648	15.700	15.519

FeO, Fe<sub>2</sub>O<sub>3</sub>, and H<sub>2</sub>O were calculated stoichiometrically. Cation calculation is based on 22 oxygen and 2 OH.



**Table C2.1 (continued):** Representative composition of sodic-calcic amphiboles (in wt%), further analyses in electronic appendix.

Analysis	winchite	winchite	winchite	winchite	winchite	winchite	winchite	winchite	winchite	winchite	mg-kat	mg-kat	barroisite	barroisite
	D1H4-1A_02	D1H4-1A_03	D1H4-1A_04	E1H3-5_41	F1H4-5_10	F2H2-1A_05	F2H2-1A_20	F2H2-4H_21	F2H2-4H_46	MAK2A_20	E1H3-4B_70	E1H3-4B_72	E1H3-5_32	F2H2-1A_16
<b>SiO<sub>2</sub></b>	55.96	56.98	56.27	55.42	54.88	55.37	53.78	55.03	53.71	56.45	47.98	48.28	51.30	46.59
<b>TiO<sub>2</sub></b>	0.03	0.01	0.04	0.02	0.01	0.00	0.03	0.07	0.09	0.02	0.52	0.43	0.11	0.29
<b>Al<sub>2</sub>O<sub>3</sub></b>	1.31	0.95	1.48	1.71	1.83	1.40	1.91	1.79	2.22	0.79	8.12	7.79	5.25	10.78
<b>Cr<sub>2</sub>O<sub>3</sub></b>	0.11	0.07	0.04	0.09	0.13	0.01	0.00	0.00	0.04	0.02	0.22	0.03	0.14	0.04
<b>Fe<sub>2</sub>O<sub>3</sub></b>	5.14	5.29	10.21	3.12	3.57	4.20	4.03	4.92	3.58	3.46	3.03	2.79	3.54	6.40
<b>FeO</b>	6.64	4.08	5.02	5.83	6.33	9.42	10.78	9.30	8.16	5.49	11.03	10.61	6.46	7.25
<b>MnO</b>	0.76	1.34	0.49	0.51	0.57	0.77	0.62	0.74	0.72	0.29	0.40	0.35	0.72	0.73
<b>MgO</b>	16.49	18.01	14.35	17.79	17.27	15.74	14.51	14.35	16.22	18.79	13.02	13.19	16.01	13.17
<b>CaO</b>	7.24	8.05	3.99	8.36	8.16	7.77	7.87	5.92	7.85	9.34	8.61	8.79	8.92	7.44
<b>Na<sub>2</sub>O</b>	3.33	2.94	4.96	2.77	2.85	2.91	3.04	4.39	2.48	2.24	3.99	3.47	2.70	3.22
<b>K<sub>2</sub>O</b>	0.11	0.04	0.03	0.08	0.09	0.07	0.10	0.07	0.07	0.02	0.17	0.26	0.04	0.93
<b>H<sub>2</sub>O</b>	2.11	2.15	2.11	2.10	2.09	2.10	2.06	2.08	2.06	2.13	2.05	2.03	2.06	2.06
<b>Total</b>	99.24	99.90	98.98	97.79	97.77	99.75	98.73	99.25	99.69	99.07	99.16	98.02	97.28	98.87
<b>T-site</b>														
<b>Si</b>	7.943	7.962	7.994	7.915	7.876	7.903	7.821	7.944	7.817	7.951	7.031	7.121	7.454	6.785
<b>Al<sup>IV</sup></b>	0.057	0.038	0.006	0.085	0.124	0.097	0.179	0.056	0.183	0.049	0.969	0.879	0.546	1.215
<b>C-site</b>														
<b>Al<sup>VI</sup></b>	0.162	0.118	0.242	0.203	0.185	0.139	0.149	0.249	0.198	0.082	0.433	0.475	0.354	0.636
<b>Ti</b>	0.003	0.001	0.004	0.002	0.001	0.000	0.004	0.008	0.009	0.002	0.057	0.047	0.011	0.031
<b>Fe<sup>3+</sup></b>	0.549	0.556	1.092	0.335	0.385	0.451	0.441	0.534	0.392	0.367	0.334	0.310	0.387	0.702
<b>Cr</b>	0.012	0.008	0.005	0.010	0.014	0.001	0.000	0.000	0.004	0.002	0.026	0.004	0.016	0.004
<b>Mg</b>	3.489	3.751	3.038	3.787	3.695	3.348	3.145	3.088	3.519	3.945	2.844	2.900	3.467	2.859
<b>Mn</b>	0.091	0.159	0.059	0.062	0.070	0.093	0.076	0.090	0.089	0.035	0.050	0.043	0.089	0.090
<b>Fe<sup>2+</sup></b>	0.695	0.408	0.560	0.601	0.650	0.967	1.185	1.031	0.789	0.567	1.257	1.220	0.675	0.679
<b>B-site</b>														
<b>Mg</b>	0.000	0.000	0.000	0.000	0.000	0.000	0.000	0.000	0.000	0.000	0.000	0.000	0.000	0.000
<b>Mn</b>	0.000	0.000	0.000	0.000	0.000	0.000	0.000	0.000	0.000	0.000	0.000	0.000	0.000	0.000
<b>Fe<sup>2+</sup></b>	0.094	0.069	0.037	0.096	0.110	0.157	0.127	0.092	0.204	0.080	0.095	0.088	0.111	0.204
<b>Ca</b>	1.101	1.206	0.607	1.280	1.254	1.187	1.226	0.916	1.224	1.410	1.352	1.389	1.388	1.161
<b>Na</b>	0.805	0.725	1.356	0.625	0.636	0.656	0.647	0.992	0.571	0.510	0.552	0.523	0.501	0.635
<b>A-site</b>														
<b>Na</b>	0.113	0.072	0.011	0.142	0.157	0.150	0.210	0.237	0.129	0.101	0.582	0.470	0.258	0.273
<b>K</b>	0.021	0.007	0.005	0.015	0.016	0.012	0.019	0.013	0.013	0.003	0.032	0.048	0.008	0.173
<b>Total</b>	15.133	15.080	15.015	15.157	15.173	15.161	15.229	15.250	15.142	15.104	15.615	15.518	15.266	15.446

FeO, Fe<sub>2</sub>O<sub>3</sub>, and H<sub>2</sub>O were calculated stoichiometrically. Cation calculation is based on 22 oxygen and 2 OH.

**Table C2.1 (continued):** Representative composition of sodic amphiboles (in wt%), further analyses in electronic appendix.

Analysis	mg-rieb D1H4- 1A_20	mg-rieb D1H4- 1A_40	mg-rieb D1H4- 1A_46	mg-rieb E1H3- 2D_03	mg-rieb E1H3- 4A_68	mg-rieb E1H3- 4C_10	mg-rieb F1H4- 5_28	mg-rieb F2H2-1A- 10	mg-rieb F2H2-1A- 25	mg-rieb F2H2-4A- 47	mg-rieb F2H2-4B- 02	mg-rieb F2H2-4H- 05	mg-rieb F2H2-4H- 06	mg-rieb F2H2-5A- 30
<b>SiO<sub>2</sub></b>	56.61	56.42	56.74	57.23	55.99	54.81	56.08	55.54	55.62	55.64	56.36	55.54	54.66	55.91
<b>TiO<sub>2</sub></b>	0.13	0.07	0.02	0.03	0.38	0.06	0.05	0.06	0.05	0.06	0.02	0.05	0.02	0.02
<b>Al<sub>2</sub>O<sub>3</sub></b>	1.70	1.91	1.68	2.51	1.91	1.82	3.56	1.80	1.75	2.80	2.69	2.76	1.89	2.51
<b>Cr<sub>2</sub>O<sub>3</sub></b>	0.08	0.04	0.00	0.09	0.02	0.07	0.14	0.00	0.03	0.00	0.00	0.03	0.00	0.04
<b>Fe<sub>2</sub>O<sub>3</sub></b>	12.59	11.41	12.51	13.75	12.53	11.42	10.41	12.53	12.76	9.79	11.08	11.19	14.25	11.97
<b>FeO</b>	6.10	6.09	5.11	3.88	6.48	7.71	4.75	7.87	8.03	6.97	5.61	6.57	8.15	7.21
<b>MnO</b>	0.20	0.44	0.45	0.23	0.28	0.53	0.21	0.44	0.96	0.31	0.44	0.49	0.25	0.40
<b>MgO</b>	12.92	13.02	13.14	12.73	11.72	11.85	12.67	11.33	11.14	12.29	12.69	12.12	9.63	11.38
<b>CaO</b>	1.75	2.40	2.41	0.75	1.53	2.03	1.52	1.60	1.44	2.46	2.13	1.44	0.38	1.45
<b>Na<sub>2</sub>O</b>	6.21	5.70	5.98	6.98	6.39	6.09	6.43	6.45	6.42	5.99	6.00	6.33	6.94	6.24
<b>K<sub>2</sub>O</b>	0.03	0.04	0.06	0.04	0.02	0.07	0.04	0.02	0.10	0.07	0.03	0.05	0.02	0.03
<b>H<sub>2</sub>O</b>	2.13	2.11	2.13	2.15	2.10	2.07	2.10	2.09	2.10	2.09	2.11	2.09	2.05	2.10
<b>Total</b>	100.46	99.64	100.24	100.35	99.36	98.52	97.96	99.72	100.39	98.47	99.16	100.64	101.06	99.67
<b>T-site</b>														
<b>Si</b>	7.979	7.998	7.993	7.999	7.995	7.949	7.993	7.968	7.956	7.985	7.996	7.964	7.991	7.997
<b>Al<sup>IV</sup></b>	0.021	0.002	0.007	0.001	0.005	0.051	0.007	0.032	0.044	0.015	0.004	0.036	0.009	0.003
<b>C-site</b>														
<b>Al<sup>VI</sup></b>	0.261	0.317	0.272	0.412	0.315	0.260	0.591	0.273	0.251	0.458	0.446	0.431	0.318	0.420
<b>Ti</b>	0.014	0.008	0.002	0.003	0.041	0.007	0.006	0.007	0.005	0.007	0.002	0.005	0.003	0.002
<b>Fe<sup>3+</sup></b>	1.335	1.218	1.326	1.446	1.347	1.247	1.117	1.353	1.373	1.058	1.183	1.208	1.567	1.289
<b>Cr</b>	0.009	0.005	0.000	0.010	0.003	0.008	0.016	0.000	0.003	0.000	0.000	0.004	0.000	0.004
<b>Mg</b>	2.715	2.752	2.760	2.651	2.495	2.563	2.691	2.423	2.374	2.629	2.684	2.590	2.099	2.427
<b>Mn</b>	0.024	0.052	0.053	0.027	0.034	0.065	0.026	0.053	0.116	0.038	0.053	0.059	0.031	0.048
<b>Fe<sup>2+</sup></b>	0.641	0.649	0.586	0.451	0.766	0.851	0.554	0.892	0.877	0.811	0.632	0.703	0.982	0.809
<b>B-site</b>														
<b>Mg</b>	0.000	0.000	0.000	0.000	0.000	0.000	0.000	0.000	0.000	0.000	0.000	0.000	0.000	0.000
<b>Mn</b>	0.000	0.000	0.000	0.000	0.000	0.000	0.000	0.000	0.000	0.000	0.000	0.000	0.000	0.000
<b>Fe<sup>2+</sup></b>	0.078	0.073	0.016	0.002	0.008	0.084	0.012	0.052	0.084	0.025	0.034	0.085	0.014	0.053
<b>Ca</b>	0.265	0.365	0.363	0.112	0.234	0.316	0.232	0.245	0.220	0.378	0.323	0.222	0.060	0.223
<b>Na</b>	1.657	1.562	1.620	1.886	1.757	1.601	1.755	1.703	1.696	1.596	1.642	1.693	1.926	1.725
<b>A-site</b>														
<b>Na</b>	0.040	0.003	0.014	0.006	0.012	0.111	0.022	0.092	0.084	0.069	0.008	0.068	0.042	0.005
<b>K</b>	0.004	0.006	0.012	0.007	0.003	0.012	0.007	0.003	0.018	0.013	0.005	0.009	0.003	0.005
<b>Total</b>	15.045	15.010	15.025	15.013	15.016	15.123	15.028	15.096	15.102	15.083	15.013	15.077	15.045	15.010

FeO, Fe<sub>2</sub>O<sub>3</sub>, and H<sub>2</sub>O were calculated stoichiometrically. Cation calculation is based on 22 oxygen and 2 OH.

## C2.2: Chlorite

Table C2.2: Representative composition of chlorite (in wt%), further analyses in electronic appendix.

Analysis	D1H4-1A_01	D1H4-1A_05	D1H4-1A_26	D1H4-2D_08	D1H4-2D_12	D3H1-8C_01	D3H1-8C_07	E1H3-2F_01	E1H3-2F_02	E1H3-3D_39	E1H3-3D_40	E1H3-4A_05	E1H3-4A_06
SiO <sub>2</sub>	29.68	30.21	31.20	32.65	32.05	35.48	35.33	31.43	30.41	32.48	33.77	29.70	29.26
TiO <sub>2</sub>	0.01	0.01	0.00	0.04	0.05	0.04	0.02	0.02	0.02	0.02	0.01	0.02	0.03
Al <sub>2</sub> O <sub>3</sub>	18.70	17.85	16.96	14.47	14.81	10.49	12.02	15.24	17.37	12.37	13.08	17.63	19.07
Cr <sub>2</sub> O <sub>3</sub>	0.50	0.46	0.29	0.01	0.00	0.50	0.40	0.19	0.23	0.01	0.03	0.05	0.06
FeO	9.41	9.50	9.11	9.46	9.78	6.75	7.25	9.41	9.75	8.75	8.42	15.03	11.07
MnO	1.11	0.88	0.88	0.19	0.19	0.07	0.03	0.42	0.36	0.25	0.18	0.54	0.58
NiO	0.12	0.21	0.25	0.27	0.17	0.31	0.26	0.22	0.19	0.03	0.05	0.05	0.05
MgO	26.84	27.15	28.11	29.49	29.32	32.79	31.86	27.07	27.46	30.06	30.50	24.13	26.33
CaO	0.03	0.05	0.18	0.04	0.07	0.02	0.02	0.43	0.22	0.20	0.18	0.06	0.07
Na <sub>2</sub> O	0.00	0.02	0.05	0.02	0.03	0.03	0.04	0.18	0.12	0.21	0.18	0.03	0.00
K <sub>2</sub> O	0.00	0.01	0.02	0.00	0.00	0.26	0.60	0.06	0.01	0.02	0.03	0.02	0.00
H <sub>2</sub> O	12.16	12.16	12.29	12.27	12.22	12.44	12.56	11.95	12.14	11.96	12.32	11.97	12.12
Total	98.57	98.49	99.33	98.90	98.69	99.16	100.38	96.61	98.27	96.36	98.74	99.22	98.64
Si	2.927	2.980	3.045	3.191	3.145	3.421	3.373	3.154	3.004	3.256	3.288	2.975	2.896
Ti	0.001	0.000	0.000	0.003	0.004	0.003	0.001	0.002	0.001	0.001	0.001	0.001	0.002
Al <sup>IV</sup>	1.073	1.020	0.955	0.809	0.855	0.579	0.627	0.846	0.996	0.744	0.712	1.025	1.104
Al <sup>VI</sup>	1.099	1.055	0.995	0.857	0.858	0.613	0.726	0.957	1.026	0.717	0.788	1.055	1.120
Cr	0.039	0.036	0.022	0.001	0.000	0.038	0.030	0.015	0.018	0.001	0.003	0.004	0.005
Fe <sup>2+</sup>	0.776	0.784	0.744	0.773	0.802	0.544	0.579	0.790	0.805	0.733	0.686	1.259	0.916
Mn	0.093	0.073	0.073	0.015	0.015	0.006	0.002	0.036	0.030	0.022	0.015	0.046	0.048
Ni	0.010	0.016	0.019	0.021	0.014	0.024	0.020	0.017	0.015	0.002	0.004	0.004	0.004
Mg	3.946	3.992	4.090	4.296	4.290	4.713	4.535	4.050	4.043	4.492	4.427	3.602	3.884
Ca	0.003	0.005	0.019	0.004	0.008	0.002	0.002	0.046	0.023	0.021	0.018	0.006	0.007
Na	0.000	0.003	0.010	0.004	0.006	0.006	0.008	0.034	0.022	0.042	0.033	0.006	0.001
K	0.000	0.001	0.002	0.000	0.000	0.032	0.073	0.008	0.002	0.003	0.004	0.003	0.000
Total	9.966	9.966	9.975	9.975	9.997	9.980	9.975	9.956	9.986	10.034	9.979	9.986	9.988
Mg#	83.57	83.59	84.61	84.75	84.24	89.65	88.68	83.68	83.39	85.97	86.59	74.10	80.92
clinocllore	81.28	81.72	82.98	84.44	83.93	88.86	88.11	82.78	82.54	85.58	86.28	73.34	80.00
chamosite	15.98	16.04	15.09	15.19	15.70	10.26	11.24	16.14	16.44	13.97	13.36	25.63	18.86
Cr-fraction	0.80	0.73	0.45	0.02	0.00	0.72	0.59	0.31	0.37	0.02	0.05	0.08	0.09
pennantite (Mn)	1.91	1.50	1.48	0.30	0.30	0.11	0.04	0.73	0.62	0.41	0.29	0.93	0.99
Ti-fraction	0.02	0.01	0.00	0.05	0.08	0.05	0.02	0.04	0.03	0.02	0.01	0.03	0.05

H<sub>2</sub>O was calculated stoichiometrically; cation calculation is based on 10 oxygens and 4 OH; Fe<sup>2+</sup> = F Nomenclature after Bayliss (1975).

Analysis	E1H3-4A_72	E1H3-4A_73	E1H3-4B_05	E1H3-4B_06	E4H2-2B_02	E4H2-2B_07	E7H2-2A_04	E7H2-2A_11	F1H1-3C_13	F1H1-3D_03	F2H2-4F_14	F2H2-4F_16	F2H2-4G_02
SiO <sub>2</sub>	30.13	28.84	27.90	27.85	28.09	27.68	31.50	30.09	30.89	29.35	30.07	30.65	29.69
TiO <sub>2</sub>	0.01	0.00	0.03	0.03	0.07	0.03	0.02	0.03	0.01	0.00	0.04	0.03	0.03
Al <sub>2</sub> O <sub>3</sub>	17.29	19.75	19.55	19.82	19.17	18.92	16.64	18.05	16.46	18.71	17.91	16.86	17.86
Cr <sub>2</sub> O <sub>3</sub>	0.06	0.05	0.24	0.12	0.03	0.02	0.11	0.05	1.07	0.00	0.39	0.26	0.35
FeO	13.73	10.97	15.27	14.52	16.32	16.85	9.43	10.81	8.79	11.75	6.47	5.91	6.66
MnO	0.51	0.46	0.45	0.45	0.35	0.44	0.37	0.39	0.44	0.62	0.41	0.41	0.37
NiO	0.04	0.03	0.04	0.04	0.07	0.03	0.20	0.16	0.42	0.05	0.20	0.24	0.18
MgO	24.62	26.34	23.26	23.36	22.30	22.31	28.58	27.54	28.98	25.63	30.17	30.96	29.64
CaO	0.21	0.02	0.08	0.10	0.25	0.13	0.35	0.07	0.06	0.00	0.00	0.00	0.01
Na <sub>2</sub> O	0.02	0.00	0.01	0.04	0.05	0.00	0.13	0.02	0.00	0.00	0.00	0.00	0.00
K <sub>2</sub> O	0.01	0.02	0.02	0.02	0.01	0.00	0.00	0.02	0.01	0.00	0.01	0.00	0.00
H <sub>2</sub> O	11.98	12.12	11.88	11.86	11.80	11.72	12.34	12.24	12.29	12.03	12.27	12.26	12.13
Total	98.61	98.60	98.72	98.20	98.50	98.12	99.65	99.47	99.42	98.14	97.95	97.58	96.92
Si	3.017	2.853	2.817	2.816	2.855	2.833	3.062	2.949	3.014	2.927	2.939	2.999	2.934
Ti	0.001	0.000	0.002	0.002	0.005	0.002	0.001	0.002	0.001	0.000	0.003	0.002	0.002
Al <sup>IV</sup>	0.983	1.147	1.183	1.184	1.145	1.167	0.938	1.051	0.986	1.073	1.061	1.001	1.066
Al <sup>VI</sup>	1.058	1.155	1.144	1.178	1.150	1.117	0.968	1.033	0.907	1.126	1.002	0.943	1.015
Cr	0.005	0.004	0.019	0.010	0.002	0.002	0.008	0.004	0.082	0.000	0.030	0.020	0.028
Fe <sup>2+</sup>	1.150	0.908	1.289	1.228	1.387	1.443	0.766	0.886	0.717	0.980	0.529	0.483	0.550
Mn	0.043	0.038	0.038	0.039	0.030	0.038	0.030	0.033	0.036	0.053	0.034	0.034	0.031
Ni	0.003	0.003	0.003	0.003	0.005	0.002	0.015	0.013	0.033	0.004	0.016	0.019	0.014
Mg	3.675	3.884	3.501	3.522	3.378	3.404	4.142	4.023	4.215	3.810	4.396	4.515	4.367
Ca	0.022	0.002	0.009	0.011	0.027	0.015	0.037	0.007	0.006	0.000	0.000	0.000	0.001
Na	0.004	0.000	0.002	0.007	0.010	0.000	0.024	0.004	0.000	0.001	0.000	0.001	0.000
K	0.001	0.002	0.003	0.003	0.001	0.000	0.000	0.003	0.002	0.000	0.001	0.000	0.000
Total	9.962	9.995	10.010	10.001	9.996	10.022	9.992	10.008	9.998	9.974	10.012	10.017	10.009
Mg#	76.17	81.05	73.09	74.15	70.89	70.24	84.39	81.95	85.46	79.54	89.26	90.33	88.81
clinocllore	75.40	80.35	72.19	73.37	70.33	69.64	83.71	81.30	83.44	78.67	88.06	89.32	87.72
chamosite	23.59	18.78	26.58	25.58	28.88	29.51	15.49	17.91	14.20	20.24	10.60	9.56	11.05
Cr-fraction	0.10	0.07	0.40	0.20	0.05	0.03	0.17	0.08	1.63	0.00	0.60	0.39	0.56
pennantite (Mn)	0.89	0.79	0.79	0.81	0.63	0.78	0.61	0.66	0.72	1.09	0.68	0.67	0.63
Ti-fraction	0.02	0.00	0.04	0.04	0.11	0.04	0.03	0.04	0.02	0.00	0.06	0.05	0.04

H<sub>2</sub>O was calculated stoichiometrically; cation calculation is based on 10 oxygens and 4 OH; Fe<sup>2+</sup> = F Nomenclature after Bayliss (1975).

## C2.3: Talc

Table C2.3: Composition of talc (in wt%), analyses also in electronic appendix.

Analysis	D1H4- 1A_29	E2H2-5D- 04	E2H2-5D- 06	E2H2-5D- 07	E2H2-5D- 16	E2H2-5J- 02	F1H3-2C- 12	F1H3-2C- 21	F1H3-2C- 25	F1H3-2C- 27	F1H3-2C- 31	F1H3-2C- 32	F1H3-2C- 35
SiO <sub>2</sub>	64.14	63.20	63.12	62.35	62.96	63.12	63.82	63.10	61.27	61.69	62.31	62.34	61.37
TiO <sub>2</sub>	0.01	0.02	0.00	0.00	0.00	0.03	0.00	0.00	0.00	0.00	0.00	0.01	0.00
Al <sub>2</sub> O <sub>3</sub>	0.18	0.11	0.11	0.12	0.12	0.12	0.09	0.08	0.16	0.13	0.16	0.03	0.03
Cr <sub>2</sub> O <sub>3</sub>	0.00	0.03	0.05	0.03	0.03	0.05	0.00	0.00	0.02	0.00	0.01	0.04	0.04
FeO	3.84	3.79	3.90	3.86	4.05	1.07	2.09	2.31	2.33	2.20	2.49	2.30	2.58
MnO	0.25	0.14	0.13	0.15	0.09	0.00	0.05	0.04	0.05	0.09	0.06	0.13	0.08
NiO	0.22	0.29	0.27	0.26	0.28	0.37	0.45	0.57	0.55	0.50	0.47	0.51	0.52
MgO	29.07	28.93	29.00	28.66	28.49	30.80	30.74	30.66	30.69	30.55	31.35	30.72	29.65
CaO	0.11	0.07	0.07	0.06	0.05	0.00	0.02	0.03	0.03	0.05	0.02	0.06	0.04
Na <sub>2</sub> O	0.03	0.04	0.05	0.04	0.02	0.04	0.01	0.01	0.01	0.00	0.00	0.02	0.00
K <sub>2</sub> O	0.00	0.02	0.00	0.01	0.00	0.00	0.01	0.00	0.00	0.00	0.00	0.00	0.02
<b>Total</b>	<b>97.85</b>	<b>96.64</b>	<b>96.69</b>	<b>95.52</b>	<b>96.08</b>	<b>95.59</b>	<b>97.28</b>	<b>96.80</b>	<b>95.11</b>	<b>95.21</b>	<b>96.88</b>	<b>96.16</b>	<b>94.32</b>
Si	4.011	4.002	3.997	3.997	4.011	3.989	3.983	3.964	3.927	3.945	3.924	3.949	3.965
Ti	0.000	0.001	0.000	0.000	0.000	0.001	0.000	0.000	0.000	0.000	0.000	0.000	0.000
Al	0.013	0.008	0.008	0.009	0.009	0.009	0.006	0.006	0.012	0.010	0.012	0.002	0.002
Cr	0.000	0.001	0.003	0.001	0.001	0.002	0.000	0.000	0.001	0.000	0.001	0.002	0.002
Fe <sup>2+</sup>	0.201	0.201	0.206	0.207	0.216	0.057	0.109	0.121	0.125	0.117	0.131	0.122	0.140
Mn	0.013	0.008	0.007	0.008	0.005	0.000	0.003	0.002	0.003	0.005	0.003	0.007	0.004
Ni	0.049	0.066	0.061	0.060	0.065	0.083	0.102	0.130	0.128	0.115	0.107	0.117	0.121
Mg	2.709	2.731	2.738	2.739	2.706	2.901	2.860	2.872	2.932	2.912	2.943	2.902	2.856
Ca	0.007	0.005	0.005	0.004	0.003	0.000	0.001	0.002	0.002	0.004	0.001	0.004	0.002
Na	0.004	0.005	0.007	0.005	0.002	0.004	0.001	0.001	0.001	0.000	0.000	0.003	0.000
K	0.000	0.002	0.000	0.001	0.000	0.000	0.000	0.000	0.000	0.000	0.000	0.000	0.002
<b>Total</b>	<b>7.009</b>	<b>7.029</b>	<b>7.031</b>	<b>7.031</b>	<b>7.017</b>	<b>7.048</b>	<b>7.066</b>	<b>7.098</b>	<b>7.131</b>	<b>7.108</b>	<b>7.123</b>	<b>7.108</b>	<b>7.094</b>
<b>Mg#</b>	<b>92.67</b>	<b>92.91</b>	<b>92.77</b>	<b>92.72</b>	<b>92.47</b>	<b>98.09</b>	<b>96.24</b>	<b>95.88</b>	<b>95.82</b>	<b>95.97</b>	<b>95.63</b>	<b>95.76</b>	<b>95.20</b>

Cation calculation is based on 10 oxygens and 2 OH; Fe<sup>2+</sup> = Fe<sup>3+</sup>.

Analysis	F1H3-2F- 04	F1H3-2F- 05	F2H2-4E- 27	F2H2-4E- 28	F2H2-4F- 04	F2H2-4F- 05	F2H2-4F- 13	F2H2-4G- 06	F2H2-4G- 22	F2H2-4G- 24
SiO <sub>2</sub>	59.91	60.44	60.98	62.13	62.66	62.60	60.73	62.89	61.50	61.14
TiO <sub>2</sub>	0.00	0.01	0.03	0.02	0.01	0.02	0.03	0.00	0.02	0.02
Al <sub>2</sub> O <sub>3</sub>	0.15	0.11	0.35	0.04	0.16	0.28	0.63	0.16	0.37	0.25
Cr <sub>2</sub> O <sub>3</sub>	0.04	0.00	0.04	0.02	0.05	0.01	0.05	0.03	0.00	0.01
FeO	1.67	2.03	2.44	2.13	2.50	2.27	2.63	2.50	2.48	2.56
MnO	0.04	0.06	0.13	0.12	0.13	0.08	0.18	0.07	0.10	0.08
NiO	0.32	0.37	0.29	0.13	0.20	0.19	0.22	0.24	0.27	0.30
MgO	32.53	30.99	30.08	29.97	29.94	30.06	29.66	30.27	29.37	29.88
CaO	0.07	0.15	0.04	0.01	0.02	0.01	0.02	0.03	0.04	0.02
Na <sub>2</sub> O	0.01	0.02	0.03	0.02	0.03	0.02	0.04	0.00	0.03	0.02
K <sub>2</sub> O	0.00	0.01	0.02	0.01	0.00	0.01	0.00	0.01	0.02	0.01
<b>Total</b>	<b>94.72</b>	<b>94.19</b>	<b>94.42</b>	<b>94.58</b>	<b>95.67</b>	<b>95.55</b>	<b>94.20</b>	<b>96.21</b>	<b>94.19</b>	<b>94.27</b>
Si	3.861	3.914	3.940	3.992	3.986	3.983	3.936	3.979	3.975	3.954
Ti	0.000	0.001	0.001	0.001	0.001	0.001	0.002	0.000	0.001	0.001
Al	0.011	0.008	0.027	0.003	0.012	0.021	0.048	0.012	0.028	0.019
Cr	0.002	0.000	0.002	0.001	0.002	0.001	0.002	0.002	0.000	0.001
Fe <sup>2+</sup>	0.090	0.110	0.132	0.114	0.133	0.121	0.143	0.132	0.134	0.138
Mn	0.002	0.003	0.007	0.006	0.007	0.005	0.010	0.004	0.006	0.005
Ni	0.073	0.085	0.067	0.029	0.046	0.044	0.052	0.054	0.062	0.069
Mg	3.125	2.992	2.897	2.871	2.839	2.851	2.865	2.855	2.830	2.881
Ca	0.005	0.010	0.003	0.001	0.001	0.000	0.002	0.002	0.003	0.002
Na	0.001	0.002	0.004	0.002	0.004	0.003	0.005	0.000	0.003	0.002
K	0.000	0.001	0.002	0.000	0.000	0.001	0.000	0.001	0.001	0.001
<b>Total</b>	<b>7.170</b>	<b>7.126</b>	<b>7.081</b>	<b>7.020</b>	<b>7.031</b>	<b>7.029</b>	<b>7.065</b>	<b>7.042</b>	<b>7.044</b>	<b>7.071</b>
<b>Mg#</b>	<b>97.14</b>	<b>96.35</b>	<b>95.44</b>	<b>95.96</b>	<b>95.31</b>	<b>95.78</b>	<b>94.94</b>	<b>95.44</b>	<b>95.29</b>	<b>95.28</b>

Cation calculation is based on 10 oxygens and 2 OH; Fe<sup>2+</sup> = Fe<sup>3+</sup>.

## C2.4: Pumpellyite, epidote and allanite

Table C2.4: Composition of pumpellyite (in wt%), analyses also in electronic appendix.

Analysis	E1H3-4B_43	E1H3-4B_51	E1H3-4B_53	E1H3-4B_54	E1H3-4B_59	E1H3-4B_60	E1H3-4B_63	E1H3-4B_65	E1H3-4B_66	E1H3-4B_75	E1H3-4B_76	E1H3-4B_84
SiO <sub>2</sub>	35.83	35.98	35.88	36.12	36.13	37.70	36.14	36.89	36.80	35.97	35.91	35.68
TiO <sub>2</sub>	0.77	0.88	0.68	0.21	0.31	0.33	1.71	0.23	0.26	0.33	1.49	0.39
Al <sub>2</sub> O <sub>3</sub>	19.72	20.33	20.81	22.36	21.78	21.86	20.33	22.63	22.47	19.59	18.59	20.48
Cr <sub>2</sub> O <sub>3</sub>	0.92	1.82	1.20	0.01	0.04	0.02	0.28	0.01	0.05	0.70	1.57	0.20
Fe <sub>2</sub> O <sub>3</sub>	10.68	7.97	8.20	7.66	8.12	7.63	8.09	6.63	7.15	10.46	8.12	8.63
MnO	0.20	0.31	0.31	0.29	0.41	0.47	0.41	0.42	0.28	0.28	0.22	0.31
MgO	2.33	2.65	2.72	3.23	2.95	3.64	2.82	3.32	3.25	2.76	3.09	3.02
CaO	21.85	21.53	21.50	22.07	21.84	21.43	22.48	22.05	21.88	21.85	22.47	22.12
Na <sub>2</sub> O	0.22	0.30	0.28	0.21	0.18	0.31	0.23	0.21	0.25	0.13	0.18	0.19
K <sub>2</sub> O	0.00	0.00	0.00	0.02	0.01	0.00	0.00	0.01	0.01	0.00	0.00	0.00
NiO	0.00	0.01	0.00	0.00	0.01	0.03	0.00	0.02	0.01	0.02	0.02	0.02
Total	92.50	91.79	91.59	92.17	91.78	93.40	92.49	92.40	92.40	92.09	91.65	91.04
Si	3.145	3.161	3.154	3.138	3.157	3.218	3.151	3.180	3.176	3.168	3.176	3.159
Al	2.041	2.104	2.156	2.289	2.243	2.199	2.089	2.299	2.286	2.033	1.937	2.138
Fe <sup>3+</sup>	0.705	0.527	0.542	0.500	0.534	0.490	0.531	0.430	0.464	0.693	0.541	0.575
Ti	0.051	0.058	0.045	0.014	0.020	0.021	0.112	0.015	0.017	0.022	0.099	0.026
Cr	0.064	0.127	0.084	0.000	0.003	0.001	0.019	0.000	0.003	0.049	0.110	0.014
Mn	0.015	0.023	0.023	0.022	0.030	0.034	0.030	0.031	0.020	0.021	0.017	0.023
Mg	0.305	0.347	0.357	0.418	0.384	0.463	0.367	0.427	0.418	0.362	0.407	0.399
Ca	2.055	2.027	2.025	2.054	2.045	1.960	2.100	2.037	2.023	2.061	2.129	2.099
Na	0.037	0.051	0.048	0.036	0.031	0.051	0.038	0.036	0.042	0.023	0.031	0.032
K	0.000	0.000	0.000	0.002	0.001	0.000	0.000	0.001	0.001	0.000	0.000	0.000
Ni	0.000	0.004	0.000	0.000	0.003	0.008	0.000	0.007	0.003	0.005	0.005	0.005
Total	8.417	8.430	8.434	8.472	8.451	8.445	8.437	8.462	8.453	8.437	8.449	8.470
Fe <sup>3+</sup> /(Al+Fe <sup>3+</sup> )	0.26	0.20	0.20	0.18	0.19	0.18	0.20	0.16	0.17	0.25	0.22	0.21

Cation calculation based on 13 (O,OH) and Fe<sup>3+</sup> = Fe<sup>2+</sup>.

Table C2.4 (continued): Composition of epidote (in wt%), analyses also in electronic appendix.

Analysis	D1H4-1	E1H3-4A_11	E1H3-4B_28	E1H3-4B_32	E1H3-4B_50	E1H3-4C_02	E1H3-4C_05	E1H3-4C_07	E1H3-4C_15	F1H4-3A_14	F1H4-3A_16	F2H2-1A-26	F2H2-1A-27
SiO <sub>2</sub>	38.02	37.72	36.99	36.93	36.51	37.30	37.08	37.11	37.35	37.32	37.51	36.86	37.25
TiO <sub>2</sub>	0.15	0.25	0.07	0.09	0.33	0.19	0.05	0.05	0.27	0.17	0.05	0.06	0.10
Al <sub>2</sub> O <sub>3</sub>	25.30	23.60	22.94	22.10	23.18	23.78	24.36	23.72	23.61	21.24	21.36	21.63	22.95
Cr <sub>2</sub> O <sub>3</sub>	0.07	0.05	0.20	0.18	0.16	0.08	0.02	0.07	0.05	0.02	0.01	0.02	0.04
Fe <sub>2</sub> O <sub>3</sub>	10.65	14.03	14.06	14.91	12.83	12.67	11.75	12.50	12.58	15.54	15.69	15.17	13.46
MnO	0.17	0.24	0.20	0.32	0.20	1.08	0.87	0.96	0.98	0.38	0.30	0.70	1.22
MgO	0.10	0.02	0.02	0.00	0.03	0.04	0.11	0.10	0.13	0.00	0.00	0.13	0.09
CaO	22.73	22.76	23.00	22.75	23.05	22.27	22.17	22.23	22.19	22.77	22.76	21.89	22.48
Na <sub>2</sub> O	0.01	0.06	0.00	0.00	0.00	0.01	0.01	0.01	0.02	0.02	0.00	0.03	0.00
K <sub>2</sub> O	0.01	0.01	0.01	0.02	0.00	0.00	0.01	0.01	0.01	0.02	0.01	0.00	0.00
NiO	0.03	0.00	0.01	0.00	0.02	0.00	0.02	0.00	0.00	0.01	0.00	0.01	0.00
H <sub>2</sub> O	1.89	1.90	1.87	1.86	1.85	1.87	1.86	1.86	1.87	1.86	1.86	1.84	1.87
Total	99.14	100.63	99.36	99.14	98.14	99.28	98.31	98.60	99.05	99.34	99.55	98.33	99.47
Si	3.011	2.982	2.971	2.983	2.962	2.986	2.984	2.989	2.994	3.014	3.021	3.002	2.990
Al	2.362	2.199	2.172	2.104	2.216	2.244	2.311	2.251	2.230	2.022	2.027	2.076	2.171
Fe <sup>3+</sup>	0.635	0.835	0.850	0.906	0.783	0.763	0.712	0.757	0.759	0.944	0.951	0.929	0.813
Ti	0.009	0.015	0.004	0.005	0.020	0.011	0.003	0.003	0.016	0.010	0.003	0.004	0.006
Cr	0.004	0.003	0.012	0.011	0.010	0.005	0.001	0.005	0.003	0.001	0.001	0.001	0.003
sum	3.009	3.052	3.039	3.027	3.029	3.023	3.027	3.016	3.009	2.978	2.982	3.011	2.993
Mn	0.012	0.016	0.014	0.022	0.013	0.073	0.059	0.065	0.066	0.026	0.020	0.049	0.083
Mg	0.012	0.002	0.002	0.000	0.003	0.005	0.013	0.012	0.016	0.000	0.000	0.016	0.011
Ca	1.929	1.928	1.980	1.969	2.003	1.910	1.912	1.918	1.906	1.971	1.964	1.910	1.934
Na	0.001	0.010	0.000	0.000	0.000	0.001	0.001	0.002	0.003	0.002	0.000	0.005	0.000
K	0.001	0.001	0.001	0.002	0.000	0.000	0.001	0.001	0.001	0.002	0.001	0.000	0.000
Ni	0.010	0.000	0.002	0.000	0.005	0.000	0.007	0.000	0.000	0.003	0.000	0.001	0.000
sum	1.973	1.973	1.973	1.973	1.973	1.989	1.994	1.997	1.993	2.004	1.985	1.980	2.028
Fe <sup>3+</sup> /(Al+Fe <sup>3+</sup> )	0.21	0.28	0.28	0.30	0.26	0.25	0.24	0.25	0.25	0.32	0.32	0.31	0.27

H<sub>2</sub>O was calculated stoichiometrically. Cation calculation based on 12.5 (O,OH) and Fe<sup>3+</sup> = Fe<sup>2+</sup>.

**Table C2.4 (continued):** Composition of allanite (in wt%), analyses also in electronic appendix.

Analysis	E1H3- 4B_19	E1H3- 4B_20	E1H3- 4B_49	E1H3- 4B_74	F2H2- 1A-35	F2H2- 1A-36	F2H2- 1A-56	F2H2- 1A-59	E1H3- 4B_25	E1H3- 4B_26	E1H3- 4B_24	F1H4- 3A_12	F2H2- 1A-95
<b>SiO<sub>2</sub></b>	33.33	32.19	32.03	31.65	34.49	33.60	33.88	34.30	35.70	33.83	32.71	30.90	34.53
<b>TiO<sub>2</sub></b>	0.16	0.17	0.27	0.26	0.07	0.00	0.05	0.17	0.09	0.09	0.11	0.23	0.01
<b>Al<sub>2</sub>O<sub>3</sub></b>	19.24	18.55	18.26	17.68	18.97	17.92	18.39	18.75	22.62	20.22	18.56	17.04	19.01
<b>Cr<sub>2</sub>O<sub>3</sub></b>	0.09	0.05	0.04	0.07	0.03	0.08	0.12	0.18	0.12	0.51	0.08	0.14	0.33
<b>Fe<sub>2</sub>O<sub>3</sub></b>	11.16	11.17	11.18	11.23	15.96	16.29	16.18	15.93	11.61	11.20	11.20	16.60	14.11
<b>MnO</b>	0.33	0.33	0.35	0.40	0.78	0.80	1.10	0.90	0.27	0.26	0.35	1.24	0.85
<b>MgO</b>	1.31	1.62	1.65	1.70	0.08	0.12	0.10	0.19	0.41	0.90	1.49	0.22	0.14
<b>CaO</b>	16.35	15.68	15.36	14.95	19.05	17.99	17.98	18.59	20.34	17.83	16.06	14.02	18.61
<b>Na<sub>2</sub>O</b>	0.01	0.03	0.04	0.04	0.01	0.04	0.03	0.03	0.00	0.04	0.04	0.07	0.04
<b>K<sub>2</sub>O</b>	0.00	0.00	0.00	0.00	0.01	0.00	0.00	0.00	0.00	0.00	0.00	0.01	0.00
<b>NiO</b>	0.02	0.00	0.01	0.02	0.03	0.05	0.00	0.03	0.00	0.00	0.00	0.02	0.00
<b>Total</b>	82.01	79.79	79.18	77.98	89.48	86.88	87.83	89.06	91.16	84.88	80.61	80.48	87.63
<b>Si</b>	3.122	3.105	3.111	3.123	3.038	3.052	3.044	3.036	3.027	3.075	3.123	3.026	1.272
<b>Al</b>	2.125	2.108	2.090	2.057	1.969	1.918	1.947	1.956	2.261	2.166	2.089	1.967	0.825
<b>Fe<sup>3+</sup></b>	0.787	0.811	0.817	0.834	1.057	1.114	1.094	1.061	0.741	0.766	0.805	1.223	0.434
<b>Ti</b>	0.011	0.012	0.020	0.019	0.005	0.000	0.003	0.011	0.006	0.006	0.008	0.017	0.000
<b>Cr</b>	0.007	0.004	0.003	0.005	0.002	0.006	0.008	0.012	0.008	0.037	0.006	0.011	0.010
<b>sum</b>	2.929	2.935	2.930	2.916	3.034	3.038	3.053	3.041	3.016	2.975	2.908	3.217	1.269
<b>Mn</b>	0.026	0.027	0.028	0.033	0.058	0.062	0.084	0.067	0.020	0.020	0.028	0.103	0.027
<b>Mg</b>	0.183	0.232	0.239	0.249	0.010	0.016	0.014	0.025	0.052	0.122	0.212	0.032	0.007
<b>Ca</b>	1.641	1.620	1.599	1.580	1.797	1.751	1.731	1.763	1.848	1.737	1.643	1.471	0.734
<b>Na</b>	0.002	0.006	0.008	0.008	0.002	0.006	0.005	0.006	0.000	0.007	0.007	0.013	0.003
<b>K</b>	0.000	0.000	0.000	0.000	0.001	0.000	0.000	0.000	0.000	0.000	0.000	0.002	0.000
<b>Ni</b>	0.008	0.000	0.003	0.007	0.010	0.015	0.001	0.009	0.000	0.001	0.000	0.005	0.000
<b>sum</b>	1.973	1.973	1.973	1.973	1.973	1.973	1.973	1.973	1.973	1.973	1.973	1.973	1.973
<b>Fe<sup>3+</sup>/(Al+Fe<sup>3+</sup>)</b>	0.27	0.28	0.28	0.29	0.35	0.37	0.36	0.35	0.25	0.26	0.28	0.38	0.34

Cation calculation based on 12.5 (O,OH) and Fe<sup>3+</sup> = Fe<sup>2+</sup>.

## C2.5: Phengite and Biotite

*Table C2.5: Representative composition of phengite and biotite (in wt%), further analyses in electronic appendix.*

Analysis	E1H3-4A_18	E1H3-4A_24	E1H3-4A_31	E1H3-4A_36	E1H3-4A_47	E1H3-4A_61	E1H3-4D_03	E1H3-5_53	E1H3-5_52	E1H3-5_27	F1H1-3D 01	F1H1-3D 02	F1H1-3D 05
SiO <sub>2</sub>	48.54	48.79	48.56	49.58	54.16	49.42	48.41	45.52	45.76	46.62	52.71	52.59	54.25
TiO <sub>2</sub>	0.54	0.48	0.47	0.41	0.13	0.53	0.63	0.34	0.34	0.41	0.16	0.12	0.09
Al <sub>2</sub> O <sub>3</sub>	27.31	27.01	27.17	24.65	21.63	26.54	25.84	32.25	32.44	31.24	23.82	23.46	24.44
Cr <sub>2</sub> O <sub>3</sub>	0.10	0.09	0.09	0.13	0.01	0.10	0.27	0.00	0.03	0.01	0.00	0.01	0.01
FeO	5.91	6.20	6.34	6.84	6.24	5.14	6.68	3.52	3.69	3.72	6.63	6.13	5.26
MnO	0.01	0.04	0.03	0.07	0.07	0.02	0.04	0.04	0.07	0.06	0.05	0.05	0.09
NiO	0.00	0.00	0.00	0.00	0.05	0.03	0.06	0.00	0.05	0.00	0.01	0.00	0.03
MgO	2.82	2.89	2.78	3.74	4.71	3.01	3.49	1.36	1.38	1.70	4.04	4.35	4.15
CaO	0.01	0.00	0.00	0.00	0.01	0.00	0.00	0.01	0.01	0.01	0.12	0.07	0.01
Na <sub>2</sub> O	0.40	0.42	0.35	0.19	0.07	0.43	0.23	1.38	1.32	1.29	0.14	0.14	0.10
K <sub>2</sub> O	10.22	10.05	10.34	10.71	10.72	10.46	9.74	9.04	9.06	9.16	8.66	9.31	10.36
H <sub>2</sub> O	4.43	4.43	4.43	4.41	4.53	4.43	4.39	4.38	4.41	4.41	4.50	4.49	4.61
<b>Total</b>	<b>100.27</b>	<b>100.38</b>	<b>100.53</b>	<b>100.71</b>	<b>102.31</b>	<b>100.10</b>	<b>99.78</b>	<b>97.85</b>	<b>98.55</b>	<b>98.63</b>	<b>100.83</b>	<b>100.70</b>	<b>103.40</b>
Si	3.289	3.303	3.290	3.370	3.588	3.343	3.305	3.116	3.112	3.167	3.510	3.514	3.525
Al <sup>(IV)</sup>	0.711	0.697	0.710	0.630	0.412	0.657	0.695	0.884	0.888	0.833	0.490	0.486	0.475
Al <sup>(VI)</sup>	1.470	1.458	1.460	1.344	1.277	1.459	1.384	1.718	1.711	1.669	1.380	1.361	1.397
Ti	0.027	0.024	0.024	0.021	0.006	0.027	0.032	0.018	0.018	0.021	0.008	0.006	0.004
Cr	0.005	0.005	0.005	0.007	0.000	0.005	0.015	0.000	0.002	0.000	0.000	0.001	0.000
Fe <sup>2+</sup>	0.335	0.351	0.359	0.388	0.346	0.291	0.381	0.201	0.210	0.211	0.369	0.342	0.286
Mn	0.000	0.002	0.002	0.004	0.004	0.001	0.002	0.002	0.004	0.004	0.003	0.003	0.005
Mg	0.285	0.292	0.280	0.379	0.465	0.303	0.356	0.139	0.140	0.172	0.401	0.433	0.402
Ca	0.001	0.000	0.000	0.000	0.001	0.000	0.000	0.000	0.001	0.001	0.008	0.005	0.000
Na	0.052	0.055	0.046	0.024	0.009	0.056	0.031	0.183	0.174	0.170	0.018	0.018	0.012
K	0.884	0.868	0.893	0.928	0.906	0.903	0.848	0.789	0.786	0.794	0.736	0.793	0.859
<b>Total</b>	<b>7.059</b>	<b>7.054</b>	<b>7.068</b>	<b>7.095</b>	<b>7.013</b>	<b>7.045</b>	<b>7.049</b>	<b>7.051</b>	<b>7.045</b>	<b>7.042</b>	<b>6.923</b>	<b>6.962</b>	<b>6.966</b>
<b>celadonite %</b>	<b>0.29</b>	<b>0.30</b>	<b>0.29</b>	<b>0.37</b>	<b>0.59</b>	<b>0.34</b>	<b>0.30</b>	<b>0.12</b>	<b>0.11</b>	<b>0.17</b>	<b>0.51</b>	<b>0.51</b>	<b>0.52</b>

H<sub>2</sub>O was calculated stoichiometrically. Cation calculation is based on 11 oxygen and 2 OH.

Analysis	Phengite							Biotite			
	F1H4-5_15	F1H4-5_20	F2H2-4A 12	F2H2-4A 13	F2H2-5A 05	F2H2-5A 07	F2H2-5A 27	D3H1-8C 03	D3H1-8C 04	D3H1-8C 05	D3H1-8C 06
SiO <sub>2</sub>	48.89	44.63	47.64	50.82	51.23	49.27	54.24	42.78	42.77	42.81	42.67
TiO <sub>2</sub>	0.35	0.08	0.57	0.55	0.20	0.64	0.22	0.12	0.10	0.11	0.10
Al <sub>2</sub> O <sub>3</sub>	24.13	27.50	26.31	25.96	25.80	27.79	23.17	11.44	11.24	11.46	11.33
Cr <sub>2</sub> O <sub>3</sub>	0.00	0.04	0.04	0.07	0.01	0.07	0.09	0.57	0.55	0.53	0.57
FeO	6.59	4.68	6.03	5.63	6.62	5.89	5.15	4.32	4.07	3.84	4.08
MnO	0.03	0.08	0.00	0.07	0.07	0.02	0.01	0.03	0.03	0.00	0.00
NiO	0.04	0.00	0.00	0.00	0.00	0.04	0.02	0.27	0.25	0.23	0.29
MgO	3.56	3.84	2.95	3.48	3.40	2.91	4.43	27.69	27.66	27.14	27.03
CaO	0.00	0.02	0.00	0.00	0.00	0.04	0.02	0.00	0.00	0.02	0.06
Na <sub>2</sub> O	0.13	0.50	0.36	0.24	0.12	0.44	0.12	0.40	0.40	0.49	0.48
K <sub>2</sub> O	10.08	9.32	10.68	10.24	9.45	10.37	9.62	7.36	7.65	8.04	8.35
H <sub>2</sub> O	4.32	4.20	4.34	4.50	4.50	4.50	4.56	4.28	4.27	4.26	4.26
<b>Total</b>	<b>98.11</b>	<b>94.89</b>	<b>98.92</b>	<b>101.57</b>	<b>101.40</b>	<b>101.98</b>	<b>101.65</b>	<b>99.25</b>	<b>98.99</b>	<b>98.93</b>	<b>99.23</b>
Si	3.395	3.184	3.290	3.385	3.411	3.282	3.570	2.995	3.005	3.011	3.003
Al <sup>(IV)</sup>	0.605	0.816	0.710	0.615	0.589	0.718	0.430	0.944	0.931	0.950	0.940
Al <sup>(VI)</sup>	1.369	1.496	1.431	1.422	1.436	1.463	1.368				
Ti	0.018	0.004	0.030	0.028	0.010	0.032	0.011	0.006	0.005	0.006	0.005
Cr	0.000	0.002	0.002	0.003	0.001	0.004	0.005	0.032	0.031	0.029	0.032
Fe <sup>2+</sup>	0.382	0.279	0.348	0.313	0.368	0.328	0.283	0.253	0.239	0.226	0.240
Mn	0.002	0.005	0.000	0.004	0.004	0.001	0.001	0.002	0.002	0.000	0.000
Mg	0.368	0.408	0.304	0.346	0.338	0.289	0.435	2.890	2.897	2.846	2.836
Ca	0.000	0.001	0.000	0.000	0.000	0.003	0.001	0.000	0.000	0.002	0.005
Na	0.018	0.068	0.048	0.031	0.015	0.056	0.015	0.054	0.055	0.066	0.065
K	0.893	0.848	0.941	0.870	0.802	0.881	0.808	0.657	0.686	0.721	0.750
<b>Total</b>	<b>7.050</b>	<b>7.113</b>	<b>7.103</b>	<b>7.018</b>	<b>6.975</b>	<b>7.058</b>	<b>6.927</b>	<b>7.833</b>	<b>7.849</b>	<b>7.858</b>	<b>7.876</b>
<b>celadonite %</b>	<b>0.39</b>	<b>0.18</b>	<b>0.29</b>	<b>0.38</b>	<b>0.41</b>	<b>0.28</b>	<b>0.57</b>				

H<sub>2</sub>O was calculated stoichiometrically. Cation calculation is based on 11 oxygen and 2 OH.

**C2.6: Garnet***Table C2.6: Representative composition of garnet (in wt%), further analyses in electronic appendix.*

Analysis	ETH3-4C	ETH3-4C	ETH3-4C	ETH3-4C	ETH3-4C	ETH3-4C	ETH3-4C	ETH3-4C	ETH3-4C	ETH3-4C	ETH3-4C	ETH3-4C	ETH3-4C
	grt1	grt1	grt1	grt1	grt1	grt1	grt1	grt1	grt1	grt2	grt2	grt2	grt2
<b>SiO<sub>2</sub></b>	37.28	36.80	36.68	36.63	37.17	37.04	37.30	36.83	36.91	37.30	37.27	36.93	36.54
<b>TiO<sub>2</sub></b>	0.10	0.08	0.45	0.41	0.31	0.22	0.14	0.07	0.07	0.09	0.18	0.37	0.38
<b>Al<sub>2</sub>O<sub>3</sub></b>	20.29	20.44	19.26	19.38	19.95	20.11	20.43	20.65	20.72	20.62	20.43	20.00	19.92
<b>Cr<sub>2</sub>O<sub>3</sub></b>	0.05	0.08	0.01	0.03	0.00	0.02	0.01	0.03	0.01	0.00	0.01	0.01	0.00
<b>FeO</b>	11.66	11.70	12.03	12.58	11.76	11.51	11.86	11.84	11.57	11.87	11.69	11.75	11.68
<b>MnO</b>	19.64	20.95	20.44	20.62	20.40	20.92	21.44	20.92	21.20	21.88	21.44	21.07	20.69
<b>MgO</b>	2.92	2.84	2.66	2.68	2.86	2.89	3.14	3.10	3.25	3.16	2.67	2.82	2.79
<b>CaO</b>	7.49	6.56	6.89	6.68	6.76	6.37	5.68	6.23	5.22	5.15	6.15	6.61	6.58
<b>Na<sub>2</sub>O</b>	0.04	0.03	0.06	0.01	0.02	0.01	0.02	0.03	0.03	0.01	0.02	0.05	0.05
<b>K<sub>2</sub>O</b>	0.00	0.00	0.01	0.00	0.00	0.00	0.00	0.00	0.02	0.00	0.01	0.00	0.01
<b>Total</b>	99.47	99.47	98.48	99.00	99.24	99.09	100.02	99.70	99.00	100.08	99.86	99.60	98.62
<b>FeO*</b>	9.78	9.27	9.73	9.90	10.21	9.97	10.02	9.28	10.09	10.26	10.29	9.44	9.46
<b>Fe<sub>2</sub>O<sub>3</sub>*</b>	2.09	2.70	2.55	2.97	1.73	1.71	2.04	2.85	1.64	1.79	1.55	2.57	2.47
<b>Total</b>	99.68	99.74	98.73	99.30	99.42	99.25	100.23	99.99	99.16	100.25	100.02	99.86	98.87
<b>Si</b>	2.987	2.949	2.939	2.935	2.978	2.968	2.989	2.951	2.957	2.989	2.986	2.959	2.928
<b>Ti</b>	0.006	0.005	0.027	0.025	0.019	0.013	0.008	0.004	0.004	0.005	0.011	0.022	0.023
<b>Al</b>	0.958	0.965	0.909	0.915	0.942	0.950	0.965	0.975	0.978	0.974	0.965	0.944	0.940
<b>Cr</b>	0.002	0.003	0.000	0.001	0.000	0.001	0.000	0.001	0.000	0.000	0.000	0.000	0.000
<b>Fe<sup>3+</sup></b>	0.063	0.081	0.077	0.090	0.052	0.052	0.062	0.086	0.049	0.054	0.047	0.077	0.074
<b>Fe<sup>2+</sup></b>	0.655	0.621	0.652	0.663	0.684	0.668	0.671	0.622	0.676	0.688	0.690	0.633	0.634
<b>Mn</b>	1.333	1.422	1.387	1.399	1.385	1.420	1.455	1.420	1.439	1.485	1.455	1.430	1.404
<b>Mg</b>	0.348	0.339	0.318	0.321	0.341	0.345	0.376	0.370	0.388	0.377	0.319	0.337	0.334
<b>Ca</b>	0.643	0.563	0.591	0.573	0.580	0.547	0.488	0.535	0.448	0.442	0.528	0.567	0.565
<b>Na</b>	0.003	0.002	0.004	0.001	0.002	0.000	0.002	0.002	0.002	0.001	0.001	0.004	0.004
<b>K</b>	0.000	0.000	0.000	0.000	0.000	0.000	0.000	0.000	0.001	0.000	0.001	0.000	0.001
<b>Total</b>	6.999	6.950	6.907	6.922	6.984	6.963	7.015	6.966	6.945	7.014	7.002	6.973	6.905
<b>Mg#</b>	34.70	35.32	32.79	32.58	33.28	34.03	35.87	37.29	36.47	35.42	31.61	34.74	34.47
<b>Prp</b>	11.7%	11.5%	10.8%	10.8%	11.4%	11.6%	12.6%	12.6%	13.2%	12.6%	10.7%	11.4%	11.4%
<b>Alm</b>	22.0%	21.2%	22.1%	22.5%	22.9%	22.5%	22.5%	21.2%	22.9%	23.0%	23.0%	21.4%	21.6%
<b>Sps</b>	44.7%	48.3%	47.1%	47.3%	46.3%	47.6%	48.7%	48.2%	48.8%	49.6%	48.7%	48.2%	47.9%
<b>Grs</b>	15.3%	11.1%	12.2%	10.4%	14.2%	13.2%	10.3%	9.9%	10.2%	9.6%	12.9%	11.5%	11.8%
<b>Adr</b>	6.1%	7.7%	7.8%	8.8%	5.2%	5.1%	5.9%	8.0%	4.9%	5.2%	4.7%	7.5%	7.3%
<b>Uw</b>	0.2%	0.2%	0.0%	0.1%	0.0%	0.1%	0.0%	0.1%	0.0%	0.0%	0.0%	0.0%	0.0%

FeO and Fe<sub>2</sub>O<sub>3</sub> calculation is based on charge balance. Cation calculation based on 12 oxygens.

Formula calculation after Locock (2008).



## C2.7: Pyroxene

Table C2.7: Representative composition of pyroxene (in wt%), further analyses in electronic appendix.

Analysis	E1H3-4B_107	E1H3-4B_108	E1H3-4B_109	E1H3-4B_94	E1H3-4B_95	F2H2-4A-25	F2H2-4A-26	F2H2-4H-01	F2H2-4H-04	F2H2-4H-07	F2H2-5A-25	F2H2-5A-26	F2H2-5A-29
SiO <sub>2</sub>	53.43	53.55	53.10	53.53	53.49	53.01	52.90	52.40	52.26	52.74	53.75	53.48	53.32
TiO <sub>2</sub>	0.04	0.24	0.16	0.17	0.01	0.51	0.42	0.00	0.02	0.36	0.02	0.10	0.01
Al <sub>2</sub> O <sub>3</sub>	3.17	3.20	2.18	3.38	3.27	3.70	3.43	4.50	4.62	4.46	4.41	4.23	2.29
Cr <sub>2</sub> O <sub>3</sub>	0.03	0.05	0.08	0.10	0.02	0.06	0.02	0.00	0.00	0.06	0.00	0.03	0.00
FeO	20.90	15.25	17.01	13.92	16.85	22.15	23.21	24.70	23.80	21.98	22.45	23.54	23.43
MnO	0.10	0.15	0.20	0.11	0.22	0.15	0.11	0.04	0.03	0.01	0.00	0.00	0.03
MgO	4.07	7.12	6.86	7.94	6.09	2.52	1.93	0.56	0.86	2.29	1.08	0.95	2.79
CaO	6.65	11.60	10.76	12.46	9.36	3.74	3.08	2.10	2.36	3.23	2.97	2.27	4.16
Na <sub>2</sub> O	10.15	7.66	7.67	7.15	8.67	11.74	11.87	12.75	12.48	11.73	12.41	12.08	11.35
K <sub>2</sub> O	0.00	0.02	0.00	0.01	0.00	0.02	0.04	0.01	0.01	0.02	0.02	0.03	0.02
Total	98.53	98.83	98.00	98.75	97.97	97.61	97.00	97.06	96.43	96.88	97.10	96.71	97.38
Si	1.985	1.977	1.987	1.973	1.989	1.981	1.996	1.973	1.978	1.984	2.017	2.026	2.007
Ti	0.001	0.007	0.004	0.005	0.000	0.014	0.012	0.000	0.000	0.010	0.000	0.003	0.000
Al	0.139	0.139	0.096	0.147	0.143	0.163	0.152	0.200	0.206	0.198	0.195	0.189	0.101
Fe <sup>3+</sup>	0.619	0.441	0.475	0.405	0.503	0.693	0.701	0.778	0.752	0.669	0.674	0.641	0.713
Cr	0.001	0.001	0.002	0.003	0.001	0.002	0.001	0.000	0.000	0.002	0.000	0.001	0.000
Fe <sup>2+</sup>	0.031	0.030	0.058	0.024	0.021	0.000	0.031	0.000	0.001	0.023	0.030	0.105	0.024
Mn	0.003	0.005	0.006	0.004	0.007	0.005	0.003	0.001	0.001	0.000	0.000	0.000	0.001
Mg	0.225	0.392	0.383	0.436	0.338	0.140	0.109	0.031	0.048	0.128	0.060	0.054	0.156
Ca	0.265	0.459	0.431	0.492	0.373	0.150	0.125	0.085	0.096	0.130	0.119	0.092	0.168
Na	0.731	0.549	0.557	0.511	0.625	0.851	0.868	0.931	0.916	0.855	0.903	0.888	0.828
K	0.000	0.001	0.000	0.000	0.000	0.001	0.002	0.000	0.000	0.001	0.001	0.001	0.001
Mg#	0.88	0.93	0.87	0.95	0.94	1.00	0.78	1.00	0.98	0.85	0.67	0.34	0.87
Aegerine	62.1	43.8	48.0	40.4	50.4	69.2	70.6	76.6	74.4	67.9	66.0	65.4	71.6
Jadeite	11.3	10.7	8.3	10.5	12.3	15.8	16.8	15.1	16.2	18.9	22.4	25.2	11.5
Diopside	26.6	45.6	43.6	49.1	37.4	15.0	12.6	8.4	9.4	13.2	11.7	9.4	16.8

FeO and Fe<sub>2</sub>O<sub>3</sub> calculation is based on charge balance. Cation calculation based on 12 oxygens.

Analysis	magmatic Px											
	E2H2-4B-13	E2H2-4B-24	F1H1-3E-05	F1H1-3E-08	F2H2-4D-10	F2H2-4D-11	F2H2-4D-12	F2H2-5C-06	F2H2-5C-09	MAK10F-01	MAK10F-02	MAK10F-03
SiO <sub>2</sub>	53.02	52.64	53.21	54.14	52.96	53.38	52.95	52.22	45.46	44.68	47.73	49.58
TiO <sub>2</sub>	0.14	0.18	0.06	0.05	0.40	0.16	0.13	0.67	3.11	2.71	2.47	1.89
Al <sub>2</sub> O <sub>3</sub>	0.34	0.60	1.43	1.41	0.78	0.76	0.78	2.37	7.23	8.20	4.97	3.86
Cr <sub>2</sub> O <sub>3</sub>	0.05	0.10	0.18	0.13	0.22	0.12	0.21	0.87	0.06	0.00	0.10	0.34
FeO	11.47	10.90	8.03	7.34	7.52	6.91	6.88	4.74	8.26	11.31	8.43	6.81
MnO	0.27	0.28	0.71	0.56	0.21	0.16	0.15	0.10	0.18	0.11	0.13	0.11
MgO	13.80	13.85	14.72	13.97	15.40	15.62	15.26	16.66	12.86	10.87	13.84	14.86
CaO	20.68	20.80	18.34	19.54	22.27	22.59	22.64	21.95	20.98	21.04	21.59	21.57
Na <sub>2</sub> O	0.34	0.32	0.72	0.98	0.37	0.28	0.28	0.30	0.39	0.51	0.40	0.36
K <sub>2</sub> O	0.00	0.01	0.00	0.00	0.00	0.00	0.00	0.02	0.00	0.03	0.00	0.01
Total	100.11	99.67	97.40	98.12	100.13	99.97	99.28	99.90	98.52	99.46	99.63	99.39
Si	1.986	1.978	2.019	2.039	1.955	1.969	1.969	1.913	1.718	1.691	1.781	1.843
Ti	0.004	0.005	0.002	0.001	0.011	0.004	0.004	0.019	0.088	0.077	0.069	0.053
Al	0.015	0.026	0.064	0.063	0.034	0.033	0.034	0.102	0.322	0.366	0.219	0.169
Fe <sup>3+</sup>	0.028	0.029	0.000	0.000	0.054	0.036	0.035	0.033	0.092	0.138	0.107	0.055
Cr	0.002	0.003	0.005	0.004	0.006	0.003	0.006	0.025	0.002	0.000	0.003	0.010
Fe <sup>2+</sup>	0.331	0.314	0.255	0.231	0.178	0.177	0.180	0.113	0.169	0.220	0.156	0.156
Mn	0.009	0.009	0.023	0.018	0.007	0.005	0.005	0.003	0.006	0.003	0.004	0.003
Mg	0.771	0.776	0.833	0.784	0.848	0.859	0.846	0.910	0.724	0.613	0.770	0.824
Ca	0.830	0.837	0.746	0.788	0.881	0.893	0.902	0.861	0.850	0.853	0.863	0.859
Na	0.025	0.023	0.053	0.071	0.027	0.020	0.020	0.021	0.029	0.037	0.029	0.026
K	0.000	0.000	0.000	0.000	0.000	0.000	0.000	0.001	0.000	0.001	0.000	0.001
Mg#	0.70	0.71	0.77	0.77	0.83	0.83	0.82	0.89	0.81	0.74	0.83	0.84
Wo	43.0	43.5	40.7	43.7	46.2	46.3	46.8	45.7	48.7	50.6	48.3	46.7
En	39.9	40.3	45.4	43.5	44.5	44.5	43.9	48.3	41.6	36.4	43.0	44.8
Fs	17.2	16.3	13.9	12.8	9.3	9.2	9.3	6.0	9.7	13.1	8.7	8.5

FeO and Fe<sub>2</sub>O<sub>3</sub> calculation is based on charge balance. Cation calculation based on 12 oxygens.

**C2.8: Rutile, titanite, ilmenite, picotite and magnetite***Table C2.8: Representative composition of rutile (in wt%), further analyses in electronic appendix.*

Analysis	E1H3-4B_10	E1H3-4B_12	E1H3-4B_13	E1H3-4B_44	E1H3-4B_46	E1H3-4B_79	E1H3-4C_16	F2H2-5A_21	F2H2-5A_24	F1H1-3E_18	E1H3-4A_08	E1H3-4A_10
SiO <sub>2</sub>	0.00	0.03	0.00	0.01	0.01	0.08	0.05	0.08	0.04	2.26	0.00	0.00
TiO <sub>2</sub>	96.98	96.84	96.87	96.65	97.42	96.90	97.77	98.11	98.25	94.20	97.12	96.67
Al <sub>2</sub> O <sub>3</sub>	0.00	0.00	0.00	0.00	0.00	0.00	0.00	0.00	0.00	0.00	0.00	0.00
Fe <sub>2</sub> O <sub>3</sub>	1.69	1.16	1.19	1.11	1.17	1.23	0.80	1.27	1.17	0.71	2.47	2.92
Cr <sub>2</sub> O <sub>3</sub>	0.25	0.22	0.20	0.21	0.23	0.23	0.26	0.02	0.03	0.27	0.07	0.05
MnO	0.00	0.03	0.00	0.01	0.06	0.00	0.05	0.01	0.00	0.03	0.00	0.02
MgO	0.00	0.00	0.00	0.00	0.00	0.00	0.00	0.01	0.00	0.01	0.00	0.00
CaO	0.11	0.02	0.07	0.23	0.03	0.66	1.18	0.29	0.78	3.21	0.03	0.08
Na <sub>2</sub> O	0.01	0.00	0.00	0.01	0.00	0.02	0.00	0.00	0.01	0.00	0.01	0.02
K <sub>2</sub> O	0.01	0.00	0.00	0.00	0.01	0.00	0.00	0.04	0.06	0.02	0.00	0.00
NiO	0.04	0.03	0.07	0.02	0.02	0.05	0.00	0.01	0.04	0.00	0.03	0.01
<b>Total</b>	<b>99.08</b>	<b>98.32</b>	<b>98.40</b>	<b>98.27</b>	<b>98.94</b>	<b>99.16</b>	<b>100.11</b>	<b>99.83</b>	<b>100.38</b>	<b>100.71</b>	<b>99.73</b>	<b>99.77</b>
Si	0.000	0.000	0.000	0.000	0.000	0.001	0.001	0.001	0.001	0.030	0.000	0.000
Ti	0.984	0.988	0.988	0.987	0.988	0.982	0.983	0.987	0.984	0.939	0.980	0.977
Al	0.000	0.000	0.000	0.000	0.000	0.000	0.000	0.000	0.000	0.000	0.000	0.000
Fe <sup>3+</sup>	0.017	0.012	0.012	0.011	0.012	0.013	0.008	0.013	0.012	0.007	0.025	0.029
Cr	0.003	0.002	0.002	0.002	0.002	0.002	0.003	0.000	0.000	0.003	0.001	0.001
Mn	0.000	0.000	0.000	0.000	0.001	0.000	0.001	0.000	0.000	0.000	0.000	0.000
Mg	0.000	0.000	0.000	0.000	0.000	0.000	0.000	0.000	0.000	0.000	0.000	0.000
Ca	0.002	0.000	0.001	0.003	0.000	0.010	0.017	0.004	0.011	0.046	0.000	0.001
Na	0.000	0.000	0.000	0.000	0.000	0.001	0.000	0.000	0.000	0.000	0.000	0.001
K	0.000	0.000	0.000	0.000	0.000	0.000	0.000	0.001	0.001	0.000	0.000	0.000
Ni	0.002	0.001	0.003	0.001	0.001	0.002	0.000	0.001	0.002	0.000	0.001	0.000
<b>Total</b>	<b>1.008</b>	<b>1.005</b>	<b>1.007</b>	<b>1.006</b>	<b>1.005</b>	<b>1.011</b>	<b>1.011</b>	<b>1.006</b>	<b>1.011</b>	<b>1.026</b>	<b>1.008</b>	<b>1.009</b>

Cation calculation based on 2 oxygens. Fe<sup>3+</sup> = Fe<sup>4+</sup>.*Table C2.8 (continued): Representative composition of titanite, further analyses in electronic appendix.*

Analysis	D1H4-2D_05	D1H4-2D_11	D1H4-2D_13	E1H3-4A_13	E1H3-4A_19	E1H3-4A_25	E1H3-4B_103	E1H3-4B_21	E1H3-4B_37	E7H2-8A_06	E7H2-8A_08	E7H2-8A_11
SiO <sub>2</sub>	30.47	30.63	30.28	30.57	30.09	30.49	30.07	30.10	30.07	29.59	30.85	30.22
TiO <sub>2</sub>	38.47	39.47	38.59	37.95	38.02	38.83	37.50	37.96	35.75	37.80	39.37	38.22
Al <sub>2</sub> O <sub>3</sub>	0.02	0.04	0.21	0.78	0.44	0.30	1.00	0.54	1.76	1.26	1.20	1.05
Fe <sub>2</sub> O <sub>3</sub>	0.06	0.02	0.01	0.00	0.04	0.00	0.05	0.09	0.20	0.00	0.05	0.07
Cr <sub>2</sub> O <sub>3</sub>	0.81	0.79	0.77	1.38	1.05	1.48	1.44	0.96	0.96	1.42	1.34	1.31
MnO	0.09	0.02	0.07	0.00	0.10	0.03	0.06	0.13	0.02	0.08	0.08	0.19
MgO	0.00	0.00	0.00	0.00	0.00	0.00	0.01	0.00	0.00	0.00	0.33	0.15
CaO	28.08	28.05	27.72	28.26	27.45	28.19	28.14	27.86	28.11	28.10	26.39	27.51
Na <sub>2</sub> O	0.01	0.05	0.04	0.02	0.00	0.03	0.02	0.01	0.02	0.00	0.02	0.04
K <sub>2</sub> O	0.00	0.00	0.00	0.01	0.06	0.00	0.00	0.00	0.01	0.00	0.00	0.00
NiO	0.02	0.02	0.00	0.01	0.00	0.00	0.00	0.02	0.00	0.00	0.00	0.00
<b>Total</b>	<b>98.03</b>	<b>99.09</b>	<b>97.68</b>	<b>98.98</b>	<b>97.26</b>	<b>99.35</b>	<b>98.28</b>	<b>97.68</b>	<b>96.90</b>	<b>98.25</b>	<b>99.64</b>	<b>98.75</b>
Si	1.015	1.009	1.011	1.009	1.010	1.004	1.001	1.007	1.012	0.986	1.005	0.999
Ti	0.964	0.978	0.970	0.942	0.960	0.962	0.939	0.955	0.905	0.948	0.965	0.950
Al	0.001	0.002	0.008	0.030	0.018	0.012	0.039	0.021	0.070	0.050	0.046	0.041
Fe <sup>3+</sup>	0.002	0.000	0.000	0.000	0.001	0.000	0.001	0.002	0.005	0.000	0.001	0.002
Cr	0.020	0.020	0.019	0.034	0.027	0.037	0.036	0.024	0.024	0.036	0.033	0.032
Mn	0.002	0.000	0.002	0.000	0.003	0.001	0.002	0.004	0.000	0.002	0.002	0.005
Mg	0.000	0.000	0.000	0.000	0.000	0.000	0.000	0.000	0.000	0.000	0.016	0.007
Ca	1.003	0.990	0.992	0.999	0.987	0.995	1.003	0.999	1.014	1.003	0.921	0.974
Na	0.001	0.003	0.002	0.001	0.000	0.002	0.001	0.001	0.002	0.000	0.001	0.003
K	0.000	0.000	0.000	0.000	0.002	0.000	0.000	0.000	0.000	0.000	0.000	0.000
Ni	0.002	0.003	0.000	0.001	0.000	0.000	0.000	0.003	0.000	0.000	0.000	0.000
<b>Total</b>	<b>3.010</b>	<b>3.005</b>	<b>3.006</b>	<b>3.018</b>	<b>3.008</b>	<b>3.011</b>	<b>3.023</b>	<b>3.016</b>	<b>3.034</b>	<b>3.024</b>	<b>2.991</b>	<b>3.014</b>

Cation calculation based on 5 oxygens. Fe<sup>3+</sup> = Fe<sup>4+</sup>.

**Table C2.8 (continued):** Composition of ilmenite (in wt%), analyses also in electronic appendix.

Analysis	Ilmenite												
	E1H3-4A_07	E1H3-4A_09	E1H3-4A_12	E1H3-4A_14	E1H3-4A_21	E1H3-4A_26	E1H3-4B_09	E1H3-4B_11	E1H3-4B_47	E1H3-4C_18	F2H2-4E_01	F2H2-4E_05	F2H2-5G_01
<b>TiO<sub>2</sub></b>	5.54	5.82	2.08	4.84	6.04	1.05	11.95	10.39	10.66	1.21	5.25	4.61	9.58
<b>Al<sub>2</sub>O<sub>3</sub></b>	0.01	0.04	0.00	0.03	0.00	0.01	0.00	0.00	0.00	0.00	0.07	0.04	0.06
<b>Cr<sub>2</sub>O<sub>3</sub></b>	0.19	0.17	0.16	0.12	0.16	0.11	0.63	0.62	0.62	0.25	1.32	1.23	1.46
<b>Fe<sub>2</sub>O<sub>3</sub></b>	85.10	84.72	88.72	86.30	93.42	89.00	86.99	72.43	63.60	98.07	93.03	93.37	87.15
<b>FeO</b>	8.51	8.47	8.87	8.63	0.00	8.90	0.00	16.29	24.53	0.00	0.00	0.00	0.00
<b>MnO</b>	0.09	0.09	0.01	0.00	0.02	0.01	0.09	0.10	0.07	0.06	0.09	0.05	0.00
<b>MgO</b>	0.02	0.01	0.00	0.02	0.01	0.00	0.00	0.04	0.01	0.00	0.00	0.02	0.02
<b>CaO</b>	0.02	0.00	0.03	0.00	0.06	0.02	0.03	0.01	0.02	0.24	0.03	0.04	0.00
<b>Total</b>	99.48	99.32	99.86	99.94	99.71	99.10	99.69	99.88	99.50	99.83	99.80	99.36	98.27
<b>Ti</b>	0.112	0.117	0.042	0.097	0.119	0.022	0.230	0.210	0.220	0.024	0.103	0.091	0.188
<b>Al</b>	0.000	0.001	0.000	0.001	0.000	0.000	0.000	0.000	0.000	0.000	0.002	0.001	0.002
<b>Cr</b>	0.004	0.004	0.003	0.003	0.003	0.002	0.013	0.013	0.014	0.005	0.027	0.026	0.030
<b>Fe<sup>3+</sup></b>	1.717	1.710	1.806	1.737	1.837	1.832	1.678	1.461	1.315	1.957	1.831	1.849	1.716
<b>Fe<sup>2+</sup></b>	0.191	0.190	0.201	0.193	0.000	0.204	0.000	0.365	0.564	0.000	0.000	0.000	0.000
<b>Mn</b>	0.002	0.002	0.000	0.000	0.000	0.000	0.002	0.002	0.002	0.001	0.002	0.001	0.000
<b>Zn</b>	0.000	0.000	0.000	0.000	0.000	0.000	0.000	0.000	0.000	0.000	0.000	0.000	0.000
<b>Mg</b>	0.001	0.000	0.000	0.001	0.000	0.000	0.000	0.001	0.000	0.000	0.000	0.001	0.001
<b>Ca</b>	0.001	0.000	0.001	0.000	0.002	0.001	0.001	0.000	0.001	0.007	0.001	0.001	0.000
<b>Total</b>	2.027	2.025	2.053	2.032	1.961	2.061	1.924	2.053	2.115	1.995	1.967	1.971	1.937

FeO, Fe<sub>2</sub>O<sub>3</sub> were calculated stoichiometrically for Ilm and Mag. Cation calculation based on 3 oxygens for Ilm, and Picotite and 4 oxygens for magnetite

**Table C2.8 (continued):** Composition of ilmenite, picotite and magnetite, analyses also in electronic appendix.

Analysis	Ilmenite		Picotite					Magnetite				
	E1H3-4C_13	E1H3-4A_80	D1H4mu d_16	E4H2-2A_05	E4H2-2A_06	D1H4mu d_69	E7H2mu d_30	E2H2-5J_03	E2H2-5J_04	E7H2mu d_80	F1H3-2C_14	
<b>TiO<sub>2</sub></b>	2.95	13.83	0.03	0.07	0.05	0.03	0.07	0.02	0.01	0.89	0.00	
<b>Al<sub>2</sub>O<sub>3</sub></b>	0.00	0.00	19.26	21.57	21.38	19.48	8.96	0.01	0.00	0.17	0.02	
<b>Cr<sub>2</sub>O<sub>3</sub></b>	0.18	0.15	50.56	43.82	44.39	47.77	59.40	3.12	2.95	0.14	0.18	
<b>Fe<sub>2</sub>O<sub>3</sub></b>	87.27	70.05	13.04	21.37	20.34	20.24	19.72	65.49	65.35	61.18	67.79	
<b>FeO</b>	8.73	15.76	5.03	0.00	0.00	0.00	1.97	30.89	30.82	28.85	29.38	
<b>MnO</b>	0.01	0.00	0.17	0.13	0.05	0.10	0.11	0.05	0.00	0.04	0.06	
<b>MgO</b>	0.01	0.01	11.91	11.52	11.64	11.35	9.63	0.02	0.00	0.18	0.59	
<b>CaO</b>	0.50	0.03	0.00	0.48	0.57	0.02	0.01	0.01	0.00	0.08	0.08	
<b>Total</b>	99.65	99.82	99.99	98.95	98.42	98.98	99.85	99.60	99.14	91.52	98.10	
<b>Ti</b>	0.060	0.275	0.001	0.001	0.001	0.000	0.001	0.000	0.000	0.028	0.000	
<b>Al</b>	0.000	0.000	0.520	0.577	0.575	0.526	0.254	0.000	0.000	0.009	0.001	
<b>Cr</b>	0.004	0.003	0.916	0.787	0.801	0.865	1.129	0.095	0.091	0.005	0.005	
<b>Fe<sup>3+</sup></b>	1.775	1.396	0.225	0.365	0.349	0.349	0.357	1.903	1.909	1.931	1.993	
<b>Fe<sup>2+</sup></b>	0.197	0.349	0.096	0.000	0.000	0.000	0.040	0.998	1.000	1.012	0.960	
<b>Mn</b>	0.000	0.000	0.003	0.002	0.001	0.002	0.002	0.002	0.000	0.001	0.002	
<b>Zn</b>	0.000	0.000	0.000	0.000	0.000	0.000	0.000	0.000	0.000	0.000	0.000	
<b>Mg</b>	0.000	0.000	0.407	0.390	0.396	0.387	0.345	0.001	0.000	0.011	0.034	
<b>Ca</b>	0.014	0.001	0.000	0.012	0.014	0.000	0.000	0.000	0.000	0.003	0.003	
<b>Total</b>	2.051	2.025	2.169	2.134	2.137	2.130	2.129	3.000	3.000	3.000	3.000	

FeO, Fe<sub>2</sub>O<sub>3</sub> were calculated stoichiometrically for Ilm and Mag. Cation calculation based on 3 oxygens for Ilm, and Picotite and 4 oxygens for magnetite

## C2.9: Apatite and zircon

*Table C2.9: Representative composition of apatite (in wt%), further analyses in electronic appendix.*

Analysis	D1H4- 2D_37	D1H4- 2D_39	D1H4- 2D_43	E1H3- 3D_14	E1H3- 3D_18	E1H3- 3D_32	E2H2-4B 01	E2H2-4B 30	E2H2-5D 10	E2H2-5D 11	F2H2-4E 08	F2H2-4E 09	F2H2-4H 25
SiO <sub>2</sub>	0.05	0.23	0.21	11.44	4.91	0.28	0.33	0.50	0.03	0.02	0.10	0.16	0.20
TiO <sub>2</sub>	0.57	0.01	0.04	0.05	0.06	0.02	0.03	0.01	0.01	0.00	0.02	0.01	0.01
Al <sub>2</sub> O <sub>3</sub>	0.00	0.03	0.04	2.67	1.12	0.02	0.01	0.05	0.00	0.02	0.00	0.00	0.01
Cr <sub>2</sub> O <sub>3</sub>	0.04	0.04	0.06	0.95	0.36	0.06	0.04	0.00	0.03	0.01	0.04	0.03	0.00
FeO	0.29	0.22	0.18	3.26	1.27	0.93	0.78	0.95	0.06	0.11	0.35	0.30	0.46
MnO	0.03	0.00	0.01	0.05	0.15	0.04	0.09	0.09	0.13	0.00	0.17	0.25	0.05
MgO	0.00	0.00	0.05	3.11	1.14	0.40	0.20	0.25	0.00	0.00	0.03	0.01	0.02
CaO	52.25	53.98	54.14	40.15	48.34	52.32	53.90	53.06	55.06	55.06	54.57	54.88	55.00
Na <sub>2</sub> O	0.00	0.00	0.02	0.40	0.19	0.22	0.05	0.08	0.05	0.01	0.06	0.08	0.04
K <sub>2</sub> O	0.01	0.00	0.00	0.17	0.07	0.03	0.01	0.00	0.01	0.00	0.00	0.00	0.02
NiO	0.06	0.10	0.04	0.00	0.00	0.04	0.03	0.00	0.04	0.00	0.07	0.05	0.01
<b>Total</b>	<b>53.29</b>	<b>54.60</b>	<b>54.79</b>	<b>62.25</b>	<b>57.62</b>	<b>54.35</b>	<b>55.46</b>	<b>54.97</b>	<b>55.41</b>	<b>55.22</b>	<b>55.41</b>	<b>55.76</b>	<b>55.82</b>
Si	0.012	0.052	0.045	1.866	0.950	0.063	0.073	0.109	0.007	0.004	0.023	0.034	0.044
Ti	0.096	0.001	0.007	0.006	0.009	0.003	0.005	0.001	0.001	0.000	0.002	0.001	0.001
Al	0.001	0.007	0.010	0.514	0.255	0.004	0.003	0.012	0.000	0.004	0.001	0.000	0.003
Fe <sup>3+</sup>	0.007	0.006	0.010	0.122	0.055	0.011	0.007	0.001	0.005	0.001	0.008	0.006	0.000
Cr	0.055	0.040	0.033	0.444	0.206	0.173	0.142	0.174	0.011	0.020	0.064	0.055	0.084
Mn	0.005	0.000	0.002	0.007	0.024	0.007	0.016	0.017	0.025	0.000	0.031	0.046	0.009
Mg	0.000	0.000	0.017	0.755	0.330	0.133	0.064	0.081	0.000	0.000	0.009	0.003	0.006
Ca	12.686	12.796	12.794	7.016	10.013	12.466	12.586	12.472	12.916	12.963	12.794	12.782	12.792
Na	0.000	0.000	0.009	0.127	0.073	0.097	0.020	0.033	0.020	0.003	0.026	0.032	0.015
K	0.004	0.001	0.001	0.035	0.017	0.008	0.002	0.000	0.003	0.000	0.000	0.000	0.006
Ni	0.049	0.077	0.029	0.000	0.000	0.031	0.023	0.000	0.030	0.000	0.055	0.040	0.010
<b>Total</b>	<b>12.915</b>	<b>12.980</b>	<b>12.957</b>	<b>10.892</b>	<b>11.931</b>	<b>12.994</b>	<b>12.940</b>	<b>12.900</b>	<b>13.016</b>	<b>12.995</b>	<b>13.011</b>	<b>12.998</b>	<b>12.969</b>

Cation calculation based on 13 oxygens. P<sub>2</sub>O<sub>5</sub> was not analyzed.

*Table C2.9 (continued): Composition of zircon (in wt%), analyses also in electronic appendix.*

Analysis	D1H4- 2D_31	D1H4- 2D_38	E1H3- 4B_16	E1H3- 4B_17	F2H2-4G 01	F2H2-1A 62	F2H2-1A 63	F2H2-1A 83	F2H2-4A 11
SiO <sub>2</sub>	37.62	37.82	37.65	36.79	35.35	37.60	38.97	38.47	37.57
TiO <sub>2</sub>	0.22	0.03	0.01	0.00	0.02	0.00	0.01	0.01	0.01
Al <sub>2</sub> O <sub>3</sub>	0.48	0.70	0.52	0.00	0.02	0.19	0.32	0.39	0.99
Cr <sub>2</sub> O <sub>3</sub>	0.01	0.02	0.05	0.00	0.00	0.04	0.02	0.03	0.00
FeO	0.90	1.61	1.53	0.65	0.57	1.14	1.49	1.52	1.19
MnO	0.03	0.00	0.00	0.00	0.00	0.01	0.13	0.12	0.00
MgO	1.25	3.23	0.57	0.01	0.05	0.23	0.90	1.01	0.53
CaO	1.47	3.14	0.65	0.06	0.32	0.28	0.96	0.51	0.08
Na <sub>2</sub> O	0.00	0.04	0.00	0.00	0.00	0.00	0.00	0.09	0.00
K <sub>2</sub> O	0.00	0.00	0.03	0.01	0.00	0.00	0.01	0.02	1.49
NiO	0.00	0.01	0.00	0.06	0.03	0.00	0.00	0.01	0.01
<b>Total</b>	<b>41.97</b>	<b>46.60</b>	<b>41.02</b>	<b>37.58</b>	<b>36.34</b>	<b>39.49</b>	<b>42.81</b>	<b>42.17</b>	<b>41.86</b>
Si	1.866	1.749	1.903	1.980	1.972	1.949	1.895	1.895	1.885
Ti	0.008	0.001	0.000	0.000	0.001	0.000	0.000	0.000	0.000
Al	0.028	0.038	0.031	0.000	0.001	0.011	0.018	0.023	0.058
Fe <sup>3+</sup>	0.000	0.001	0.002	0.000	0.000	0.002	0.001	0.001	0.000
Cr	0.037	0.062	0.065	0.029	0.026	0.049	0.061	0.063	0.050
Mn	0.001	0.000	0.000	0.000	0.000	0.000	0.005	0.005	0.000
Mg	0.092	0.223	0.043	0.001	0.004	0.018	0.065	0.074	0.040
Ca	0.078	0.155	0.035	0.004	0.019	0.016	0.050	0.027	0.004
Na	0.000	0.004	0.000	0.000	0.000	0.000	0.000	0.008	0.000
K	0.000	0.000	0.002	0.000	0.000	0.000	0.001	0.001	0.095
Ni	0.000	0.002	0.000	0.011	0.005	0.000	0.000	0.001	0.001
<b>Total</b>	<b>2.112</b>	<b>2.234</b>	<b>2.081</b>	<b>2.025</b>	<b>2.029</b>	<b>2.045</b>	<b>2.096</b>	<b>2.098</b>	<b>2.134</b>

Cation calculation based on 4oxygens. ZrO was not analyzed.

## C2.10: Serpentine (antigorite)

*Table C2.10: Composition of serpentine (in wt%), analyses also in electronic appendix.*

Analysis	E4H2-2A 01	E4H2-2A 02	E4H2-2A 09	E4H2-2A 10	E2H2-4G 05	E2H2-4G 06	E2H2-4G 07	E2H2-4G 08	E2H2-4G 09	E2H2-4G 10	E2H2-4G 11	E2H2-4G 12	E2H2-5H 08	E2H2-5H 10	E2H2-5H 11
<b>SiO<sub>2</sub></b>	38.69	38.56	35.54	36.63	43.78	43.25	41.24	42.39	40.01	43.43	38.67	41.51	41.75	41.45	40.67
<b>TiO<sub>2</sub></b>	0.02	0.01	0.02	0.03	0.00	0.02	0.00	0.02	0.00	0.00	0.00	0.01	0.00	0.02	0.00
<b>Al<sub>2</sub>O<sub>3</sub></b>	0.62	0.56	0.98	0.60	0.44	0.49	0.17	0.14	0.18	0.15	0.19	0.44	0.12	0.15	0.16
<b>Cr<sub>2</sub>O<sub>3</sub></b>	0.82	0.89	0.94	0.87	0.01	0.00	0.01	0.00	0.02	0.02	0.00	0.00	0.00	0.01	0.00
<b>FeO</b>	5.54	5.37	5.48	4.62	5.85	5.83	4.52	3.75	4.57	4.01	4.68	5.77	3.57	3.34	3.68
<b>MnO</b>	0.05	0.08	0.19	0.10	0.12	0.05	0.07	0.16	0.05	0.07	0.03	0.06	0.09	0.11	0.10
<b>MgO</b>	37.71	37.11	35.06	35.01	37.14	37.14	36.97	36.66	37.06	40.05	35.02	36.72	38.67	37.79	39.37
<b>CaO</b>	0.25	0.20	0.08	0.04	0.11	0.08	0.07	0.05	0.06	0.09	0.11	0.08	0.22	0.14	0.17
<b>Na<sub>2</sub>O</b>	0.06	0.07	0.09	0.09	0.07	0.06	0.01	0.06	0.06	0.03	0.09	0.06	0.15	0.17	0.19
<b>K<sub>2</sub>O</b>	0.02	0.01	0.00	0.02	0.00	0.01	0.00	0.00	0.02	0.01	0.02	0.03	0.01	0.02	0.00
<b>NiO</b>	0.24	0.28	0.41	0.50	0.00	0.04	0.02	0.05	0.00	0.03	0.03	0.04	0.04	0.04	0.02
<b>Total</b>	84.01	83.14	78.78	78.50	87.52	86.98	83.07	83.27	82.02	87.87	78.82	84.71	84.61	83.24	84.36
<b>Si</b>	3.290	3.309	3.234	3.316	3.528	3.509	3.489	3.553	3.439	3.464	3.461	3.468	3.458	3.483	3.392
<b>Ti</b>	0.001	0.001	0.001	0.002	0.000	0.001	0.000	0.001	0.000	0.000	0.000	0.000	0.000	0.001	0.000
<b>Al</b>	0.062	0.057	0.106	0.064	0.042	0.047	0.017	0.014	0.018	0.014	0.020	0.043	0.012	0.015	0.015
<b>Cr</b>	0.055	0.061	0.067	0.062	0.000	0.000	0.001	0.000	0.001	0.001	0.000	0.000	0.000	0.000	0.000
<b>Fe</b>	0.394	0.386	0.417	0.350	0.394	0.396	0.320	0.263	0.329	0.267	0.350	0.403	0.247	0.234	0.256
<b>Mn</b>	0.003	0.006	0.014	0.008	0.008	0.004	0.005	0.011	0.003	0.005	0.002	0.004	0.006	0.008	0.007
<b>Mg</b>	4.779	4.746	4.756	4.724	4.462	4.491	4.662	4.581	4.750	4.763	4.672	4.573	4.775	4.733	4.895
<b>Ca</b>	0.022	0.019	0.008	0.004	0.009	0.007	0.006	0.004	0.005	0.007	0.010	0.007	0.020	0.013	0.015
<b>Na</b>	0.010	0.011	0.016	0.016	0.010	0.010	0.001	0.009	0.010	0.005	0.015	0.010	0.024	0.028	0.031
<b>K</b>	0.002	0.001	0.000	0.002	0.000	0.001	0.000	0.000	0.002	0.001	0.002	0.003	0.001	0.002	0.000
<b>Ni</b>	0.075	0.087	0.133	0.164	0.000	0.011	0.006	0.016	0.000	0.008	0.008	0.011	0.011	0.013	0.007
<b>Total</b>	8.694	8.681	8.752	8.711	8.455	8.477	8.506	8.452	8.557	8.535	8.541	8.522	8.554	8.530	8.619
<b>Mg#</b>	92.33	92.39	91.69	92.97	91.73	91.83	93.50	94.35	93.46	94.60	92.98	91.81	94.96	95.13	94.90

Cation calculation based on 12 oxygens.

## C3: SIMS data

Table C3: Li, Be, B, Sr contents and  $\delta^{11}\text{B}$  values of metabasite minerals, analyzed by SIMS.

Analysis	Mineral	Li ( $\mu\text{g/g}$ )	$2\sigma_{\text{mean}}$	Be ( $\mu\text{g/g}$ )	$2\sigma_{\text{mean}}$	B ( $\mu\text{g/g}$ )	$2\sigma_{\text{mean}}$	Sr ( $\mu\text{g/g}$ )	$2\sigma_{\text{mean}}$	Analysis	$I_p$ (nA)	n	$^{11}\text{B}/^{10}\text{B}$ measured	$\alpha_{\text{inst}}$	$^{11}\text{B}/^{10}\text{B}$ corrected	$\delta^{11}\text{B}$ (‰)	$2\sigma_{\text{mean}}$
D1H4-1A-1	Am	2.86	3.9%	0.594	8.7%	3.60	6.0%	2.54	14.9%	-	-	400	-	-	-	-	-
D1H4-1A-10	Am	0.97	4.5%	0.617	4.5%	3.17	3.4%	4.83	9.6%	D1H4-1A-10	10	400	3.862	1.045	4.037	1.34	1.20%
D1H4-1A-11	Am	5.34	2.4%	0.783	10.3%	2.56	3.6%	1.80	14.0%	-	-	-	-	-	-	-	-
D1H4-1A-12	Am	6.67	1.9%	0.708	3.7%	1.94	8.7%	5.31	8.7%	-	-	-	-	-	-	-	-
D1H4-1A-13	Am	1.43	20.2%	0.473	8.6%	1.94	8.5%	5.31	13.8%	D1H4-1A-13	10	400	3.826	1.045	3.999	-8.09	1.03%
D1H4-1A-14	Am	1.87	8.9%	0.393	11.4%	2.78	4.4%	5.29	10.6%	-	-	-	-	-	-	-	-
D1H4-1A-15	Am	1.93	3.3%	0.828	6.4%	2.67	5.4%	4.38	6.5%	-	-	-	-	-	-	-	-
D1H4-1A-16	Am	2.52	4.0%	0.893	7.5%	11.18	2.5%	4.70	12.8%	D1H4-1A-16 <sup>a</sup>	10	400	3.851	1.045	4.025	-1.58	1.01%
D1H4-1A-17	Am	0.31	10.5%	0.281	13.2%	2.23	3.2%	20.55	4.6%	-	-	-	-	-	-	-	-
D1H4-1A-18	Am	2.94	4.3%	0.653	7.9%	6.38	5.7%	4.52	13.4%	D1H4-1A-18	10	400	3.920	1.045	4.097	16.28	1.28%
D1H4-1A-19	Am	1.04	7.7%	0.510	9.8%	3.36	4.6%	3.24	11.6%	-	-	-	-	-	-	-	-
D1H4-1A-2	Am	1.13	7.5%	0.584	10.7%	3.25	3.5%	5.00	3.5%	-	-	-	-	-	-	-	-
D1H4-1A-20	Am	3.57	3.7%	1.053	7.7%	8.64	3.9%	3.69	9.0%	-	-	-	-	-	-	-	-
D1H4-1A-21	Am	8.09	3.1%	0.925	4.7%	2.44	4.5%	0.51	20.9%	-	-	-	-	-	-	-	-
D1H4-1A-22	Chl	26.87	1.4%	0.083	22.8%	0.28	13.4%	0.49	30.2%	-	-	-	-	-	-	-	-
D1H4-1A-23	Am	0.87	6.3%	0.738	6.6%	9.59	2.5%	7.88	6.8%	-	-	-	-	-	-	-	-
D1H4-1A-24	Am	4.11	3.3%	1.094	7.1%	12.98	2.8%	3.54	15.9%	-	-	-	-	-	-	-	-
D1H4-1A-25	Chl	32.65	1.4%	0.105	13.5%	1.10	8.7%	2.00	24.5%	-	-	-	-	-	-	-	-
D1H4-1A-26	Am	3.19	5.3%	0.720	7.3%	3.54	3.3%	2.37	14.8%	D1H4-1A-26	10	400	3.859	1.045	4.034	0.63	0.96%
D1H4-1A-3	Am	30.68	1.6%	0.088	12.9%	0.46	8.3%	0.30	47.8%	D1H4-1A-3	10	400	3.866	1.045	4.041	2.24	0.96%
D1H4-1A-4	Chl	38.07	0.9%	0.112	21.6%	0.87	19.3%	0.87	18.3%	-	-	-	-	-	-	-	-
D1H4-1A-5	Am	1.68	5.1%	0.604	6.6%	3.04	3.2%	4.82	10.8%	D1H4-1A-5 <sup>a</sup>	10	400	3.865	1.045	4.040	2.11	0.53%
D1H4-1A-7	Am	5.79	2.3%	0.692	5.8%	2.97	4.9%	2.37	11.0%	-	-	-	-	-	-	-	-
D1H4-1A-8	Am	6.28	1.8%	0.872	2.7%	2.46	3.1%	1.45	18.4%	-	-	-	-	-	-	-	-
D1H4-1A-9	Am	0.82	6.5%	0.505	9.1%	1.68	5.4%	8.46	7.8%	-	-	-	-	-	-	-	-
D1H4-1A-x	Am	-	-	-	-	-	-	-	-	D1H4-1A-x	10	400	3.874	1.045	4.049	4.33	0.50%
D1H4-2D-1	Am	0.17	30.0%	3.535	17.4%	4.65	7.0%	8.82	13.4%	D1H4-2D-1	10	400	3.881	1.045	4.002	-7.29	0.92%
D1H4-2D-10	Chl	11.59	1.5%	0.030	47.5%	2.63	5.5%	0.57	41.4%	-	-	-	-	-	-	-	-
D1H4-2D-11	Am	0.08	16.2%	2.817	8.6%	6.45	3.9%	8.13	5.3%	D1H4-2D-11	10	400	3.832	1.045	4.003	-7.04	0.74%
D1H4-2D-12	Chl	25.94	1.4%	0.071	35.4%	7.92	5.3%	31.17	4.2%	-	-	-	-	-	-	-	-
D1H4-2D-13	Am	0.13	15.7%	6.632	4.7%	10.99	2.9%	8.30	8.5%	D1H4-2D-13	10	400	3.886	1.045	4.007	-5.94	0.82%
D1H4-2D-14	Ttn	0.47	8.6%	0.054	26.5%	0.59	13.4%	129.19	1.6%	-	-	-	-	-	-	-	-
D1H4-2D-15	Am	0.09	18.6%	2.038	25.2%	4.74	4.5%	9.17	11.6%	D1H4-2D-15	10	400	3.857	1.045	4.029	-0.59	0.88%
D1H4-2D-2	Am	0.31	11.5%	4.494	3.6%	6.18	5.4%	9.84	7.2%	-	-	-	-	-	-	-	-
D1H4-2D-3	Chl	6.82	2.5%	0.025	40.2%	1.06	14.0%	0.41	48.5%	-	-	-	-	-	-	-	-
D1H4-2D-4	Chl	6.89	9.1%	0.013	91.3%	0.81	13.5%	0.35	55.4%	-	-	-	-	-	-	-	-
D1H4-2D-5	Am	0.10	28.8%	2.034	6.2%	7.73	3.9%	8.95	11.0%	D1H4-2D-5	10	400	3.851	1.045	4.023	-2.01	0.80%
D1H4-2D-6	Am	0.09	20.2%	1.361	5.6%	9.95	3.6%	6.71	15.8%	-	-	-	-	-	-	-	-
D1H4-2D-7	Chl	13.25	4.2%	0.589	9.9%	6.61	3.4%	3.43	15.9%	-	-	-	-	-	-	-	-
D1H4-2D-8	Am	0.16	15.4%	1.445	7.0%	3.53	5.3%	8.08	7.7%	D1H4-2D-8	10	400	3.846	1.045	4.018	-3.38	0.84%
D1H4-2D-9	Am	0.07	29.2%	6.004	5.4%	23.32	3.2%	11.14	7.9%	D1H4-2D-9	10	400	3.832	1.045	4.003	-7.02	0.70%

<sup>a</sup> = matrix corrected

Table C3 (continued): Li, Be, B, Sr contents and  $\delta^{11}\text{B}$  values of metabasite minerals, analyzed by SIMS.

Analysis	Mineral	Li ( $\mu\text{g/g}$ )	$2\sigma_{\text{mean}}$	Be ( $\mu\text{g/g}$ )	$2\sigma_{\text{mean}}$	B ( $\mu\text{g/g}$ )	$2\sigma_{\text{mean}}$	Sr ( $\mu\text{g/g}$ )	$2\sigma_{\text{mean}}$	Analysis	$I_p$ (nA)	n	$^{11}\text{B}/^{10}\text{B}$ measured	$\alpha_{\text{inst}}$	$^{11}\text{B}/^{10}\text{B}$ corrected	$\delta^{11}\text{B}$ (‰) <sup>f</sup>	$2\sigma_{\text{mean}}$
EIH3-3D-1	Am	2.47	17.2%	1.414	7.5%	4.27	7.0%	9.84	7.8%	-	-	400	3.842	1.045	4.014	-4.41	0.44%
EIH3-3D-10	Am	1.31	6.7%	1.049	6.5%	0.14	39.2%	877.98	0.7%	-	-	10	3.842	1.045	4.014	-4.41	0.44%
EIH3-3D-11	Chl	25.17	5.3%	0.377	15.3%	9.54	3.8%	9.28	9.7%	-	-	10	3.842	1.045	4.014	-4.41	0.44%
EIH3-3D-12	Chl	18.52	1.1%	0.205	16.3%	11.64	3.9%	9.62	8.3%	EIH3-3D-12	10	400	3.842	1.045	4.014	-4.41	0.44%
EIH3-3D-13	Am	1.84	8.2%	1.156	7.5%	0.45	29.8%	899.69	3.6%	-	-	400	3.842	1.045	4.014	-4.41	0.44%
EIH3-3D-14	Am	1.62	4.7%	1.123	8.1%	0.09	19.7%	776.50	1.1%	-	-	400	3.842	1.045	4.014	-4.41	0.44%
EIH3-3D-2	Am	2.32	4.3%	1.542	7.1%	3.54	6.7%	12.79	8.5%	-	-	400	3.842	1.045	4.014	-4.41	0.44%
EIH3-3D-3	Am	1.50	6.3%	1.083	5.6%	0.22	22.6%	888.55	1.0%	-	-	400	3.842	1.045	4.014	-4.41	0.44%
EIH3-3D-4	Am	1.56	5.8%	0.943	6.9%	0.11	29.9%	954.61	1.5%	-	-	400	3.842	1.045	4.014	-4.41	0.44%
EIH3-3D-5	Am	0.54	12.4%	5.080	4.2%	7.92	11.0%	12.77	11.5%	-	-	400	3.842	1.045	4.014	-4.41	0.44%
EIH3-3D-6	Am	1.52	7.8%	0.790	8.6%	0.09	41.4%	1018.32	1.6%	-	-	400	3.842	1.045	4.014	-4.41	0.44%
EIH3-3D-7	Chl	23.88	4.1%	0.374	12.3%	13.16	2.3%	12.57	6.7%	-	-	400	3.842	1.045	4.014	-4.41	0.44%
EIH3-3D-8	Am	1.85	6.0%	1.352	7.4%	0.48	16.0%	904.59	1.5%	EIH3-3D-8	10	400	3.904	1.045	4.078	11.55	1.37%
EIH3-3D-9	Chl	21.62	3.3%	0.265	14.8%	11.59	3.0%	12.94	4.9%	EIH3-3D-9	10	400	3.844	1.045	4.016	-3.86	0.47%
EIH3-4A-1	Am	13.71	2.3%	0.700	10.0%	5.75	3.1%	2.20	21.0%	EIH3-4A-1	20	200	3.831	1.048	4.015	-3.99	0.65%
EIH3-4A-10	Am	2.54	2.6%	1.472	6.2%	9.17	3.8%	6.86	10.8%	-	-	200	3.831	1.048	4.015	-3.99	0.65%
EIH3-4A-11	Chl	49.95	1.2%	0.107	24.1%	0.86	12.6%	5.30	11.7%	-	-	20	3.811	1.048	3.994	-9.17	0.52%
EIH3-4A-12	Phe	62.16	4.4%	1.702	8.9%	40.89	0.7%	29.86	10.5%	EIH3-4A-12	20	400	3.816	1.048	4.000	-7.77	0.14%
EIH3-4A-13	Phe	76.85	0.8%	2.002	5.8%	37.91	1.6%	41.29	4.6%	EIH3-4A-13	20	400	3.825	1.048	4.010	-5.43	0.15%
EIH3-4A-14	Am	12.90	5.2%	0.457	7.9%	3.32	6.4%	1.10	22.2%	EIH3-4A-14	20	400	3.813	1.048	3.997	-8.45	0.49%
EIH3-4A-2	Am	1.95	4.6%	0.736	9.7%	7.39	3.9%	6.43	7.9%	EIH3-4A-2	20	200	3.841	1.048	4.026	-1.36	0.61%
EIH3-4A-3	Am	15.89	8.4%	0.439	29.6%	2.50	7.8%	4.51	26.5%	EIH3-4A-3	20	400	3.811	1.048	3.994	-9.17	0.52%
EIH3-4A-4	Chl	72.33	1.2%	0.261	17.9%	1.30	8.6%	5.85	15.8%	-	-	20	3.811	1.048	3.994	-9.17	0.52%
EIH3-4A-5	Chl	54.73	1.3%	0.089	30.0%	1.68	12.6%	1.59	16.0%	-	-	20	3.811	1.048	3.994	-9.17	0.52%
EIH3-4A-6	Phe	73.88	1.1%	2.044	6.3%	32.52	1.4%	38.34	2.8%	-	-	20	3.811	1.048	3.994	-9.17	0.52%
EIH3-4A-7	Phe	66.82	1.6%	1.837	4.6%	41.52	2.2%	50.08	4.7%	EIH3-4A-7	20	400	3.824	1.048	4.008	-5.72	0.14%
EIH3-4A-8	Am	5.10	3.4%	0.641	10.9%	4.79	5.9%	5.18	17.2%	-	-	400	3.824	1.048	4.008	-5.72	0.14%
EIH3-4A-9	Chl	33.38	1.1%	0.238	15.5%	12.75	3.5%	7.03	10.1%	-	-	400	3.824	1.048	4.008	-5.72	0.14%
EIH3-4B-1	Am	8.34	3.5%	3.262	5.8%	4.37	6.3%	37.02	3.5%	EIH3-4B-1	20	400	3.813	1.048	3.997	-8.59	0.45%
EIH3-4B-11	Ep	0.01	56.6%	0.017	73.6%	0.48	18.7%	641.75	4.2%	-	-	20	3.813	1.048	3.997	-8.59	0.45%
EIH3-4B-12	Chl	87.20	1.0%	0.140	21.3%	0.58	17.6%	0.41	37.4%	-	-	20	3.813	1.048	3.997	-8.59	0.45%
EIH3-4B-13	Am	9.02	1.9%	4.163	4.0%	5.11	4.0%	48.22	3.6%	-	-	400	3.813	1.048	3.997	-8.59	0.45%
EIH3-4B-14	Phe	83.78	3.0%	2.882	3.2%	36.98	1.8%	1.53	20.8%	EIH3-4B-14	20	400	3.821	1.048	4.005	-6.54	0.18%
EIH3-4B-15	Aln	0.41	11.2%	0.208	18.5%	2.87	6.5%	1354.40	1.0%	-	-	400	3.821	1.048	4.005	-6.54	0.18%
EIH3-4B-16	Ep	0.13	23.8%	0.161	21.8%	2.55	7.2%	1391.56	2.6%	EIH3-4B-16	20	400	3.848	1.048	4.034	-2.45	0.92%
EIH3-4B-17	Chl	80.49	3.3%	0.057	29.3%	2.29	11.6%	1.50	17.3%	-	-	400	3.848	1.048	4.034	-2.45	0.92%
EIH3-4B-18	Am	7.37	1.9%	3.027	2.8%	3.91	6.4%	33.88	6.4%	EIH3-4B-17	20	400	3.812	1.048	3.996	-8.71	0.52%
EIH3-4B-19	Chl	99.59	1.1%	0.120	16.2%	7.00	14.5%	0.66	30.5%	EIH3-4B-12	20	400	3.821	1.048	4.006	-6.37	0.99%
EIH3-4B-2	Chl	8.54	3.4%	3.562	3.2%	4.73	5.6%	34.62	5.8%	EIH3-4B-3	20	400	3.819	1.048	4.003	-7.00	0.45%
EIH3-4B-3	Am	0.04	39.4%	0.036	47.0%	0.77	15.6%	1499.67	1.8%	-	-	400	3.819	1.048	4.003	-7.00	0.45%
EIH3-4B-4	Ep	0.04	39.4%	0.036	47.0%	0.77	15.6%	1499.67	1.8%	-	-	400	3.819	1.048	4.003	-7.00	0.45%
EIH3-4B-5	Am	8.40	2.4%	3.682	4.0%	4.78	5.2%	40.27	6.2%	-	-	400	3.819	1.048	4.003	-7.00	0.45%

\* = matrix corrected

Table C3 (continued): Li, Be, B, Sr contents and  $\delta^{11}\text{B}$  values of metabasite minerals, analyzed by SIMS.

Analysis	Mineral	Li ( $\mu\text{g/g}$ )	$2\sigma_{\text{mean}}$	Be ( $\mu\text{g/g}$ )	$2\sigma_{\text{mean}}$	B ( $\mu\text{g/g}$ )	$2\sigma_{\text{mean}}$	Sr ( $\mu\text{g/g}$ )	$2\sigma_{\text{mean}}$	Analysis	$I_P$ (nA)	n	$^{11}\text{B}/^{10}\text{B}$ measured	$\alpha_{\text{inst}}$	$^{11}\text{B}/^{10}\text{B}$ corrected	$\delta^{11}\text{B}$ (‰) <sup>#</sup>	$2\sigma_{\text{mean}}$
E1H3-4B-6	Am	9.41	1.9%	4.063	3.6%	3.18	7.8%	40.88	5.7%	E1H3-4B-6	20	400	3.813	1.048	3.996	-8.66	0.50%
E1H3-4B-7	Chl	29.93	1.0%	0.100	19.0%	7.01	2.8%	15.70	5.6%	E1H3-4B-8	20	400	3.843	1.048	4.029	-0.66	0.33%
E1H3-4B-8	Chl	9.24	2.3%	6.837	3.3%	12.71	2.1%	6.70	10.9%	-	-	-	-	-	-	-	-
E1H3-4B-9	Chl	31.67	1.6%	0.106	25.0%	6.58	6.7%	6.56	11.5%	-	-	-	-	-	-	-	-
E1H3-4C-1	Ep	0.02	56.8%	0.153	20.4%	1.59	17.0%	371.38	1.3%	-	-	-	-	-	-	-	-
E1H3-4C-2	Chl	35.91	1.3%	0.081	17.5%	0.83	10.4%	9.53	3.9%	-	-	-	-	-	-	-	-
E1H3-4C-3	Grt	4.38	3.4%	0.005	96.6%	0.06	43.2%	0.12	51.6%	-	-	-	-	-	-	-	-
E1H3-4C-4	Chl	37.26	0.9%	0.517	11.2%	0.42	20.7%	2.73	20.7%	-	-	-	-	-	-	-	-
E1H3-4D-01	Phe	79.69	0.8%	1.722	6.4%	30.16	3.2%	6.70	8.9%	-	-	-	-	-	-	-	-
E1H3-4D-10	Am	19.51	0.8%	1.216	6.8%	3.24	6.1%	8.64	11.2%	-	-	-	-	-	-	-	-
E1H3-4D-11	Phe	82.82	2.7%	1.438	4.9%	43.37	1.5%	11.70	8.7%	-	-	-	-	-	-	-	-
E1H3-4D-12	Chl	65.21	1.0%	0.156	18.1%	0.84	10.7%	1.43	28.3%	-	-	-	-	-	-	-	-
E1H3-4D-13	Am	3.92	4.4%	1.364	8.5%	2.28	8.9%	11.93	6.9%	-	-	-	-	-	-	-	-
E1H3-4D-14	Am	17.32	2.1%	1.909	4.7%	3.31	8.1%	10.76	9.0%	E1H3-4D-14	20	400	3.817	1.048	4.001	-7.55	0.65%
E1H3-4D-15	Am	12.04	2.0%	0.163	7.2%	2.07	5.4%	0.84	28.7%	E1H3-4D-15	20	400	3.796	1.048	3.980	-12.83	0.19%
E1H3-4D-16	Am	18.61	2.1%	1.376	6.6%	3.49	6.6%	10.01	11.9%	E1H3-4D-16	20	400	3.819	1.048	4.003	-7.04	0.56%
E1H3-4D-17	Am	19.60	1.3%	1.744	5.3%	3.31	6.5%	11.22	7.5%	-	-	-	-	-	-	-	-
E1H3-4D-18	Chl	73.39	1.0%	0.145	27.9%	0.39	16.7%	0.95	33.1%	E1H3-4D-18*	20	400	3.817	1.048	4.001	-7.62	0.14%
E1H3-4D-19	Phe	77.44	3.5%	1.861	4.4%	43.52	1.9%	4.03	10.9%	-	-	-	-	-	-	-	-
E1H3-4D-2	Phe	97.19	0.5%	1.961	5.8%	41.27	1.6%	12.94	7.0%	E1H3-4D-2	20	200	3.819	1.048	4.003	-6.98	0.25%
E1H3-4D-20	Chl	65.12	1.3%	0.152	14.9%	1.47	8.6%	1.75	21.4%	-	-	-	-	-	-	-	-
E1H3-4D-21	Am	14.76	1.8%	1.498	7.2%	2.98	6.5%	10.22	5.8%	-	-	-	-	-	-	-	-
E1H3-4D-22	Chl	5.88	11.6%	1.016	5.0%	3.01	4.5%	7.32	7.7%	-	-	-	-	-	-	-	-
E1H3-4D-23	Phe	94.19	1.5%	1.047	7.1%	35.65	1.4%	30.49	5.1%	E1H3-4D-23	20	400	3.823	1.048	4.007	-6.01	0.15%
E1H3-4D-24	Phe	96.79	1.1%	1.007	7.6%	36.99	1.4%	31.91	3.5%	E1H3-4D-24	20	400	3.817	1.048	4.002	-7.40	0.15%
E1H3-4D-25	Chl	79.86	1.1%	0.152	26.0%	0.35	11.6%	1.08	31.2%	-	-	-	-	-	-	-	-
E1H3-4D-26	Am	17.11	1.7%	1.871	7.1%	3.36	5.3%	10.49	9.8%	E1H3-4D-26	20	400	3.811	1.048	3.995	-9.02	0.60%
E1H3-4D-27	Am	1.80	5.5%	0.852	7.6%	1.94	12.5%	11.28	6.8%	-	-	-	-	-	-	-	-
E1H3-4D-28	Chl	76.76	0.7%	0.146	17.7%	0.41	14.2%	1.16	39.3%	-	-	-	-	-	-	-	-
E1H3-4D-29	Phe	105.35	0.5%	1.776	4.1%	29.31	2.1%	12.95	7.9%	E1H3-4D-29	20	400	3.829	1.048	4.014	-4.41	0.14%
E1H3-4D-3	Phe	103.11	0.8%	1.691	8.2%	39.80	1.7%	17.29	8.3%	-	-	-	-	-	-	-	-
E1H3-4D-30	Phe	78.67	0.9%	1.565	4.6%	43.32	1.1%	3.45	9.4%	E1H3-4D-30	20	400	3.836	1.048	4.021	-2.61	0.13%
E1H3-4D-31	Chl	58.34	0.7%	0.238	15.8%	4.55	9.2%	3.79	16.6%	E1H3-4D-31	20	400	3.823	1.048	4.007	-6.07	0.14%
E1H3-4D-32	Phe	76.50	1.5%	1.647	6.4%	53.86	1.6%	2.51	14.8%	-	-	-	-	-	-	-	-
E1H3-4D-33	Am	1.72	3.9%	1.184	8.8%	2.55	6.6%	9.96	9.6%	-	-	-	-	-	-	-	-
E1H3-4D-34	Am	3.93	2.2%	1.574	5.8%	2.64	9.0%	12.59	6.7%	E1H3-4D-34	20	400	3.821	1.048	4.006	-6.41	0.68%
E1H3-4D-4	Phe	100.90	1.0%	1.373	7.5%	34.72	2.4%	24.74	4.5%	E1H3-4D-4	20	200	3.826	1.048	4.011	-5.19	0.21%
E1H3-4D-5	Am	6.86	3.8%	1.017	10.3%	2.28	11.8%	8.22	16.1%	E1H3-4D-5	20	200	3.784	1.048	3.966	-16.11	0.97%
E1H3-4D-6	Am	11.38	3.1%	3.155	4.0%	3.54	5.5%	11.70	9.4%	-	-	-	-	-	-	-	-
E1H3-4D-7	Am	11.01	2.8%	3.462	4.1%	3.09	5.2%	11.72	8.1%	E1H3-4D-7	20	400	3.802	1.048	3.986	-11.30	0.64%
E1H3-4D-8	Am	14.84	2.0%	1.371	9.8%	3.14	4.9%	11.41	11.0%	-	-	-	-	-	-	-	-
E1H3-4D-9	Chl	70.68	0.9%	0.125	27.6%	0.85	12.0%	1.90	19.3%	-	-	-	-	-	-	-	-
E2H2-4G-1	Grt	0.01	126.5%	0.006	189.7%	1.38	12.3%	1.43	28.3%	-	-	-	-	-	-	-	-

\* = matrix corrected



Table C3 (continued): Li, Be, B, Sr contents and  $\delta^{11}\text{B}$  values of metabasite minerals, analyzed by SIMS.

Analysis	Mineral	Li ( $\mu\text{g/g}$ )	$2\sigma_{\text{mean}}$	Be ( $\mu\text{g/g}$ )	$2\sigma_{\text{mean}}$	B ( $\mu\text{g/g}$ )	$2\sigma_{\text{mean}}$	Sr ( $\mu\text{g/g}$ )	$2\sigma_{\text{mean}}$	Analysis	$I_p$ (nA)	n	$^{11}\text{B}/^{10}\text{B}$ measured	$\alpha_{\text{inst}}$	$^{11}\text{B}/^{10}\text{B}$ corrected	$\delta^{11}\text{B}$ (‰) <sup>f</sup>	$2\sigma_{\text{mean}}$
E2H2-4G-2	Grt	b.d.l.	0.005	126.5%	2.16	9.1%	1.69	27.1%	-	-	-	-	-	-	-	-	-
E2H2-4G-3	Srp	0.23	14.6%	0.001	189.7%	165.11	2.9%	0.38	28.6%	-	-	-	-	-	-	-	-
E2H2-4G-4	Srp	0.20	12.8%	0.002	189.7%	178.77	7.1%	0.28	46.1%	-	-	-	-	-	-	-	-
E2H2-4G-5	Srp	7.63	2.0%	0.006	77.5%	118.58	4.4%	0.73	36.4%	-	-	-	-	-	-	-	-
E2H2-4G-6	Grt	0.00	189.7%	b.d.l.	0.34	27.7%	1.52	22.8%	-	-	-	-	-	-	-	-	-
E2H2-4G-7	Grt	b.d.l.	0.003	189.7%	0.69	12.3%	1.79	22.5%	-	-	-	-	-	-	-	-	-
E2H2-4G-8	Srp	0.20	15.3%	0.007	105.6%	164.90	5.4%	5.70	10.7%	-	-	-	-	-	-	-	-
E2H2-4J-1	Am	0.55	8.7%	0.079	29.8%	2.75	8.6%	1.01	34.2%	E2H2-4J-2	10	400	3.829	1.045	4.000	-7.69	0.99%
E2H2-4J-2	Am	0.02	38.8%	0.060	34.2%	3.17	7.2%	1.15	38.6%	-	-	-	-	-	-	-	-
E2H2-4J-3	Am	0.21	39.6%	0.060	49.4%	1.46	15.3%	7.13	10.2%	-	-	-	-	-	-	-	-
E2H2-5D-1	Am	13.82	1.9%	0.820	5.8%	2.81	10.2%	8.97	9.9%	-	-	-	-	-	-	-	-
E2H2-5D-2	Chl	13.68	6.4%	0.612	5.5%	1.85	7.0%	7.20	7.3%	-	-	-	-	-	-	-	-
E2H2-5D-3	Am	19.23	1.8%	1.420	7.2%	2.97	8.6%	11.08	10.5%	-	-	-	-	-	-	-	-
E2H2-5D-4	Tlc	9.16	2.1%	0.229	28.5%	9.23	10.0%	3.75	21.8%	-	-	-	-	-	-	-	-
E2H2-5H-1	Grt	b.d.l.	0.007	126.5%	0.14	44.1%	0.86	49.6%	-	-	-	-	-	-	-	-	-
E2H2-5H-2	Srp	0.25	16.3%	0.009	104.8%	106.62	7.8%	3.81	17.1%	-	-	-	-	-	-	-	-
E4H1-2A-1	Am	3.38	7.7%	0.056	30.6%	0.42	27.1%	7.19	14.6%	-	-	-	-	-	-	-	-
E4H1-2A-2	Am	0.01	101.9%	0.088	34.5%	0.18	31.5%	8.06	11.6%	-	-	-	-	-	-	-	-
E4H1-2A-3	Chl	4.02	6.3%	0.020	69.6%	17.16	3.8%	38.23	7.4%	E4H1-2A-3	10	400	3.888	1.045	4.063	7.88	0.42%
E4H1-2A-4	Chl	1.58	7.9%	0.003	189.7%	3.38	5.9%	3.57	17.9%	E4H1-2A-4	10	400	3.898	1.045	4.074	10.45	0.77%
E4H1-2A-5	Am	0.02	66.1%	0.102	44.7%	0.21	28.9%	7.15	11.9%	-	-	-	-	-	-	-	-
E4H1-2A-6	Chl	4.71	3.6%	0.017	69.5%	5.54	8.1%	5.27	21.3%	-	-	-	-	-	-	-	-
E4H2-2B-1	Ep	0.06	47.4%	0.698	15.6%	150.84	2.0%	727.72	1.4%	-	-	-	-	-	-	-	-
E4H2-2B-2	Ep	0.80	14.5%	0.902	13.2%	27.93	3.5%	818.51	1.6%	-	-	-	-	-	-	-	-
E4H2-2B-3	Ep	0.09	44.1%	0.813	6.9%	51.41	5.3%	811.60	2.0%	E4H2-2B-3d	10	400	3.822	1.046	3.992	-12.74	0.32%
E4H2-2B-4	Ep	0.13	30.2%	1.039	10.8%	25.19	2.2%	683.21	1.1%	E4H2-2B-4	10	400	3.826	1.046	4.003	-10.17	0.41%
E4H2-2B-5	Chl	48.42	3.8%	0.332	17.5%	1.47	5.1%	13.01	9.1%	E4H2-2B-5	10	400	3.862	1.046	4.040	2.11	0.30%
E4H2-2B-6	Ep	5.45	4.4%	0.444	15.9%	8.77	7.7%	840.37	1.3%	-	-	-	-	-	-	-	-
E4H2-2B-7	Chl	49.51	1.4%	0.383	16.5%	3.52	11.3%	2.25	25.3%	-	-	-	-	-	-	-	-
E7H2-1A-1	Am	0.94	7.0%	0.865	3.3%	10.15	2.2%	5.37	7.1%	-	-	-	-	-	-	-	-
E7H2-1A-2	Am	0.07	12.0%	0.099	16.9%	0.89	6.4%	2.62	12.6%	-	-	-	-	-	-	-	-
E7H2-1B-1	Am	1.76	8.1%	0.780	10.4%	7.72	6.4%	3.62	19.0%	-	-	-	-	-	-	-	-
E7H2-2A-1	Am	0.15	10.9%	0.107	21.7%	0.52	14.6%	6.61	9.9%	-	-	-	-	-	-	-	-
E7H2-2A-11	Am	0.50	17.4%	0.531	7.4%	2.72	6.1%	4.63	12.1%	-	-	-	-	-	-	-	-
E7H2-2A-2	Am	0.46	8.1%	0.416	7.2%	2.40	7.3%	5.64	8.6%	-	-	-	-	-	-	-	-
E7H2-2A-3	Am	1.93	3.4%	0.900	4.6%	2.43	7.4%	7.33	7.8%	-	-	-	-	-	-	-	-
E7H2-2A-4	Am	1.44	5.5%	0.628	9.4%	2.75	7.6%	11.15	5.6%	-	-	-	-	-	-	-	-
E7H2-2A-5	Am	0.40	6.5%	0.476	9.6%	2.61	6.7%	3.27	14.1%	-	-	-	-	-	-	-	-
E7H2-2A-6	Am	0.03	42.8%	0.133	20.3%	0.66	12.7%	3.04	10.5%	-	-	-	-	-	-	-	-
E7H2-2A-7	Am	0.31	11.5%	0.167	9.3%	0.87	10.2%	6.26	5.2%	-	-	-	-	-	-	-	-
E7H2-2A-8	Am	0.37	13.2%	0.252	6.7%	0.78	14.4%	3.99	11.3%	-	-	-	-	-	-	-	-
E7H2-2A-9	Am	0.24	10.2%	0.607	8.2%	4.78	2.2%	3.21	10.8%	-	-	-	-	-	-	-	-

\* = matrix corrected

Table C3 (continued): Li, Be, B, Sr contents and  $\delta^{11}\text{B}$  values of metabasite minerals, analyzed by SIMS.

Analysis	Mineral	Li ( $\mu\text{g/g}$ )	$2\sigma_{\text{mean}}$	Be ( $\mu\text{g/g}$ )	$2\sigma_{\text{mean}}$	B ( $\mu\text{g/g}$ )	$2\sigma_{\text{mean}}$	Sr ( $\mu\text{g/g}$ )	$2\sigma_{\text{mean}}$	Analysis	$I_p$ (nA)	n	$^{11}\text{B}/^{10}\text{B}$ measured	$\alpha_{\text{inst}}$	$^{11}\text{B}/^{10}\text{B}$ corrected	$\delta^{11}\text{B}$ (‰) <sup>#</sup>	$2\sigma_{\text{mean}}$
E7H2-A-10	Am	0.24	14.1%	0.129	19.5%	0.70	9.4%	2.85	9.5%	-	-	-	-	-	-	-	-
F1H1-3D-1	Chl	45.07	1.9%	0.172	34.6%	0.83	13.1%	0.06	189.7%	-	-	-	-	-	-	-	-
F1H1-3E-1	Am	5.63	3.6%	1.032	12.8%	2.80	11.3%	12.19	11.3%	-	-	-	-	-	-	-	-
F1H1-3E-2	Am	6.98	7.3%	0.088	6.8%	2.46	6.8%	185.72	3.5%	-	-	-	-	-	-	-	-
F1H1-3E-3	Chl	140.00	2.0%	0.009	126.5%	2.29	11.6%	1.23	30.8%	F1H1-3E-3	10	400	3.861	1.046	4.040	2.04	0.79%
F1H1-3F-1	Am	0.04	34.2%	0.357	21.6%	6.49	5.2%	5.21	17.4%	F1H1-3F-1	10	400	3.863	1.046	4.041	2.44	0.68%
F1H1-3F-2	Chl	16.24	3.0%	0.251	17.6%	13.59	3.5%	11.50	10.1%	-	-	-	-	-	-	-	-
F1H1-3F-3	Am	0.04	47.6%	0.336	12.8%	3.91	5.4%	2.85	28.1%	-	-	-	-	-	-	-	-
F1H1-3F-4	Am	0.44	15.2%	0.586	12.3%	3.47	10.0%	10.26	11.2%	-	-	-	-	-	-	-	-
F1H3-2C-1	Am	0.07	45.5%	2.698	7.6%	3.93	9.8%	5.55	19.6%	-	-	-	-	-	-	-	-
F1H3-2C-2	Am	0.04	31.6%	1.510	18.4%	4.03	7.4%	7.89	10.4%	F1H3-2C-2	10	400	3.837	1.045	4.010	-5.32	0.97%
F1H3-2C-3	Am	0.10	31.6%	0.828	18.4%	2.65	7.4%	10.00	10.4%	-	-	-	-	-	-	-	-
F1H3-2C-4	Chl	7.90	6.2%	0.107	61.3%	15.42	7.0%	2.15	37.9%	F1H3-2C-4	10	400	3.844	1.045	4.017	-3.62	0.75%
F1H3-2D-1	Ttn	5.06	5.9%	2.260	8.5%	46.76	2.8%	214.74	3.2%	-	-	-	-	-	-	-	-
F1H3-2D-2	Chl	17.14	2.3%	0.271	22.9%	17.36	2.4%	13.66	15.2%	F1H3-2D-2	10	400	3.839	1.045	4.012	-4.93	0.36%
F1H4-3A-1	Ep	0.01	69.7%	0.090	28.4%	0.47	12.8%	2292.13	0.8%	-	-	-	-	-	-	-	-
F1H4-3A-2	Aln	0.40	11.1%	1.013	12.6%	17.47	5.1%	5619.67	1.3%	-	-	-	-	-	-	-	-
F1H4-3A-3	Ep	0.02	79.8%	b.d.l.		0.07	54.3%	3068.95	2.6%	-	-	-	-	-	-	-	-
F1H4-3A-4	Chl	82.51	1.5%	0.433	11.8%	1.83	5.8%	0.43	45.6%	F1H4-3A-4	10	400	3.809	1.046	3.984		1.12%
F1H4-3A-5	Chl	79.92	1.5%	0.252	16.5%	0.93	11.4%	0.10	133.9%	-	-	-	-	-	-	-	-
F1H4-3A-6	Ep	0.05	34.9%	0.010	96.6%	0.06	58.3%	1586.40	1.7%	-	-	-	-	-	-	-	-
F1H4-3A-7	Chl	126.75	0.6%	0.947	13.2%	2.72	4.2%	1.95	21.1%	-	-	-	-	-	-	-	-
F2H2-1A-1	Am	0.44	15.6%	0.884	15.2%	2.36	8.0%	12.02	5.0%	-	-	-	-	-	-	-	-
F2H2-1A-2	Chl	1.11	12.4%	0.498	18.0%	1.18	12.8%	2.77	17.4%	F2H2-1A-2	10	400	3.824	1.046	4.000	-7.70	0.83%
F2H2-1A-3	Ep	0.01	96.6%	0.178	28.1%	0.24	29.8%	1237.95	1.5%	-	-	-	-	-	-	-	-
F2H2-1A-4	Ep	0.01	126.5%	0.177	39.9%	0.25	34.5%	1076.37	1.6%	-	-	-	-	-	-	-	-
F2H2-1A-5	Am	0.57	14.0%	1.098	12.8%	2.19	10.3%	11.20	12.5%	-	-	-	-	-	-	-	-
F2H2-4A-1	Am	1.32	4.5%	0.381	11.0%	1.48	12.1%	9.69	11.1%	-	-	-	-	-	-	-	-
F2H2-4A-2	Phe	42.42	1.2%	0.827	11.1%	27.01	2.9%	7.80	8.6%	-	-	-	-	-	-	-	-
F2H2-4A-3	Phe	39.45	3.0%	0.793	8.8%	29.98	2.9%	6.45	9.4%	F2H2-4A-3	10	400	3.822	1.045	3.994	-9.30	0.24%
F2H2-4A-4	Am	10.23	3.7%	1.015	5.8%	5.81	6.5%	3.06	18.2%	-	-	-	-	-	-	-	-
F2H2-4A-5	Phe	42.98	1.1%	0.796	9.7%	32.10	2.1%	21.86	5.6%	F2H2-4A-5	10	400	3.843	1.045	4.016	-3.81	0.26%
F2H2-4A-6	Am	1.84	8.4%	0.364	18.3%	3.72	9.3%	11.72	15.7%	F2H2-4A-6	10	400	3.861	1.045	4.034	0.72	0.92%
F2H2-4B-1	Am	1.22	12.1%	1.101	8.8%	3.05	6.1%	12.90	5.5%	-	-	-	-	-	-	-	-
F2H2-4B-2	Phe	39.00	3.8%	1.059	5.5%	34.80	2.3%	4.52	17.6%	F2H2-4B-2	10	400	3.835	1.045	4.008	-5.89	0.21%
F2H2-4B-3	Phe	56.39	2.5%	1.928	10.4%	36.42	3.7%	13.37	16.6%	F2H2-4B-3	10	400	3.850	1.045	4.024	-1.96	0.24%
F2H2-4B-4	Am	7.31	3.0%	3.477	4.5%	3.85	7.3%	7.97	12.5%	F2H2-4B-4	10	400	3.835	1.045	4.008	-5.81	0.86%
F2H2-4B-5	Am	0.66	11.0%	2.701	3.8%	2.82	6.8%	10.02	12.5%	F2H2-4B-5	10	400	3.876	1.045	4.051	4.71	0.98%
F2H2-4B-6	Phe	50.89	3.1%	1.342	9.4%	37.86	2.7%	5.57	16.6%	F2H2-4B-6	10	400	3.839	1.045	4.012	-4.89	0.24%
F2H2-4B-7	Am	0.65	8.6%	2.785	3.4%	2.93	6.0%	10.41	13.0%	-	-	-	-	-	-	-	-
F2H2-4D-1	Px	2.74	8.2%	0.725	11.3%	3.38	10.7%	3.72	25.9%	-	-	-	-	-	-	-	-
F2H2-4D-2	Am	0.37	11.4%	0.074	34.7%	2.47	8.9%	3.15	26.8%	-	-	-	-	-	-	-	-
F2H2-4D-3	Chl	10.73	2.3%	0.012	84.7%	10.54	5.2%	10.16	9.2%	-	-	-	-	-	-	-	-

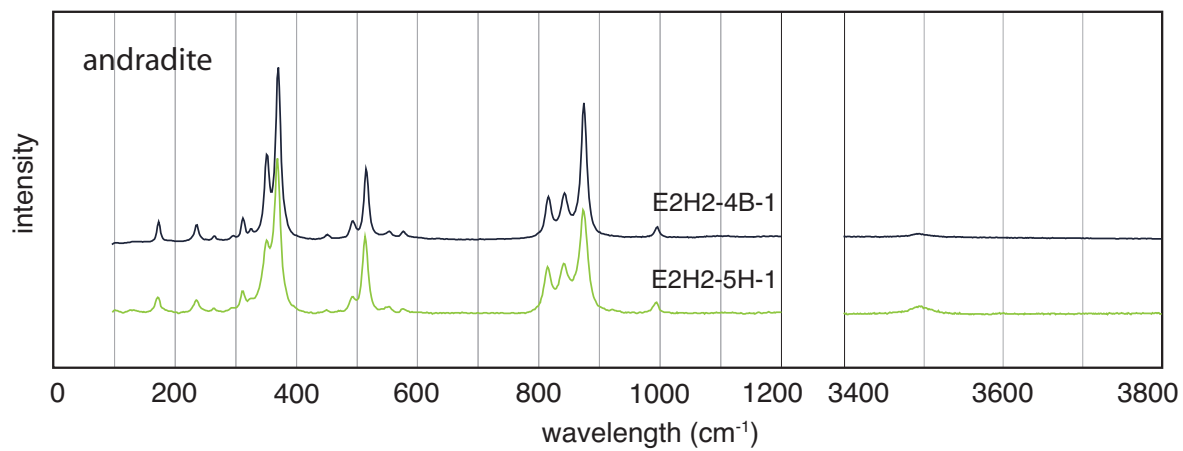
# = matrix corrected

Table C3 (continued): Li, Be, B, Sr contents and  $\delta^{11}\text{B}$  values of metabasite minerals, analyzed by SIMS.

Analysis	Mineral	Li ( $\mu\text{g/g}$ )	$2\sigma_{\text{mean}}$	Be ( $\mu\text{g/g}$ )	$2\sigma_{\text{mean}}$	B ( $\mu\text{g/g}$ )	$2\sigma_{\text{mean}}$	Sr ( $\mu\text{g/g}$ )	$2\sigma_{\text{mean}}$	Analysis	$I_P$ (nA)	n	$^{11}\text{B}/^{10}\text{B}$ measured	$\alpha_{\text{inst}}$	$^{11}\text{B}/^{10}\text{B}$ corrected	$\delta^{11}\text{B}$ (‰) <sup>#</sup>	$2\sigma_{\text{mean}}$
F2H2-4E-1	Chl	40.10	0.9%	0.204	12.8%	0.92	11.5%	0.38	39.8%	-	-	400	3.804	1.045	3.975	-13.96	0.87%
F2H2-4E-2	Am	0.19	18.9%	0.503	15.3%	2.82	8.0%	8.59	10.7%	-	-	400	3.845	1.045	4.018	-3.23	0.96%
F2H2-4E-3	Am	0.91	16.6%	0.629	7.4%	3.32	6.0%	7.79	13.2%	-	-	400	3.843	1.045	4.015	-3.96	0.27%
F2H2-4E-4	Chl	32.56	2.0%	0.180	27.2%	1.24	30.1%	0.18	77.5%	-	-	400	3.867	1.045	4.041	-0.77	0.80%
F2H2-4E-5	Am	0.10	24.1%	0.432	10.9%	1.71	14.2%	8.54	16.3%	-	-	400	3.827	1.046	4.004	-6.91	0.19%
F2H2-4E-6	Chl	34.85	1.9%	0.190	26.2%	0.68	17.8%	0.42	70.1%	-	-	400	3.872	1.046	4.051	-4.86	0.64%
F2H2-4F-1	Chl	23.21	2.3%	0.138	32.6%	1.94	23.3%	0.53	67.7%	-	-	400	3.861	1.046	4.039	1.97	0.87%
F2H2-4F-2	Am	0.13	25.2%	0.814	10.6%	2.41	9.8%	11.56	11.1%	-	-	400	3.850	1.046	4.028	-0.94	0.25%
F2H2-4F-3	Chl	20.44	2.3%	0.170	31.4%	0.45	20.4%	0.50	60.1%	-	-	400	3.870	1.046	4.049	1.26	0.38%
F2H2-4G-1	Am	0.07	39.2%	0.527	10.2%	1.95	8.4%	10.98	12.2%	-	-	400	3.882	1.046	4.061	4.25	0.71%
F2H2-4G-2	Chl	35.42	1.7%	0.164	30.9%	1.71	28.1%	0.29	70.5%	F2H2-4G-2	10	400	3.804	1.045	3.975	-13.96	0.87%
F2H2-4G-3	Chl	36.18	1.6%	0.206	20.2%	1.44	19.5%	0.32	58.8%	-	-	400	3.844	1.045	4.017	-3.52	0.27%
F2H2-4G-4	Am	0.28	17.5%	0.519	10.3%	1.88	8.9%	9.68	17.4%	-	-	400	3.827	1.046	4.004	-6.91	0.19%
F2H2-4H-1	Am	1.57	6.0%	2.012	7.1%	3.15	7.9%	9.15	6.9%	F2H2-4H-1	10	400	3.845	1.045	4.018	-3.23	0.96%
F2H2-4H-2	Phe	35.41	3.7%	1.316	8.3%	45.04	1.5%	7.32	14.1%	F2H2-4H-2	10	400	3.843	1.045	4.015	-3.96	0.27%
F2H2-4H-3	Px	1.19	6.8%	0.235	15.8%	3.73	9.9%	1.18	50.7%	F2H2-4H-3	10	400	3.867	1.045	4.041	-0.77	0.80%
F2H2-4H-4	Am	1.80	3.9%	3.505	4.2%	2.19	10.2%	9.66	9.7%	-	-	400	3.864	1.045	4.038	1.56	0.90%
F2H2-4H-5	Phe	53.81	1.2%	3.019	7.3%	33.63	2.8%	25.18	7.6%	F2H2-4H-4b	10	400	3.864	1.045	4.038	1.56	0.90%
F2H2-4J-1	Chl	28.42	2.3%	0.182	30.8%	0.94	24.8%	0.48	56.8%	F2H2-4H-5	10	400	3.844	1.045	4.017	-3.52	0.27%
F2H2-4J-2	Am	1.30	8.8%	0.521	10.8%	2.80	10.4%	8.83	15.5%	-	-	400	3.827	1.046	4.004	-6.91	0.19%
F2H2-4J-3	Chl	31.30	2.4%	0.230	18.0%	2.31	18.3%	0.32	82.1%	-	-	400	3.872	1.046	4.051	-4.86	0.64%
F2H2-4J-4	Chl	22.35	1.4%	0.189	21.9%	0.34	30.0%	0.24	63.2%	-	-	400	3.861	1.046	4.039	1.97	0.87%
F2H2-5A-1	Phe	26.98	5.1%	1.307	7.6%	49.74	1.7%	2.18	15.9%	F2H2-5A-1	10	400	3.827	1.046	4.004	-6.91	0.19%
F2H2-5A-2	Am	7.98	5.2%	8.279	3.5%	3.74	7.7%	9.24	14.3%	F2H2-5A-2	10	400	3.851	1.046	4.029	-0.66	0.74%
F2H2-5A-3	Chl	10.23	3.2%	0.025	59.1%	8.42	5.3%	26.48	7.1%	F2H2-5A-3	10	400	3.872	1.046	4.051	-4.86	0.64%
F2H2-5A-4	Am	36.55	1.9%	0.311	14.9%	2.23	7.6%	0.83	25.7%	F2H2-5A-4	10	400	3.861	1.046	4.039	1.97	0.87%
F2H2-5A-5	Phe	37.46	1.4%	1.540	8.3%	40.09	2.1%	9.60	9.2%	F2H2-5A-5	10	400	3.850	1.046	4.028	-0.94	0.25%
F2H2-5A-6	Px	0.47	17.6%	0.019	63.2%	0.07	37.9%	41.60	6.3%	F2H2-5A-6	10	400	3.870	1.046	4.049	1.26	0.38%
F2H2-5C-1	Px	0.42	27.9%	0.147	29.6%	0.37	32.9%	45.97	7.1%	-	-	400	3.882	1.046	4.061	4.25	0.71%
F2H2-5C-2	Chl	7.13	3.1%	0.501	17.0%	10.61	7.6%	36.84	6.4%	F2H2-5C-2	10	400	3.882	1.046	4.061	4.25	0.71%
F2H2-5C-3	Chl	51.70	1.8%	0.855	13.7%	6.94	5.8%	8.83	10.4%	-	-	400	3.913	1.046	4.094	15.40	0.72%
F2H2-5D-1	Px	0.92	9.8%	0.269	16.7%	0.52	11.0%	38.05	9.6%	F2H2-5C-4	10	400	3.913	1.046	4.094	15.40	0.72%
F2H2-5D-2	Chl	7.48	3.2%	2.296	4.5%	13.69	2.9%	56.29	5.1%	-	-	400	3.821	1.046	3.988	-8.32	0.44%
F2H2-5G-1	Am	0.92	10.1%	0.827	10.9%	2.12	12.1%	11.86	9.9%	F2H2-5D-2	10	400	3.821	1.046	3.988	-8.32	0.44%
F2H2-5G-2	Chl	38.09	1.5%	0.223	24.9%	0.87	17.0%	0.68	36.5%	-	-	400	3.821	1.046	3.988	-8.32	0.44%
F2H2-5G-3	Chl	37.96	1.7%	0.232	26.4%	1.36	17.4%	0.40	49.6%	-	-	400	3.821	1.046	3.988	-8.32	0.44%

# = matrix corrected

### C4: Micro-Raman spectra of andradite garnet



*Fig. C4: Micro-Raman spectra of 2 garnet, which can be identified as andradite.*

## Appendix D: Supplementary Results

D1: Sr - light element variation in blueschist minerals	220
D2: Sr - light element variation in serpentinites	220
D3: U concentration in rutile – a possibility for dating	221
D3.1 Analytic	222

## D1: Sr - light element variation in blueschist minerals

Along with Li, Be, and B concentrations, strontium (Sr) was included in most SIMS analyses. Strontium contents of chlorite, amphibole and phengite form a field at low concentrations (Fig. D3). At little higher concentration of about 40–50  $\mu\text{g/g}$ , pyroxene and garnet from serpentine-grt-rocks form a distinct compositional field. Garnet from sample E1H3-4 has low Sr contents similar to chlorite and amphibole. Highest Sr contents of analyzed minerals are found in epidote and kaersutite amphibole.

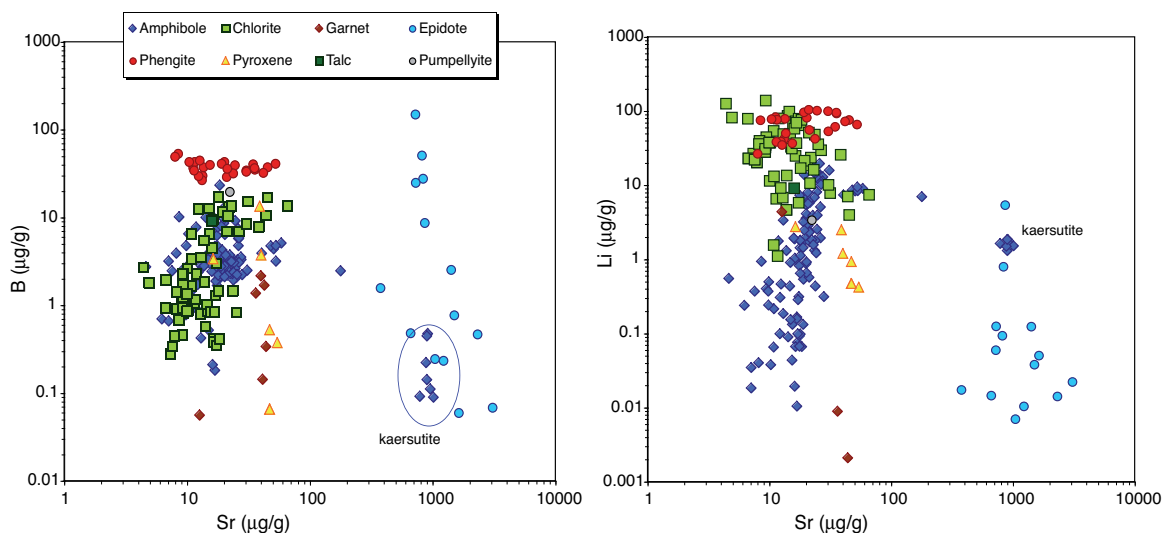


**Fig. D1:** Sr vs Li and B concentration of minerals found in slab-derived blueschist-facies clasts. Phengite, chlorite and amphibole have a distinct Sr range at relatively low concentration, garnet and pyroxene have higher Sr contents, epidote and kaersutite are Sr-enriched.

## D2: Sr - light element variation in serpentinites

Strontium (Sr) concentrations of primary minerals Ol, Opx and Cpx are low ( $<1 \mu\text{g/g}$ ; Fig. D2) and lower than depleted mantle values ( $9.8 \mu\text{g/g}$ ) estimated by Salters & Stracke (2004). These low Sr values ( $<1 \mu\text{g/g}$ ) in primary minerals coincide with concentrations in mantle minerals from Cr-diopside-bearing harzburgite xenoliths from the Kerguelen Islands studied by Grégoire et al. (2000); Sr concentrations in these rocks are  $<0.01$ – $1.36 \mu\text{g/g}$  in olivines,  $<0.12$ – $2.14 \mu\text{g/g}$  in orthopyroxenes and  $0.72$ – $458 \mu\text{g/g}$  in clinopyroxenes.

Compared to depleted mantle, Sr contents in serpentine are variably enriched or even depleted. Concentrations range from  $0.05 \mu\text{g/g}$  in some veins to  $700 \mu\text{g/g}$ . The majority of serpentine reveals Sr contents between  $1$  and  $60 \mu\text{g/g}$  (Fig. D2), which is an enrichment in Sr relative to primary minerals. Sr contents in brucite range from  $0.65$  to  $8.83 \mu\text{g/g}$  and correlate positively with Li contents.

The serpentine composition correlates with bulk rock compositions given for serpentinized peridotites from South Chamorro ( $3.5$ – $34 \mu\text{g/g}$ ), Conical ( $2.8$ – $5.3 \mu\text{g/g}$ ) and Torishima Seamounts ( $5.6$ – $5.8 \mu\text{g/g}$ ) (Zanetti et al., 2006). This bulk rock Sr enrichment was also reported by Savov et al. (2005a, 2005b, 2007) for Mariana serpentinites. Mottl et al. (2003) suggested that serpentinization

leads to Ca and Sr removal from the fluid by aragonite precipitation. Since the sampled studied are free of aragonite, Sr instead is suggested to be consumed by the serpentine minerals.

No correlation is observed between Sr concentrations and  $\delta^{11}\text{B}$  value in serpentine.

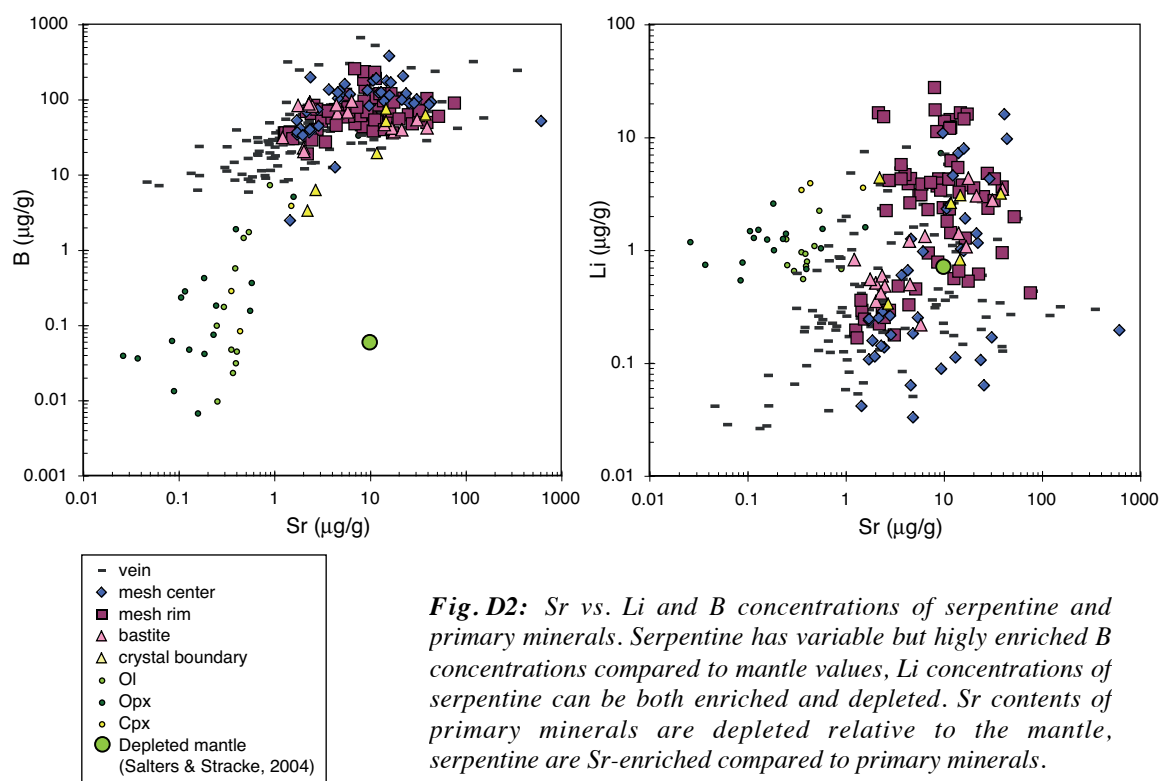


**Fig. D2:** Sr vs. Li and B concentrations of serpentine and primary minerals. Serpentine has variable but highly enriched B concentrations compared to mantle values, Li concentrations of serpentine can be both enriched and depleted. Sr contents of primary minerals are depleted relative to the mantle, serpentine are Sr-enriched compared to primary minerals.

### D3: U concentration in rutile – a possibility for dating

Some metabasic rocks from the Mariana subduction mélangé zone contain rutile-ilmenite + titanite paragenesis in a (Na-)amphibole + chlorite matrix (Fig. D). In sample E1H3-4b, rutile grains are large enough for SIMS analyses. Zr concentrations in rutile range from 245 to 446  $\mu\text{g/g}$  (Table D). Tomkins et al. (2007) formulated a thermometer based on the Zr contents of rutile at a given pressure. The following equation is given in the a-quartz field:

$$T (^{\circ}\text{C}) = ((83.9 + 0.410 P) / (0.1428 - R \ln x)) - 273$$

in which  $x$  is  $\mu\text{g/g}$  Zr,  $P$  is in kbar and  $R$  is the gas constant, 0.0083144 kJ/K.

Applying this equation, the temperature calculated for the rutile-bearing Mariana blueschist-facies rocks is  $\sim 650^{\circ}\text{C}$  at 0.7 GPa. Such high temperatures are unrealistic, as geothermometry on phase relationships give evidence for conditions at  $300\text{--}350^{\circ}\text{C}$ .

An unexpected result is the relatively high U concentration in rutile of  $19\text{--}39 \mu\text{g/g}$  (Table D). Though still low, this concentration allows dating – if the sample directly derived from the subducting

slab, we expect a relatively young age of <3 Ma (at ~3 cm/a subduction until ~27 km depth). The small mineral size requires analytical conditions such as a small beam size (e.g., laser) and a low detection limit. Furthermore, zircon grains reveal another possibility for U-Pb-dating, but the small grain size requires high-resolution analytics.

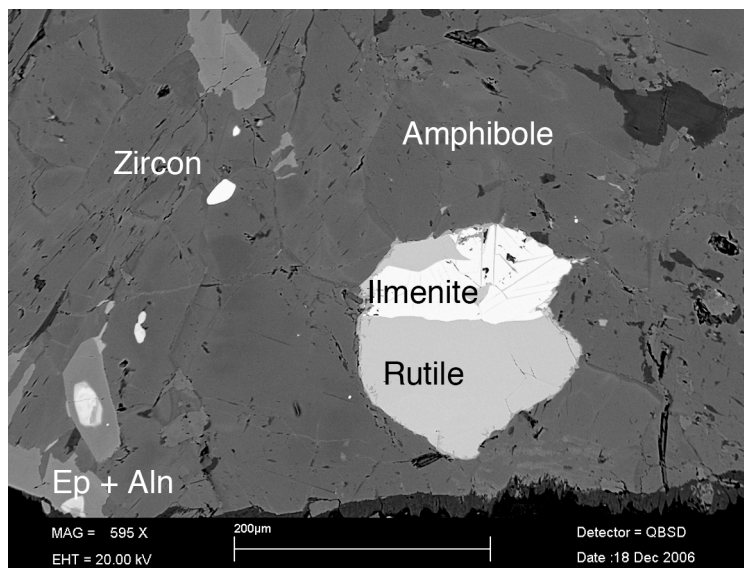


**Fig. D3:** Rutile + ilmenite in (Na-)amphibole, sample E1H3-4b.

**Table D3:** Rare earth element concentrations of rutile in E1H3-4B analyzed by SIMS ( $\mu\text{g/g}$ ).

		$^{90}\text{Zr}$	$^{93}\text{Nb}$	$^{118}\text{Sn}$	$^{120}\text{Sn}$	$^{121}\text{Sb}$	$^{123}\text{Sb}$	$^{178}\text{Hf}$	$^{181}\text{Ta}$	$^{184}\text{W}$	$^{186}\text{W}$	$^{232}\text{Th}$	$^{238}\text{U}$
E1H3-4B-1	rutile	330	3,222	93	104	99	113	12	68	131	149	0.07	28
E1H3-4B-2	rutile	392	3518	109	110	56	79	9	28	76	84	0.05	30
E1H3-4B-3	rutile	245	2,991	105	99	107	101	10	54	148	163		19
E1H3-4B-4	rutile	446	3,537	96	98	79	108	12	73	166	176	0.19	39
E1H3-4B-5	rutile	420	3,505	115	105	75	64	13	74	167	193	0.20	21

### D3.1 Analytic

Large rutile grains identified in some blueschist facies fragments were also analyzed by SIMS for the following isotopes:  $^{47}\text{Ti}$ ,  $^{90}\text{Zr}$ ,  $^{93}\text{Nb}$ ,  $^{118}\text{Sn}$ ,  $^{120}\text{Sn}$ ,  $^{121}\text{Sb}$ ,  $^{123}\text{Sb}$ ,  $^{178}\text{Hf}$ ,  $^{181}\text{Ta}$ ,  $^{184}\text{W}$ ,  $^{186}\text{W}$ ,  $^{232}\text{Th}$ ,  $^{238}\text{U}$ . Analyses were performed using a 14.5 keV / 10 nA  $^{16}\text{O}^+$  primary ion beam. Positive secondary ions were nominally accelerated to 4.5 keV. The energy window was set to  $\pm 40$  eV and the energy filtering technique was used with an offset of 90 eV at a mass resolution of  $\sim 400$  m/ $\Delta$ m (10%). Count rates were normalized to  $^{47}\text{Ti}$ . Reference concentration was  $\text{TiO}_2$ , assumed to be 100 wt% in rutile, unless other elements exceeded 1 wt%. In such cases,  $\text{TiO}_2$  concentrations obtained by EMP were used instead. Standard reference material was the SRM 610 glass (Pearce *et al.*, 1997).





## Danksagung

Zunächst möchte ich mich bei meinem Doktorvater Dr. Thomas Zack bedanken, der mir diese Arbeit ermöglichte und mir alle Freiheiten der Umsetzung gelassen hat. Ein großer Dank geht auch an Prof. Alan Woodland, der sich bereit erklärt hat, als Zweitgutachter aufzutreten.

Ganz besonders möchte ich Thomas Ludwig danken. Zum einen für die Betreuung an der SIMS, aber vor allem für seinen enormen Einsatz und seine Ausdauer bei den Korrekturen der Arbeit.

Weiterhin danke ich Hans-Peter Meyer für die Betreuung an der Mikrosonde, Ilse Glass und Alexander Varychev für die Unterstützung am REM sowie für XRD Analysen und Ilona Fin und Oliver Wienand aus der Dünnschliffwerkstatt für zahlreiche An- und Dünnschliffe. Ich danke auch Petra Fuchs und Prof. Rainer Altherr für ihre Aufmunterungen und Unterstützung während der letzten Jahre.

Des Weiteren danke ich Burkhard Schmidt (Uni Göttingen) für die Einführung am Raman, Detlef Rost und Ed Vicenzi für die Hilfe bei den ToF-SIMS Messungen am Smithsonian History Museum, (Washington DC.). Auch danke ich Sonia Tonarini (Pisa) für die TIMS Messungen. Ivan Savov danke ich u.a. für die zur Verfügung gestellten Proben und seine fachlichen Anregungen.

Jens Hopp und Gültekin Topuz danke ich für ihre Begeisterung, Diskussionen und Unterstützung beim Korrigieren vom Manuskript und diversen Abstracts. Danke auch an Flurin Vils für zahlreiche paper, Tipps und Korrekturen.

Danke an Kevin, Carsten, Fabio und Thomas für einen erlebnisreichen Start in Heidelberg und besonders Iris für Spaß und Beistand bei Exkursionen, Kursen, Konferenzen und an der Uni.

... Branimir, Ewa und vor allem Sandra – danke für viele lustige und entspannende Momente, sowie eure Hilfe bei fachlichen und anderen Problemen.

... Christian, Natalia, Jorham y Judith – muchas gracias por compartir el café, las charlas, algunos viajes y mucho mas.

Danke auch an George, Emily, Joan, Ines, Höpke, Stefan, Francis, Carolina, Daniel und Rosario und an alle, die ich vergessen haben sollte – es war immer gut zu wissen, dass man für Kekse, Kaffee, Tee, einen Plausch und fachlichen Rat zu Euch kommen konnte.

Des Weiteren möchte ich mich bei allen Freunden und Kollegen bedanken, die mir auch aus weiter Ferne beigestanden haben.

Mein herzlichster Dank geht an meine Eltern und meine Schwester, die zwar meinten, ich müsse das nicht tun, aber auch nie einen Zweifel daran gelassen haben, dass ich es kann! Ihr seid die Besten!



## Eidesstattliche Erklärung

Hiermit erkläre ich, Sonja Pabst, geboren am 06.08.1979 in Nordenham, an Eides statt, dass ich die vorliegende Dissertation selbst verfasst und mich dabei keiner anderen als der von mir ausdrücklich bezeichneten Quellen und Hilfen bedient habe.

Ich, Sonja Pabst, geboren am 06.08.1979 in Nordenham, erkläre zudem an Eides statt, dass ich an keiner anderen Stelle ein Prüfungsverfahren beantragt habe, dass ich die Dissertation nicht in dieser oder anderer Form bereits anderweitig als Prüfungsarbeit verwendet habe und dass ich sie an keiner anderen Fakultät als Dissertation vorgelegt habe.

Heidelberg, den 20. Oktober 2009